THE TELESCOPE ARRAY MIDDLE DRUM MONOCULAR ENERGY SPECTRUM AND A SEARCH FOR COINCIDENT SHOWERS USING HIGH RESOLUTION FLY'S EYE HIRES-1 MONOCULAR DATA

by

Douglas Chase Rodriguez

A dissertation submitted to the faculty of
The University of Utah
in partial fulfillment of the requirements for the degree of

Doctor of Philosophy

in

Physics

Department of Physics and Astronomy

The University of Utah

May 2011

The University of Utah Graduate School

STATEMENT OF DISSERTATION APPROVAL

This dissertation of Douglas Chase Rodriguez

has been approved by the following supervisory committee members:

Charles Jui	, Co-Chair	2/15/2011 Date Approved
John N. Matthews	, Co-Chair	2/15/2011 Date Approved
Pierre Sokolsky	, Member	2/15/2011 Date Approved
Orest Symko	, Member	2/15/2011 Date Approved
Yong-Shi Wu	, Member	2/15/2011 Date Approved
Theresa Martinez	, Member	2/15/2011 Date Approved

and by David Kieda, Chair of

the Department of Physics and Astronomy

and by Charles A. Wright of the Graduate School.

ABSTRACT

The transition from the High Resolution Fly's Eye (HiRes) experiment to the Telescope Array (TA) experiment has been completed. The TA Middle Drum fluorescence detector was built using refurbished telescopes from the HiRes-1 site so that a direct comparison could be made between the energy scales of the two experiments. I have made a comparison between the published HiRes spectrum [3] and a preliminary energy spectrum using data collected with the Middle Drum telescopes. Both sets of data represent measurements made via the monocular observation technique and were analyzed using the HiRes-1 profile-constrained geometry reconstruction technique. The HiRes-1 data represents almost nine years of exposure and was collected between May 29, 1997 and May 26, 2006. The Middle Drum data were collected over a three-year period between December 16, 2007 and December 16, 2010. The Middle Drum exposure is about one third of the HiRes-1 total exposure. I have demonstrated that the Middle Drum detector has the same energy scale as HiRes-1.

The published HiRes-1 and Middle Drum spectra presented in this dissertation were measured using average calibrations. A study was preformed on the HiRes-1 data to determine the systematic effects of using the nightly atmospheric and electronic-calibration databases instead of average values. The difference between using the average values and using the detailed nightly databases was less than 1%, indicating the spectral results are robust to these differences.

Finally, a search was made for the interaction between cosmic rays and ions in the heliosphere. This interaction could result in a unique signature of parallel, simultaneous photon showers. The HiRes-1 data were chosen for this search due to its large exposure and resulting data set. Unfortunately, detector limitations restricted the potential observations. No double-shower events were detected; however, if observed, this would be suggestive of new physics. Monte Carlo simulated events were used to calculate a preliminary aperture of the HiRes-1 detector for these exotic events and future refinements will allow us to set a physical limit on the rate of events.

I would like to dedicate this work to my wife, Larissa. Your support through this process has been the island in my stream. I would also like to dedicate this work to my son, Evan, and soon-to-be daughter, Shaye, who came at just the right time to keep me smiling.

CONTENTS

LIST OF TABLES

LIST OF FIGURES

ACKNOWLEDGMENTS

The author would like to give special thanks to Charles Jui, S. Adam Blake, John Matthews, Tareq Abu-Zayyad, Dimitri Ivanov, and the other members of the HiRes and Telescope Array collaborations. This work would not have been possible without their assistance. The author would also like to thank his wife, Larissa Rodriguez, whose support was invaluable during the years spent gathering and analyzing the data for this work.

The HiRes experiment is supported by the U.S. National Science Foundation. We gratefully acknowledge the contributions from the technical staffs of our home institutions. An allocation of computer time from the Center for High Performance Computing at the University of Utah is gratefully acknowledged. The cooperation of Colonels E. Fisher, G. Harter, and G. Olsen, the U.S. Army, and the Dugway Proving Ground staff is greatly appreciated.

The Telescope Array experiment is supported by the Ministry of Education, Culture, Sports, Science and Technology-Japan; the U.S. National Science Foundation; the Korea Research Foundation; the Korean Science and Engineering Foundation; the Russian Academy of Sciences; and the Belgian Science Policy. The foundations of Dr. Ezekiel R. and Edna Wattis Dumke, Willard L. Eccles and the George S. and Dolores Dore Eccles all helped with generous donations. The State of Utah supported the project through its Economic Development Board, and the University of Utah through the Office of the Vice President for Research. The experimental site became available through the cooperation of the Utah School and Institutional Trust Lands Administration (SITLA), U.S. Bureau of Land Management and the U.S. Air Force. We also wish to thank the people and the officials of Millard County, Utah, for their steadfast and warm support.

CHAPTER 1

INTRODUCTION

As University of Utah physics professor Dan Mattis once told me, "Everything comes down to sociology." Take, for instance, the parallels between the ideas of Dr. Martin Luther King, Jr. and Galileo Galilei. Both introduced radical ideas which became stepping stones towards the whole of progress. King reminded us that each person is important, not just White, Anglo-Saxon Protestants, while Galileo advocated that the Earth was not the center of the universe. King further emphasized the idea that advancement of society depends on everyone, with the minority showing where society needs to change most. Galileo reinforced the precept that progress depends on understanding of what is observed, not on what is assumed.

There are many modes of sociological connections within the field of physics research: the interaction between scientists and the public, between researchers and other researchers, etc. Each individual perceives thoughts and ideas differently. The most outspoken then become the driving force behind what society and researchers deem important. Within the field of physics, there is strong dynamical interplay between theoretical ideas and experimental research. Theory explains what experimentalists search for, but it takes real data to find the anomalies that theorists need to explain; science then advances through this cyclical process.

Recently, the well-established physics of radioactive decay came under scrutiny. Jenkins [50] correlated the rate of nuclear decay with the distance between the Earth and Sun that changed over the course of the year. This was quickly shown to be a fallacy by analyzing similar decays in the nuclear power sources from a satellite travelling to distances that varied on a much larger scale to look for the same result [31]. Simplicity, guided by Occam's razor, would attribute temperature or pressure variations of the detector as the more likely cause of the annual modulation. Sociological discussions soon arose as to whether such abstruse proposals that question established knowledge should be given any merit.

It has been said that "men often sense that older ways of feeling and thinking have collapsed, and that newer beginnings are ambiguous to the point of moral stasis" [67]. An intellectual parallel of this statement haunts the field of physics, especially concerning

the fundamental nature of matter and interactions. As scientists, we are compelled to question what has been observed, even if it means to overthrow established paradigms. Only by delving into the exotic or heretical can we solidify our understanding and expand our knowledge to greater possibilities. The results of new investigations will either uphold the status quo to greater precision, or lead to new and enticing advances in knowledge.

This dissertation addresses two aspects of scientific sociology within the field of cosmic-ray physics. Conventionally, new experiments incorporate new technologies in their design, but must corroborate the results of previous measurements at some level. Primarily, this would be performed by observing similar regions (e.g., the High Resolution Fly's Eye observing events triggering the Chicago Air Shower Array/Michigan Array detectors [20]) or using similar subsets of equipment (e.g., Telescope Array using scintillating plastic like the Akeno Giant Air Shower Array [12]). Rarely have two experiments been comprised of the exact same equipment. A comparison between the High Resolution Fly's Eye HiRes-1 energy flux and the Telescope Array Middle Drum energy flux, which both use the same telescopes, therefore provides an inherent bridge between these two experiments. The results of the new Middle Drum configuration must either support the energy spectrum measured by HiRes, or show that there is a difference that must then be explained.

Additionally, experiments are typically designed to answer some well-defined question with some guarantee of an answer. Often, the capabilities of the instruments also allow us to probe for anomalies that might extend beyond standard explanations (e.g., Blake [24] used the HiRes experiment to look for events travelling faster than the speed of light). A search for the unexpected expands the understanding and limits of observable physics. As a part of this dissertation, a search is made for simultaneous showers in order to probe for the possibility of cosmic rays interacting with heliospheric ions producing neutral pions which then decay into two photons and arrive at the earth as double showers. This highly unlikely occurrence is such an improbability (only one in a trillion chances of happening), that the observation of an event would necessarily imply new physics.

1.1 Organization

The chapters of this dissertation will support the physical and sociological observations through the following breakdown:

Chapters 2, 3, and 4 provide the foundation of what is currently known in cosmic ray physics and how experimental measurements are made on ultra-high energy cosmic rays.

Chapters 5 and 6 describe the HiRes and Telescope Array experiments. A critical goal of these chapters is to provide a bridge between these successive experiments by describing

their similarities and differences. Specifically, a direct comparison of the energy spectrum observed by HiRes and by Telescope Array's Middle Drum fluorescence site can be made because the same equipment was used in both experiments.

Chapters 7, 8, and 9 document the three different sets of programs used to analyze the data of HiRes-1 and Middle Drum. The Middle Drum data is processed using the stereo_TA program set. Critical for a comparative understanding of the experiments, a parallel analysis is made between the Middle Drum data and the HiRes-1 data using the stereo_TA processing suite. The simultaneous-shower search using the HiRes-1 data can only be accomplished using the AlphaProc code set, so a justification between the original and AlphaProc event-selection process becomes vital for this exotic event search. The HiRes-1 Monte Carlo simulations are each processed and reconstructed using these three program sets and then compared on an event-by-event basis, defining differences between the sets.

Chapters 10 and 11 show the energy flux spectrum of the HiRes-1 and Middle Drum data, respectively. These analyses are intended to support the published HiRes spectrum [3]. The respective aperture, resolutions, and data-Monte Carlo comparisons are also presented as justification for the spectra. As such, these chapters define another bridge by comparing results of old and new experiments.

Chapter 12 describes efforts to analyze the variable aerosol content of the atmosphere. Studies were made to 1) be able to retro-analyze the HiRes-1 reconstruction and 2) to demonstrate a sufficient understanding of the attenuation for reliable energy measurements of the Middle Drum data.

Chapters 13, 14, and 15 describe the search for interactions between cosmic rays and ions in the Sun's heliosphere. Such interactions can potentially produce many neutral pions which would decay into a pair of photons. These photons would follow parallel trajectories and arrive at the earth to produce two separate, coincidental showers. Density studies show very little chance of this occurring, but this search was performed with the understanding that rare and unique observations can become the driving force of revolutionary discoveries.

CHAPTER 2

COSMIC RAY PHYSICS

Cosmic ray particles have been observed over a wide range of energies. Figure 2.1 shows a compilation of the inclusive flux of cosmic rays from many experiments [40]. It is striking that a simple single power law gives a good description of the data for over 10 orders of magnitude in energy. The low-energy cosmic rays have been observed to come from nearby sources, roughly increasing in distance as energy increases to those observed by HiRes at the highest energies. Cosmic rays with energy $\sim 10^{9-12}$ electron volts (eV) are quite abundant since the closest source of these is the Sun. Very High Energy (VHE) cosmic rays (between $\sim 10^{12-16}$ eV) are thought to come from sources within the galaxy [21] [23]. Within the VHE energy range there is only one spectral feature, the knee, and the cause of this softening of the spectrum has not been established.

Ultra-High Energy (UHE) cosmic rays refer to particles of extragalactic origin with energies above 10^{16} eV and up to $\sim 10^{20}$ eV. This is the region of interest of both the High Resolution Fly's Eye (HiRes) and the Telescope Array (TA) experiments. The physics of UHE cosmic rays (UHECRs) are not very well understood, in part because of the very small flux ($\leq$ 1 particle/century/km^2 at $\sim 10^{18}$ eV and above). There are three main questions that have not yet been answered in any authoritative manner: (A) how are the UHECR particles created or accelerated? (B) where do they come from? (C) what are they made of? Anisotropy studies search for objects capable of accelerating the particles to UHECR energies. Composition studies try to determine and explain the chemical make-up of the cosmic ray primaries. Energy spectra measurements describe the flux of cosmic rays as a function of energy. This gives insight into production mechanisms and propagation factors. Each of these studies relates to the others and helps form an understanding of the overall picture.

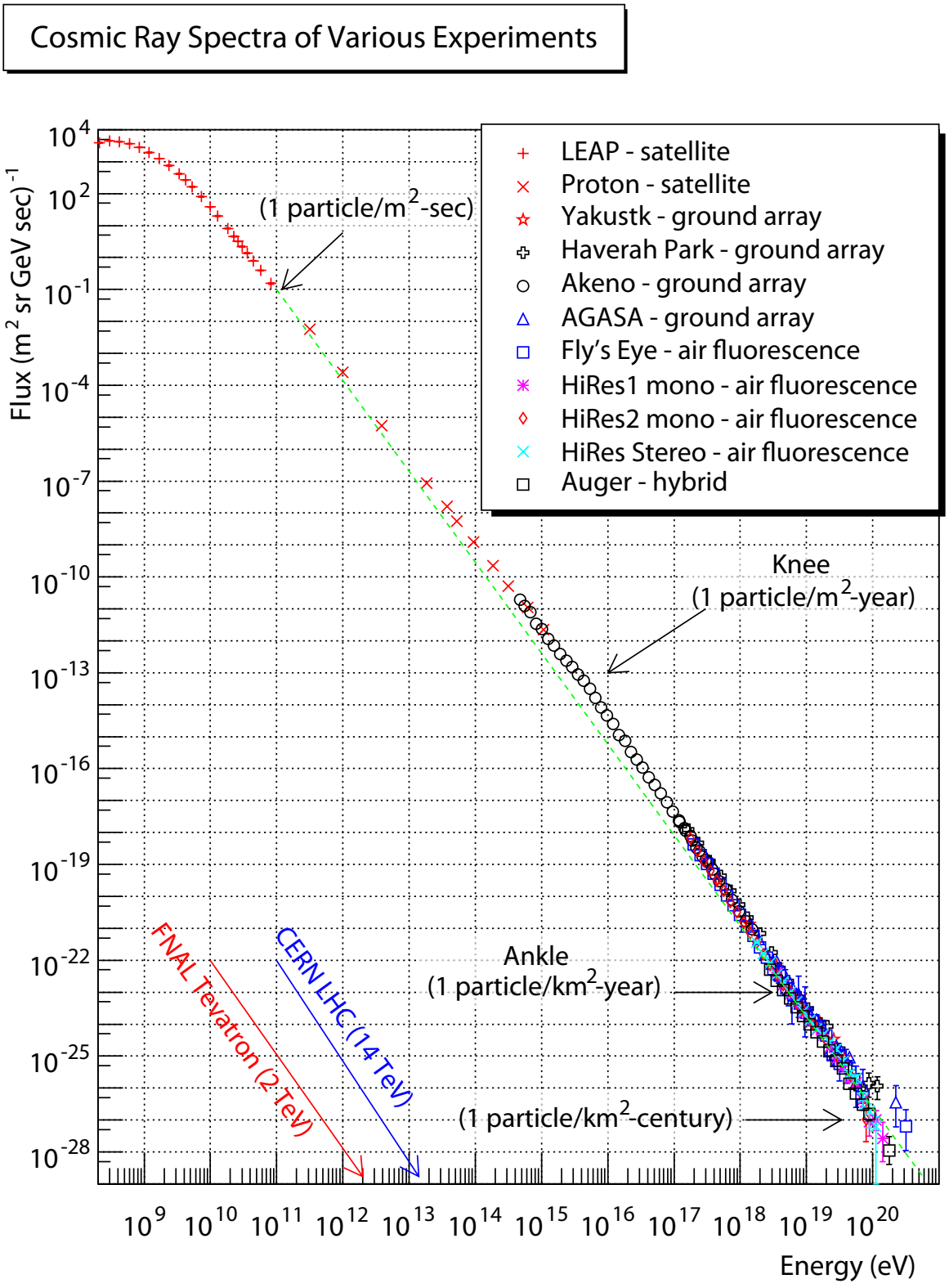

Figure 2.1: A compilation of cosmic ray experimental fluxes. For a comparison, Fermi Lab's Tevatron and CERN's LHC signal-squared upper limits are shown.

2.1 Anisotropy

2.1.1 Acceleration

It is unclear how cosmic rays are accelerated to the UHE regime. The numerous theoretical ideas about the origin of cosmic rays with energies $> 10^{17}$ eV fall into two broad categories: top-down models and bottom-up models. Top-down models refer to theories in which observed UHECRs result from the decay of rare, massive objects. These models include relic particles left over from the Big Bang (monopoles and dark matter/energy), superconducting strings, and Weakly Interacting Massive Particles (WIMPS).

Bottom-up models describe mechanisms that actively accelerate the cosmic rays into the UHECR energy range from much lower initial energies. In these models, UHE cosmic rays are, in general, believed to come from observable objects. There are two different approaches to explain this acceleration: statistical acceleration and direct acceleration. Longair [61] describes two forms of Fermi statistical acceleration: second-order shock acceleration, in which the relativistic particle would collide with chaotic magnetic clouds or plasma waves in the interstellar medium; and first-order Fermi shock acceleration, which takes place in strong-shock regions like those of supernovae explosions. The first-order acceleration model naturally produces a power law energy spectrum of $N \propto E^{-2}$, but it also has the disadvantage that the energy losses exceed the energy gained.

Direct acceleration models assume the particle is travelling within a strong, rotating magnetic field, similar to synchrotron accelerators (e.g., the circular accelerators at the CERN complex). Examples of these objects include neutron stars, colliding galaxies and black hole accretion disks. Direct acceleration increases a particle's energy up to a limit described by the relativistic equation

$$E_{max} \propto zeBcL \tag{2.1}$$

where ze is the atomic charge of the particle, c is the speed of light, and B and L are the magnetic field strength and scale, respectively. A typical neutron star can have a magnetic field strength of $B = 10^6$ T at its surface and a scale of ~ 100 km, which can boost the energy of a proton to $E_{max} = 3 \times 10^{19}$ eV. This form of acceleration is able to describe the production of particles with energies in the UHECR region.

Candidate sources inside the galaxy (e.g., supernovae remnants) can account for observed events with energy only up to $\sim 10^{15-16}$ eV. Assuming particles with greater energies must come from sources outside of the Milky Way, they must traverse the interstellar mediums of the galaxy where they are created, of the intergalactic medium, and of the Milky Way galaxy.

2.1.2 Propagation

Another problem in identifying the sources of UHE cosmic rays is that the magnetic fields the particle pass through deflect the original trajectory of the particle. Regular, galactic magnetic fields (of the order of a few μG) can bend the trajectory of the particles proportional to the Larmour radius,

$$R_L(cm) = \frac{E}{300BZ} \tag{2.2}$$

where E is the energy of the cosmic ray in eV, B is the magnetic field strength in gauss, and Z is the charge of the cosmic ray. A particle passing through a magnetic cloud of thickness L will experience a deflection of L/R_L radians. The trajectory of a 10^{15} eV proton passing through a 0.1 parsec galactic magnetic cloud with a strength of 1 μG will bend by $\sim 5^\circ$. Such a particle needs to pass through only ~ 100 such clouds before it significantly diverges from its initial path. Assuming the cloud density to be $\sim 10^{24}\text{cm}^{-3}$, this scenario is possible [78]. This same cloud would have little effect on particles with energy in the 10^{18} eV range, bending the particle only $\sim 0.005^\circ$ and requiring $\sim 10^8$ collisions before there is a significant deflection from the original pointing direction. The field strength of intergalactic magnetic clouds is on the order of 10^{-2} μG. Particles with energies > 30 EeV will not be significantly affected, allowing particles from as far away as 50 Mpc (from Earth to the center of the Virgo supercluster) to arrive without significant bending ($\sim 2 - 5^\circ$).

Figure 2.2 shows the arrival directions of the highest energy particles ($E > 40$ EeV) from the Akeno Giant Air Shower Array (AGASA) as well as the HiRes stereo data. AGASA has a 5° resolution, but even with a 1° resolution for HiRes stereo data, the distribution of pointing directions to sources of the cosmic rays quantify isotropic. Both AGASA and HiRes were located in the northern hemisphere, which is why events are not below 30° in the southern hemisphere. The Pierre Auger collaboration, located in the southern hemisphere, has stated that they observe a correlation between Active Galactic Nuclei (AGN) and cosmic rays with $E > 10^{19.3}$ eV [5]. When the same cuts are applied to HiRes data, no correlation is found [4].

2.2 Composition

When discussing the chemical make-up of UHECRs there are two factors that need to be considered: the source spectrum and the observed spectrum. Low-energy cosmic rays are known to come with any atomic number up to 26 (iron), the heaviest stable element produced by solar fusion (see Figure 2.3). The energy cutoff of the galactic spectrum seems to be proportional to the atomic number, with protons cutting off at the

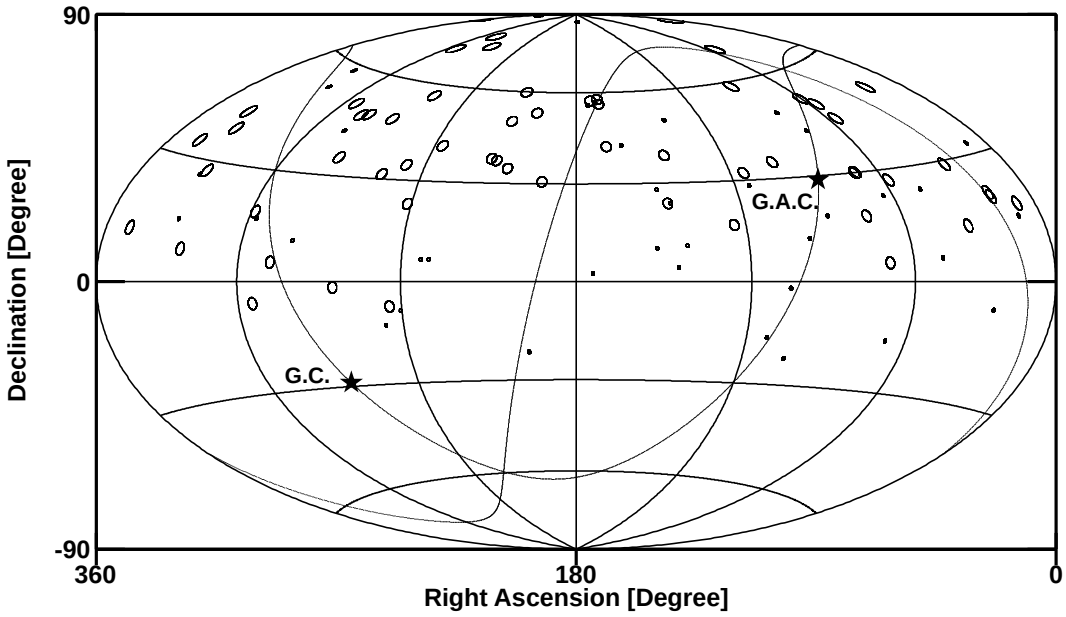

Figure 2.2: This map shows the AGASA and HiRes stereo anisotropy (pointing directions) of cosmic rays with minimum 40 EeV energies.

knee, $\sim 5 \times 10^{15}$ eV (see Figure 2.1) and iron being ~ 30 times higher [41]. Diffusive propagation (where a particle's trajectory randomly bends based on external factors) can describe this process, with particles traversing regions with ≤ 10 g/cm^2 of material (e.g., the Milky Way galaxy). Protons with interaction lengths of ~ 70 g/cm^2 will hardly be affected and will escape the galactic confinement. Heavy nuclei with interaction lengths of ~ 10 g/cm^2 will be confined longer and potentially spallate, affecting the cosmic ray flux from galactic sources. This then leads to the understanding that high-energy galactic cosmic rays tend to have higher atomic numbers (but energies only up to $\sim 10^{16-17}$ eV), and those particles with lower atomic numbers are more likely to escape through the "leaky box model" of diffusion. These lighter particles can then propagate through interstellar space where the spallation length is much longer but where the heavier nuclei are filtered out.

The flux of particles is known to decrease with increasing energy (see Figure 2.1). The measurement of the composition of cosmic rays above $\sim 10^{15}$ eV cannot be measured for each cosmic ray particle. Instead, statistical methods must be used to determine the average composition along with the change in composition as a function of energy (the elongation rate). There is a known intrinsic fluctuation in the mean of the penetration depth of the maximum energy deposition ($\langle X_{max} \rangle$) for a given mass and energy. The model-dependent elongation rates can then be described through the equation

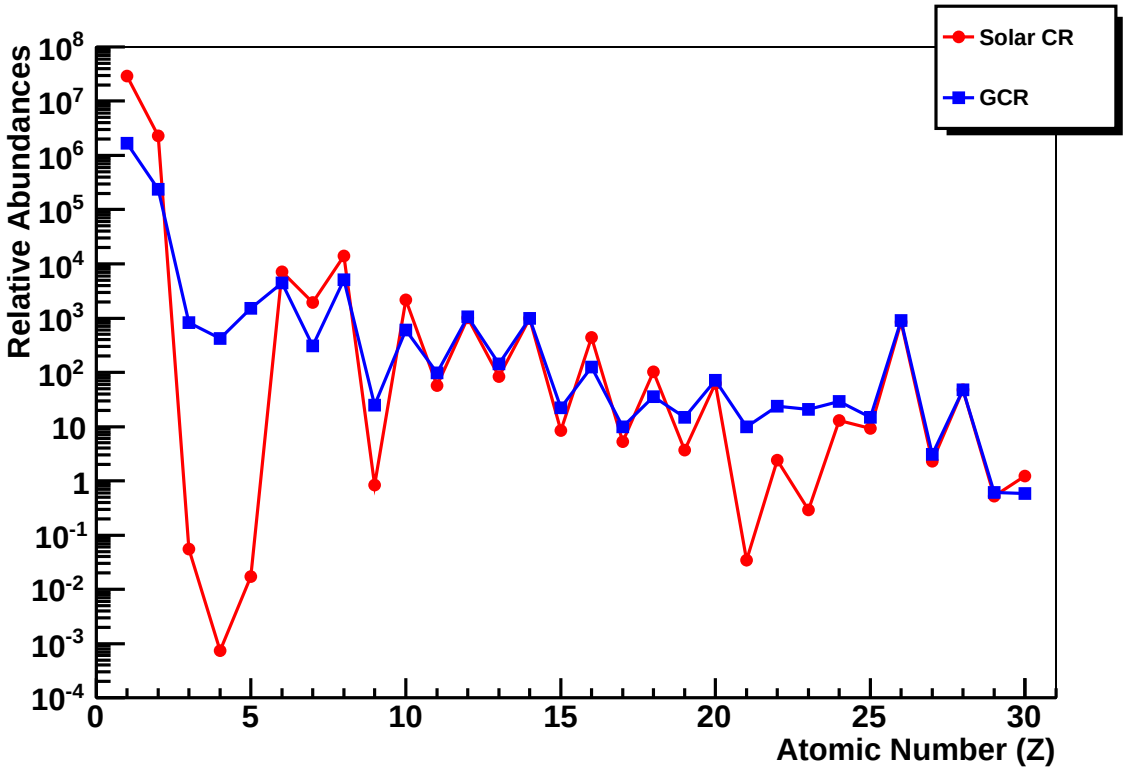

Figure 2.3: This graph shows the relative abundance of low-energy cosmic rays for both the solar spectrum and the galactic spectrum. The indicated atomic composition is normalized to silicon, atomic number 14, at 1000. The data are collected by Lodders [60] and Simpson [88].

$$\zeta = \frac{d(\langle X_{max} \rangle)}{d(\log_{10} E_0)} \tag{2.3}$$

where E_0 is the energy of the cosmic ray primary particle. This will be further discussed in Chapter 3. As can be seen in Figure 2.4, the HiRes-Prototype-MIA composition appears to shift from predominantly heavy particles (like iron nuclei) to predominantly light particles (like protons) as the energy increases from 10^{17} eV to 10^{18} eV. Above about 10^{18} eV, the data supports a predominantly light composition. Acceleration mechanism and propagation theories support this trend, but the exact energy at which this transition takes place is model-dependent. More information can be found in the literature by Sokolsky, Belz, et al. [92].

2.3 Energy Spectrum

Figure 2.1 shows that there is an overall power law that can describe the cosmic ray spectrum with one break around 1 PeV. This power law restricts potential acceleration mechanisms. Integrating this spectrum results in an energy density on the order of 1 eV/cm^3 (compared to 0.6 eV/cm^3 for star light and 0.2 eV/cm^3 for the galactic magnetic field) [93].

The matter density of intergalactic space is $\sim 10^{-29}$ g/cm^3 and the particles will traverse ~ 0.02 g/cm^2 of matter over a 50 Mpc distance, resulting in negligible hadronic interactions. Meson photo-production (cross section $\sim 10^{-28}$ cm^2), photo-nuclear fission ($\sim 10^{-26}$ cm^2), and electron-positron pair-production all play major roles in the energy loss of particles. The primary loss mechanism comes from collisions with the photons of the Comic Microwave Background Radiation (CMBR), which has a density on the order of 500 photons/cm^3 [79]. Greisen [39] and, independently, Zatsepin and Kuzmin [105] calculated that protons of $\gtrsim 60$ EeV will collide inelastically with the CMBR photons at the rest-frame pion photo-production of the Δ^+ resonance (1232 GeV). This results in a suppression (commonly known as the GZK cutoff) of cosmic rays with energy above this energy and a pile-up in the flux of protons with energies just below this energy [46]. Heavier nuclei, with energy above this, will go through photo-spallation, resulting in few particles with atomic numbers greater than one.

It was the search for the GZK cutoff that motivated the construction of the High Resolution Fly's Eye (HiRes) experiment, which published a monocular spectrum for both HiRes-1 and HiRes-2 [3] as well as a stereoscopic spectrum [40] (see Figure 2.5). In all three spectra the GZK suppression was found around $10^{19.8}$ eV and an ankle/dip structure was seen around $10^{18.5}$ eV. This observation of the GZK suppression supports the hypothesis that the highest energy particles tend to be dominated by protons, in

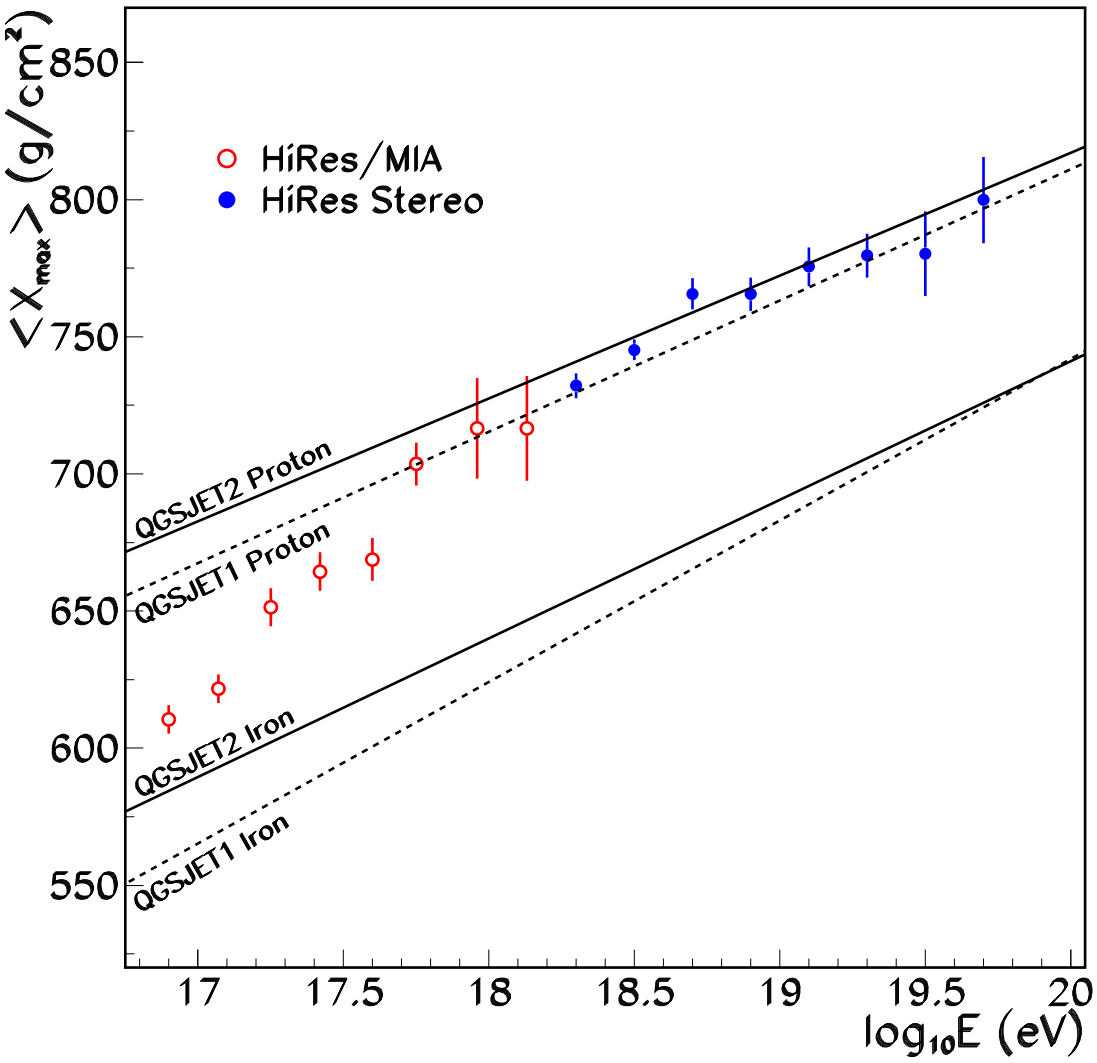

Figure 2.4: Measured composition of HiRes-observed cosmic rays.

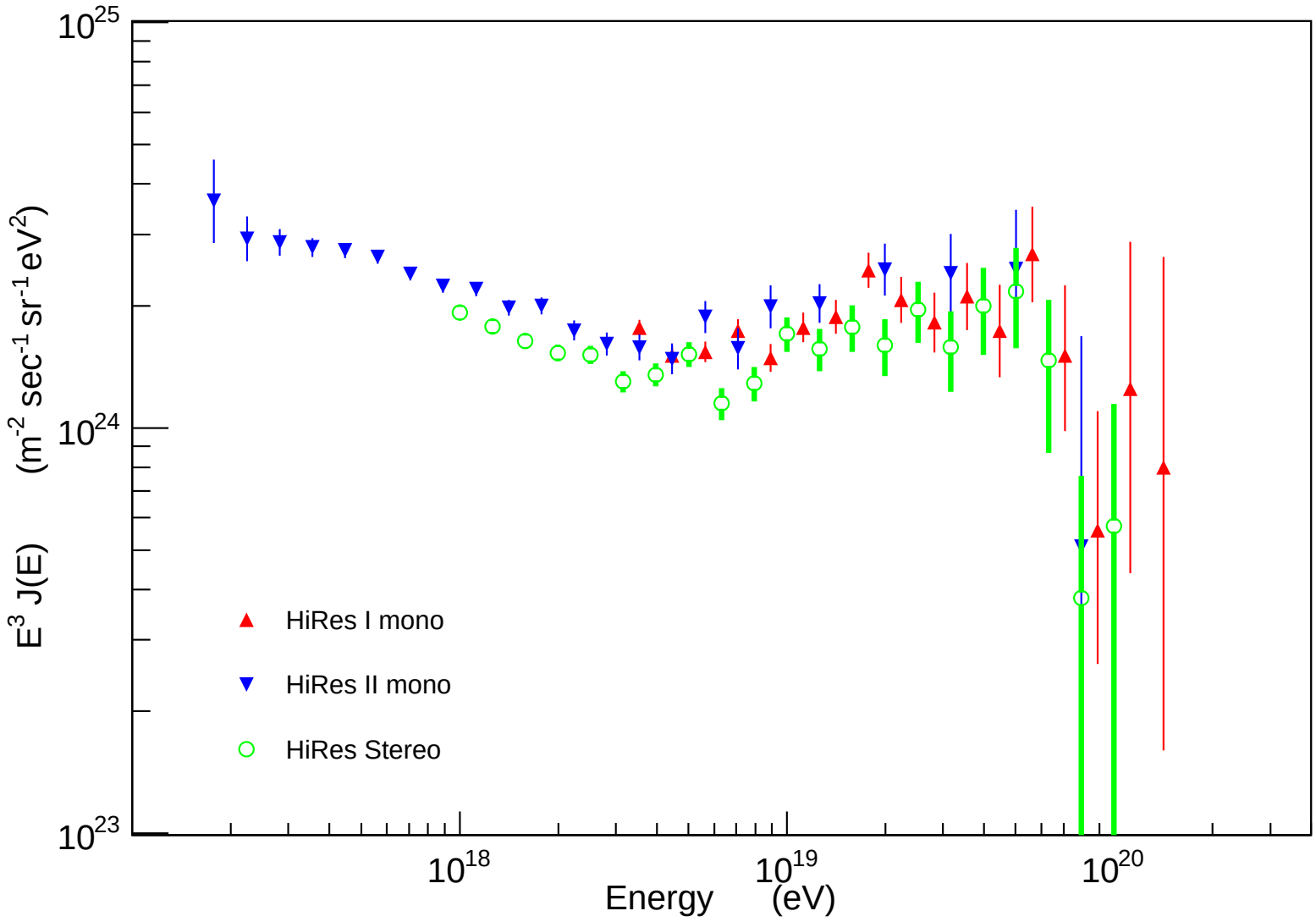

Figure 2.5: The published spectra for HiRes-1 and HiRes-2 monocular observations [3] and the HiRes stereoscopic observations [40].

agreement with what is observed in th $\langle X_{max} \rangle$ composition measurements shown in Figure 2.4. The HiRes-2 monocular spectrum is reliable to energies as low as $10^{17.1}$ eV and shows the hint of a second knee (a softening of the spectrum) around $10^{17.5}$ eV, though it is not statistically significant. With this possibility, however, the TALE experiment (Telescope Array Low-energy Extension) becomes scientifically compelling because it is designed to measure cosmic rays using fluorescence detection down to energies as low as $10^{16.5}$ eV. TALE is therefore perfectly able to study this unexplained spectral feature.

The HiRes spectrum was also compared to a parameterization of the cosmological distribution of sources. Bergman [18] produced a graph (see Figure 2.6) which describes the fraction of proton interactions with the CMBR as a function of red-shift. Individual peaks for each red-shift (visibly starting at z = 4) form for all energies but are compressed to lower energies due to energy losses. Integrating these red-shift bands produces a spectral shape which is then compared to the cosmic ray energy spectrum measured by the HiRes experiment. A pile-up from pion production then forms the peak observed at $10^{19.5}$ eV. It also shows electron-positron pair-production excavating the dip at the region of the ankle ($10^{18.5}$ eV). Quasars, which are very young cosmological objects in the universe, could be responsible for the deficit starting at a red-shift of $z = 1$. This deficit arises close to the energy of the second knee.

There are significant differences in the energy scale spectra obtained by the various collaborations. Figure 2.7 shows that spectra from different experiments can be shifted by $\sim 10\%$ in order to fit the same features for the various energy ranges. Beyond that, HiRes observes the GZK cutoff with greater than 5σ significance. However, AGASA data is indicative of a flux that continues unabated above 5×10^{19} eV. Since these measurements were made using different types of detectors, this has driven researchers to create hybrid detectors that combine fluorescence telescopes and scintillation ground arrays such as the Telescope Array and the Pierre Auger Observatory. There are still many questions to be answered and each new generation of detector provides more valuable insight.

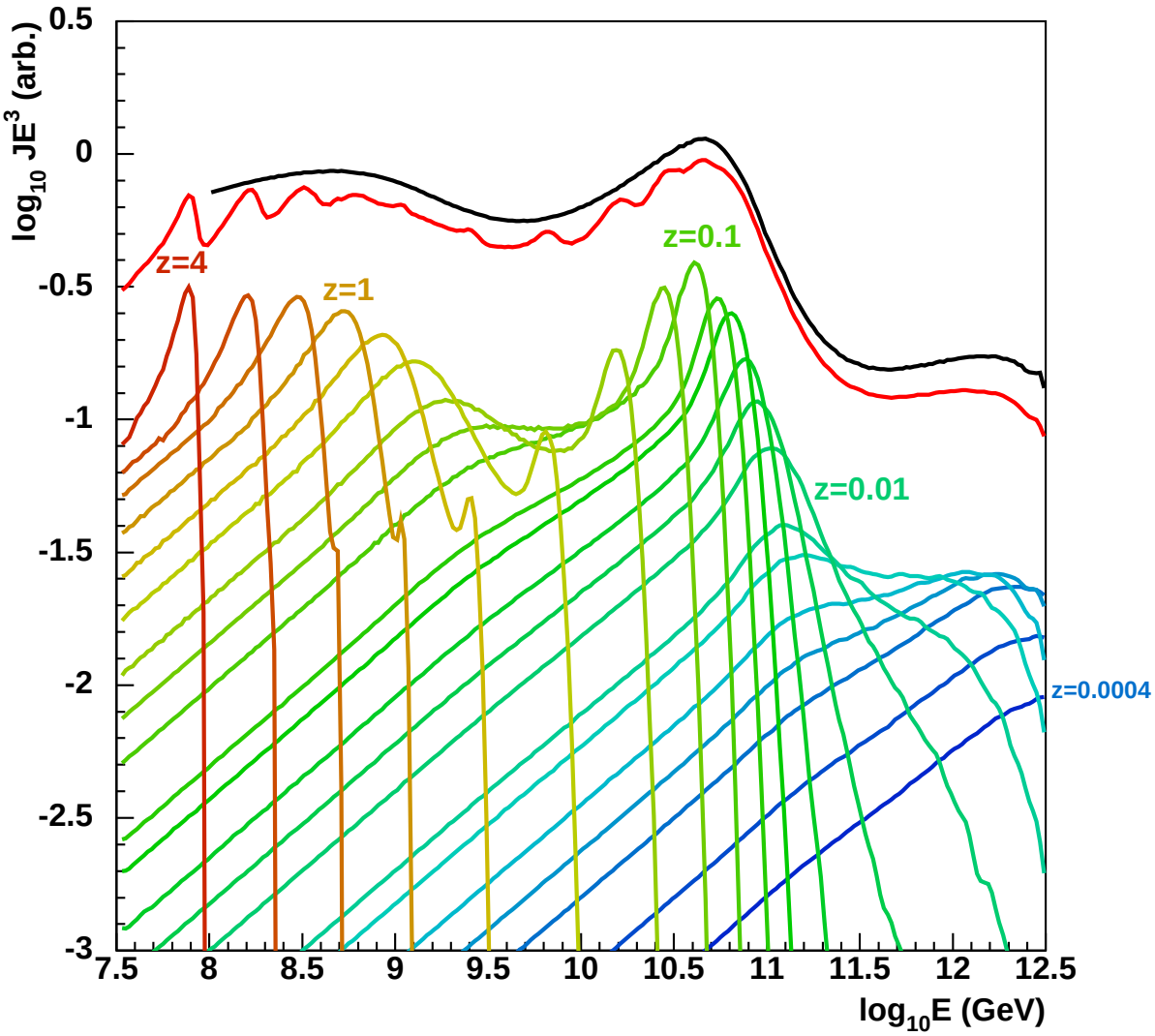

Figure 2.6: The lower lines show the fraction of proton interactions with the cosmic microwave background radiation plotted as a function of energy for various red-shifts. These are then integrated (the lower-upper line) and compared to the HiRes spectral data (the higher-upper line).

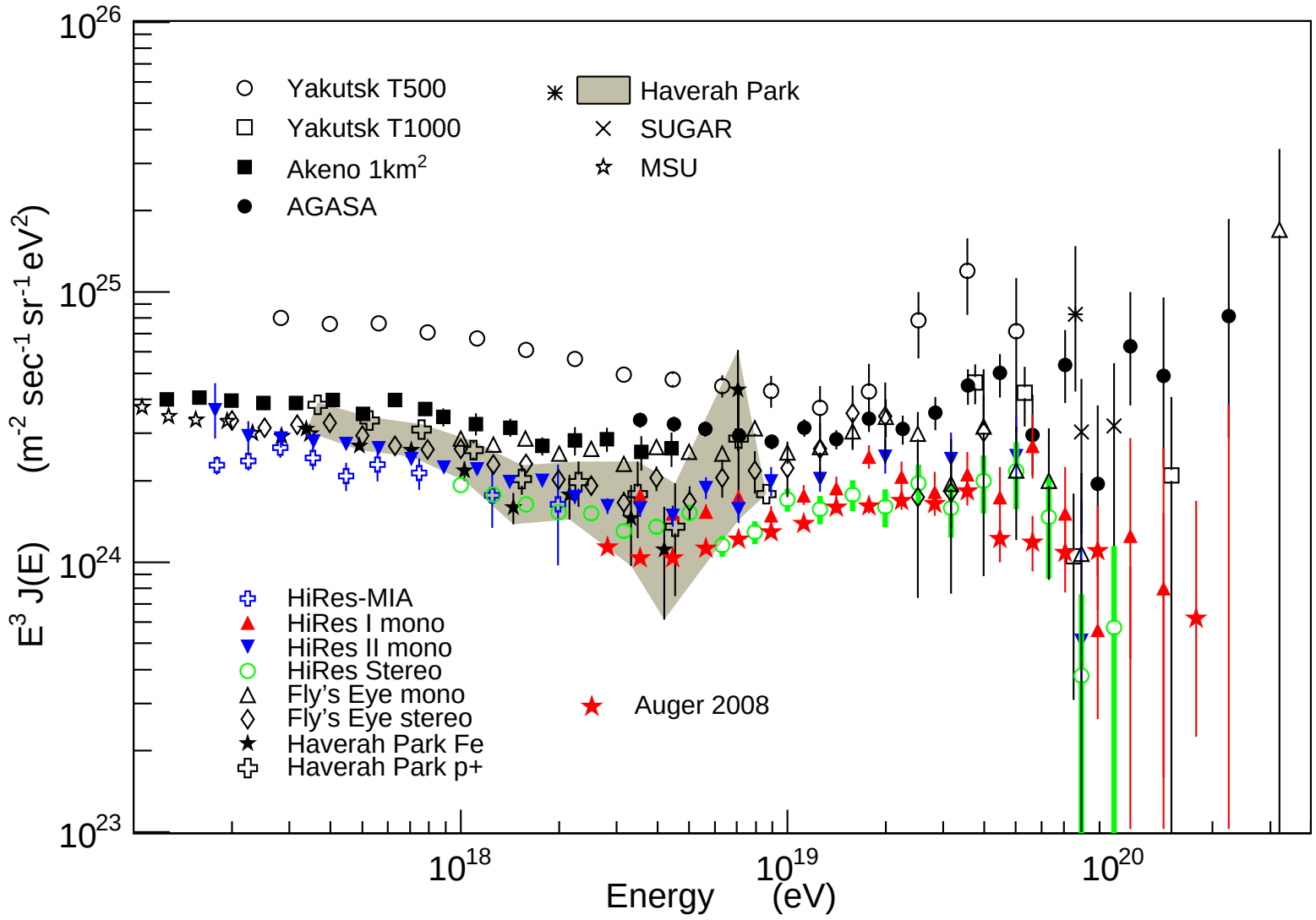

Figure 2.7: All UHECR experiments.

CHAPTER 3

EXTENSIVE AIR SHOWERS

Extensive air showers (EAS) were discovered by Pierre Auger [13] in 1937 when he measured high energy particles arriving at ground level in time coincidence, spread over an area of hundreds of square meters. These correlated particles were interpreted to come from a single primary cosmic ray particle interacting with the atmosphere, resulting in an avalanche of secondary particles. Because of the rarity of Ultra-High Energy (UHE) cosmic rays, the measurement of extensive air showers has become the only practical technique for detecting cosmic rays with energies above $\sim 10^{16}$ eV. These measurements are indirect in nature because we are able to observe only the resulting particle cascade and cannot measure the properties of the original particle. For this reason, the interpretation of these measurements depends on the model used to describe the properties of the shower. There are several air shower simulation packages available, including AIRES [86] and Cosmos [55]. However, the standard program currently used by the UHECR field is CORSIKA [44].

The measurement of UHECR air showers uses the atmosphere itself as part of a very large sampling calorimeter. Cosmic ray shower development can be considered a sequence of particle interactions cascading through the atmosphere. Proton and nuclear primaries produce hadronic showers, which in turn generate electromagnetic subshowers (see Figure 3.1). Photons and electrons create purely electromagnetic showers.

3.1 Hadronic Cascade

A typical UHECR shower starts when a cosmic ray particle (usually a proton, though larger nuclei can be considered a conglomerate of A nucleons, each with an energy of E_0/A [94]) enters the atmosphere and collides with a nitrogen or oxygen nucleus (respectively 78% and 20% of the time due to abundance) (see Figure 3.1). A typical 10^{19} eV proton primary can produce ~ 100 particles (mesons and a few baryons) in the first hadronic interaction. Of these, about 60% are pions in equal charge distributions due to isospin invariance of strong interactions. The neutral pions will decay electromagnetically.

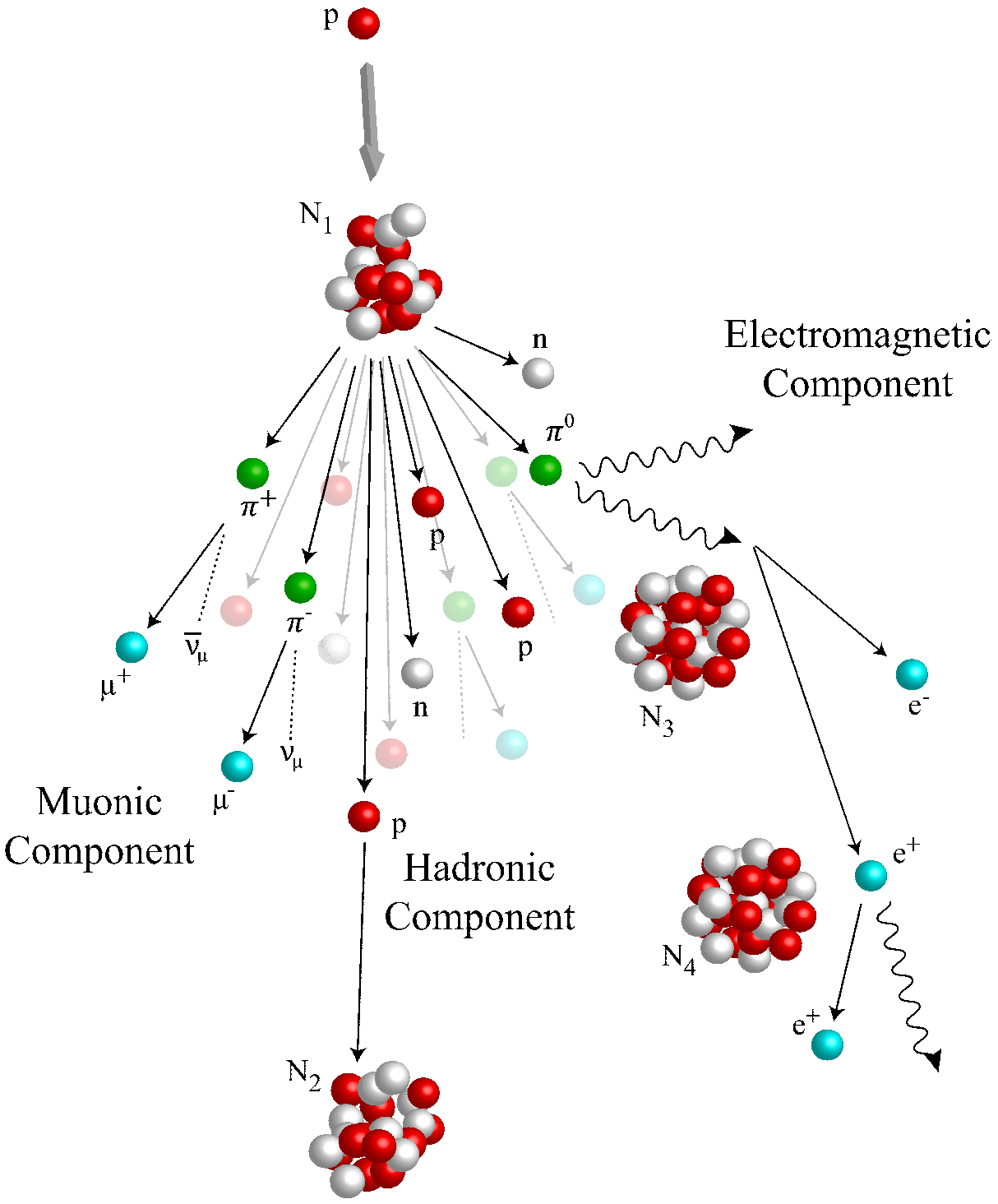

Figure 3.1: An air shower schematic of the most common particle interactions and decays that take place in a cosmic ray shower as it penetrates the Earth's atmosphere.

After a collision, each of the secondary particles will either decay or suffer another collision, depending on the density of nuclei in the surrounding medium and the intrinsic lifetime of the particle. For example, about 40% of the particles produced in a hadronic collision are charged pions, which have long (weak-interaction) decay times. In the rarified upper atmosphere, essentially all of these pions will decay leptonically

$$\pi^{\pm} \rightarrow \mu^{\pm} + \nu_{\mu}(99.99\%). \tag{3.1}$$

The muons and neutrinos produced in the upper atmosphere from this decay rarely interact with the atmosphere; the muons likely hitting the ground before any additional interaction takes place, the neutrinos passing through the ground.

At lower elevations, the charged pions are increasingly likely to collide with another nucleus. These secondary collisions are identical in nature to the primary interaction, but with less energy available. In this manner, a cascade of hadronic collisions lead to the formation of a "core" hadronic shower, but 20% of the energy in any given hadronic collision is transferred into the electromagnetic part of the EAS. After the first few interactions, the shower becomes primarily electromagnetic in nature, with only a small hadronic core remaining. The cascade continues to grow until the hadrons reach an average energy equal to a critical energy, ϵ_c^h (in air), below which they will lose energy only through ionization.

3.1.1 Hadronic Interactions

Two hadrons can interact via the strong force as long as they are within a radius of $\sim 1 \times 10^{-15}\ A^{\frac{1}{3}}$ meters, where A is the mass number of the target hadron. This describes a typical collision between a cosmic ray particle with a target nucleus. This can be described as a bag of quarks, surrounded by a virtual gluon cloud, interacting with a stationary bag of closely-bound quarks and gluons. The result of such a collision is the complete break-up of both the projectile and target into their constituent quarks and gluons. These recombine into $\sim 20\%$ π^+, π^0 and π^- in roughly equal numbers, 15% kaons, $\sim 10\%$ protons and neutrons, and a small number of short-lived heavier hadrons (see Figure 3.2).

3.2 Electromagnetic Cascade

In contrast to charged pions, which decay via the weak interaction, neutral pions decay electromagnetically with a lifetime of $\sim 10^{-16}$ seconds. This means that essentially all π^0s do not interact further, but instead decay into a photon pair

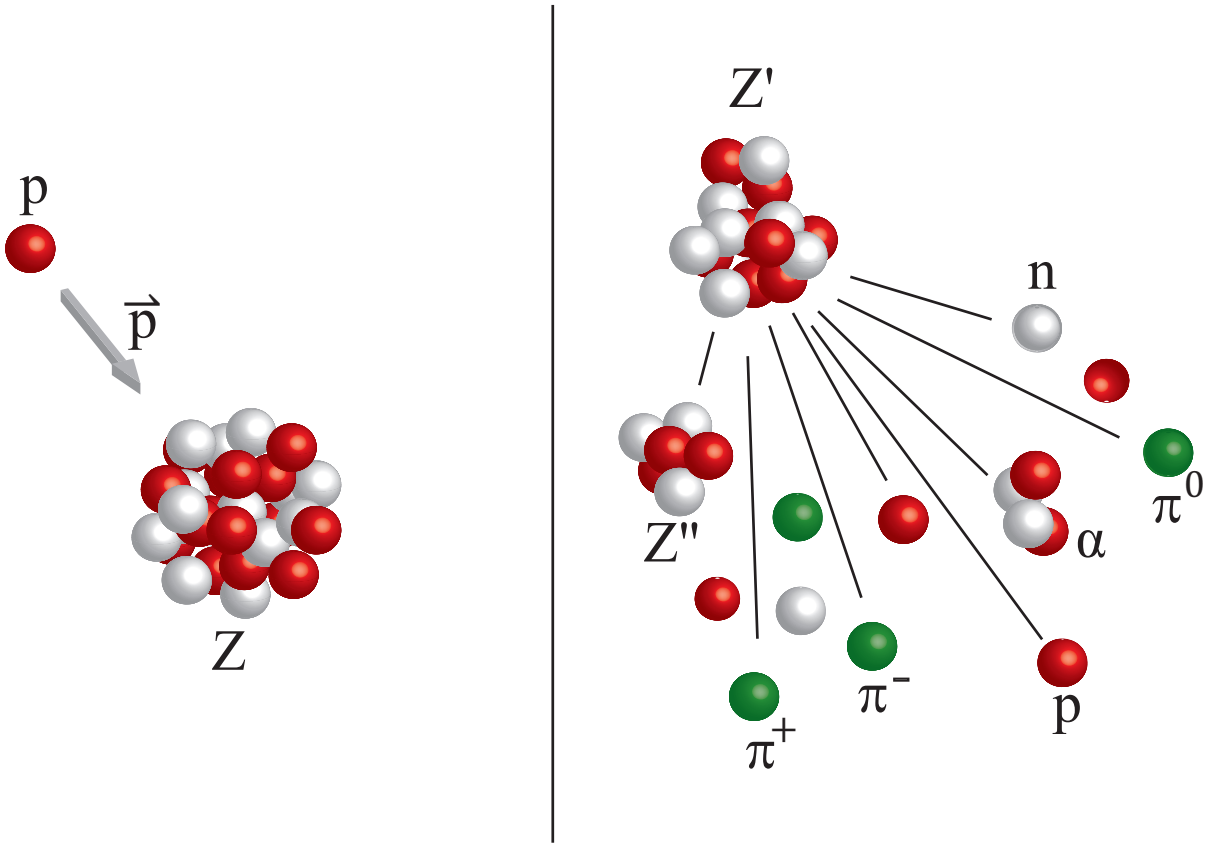

Figure 3.2: Hadronic interaction.

$$\pi^0 \rightarrow \gamma + \gamma \ (98.8\%). \tag{3.2}$$

These photons then produce an electromagnetic cascade through combinations of pair-production and bremsstrahlung. The Heitler model (see Figure 3.3) [45] illustrates this process in a simple manner and gives a good approximation. This model shows how electrons, positrons and photons split into two particles after one interaction length, λ. This process continues until the particles diagramed as individual lines have reached a critical energy of ~ 1 GeV. The electrons (and positrons, though these will henceforth be referred to as electrons) and photons undergo two-body splitting (bremsstrahlung and pair-production, respectively) after an average distance equal to the radiation length of air, λ_0. After n splittings there are 2^n particles, each with an energy $\sim E_0/2^n$, at a depth of $x = n\lambda_0 \ln 2$ in the atmosphere. This process continues until an individual electron's or photon's energy drops below a critical energy, $\epsilon_c^e = 87$ MeV, when ionisation losses exceed radiative processes. A maximum number of particles in the shower occurs when essentially all particles reach this energy, $N_{max} = E_0/\epsilon_c^e$, where E_0 is the energy of the primary particle. The penetration depth at which this occurs is then

$$X_{max} = n_c \lambda_0 \ln 2 = \lambda_0 \ln \frac{E_0}{\epsilon_c^e}, \tag{3.3}$$

where n_c is the average number of splittings to reach ϵ_c^e. The rate at which X_{max} increases as a function of $\ln E_0$ is the elongation rate (see equation 2.3).

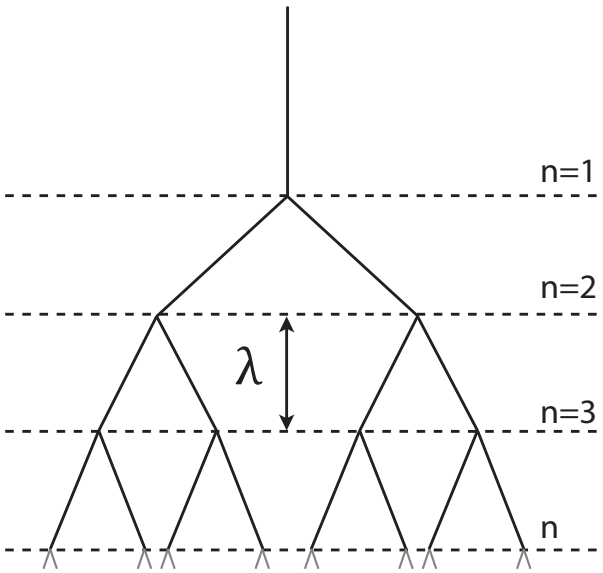

Figure 3.3: The Heitler Model. Adapted from Heitler [45]

3.2.1 Electromagnetic Interactions

There are several types of electromagnetic interactions involved in the development of an electromagnetic (sub)shower. These are easily observed and studied in lower-energy particle interactions with accelerators.

1. Pair Production

   From the decay of neutral pions, high-energy photons are created that initiate electromagnetic subshowers. At high energies ($\gtrsim$ 10 MeV) a photon undergoes pair-production in collisions with charged nuclei (see Figure 3.4):

   $$\gamma + A \rightarrow e^- + e^+ + A. \tag{3.4}$$

   Here the nucleus absorbs the excess momentum while essentially all of the energy of the photon is imparted into the electron-positron pair. At lower energies, Compton scattering ($\gamma + A \rightarrow \gamma + e^- + A^+$) becomes more likely.

   For a given material, the characteristic depth traversed by the photon before interacting is called the radiation length, given by the equation [33]

   $$X_0 = \frac{716.4A}{Z(Z+1)\ln\frac{287}{\sqrt{Z}}}\text{g/cm}^2 \tag{3.5}$$

   where A is the mass number and Z is the atomic number. For pair-production, $X_0 = 7/9$ of the mean free path of a photon [61].

2. Bremsstrahlung

   Electrons scattering from a heavy nucleus can result in the emission of a photon that carries off some of the energy of the incident electron. Again, the nucleus in such interactions absorbs the excess momentum without taking away a significant amount of the energy. This process is known as bremsstrahlung (see Figure 3.5):

   $$e^\pm + A \rightarrow e^\pm + A + \gamma. \tag{3.6}$$

   It is convenient to describe the energy loss as a function of radiation lengths, X_0. This is the distance over which the electron retains 1/e of its original energy (on average) in a given medium. The radiation length in air (at standard temperature and pressure) is $X_0 = 36.5$ g/cm^2. The energy loss can be written as a function of "depth" rather than distance:

   $$-\frac{dE}{dX_r} = \frac{E}{X_0}. \tag{3.7}$$

   Calculating interactions as a function of the amount of material the particle must pass through is more appropriate since the density of the atmosphere changes.

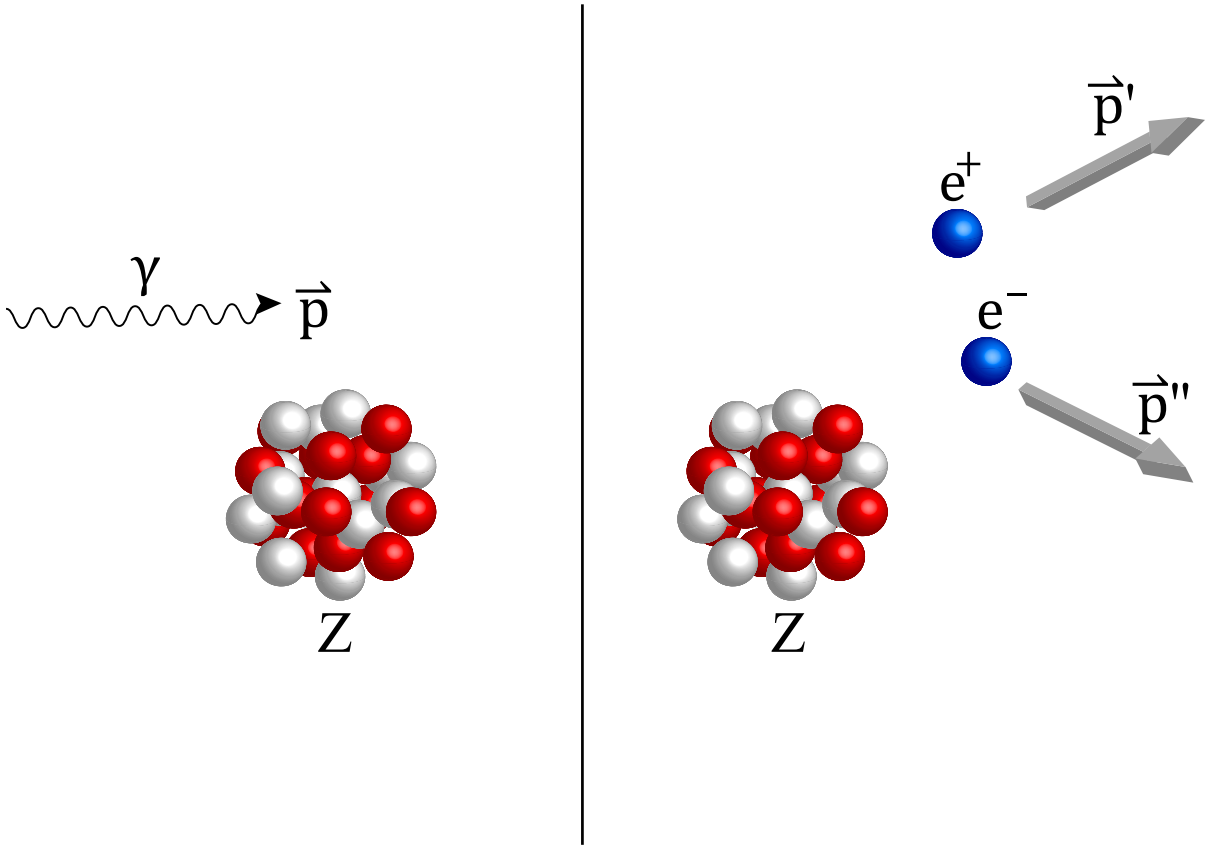

Figure 3.4: Pair production.

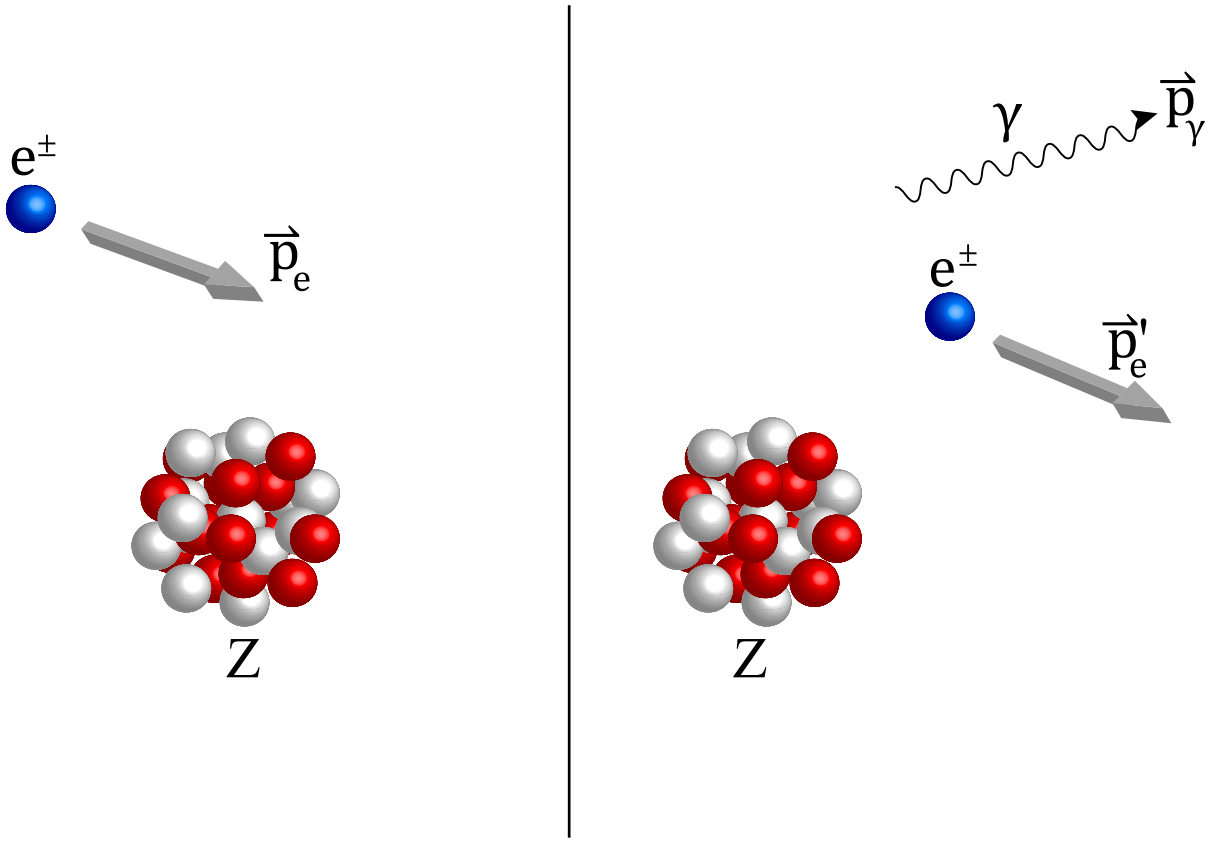

Figure 3.5: Bremsstrahlung.

3. Ionisation

   Ionisation is the process by which high-energy, charged particles lose energy to atomic electrons through Coulomb interactions. The (relativistic) projectile will interact with the bound electron (see Figure 3.6), producing a net impulse in the direction perpendicular to that in which the projectile is moving. The average energy the projectile loses per unit length is given by the Bethe-Bloch equation

$$-\frac{dE}{dx} = \frac{Z^2 e^4 N_e}{4\pi\epsilon_0^2 m_e v^2}\left[\ln(\frac{2\gamma^2 m_e v^2}{\overline{I}}) - \frac{v^2}{c^2}\right] \tag{3.8}$$

   where Ze is the charge of the projectile, ϵ_0 is the permittivity of free space, v is the speed of the proton, $\gamma = [1-(v/c)^2]^{-1/2}$ is the Lorentz factor, and $\overline{I}$ is the mean ionisation potential of the atomic electrons and is dependent upon the interaction length, b. A more detailed derivation can be found in Rossi [84].

3.3 Čerenkov Radiation

All of the high-energy particles produced in an EAS are moving at ultra-relativistic speeds as they pass through the atmosphere. Since 90% of these are electrons, they are

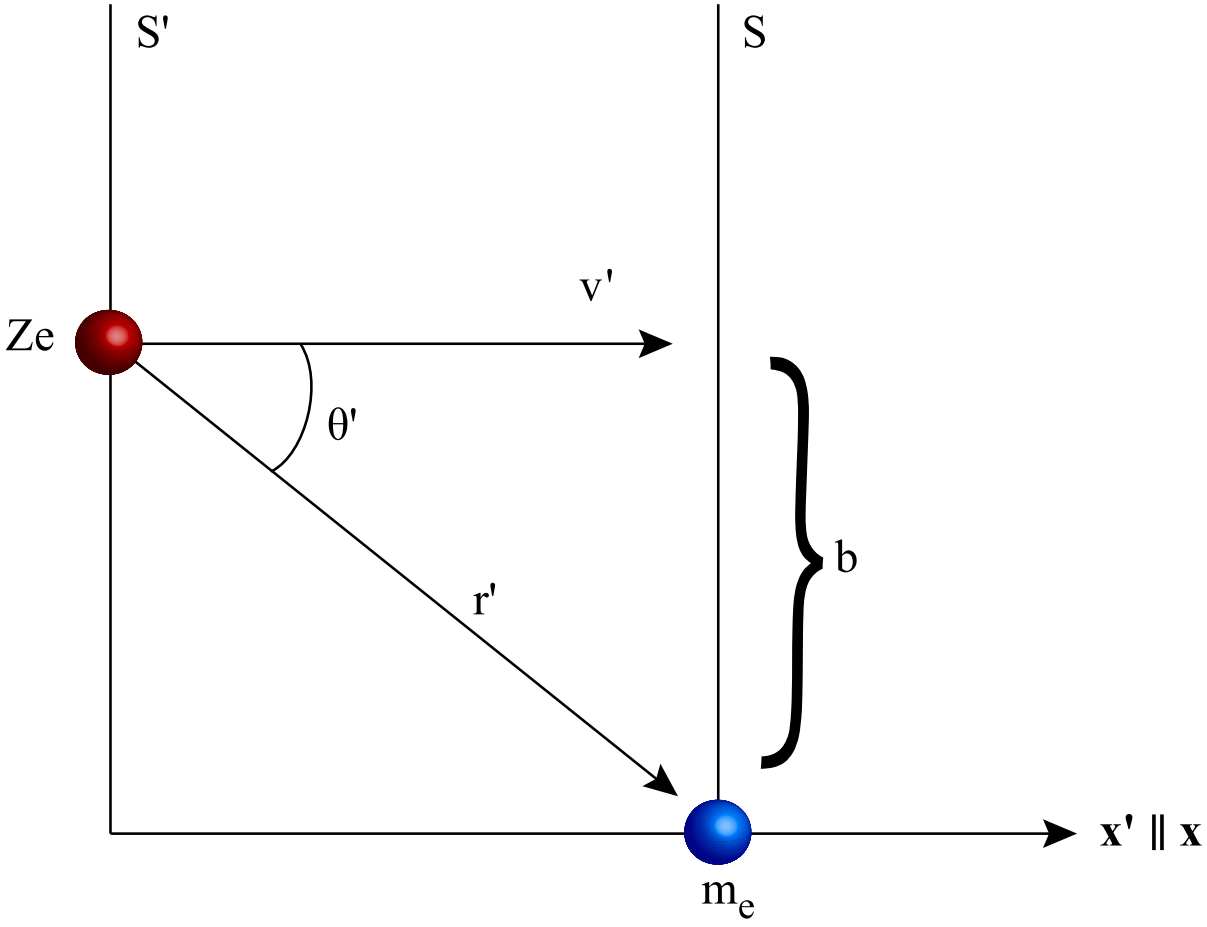

Figure 3.6: Ionisation.

the primary producers of Čerenkov radiation in the EAS. The electrons only produce Čerenkov light if their velocity is greater than the speed of light in the local medium

$$v = \frac{c}{n(H)} \tag{3.9}$$

where c is the speed of light and n is the index of refraction, which changes as a function of altitude (H). Since atmospheric pressure changes as a function of height, the energy threshold for this process is described by the equation

$$E_{min} = \frac{m_e}{\sqrt{2\delta}} \tag{3.10}$$

where $m_e = 511$ keV is the mass of an electron, $\delta = n - 1$ and is proportional to $\exp(-H/H_s)$, with H_s being the scale height of the atmosphere. The wavefront of this direct-Čerenkov light propagates at a fixed angle with respect to the particle's initial velocity according to Huygens' principle (see Figure 3.7)

$$\cos\theta = \frac{c}{nv} \tag{3.11}$$

where θ is the angle of the wave vector, n is the refractive index of a medium, c is the speed of light in a vacuum and v is the speed of the particle.

The number of Čerenkov photons produced per meter in the atmosphere is dependent on the energy, E, of the primary cosmic ray and is described by the equation [93]:

$$\frac{dN_\gamma}{dl} = 4\pi\alpha \left[1 - \left(\frac{E_{min}}{E}\right)^2\right] \int \frac{\delta}{\lambda^2} d\lambda \tag{3.12}$$

where α is the fine structure constant and λ is the wavelength of the light emitted. The angular distribution of the photons can be described by the equation

$$\frac{dN_p}{d\Omega} \propto \frac{e^{-\theta/\theta_0}}{\sin\theta} \tag{3.13}$$

where $\theta_0 = aE_{min}^{-b}$, $a = 0.83$, and $b = 0.67$. This shows that most of the photons are contained within 6° of the primary particle's initial direction vector, however the atmosphere can scatter them as far as 25° away.

3.4 Fluorescence

The charged particles passing through the atmosphere also excite the gas molecules. After $\sim 10 - 15$ nanoseconds, the excited electrons will relax and release the energy they gained in the form of scintillation light, a form of luminescence [47]. (While "fluorescence" is the common vernacular in cosmic ray physics, it is misleading because fluorescence is

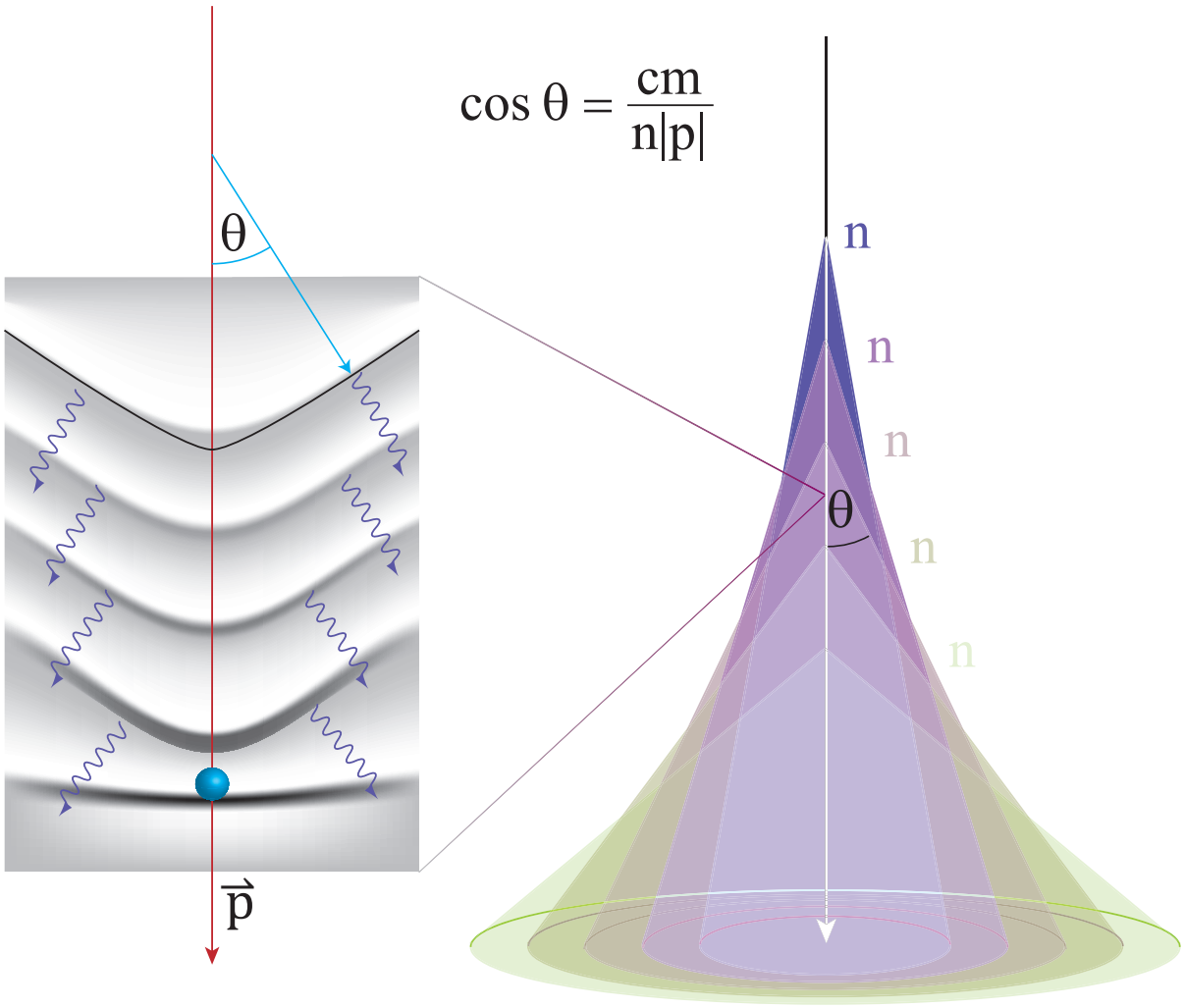

Figure 3.7: Čerenkov radiation wave front.

the process of light emitted by electrons after being excited by photons, specifically. The more appropriate term is "scintillation," which can be caused by emission after any form of ionizing excitation.) Due to their relative abundance, most of the light will come from nitrogen molecules. Bunner [27], FLASH [17] [2] and AIRFLY [14] have all produced spectra of nitrogen luminescence. The main de-excitation transition occurs between the N_2^+ ion's 1N band and the N_2 molecule's 2P band, which primarily produce light in the UV range between 310 nm and 390 nm with a primary peak at 337 nm (see Figure 3.8).

The fluorescence yield is determined by the number of fluorescence photons produced per particle, per unit path length of the ionizing particle (see Figure 3.9). Since $\sim 90\%$ of the particles that ionize the atmosphere are electrons and positrons with energy $< 10^{12}$ eV, measurements of this value can be performed in a laboratory using electron beams. The parameterization used by the HiRes and Middle Drum reconstruction routines is [53]

$$Y_\gamma = \frac{1}{(dE/dx)_{dep}} \frac{\rho A_\gamma}{1 + \rho\alpha A_\gamma \sqrt{T}} \tag{3.14}$$

where $(dE/dx)_{dep}$ is the energy deposited into the atmosphere per unit path length, ρ is the density of the atmosphere at a given altitude, and A_γ and T are the transmission coefficient and temperature of the atmosphere at that altitude. A single 1 GeV electron

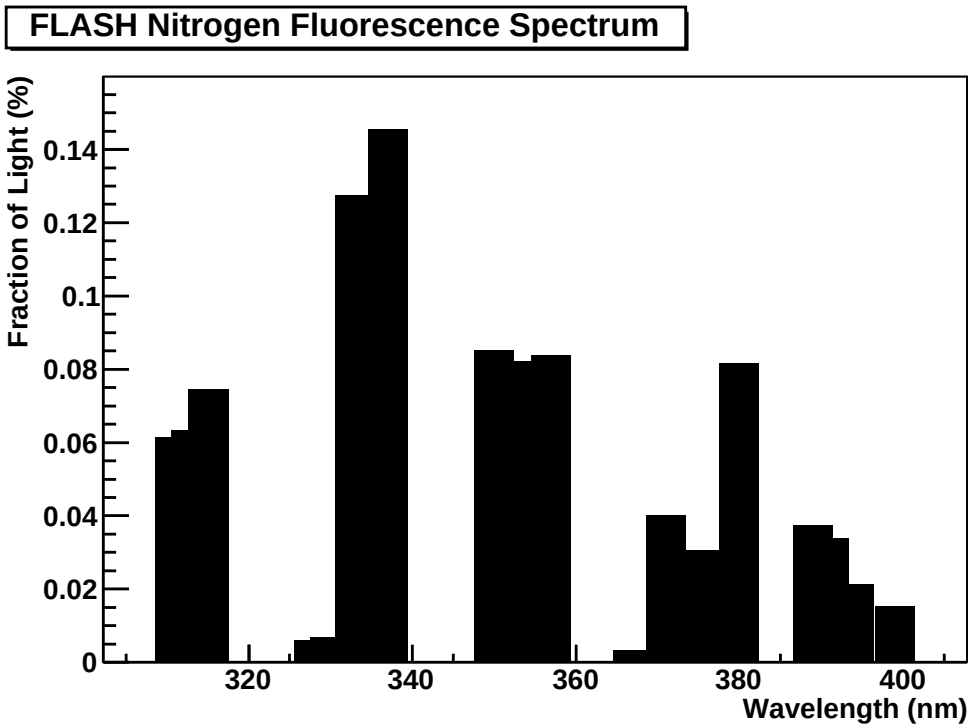

Figure 3.8: The FLASH collaboration's nitrogen fluorescence spectrum between 300 nm and 400 nm.

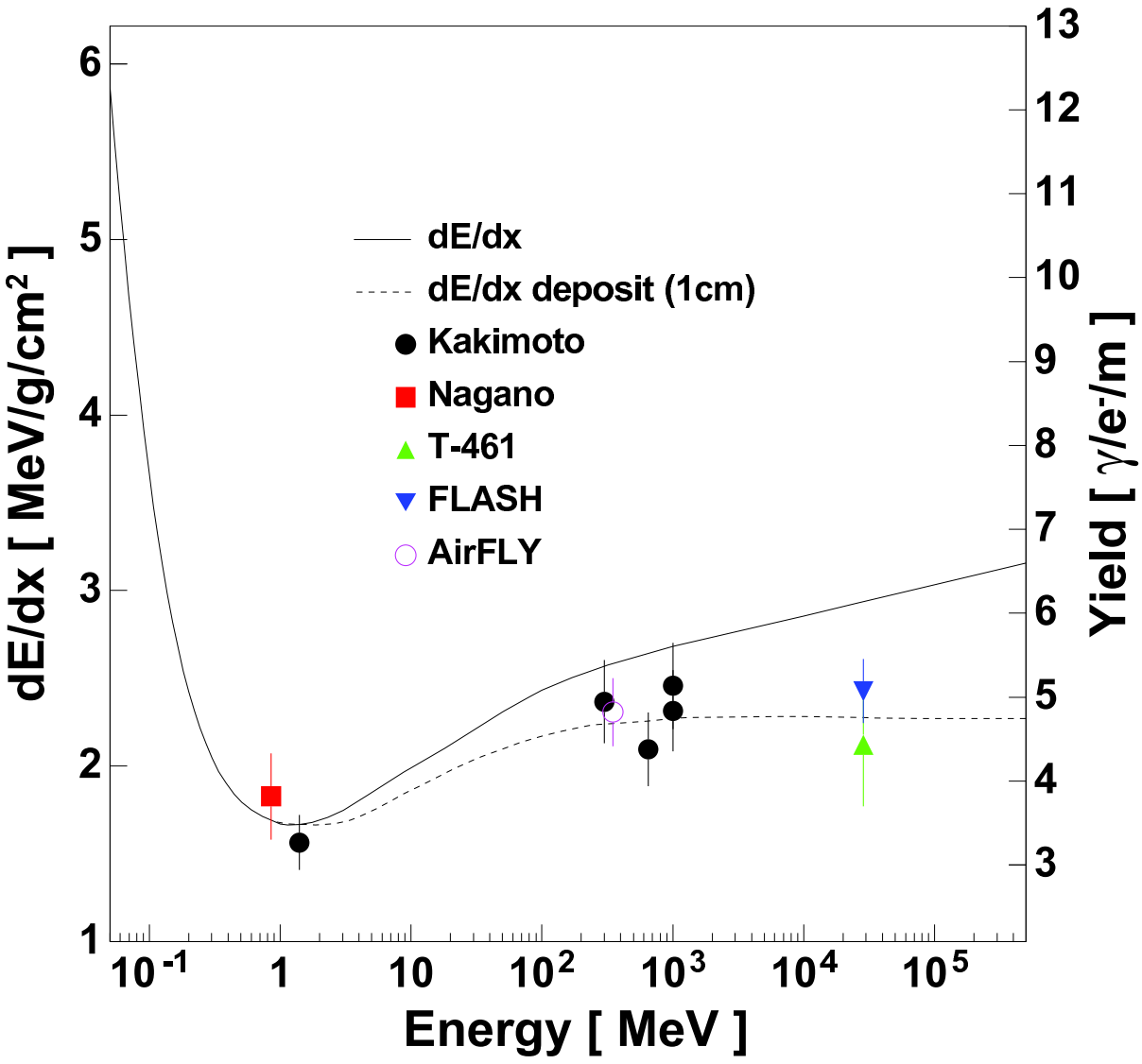

Figure 3.9: A composite of measurements of the nitrogen fluorescence yield.

will produce $\sim$ 5 fluorescence photons (see Figure 3.9), but a typical 10^{19} eV proton-induced shower produces $\sim 6 \times 10^9$ ionizing electrons at shower maximum.

CHAPTER 4

FLUORESCENCE OBSERVATION

4.1 Detection Methods

Presently, ultra-high energy cosmic rays or very-high energy gamma rays can only be studied through the measurement of extensive air showers. Because of the rarity of these particles, detectors must be able to observe large areas of space over long periods of time. There are three types of detectors used in the search for cosmic rays: Čerenkov telescopes, ground arrays, and fluorescence telescopes.

4.1.1 Čerenkov Telescopes

Cosmic rays with energy $\gtrsim 10^{12}$ eV will produce detectable Čerenkov radiation. Since the angle between the shower core and the extent of direct Čerenkov light is quite narrow ($\leq 6^{\circ}$), Čerenkov telescopes must be placed in the path of the shower. These are ideal for observing gamma-rays and cosmic rays with energy less than $\sim 10^{15}$ eV since there is a large enough flux of these particles. One way Čerenkov telescopes are used is by imaging the intensity of the Čerenkov radiation as the shower develops in the atmosphere. The DICE cosmic ray experiment [26] observed cosmic-ray air shower Čerenkov radiation in an effort to determine the mass composition of cosmic rays with energies around a few PeV. The VERITAS experiment [97] uses an imaging technique to discern the sources of very-high energy gamma-rays. A nonimaging Čerenkov observation method measures the lateral distribution of the light as a function of the distance to the core of the shower (e.g., the BLANCA experiment [29] and AIROBICC [54]). Both of these methods have been used to try to explain the nature of the "knee" in the cosmic ray spectrum.

4.1.2 Ground Arrays

By far the most common technique for studying UHE cosmic ray showers is to build an array of particle counters over the ground to sample the electromagnetic footprint of

the EAS shower front as it reaches the surface of the Earth. The individual detectors can be placed from tens of meters (e.g., CASA [74]) to kilometers apart (e.g., Telescope Array and the Pierre Auger Observatory [72]), a distance that is optimized for the energy range of primary particles that the experiment is studying.

Ground arrays include many forms of detectors. The most common type consists of plastic scintillators that produce light when the charged components of a shower pass through it. The charged electromagnetic particles passing through the plastic leaves a trail of ionization which then produces photoluminescence during recombination. Water-Čerenkov tanks can detect both electromagnetic and muonic particles by the Čerenkov radiation produced as shower particles pass through the water. In both cases, photomultiplier tubes are used to collect the resulting light. Experiments like AGASA [12] and Telescope Array use scintillators. The Pierre Auger experiment [72] and MILAGRO/HAWC [73] [71] use the water-Čerenkov method.

4.1.3 Fluorescence Telescopes

Fluorescence telescopes observe scintillation light produced by atmospheric nitrogen molecules after they are excited by the EAS. The atmosphere acts like a large-volume scintillator and produces UltraViolet (UV) light isotropically around the shower (see section 3.4). The observable signal is limited only by the amount of light produced and by attenuation by the atmosphere that the UV light must pass through on its way to the telescope. In this way a compact telescope can observe cosmic rays over a large area, which increases in size with shower energy, and, hence, of the primary cosmic ray.

Fluorescence telescopes measure light from the shower. This is inherently dominated by the shower axis, which has the highest density of charged particles, and hence generates most of the fluorescence light. By measuring the amount of light along the shower track, the number of particles can be measured and the longitudinal profile is measured. By examining the shape of the shower profile and integrating the observed light of shower, one can determine the energy of the cosmic ray primary. However, one can determine the chemical composition only on a statistical basis due to shower-to-shower variations in the first interaction depth and the depth of X_{max}. By looking at the illuminated pixels in the camera, one can find the best fit line of the track. That line, combined with the center of the spherical mirror, determine the shower-detector plane. Adding the timing information (from each pixel), one can determine thr pointing direction of the original cosmic ray. Of course, when the track is observed by two different fluorescence detector sites, one can intersect their shower-detector planes to get a better, more precise, geometrical reconstruction. The High Resolution Fly's Eye detectors as well as the

Telescope Array Middle Drum detector are fluorescence detectors and so this dissertation will focus on this form of observation.

4.1.3.1 Fluorescence Detection

When a cosmic ray penetrates the atmosphere it produces a cascade of particles called an extensive air shower, as described in Chapter 3. The ultraviolet light produced (~ 5 photons/meter/charged particle) will travel isotropically away from the shower axis and be attenuated by the same atmosphere that produced it. The dominant attenuation processes are Rayleigh (molecular) and aerosol (particulate) scattering. In addition, a very small amount will be absorbed by the ozone in the air. A tiny fraction of that light will be collected by the telescope mirror and be focused on its camera (see Figure 4.1). The telescopes at HiRes and TA each consist of a mirror and a camera composed of PhotoMultiplier Tubes (PMTs). The spherical mirrors gather the light and focus it onto the PMTs in a time-ordered pattern corresponding to the angle at which the photons were produced.

A PMT converts the photons into electrons through the photoelectric effect and these signals are amplified through high-voltage-driven avalanche multiplication, producing gains of $\sim 1 \times 10^5$ at the anode. The signal current from the anode is converted to a signal voltage via a preamplifier built into the base of the PMT. This voltage is then sent over ribbon cables to the main DAQ readout system. Each channel is split into a single-threshold trigger discriminator and a delayed sample-and-hold circuit to provide trigger, timing, and charge integration information from that PMT.

4.2 Atmospheric Considerations

4.2.1 Air Density

For this analysis, the reconstruction routines which determine the density, pressure, and temperature of the atmosphere use the U.S. 1976 standard model (see Figure 4.2) which, apart from assuming a nonconstant temperature, is not too far from the isothermal approximation

$$P = P_0 \exp^{-\frac{h}{kT/mg}} \tag{4.1}$$

where P is the pressure change from P_0 of 1 atm, T is the temperature, m is the average molecular mass of air at height, h, above the ground, k is the Boltzmann constant and g is the gravitational constant.

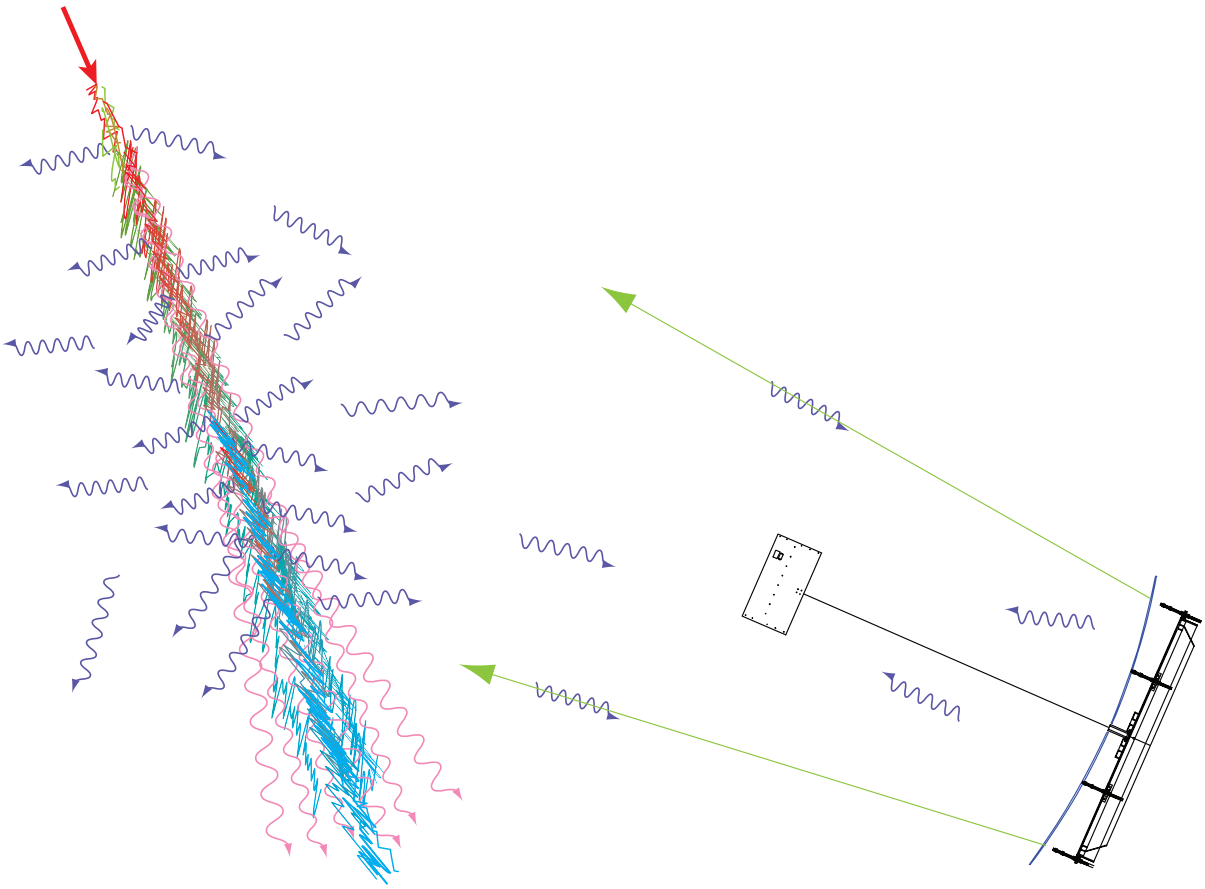

Figure 4.1: Fluorescence detection schematic. In the figure, a cosmic ray initiated air shower develops (left) and heads to the surface fo the Earth. As the shower traverses the atmosphere, it excites the gases causing them to isotropically emit ultraviolet photons. A small fraction of that light hits the telescope mirror where it is gatherd and focused onto the camera.

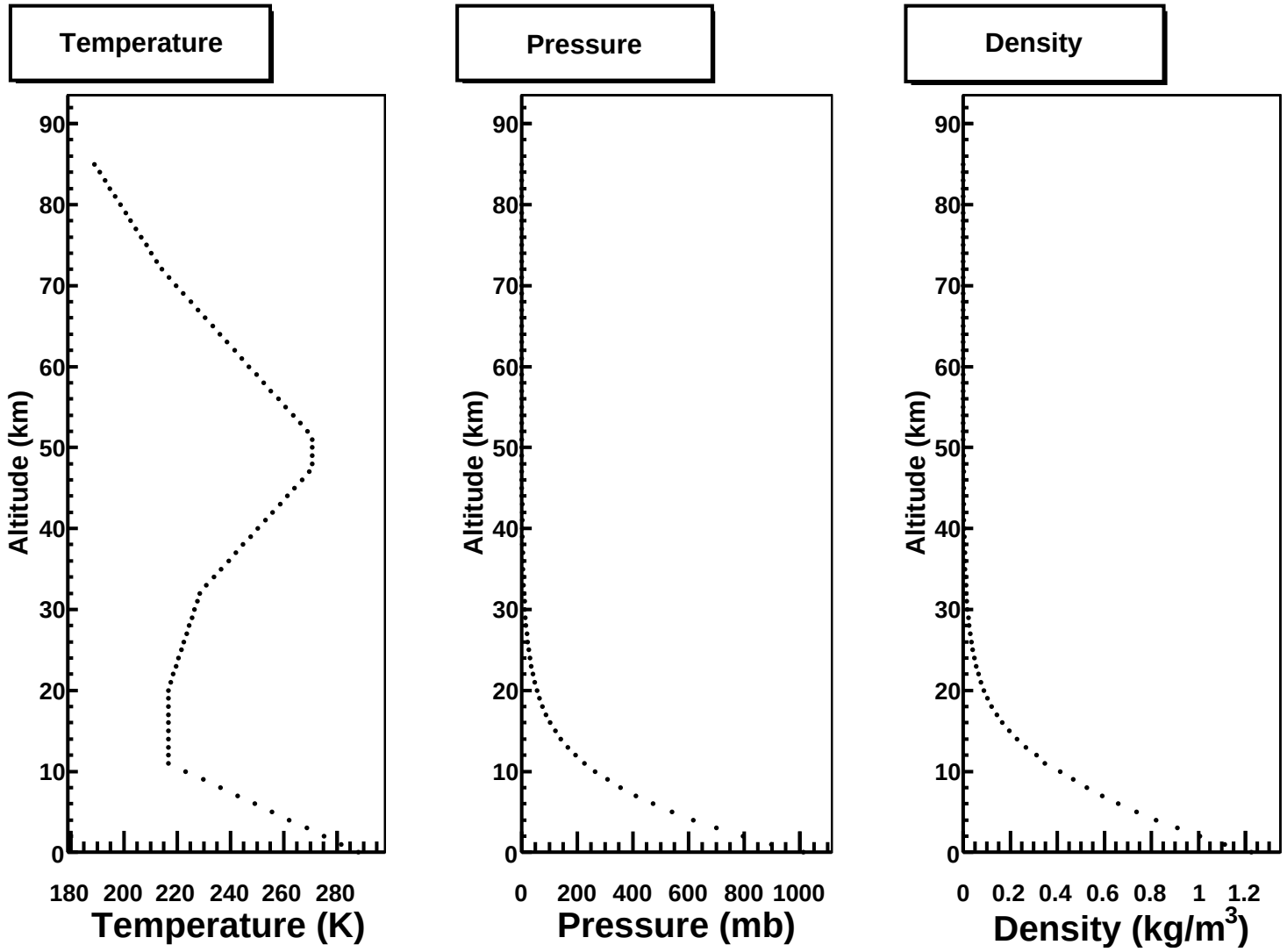

Figure 4.2: The U.S. 1976 standard atmosphere temperature, pressure, and density profiles.

Using the Salt Lake City international airport radiosonde information, a study was made to determine the annual pressure profile of the atmosphere during the operation of the HiRes experiment between January, 1998 and May, 2006 (see Figure 4.3). Between 6 and 12 km above sea level the average atmospheric pressure is seen to cycle with the seasons. The data were reconstructed again using the radiosonde database as well as a three-season atmospheric model. The results of these two analyses were then compared to the reconstruction which utilized the U.S. 1976 standard atmosphere (see Figure 4.4). The reconstructed X_{max} using a three-season model fits closer to the radiosonde data and compensates for the discrepancy produced in the standard model. The radiosonde values collected twice a day were used in the final reconstruction.

4.2.2 Rayleigh Scattering

Rayleigh scattering is the highly-wavelength-dependent scattering of light off air molecules. The number of photons, N_γ, scattered as a function of wavelength per a unit track length, dl,is given by [95]

$$\frac{dN_\gamma}{dl} = \frac{-\rho N_\gamma}{X_R(400/\lambda)^4} \tag{4.2}$$

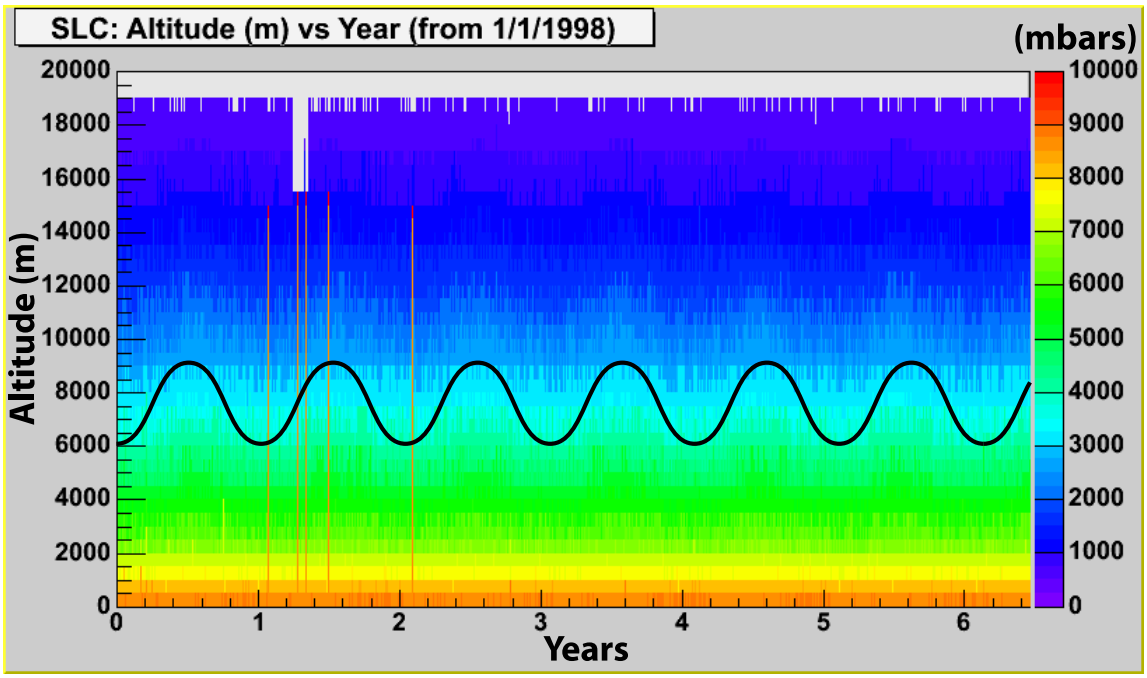

Figure 4.3: Annual atmospheric pressure profile in millibars from the Salt Lake International Airport radiosonde. As highlighted by the black wavy line, the pressure changes by $\sim$ 4000 millibar over the course of a year on an annual cycle.

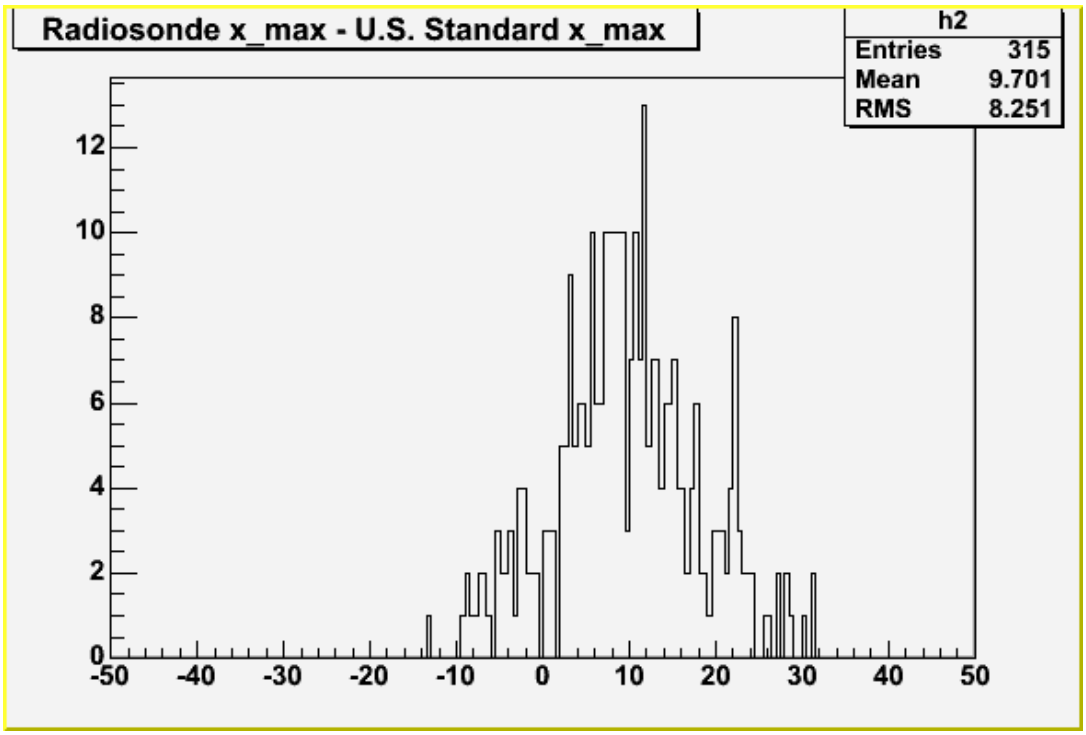

(a) Radiosonde vs. Standard Model

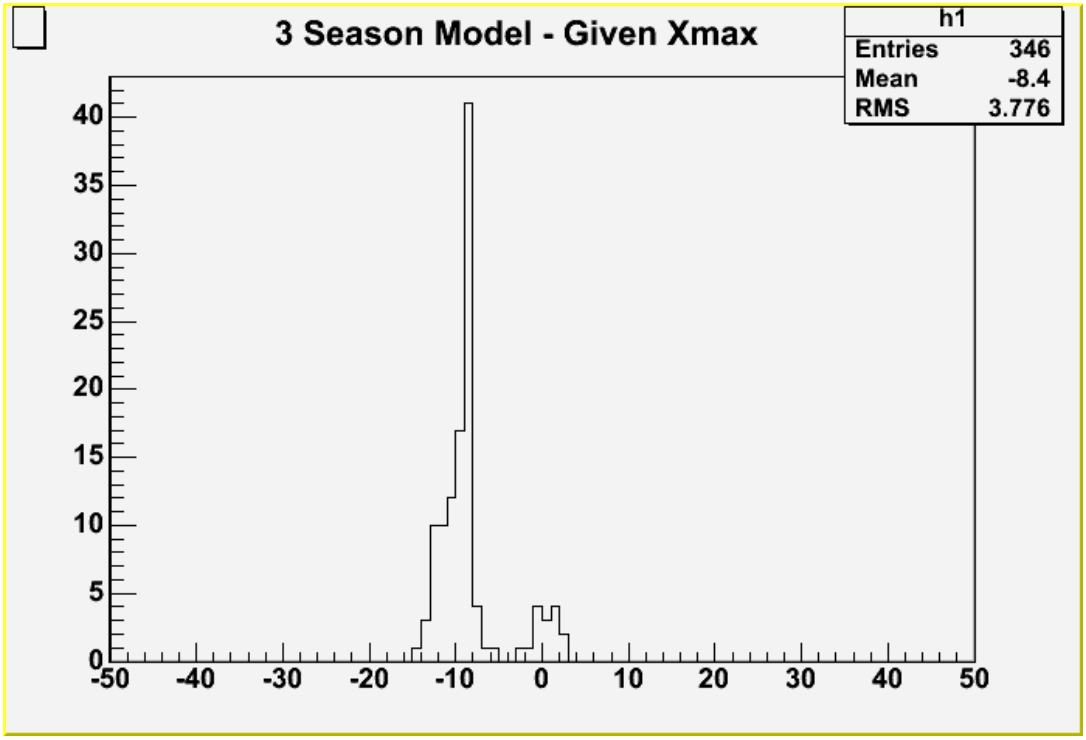

(b) 3-season vs. Standard Model

Figure 4.4: Standard atmosphere vs. radiosonde and three-season models.

where ρ is the atmospheric density, $X_R = 2970\text{g/cm}^2$ is the mean free path of photons at 400 nm, and λ is the wavelength of the light in nanometers. The angular distribution of the scattered light into a unit solid angle, Ω, is given by

$$\frac{d^2N_\gamma}{dld\Omega} = \left(\frac{3}{16\pi}\right)\left|\frac{dN_\gamma}{dl}\right|\left(1+\cos^2\theta\right) \tag{4.3}$$

where θ is the zenith angle of the light and the initial photons are assumed to be randomly polarized. This is used to calculate the amount of light from both Čerenkov light scattered away from the shower axis as well as of UV light produced in the electromagnetic cascade.

The transmission factor of Rayleigh scattered light is given by

$$T_R = \exp\left[\frac{-\Delta x}{X_R(400/\lambda)^4}\right] \tag{4.4}$$

where Δx (given in g/cm^2) is the slant depth path length. This then gives the amount of attenuation of light during propagation to the detector.

4.2.3 Aerosol Scattering

Aerosol scattering refers to the scattering and absorption of light from particles with a diameter greater than its wavelength. The only well-defined information known about aerosols is that the concentration drops as a function of height above the ground. Otherwise, winds, soil type, and time are all factors in adjusting the amount of scattering that will occur.

The attenuation of photons due to aerosols is given by

$$\frac{dN_\gamma}{dl} = \frac{N_\gamma\rho_a(h)}{L_M(\lambda)} \tag{4.5}$$

where L_M is the horizontal extinction length (HiRes reconstruction uses $L_M = 25$ km at 334 nm from the Etterman model) (see Figure 4.5) and

$$\rho_a = e^{\frac{-h}{H_a}} \tag{4.6}$$

where h is the height of the interaction above the ground and $H_a = 1.0$ km is the estimated average aerosol scale height. The vertical aerosol optical depth (VAOD) is determined by dividing the scale height by the extinction length, measured to have an average of 0.04 for HiRes. Figure 4.6 shows the VAOD experienced around the HiRes detectors. Additionally, a Monte Carlo study was performed which predicted how well the detectors would respond to calibration lasers with varying amounts of aerosols [104]. The study showed that if the lasers were set at ~ 3 km away, the amount of scattered

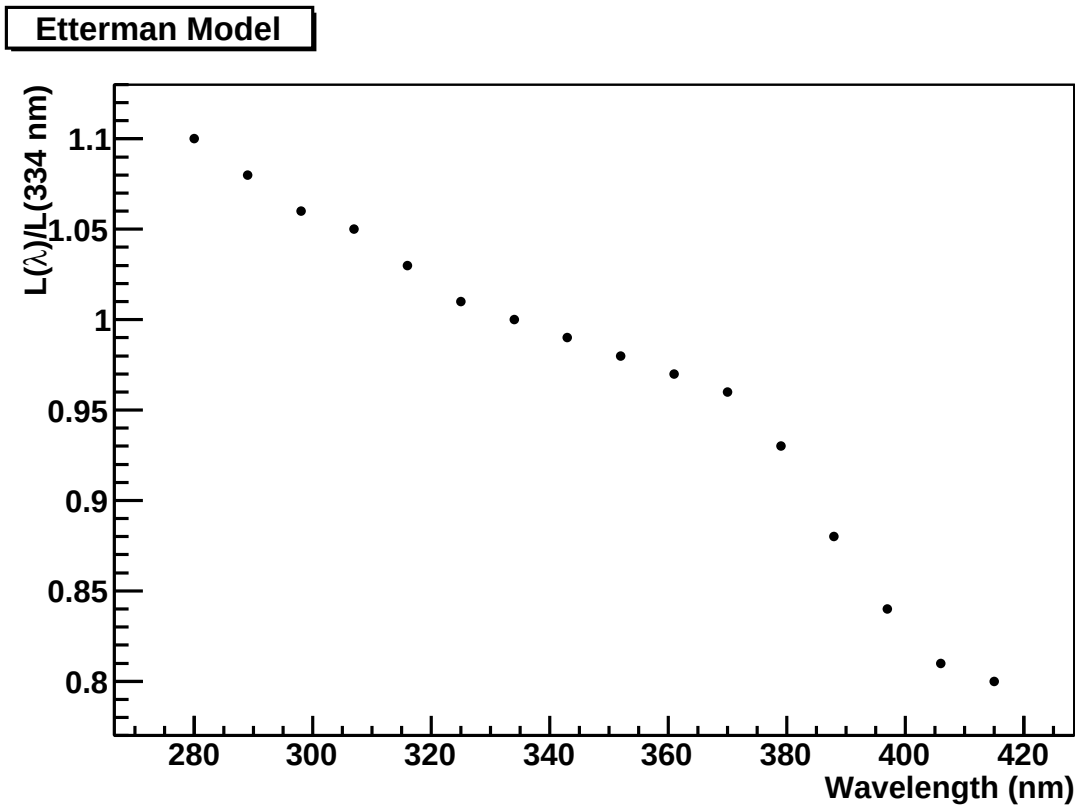

Figure 4.5: The Etterman model showing the aerosol extinction length as a function of the scattered light's wavelength.

laser light generated would balance the attenuation for any amount of aerosol content (see Figure 4.7). The angular distribution of the scattered light is given by

$$\frac{d^2N_\gamma}{dld\Omega} = -\left|\frac{dN_\gamma}{dl}\right| \times \phi(\theta) \tag{4.7}$$

where ϕ is the scattering phase function based on the Longtin desert aerosol model (see Figure 4.8) at 10 m/s wind speeds for 550 nm particulates [63]. The transmission factor of aerosol scattering for a flat-earth model is [95]

$$T_A = \exp\left[\frac{H_a}{L_M \cos\theta}\right]\left[e^{\frac{-h_1}{H_a}} - e^{\frac{-h_2}{H_a}}\right]. \tag{4.8}$$

4.2.4 Ozone Absorption

The amount of light the ozone in the atmosphere absorbs is given by

$$\frac{dN_\gamma}{dl} = -N_\gamma \rho_{O3}(h) A_{O3}(\lambda) \tag{4.9}$$

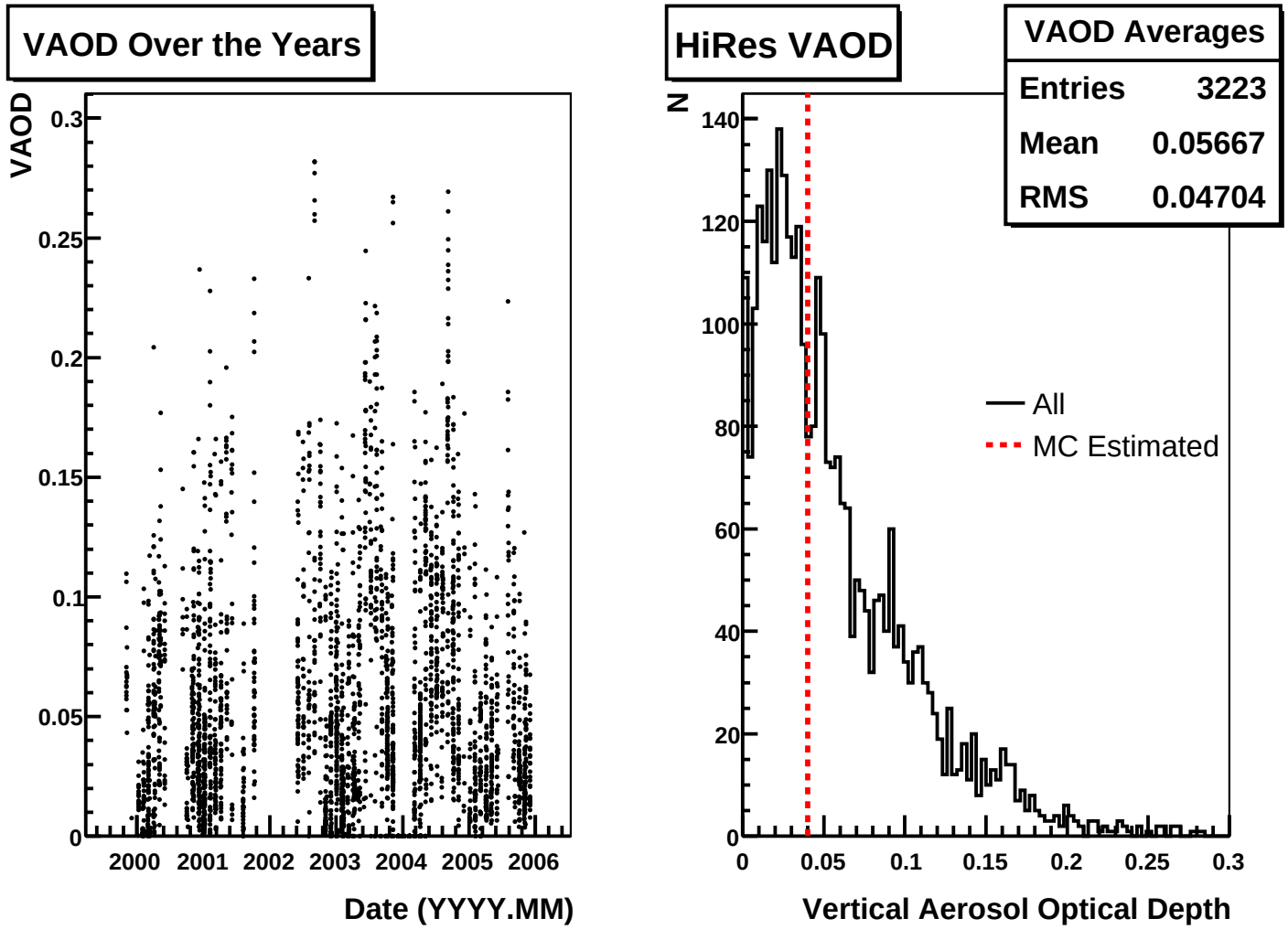

Figure 4.6: The average vertical aerosol optical depth around HiRes. The graph on the left shows monthly VAOD in which an annual trend can be seen. The plot on the right shows three different histograms showing all of the VAOD values with a vertical line showing the average value used for the HiRes-1 Monte Carlo.

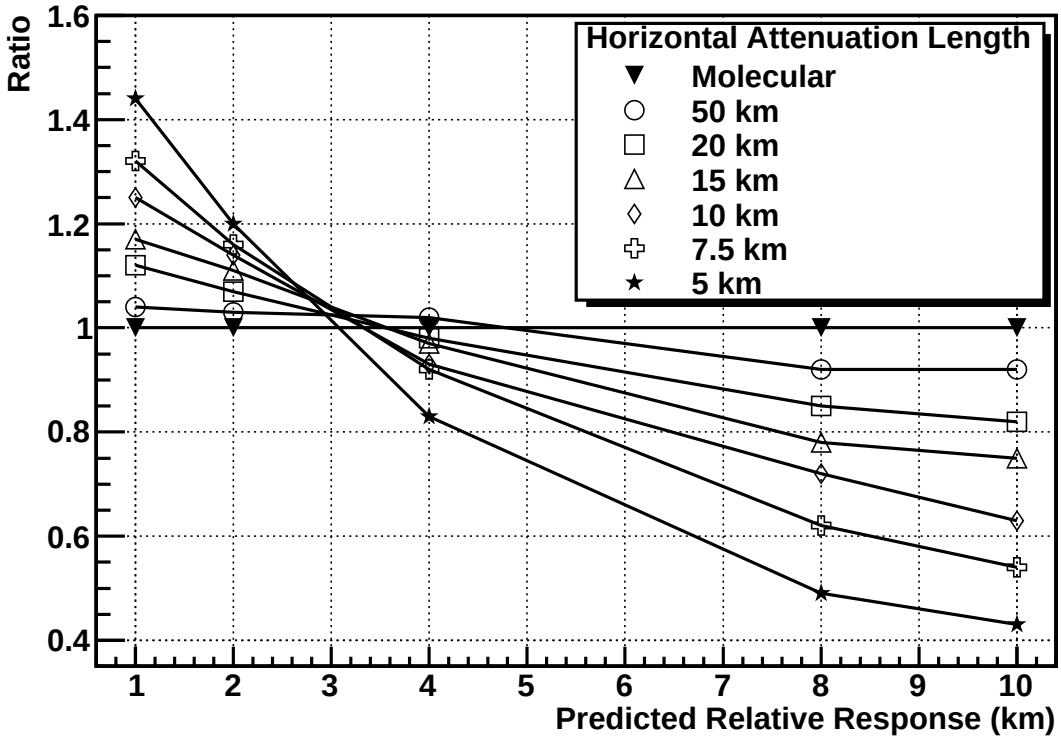

Figure 4.7: This predicted response of calibration lasers compared to aerosol content around HiRes.

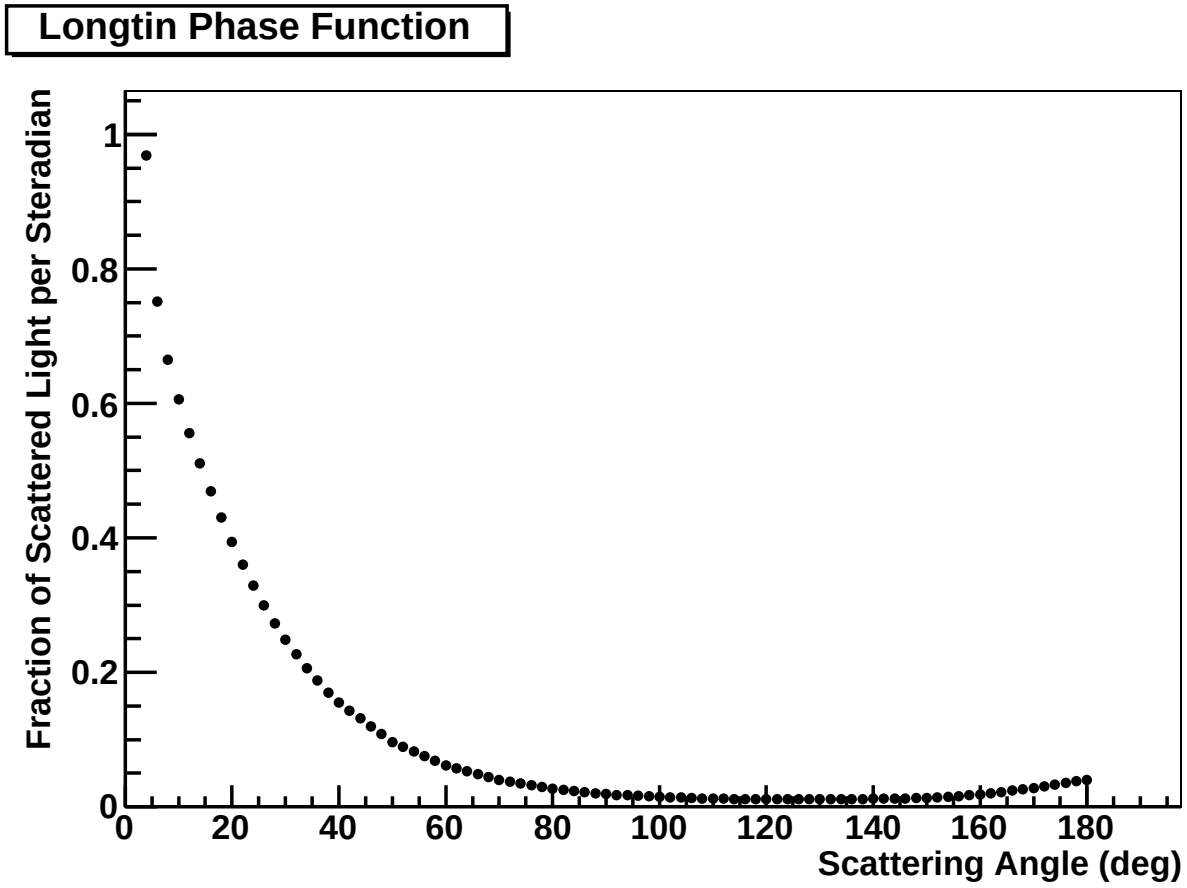

Figure 4.8: The Longtin phase function showing the amount of light scattered as a function of scattering angle.

where ρ_{O3} is the altitude-dependent ozone concentration (see Figure 4.9) and A_{O3} is a wavelength dependent attenuation coefficient (see Figure 4.10) [52]. The transmission factor of light passing through the ozone is

$$T_{O3} = \exp[-\Delta x_{O3} A_{O3}(\lambda)] \tag{4.10}$$

where Δx_{O3} is the integrated density over the slant depth. Ozone concentrations are significant only above 20 km in elevation and do not affect ground-based fluorescence detectors in any substantial way.

4.3 Simulation

The HiRes Monte Carlo uses showers simulated in CORSIKA [44] and fit to the Gaisser-Hillas function to obtain a shower library. The number of particles at each slant depth is then simulated with the appropriate number of photons generated isotropically and ray traced, with attenuation (see section 4.2), to the detector. The detector electron-

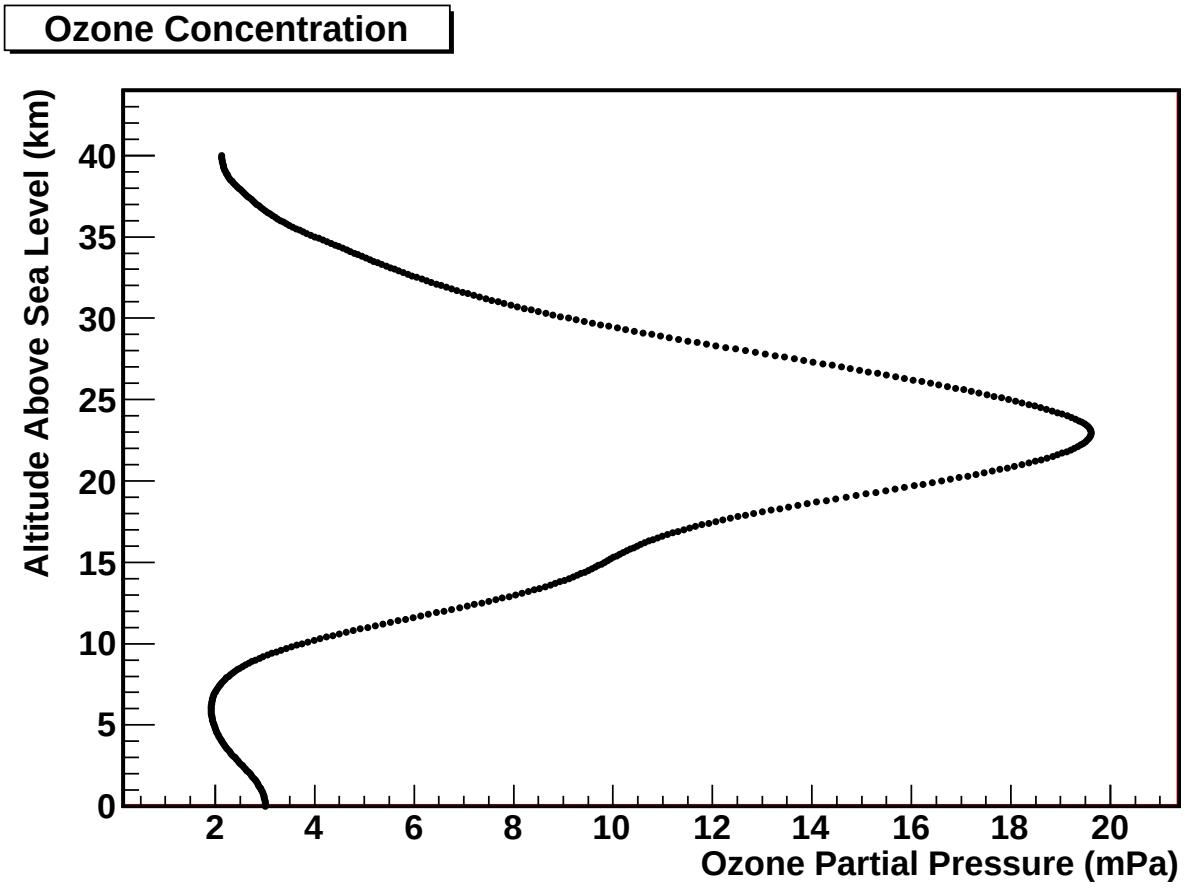

Figure 4.9: Ozone concentration as a function of altitude.

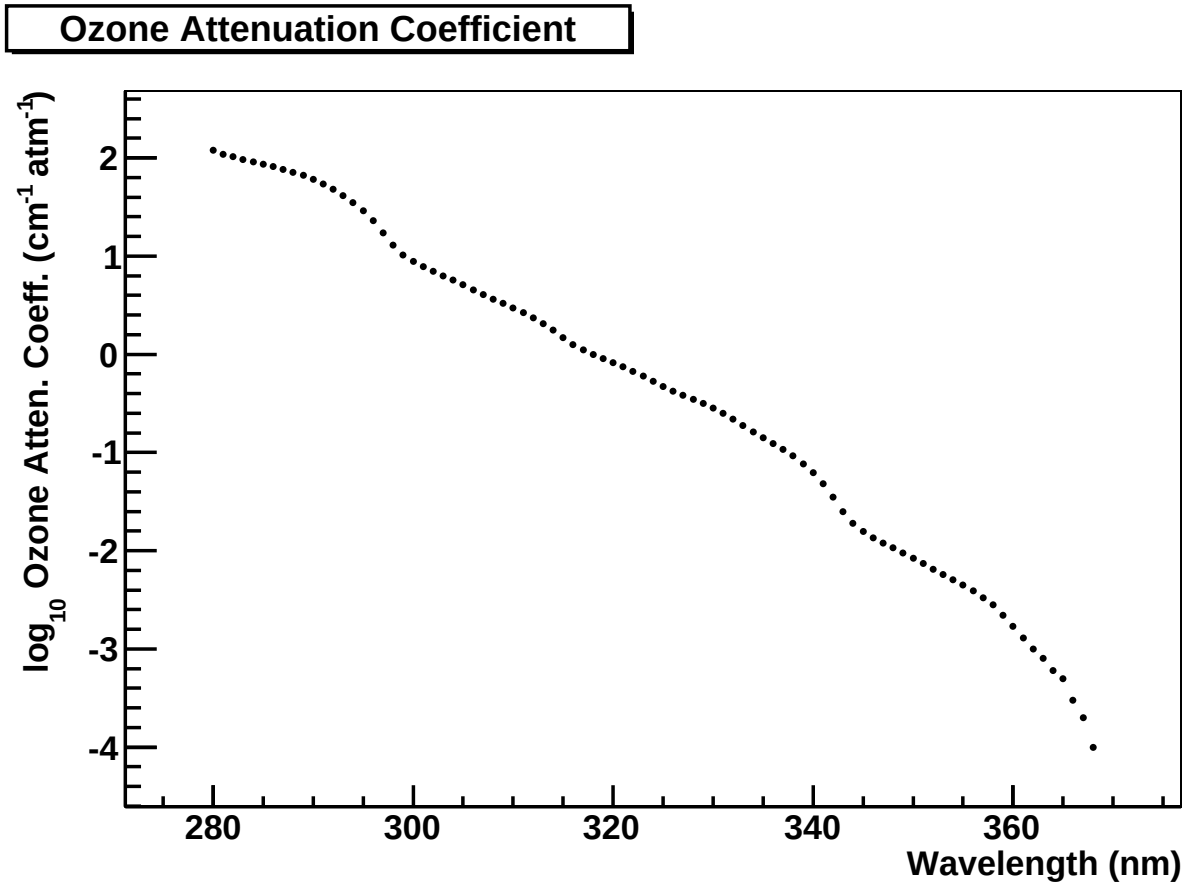

Figure 4.10: Ozone attenuation as a function of wavelength of the scattered light. Adapted from [52].

ics are also simulated to give an accurate representation of how the individual simulated showers are observed.

4.3.1 Shower Parameterization

Since most of the fluorescence light used in event detection is produced from the electromagnetic cascade, it is necessary to know how many electrons are produced along the shower track at any given moment. HiRes and Telescope Array use the parameterization given by the Gaisser-Hillas equation [36]

$$N_e(x) = N_{max} \times \left[\frac{x - X_0}{X_{max} - X_0}\right]^{\frac{X_{max}-X_0}{\lambda}} e^{\frac{X_{max}-x}{\lambda}} \tag{4.11}$$

where x is the slant depth into the atmosphere along the shower track, X_0 is the fit parameter associated with the depth inside the atmosphere of the first interaction, X_{max} is the depth of shower maximum (where $N_e = N_{max}$), and $\lambda = 60$ g/cm^2 is a scale constant for hadronic showers averaged from CORSIKA shower simulations (see Figure 4.11).

The shower depth X_{max} is dependent upon the initial interaction depth which in turn depends on the cross-section, σ_{p-air} for protons. The cross-section of larger nuclei can be estimated with the Glauber approximation [38]. This interaction usually happens within the first 70 g/cm^2 for UHE particles. The elongation rate (see equation 2.3) relates the depth of the shower maximum, X_{max}, to the energy of the shower [59]. When looking at Monte Carlo studies, it is seen that the spread in X_{max} is larger for protons than for iron since protons have a smaller cross-section, but the distributions of the two hadrons overlap and it becomes difficult to individually distinguish (see Figure 4.12). However, when looking at the mean values of all of the simulated showers, there is a clear distinction between the two primary particles for all energies (see Figure 2.4). When looking at the HiRes/MIA observed air showers (see Figure 2.4), a trend is seen showing a shift towards proton cosmic ray primaries as the energy of the cosmic ray increases.

The electrons not only increase in number along the shower track; there is an isotropic, transverse direction to the production of the electrons causing the shower to gradually expand as it penetrates farther into the atmosphere. This also allows for an isotropic angular distribution of fluorescence light defined by the equation

$$\frac{d^2N_\gamma}{dld\Omega} = \frac{YN_e}{4\pi} \tag{4.12}$$

where N_e is the number of electrons given by equation 4.11. HiRes and Telescope Array use the Nishimura-Kamata-Greisen (NKG) parametrization to describe the transverse

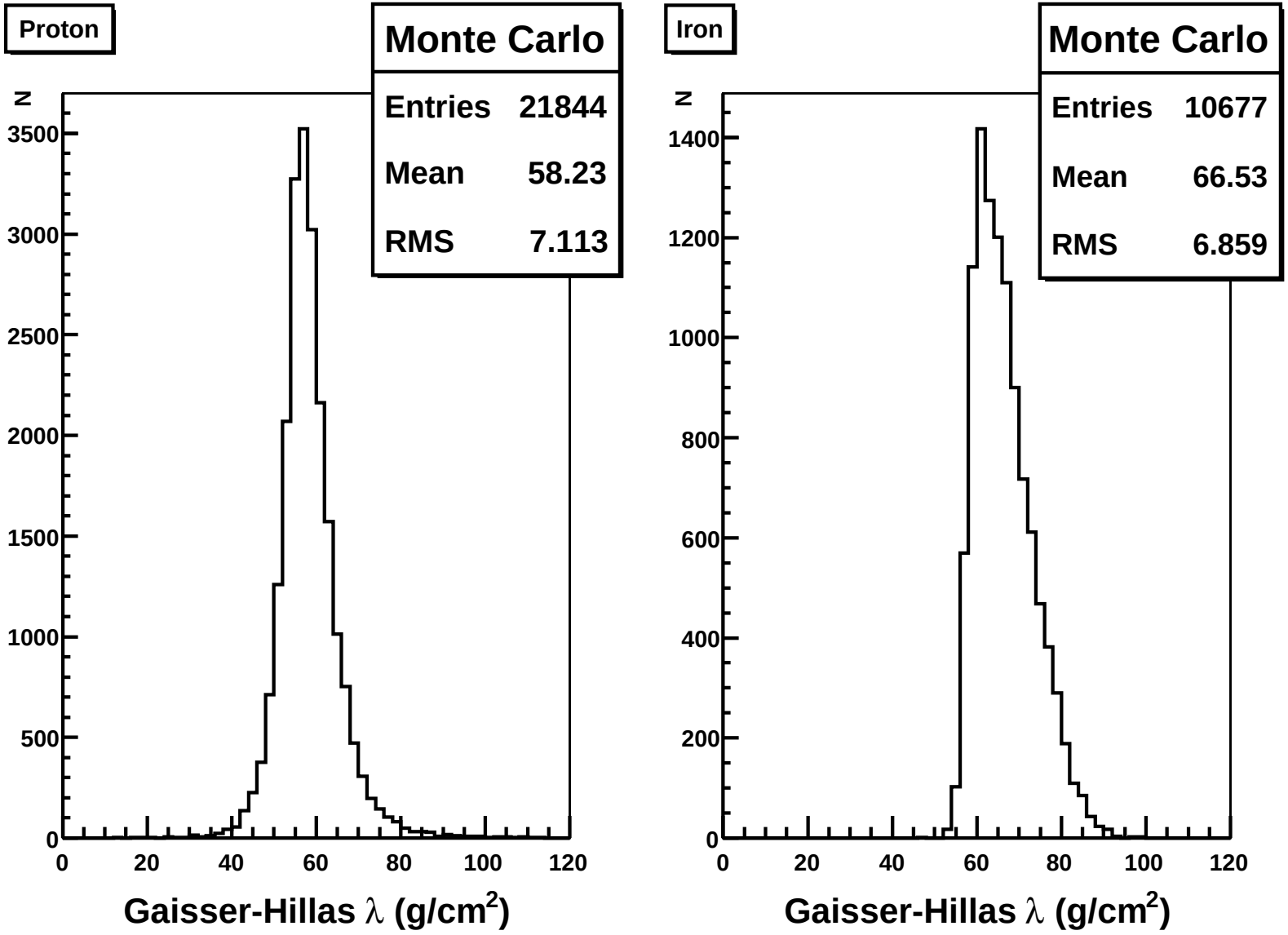

Figure 4.11: Gaisser-Hillas parameterization λ value averages.

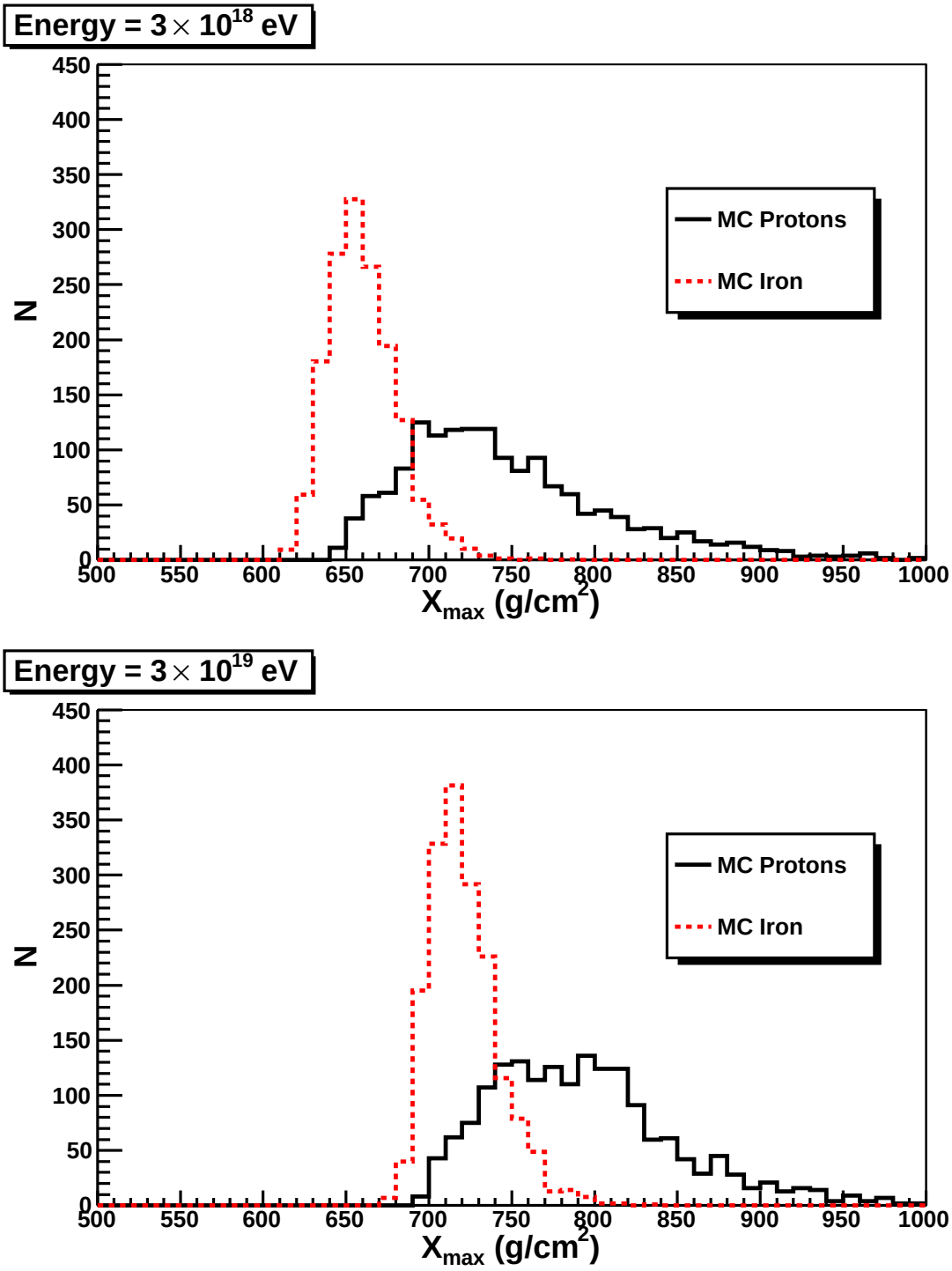

Figure 4.12: $\langle X_{max} \rangle$ depths versus energy for proton and iron cosmic ray shower simulations.

expansion [37]:

$$\rho(r) = \frac{N}{r^2} f\left(s, \frac{r}{r_M}\right) \tag{4.13}$$

where N is the total number of electrons within a radius, r, and f is the Nishimura-Kamata function

$$f\left(s, \frac{r}{r_M}\right) = \left(\frac{r}{r_M}\right)^{s-2} \left(1 + \frac{r}{r_M}\right)^{s-4.5} \frac{\Gamma(4.5-s)}{2\pi\Gamma(s)\Gamma(4.5-2s)} \tag{4.14}$$

with r_M being the Moliere radius for multiple scattering and

$$s = \frac{3}{1 + 2\frac{X_{max}}{x}} \tag{4.15}$$

being the shower age, where a shower age of 1 corresponds $x = X_{max}$.

4.3.2 Detector Optics

Using the information given in section 4.2, it is possible to predict the optical response of the detector. The first step is to determine the amount of light that would actually reach the detector. This is performed by: 1) quantifying the amount of light produced in each segment, δl, of the shower track and 2) calculating the amount of light that actually reaches the photomultiplier tubes (PMTs) after they are reflected off of the mirror. (Detector component information can be found in Chapters 5 and 6.)

The first step is to determine the number of photons produced by multiplying the above angular distributions (equations 4.12, 4.3, and 4.7) by δl. The resulting expressions are then used to calculate the number of photo-electrons (*pe*) produced in each track segment and collected by a disk mirror in the equation

$$\begin{aligned} N_{pe} \;=\; & \sum_{\lambda=300}^{420} \left[\frac{dN_\gamma}{d\Omega(\lambda,\theta_e)}|_{fluor} + \frac{dN_\gamma}{d\Omega(\lambda,\theta_e)}|_{Ray} + \frac{dN_\gamma}{d\Omega(\lambda,\theta_e)}|_{Mie} \right] \times \\ & T_R(\lambda)\; T_A(\lambda)\; T_{O3}(\lambda)\; T_{UV}(\lambda)\; R_m\; QE(\lambda)\; \delta\Omega. \end{aligned} \tag{4.16}$$

The summation over λ is performed using 1 nm steps over the spectrum (see Figure 3.8) and θ_e is the light emission angle. The labels "fluor," "Ray," and "Mie" represent the fluorescent and Rayleigh- and Mie-scattered Čerenkov light, respectively. The above-mentioned transmission factors along with the UV filter (see Chapter 5) transmission factor, the mirror reflectivity, R_m, and the PMT quantum efficiency, QE, are also taken into account to determine the number of *pe* per unit solid angle, $\delta\Omega$.

For each *pe* created, an initial position was determined using equations 4.11 and 4.13. From there, the *pe* is ray-traced to see if it hit a cloverleaf-shaped mirror (representative

of the HiRes mirrors) and reflected to the PMT camera, hit the back of the camera, or completely missed. If it did manage to hit the viewing plane of the camera, the landing position was fluctuated with a Gaussian uncertainty of $\sigma = 0.25\ cm$ to account for the mirror's morphological imperfection. If the *pe* still landed in the PMT, it was weighted by the PMT response profile (see Figure 4.13) to determine the signal contribution.

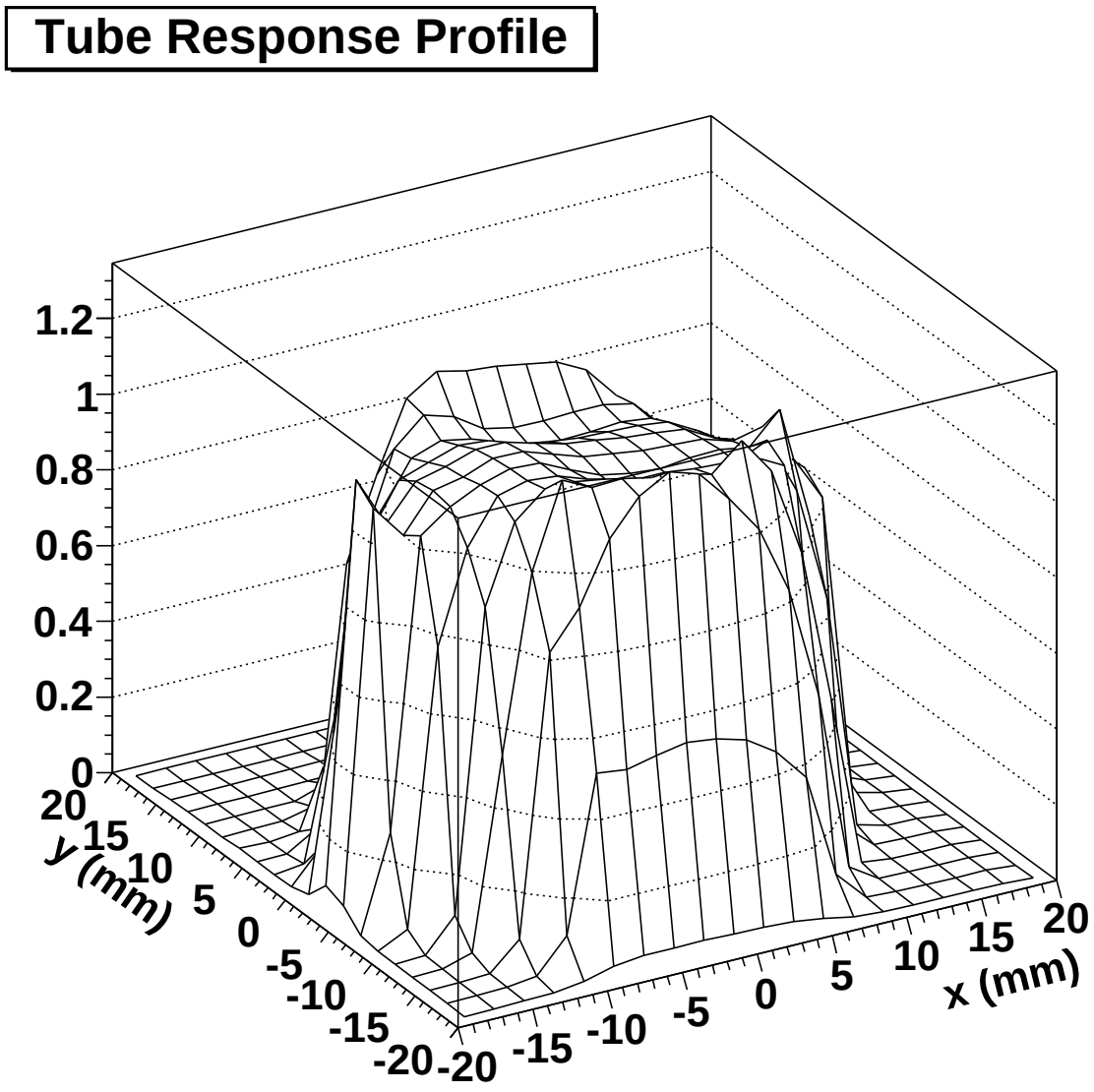

Figure 4.13: PMT response profile. This profile shows the response of an average photomultiplier tube used in the HiRes detectors.

4.3.3 Detector Electronics

Detector electronics are simulated to mimic the sample-and-hold properties and the trigger requirements implemented in the hardware. First, assuming the shower travels at the speed of light, a transit time for the event to cross the mirror view, T_{geo}, is calculated from the geometry of the shower. A period of $T_{trig} = 25\ \mu s$ is added before the actual trigger to account for noise triggering before the event trigger is saved. Finally, an interval of $T_{HO} = 50\ \mu s$ is added to simulate the hold-off delay gate implemented to allow all tubes in the mirror to be recorded as the same event.

The total time interval $T_{tot} = T_{trig} + T_{geo} + T_{HO}$ is divided into 20 ns bins and a sky background with a Poisson distribution with a mean of 40 $pe/\mu s$ [6] is added across the bins before the ray-traced tube signals are distributed to the event. The full signals are passed through emulated PMT, preamplifier, and electronics gains; a low-pass filter; trigger and integration circuitry; and compared to an average 15,000 A/W per 700 mV gain-versus-threshold (for HiRes-1). This value was different for Middle Drum (see section 11.1.3). The tube signals are then integrated over the hardware-defined 5.6 μs window and digitized into equivalent TDC and QDC values.

4.4 Fluorescence Reconstruction

Event reconstruction is performed similarly for both observational data and the Monte Carlo simulations. This is a two-step process where, first, the geometry of the shower is determined using the timing and plane-geometry and, second, the profile is determined from the number of photons observed at each geometrical slant-depth. Two main differences are applied to the reconstruction compared to the simulation to minimize computation time: using half as many track segments and 5 nm wavelength steps. Both of these resulted in a 1% or less effect on the final reconstructed values [6]. Seven parameters are needed in order to obtain an energy estimate of the shower. Three of these are used in the Gaisser-Hillas equation (see equation 4.11) to parameterize the shower profile. The other four are independent values that define the geometry of the shower with respect to the center of the detector.

The geometry of the shower is first found within a shower-detector (SD) plane. This is formed between two of the independent parameters: the axis of the shower and the center of the detector. The remaining two parameters are the impact parameter, R_p, or the point of closest approach, and the incline angle of the shower away from the horizontal, ψ (see Figure 4.14). The SD plane is determined from the PMT pointing directions by minimizing the chi-squared function

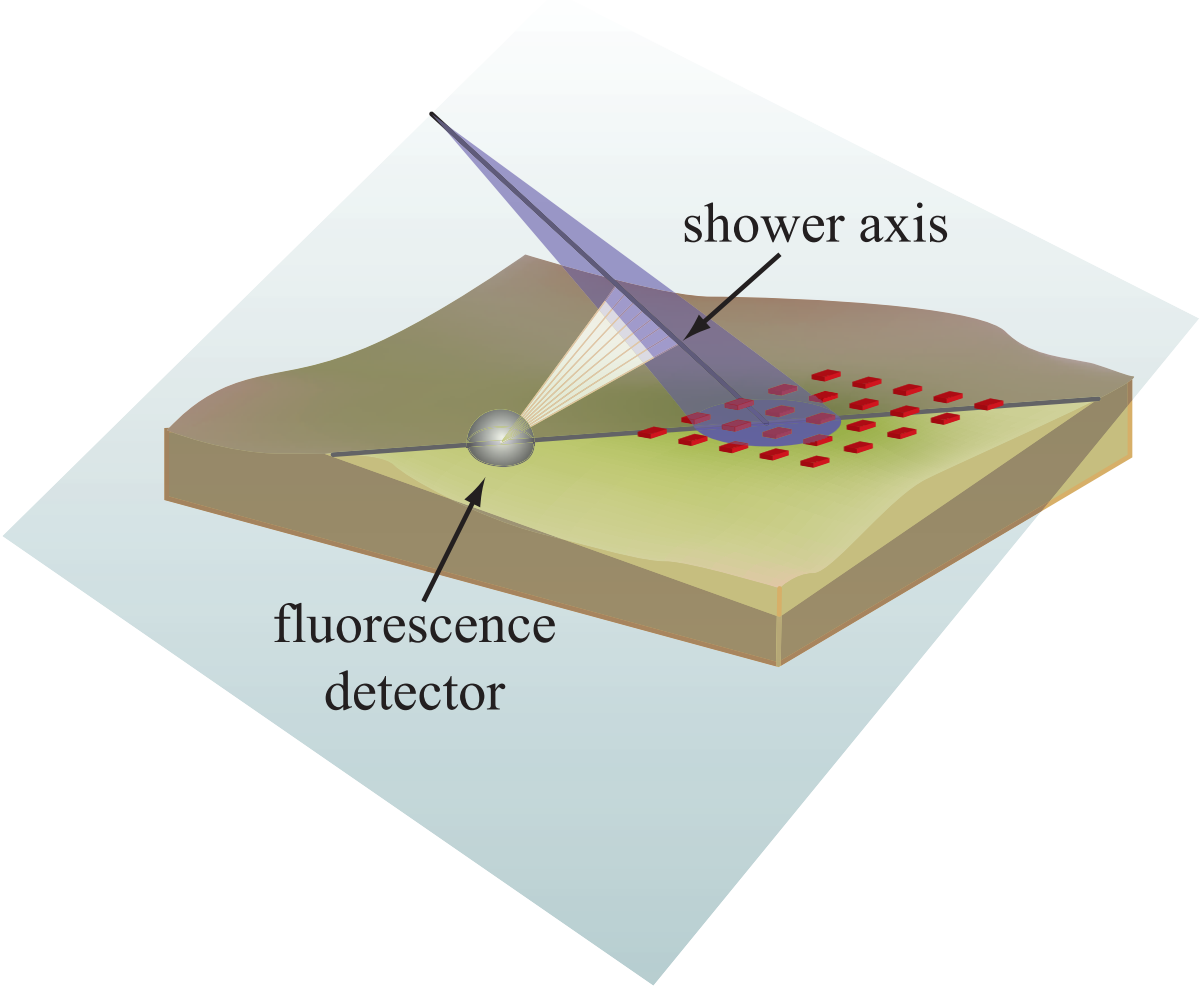

Figure 4.14: This image characterizes the observation of the shower with respect to the detector.

$$\chi^2 = \sum_i \frac{[(\hat{n} \cdot \hat{n_i})^2 \cdot w_i]}{\sigma_i^2} \tag{4.17}$$

where the sum is performed on the triggered tubes; $\hat{n}$ is the plane normal vector; $\hat{n_i}$ is the pointing vector of the PMT's viewing direction weighted by the *pe*-signal, w_i, of the tube; and σ is a 1° resolution applied to all tubes.

The impact parameter and incline angle are determined using tube trigger times fitted within the SD plane (see Figure 4.15). The time required for the shower to be observed within each tube, i, at time t_i at its viewing angle, χ_i, is given by

$$t_i = t_0 + \frac{R_p}{c} \tan\left(\frac{\pi - \psi - \chi_i}{2}\right) \tag{4.18}$$

where t_0 is the time at which the shower is at R_p. The timing fit to find R_p and ψ is then performed using the equation

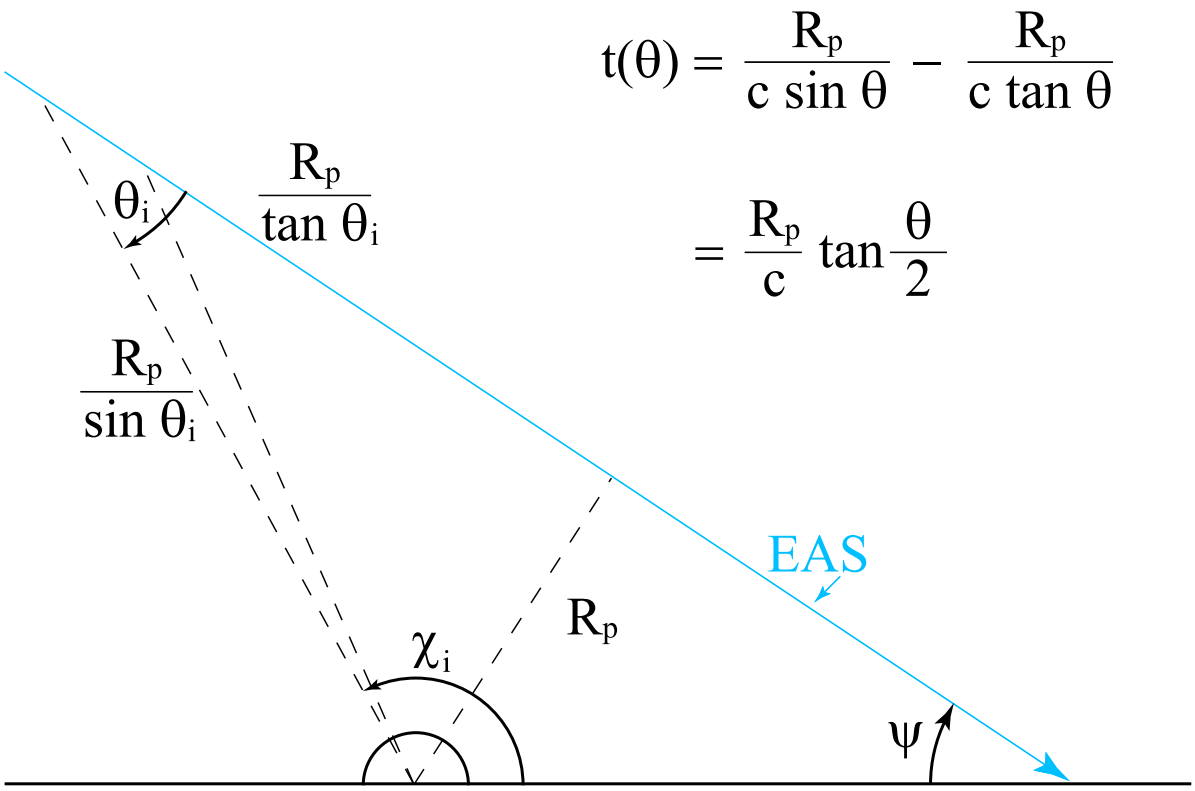

Figure 4.15: The variables calculated in track-geometry reconstruction.

$$\chi^2_{time} = \sum_i \frac{1}{\sigma_i^2} \left\{ t_i - \left[t_0 + \left(\frac{R_p}{c} \right) \tan \left(\frac{\pi - \psi - \chi_i}{2} \right) \right] \right\}^2 \tag{4.19}$$

with an error $\sigma_i = (500/\sqrt{S_i})$ ns where S_i is the tube signal in *pe* [6].

Once the geometry of the shower is determined, it is divided into bins based on the calculated slant-depth for each tube. These depths are used in conjunction with the calibrated number of photons (*npe*) to determine the best fit to the Gaisser-Hillas parameterization (see equation 4.11). The HiRes reconstruction utilizes an inverse-Monte Carlo routine to determine this profile fit. The reconstruction program searches the shower library (see section 4.3.1) for matching X_{max} simulated showers and determines the *npe* for each slant depth along the determined geometrical track. The observed tube signals, S_i^o, are then compared to the emulated tube signals, S_i^e. The quality of the fit is then obtained using the equation

$$\chi^2_{profile} = \sum_i \left(\frac{1}{\sigma_i^2} \right) (S_i^o - S_i^e)^2 \tag{4.20}$$

where, like the timing fit, the sum is performed over the tubes deemed to have a "good" geometry. The error, σ_i^2, is estimated to be $S_i^o + 200$, which is obtained through adding in quadrature the sky noise and electronic fluctuations. Details of the reconstruction codes used in HiRes-1 and TAMD analysis can be found in Chapters 7 and 8.

CHAPTER 5

HIGH RESOLUTION FLY'S EYE EXPERIMENT

This chapter describes the High Resolution Fly's Eye experiment. This project consisted of two fluorescence sites. However, only the data from HiRes-1 were analyzed for this dissertation. HiRes-2 will be referenced only where necessary.

5.1 Detectors

The High Resolution Fly's Eye (HiRes) was located $\sim$ 100 km southwest of Salt Lake City, Utah on the U.S. Army's Dugway Proving Ground (see Figure 5.1). It consisted of two detector sites located 12.6 km apart on Little Granite Mountain (HiRes-1), the site of the original University of Utah's Fly's Eye experiment, and Camel's Back Ridge (HiRes-2). The positions of these two sites were optimized for studying cosmic ray showers with energies above $10^{18.5}$ eV in stereoscopic mode.

Each detector operated independently and the data could then be analyzed in either monocular mode for each site or in a combined stereo mode. The studies in this dissertation are performed using HiRes-1 monocular data and so HiRes-2 equipment will only be described in this chapter as a comparison to that of HiRes-1.

5.1.1 HiRes Overview

The Western Utah Desert was chosen as the site of the HiRes experiment for two main reasons. First, it was the location of the original Fly's Eye experiment - the predecessor of HiRes which ran between 1981 and 1992 [15] - where a significant investment in infrastructure (i.e., the roads and power lines) was already in place. The second reason is that the atmospheric quality of the region is ideal for fluorescence detectors (see Section 4.2). The Utahan atmosphere has $\sim$ 60% less aerosol than other U.S. desert regions, resulting in less attenuation of the UV light produced in the showers, and maximizing the observational aperture of the detectors.

Figure 5.1: This figure shows the location of HiRes relative to Salt Lake City, UT.

After the Fly's Eye experiment ended in 1993 there was a period of three years of prototype development (HiRes-proto) that tested 14, 2-meter diameter mirrors and smaller, 4 cm photomultiplier tubes (PMTs) using sample-and-hold read-out electronics similar to that used by the Fly's Eye. These were placed on Little Granite Mountain (site of the original Fly's Eye I) and used in conjunction with (a) four additional, slightly different telescopes (see section 5.1.2) on Camel's Back Ridge and (b) the CASA-MIA detectors located around the Fly's Eye II site, 3.4 km northeast of Little Granite Mountain.

The results of these tests validated the suitability of the optical design of the mirror and PMT cameras for the telescopes. Further information can be found in Bird [20]. In addition, cooperation between the HiRes and CASA-MIA groups led to the world's first hybrid detector, where the timing information from MIA was included in the geometrical fit of HiRes-proto, and the muon density information provided by MIA was also analyzed as an orthogonal composition measurement. Results on the energy spectrum and composition of UHECRs in the 10^{17-18} eV decade in energy were obtained [98] [103] [11].

In September, 1996, the HiRes-proto detector ended operations and the 18 prototype telescopes were reconfigured at the HiRes-1 site. In May, 1997, the first data were taken with the new HiRes-1 detector using the 14 prototype units. Between then and March, 1998 21 mirrors were installed and collecting data. Table 5.1 describes the final numbering system of the mirrors, for both HiRes-1 and HiRes-proto configurations, as well as deployment dates and PMT type. This information is included here primarily as documentation for the HiRes and TA collaborators as a cross-reference between the two experiments. In October, 1999, the first HiRes-2 detectors were installed at Camel's Back Mountain and each detector site was referred to as an "eye."

In order to obtain the largest possible aperture for energies above 10^{19} eV, the telescopes were set up in rings covering the full azimuth and 14° in elevation angle. HiRes-1 consisted of one ring between 3° and 17° above the horizon. HiRes-2 had 42 mirrors distributed in two rings; the lower covering 3° and 17° and the higher covering 17° and 31° in elevation angle. The difference in elevation coverage resulted in the two detectors having different low-energy thresholds (see Figure 5.2): HiRes-1 could only make reliable measurements down to $10^{18.5}$ eV, while HiRes-2 was able to see down below $10^{17.5}$ eV. The overlapping fiducial volumes were optimized for stereo observation at energies above $10^{18.5}$ eV (see Figure 5.3).

By the end of the experiment, HiRes-1 consisted of 22 telescopes laid out around the mountaintop (see Figure 5.4) with relative viewing directions shown in Figure 5.5. Two of these were installed in October, 2005 and will be discussed in section 5.3. Telescope 17 was decommissioned in 2002 because the post-9/11 personnel restrictions at Dugway had forced the experiment into remote operations. Only HiRes-2 was allowed to have operators and the building doors in which HiRes-1's telescope 17 was located could not

Table 5.1: This shows the time table of when the HiRes-1 detector units were deployed as well as what version of electronics was used and the type of photomultiplier tube in each cluster. Additionally it relates the units to those from the HiRes-prototype detector phase.

HiRes#	Start Date	End Date	Proto Rack#	Proto Cluster#	PMT Type	Elect. Version	Pins	Tube Size
1	May-97	Apr-06	1	8	EMI	3	-	-
2	May-97	Apr-06	10	3	Phillips	3	10	1079
3	May-97	Apr-06	4	4	EMI	3	-	-
4	May-97	Apr-06	2	2	EMI	3	-	-
5	May-97	Apr-06	9	10	Phillips	3	10	1079
6	May-97	Apr-06	7	6	EMI	3	-	-
7	May-97	Apr-06	8	12	Phillips	3	10	1079
8	May-97	Apr-06	6	1	Phillips	3	10	1079
9	May-97	Apr-06	5	13	EMI	3	-	-
10	May-97	Apr-06	12	11	Phillips	3	10	1079
11	May-97	Apr-06	13	7	EMI	3	-	-
12	May-97	Apr-06	3	14	Phillips	3	10	1079
13	May-97	Apr-06	14	9	Phillips	3	10	1079
14	May-97	Apr-06	11	5	Phillips	3	10	1079
15	Jun-97	Apr-06	HR2-3	HR2-3	Phillips	4	-	-
16	Jun-97	Apr-06	HR2-2	HR2-2	Phillips	4	-	-
17	Apr-98	Jan-02	New	New	Phillips	R3/C4	-	-
18	-	-	HR2-4	HR2-4	Phillips	4	-	-
19	Apr-98	Apr-06	New	New	Phillips	4	-	-
20	Jun-97	Apr-06	HR2-1	HR2-1	Phillips	4	-	-
21	Mar-98	Apr-06	New	New	Phillips	4	-	-
22	Mar-98	Apr-06	New	New	Phillips	4	-	-
23	-	-	-	-	Phillips	4	-	-
24	Oct-05	Apr-06	HR1-17	HR1-17	Phillips	R3/C4	-	-
25	Oct-05	Apr-06	HR1-18	HR1-18	Phillips	4	-	-

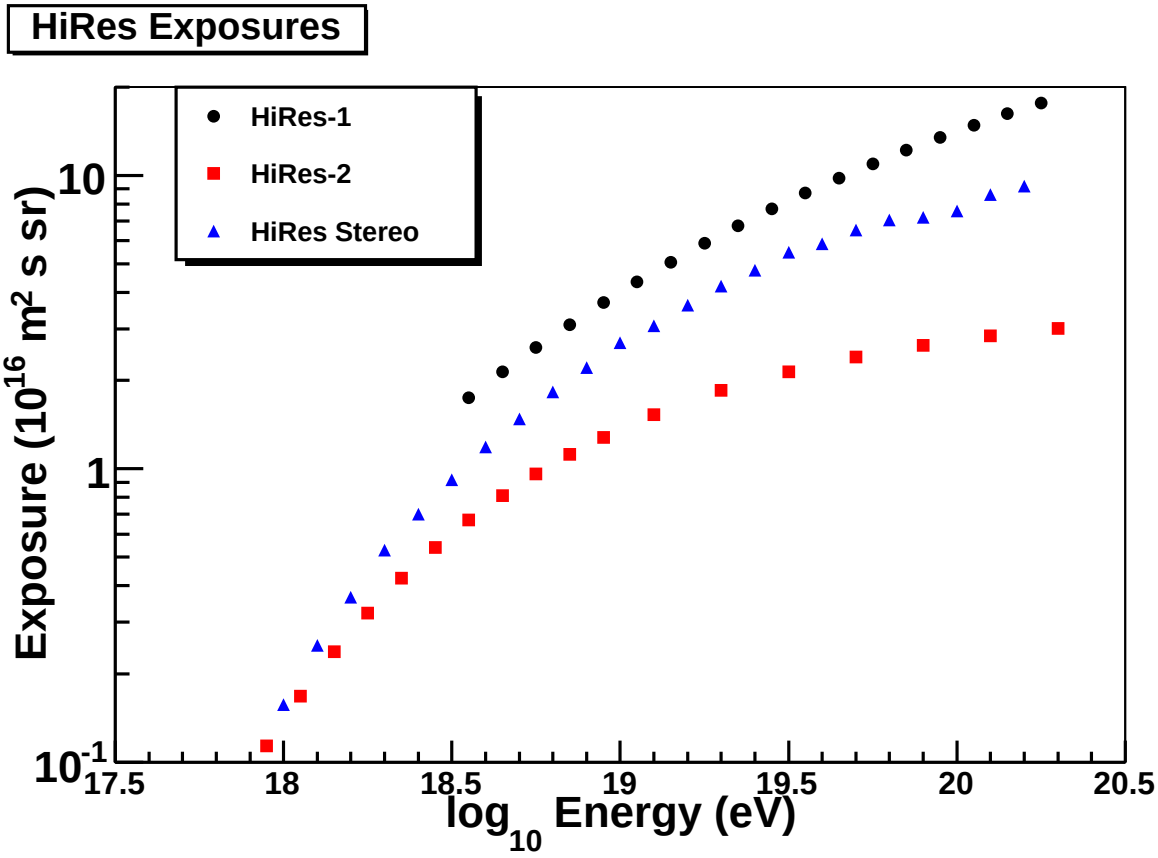

Figure 5.2: The exposures of the different HiRes detector configurations.

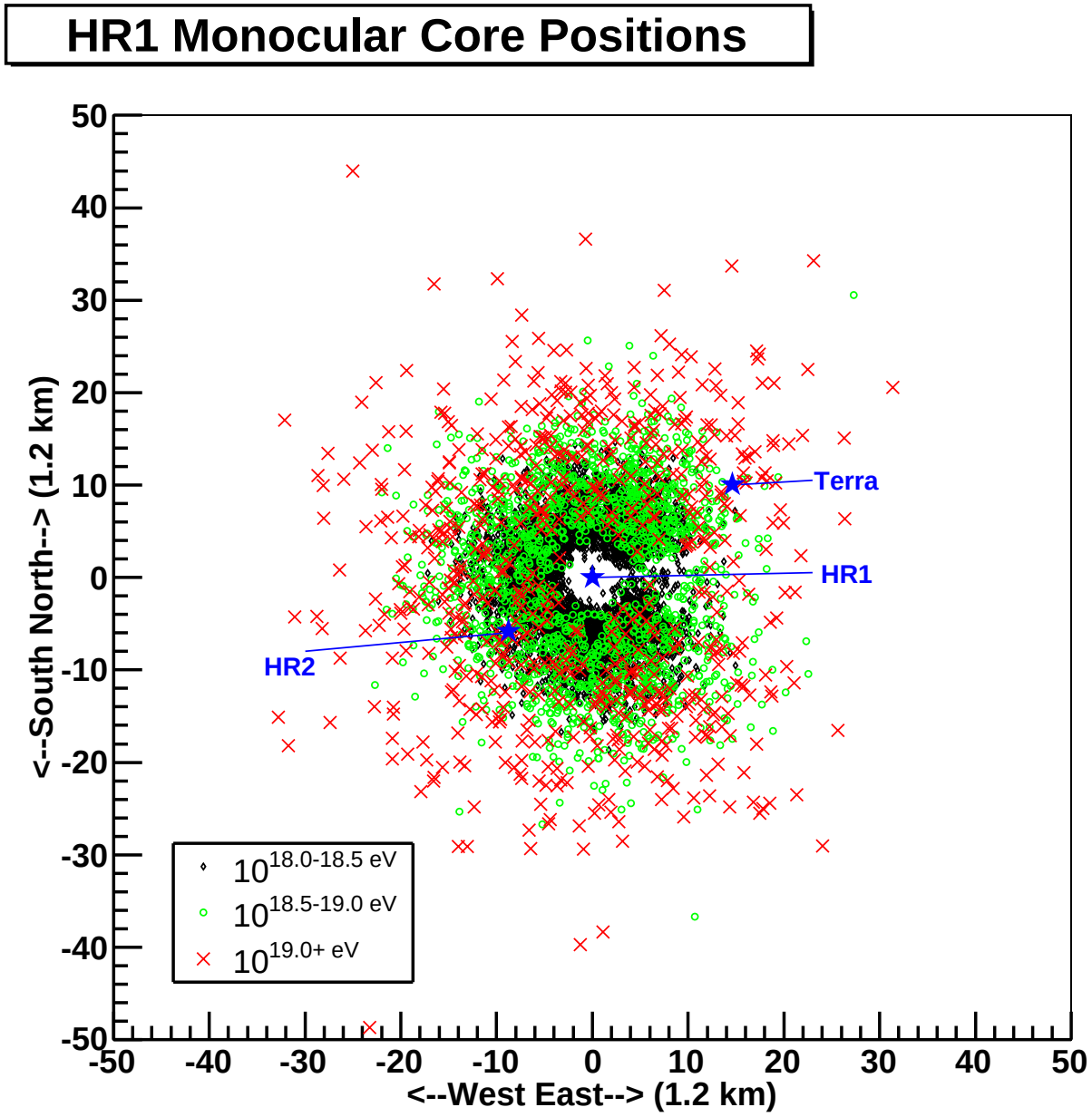

Figure 5.3: HiRes-1 AlphaProc reconstructed core locations. The lack of events to the east shows where telescopes were not pointing.

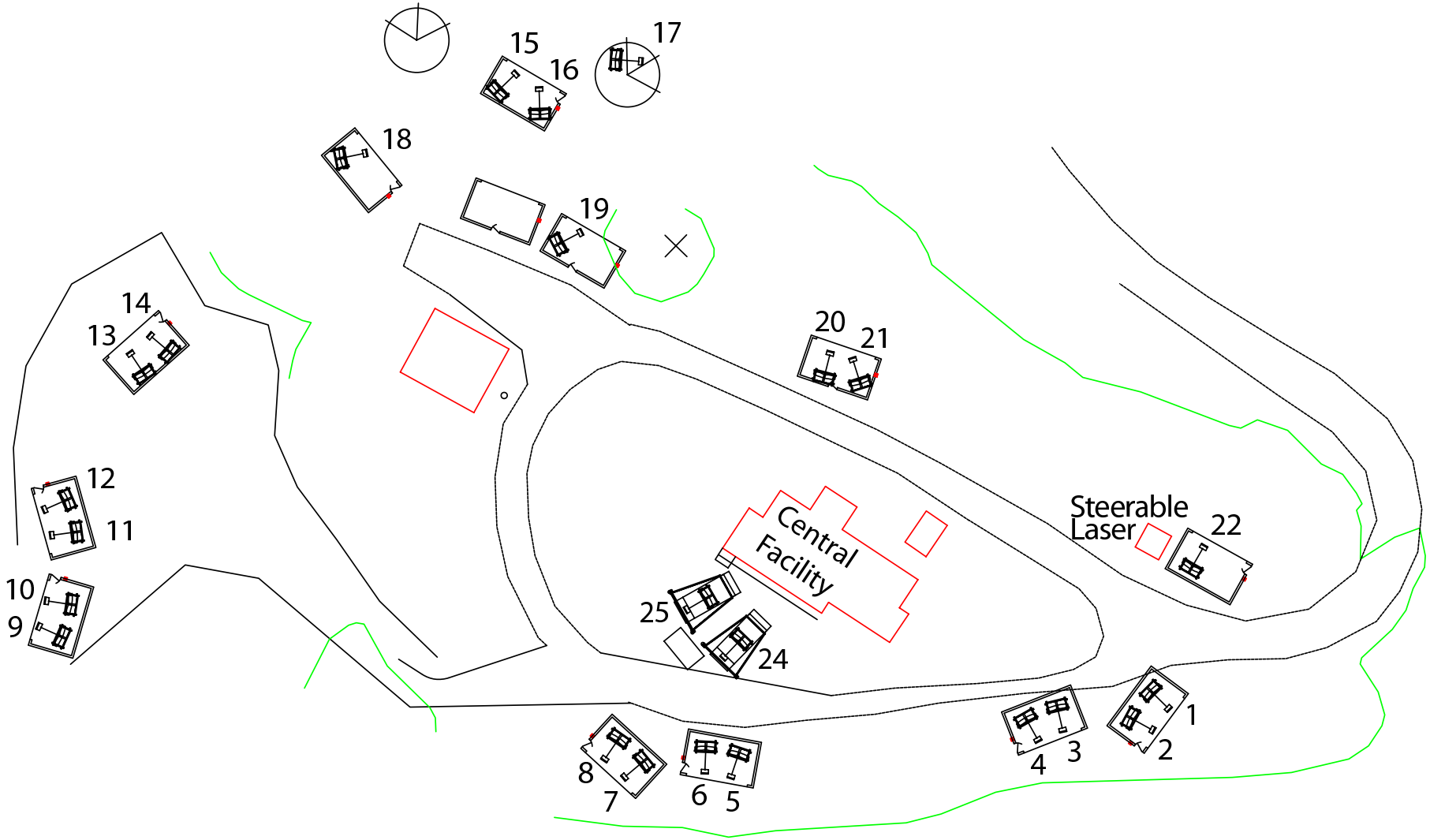

Figure 5.4: These were the final locations of each HiRes-1 telescope unit located around Little Granite Mountain.

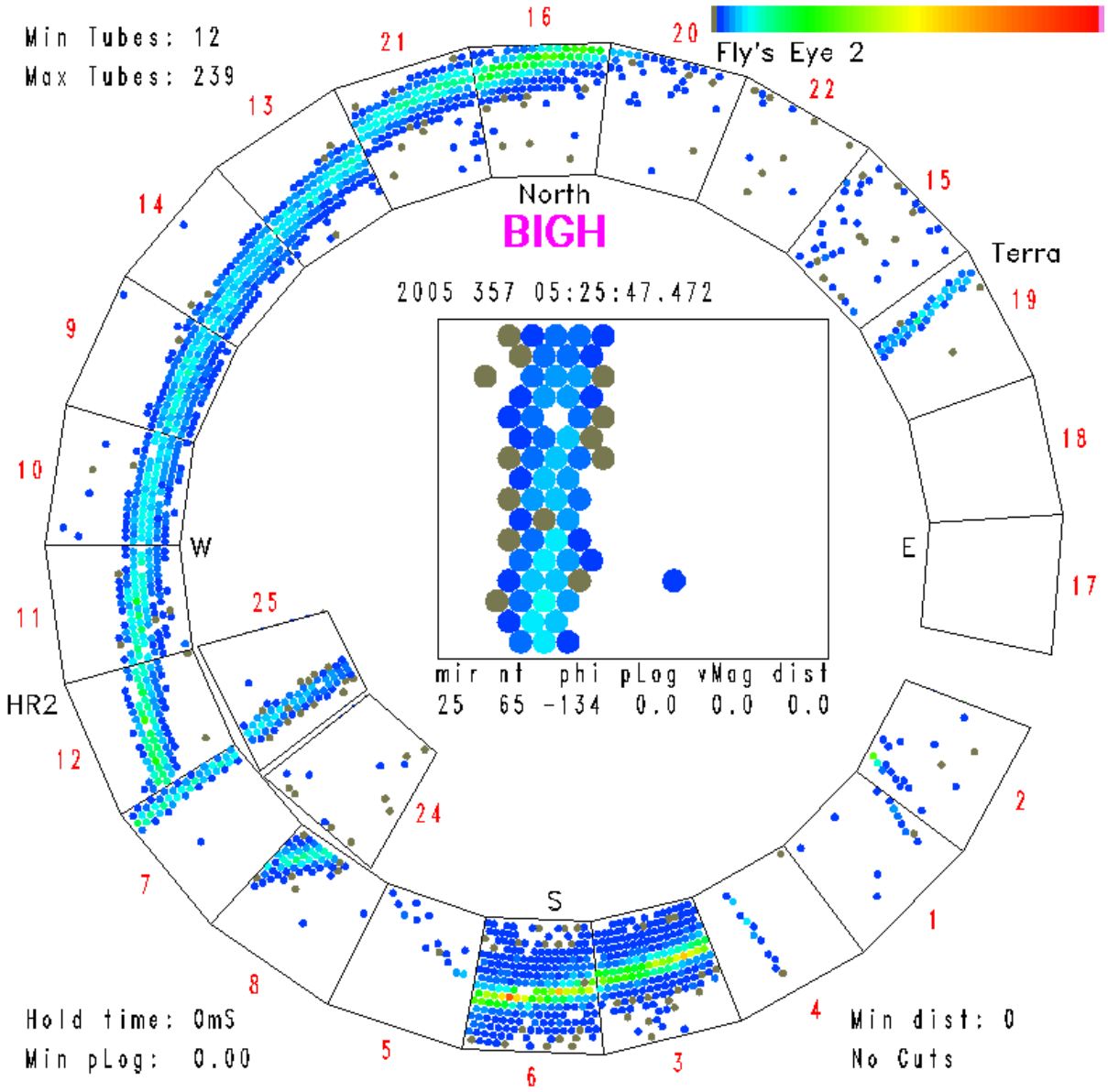

Figure 5.5: This was the event display used during data collection run-time.

be made to open and close reliably via remote control. Telescope 18 was never installed at HiRes-1, but was instead used for other prototype experiments [83].

A schematic of the entire HiRes-1 site can be seen in Figure 5.6. The GPS based Central-Timing (CT) crate, connected to each computer through timing cables, is located inside the central facility. The central facility also houses the main data acquisition (DAQ) computer that connects to each mirror through ethernet cables. The data is then extracted from this computer to be stored back at the University of Utah. The DAQ can also be run by remote desktop session (VNC [62]) software from HiRes-2, the University of Utah, or other collaborating institutions.

5.1.2 HiRes Telescopes

Each telescope consisted of three main components: a mirror, a photomultiplier tube (PMT) camera, and read-out electronics. Since these were either used in or based on the HiRes prototype detectors, the following will be a summary of the equipment used there. A more detailed description can be found by Kidd [56].

5.1.2.1 Mirrors

HiRes-1 consisted of 20 telescopes in a single ring, pointing between 3° and 17° above the horizon. This lower angle limit allowed for ambient light from ground lights to have minimal effects on the data collected. Combined, they cover almost the full 360° azimuth. Each 5.1 m^2 spherical mirror was constructed from four aluminum-plated glass segments in a clover-leaf shape. Each segment can be adjusted to focus directly to the center of the camera. The PMT camera and stand both obscure portions of the mirror making the unobstructed collection area 3.72 m^2. Operating in the open desert air, dust collected on the mirror surface and reduced the effective reflectivity (see Figure 5.7) to $\sim 80\%$ at the peak wavelength of fluorescence emission.

5.1.2.2 Cameras

A PMT camera of 256 hexagonally close-packed PMTs is situated in front of each mirror at a distance of 0.485 times the radius of curvature (474 cm) of the mirror from its center. This distance is smaller than the optimal focal length for on-axis observation of a spherical mirror. However, it allows for an optically uniform image spot size that is still significantly smaller than the pixel (PMT) size, as determined by ray-tracing studies. Each tube covers approximately $1° \times 1°$ in this placement, giving a total viewing area of

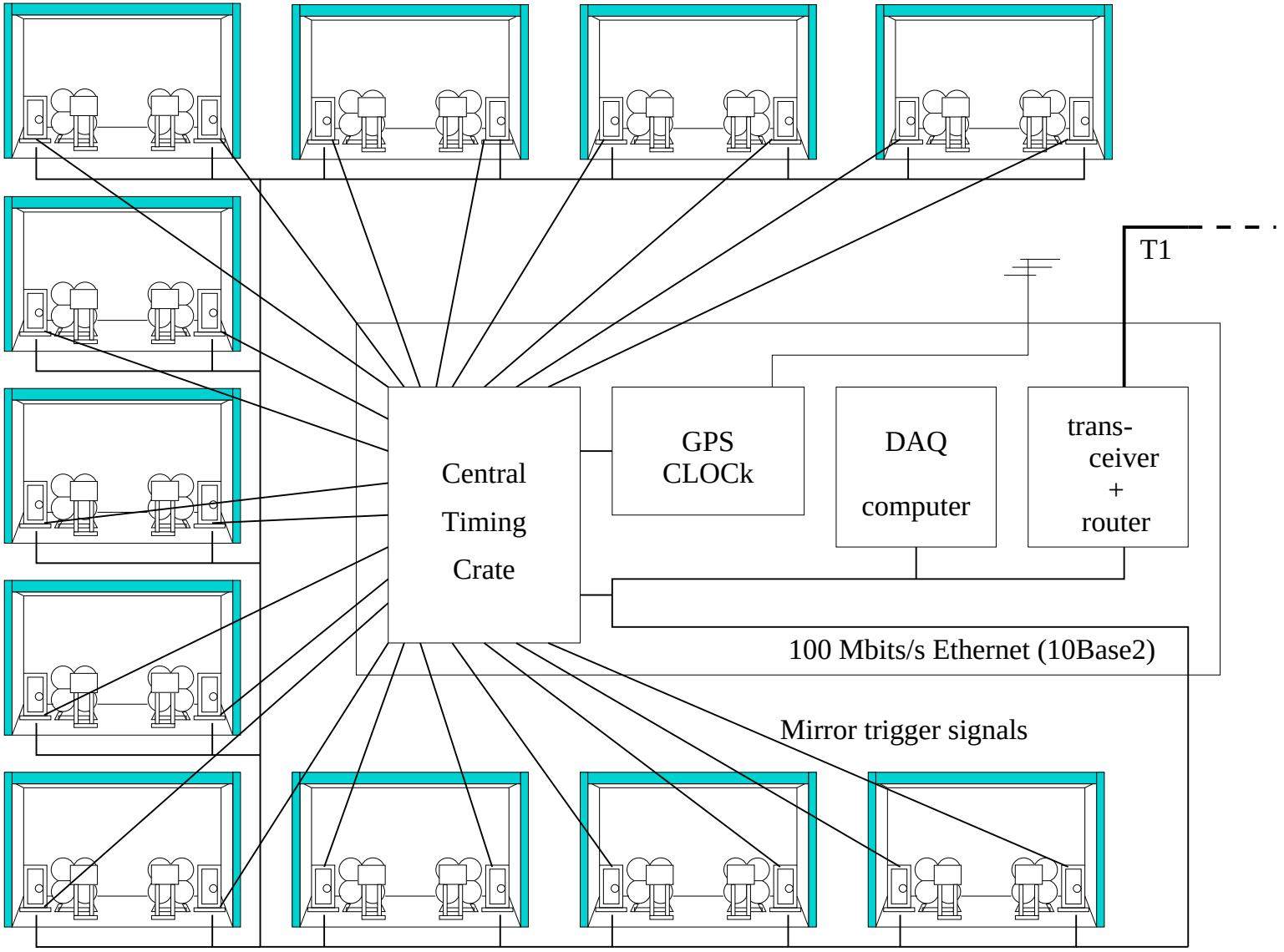

Figure 5.6: HiRes-1 detector schematic.

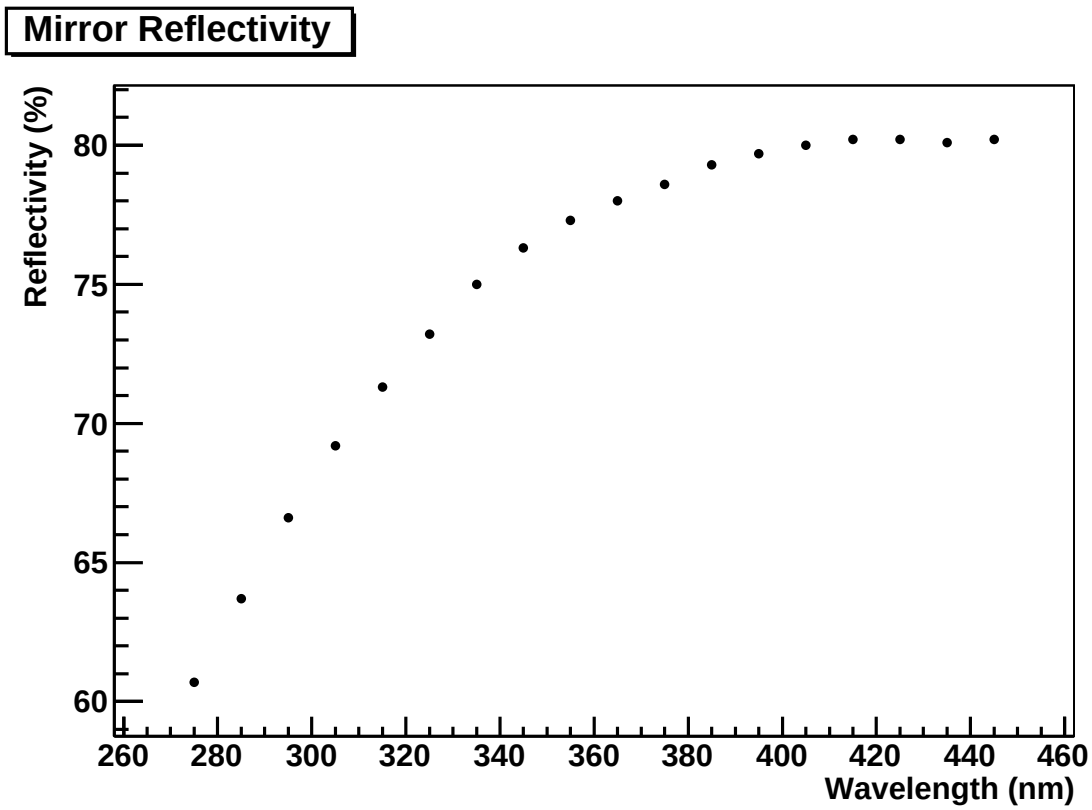

Figure 5.7: The mirror reflectivity of an average HiRes-1 mirror as a function of wavelength.

$16^\circ \times 14^\circ$. A filter was placed on the front of the camera to allow only UV light to reach the tubes (see Figure 5.8).

Two different types of PMTs were used at HiRes-1: EMI 9974KAFL and Phillips (later known as Photonis) XP3062/FL. Table 5.1 also recorded the type of tube that was used in each camera. Both types have a 40 mm diameter, however, the EMI tubes have a smaller effective detection area (1000 mm^2 compared to 1140 mm^2 for the Phillips). Additionally, the Phillips tubes have thin, flat faces while the EMI have thicker, spherical faces. As a result, the EMI tubes suffer more absorption and consequently give smaller quantum efficiencies (a mean of 24%, as compared to 28% for the Phillips). Individual tube differences can be significant, but are corrected for in the calibration process.

Each PMT is instrumented with a preamplifier and a high voltage divider chain before being mounted to the camera backplane. From the backplane, voltages and signals can be measured for debugging purposes and the signals are sent to the electronics racks through twisted-pair ribbon cables.

There were two versions of readout electronics used at HiRes-1, depending upon the age of the HiRes-prototype units (see Table 5.1). The first 14 units used at Little Granite Mountain were Revision 3 (Rev-3) while the rest were Revision 4 (Rev-4). Rev-4 electronics differ from Rev-3 in several respects. First, Rev-4 use a common high

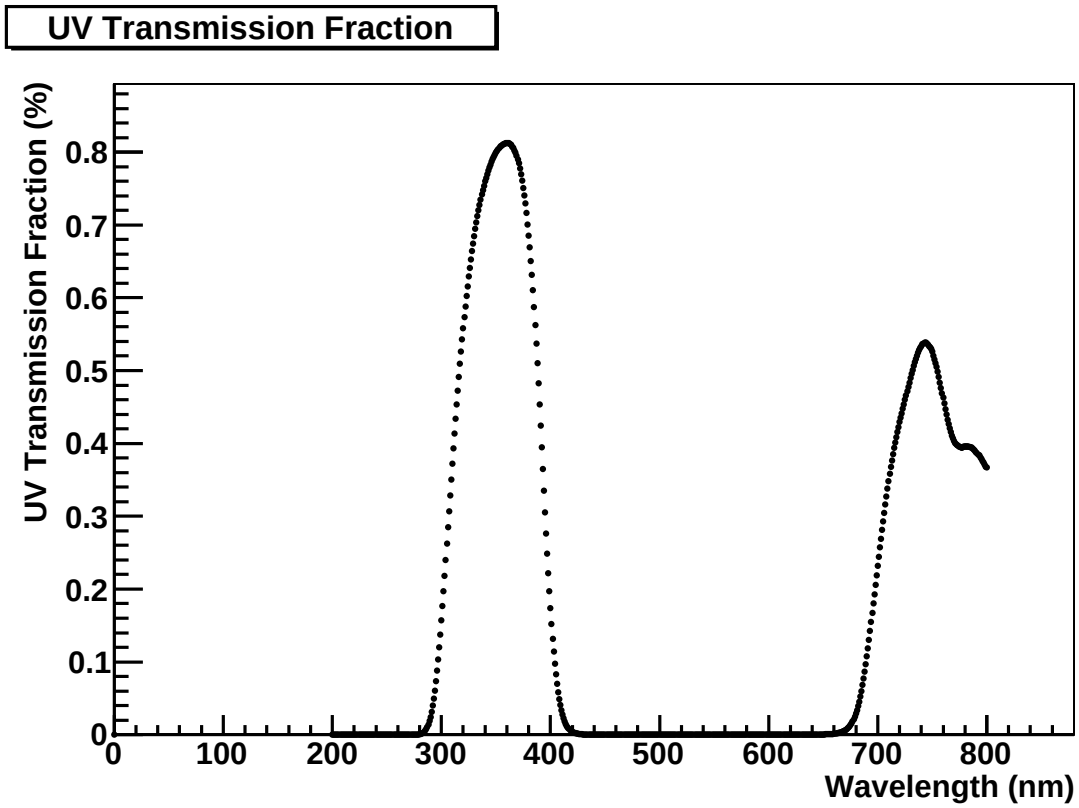

Figure 5.8: The UV filter transmission curve as a function of the wavelength.

voltage (HV) setting for neighboring groups of 16 PMTs (subclusters), whereas they are individually set on Rev-3. This means that the PMTs in a subcluster had to be gain-matched but fewer HV distribution boards were needed.

Second, Rev-4 offered two simultaneous trigger and digitization channels with different filter constants and integration windows, where this was a selectable configuration on Rev-3. In practice, for HiRes operation, only the long time-constant/window channel, QDCB (charge-to-digital converter, channel B), was used for both.

A third minor difference was that Rev-4 used single-ended signal cables whereas Rev-3 used differential input/output. This single-ended implementation caused Rev-4 to be more susceptible to feed-back oscillations. Because of this, half of the units required more expensive and bulkier linear power supplies in place of the cheaper, lightweight, switching power supplies [89].

5.1.2.3 DAQ Electronics

All of the electronics not inside the camera were housed in a single VME rack for each telescope. Figure 5.9 shows the schematics for communication between the camera and electronics rack. Each unit contains:

1. power distribution
    - separately for 110 V and 220 V;
2. power supplies
    - switching supply (housing +5 V and ±12 V): supplies power to the VME crate;
    - low voltage supply (+5 V and ± 12 V): supplies the power to the preamplifiers and miscellaneous control circuits in the camera;
    - high voltage supply: to apply high voltage to the PMTs that control and supply the energy for avalanche amplification;
3. cooling fans to keep the operating temperature of all components below 60° C;
4. high voltage (HV) crate
    - distributes the high voltage to
        - each tube on the Rev-3 clusters;
        - each subcluster on the Rev-4 clusters;
5. VME crate, which contains:

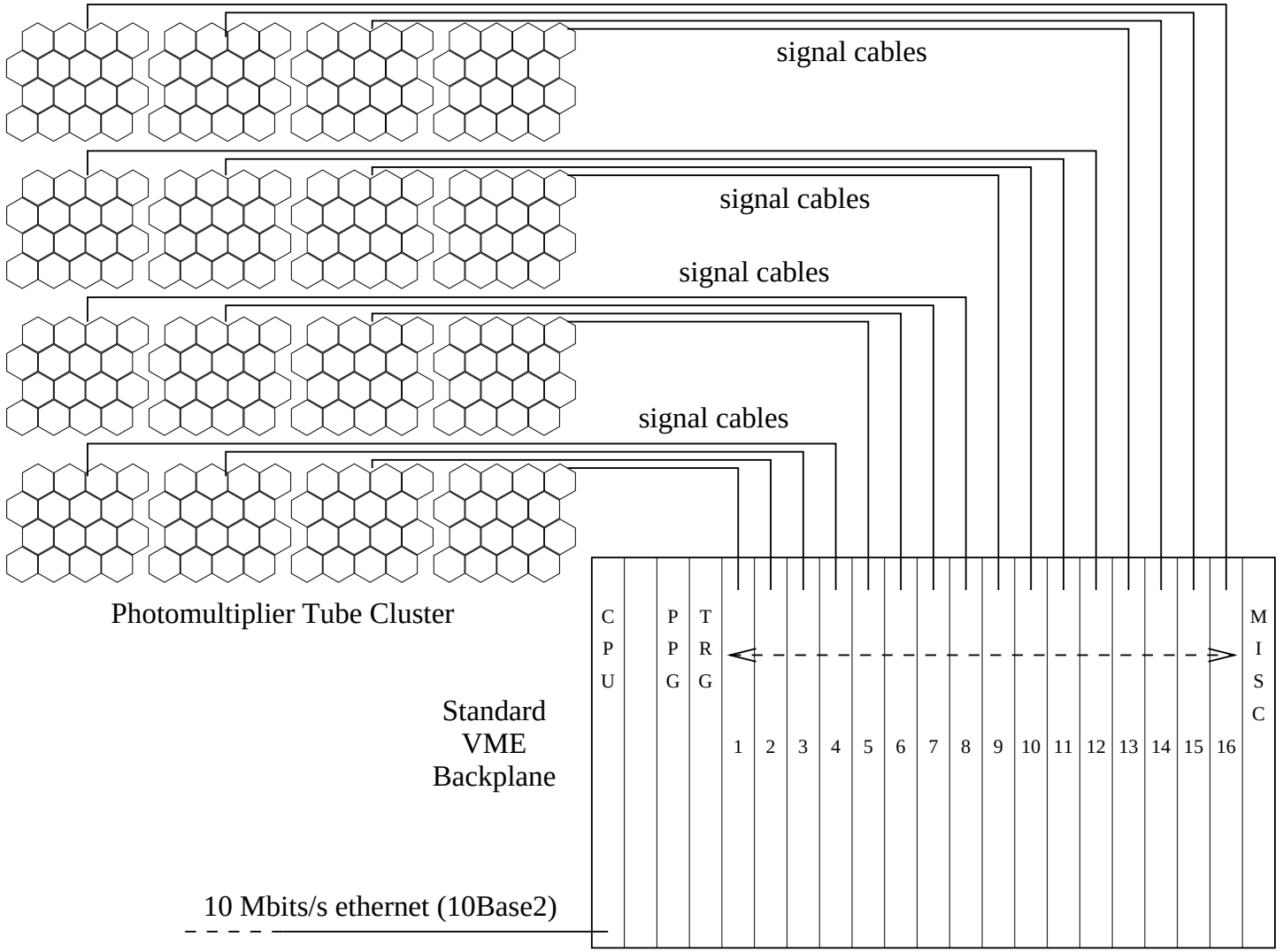

Figure 5.9: This electronics schematic shows each subcluster connecting to an individual ommatidial board on the VME backplane. Additionally, the central processing unit, programmable pulse generator, trigger, and miscellaneous "garbage" boards are also seen.

- CPU board: handles control and data communication between telescope electronics and central facility;
- Programmable Pulse Generator (PPG) board: provides calibration signal pulses with programmable amplitude and duration to the pre-amplifiers;
- Trigger board: forms telescope triggers (see Figure 5.10) from preset combinations of individual subcluster triggers (see Figure 5.11);
- Garbage board: performs temperature and voltage read-back and door control;
- Ommatidial boards (OMBs): one for each of the 16 subclusters provides secondary amplification, integration, and digitization of the signal for each tube and fires a local trigger for the subcluster. (The "ommatidial" boards were named for their functional resemblance to the nerve cells attached to the retina of the eye.)

The HV crate was composed of distribution boards that stepped down the high voltage from the HV supply in 20 V steps over a 500 V range. Depending on the type (Rev-3 or Rev-4), the 32- or 16-port output was individually set for "optimal" gain balance, as defined by (i) uniformity and (ii) as high as possible without saturating both charge-to-digital converters (QDCs) and threshold control. Each subcluster (see Figure 5.11) consisted of 16 tubes in a 4×4 grouping.

Each OMB attenuates the input signals from a subcluster by three at the input with a gain of 30 going into the trigger. There is no gain going into the integrator, so there is an overall gain of 30 through the OMB. This is then split into a comparator and a delay line (1.6 μs). If the output voltage exceeds the programmable threshold on the comparator, a PMT trigger occurs and causes the signal on the corresponding delay line to be switched into an integration capacitor over a 5.6 μs gate, which is then held for 25 μs (see Figures 5.12, 5.13, and 5.14). The PMT trigger also generates a 25 μs-long logic pulse to allow other subcluster PMT triggers to occur. Trigger patterns in look-up tables are loaded into the address of a 64k $\times$ 4 static RAM (SRAM) from an EPROM and can be

1. any tube
2. any two tubes
3. any two adjacent tubes
4. any three tubes
5. any three tubes with 2 adjacent

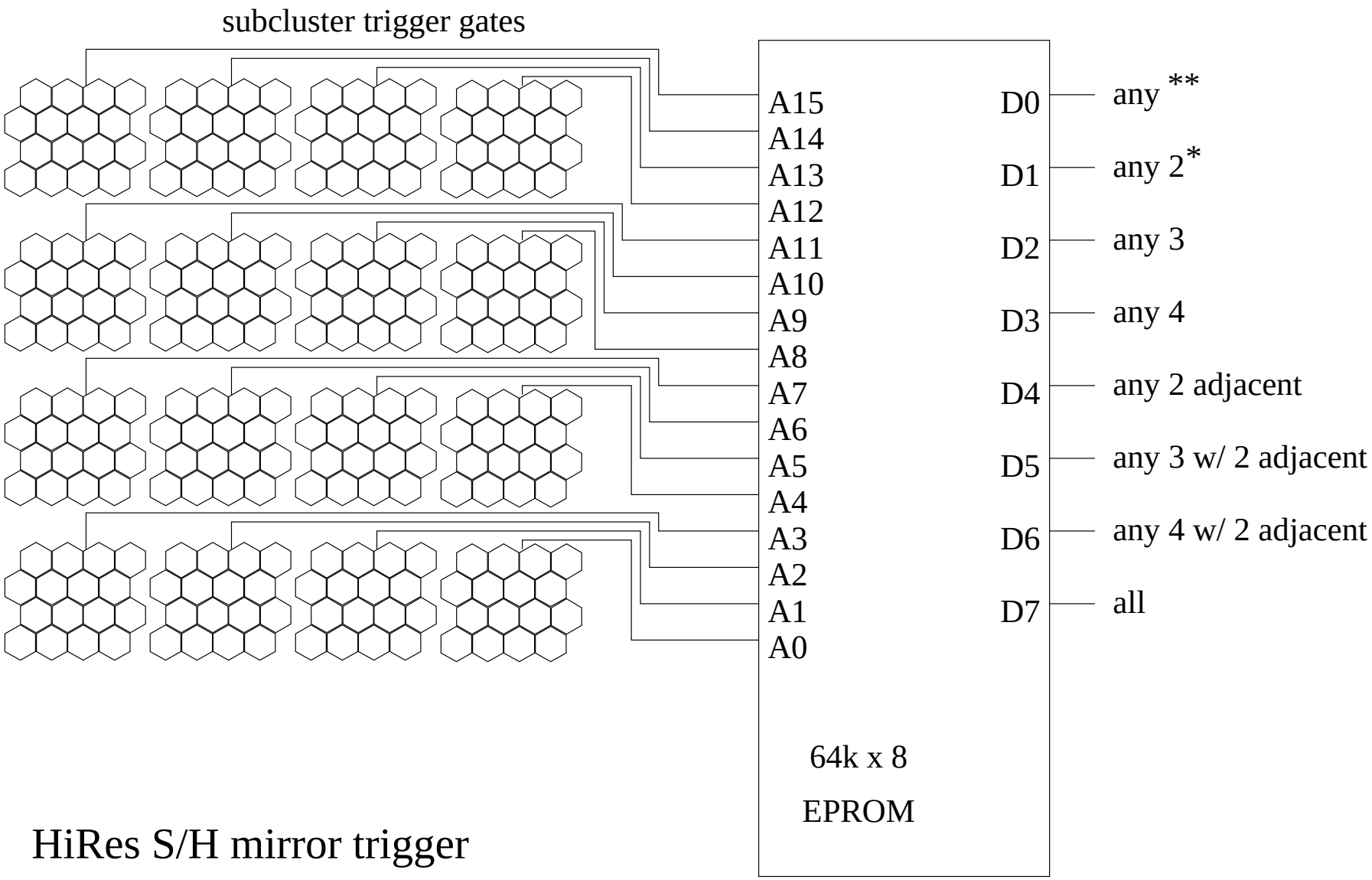

Figure 5.10: This shows the possible combinations of triggered subclusters to activate a telescope-wide trigger.

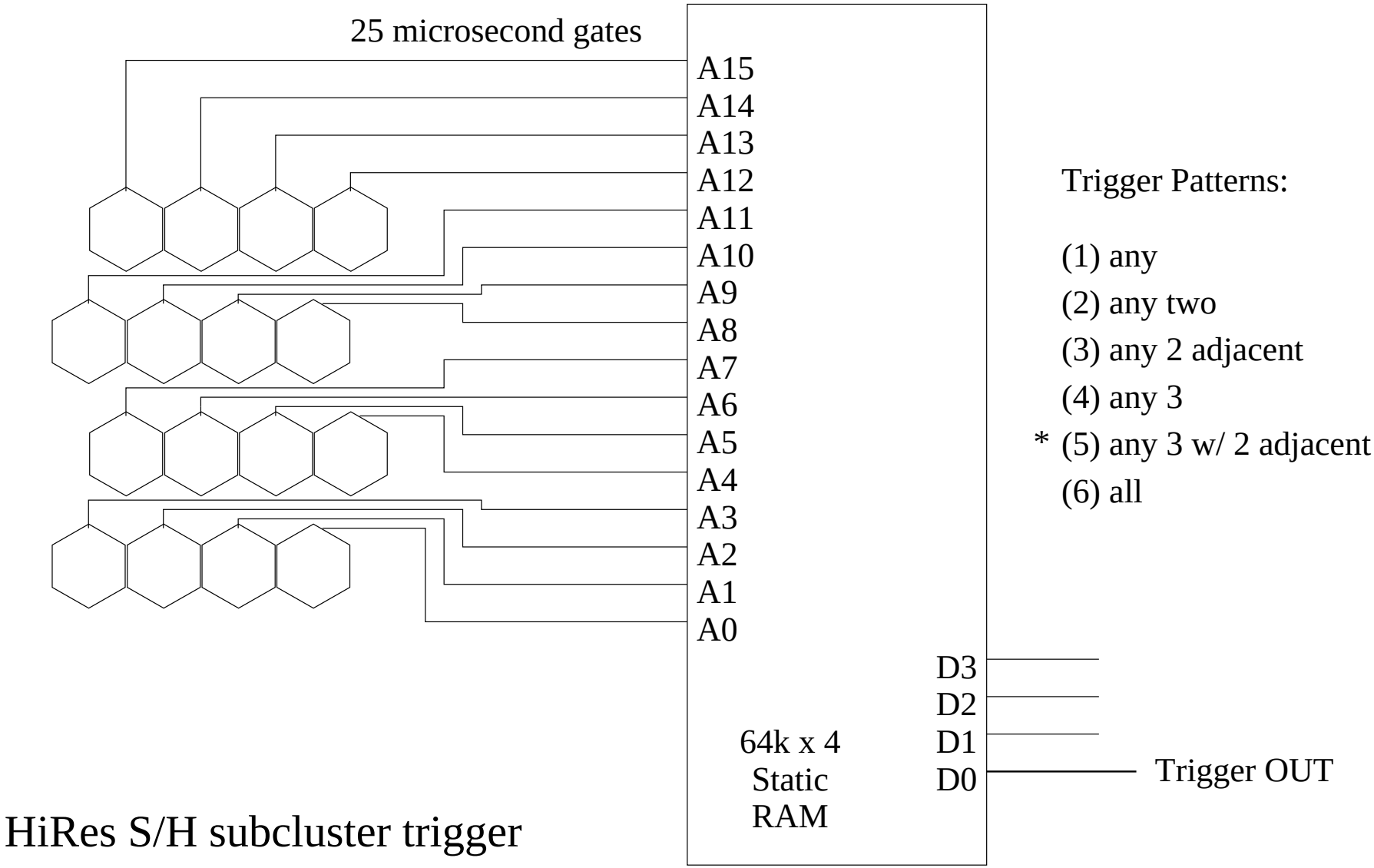

Figure 5.11: This shows the triggering possibilities for an individual subcluster on an ommatidial board.

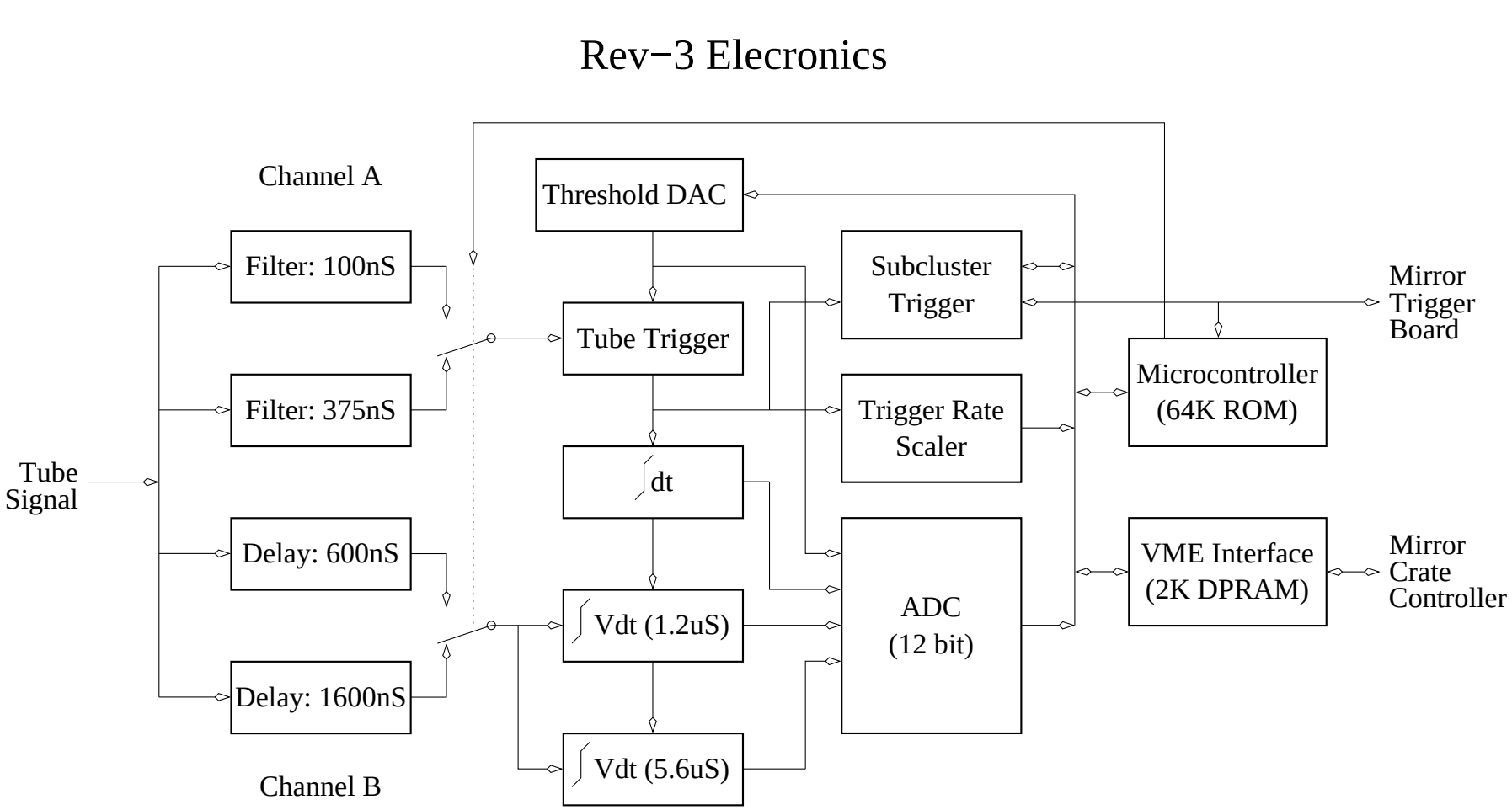

Figure 5.12: The schematics of how a standard Rev-3 ommatidial board processes a signal.

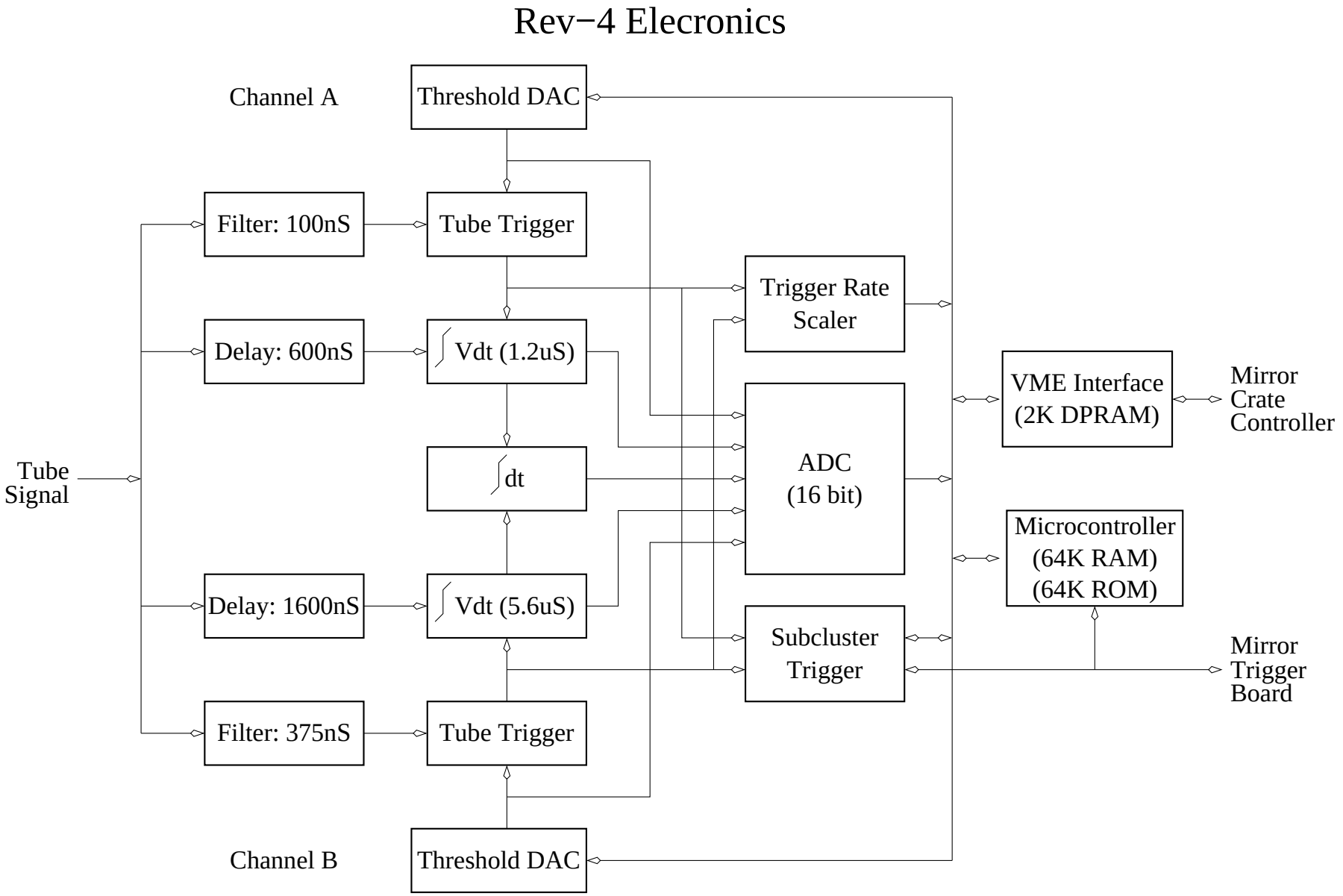

Figure 5.13: The schematics of how a standard Rev-4 ommatidial board processes a signal.

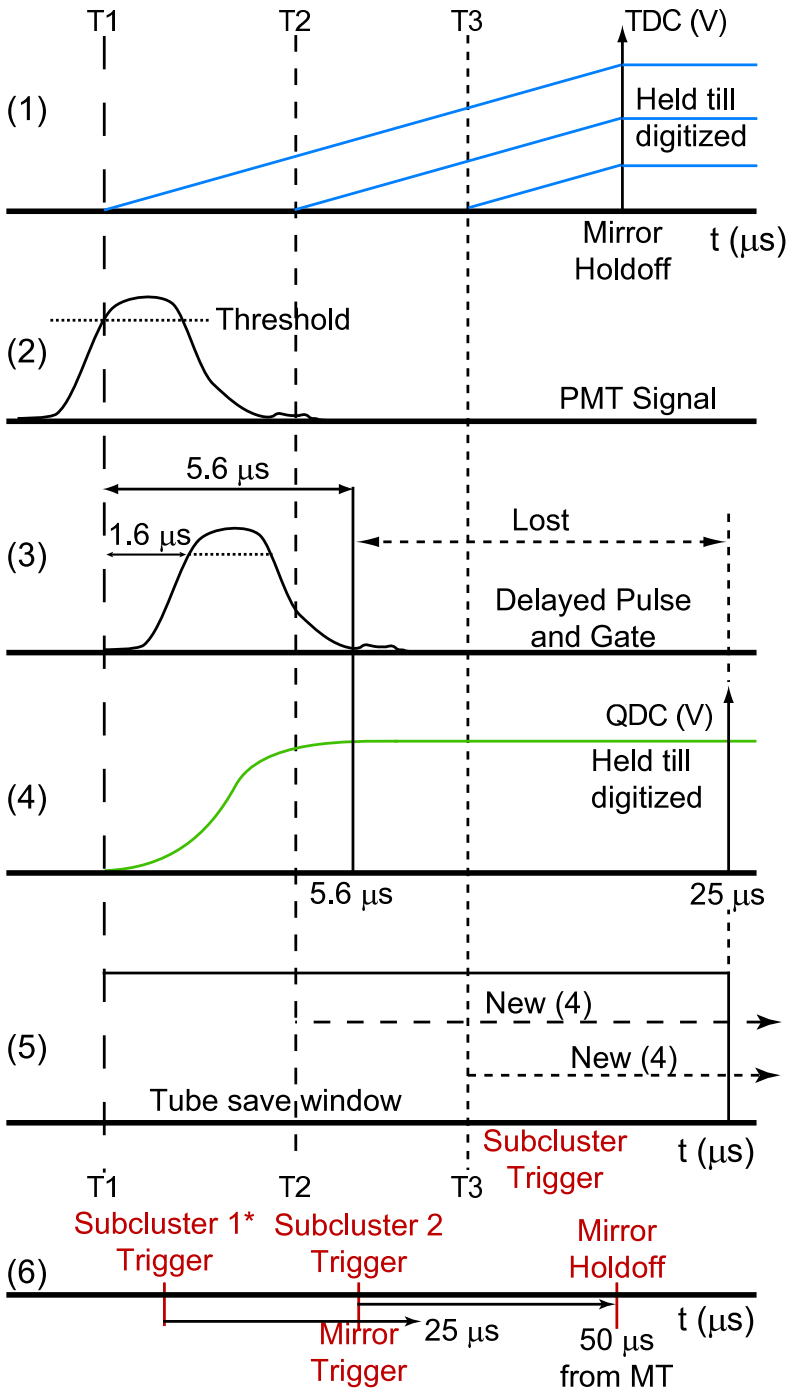

Figure 5.14: Delay response. This image shows the process of obtaining an event. Graph (1) shows the time-to-digital converter (TDC) voltage increases as time progresse. Graph (2) shows when the tube is triggered. Graph (3) records the delayed signal. Graph (4) shows the signal converted into a charge-to-digital converter (QDC) value. Graph (5) shows how each tube's QDC and TDC is forwarded into a subcluster trigger. Graph (6) shows that if a second subcluster is triggered within the previous subcluster's last 25 μs save window, a mirror trigger is activated.

6. all tubes

where the default during data collection is any three tubes with two adjacent. If the 16 subcluster trigger lines match any of the trigger pattern in the look-up tables, the subcluster trigger becomes true and the tube information is stored.

The OMB also continuously adjusts the threshold at each comparator at a level that keeps the tube trigger rate at a software-selectable rate (1.245 V over 256 steps for Rev-3 and 2.5 V over the same number of steps for Rev-4). For night sky observation this rate is set to 200 Hz. This threshold is recorded for each channel once each minute and incorporated into the data stream.

The subcluster triggers are transmitted over the VME backplane to the trigger board, where the combination of subcluster trigger lines sets the address of a 64k $\times$ 8 EPROM preset with trigger patterns for

1. any subcluster
2. any two subclusters
3. any three subclusters
4. any four subclusters
5. any two adjacent subclusters
6. any three subclusters with two adjacent
7. any four subclusters with two adjacent
8. all subclusters

which then constitutes the telescope trigger (see Figure 5.10).

A common GPS clock in the central timing (CT) rack is used to synchronize the telescopes by having the CT rack transmit a once-per-millisecond signal and a once-per-minute signal to each telescope. The individual telescopes will advance a counter after receiving the millisecond signal and clear the counter once the minute signal is received. An additional counter starts at the beginning of each data file to count the number of minutes. The central DAQ computer time-stamps the beginning of the data file with a START packet when the minute counter is cleared.

After a telescope trigger is initiated, a trigger signal is sent to CT, where the trigger signal is then routed to neighboring telescopes (based on the telescopes' pointing directions). This neighbor-trigger signal reduces the trigger requirements in those telescopes to allow smaller segments of track to be collected in the secondary telescopes. At the

end of the hold-off delay ($50\mu s$), each telescope generates a hold-off signal that stops the event collection (charge-to-digital converters, QDCs, and charge-to-digital converters, TDCs) and is also sent to CT to be time-stamped (with 25 ns resolution). The hold-off time-stamps for each mirror are then queued for each GPS second at which time they are transmitted to the central DAQ computer in a TIME packet.

The hold-off signal is also time-stamped locally at the telescope with millisecond and minute counters. This time-stamp, along with the event's QDCs and TDCs are compiled into an EVENT packet to also be sent to the central DAQ computer. When the assembling of the EVENT packets are completed, all of the TDC and QDC integrators are reset and the hold-off signal is cleared in preparation for the next event. The readout time varies between one and two milliseconds per trigger, which is the primary constituent of the dead time of each telescope since new trigger events cannot begin during this time. Each telescope monitors its dead time and trigger rate during each GPS minute and sends this information to the central DAQ computer in a MINUTE packet to be recorded in the data file. The central DAQ computer records the TIME and EVENT packets to a data file for offline matching. The matching program will be discussed in section 7.1.4 [90].

As implemented at HiRes-1, there were three additional differences between the Rev-3 and Rev-4 electronics:

1. Rev-3 allows for only one of two trigger/delay channels to be used; Rev-4 allows both, and either channel can trigger.

2. Rev-3 thresholds are set for the selected channel (B); Rev-4 thresholds are set independently for both channels.

3. Rev-3 uses a unipolar 12-bit ADC with an offset; Rev-4 uses a signed, 16-bit ADC.

5.1.2.4 Additional Upgrades

Telescope 17 was in a separate, converted corn silo before it was removed (see Figure 5.4). It had a revolving wall/door to allow the telescope to view the night sky. All of the other buildings were custom-made to hold two telescopes, with a roll-up garage door controlled by the "garbage" board with light-sensing interlocks. Additional interlocks (see Figure 5.15) were also placed on the light switches and on light sensors attached to the exterior of the buildings. The central timing connection was opened by both the operator and the dark time, but the interior light switch and the exterior ambient-light sensor also had to agree that there was no light in the building or coming from outside. These all ensured that the HV could not be turned on and the door could not be opened while there was any light visible to the PMTs.

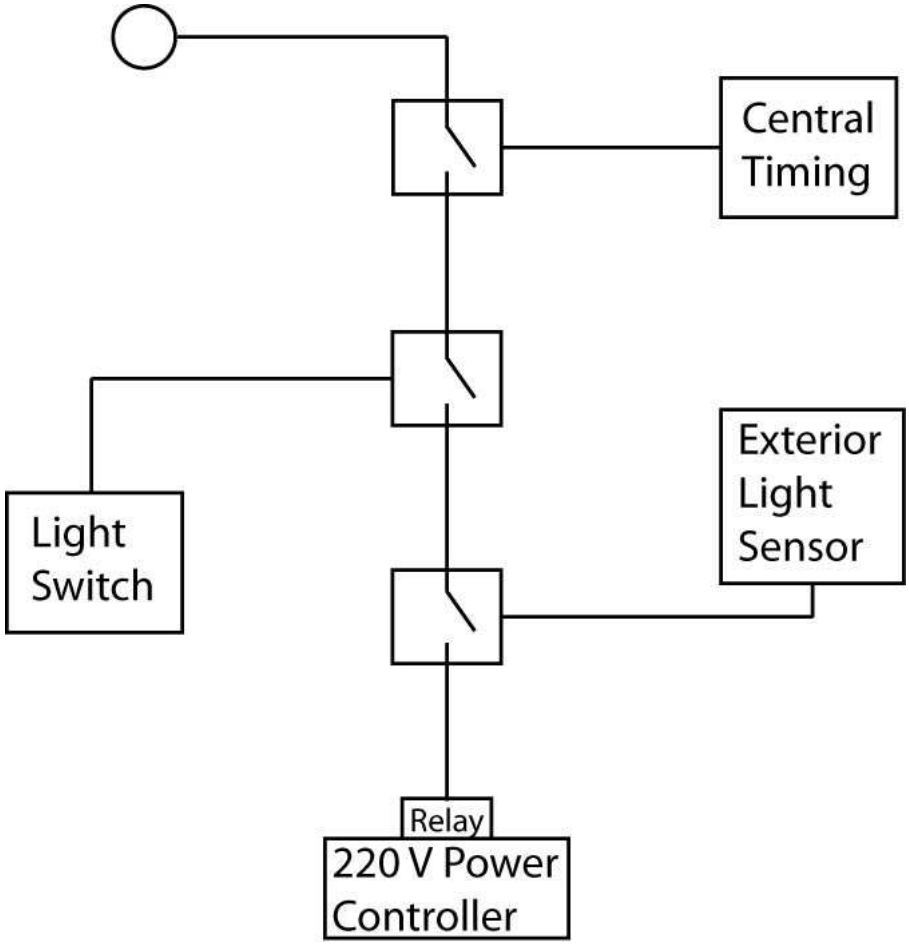

Figure 5.15: High-voltage interlocks.

One other fail-safe installed was a drop-down curtain directly in front of each mirror. Direct sunlight hitting the mirrors could focus the light onto the cluster and melt the UV filter and PMTs in its path. This curtain helped prevent that situation by dropping down to cover the mirrors when ambient light levels were discernibly higher than that of a moonless night sky. These, in fact, deployed on many occasions where operators failed to close all doors at the end of the night.

5.2 HiRes Diagnostic and Calibration

The energy calibration of the HiRes detectors involved a number of separate processes. This section will describe each type of calibration in turn: electronic, mirrors, PMT and atmospheric.

5.2.1 Electronic Diagnostic and Calibration

5.2.1.1 Electronic Functionality

Electronic functionality diagnostics is performed with two different nightly tests before and after the data is collected. The PPG board in each unit can send a square pulse of programmable amplitude and duration to each PMT preamplifier. Before the run begins, a single pulse is sent and will show in the event display which tubes are dead or have low gain.

Additionally, a sequence of diagnostics was performed on every tube to indicate potential malfunctions in (a) a preamplifier, (b) a signal cable, (c) a PPG channel (the same tube number in all subclusters), (d) a subcluster, or (e) the entire electronics. This was done through the "diag" script which specifically:

1. initialized the electronics racks to check the response
2. checked that the GPS clock was synchronized to the system
3. read the low-voltage values and checked that they were within an acceptable range
4. set and digitized the thresholds and checked that they were operational
5. generated and checked counting rates to determine if the electronics were observing all triggers
6. generated electronic triggers and checked that the charge integrators and digitizers (QDC) were operational on the ommatidial board
7. generated electronic triggers and checked that the timing read-back and hold-off integrators (TDC) were operational on the ommatidial board
8. generated PPG triggers and checked that both QDC and TDC values were simultaneously operational starting at the preamplifier and signal cable

5.2.1.2 Electronic Response

Calibration data for the DAQ electronics was collected at both the beginning and the end of each run night. This data were then used later for offline calibration of the event TDC and QDC data. The TDC integrators were calibrated by 1) forcing all the channels in a telescope to trigger simultaneously (called a "snapshot") and 2) leaving them open for a programmed, hold-off delay trigger. By varying the hold-off delay through a range of values and recording both the delay length and the TDC values for each channel, calibration constants could be calculated with a linear fit to the delay-TDC data.

The QDCs were calibrated by injecting a programmed amplitude and width pulse (using a programmable pulse generator, PPG) into the preamplifier of each PMT in the camera and generating triggers from those pulses. A range of pulse amplitude values were generated for each value in a range of widths which were recorded along with the resulting QDC value for each channel. In practice, four width values are chosen and the amplitude-QDC data are fit linearly, which is generally different for each width. When calculating a pulse area of the QDC, the pulse width is estimated from the event track geometry and the pulse amplitude is calculated by interpolating from the fitted amplitude calibration data between the two nearest calibrated widths [91].

5.2.1.3 Pedestal Calibration ("noise")

To obtain the nightly pedestal (zero-charge response), the detector was allowed to collect data once before and once after the doors were opened at both the beginning and the end of the nightly run. From data collected with the doors closed, the width of the pedestal will indicate what kind of shot-noise can be expected for the night. From data collected with the doors open, the pedestal width gives a measure of the brightness of the night sky. The mean of the closed-door data from the beginning and end of the night was used to calibrate the pedestal offset.

5.2.2 Mirror Calibration

The individual mirror reflectivity was determined using a combination of studies. First, each mirror reflectivity was measured multiple times. The first calibration used a 337 nm laser and gave the original, standard mirror reflectivity of 80% (see Figure 5.7). A second analysis [101] gave values for each individual mirror using four individual reflectometer measurements. Averaging all five measurements calibrated the reconstructed energy much lower than expected, while averaging only the reflectometer measurements calibrated the events too high. An average of these two averages was taken with an uncertainty of $\pm 5\%$ (see Figure 5.16).

Secondly, the wavelength dependance of each mirror was determined for all mirrors between 270 nm and 450 nm in 10 nm bins (see Figure 5.7). The average mirror reflectivity quoted for each mirror was then normalized to the 335 nm bin (to match the lasers used in the averaging technique), giving the wavelength dependance of each mirror's individual reflectivity.

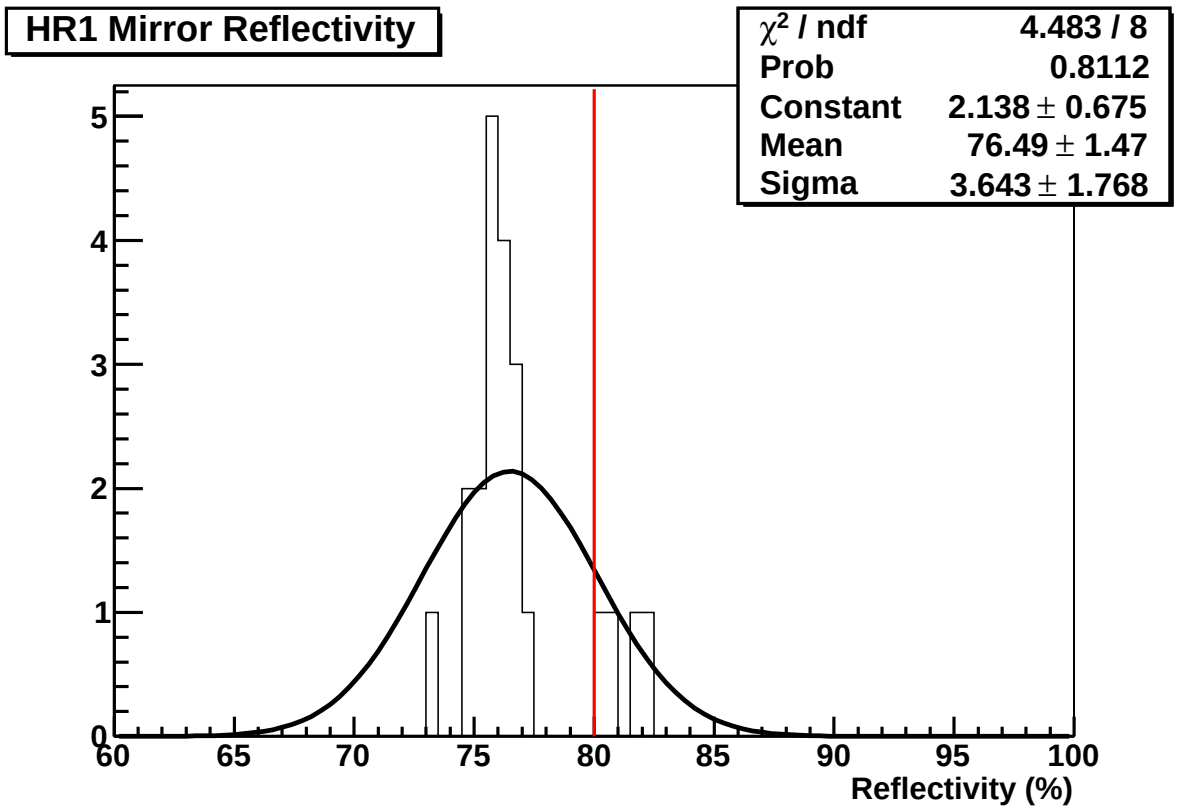

Figure 5.16: The mirror reflectivity distribution of all mirrors at HiRes-1. The vertical line shows the average value used in the original reconstruction.

5.2.3 PMT Calibration

Calibration of the PMTs was performed in several ways since knowing the individual properties of the tubes is of utmost importance to ensure correct calculations on the number of photo-electrons (NPE) in each event.

5.2.3.1 RXF

A roving xenon flasher (RXF) measurement was taken monthly in order to quantify the number of photons with a QDC value. The RXF was inserted into a holder at the center of each mirror and that telescope was then individually triggered for 5 to 20 minutes. Over the course of a year, a seasonal variation was observed in the detector due primarily to the ambient temperature (see Figures 5.17 and 5.18). The mean gain of the telescopes rose during the winter months when the ambient temperature was lower and dropped during the summer months when the ambient temperature is higher. The temperature coefficient of the quantum efficiency is quoted to be -0.2%/K between 0 and 40° Celsius at 420 nm [80]. The observed response of the tubes, however, includes the temperature dependance of the preamplifier, the ommatidial boards, and other electronics as well (see Figures 5.19 and 5.20).

The RXF itself was calibrated at the University of Utah. The RXF was set to the same distance as it would be from the telescope camera to illuminate a NIST-calibrated, hybrid photo-diode (HPD). Additionally, a light-emitting diode (LED) also illuminated the same HPD set at an intensity of single-photon emission. The value of the RXF was then compared to the single-photon peak to determine the number of photons produced by the RXF.

Folding in the quantum efficiency given by the manufacturer and the UV filter transmission curve, the individual PMT efficiency and gain values were calculated on a tube-by-tube basis [64] [10]. By knowing the effective area of the PMT type (different for EMI and Phillips as indicated in section 5.1.2.2), the tubes were calibrated with an absolute value in terms of photons per mm^2. This information was used in the calibration of the nightly runs in order to determine the NPEs of each event recorded (see section 7.1.3).

5.2.3.2 YAG

The output of an energy-tripled Nd:YAG (neodymium-doped yttrium aluminium garnet) laser, operating at 355 nm, was distributed through fiber optic cables to every telescope, where it was then diffused with Teflon discs. The diffused sources were placed at two locations. One source was placed in the center of the mirror, directly illuminating

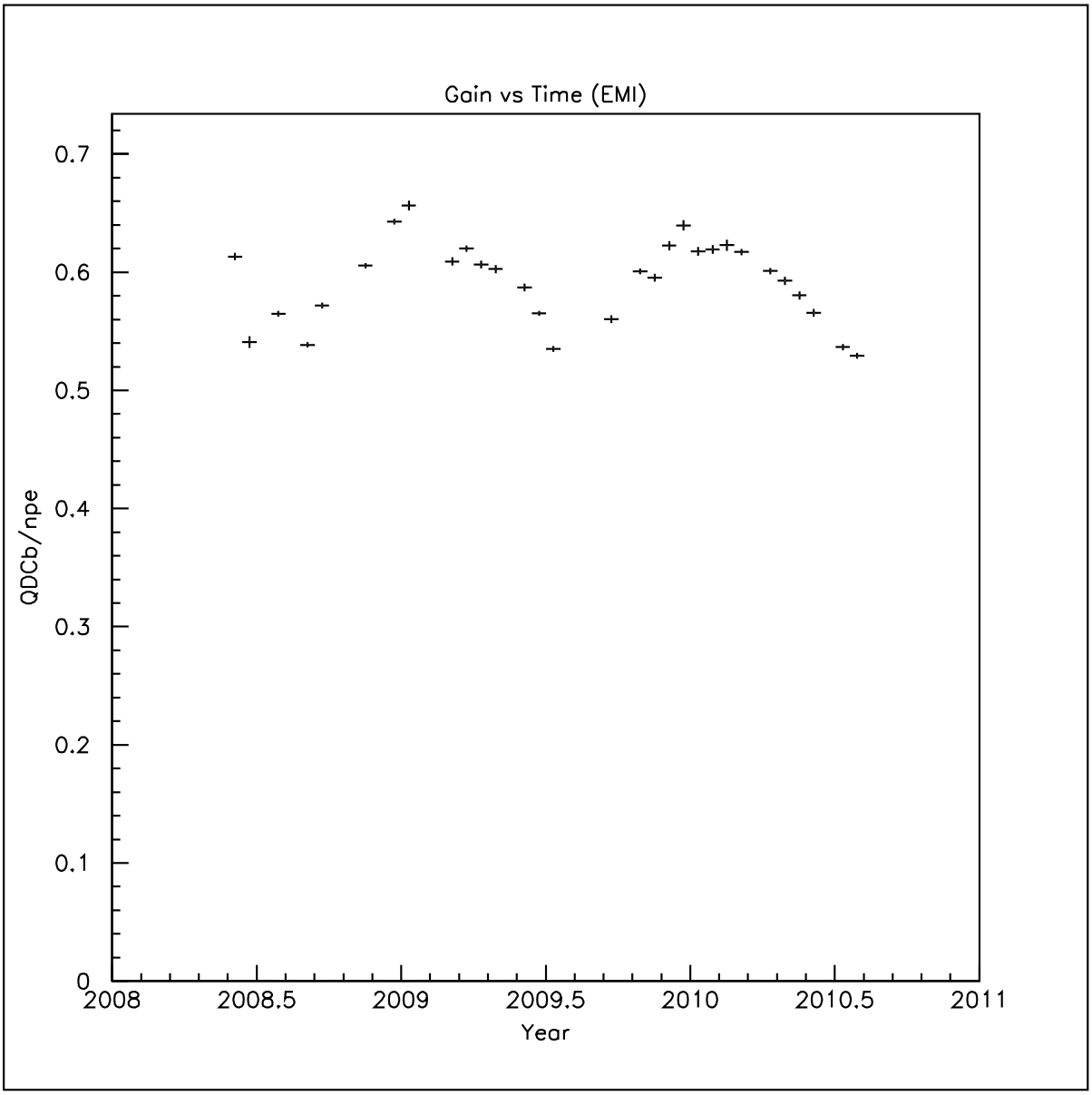

Figure 5.17: Annual response of EMI photomultiplier-tube detectors at Middle Drum. HiRes RXF data were insufficient to show this quality.

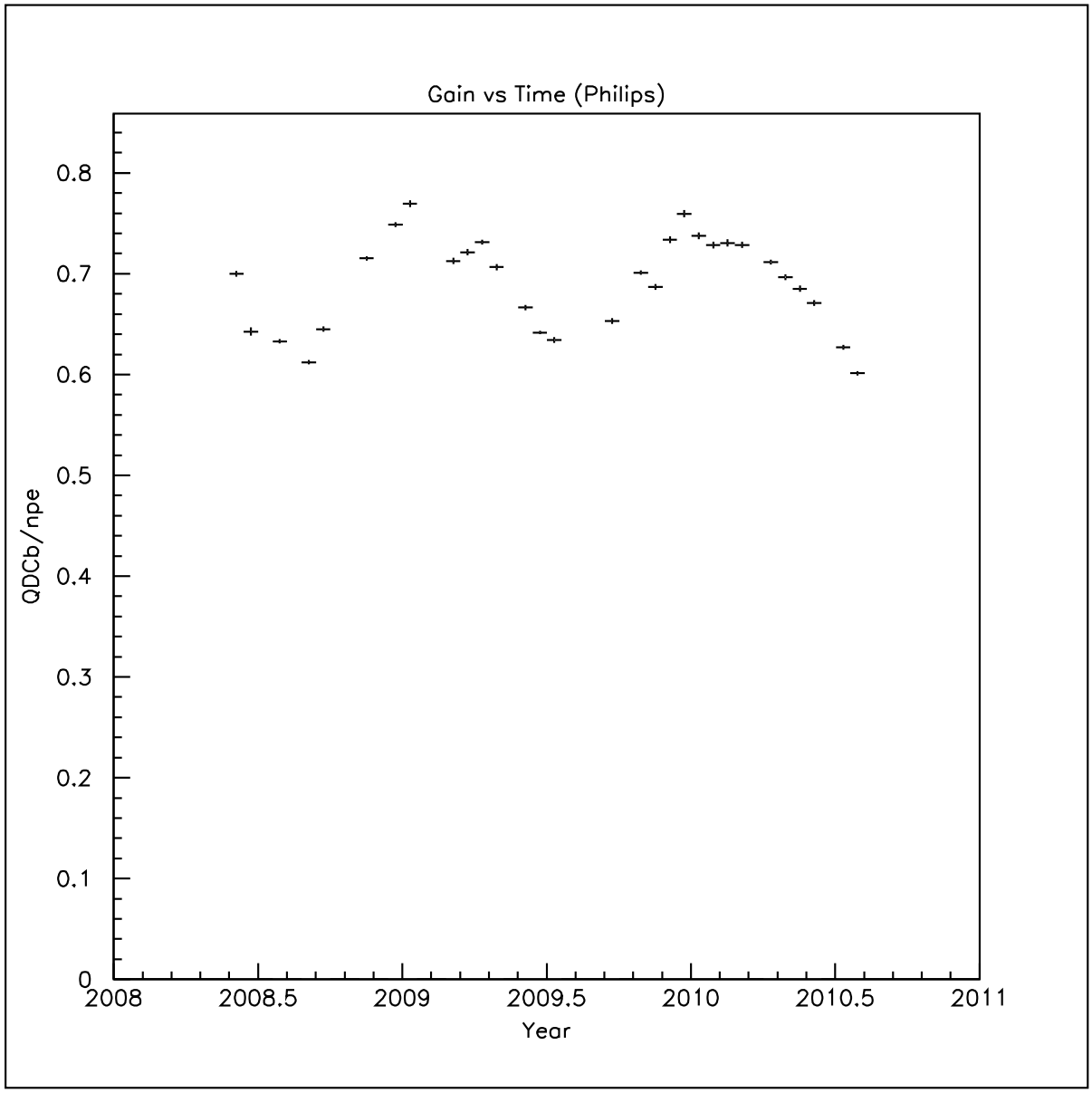

Figure 5.18: Annual response of Philips photomultiplier-tube detectors at Middle Drum. HiRes RXF data were insufficient to show this quality.

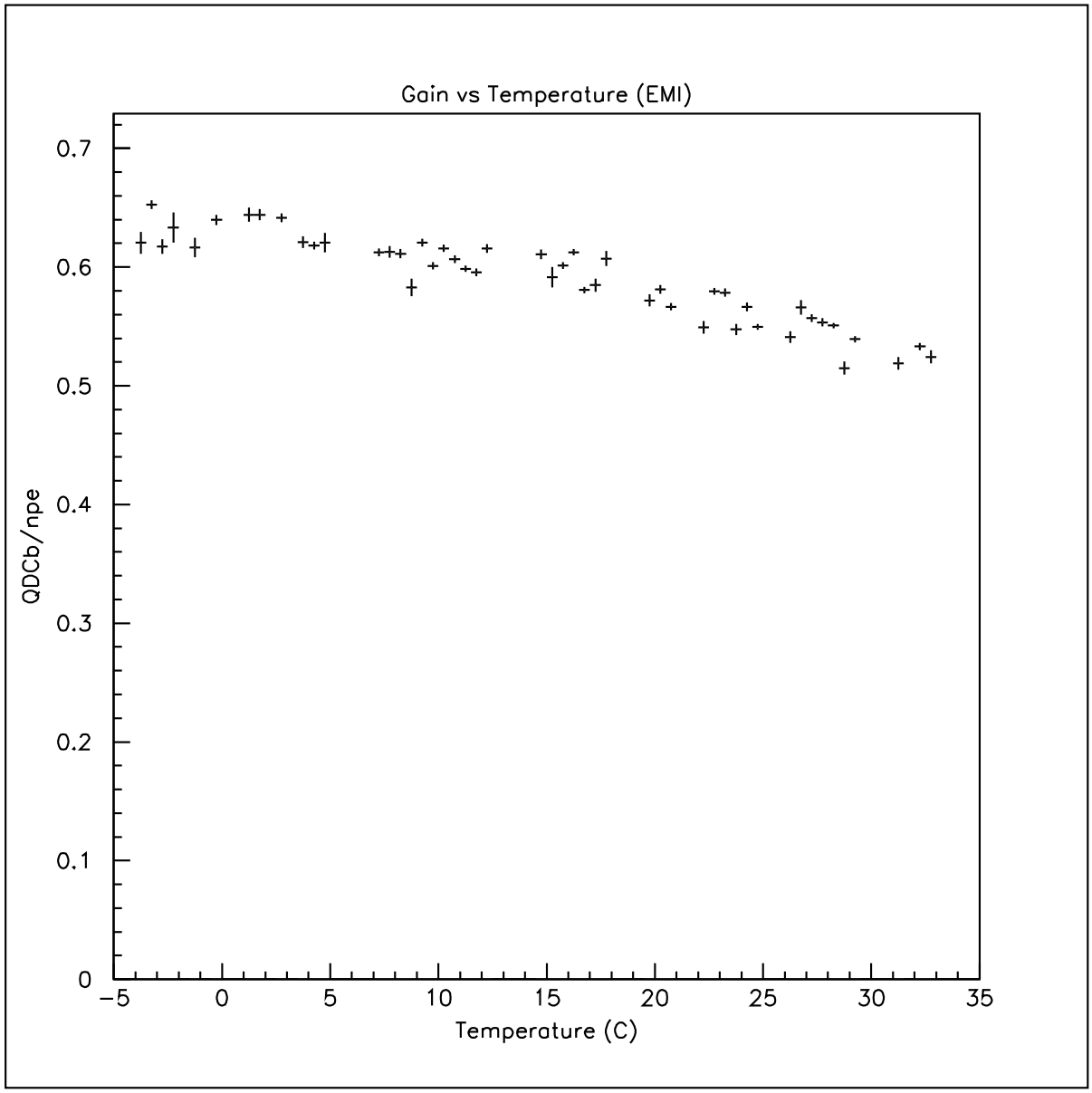

Figure 5.19: Temperature response of EMI photomultiplier-tube detectors. Middle Drum RXF data were used for consistency with Figure 5.17.

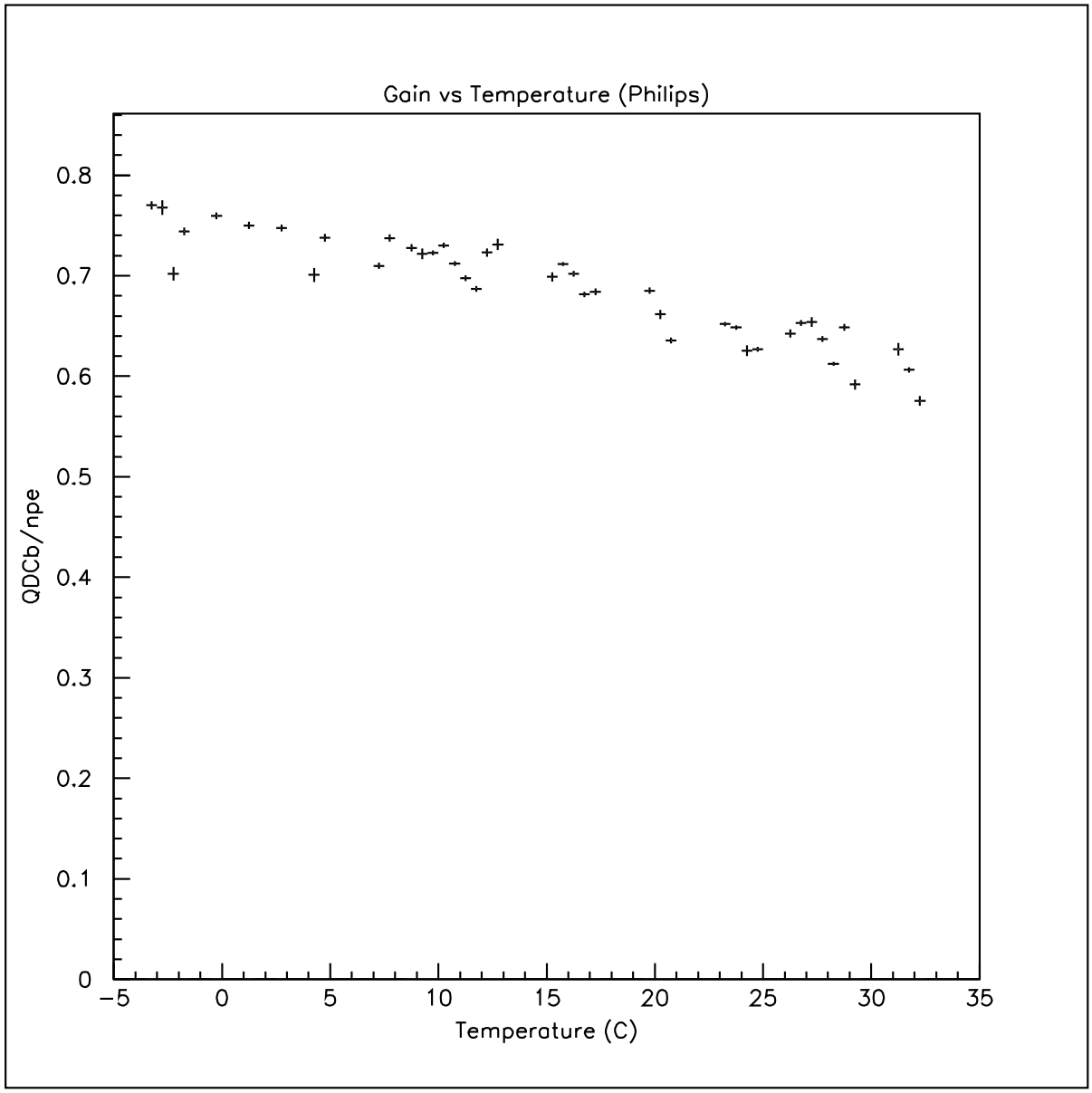

Figure 5.20: Temperature response of Philips photomultiplier-tube detectors. Middle Drum RXF data were used for consistency with Figure 5.18.

the camera. Two others were positioned on either side of the camera to reflect off the mirror, back towards the camera. This transmitted to every telescope the same calibration light from the same source, giving relative values of QDC between telescopes.

The nightly YAG laser gave a short-term diagnostic of PMT relative gain variations. It has been noted [6] that there was a 3% uncertainty in night-to-night variations. Using the RXF (with a series of neutral density filters to vary the intensity) in conjunction with the YAG data, we were been able to determine the relative gain response of PMTs according to the NPE recorded for both calibration techniques (see Figure 5.21).

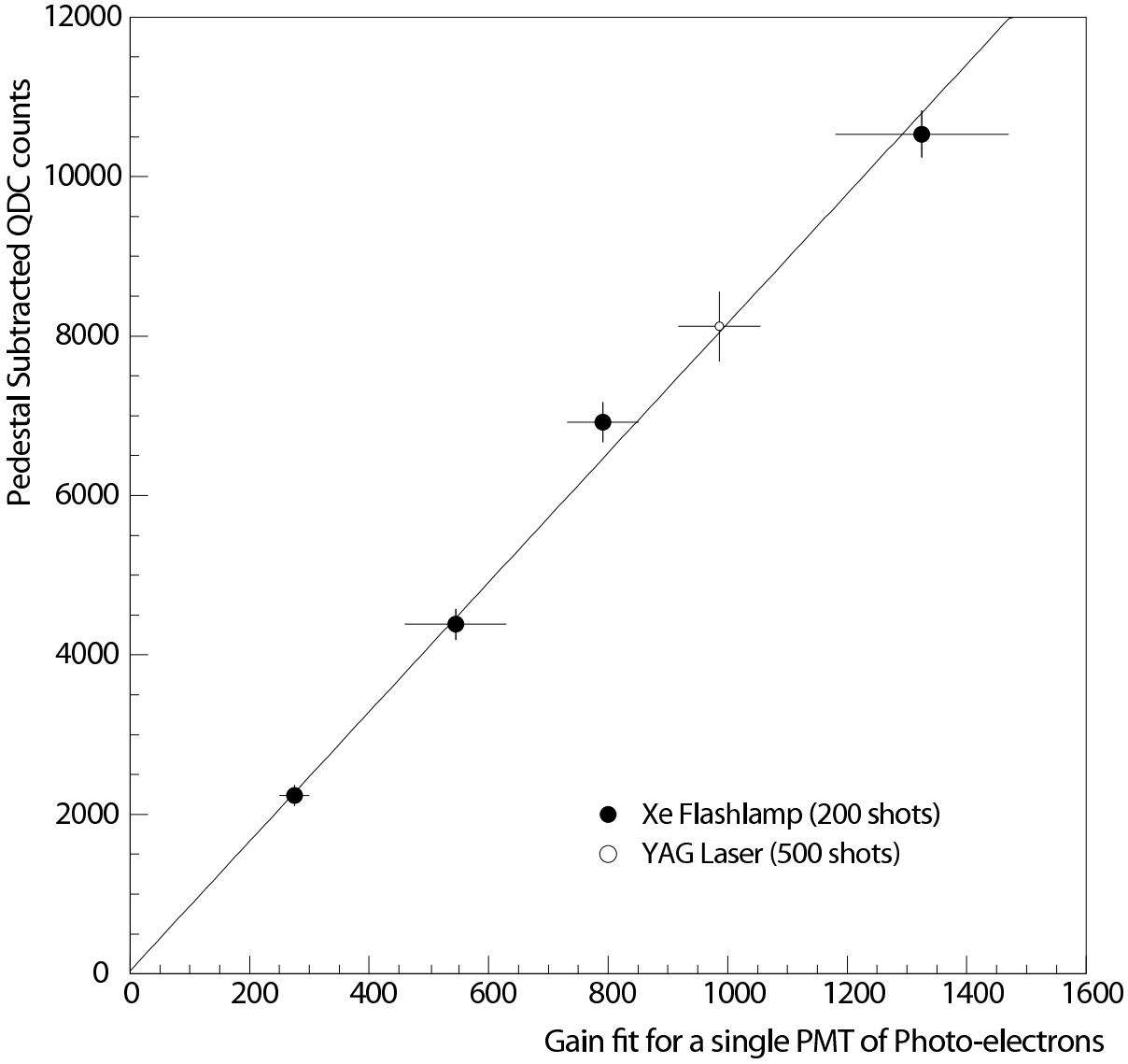

Figure 5.21: This graph shows the QDC gain response of an individual Rev-4 photo-multiplier tube as the intensity of the light source increases.

5.2.4 End-to-End Calibration

A particularly important form of calibration used in this experiment was an end-to-end calibration in lieu of a primary beam line calibration that is not available to us. A nitrogen laser was transported to various locations around the two detector sites at four kilometer distances in front of each mirror. As was discussed in section 4.2.3, this approximate distance is ideal for the scattering of light to be equally attenuated by the same amount of aerosols that produce it for any horizontal extinction length (see Figure 4.7). While the actual distance for aerosol attenuation insensitivity is closer to 3 km, restrictions on Dugway caused variations in allowable distances. This calibration method, however, allowed for a direct measurement of laser light that is minimally sensitive to the atmospheric aerosols. The analysis of these events allowed us to reconstruct the energy of each laser shot, which is then compared to the value measured by a photometer. This comparison is used to validate the photometric calibration [40].

5.2.5 Atmospheric Calibration

As described in section 4.2, the light observed from an extensive air shower is much attenuated by various forms of scattering. In order to know how much light is actually generated at the shower, we compare the amount of light (or energy) seen in laser events to what was actually fired from the laser. We use multiple lasers in order to do this because the atmosphere is the most dynamic factor of cosmic ray detection. Rayleigh scattering is mostly constant with only 3% variation, so the following lasers are used primarily to determine aerosol content, which can change hourly.

5.2.5.1 SLS

A steerable YAG laser system (SLS) [8] was installed at each of the two detector sites (noted for HiRes-1 in Figure 5.4). These were used in "bistatic" lidar mode, where the scattered light from the laser is observed at a secondary location (as compared to observing back-scattered light in "monostatic" lidar mode from a detector at the same location as the laser). Simply stated, HiRes-1 was only able to view the HiRes-2 SLS, and vice versa. The output of the laser was split at the laser head, 8% of the energy being monitored for each shot, allowing precise calculations observed by the telescope. The lasers were fired at different azimuthal and elevation angles in a ~ 50 minute preset pattern once an hour. Depending upon the angle, the scattered light would trigger between one and eight telescopes, between telescopes 2 and 21, centered on telescope 12 (see Figure 5.5). To make SLS events easily identifiable in the data, the lasers were

fired at preset millisecond marks. For example, HR1SLS fires at quarter-second intervals starting at +111 ms, while HR2SLS fired started at +222 ms. These showers allowed the aerosol density to be measured from both the vertical and incline shots, given in terms of vertical scale height (H), horizontal attenuation length (L), and vertical aerosol optical depth (VAOD).

One additional feature instituted with these lasers was known as "shoot-the-shower". When an event with an estimated energy above 10^{19} eV was observed during data collection, the laser was pointed in the vicinity of where the shower was seen in order to have a timely scan of the atmosphere in the neighborhood of the shower.

5.2.5.2 Terra Laser

Another YAG laser was positioned 21.3 km east of HiRes-1 in the town of Terra, Utah, just west of the Onaqui Mountain Range. Its primary purpose was to test how far away the detectors were able to view the highest energy events, so it was set in a permanently vertical pointing direction. The Terra laser was fired at every quarter second after +322 ms. On most clear nights the laser was easily detected and accurately reconstructed, demonstrating that HiRes was able to clearly see showers at least this distance.

Additionally, a study was performed [100] using five separate neutral density filters on the Terra laser to simulate five different air shower energies between 40 EeV and 125 EeV. The reconstructed energies were compared to an estimated, observable intensity to determine an efficiency. Figure 5.22 shows the efficiency of these five intensities compared to the laser's reconstructed energy. As can be seen, the HiRes detectors have nearly 100% efficiency for energies above the GZK threshold.

5.2.5.3 Cloud Monitors

One other set of equipment was specifically used to check for clouds: infrared (IR) cloud monitors [30]. These measured the difference between the sky temperature in their field of view to that of the ambient temperature to determine if there was a cloud in its line of sight (see Figure 5.23). Placed in each of the eleven mirror buildings was one fixed-position sensor with a 30° field of view. Additionally, a 3° steerable IR sensor placed on the SLS building scanned the sky every 12 minutes.

The data collected were used as an early warning for operators, letting them know whether it was safe to open the garage doors or if they should be closed due to an approaching storm. This information was also used as a way to sort events into good-weather or bad-weather categories.

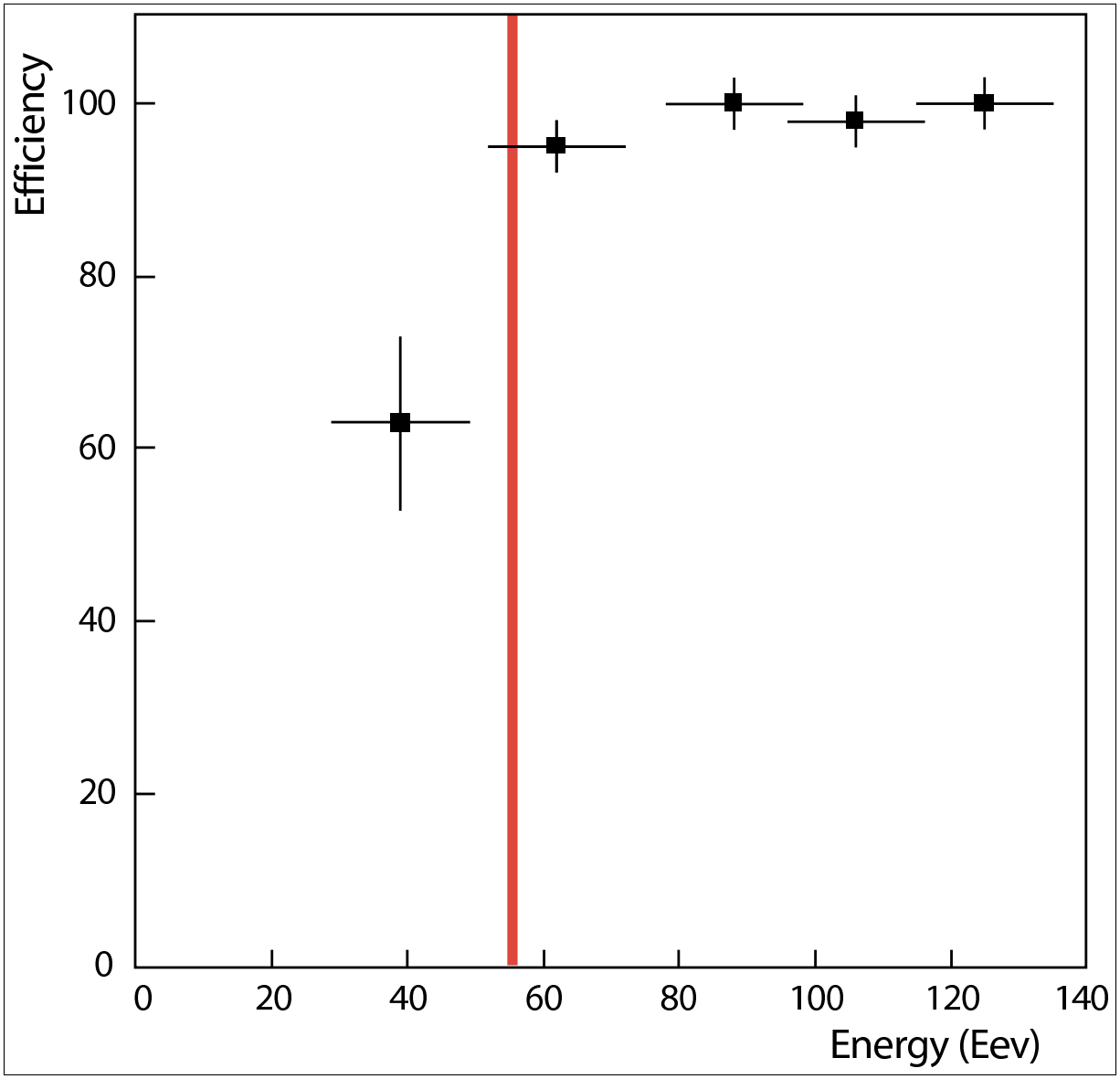

Figure 5.22: The efficiency of the Terra laser shots as a function of pseudo-energy. The GZK threshold energy is indicated by the vertical line.

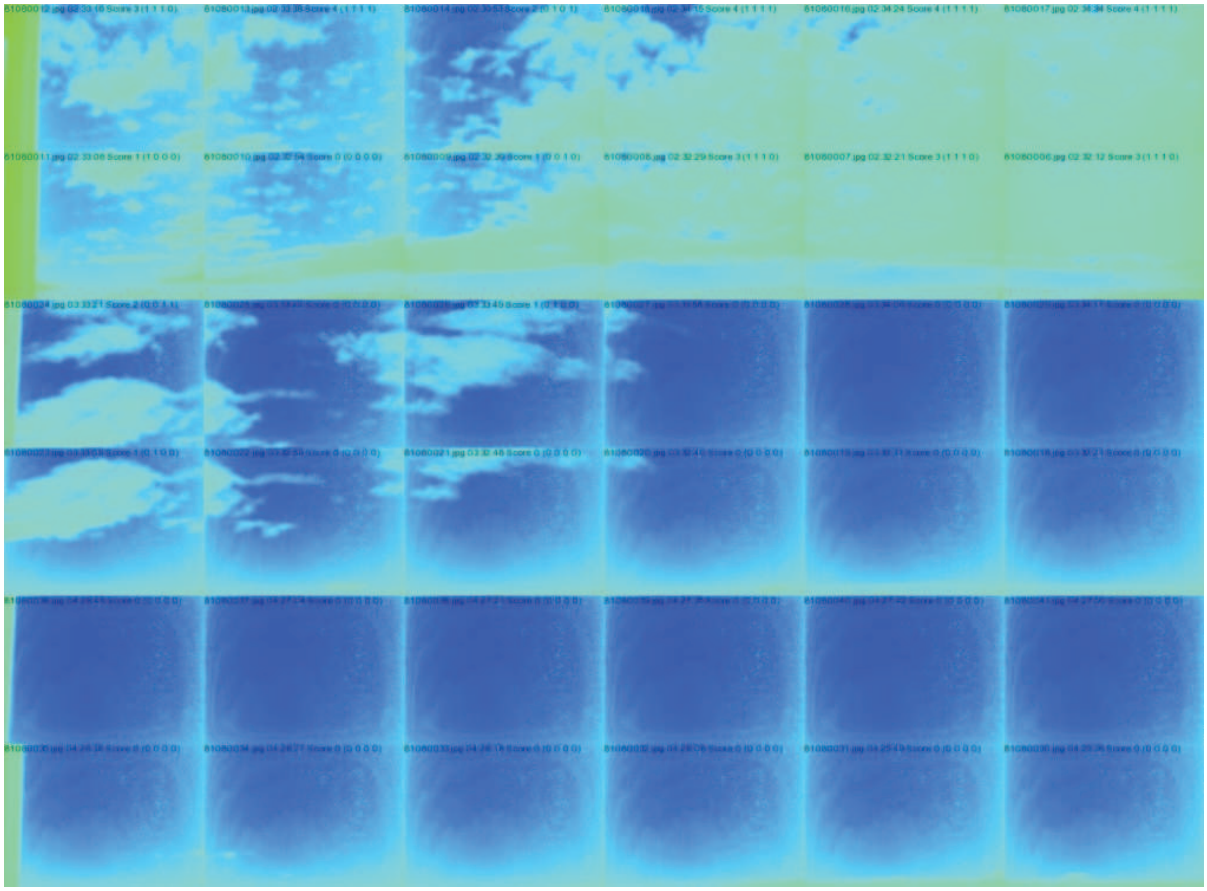

Figure 5.23: How the cloud monitor observed the sky on any given night. This is time progressed along each row, from left to right.

5.2.5.4 Operator Observation

If there was any cloud cover, the lasers would show up in the event display with the light scattering in "cloud blooms". This was one way for operators to determine if the particular data part should be excluded from a spectrum measurement because of much atmospheric uncertainty. This was also an indication that clouds had moved into the view of the detector and may indicate impending precipitation or lightning that might damage the electrical components.

A standard weather code was also used, based on visual sky observation by the operators (see Table 5.2). The cardinal directions and ground haze indications were determined from observations less than 20° above the horizon. Overhead cloud cover was recorded for elevations above 20° and by a number indicating how much of the sky was covered: 0 for no clouds, 1 for less than 1/4 of the sky covered by clouds, 2 for less that 1/2 of the sky covered, 3 for less than 3/4 of the sky covered, and 4 for between 3/4 and a fully overcast sky. A "thickness" number was also used to indicate if stars were visible through the overhead clouds. The first line of numbers in Table 5.2 were the values available for each indication. The other lines in the table show the codes used to determine whether or not the night could be considered clear enough for reasonable reconstruction. If the average night was mostly clear with an overhead coverage of 2 or less, the night was considered to have good weather. The given directional values can be permutated.

5.2.6 Flashers

Occasionally, one of the two GPS modules at the HiRes sites would malfunction and introduce an integral second offset into the data. On these occasions, timing offset corrections between the two sites were determined by the individual detectors' observations of xenon "flashers." These were comprised of a xenon flashbulb placed in front of a mirror (similar to flashlights). One flasher was situated at the Fly's Eye II site, 3.4 km northeast of Little Granite Mountain and was permanently tilted to shoot between the two sites. Operators were able to always see this "intersite" flasher in both event displays

Table 5.2: "Weather codes": the values used to determine nightly atmospheric clarity.

North	East	South	West	Overhead	Thickness	Haze
0/1	0/1	0/1	0/1	0/1/2/3/4	0/1	0/1
0	0	0	0	0/1/2	-	-
0	0	1	1	0/1/2	-	-
1	1	1	1	0/1	-	-

simultaneously and always in the same set of telescopes as long as there was no fog or haze to interfere with the view. For HiRes-1, this was always from telescopes 16/20 to telescope 7 (see Figure 5.5). Abu-Zayyad [6] performed an initial calibration of the intersite flasher (ISF) data, though further analysis of the ISF was again only used for timing corrections. Additional flashers were pointed vertically at positions in a radial pattern directly out from HiRes-2 telescope pairs 1/2 and 3/4 [9]. These were set at distances of 1 km, 2 km, 4 km, 6 km, 8 km and 10 km. From HiRes-1 these could be seen in telescopes 7 through 12 (see Figure 5.5). Primarily these gave operators a qualitative measure of atmospheric clarity [7] since they were a relic of the prototype tests and had no calibration functionality.

5.3 Low-Energy Upgrade

Except for the small upgrade towards the end of the experiment, the descriptions of the HiRes-1 electronics and other equipment can be found elsewhere [9] [7] [8] [30] [34] [19]. In October, 2005, two additional telescopes were installed at HiRes-1 for a low-energy extension prototype study. This section documents this prototype work. We include this description as this project was the sole responsibility of the author and his colleague, Samuel Adam Blake, as part of our "hardware" training in experimental particle physics. In addition, much of the work constituted developing procedures and methods for refurbishing 14 of the telescopes for use on the Telescope Array experiment to be described in the next chapter.

In section 5.1.1 it was noted that HiRes consisted of two sites designed to observe cosmic ray showers with primary energies of $10^{18.5}$ eV and above in stereo mode. This was done by overlapping the observation regions between the detector sites. As was also noted, HiRes-1 was a single ring detector that had a lower energy limit for monocular observation of $10^{18.5}$ eV while HiRes-2 was a double ring detector that was able to observe energies down to $10^{17.5}$ eV (see Figure 5.2). This asymmetry in viewing angles instigated a project which would allow HiRes-1 to extend its low-energy observation limit by adding two additional telescopes that would view higher elevations. This would then allow the stereoscopic energy threshold between the two detectors to be lower.

There were two possible options in pointing the two new telescopes. If they overlooked HiRes-2 directly, the aperture would increase, allowing for better observations of low-energy events that happen higher in the atmosphere. By allowing the telescopes to view to either side of HiRes-2, better geometrical reconstruction is obtained by avoiding events in line between the two sites. We decided that the geometrical reconstruction was more important in analyzing the stereo data.

The project had a further purpose of acting as a prototype for a low-energy extension for the Telescope Array experiment. As will be discussed in the next chapter, some equipment was already chosen to be refurbished for one of the main fluorescence detector sites. This project was used to test for a secondary aspect of the experiment, Telescope Array Low-energy Extension (TALE) [96], which could have the telescopes housed in individual shipping containers.

5.3.1 Buildings

Each telescope was placed in a "connex" box (an 8' × 8' × 20' shipping container) for individual housing while the electronics for both were placed in a ward shelter (a portable, military container) in front of and between each connex box (see Figure 5.24). The connex boxes were supported at a zenith angle of 23° by crossbeams and a movable I-beam that could raise and lower if needed. They had azimuthal viewing angles of 226° and 210° (telescope 24 and 25, respectively) and the elevation angles of both were between 17° and 31° (ring 2).

The doors were rolling garage doors similar to those on all of the other buildings, but much smaller in size. They were controlled remotely or manually by buttons or chains like all of the other doors. The only differences were that these buttons were in the central ward shelter and the chains were on the outside of the boxes.

Unlike the other mirrors at HiRes-1, there were no emergency failsafe curtains. Not only was there not enough room to set up the equipment, but the connex boxes were sitting at an angle which would not allow them to be lowered by gravity. We decided that this was not as critical for these units since the doors would only be opened during a run night and were facing away from sun/moon rise.

The height and angle of the connex boxes necessitated modifications in order to perform the monthly RXF calibration runs. A trap door was cut into the floor between the mirror and cluster and a ladder was erected for accessibility. Stairs were mounted to the floor to assist in balance at the increased angle. Prior to the installation of gravity-driven curtains at HiRes-1, a linen fitted sheet was placed over the mirrors to inhibit reflection off of the mirror segments, should a door fail to close. Later, these sheets were also used to prevent cross-reflection of the RXF during calibration runs. However, the angle of the box prevented convenient use of sheets. Instead, a pull-down curtain was mounted to the ceiling with a hole cut out to allow the RXF to sit in the mirror center.

Figure 5.24: The mirrors and photomultiplier-tube cameras were housed in the two connex boxes overlooking the ward shelter that housed the electronics for both. The door on telescope 25 is open to show the arrangement of the photomultiplier tube camera inside the connex box.

5.3.2 Hardware

As was discussed in section 5.1.1, telescopes 17 and 18 were decommissioned by 2002. One was used for other prototype experiments [83], while the other was initially set in a building that proved difficult to operate remotely and so was dismantled and placed into storage. Since this equipment was not being used, it was instead utilized for this low-energy extension project.

The mirror and camera were positioned far enough into the connex box to allow the back of the camera to fit just inside the door (see Figure 5.25). This arrangement maintained maximum mirror aperture. Due to the height of the front of the connex boxes from the ground, a special bipod was made in order to align the mirror segments. This device could be attached to the front of the connex box to hold a laser screen at the exact distance of the mirror focus. Because of the rigidity of the frame attached to the floor of the connex box, the telescope's pointing direction was only adjustable by moving the box itself.

The PMT camera was mounted in stands sitting just inside the garage door. Reflecting a laser on to the UV filter from the center of the mirror allowed for the camera face to be aligned normal to the central pointing direction of the mirror. It also gave a precise

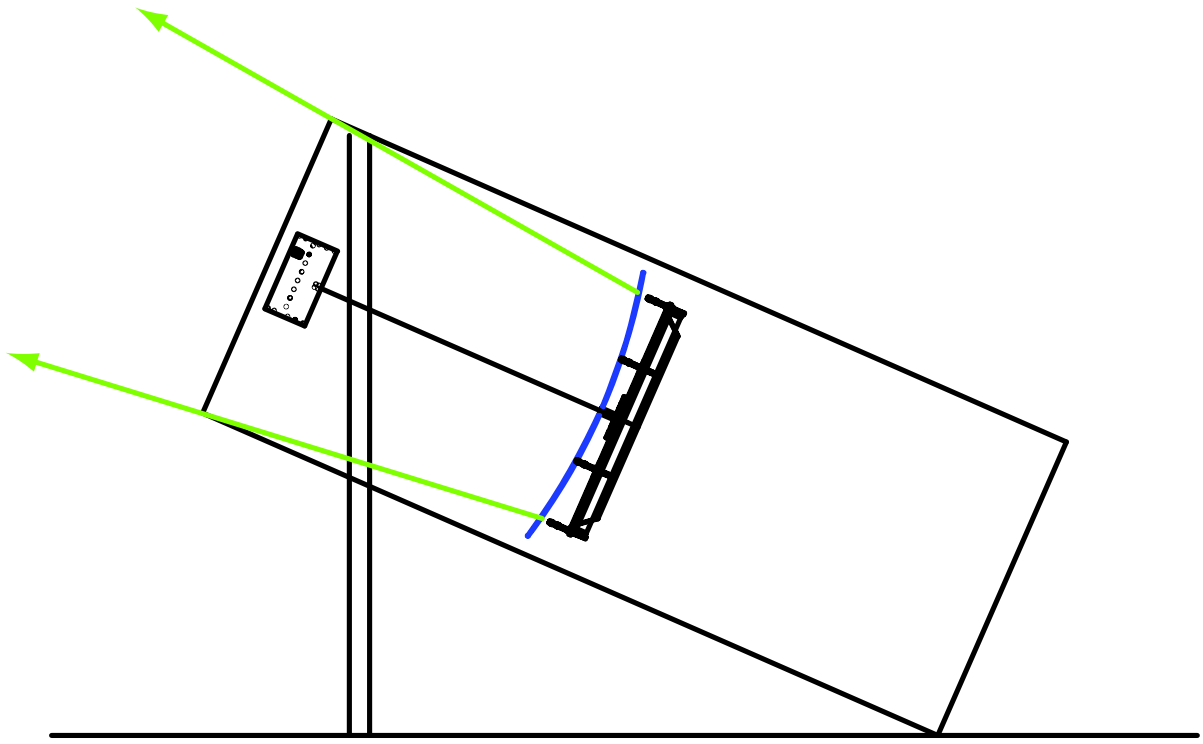

Figure 5.25: The mirrors and photomultiplier-tube cameras of telescopes 24 and 25 were positioned to allow their viewing angles to align with the edges of the connex box opening.

measurement of the optical center line of the mirror with respect to the center of the camera. A survey showed that the camera stand of telescope 25 was misaligned by 3.33 cm in the horizontal direction and 6.83 cm in the vertical direction. This was corrected for in the reconstruction programs and will be discussed in section 5.3.5.

5.3.3 Electronics

The electronic racks for the two ring-2 mirrors were housed together in a separate container box with the signal cables and voltage-supply wires running through plastic tubing into the two connex boxes. Both of the telescopes used Rev-4 cameras, but, as noted in Table 5.1, telescope 24 used Rev-3 electronics while telescope 25 used Rev-4. The high-voltage interlocks controlled both telescopes simultaneously.

5.3.4 UVLED Calibration

Since these two telescopes were housed in new buildings and commissioned very close to the end of the experiment, installing a YAG calibration system was not deemed cost-effective. Instead, these two telescopes were calibrated nightly using electronically-triggered UVLEDs (ultra-violet light emitting diodes) [70] mounted locally at the center of the mirror same location that a YAG laser fiber-optic mount would be positioned (see Figure 5.26). These were used since the wavelength of these LEDs falls within the spectral range of the UV filters (see Figure 5.27). They were controlled through an RJ-45 connection and were pulsed at 4 Hz with an intensity that produced a signal roughly equivalent to the YAG laser at the other telescopes.

The YAG system was originally intended to calibrate each telescope using the same light source. In practice, the fiber-Teflon interface changes the transmission, making the telescope-to-telescope calibration unstable over the long term, as well as being expensive and delicate. The UVLED was tested as a local light source and proved to be sufficient as a PMT calibration technique. The result of this was that the Middle Drum site of the Telescope Array experiment is now utilizing this technique.

5.3.5 Software

Since telescope 17 was removed and telescope 18 was never installed, the central timing hold-off channels for these telescopes were used by telescopes 24 and 25 respectively. The low-voltage and high-voltage channels of 24 and 25 were necessarily used in order to

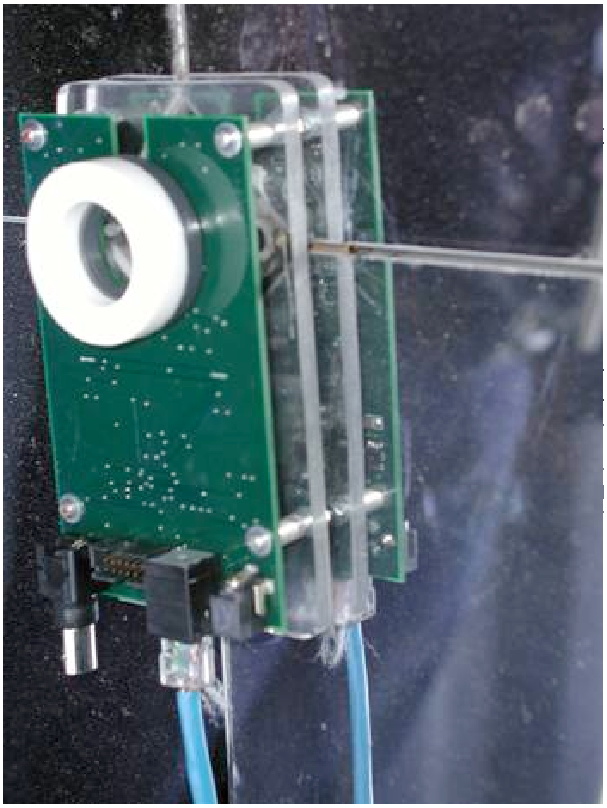

Figure 5.26: A UVLED calibration device used for HiRes-1 telescopes 24 and 25.

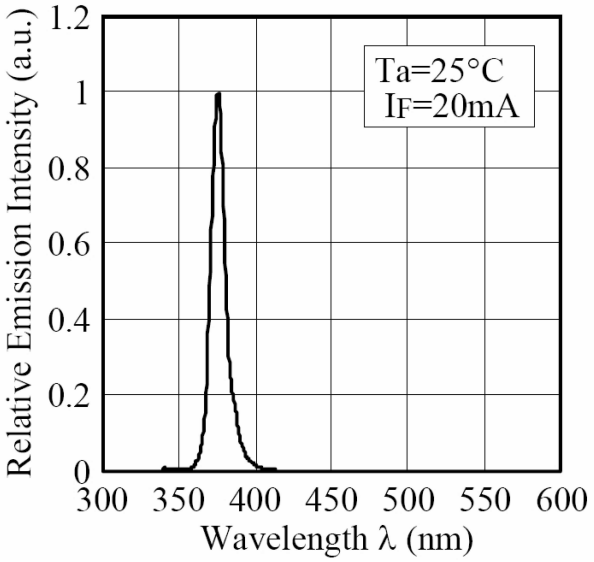

Figure 5.27: UVLED spectrum

control the interlocks. This forced the data acquisition software to understand telescopes 17 and 18 to be 24 and 25 for parts of the program. The event display was also adjusted to compensate for the locations of the two telescopes above telescopes 7, 8, 10 and 11 (see Figure 5.5).

Due to the misalignment of the camera bracket of telescope 25, a new parameter was created to compensate for the x- and y-offset of the camera in the geometry description of the analysis software suite. This program, responsible for determining the pointing directions for each tube, was the only file needing an adjustment. Beyond this, all of the analysis programming was the same as for the rest of the detector (see Chapter 7).

5.3.6 Conclusion

The Low-Energy Extension upgrade produced mixed results as a prototype. Since the shipping containers were extremely cumbersome, it was decided that they would not suffice for the TALE site. However, the utility of the UVLEDs has proven to be extremely convenient as local light calibration sources. The UVLEDs can be calibrated individually and in comparison to each other, and can also be programmed to give any pattern desired. Additionally, if one unit fails, it can be swapped out for a new one.

The construction of the Telescope Array's Middle Drum detector became a high priority after the conclusion of the HiRes experiment. As will be discussed in Chapter 6, much time was needed in order to dismantle HiRes, clean and repair the equipment, and install the telescopes at the new site. Because of this, the data analysis using telescopes 24 and 25 in HiRes-1 monocular mode was never performed on the data taken. This will be assigned as part of a later dissertation project to study the effectiveness of the TALE 6 km stereo detector design [47] (see section 6.1).

CHAPTER 6

TELESCOPE ARRAY EXPERIMENT

The Telescope Array (TA) is located in Millard County, Utah, $\sim$ 240 km southwest of Salt Lake City, Utah, and $\sim$ 160 km directly south of Dugway, Utah, the former location of the HiRes experiment (see Figure 6.1). The TA experiment is a collaborative effort between research groups from the U.S., Japan, Korea, Russia, and Belgium. It was designed as a hybrid detector, using fluorescence telescopes that look over a scintillation counter array (see Figure 6.2).

Additionally, there is a new effort to extend the low-energy limit of the experiment by constructing one more fluorescence detector site and an infill ground array. The Telescope Array Low-energy Extension (TALE) will be able to observe extensive air showers down to $10^{16.5}$ eV in hybrid mode as compared to the $10^{17.5}$ eV energy limit of HiRes-2 in monocular mode. Each fluorescence detector can operate independently and the data can be analyzed in either monocular mode for each site, in a combined stereo mode or in a hybrid mode with the ground array. This chapter describes the overall changes made to 14 HiRes-1 Rev-3 telescope units and the Telescope Array Middle Drum detector site where they were redeployed. The analyses in this dissertation are performed using the Middle Drum fluorescence detector in monocular mode, specifically to provide a direct comparison to the HiRes energy scale.

6.1 Detector Overview

Millard County, Utah was chosen as the site of the TA experiment for two main reasons. First, it was a site large enough to accomodate the ground array, but still close enough to Salt Lake City for the University of Utah to act effectively as the host institution. The second reason is that the atmospheric quality of the region is well characterized by the HiRes experiment (see Chapters 4 and 5) and is the best site for fluorescence detectors in the Northern Hemisphere.

The TA/TALE experiment will consist of a ground array, a total of four fluorescence detectors and an infill array (see Figure 6.2). The main ground array and the two

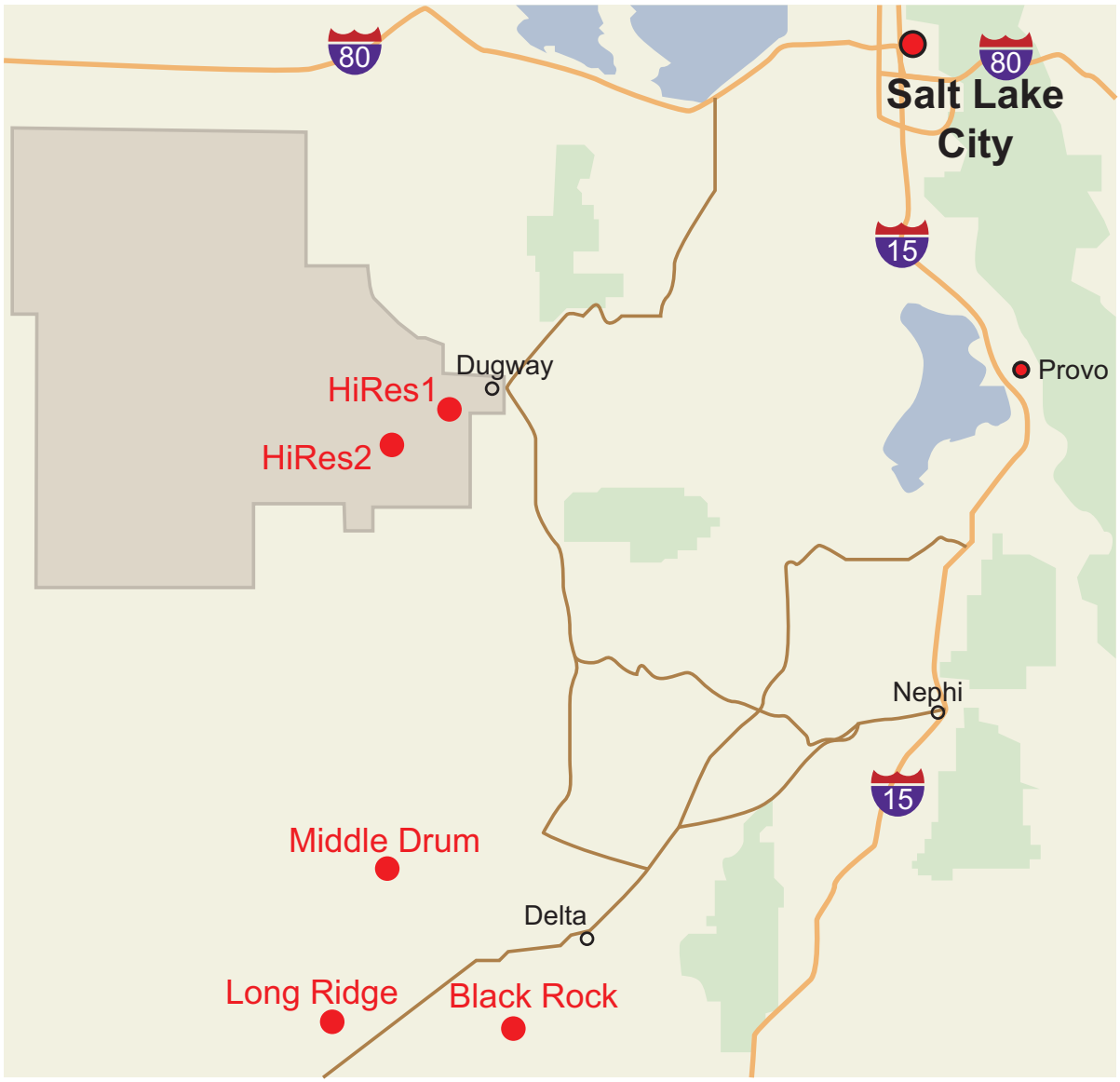

Figure 6.1: The location of Telescope Array relative to Salt Lake City and Dugway, Utah.

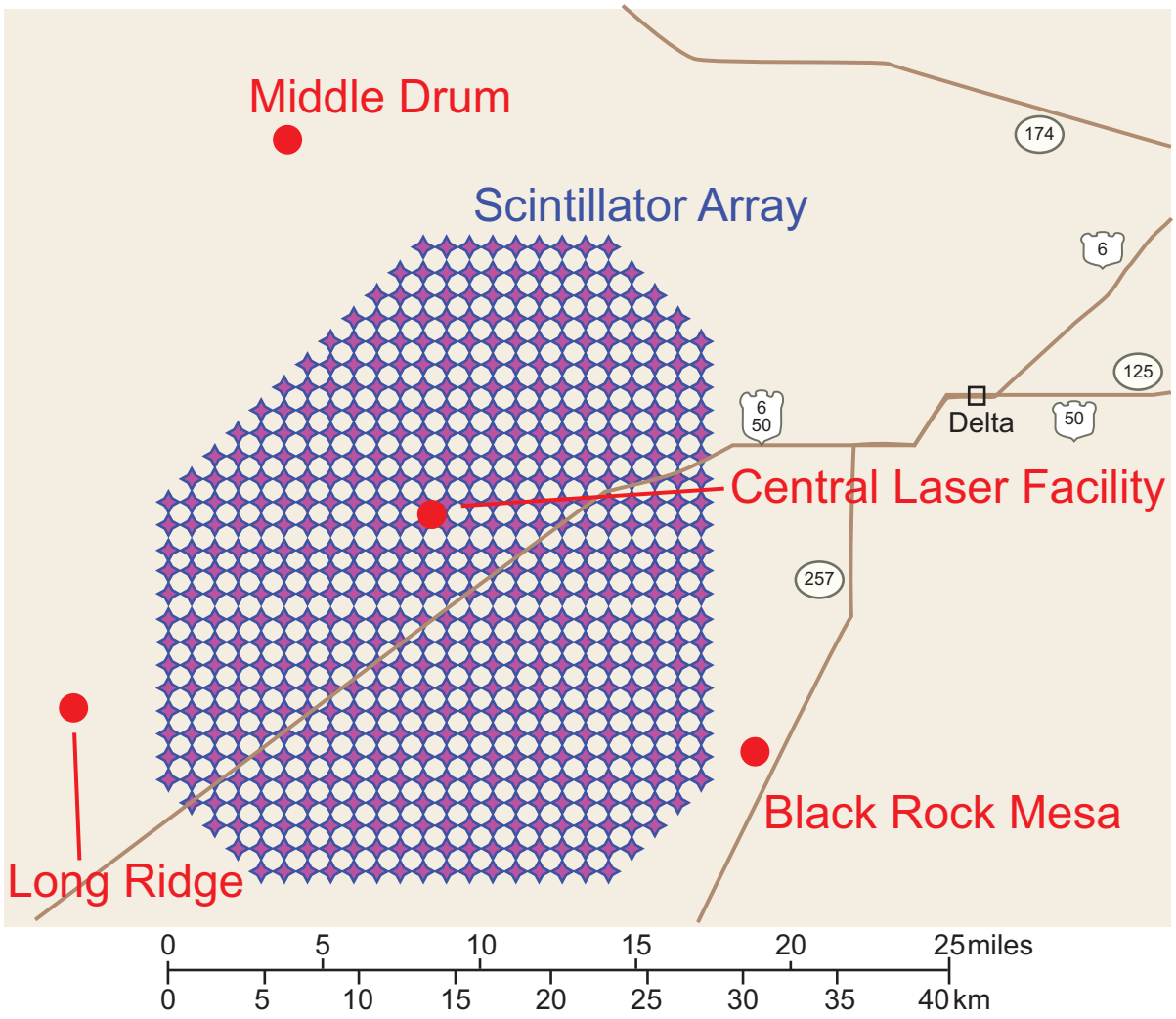

Figure 6.2: The relative locations of the Middle Drum, Black Rock Mesa and Long Ridge sites located around the scintillator ground array.

southern-most TA fluorescence detectors were funded by the Japanese government, while construction costs of the northern-most TA fluorescence detector, the TALE fluorescence detectors, and the infill array will be shared by the U.S., Japanese, Korean, and Russian funding agencies.

The ground array consists of 507 plastic scintillation counters, each 3 m^2 in area, separated by 1.2 km in a square grid (see Figure 6.3). It has a geometrically-limited aperture of 1500 km^2 steradians at energies above $10^{18.8}$ eV, and is optimized for observing showers with energy above 10^{19} eV. The array operates 24 hours a day and therefore collects data at times that the fluorescence detectors cannot. The ground array has a $\sim$ 20% energy resolution and $\sim 1.5^\circ$ pointing accuracy. Made of scintillation counters, they observe the electro-magnetic component of the cosmic ray shower (see section 3.2).

The TA fluorescence detectors look inward over the ground array. The two southern detectors each have mirrors with unobstructed light-collection areas of $\sim$ 4.58 m^2, 23% larger than those of HiRes-1/TAMD. They observe 108° in the azimuth and between 3° and 34° in elevation, which is roughly a third of the field of view of HiRes-2. These were deployed at the Black Rock Mesa and the Long Ridge sites (see Figure 6.2). These two telescopes (see Figure 6.4) are run with FADC readout electronics operating at 10 MHz.

For the initial phase of TA, the northern fluorescence detector site at Middle Drum (TAMD) was to be instrumented with the 14 Rev-3 HiRes-1 telescopes (see Table 6.1). The choice of the HiRes-1 equipment was based on three criteria: (1) the HiRes-1 telescopes required the least effort to refurbish and reintegrate into a running detector; (2)

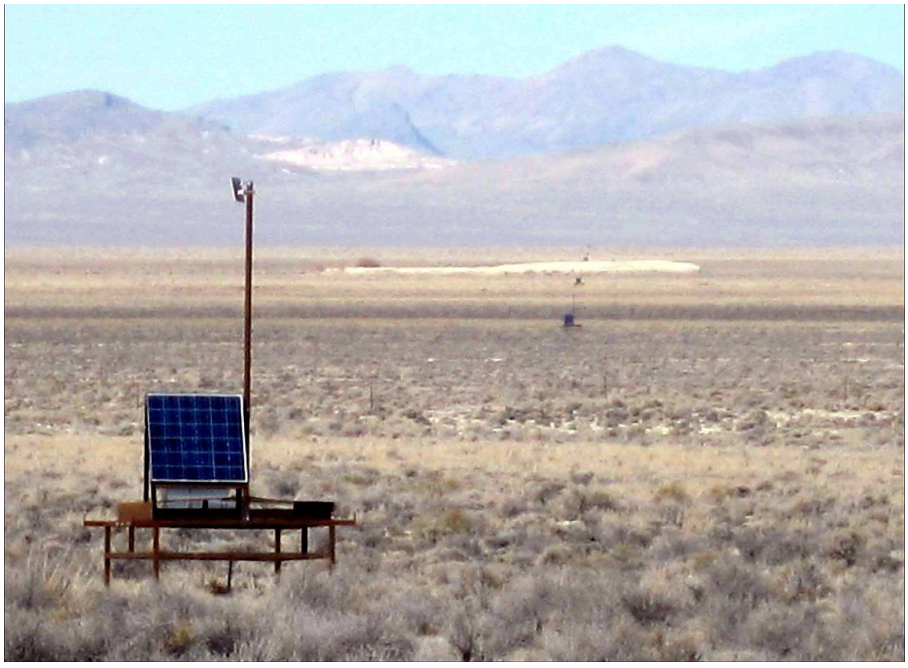

Figure 6.3: Scintillation detectors.

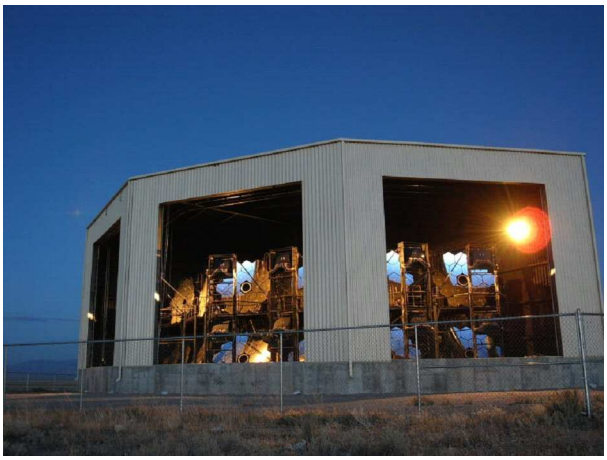

(a) BRM Building

(b) BRM Mirror

(c) BRM camera

Figure 6.4: Black Rock Mesa detector. Figure 6.4(a) shows the telescope building with open doors. Figure 6.4(b) shows one of the telescope mirrors. Figure 6.4(c) shows a telescope camera. The Long Ridge detector is similar.

Table 6.1: This table shows the Middle Drum configurations of the previous HiRes-1 electronics/camera location, the date the equipment was first used for data processing, the photomultiplier tube type, the electronics version, and the previous HiRes-2 mirror location.

Telescope Array#	HiRes-1 Elect./Camera #	TA Start Date	PMT Manufacturer	Electronics Revision	HiRes-2 Mirror #
1	1	Dec-16-2007	EMI	3	22
2	6	Dec-16-2007	EMI	3	17
3	3	Dec-16-2007	EMI	3	21
4	4	Dec-16-2007	EMI	3	18
5	9	Dec-16-2007	EMI	3	36
6	11	Dec-16-2007	EMI	3	34
7	7	Dec-16-2007	Phillips	3	35
8	8	Dec-16-2007	Phillips	3	33
9	2	Dec-16-2007	Phillips	3	32
10	10	Dec-16-2007	Phillips	3	29
11	5	Dec-16-2007	Phillips	3	31
12	12	Dec-16-2007	Phillips	3	30
13	13	Dec-16-2007	Phillips	3	19
14	14	Dec-16-2007	Phillips	3	15

TALE will require more equipment than is available at HiRes-1 so that we have reserved HiRes-2 equipment for use later on TALE; and (3) the use of the 14 HiRes-1 telescopes also allows us to make direct comparison of the energy flux measured at TAMD to that published in the HiRes paper, "First Observation of the Greisen-Zatsepin-Kuzmin Suppression" [3], in which most of the statistical significance of the GZK suppression comes from the HiRes-1 monocular data.

As stated above, fluorescence telescopes from HiRes-2 are intended to create a low-energy extension (TALE) detector. This will be deployed 6 km inward from the Long Ridge fluorescence detector. Due to overlapping coverage, TALE will provide additional high-energy stereo aperture, creating a total of 2200 km^2 steradians (half from the array, half from the telescopes). Compared to HiRes, TALE will also provide a better stereo aperture around the ankle, allowing for a better understanding of both the energy spectrum and composition in this range (see Figure 6.5).

In addition, there will be a tower detector located at the TALE site which will observe from 31° to 73° (see Figures 6.6 and 6.7) [87]. These will have a light-collection area three times that of HiRes and are optimized to observe showers with energies between $10^{16.5}$ eV and $10^{18.0}$ eV. Using an infill array of 100 scintillation counters placed in a 400 m square grid in front of the tower's observing azimuth (see Figure 6.8), the TA/TALE hybrid spectrum will be measured down to $10^{16.5}$ eV. A 300 m square grid of muon counters will

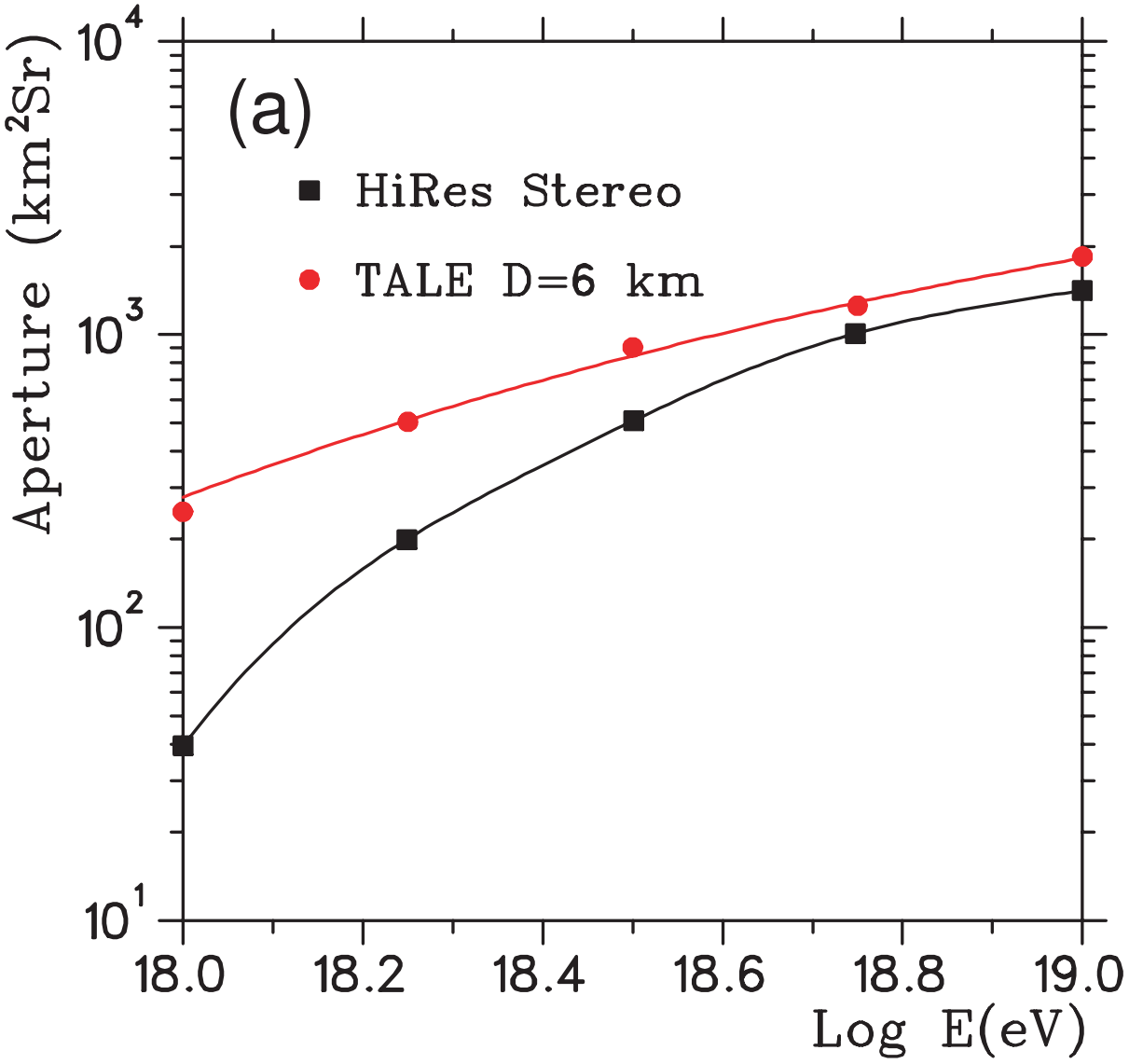

Figure 6.5: This graph shows the estimated aperture of the TALE detector compared to HiRes stereo.

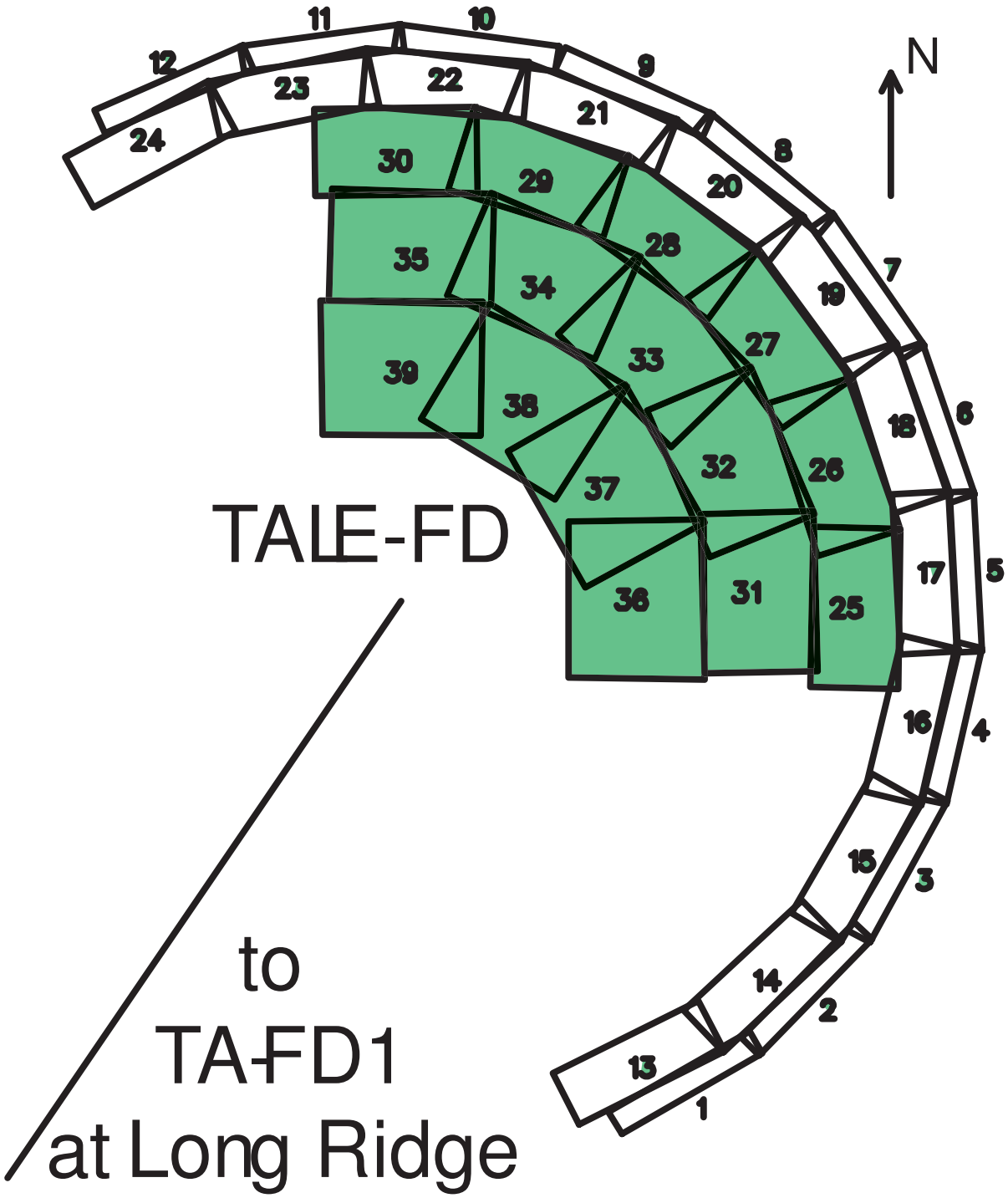

Figure 6.6: The upper image shows the layout of the TALE detector pointing directions. As can be seen in TALE-1 there are five rings, the upper three being the tower pointing directions.

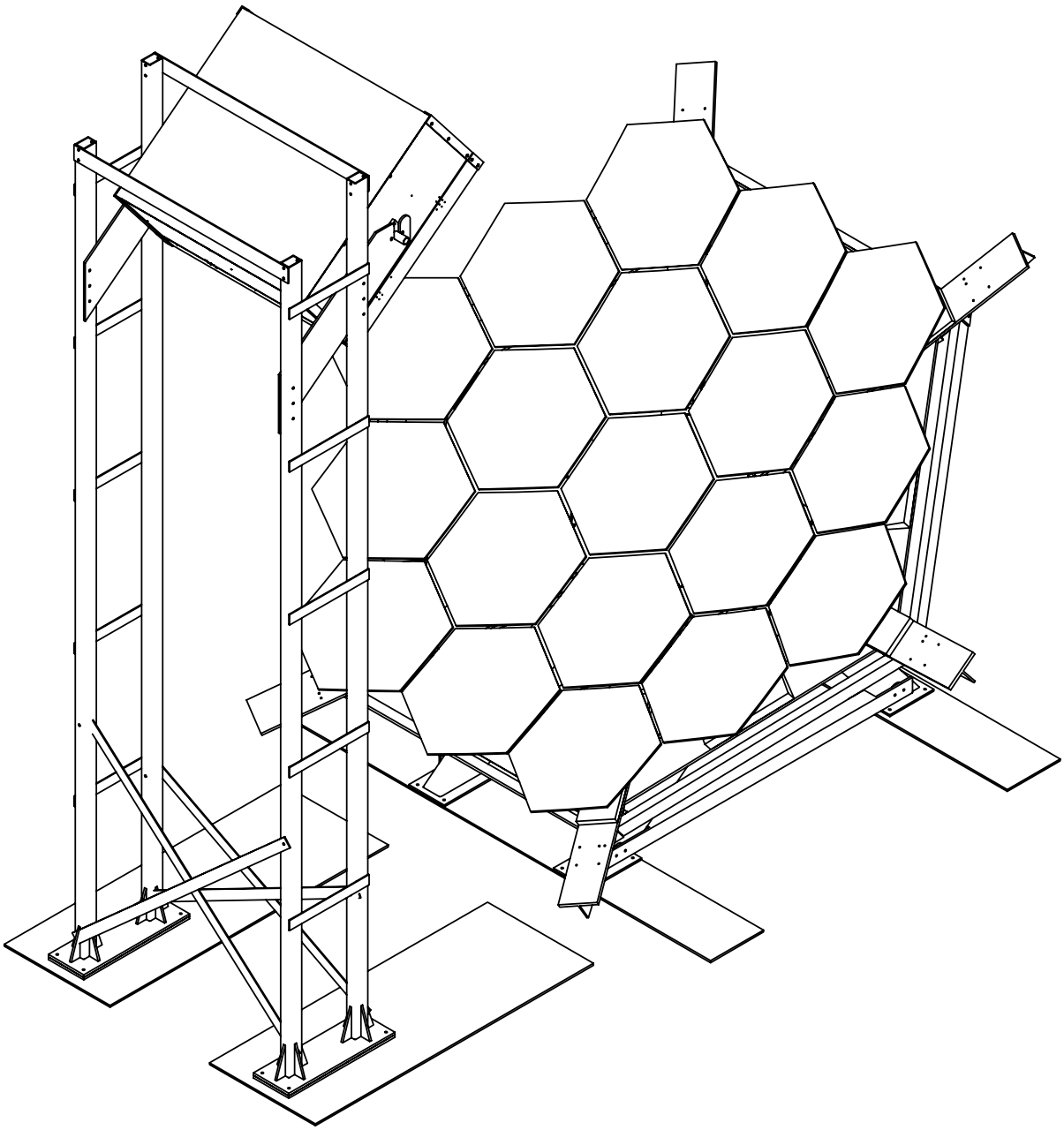

Figure 6.7: A schematic of the TALE Tower which would point in the highest elevations.

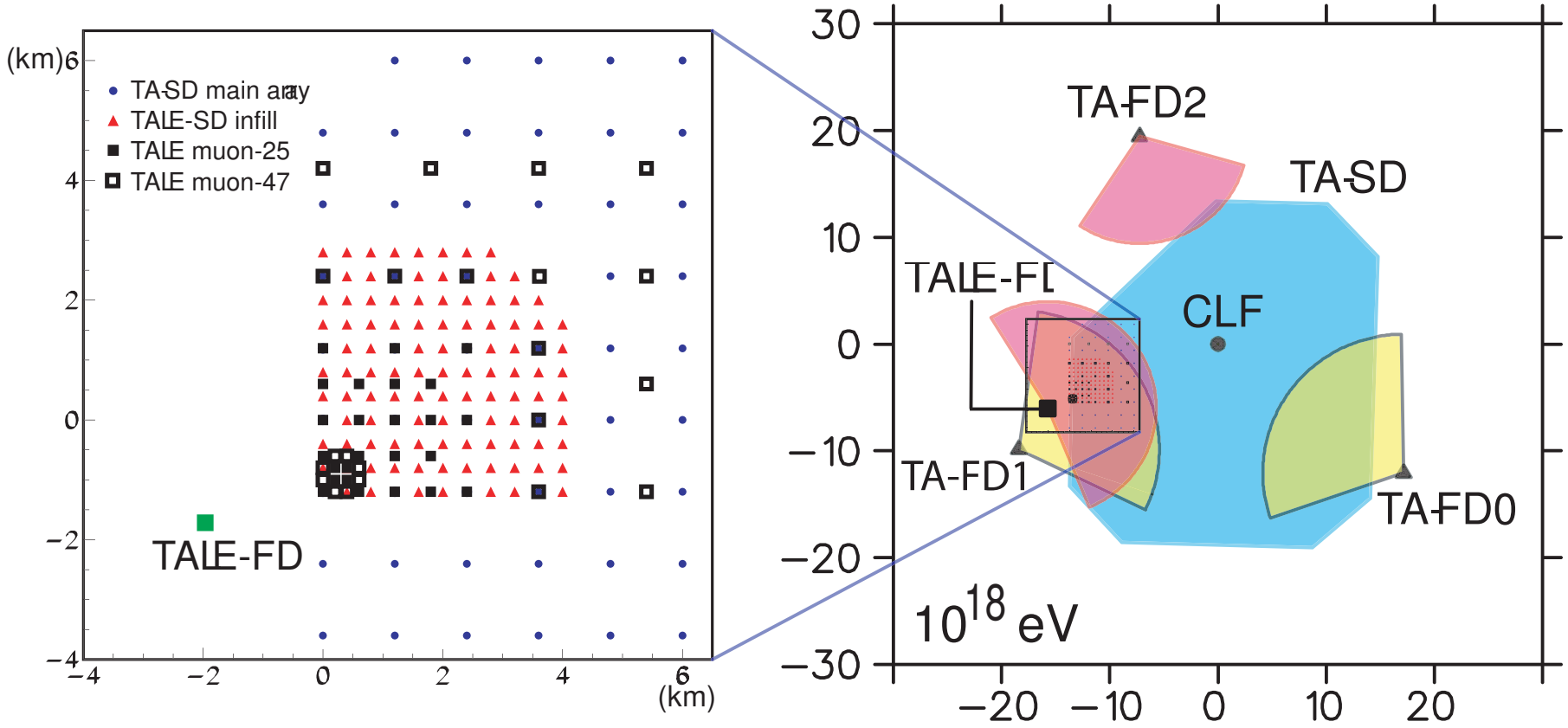

Figure 6.8: The TALE infill array is composed of 100 scintillation counters placed in front of the TALE detector within the TA ground array. Additionally, the muon counter placement can be seen overlapping the infill array.

overlap the infill array, allowing for an orthogonal measure of composition based on μ/e ratios.

Different combinations of detectors will provide overlapping coverage from $10^{16.5}$ eV to the highest energies (see Table 6.2). The Long Ridge fluorescence detector (TALR) will join in stereo observations, providing cross-checks between the detectors (see Figures 6.5 and 6.9). The 6 km TALE fluorescence detectors will operate in stereo mode with TALR to observe events with at least 10^{18} eV. For energies of 10^{19} eV and greater, the TA ground array and other fluorescence detectors will assist in the cross-calibration of events. This will be the first experiment that will effectively produce a consistent energy spectrum from $10^{16.5}$ to 10^{21} eV, which will be able to show all of the major UHECR features and their potential sources.

6.1.1 Middle Drum Refurbishment

Between November, 2006 and June, 2007, 14 HiRes-1 Rev-3 telescopes were refurbished and installed into the TA detector site at Middle Drum, at the northwest corner of the ground array (see Figure 6.2). Much work went into refurbishing and modifying the HiRes equipment in order to make it suitable for TA. This section documents efforts led by the author, with the help of Melissa Maestas, Monica Allen, and Jon Paul Lundquist, to refurbish and reach the final parameters used for the detector.

6.1.1.1 Recovery

Middle Drum (TAMD) was designed to be a two-ring detector in a concave building (see Figure 6.10) overlooking the ground array. The electronic equipment of telescopes 1 through 14 from HiRes-1 has proven to be rugged and highly flexible over its 15-year lifetime. Since TAMD was designed to be a two-ring detector, we used 14 mirrors (not including the cameras and electronics) from HiRes-2 for the new telescopes instead of

Table 6.2: This table shows what we can learn over various energy intervals concerning extragalactic sources and which detectors will observe said sources.

Energy Range	Physics	Detector Combination
$10^{16.5}$ to $10^{18.0}$	the cause of the second knee	Tower, Infill Array
$10^{16.5}$ to $10^{18.7}$	galactic/extra-galactic transition	Tower, Infill Array, LRFD
$10^{18.0}$ to $10^{18.7}$	evolution parameter	TALE-FD, LRFD
$10^{18.0}$ to $10^{19.4}$	pair-production from the CMBR	TALE-FD, Main FDs, SDs
$10^{18.0}$ to $10^{19.4}$	mean spectral index	TALE-FD, Main FDs, SDs
$10^{19.8}+$	pion production from CMBR	Main FDs, SDs

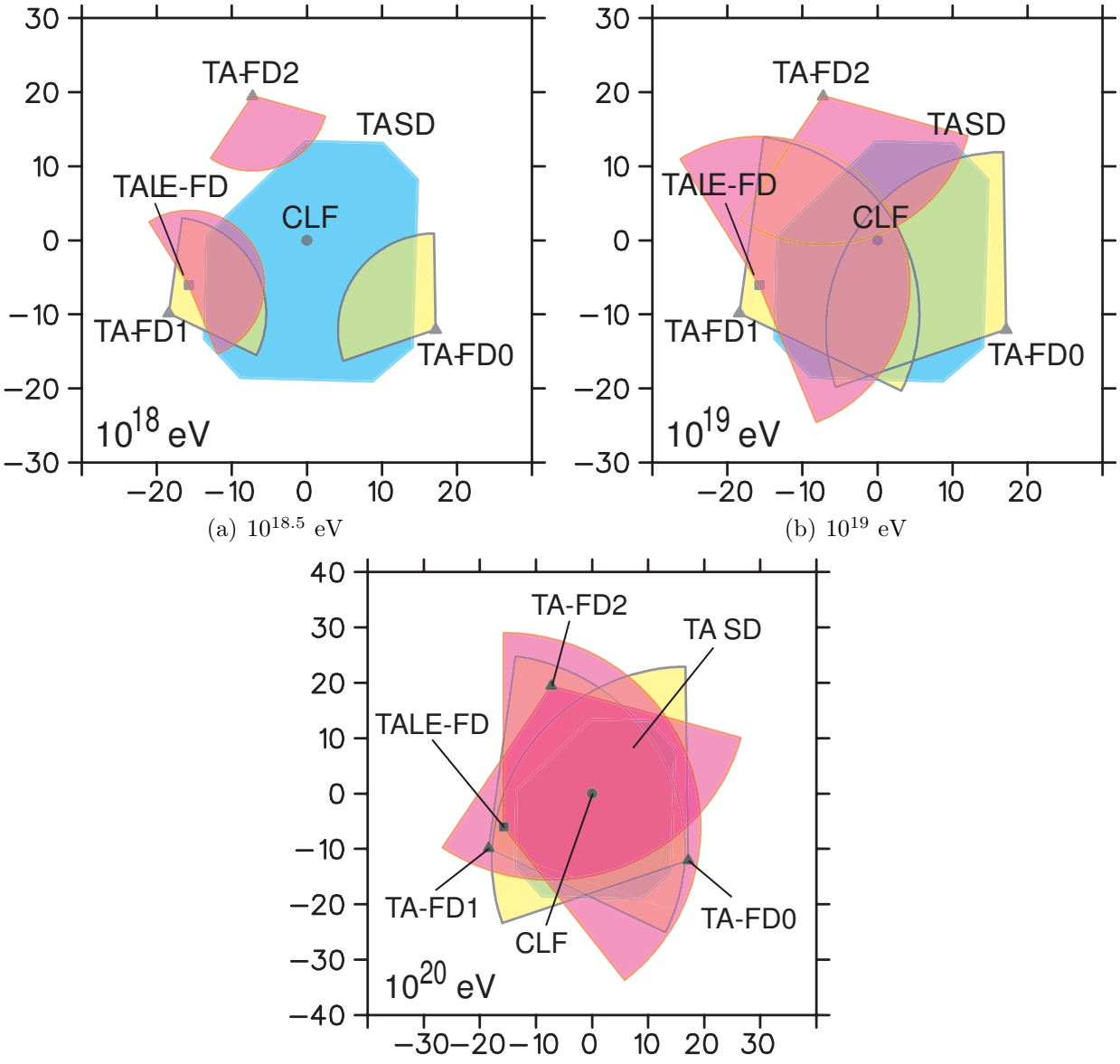

(a) $10^{18.5}$ eV

(b) 10^{19} eV

(c) 10^{20} eV

Figure 6.9: Monte Carlo studies of different energies for the TA and TALE detector sites. Figure 6.9(a) shows the observable range for the three TA sites with the TALE site at energies of 10^{18} eV. Figure 6.9(b) shows all five fluorescence detector sites at energies of 10^{19} eV and Figure 6.9(c) shows all five observing simulated showers at 10^{20} eV.

Figure 6.10: Middle Drum telescope building.

remaking mirror stands for HiRes-1 mirrors. These mirrors were transported directly to the TAMD site after extraction from Camel's Back Mountain. The readout electronics and PMT cameras both came from HiRes-1 in order to be consistent in their data collection and electronic types (see Table 5.1). They were transported back to the University of Utah to be cleaned and reconfigured (see below).

6.1.1.2 Refurbishment

This section describes the individual parts of the refurbishment process that was performed. This documentation is included for the benefit of future users of the equipment.

- Pretest:

  Before cleaning the equipment, an electronic calibration was performed on the camera and VME boards in order to verify the settings known from the last HiRes-1 data run. A "PPG test," "diagnostic," and "calibration" (see section 5.2) were run and the HV supply was turned on without being attached to the PMT camera. All were found to have essentially no variance in the values last set at Little Granite Mountain as of April of 2006 (see Figure 6.11).

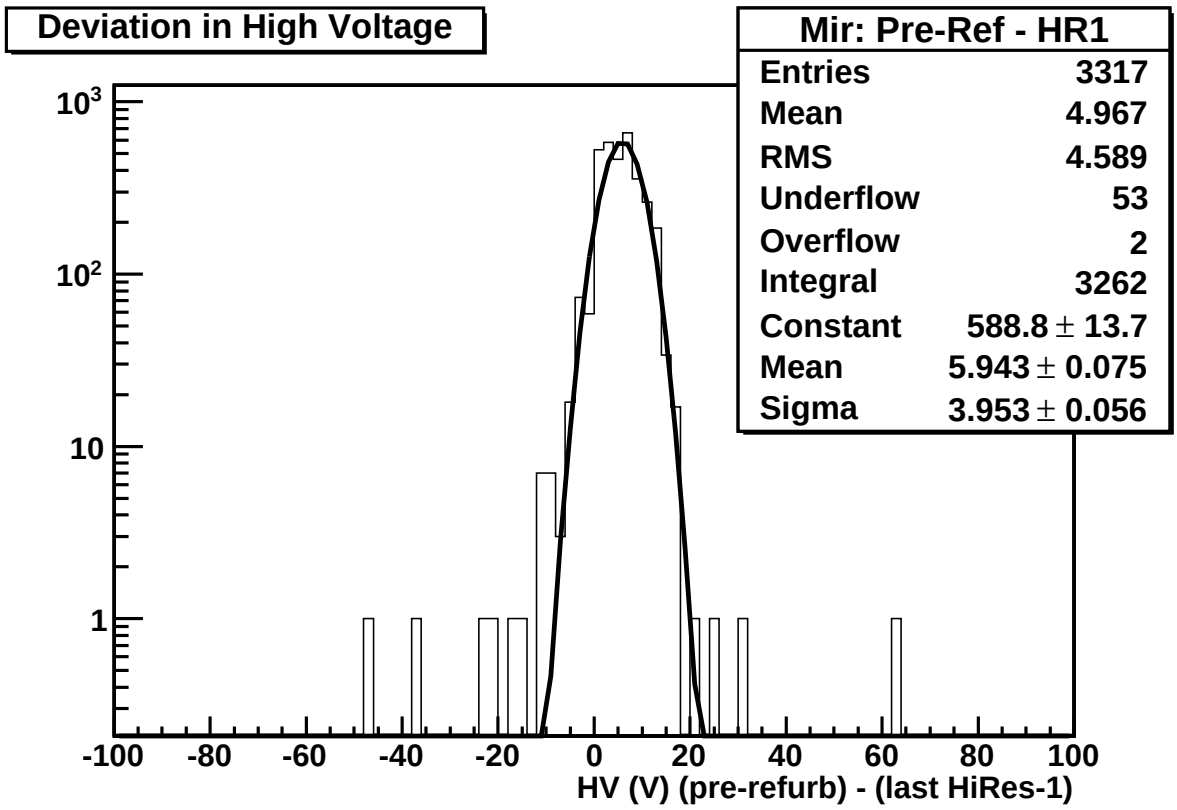

Figure 6.11: This histogram shows the difference in high voltage values between the final rxf calibration data obtained at HiRes-1 those obtained during pretesting for refurbishment.

- Cleaning:

  A significant amount of debris was found in both the electronic crates and the PMT cameras. Most of the damage was inflicted by rodents chewing up wiring and cable shielding for use as nesting material. The resulting refuse even included chewed up pieces of steel wool and cables installed specifically to prevent pest access at Dugway. In addition, rodent excrement was found. The combination of these waste materials constituted substantial hazard both for the proper electrical operations of the equipment and to the health and safety of the personnel. It was therefore essential that the recovered equipment was thoroughly cleaned before being reconfigured for use at the TAMD site.

  The caked excrement in the equipment was first chiseled away and vacuumed out. The electronic rack casing, the electronic crates, the less-delicate electronic boards, and the camera casing were then washed using bleach water and allowed to dry thoroughly. The delicate electronics were subjected to more careful but thorough cleaning with ethyl alcohol to make sure there were no urine drips down their faces. The PMT faces and the the UV filters were also washed with alcohol to remove the dust without leaving smears.

- Refurbishment Changes:

  To prevent further rodent damage, wire mesh was placed on both the floor and ceiling of the electronic racks. Additionally, the racks were mounted on raised platforms that mice and rats would have difficulty climbing. In contrast to HiRes, the signal cables, power cables and central timing wires at TAMD pass through elbow piping mounted on the roofs of the electronic rack (see Figure 6.12), across cable trays to the PMT camera, power outlets, and the central timing rack, respectively.

  To impede rodent access into the camera, rubber gaskets were installed on the sides (see Figure 6.13). Narrow slits in the gaskets allow the signal cables to pass through to the backplane, but were tight enough that they could only be opened with human strength and dexterity. By the time of this dissertation, the rodent-prevention measures seem to be effective since there has been no need to replace the signal and high-voltage cables.

  At HiRes, there were four or more Fan-Paks (integrated 3- or 6-fan modules) per rack to keep the rack temperature within operating range over the course of the night. During summer these helped to extract the heat away from the electronics. In winter they helped to keep the electronics from getting too cold. For TAMD, the number of fans was reduced and rearranged (see Figure 6.12), and a current

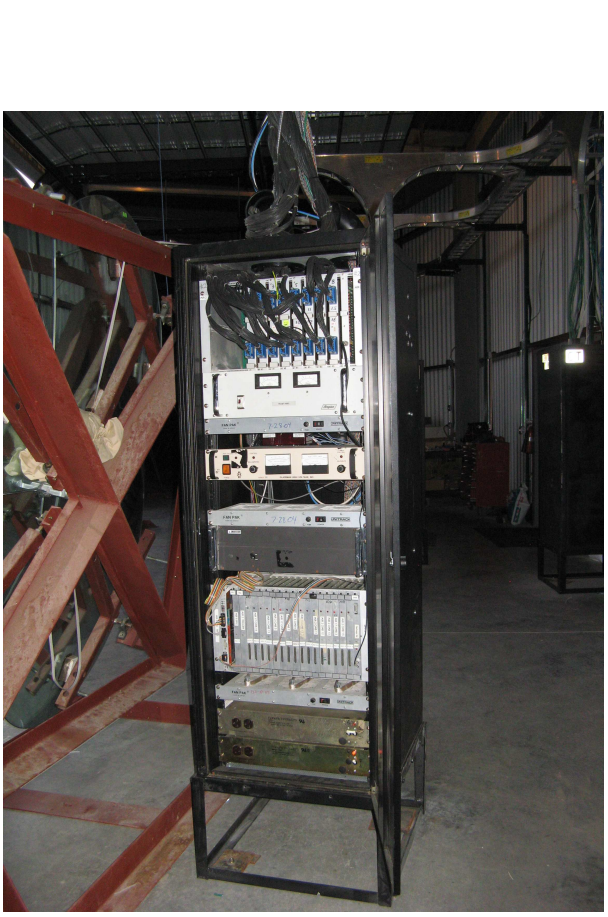

(a) picture

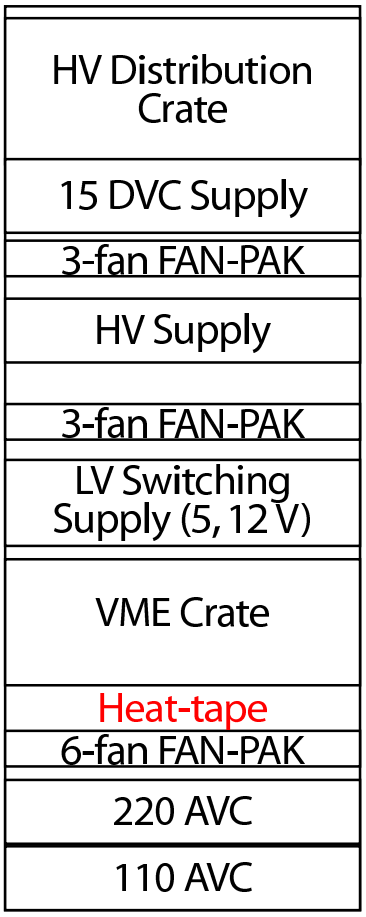

(b) schematic

Figure 6.12: These are an image and a schematic of the positions of the crates determined ideal for TAMD electronics rack crates.

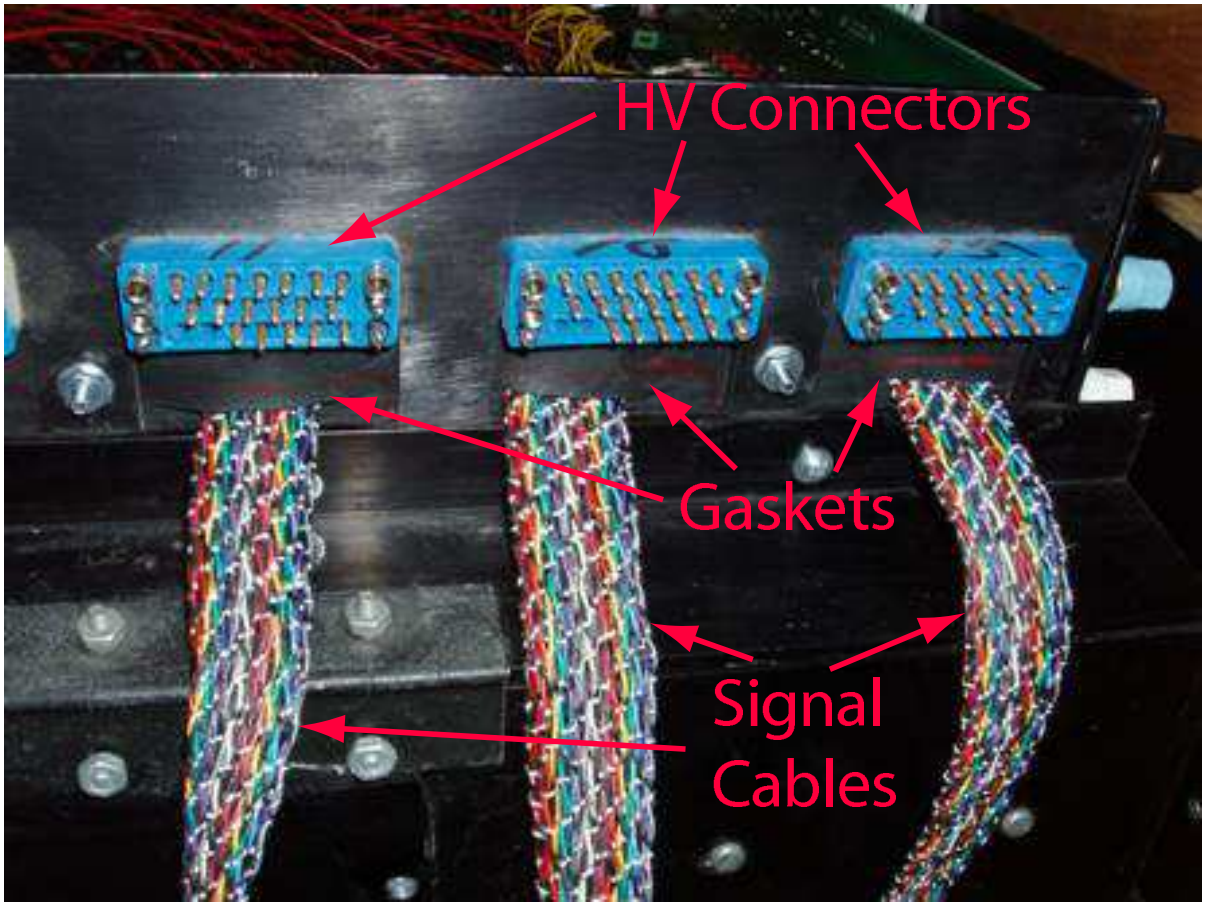

Figure 6.13: These gaskets were installed into the sides of the camera so mice can not gain access.

sensor was added to help operators identify malfunctions in the fans. A current of 2.5 A was established as the normal drain when all fans in a rack are operating correctly. A test was performed to see how the drain responded by physically stopping various numbers of fans within any of the three Fan-Paks (see Figure 6.14). Various combinations of the same number of fans were jammed, but all showed the same increase or decrease in current: since the motors are still trying to drive the stuck fans, the current increases; if a Fan-Pak is turned off, the current indicated is less than the 2.5 A maximum when all units are working.

To help keep the electronics at running temperatures during the winter, a heater was built using one of the Fan-Paks. Heat tape was threaded across the upper surface of the lowest fan which would blow the heat through the rack. If the temperature dropped below 10° F the heat tape turns on by a solid-state relay connected to a pressure-temperature-humidity (PTH) board (see Figure 6.15) .

Middle Drum is not on a power grid like HiRes was at Dugway so the detector is being converted into complete remote operation through the power of diesel generators. In order for the generators, and therefore the equipment, to turn on remotely, a computer must always be accessible. Solar panels will be used to power

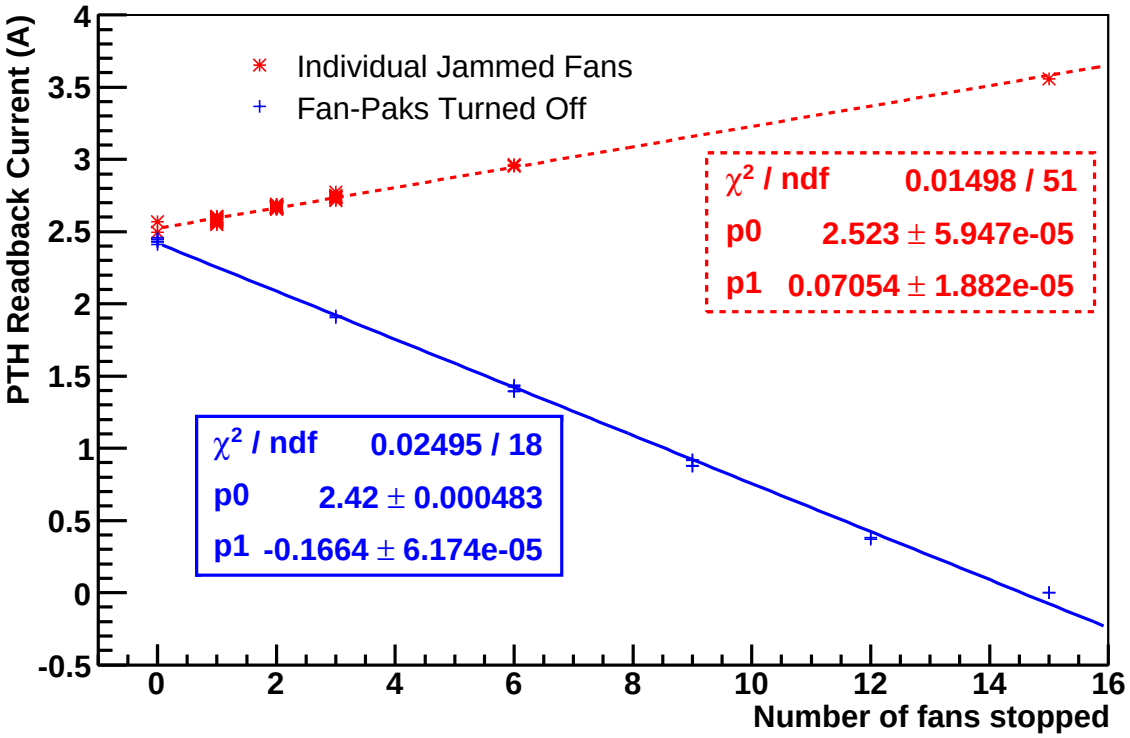

Figure 6.14: The current change as a function of the number of stopped fans.

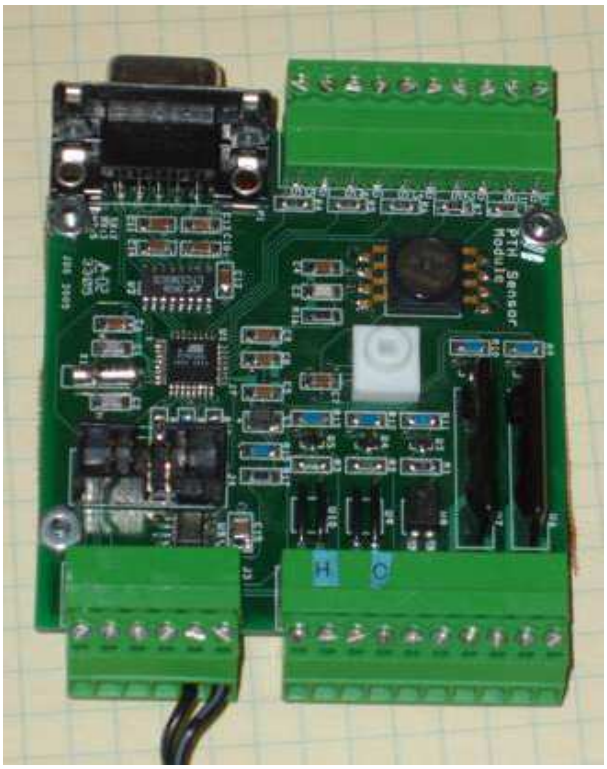

Figure 6.15: A pressure-temperature-humidity board designed and manufactured by the Utah TA group.

that computer which will also be powering the PTH board installed in each rack. Not only can they be accessed in order to turn on the racks, but they are used to monitor the actual atmospheric qualities inside the rack to ensure proper running conditions. As previously mentioned, this board also monitors the fan currents and is the interface between the rack interlocks and the central timing rack and operations computer.

The final upgrades for the TAMD telescopes were in the cabling. Unshielded twisted-pair cables that carried the common-stop ("hold-off") gates from the telescopes to central timing (CT) for GPS time-stamps were replaced with RJ-45 cables (see Figure 6.16). Whereas the HiRes-1 cable lengths varied according to the telescope building location, and the delay of each had to be individually calibrated, the new TAMD cables were cut to equal lengths with a constant 174.8 μs delay. This improvement was made feasible by the deployment of all the telescopes in a single building. In addition, the mixed twisted-pair (10base-T) and coaxial cable (10base-2) ethernet distribution used at HiRes-1 (which was the ultimate limit in data rate) was replaced with a fully parallel twisted-pair ethernet. Lastly, the console terminal (RS232) port of each telescope is now attached to a new ethernet-to-serial adapter ("R. E. Smith" interface module [81]). These provide

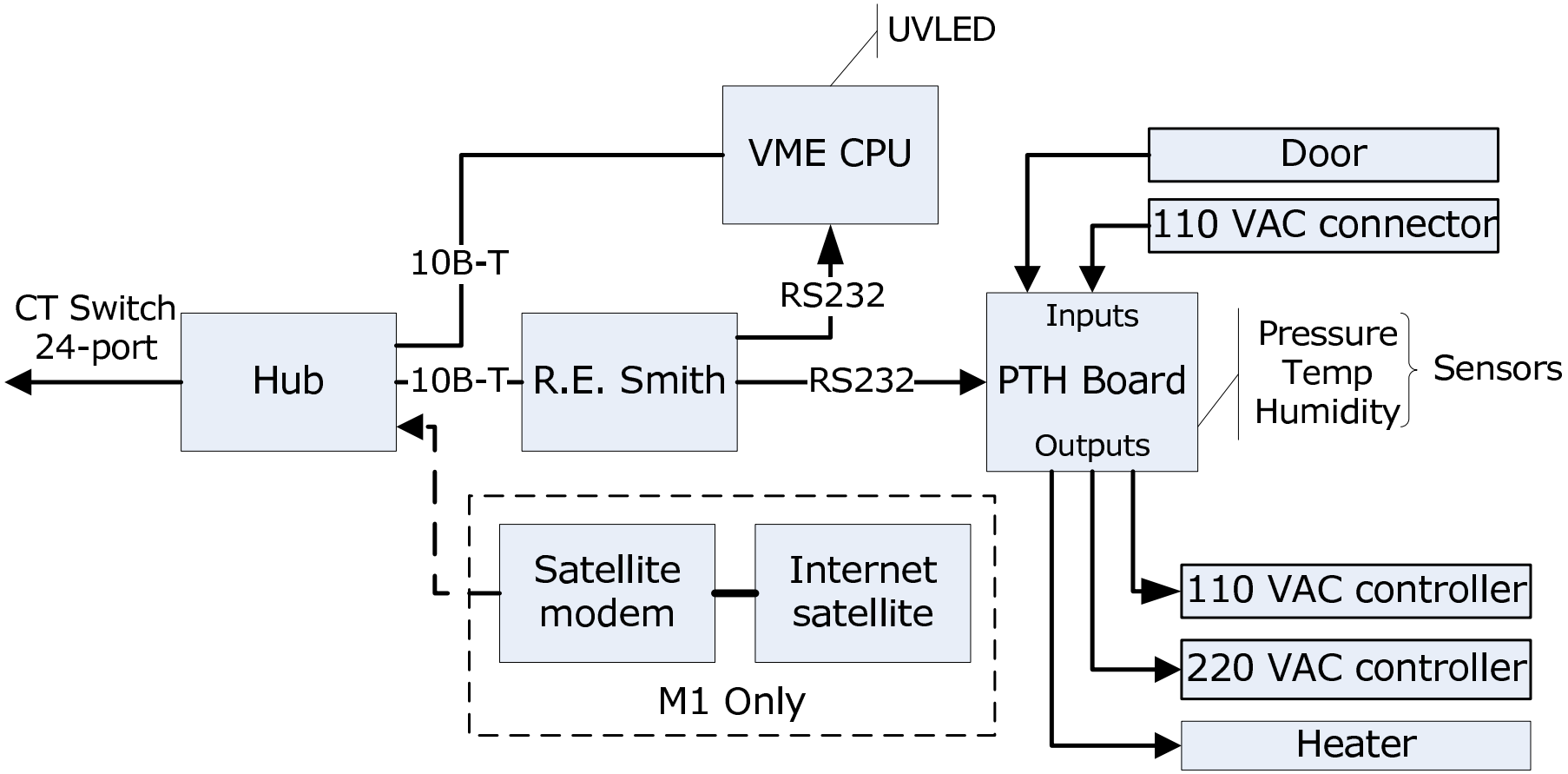

Figure 6.16: TAMD electronics schematic. An RJ-45 cable was placed between the central timing crate and the hub in each of the telescopes. This hub was then used to transmit all I/O information to the VME CPU board that controlled the data collection through a 10base-T cable. A second 10base-T cable connected the hub to the R. E. Smith interface module which was connected to both the CPU board and the PTH board to allow the electronic interlocks to control the voltage supplies.

the interface to the PTH boards, and therefore the electronic interlocks, as well as the ability to reconfigure and debug the CPU boards directly from the DAQ computer. An additional modem was placed in telescope 1's rack which connected the internet satellite to the central timing crate, allowing offsite transmission of information.

- Recalibration:

  A majority of the refurbishment time was dedicated to repairing and recalibrating the readout electronics and PMTs. The basic procedure was to run a test using programmable pulse generator (PPG) signals, a diagnostic (diag) test, and electronic calibration (calib) to make sure OMBs, PMTs, and PMT preamplifiers were working as designed (section 5.2.1). Repairs are made if the component fails any of these tests. Next, an initial roving xenon flasher (RXF) run was performed in order to measure the original gain settings of the tubes.

  The gain of each tube is given by a power law of the voltage applied:

$$\ln G = \alpha + \beta \ln V \tag{6.1}$$

  The exponent β is approximately equal to the number of amplification stages (i.e., the number of dynodes and the anode). For HiRes-1/TAMD tubes, $\beta \approx 6$ so that an approximation for the PMTs used during refurbishment was

$$\frac{\Delta G}{G} \approx 6\frac{\Delta V}{V} \tag{6.2}$$

  where G is the gain of the tube and V is the voltage applied. By knowing the target gain (corresponding to QDCB = 1492), the current gain of the tube and the current voltage, an iterative sequence of adjustments to the voltage would lead to the desired gain. RXF data were taken during each iteration in order to obtain the new gain of every tube at each adjustment until the desired value was reached.

  In order to bring the high voltage up or down, depending on whether the gain was too low or too high, placement of the wires in the HV peg boards were adjusted. This meant every tube in a camera must, ideally, be within the 500 V range available from the resistor drops from the HV supply setting. Occasionally a tube would require a finer voltage adjustment than was available, but most tubes were set within 5% of the target voltage. Individually, the necessary tube gains covered a wide range of voltage settings (see Figure 6.17). The final high voltage supply settings for each camera can be found in Table 6.3.

  As mentioned above, a mean QDCB signal voltage of 1492 V was chosen as the setting for ideal sensitivity. At the time of refurbishing, this value was

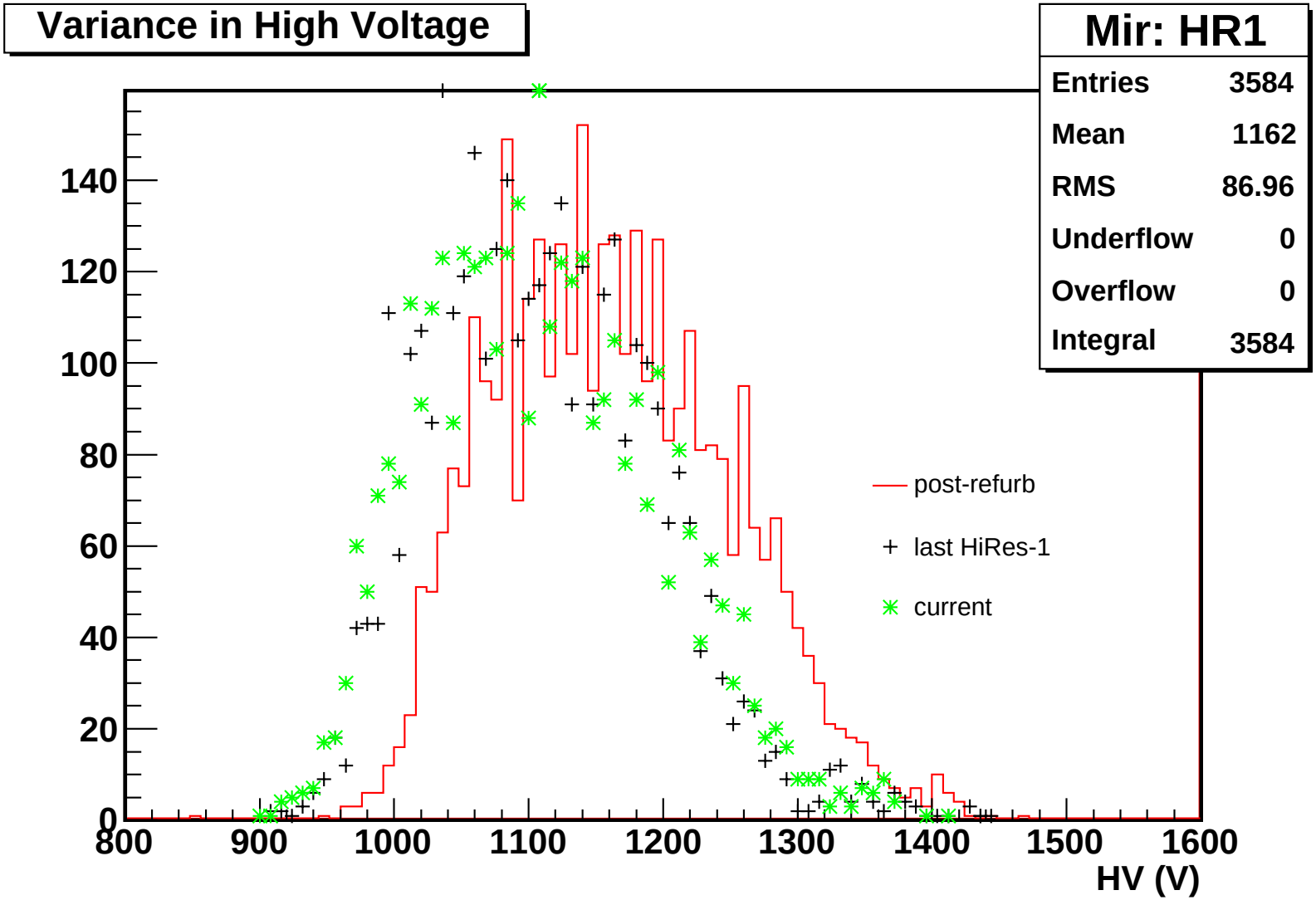

Figure 6.17: This set of histograms shows the HV values for each tube in all of the mirrors. As can be seen, the current values center on values ~ 50 V less than the values originally set to during refurbishment.

Table 6.3: These final high voltage supply settings show differences in the average high voltages depending upon the type of tube used in each camera (see Table 6.1).

Telescope	Supplied HV (V)
1	1361
2	1376
3	1357
4	1362
5	1415
6	1348
7	1275
8	1349
9	1335
10	1269
11	1287
12	1306
13	1284
14	1288

mistakenly set after pedestal subtraction, whereas the intent had been for 1492 before pedestal subtraction. The extra gain ($\sim$ 15%) actually made the detector system unstable, causing the self-adjusting thresholds to reach their upper limits and the PMTs saturate. These were lowered in the field and stable operations were established (see Figure 6.18). This adjustment of the HV values also established the first date of usable data: December 16, 2007.

6.1.2 Telescope Units

As with HiRes, each telescope unit consisted of three main parts: a mirror, a PMT camera, and an electronics rack. Since these are refurbished HiRes detectors (see section 5.1.2), this will be a summary of the differences to HiRes.

- Mirrors

  The Telescope Array Middle Drum (TAMD) site consists of 14 mirrors in two rings pointing between 3° and 31° above the horizon. (The lower limit of 3° minimized the contamination from ground-based lights.) Combined, they can see 112° azimuthally.

- Cameras

  The HiRes-1 Rev-3 photomultiplier tube cameras were used for Middle Drum (see section 5.1.2). These are the same cameras used in the HiRes-proto experiment.

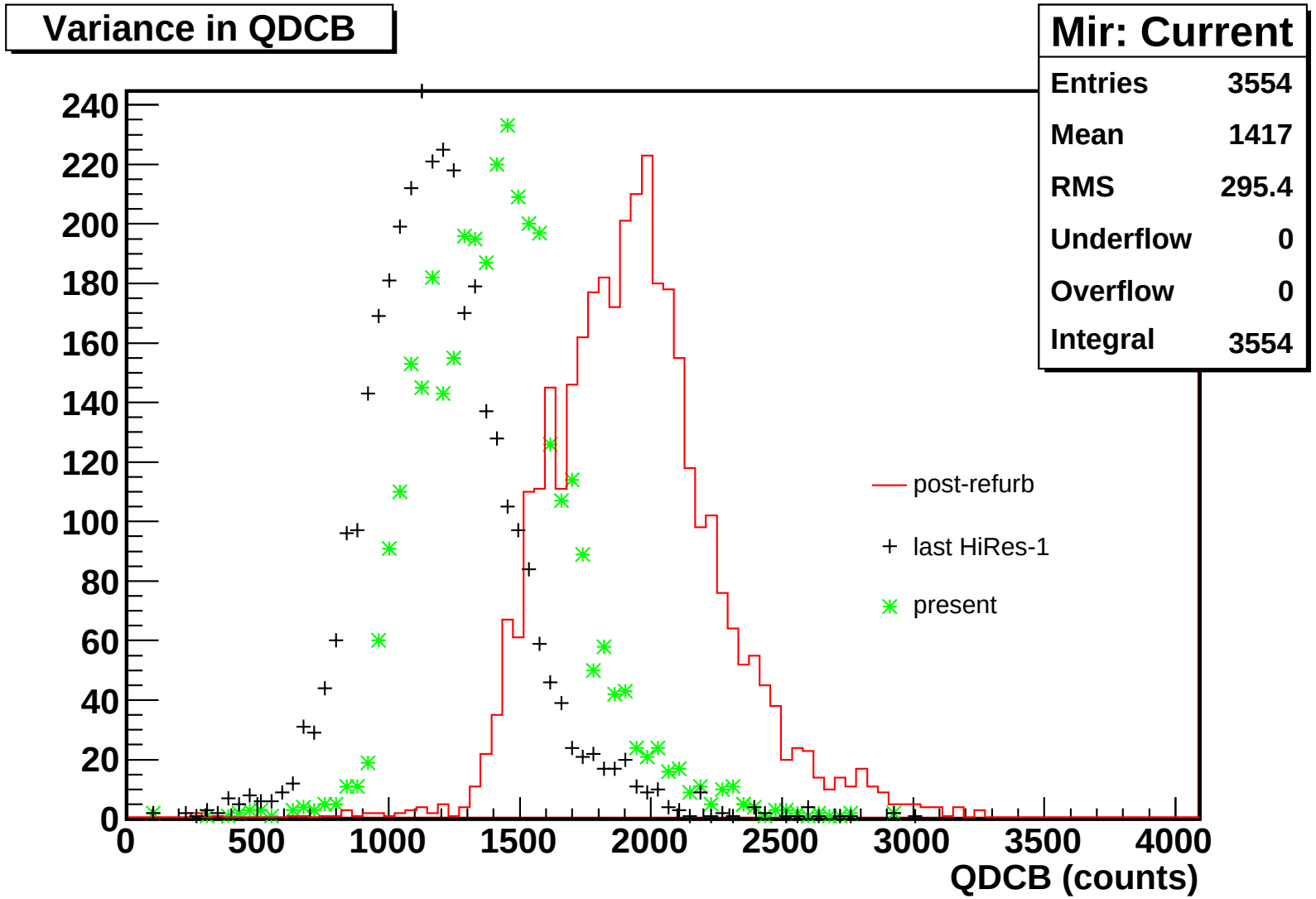

Figure 6.18: This set of histograms shows the QDCB values for each tube in all of the mirrors. As can be seen, the current values center closer to the ideal value of 1492. The last HiRes-1 setting was lower than desired and the value after refurbishment was found after pedestal subtraction, making the PMTs saturate.

Half of them (the new even-numbered units) are now sitting at a ring-2 level (17° to 31°), so HiRes-2 camera mounts were used for all of the telescopes.

Two different types of PMTs are used among the units: EMI 9974KAFL and Phillips XP3062/FL. Table 6.1 shows which type of tube was used in each mirror's camera. The units were organized according to the type of PMT in the camera. The first six telescopes contain EMI PMT cameras, the last eight contain Phillips PMT cameras. The grouping was motivated by a small difference in the tube photo-cathode live area and sensitivity profile and in their quantum efficiency. Table 6.1 also lists these positions along with the previous positions from HiRes (with Table 5.1 also showing the location during the HiRes-prototype period).

There were two electronics revisions (Rev-3 and Rev-4) used at HiRes-1 (see Table 5.1), but the 14 telescopes at TAMD are all Rev-3. Consequently, each PMT in the camera has individual high-voltage adjustability, rather than each subcluster.

- Electronics

  All of the electronics not inside the camera are housed in a single rack for each telescope. Figure 5.9 shows the schematics for communication between the camera and electronics rack, which was the same at HiRes-1. The location of the crates within the racks was analyzed over the life of HiRes and pieces were either adjusted or removed to allow for more efficient heat distributions (see Figure 6.12). Triggering remained the same as at HiRes-1 (section 5.1.1).

- Miscellaneous Equipment

  Certain aspects of the detector units were modified, removed or added in TAMD. These are described here:

  1. The mirror building. As seen in Figure 6.19, all of the telescope units are housed in a single concave building. Each bay houses a ring-1/ring-2 pair of telescopes looking at roughly the same azimuth (see Figure 6.20). Each bay has a sectional garage door controlled by the central timing (CT) rack. Since all the telescopes are in a single building, all of the doors are constrained by a series of interlocks to ensure sunlight cannot penetrate the building and hit any of the mirrors (see Figure 6.21).
  2. Garage doors. Operation of HiRes-1 showed that there were problems when trying to operate roll-up garage doors during high winds. Usually one side of the door would be pressed into the track enough to prevent that side from rising while the other side would continue to rise. This would jam the door open partway, potentially allowing light from the sun to reflect off the mirrors

Figure 6.19: The single building holding all of the telescopes at the Middle Drum site. Note the concave curvature of the building.

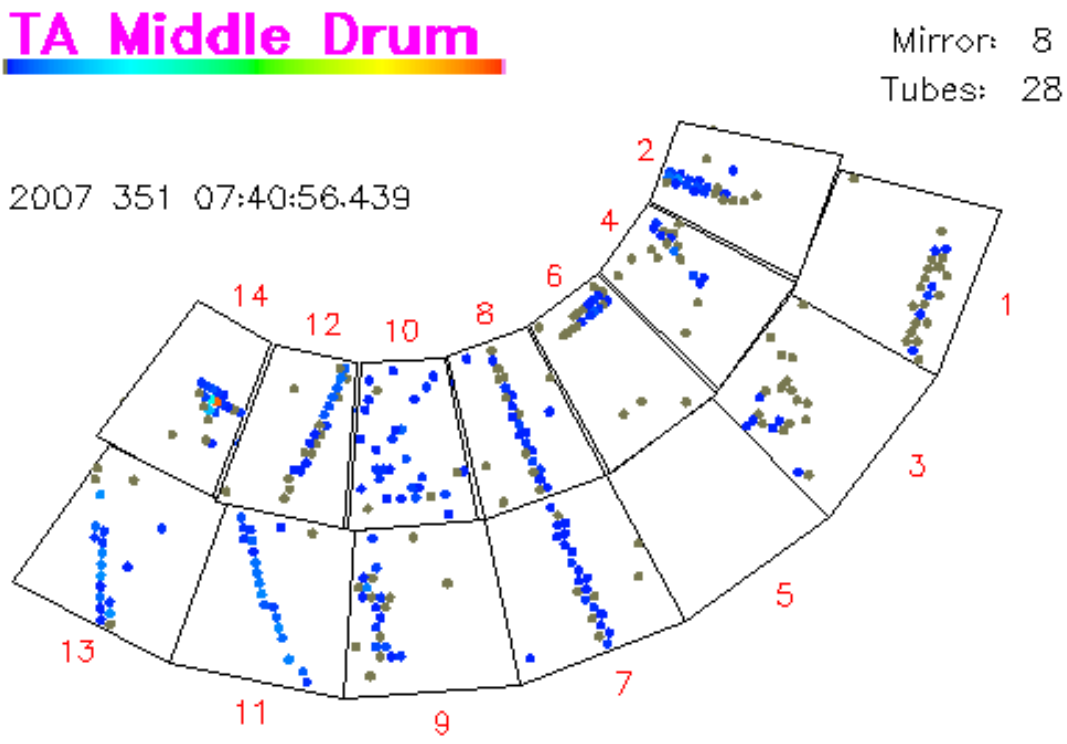

Figure 6.20: The real-time display of the Middle Drum detector. The odd-numbered telescopes view lower in elevation with the focus of the telescope outline rings pointing at zenith angle 90°. Telescopes 1 and 2 point almost due East, and the azimuthal direction changes to point South with increasing telescope number. The tubes triggered in telescopes 14 and 13 show a downward-tending cosmic ray shower; the other tubes are noise.

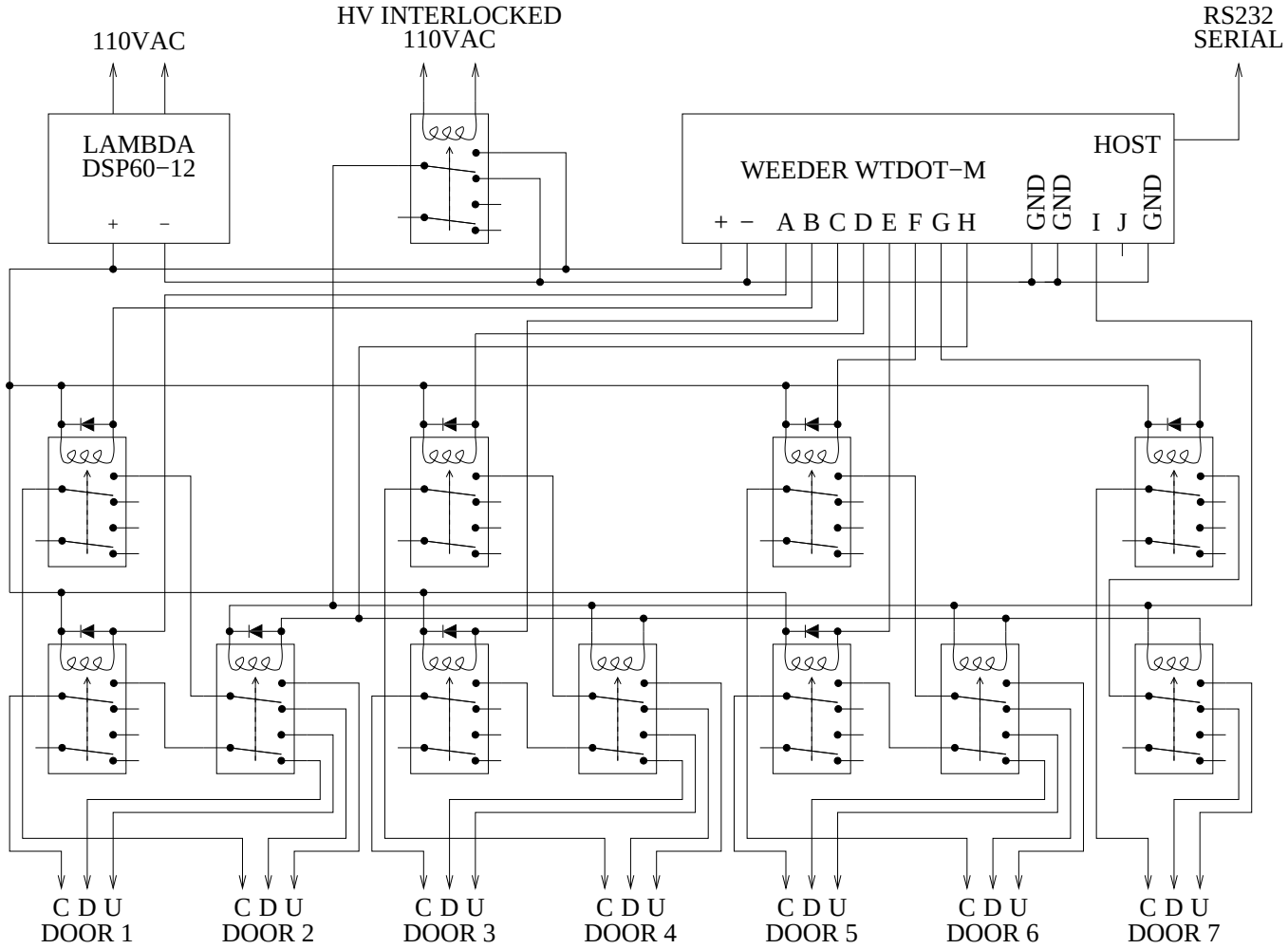

Figure 6.21: Each door on the Middle Drum telescope building contains an "up", a "down", and a "common" switch controlled by relays and interlocks (light sensors and high-voltage sensors).

and burn holes in the camera. In order to prevent that from happening at Middle Drum, segmented doors were used instead (as they were at HiRes-2), requiring extra space in the building, but proving to be far more reliable. The Black Rock and Long Ridge detectors utilize roll-up garage doors since their design specifications don't allow for extra room to utilize segmented garage doors.

3. Interlocks. Interlocks (see Figure 6.22) were also placed on the light switches and on light sensors attached to the exterior of the building. These all ensure that the HV cannot be turned on while there is any light visible to the PMTs.
4. Curtains. One other fail-safe installed at HiRes was a drop-down curtain directly in front of each mirror. By the time this dissertation was complete these had not been installed at Middle Drum. While never actually installed at HiRes-2, all the parts were fabricated for both ring-1 and ring-2 mirrors there. One for each mirror will be installed later at TAMD.
5. Rodent prevention. Rodent prevention became a major focus for TAMD. The preventative efforts described in section 6.1.1.2 exemplify the trouble experienced at HiRes.

6.2 Calibration

Like HiRes, Middle Drum requires a combination of multiple calibration methods in order to ensure a thorough understanding of the detector properties. This section will describe the differences in calibration at TAMD compared to HiRes.

6.2.1 Electronic Calibration

The programmable pulse generator (PPG) and diagnostics ("diag") tests check the electronic functionality of the tubes and preamplifiers. These, along with electronic response tests using the calibration program "calib," are the same as for HiRes. Additionally, the detector is allowed to collect data before and after the doors are opened to collect background noise. The only difference is the location of the two detectors and therefore the amount of background light they see.

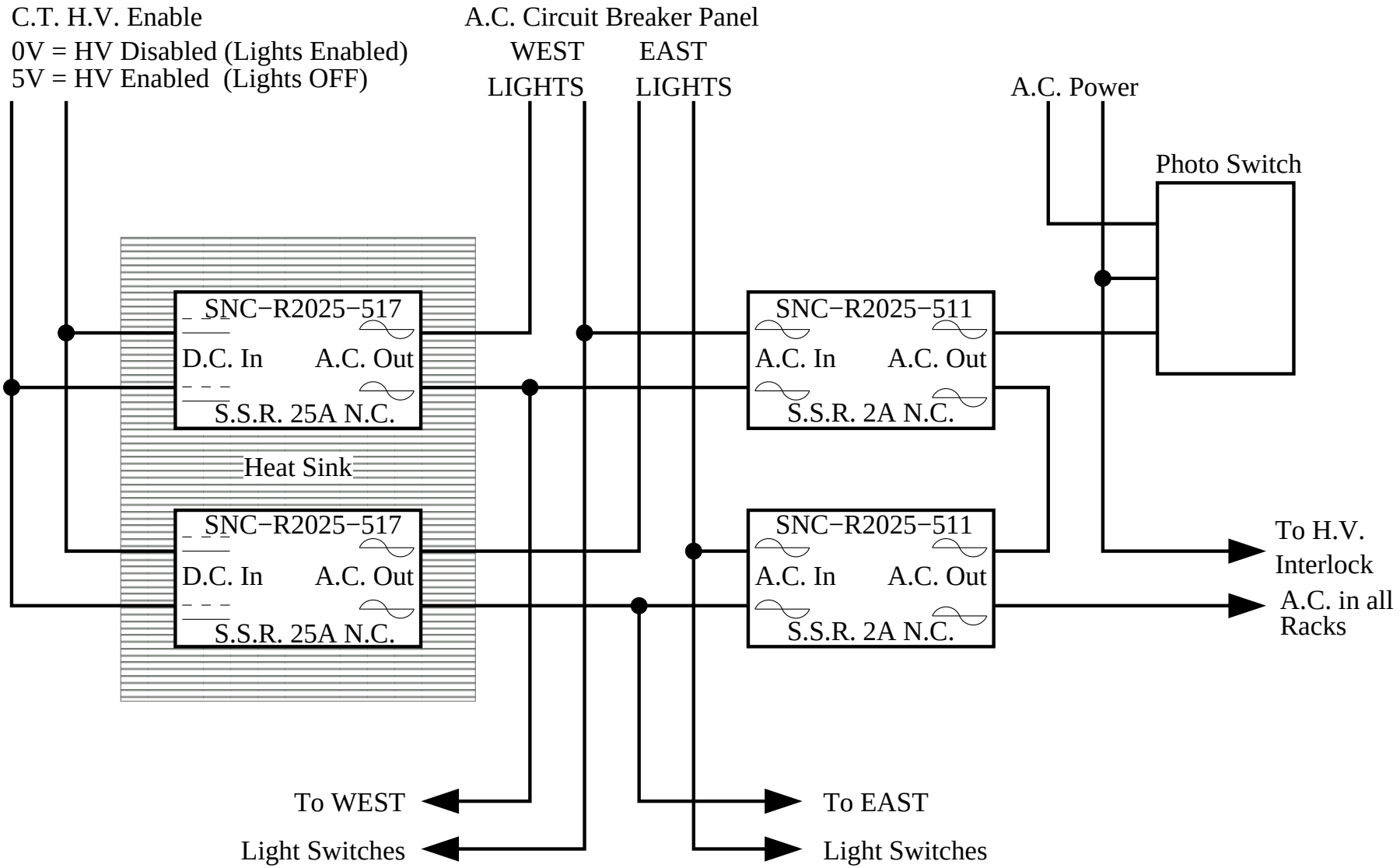

Figure 6.22: Middle Drum interlocks schematic.

6.2.2 Optometric Calibration

6.2.2.1 UVLED

The Utah group's experience with fiber-distributed laser light for nightly calibration led to the conclusion that the optical fiber and teflon differences were not capable of keeping consistent relative output at the individual telescopes. At Middle Drum we chose not to use a laser-based system, which is expensive and fragile. Instead, each telescope is instrumented with a UVLED flasher which was prototyped at the two ring-2 mirrors at HiRes-1 (see section 5.3.4).

An encased UVLED is positioned at the center of each mirror in the same mount used by the RXF. Each of these UVLEDs emit light at 355 nm, but can be switched out for a 335 nm or a 325 nm UVLED during roving calibration measurements. These are triggered once before and once after each night's data collection for calibration, as well as once per second (at 2 ms after the second) during the night's data collection.

The gain of a PMT is related to the high voltage applied according to equation 6.2. A study was performed to measure the functionality of the UVLEDs in comparison to the RXF calibration (see Figures 6.23, 6.24, 6.25, 6.26). The RXF fires at a fixed amplitude and width (based on the hardware). The width was measured using an oscilloscope and the width of the UVLED was programmed to be the same. The amplitude of the UVLED was then adjusted to obtain the same average QDCB as the RXF, and this was declared 100% illumination for both devices. The intensity of the RXF was then lowered through the use of neutral density filters to known values: 77%, 55%, and 14%. The UVLED intensity was then adjusted in 10% steps below and 25% steps above the 100% illumination in (separately) amplitude and width. The result of this showed that the response of the PMTs to both the RXF and the UVLED was similar.

6.2.2.2 CXF

A xenon flasher is positioned at the radial center of the mirror building, allowing every mirror to observe it at the same moment (see Figure 6.27). This "central xenon flasher" (CXF) is triggered once during the first data part and once during the last data part for nightly relative-mirror calibration and relative-mirror timing studies. As of the writing of this dissertation, this system still requires further analysis.

6.2.2.3 RXF

The roving xenon flasher (RXF) used at HiRes to calibrate PMTs is now used at TAMD. With plans to operate TAMD completely remotely, the RXF must be run

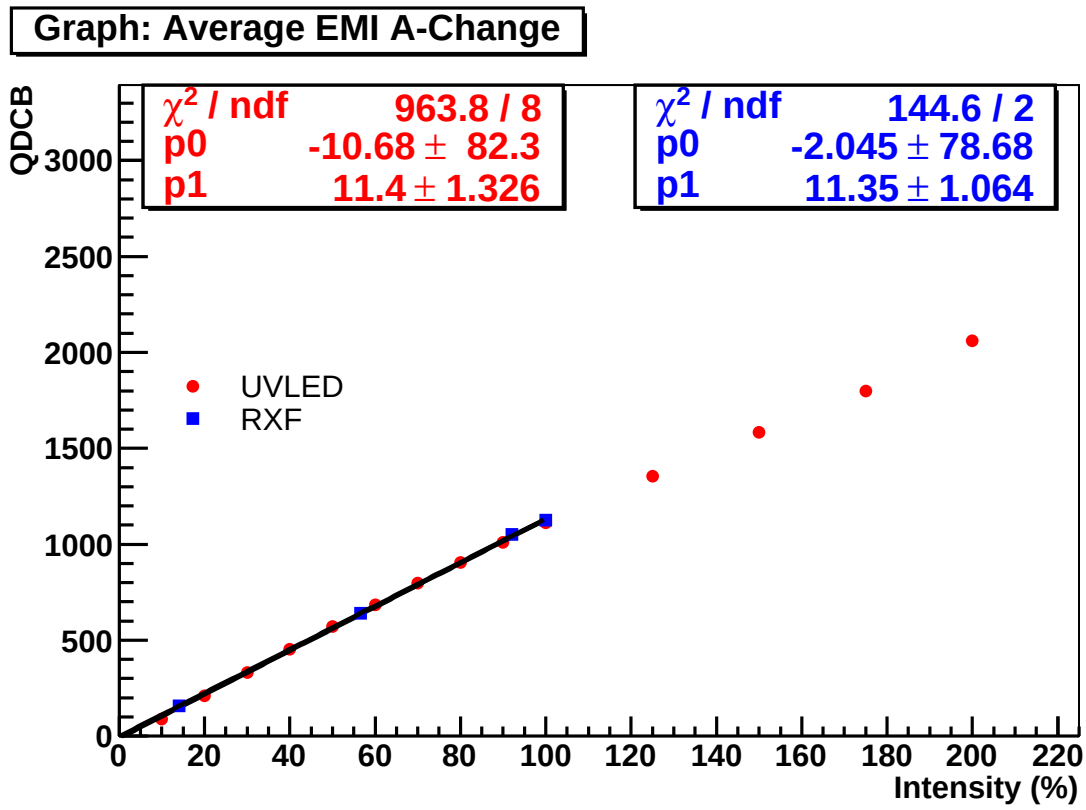

Figure 6.23: The QDCB response of an individual EMI tube as the amplitude of the UVLED pulse changes (stars) and when different neutral density filters cover the RXF (pluses).

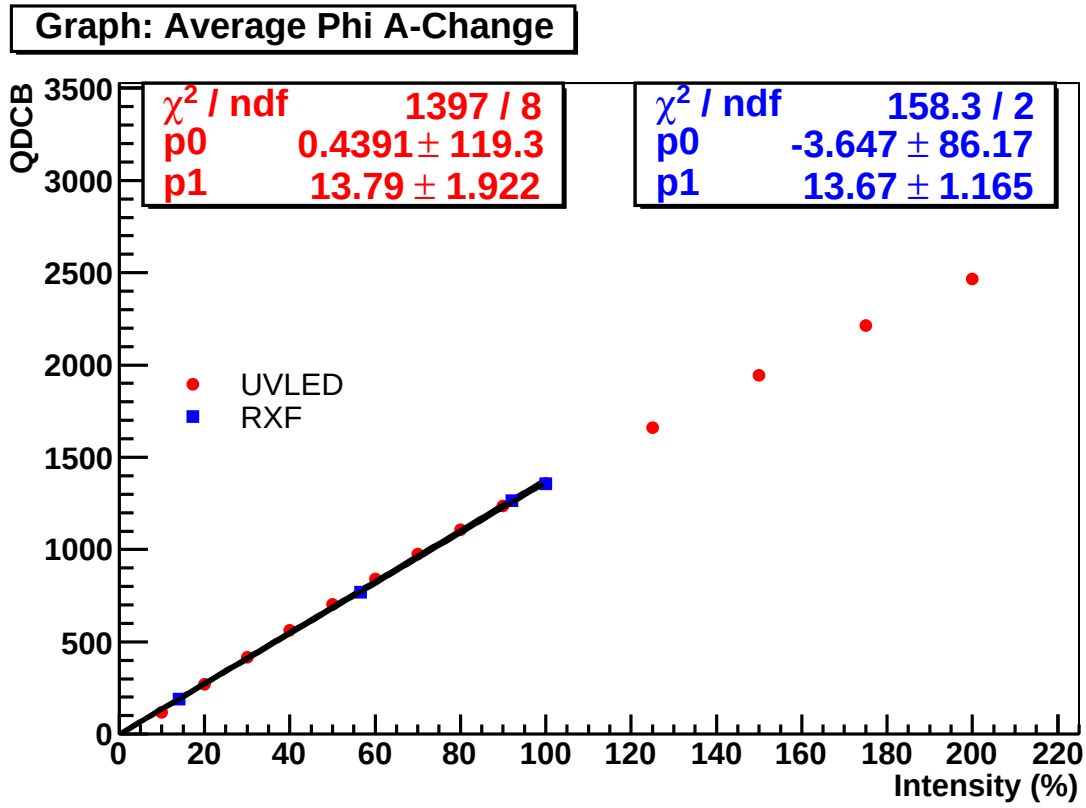

Figure 6.24: The QDCB response of an individual Philips tube as the amplitude of the UVLED pulse changes (stars) and when different neutral density filters cover the RXF (pluses).

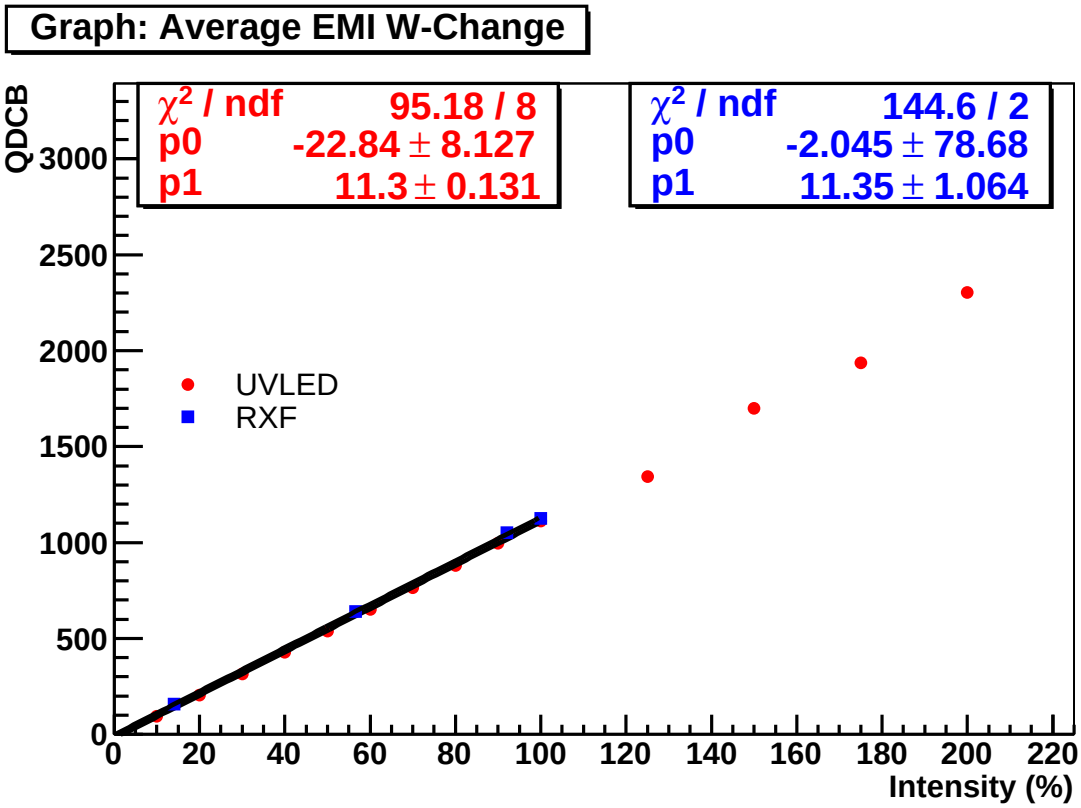

Figure 6.25: The QDCB response of an individual EMI tube as the width of the UVLED pulse changes (stars) and when different neutral density filters cover the RXF (pluses).

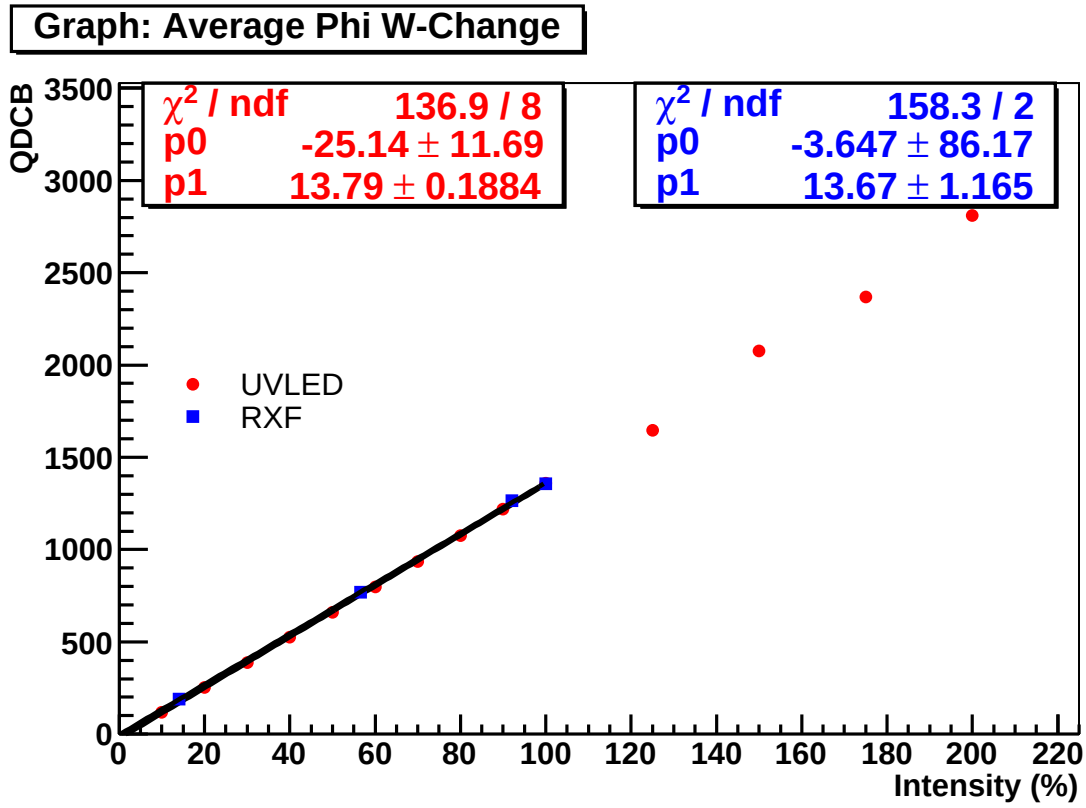

Figure 6.26: The QDCB response of an individual Philips tube as the width of the UVLED pulse changes (stars) and when different neutral density filters cover the RXF (pluses).

Figure 6.27: The central xenon flasher is centered at the focus of the concave telescope building so all telescopes see the light at the same time.

remotely as well. A track was constructed along the telescope building to allow the RXF to be suspended between the mirrors and the cameras. The RXF can be positioned in front of each mirror through the use of a trolley. As of the writing of this dissertation, the RXF was still manually inserted into a mount situated in the center of the mirror after removing the UVLED module that normally occupies it.

6.2.3 Atmospheric Calibration

As at HiRes, we assume a relatively stable ($\sim 3\%$) atmospheric profile for the purpose of modeling Rayleigh scattering, so the following lasers are mostly used to determine aerosol content in the atmosphere. The analysis of the data performed in this dissertation uses the density profile from the 1976 U.S. standard atmosphere. The collection and calibration of the atmospheric density profile for TA is beyond the scope of this work.

6.2.3.1 LIDAR

There is a central laser facility (CLF) that sits equidistant, ~ 20.86 km away, from each of the three TA fluorescence detectors; allowing for cross-optometric calibration mostly independent from aerosol conditions. At the CLF a 355 nm YAG laser system was installed to facilitate atmospheric calibration. There are plans to install a steerable reflector to direct the laser light anywhere into the sky. At the time of the writing of this dissertation, this laser is only pointed vertically. Additionally, there are plans to add a lidar receiver with this system to obtain the back-scattered light from the laser. Primarily, this system is used in "bistatic lidar" mode, where the intensity of the light is analyzed from the TA telescopes which are perpendicular to the light. This allows us to determine the vertical aerosol optical depth for nightly calibrations. Additionally, the laser is viewed by all three TA fluorescence detectors and can reveal relative timing differences between the three telescopes.

There is also a monostatic lidar system stationed at the Black Rock site. This system also uses a 355 nm YAG laser, but contains a steering head to allow the light to be redirected. This system contains a lidar receiver that observes the back-scattered light from the laser.

6.2.3.2 ELS

One unique calibration technique of the TA experiment is the use of an electron light source (ELS) (see Figure 6.28) that will simulate an upward-going, vertical shower. This is an electron beam positioned near the Black Rock fluorescence detector (see Figure 6.2)

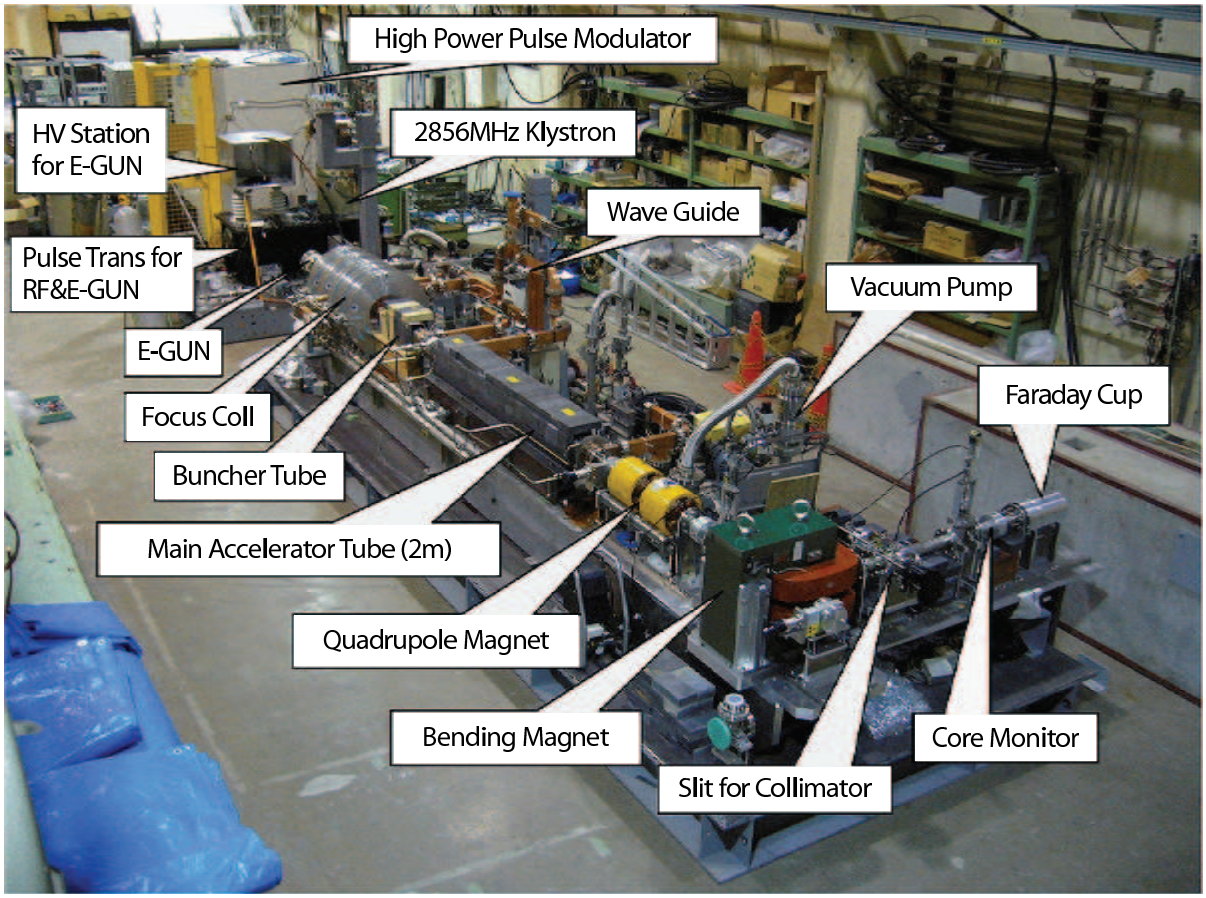

Figure 6.28: The electron light source beam equipment.

which was in the deployment phase during the writing of this dissertation. The testing of the equipment was performed at the High Energy Accelerator Research Organization (KEK) accelerator complex in Japan [77]. Studies were made at 0.5 Hz with a beam of $\sim 10^9$ electrons per pulse. The system being deployed at TA will fire a 40 MeV electron beam with the same bunch size at 100 m from the telescopes, allowing us to directly measure the fluorescence yield of an equivalent cosmic ray shower in a true end-to-end calibration.

6.2.3.3 Cloud Monitors

The cloud monitors used at HiRes were also refurbished for use at TAMD. Due to the 30° viewing angle (section 5.2.5) only four units are needed to cover the entire field of view of TAMD. These are mounted on telescopes 1, 5, 9, and 13. Measuring the atmospheric temperature differences every 12 minutes, the monitors were able to determine if a cloud came, left, or stayed in the view of the detector.

6.2.3.4 Visual Observation

On run nights, operators look for clouds once an hour and record the amount of cloud cover using a standard weather code (see Table 5.2). The information was used to determine if there was a data part of the nightly run that could be ignored due to too much atmospheric uncertainty. An adjustment was made to how HiRes good weather parts were chosen due to the directions TAMD actually observed. Since TAMD only looked in the eastern and southern directions, only these two cardinal directions, along with overhead of less than 50% cloud cover, were considered good weather (see Table 6.4). For the eastern and southern directions 0 indicates no cloud and 1 indicates some cloud cover. For the amount overhead, 0 indicates no clouds, 1 indicates $< 25\%$ cloud cover, and 2 indicates $< 50\%$ cloud cover. If the data part contained any combination within this set of recorded values the events were used in the final count.

Table 6.4: TAMD good-weather cuts.

East	South	Overhead
0	0	0
0	0	1
0	0	2
0	1	0
0	1	1
0	1	2
1	0	0
1	0	1
1	0	2
1	1	0
1	1	1

CHAPTER 7

MONOCULAR FLUORESCENCE EVENT SELECTION AND RECONSTRUCTION

This chapter describes the various program sets used for monocular event reconstruction. The first section describes the original routines used by HiRes. These are included in part as documentation for the TA and HiRes Collaborations and a great portion of the newer codes have not been previously documented.

7.1 Original Search Procedure

The HiRes-1 and Middle Drum data are passed through a processing chain that progressively filters out spurious noise events in order to find the real cosmic ray showers. Each processing routine, starting with actual data collection, created a bank of information that was then added to the collection of banks for each event listed in the file. The data used in the analyses for this dissertation (described in later sections) come from HiRes-1 and Middle Drum, so only those processes will be described here. A summary of the programs, scripts, banks used, and banks created can be found in Table 7.1.

7.1.1 Raw Data

During clear, moonless nights of three or more hours, the collected data is organized into the standard Data Storage Tape (DST) format. The raw data is organized into different types of ethernet packets transmitted over the DAQ network which describe different aspects of the gathered information bundled into the HPKT1 bank. The different types of packets include:

1. HR_TYPE_TIME - packets listing the GPS time stamps for the telescope hold-off, TDC trigger and common stop times for individual telescope events.

2. HR_TYPE_EVENT - packets generated by the individual telescope electronic triggering. These packets store the QDCs and TDCs of each triggered tube.

Table 7.1: This initial program summary lists the programs used to process the data along with the scripts run to handle the processing, the input banks used by the program, and the banks created by the program.

Program	Script	Banks Used	Banks Created
hma	hps0	HPKT1	HRAW1
hpass1	hps1	HRAW1, HCAL1, HPED1	HBAR, HRAW1
hpass2	hps2	HRAW1	PASS2
hpln	hps3	HRAW1	HPLN1, PASS3
hpln -C	hps3ad	HRAW1	HPLN1, PASS3
hpass3b	hps3b	PASS2, HPLN1	
htim_pfl		HRAW1, HPLN1	PRFC, HCTIM, HCBIN

3. HR_TYPE_CALIB - summary information (mean and RMS values) from the pre- and postrun electronic calibration of the response of the tubes to various pulse amplitudes and widths injected into the preamps by the programmable pulse generator (PPG).

4. HR_TYPE_MINUTE and HR_TYPE_NOTICE - packets generated by each triggered mirror, recording the actual times the mirror is taking data. This is given in the form of start/stop and dead-time information.

Other types of packets record threshold levels, status information, and tube trigger rates of each mirror. These are all folded into the processing of the information, but the details are not in the scope of this analysis [6].

7.1.2 Preprocessing 0

Every night after the data are collected, the "end_night" script is run, which calculates the files' checksums. This is important for data corruption detection during transfer to the central storage computers. Additionally, a weather selection is made to tag periods of cloud cover and hazy conditions. A cut is applied if clouds cover 50% or more of the sky, based on Table 5.2. At this time the on-time of each mirror is calculated twice; once for all-weather running and once for only good-weather observation.

At the end of each run period the on-time is totaled in order to quantify the mirror-by-mirror reliability and the accumulated exposure of the experiment. The total number of hours actually run, given in both the all-weather and good-weather on-times, are then divided by the number of potential hours. From this we know how well the detector performed during each run period.

The actual processing of the data was performed after each run period (lunar cycle). After the data are transferred and after each process, the checksums were verified and

recalculated in order to ensure data integrity. Before processing the actual data using the UNIX shell and Perl scripts listed in Table 7.1, diagnostic summary information was first collected in a log file in order to clarify which calibration files should be used (e.g., if there were more or less than the two scheduled pre- and postcalibrations per night) and other parameters of the run conditions for each run night. From this log file a script would call the programs "hca" and "hped" to run on the chosen calibration and pedestal files, respectively. These would create the new bank files: (beginning night).hcal1.dst and (beginning night).hped1.dst, where (beginning night) is the first night of the processed run period (e.g., y1997m05d29 for the very first HiRes-1 data collected). The data in the HCAL1 bank gives the timing calibration for each PMT and the HPED1 bank gives the pedestal, or null-charge, levels for each tube.

7.1.3 Preprocessing 1

The next step in the processing is to apply calibration to the raw data. As described in Chapter 4, fluorescence detectors depend on parameters of the atmosphere and equipment. The timing and photometric calibration parameters must be combined into files needed by Pass1 (see section 7.1.5) in order to determine the number of photons collected in each phototube of the event.

1. Source files are created from the most recent roving xenon flasher (RXF) runs with the .hped1.dst files taken that same night. These are produced using the script "hspec" and use information on reference data and spectra of the type of calibration. The standard hspec file converts the data collected from the RXF run and applies 1) the luminosity of the xenon flashbulb; 2) the known transmission coefficients of the UV filter; 3) the transmission of light due to the thickness of the scattering Teflon; and 4) the internal neutral density filter of the RXF. The measured quantum efficiency (QE) of each tube and related information is included to make the file specific to each tube.

2. The hspec files were then used to create HNPE DST files. The input file has the following format, with commas between parameters and each mirror on its own line:

    - File description
        - Beginning Julian date and end Julian date for which the hnpe file is valid
        - files for the standard UV filter and tube quantum-efficiency curves
    - Telescope description

- Telescope number
- HSPEC spectrum file, with appropriate dates, created in the previous step
- Description, usually of what was used to create the hspec file
- Pulse width, in nanoseconds
- RXF file for appropriate mirror, same used in the previous step
- Hped1 file from the date the RXF was run, obtained in the "Preprocessing 0" step
- Calibration file with the HPKT1 data from the date the RXF was run, not the hcal1 file
- Noise-closed file with the HPKT1 data from the date the RXF was run, separate from the hped1 file created with the same file
- UV filter open flag, generally 0 since the filter is closed during the regular RXF data runs.

The following example shows the first few lines of the input file for the first month of the Middle Drum runs. Note, the mirror information actually used is all on one line; it is separated here to show everything:

```
2454407 2454422 stdUV.hspec.dst stdQE.hspec.dst
        01, source_nov07_rxf.hspec.dst, RXF calib stdUV teflon2 oriel1 377nm,
                1000, y2007m11d17p01.01.rxf.hal, y2007m11d17.hped1.dst,
                y2007m11d17p01.cal.hal, y2007m11d17p01.noise-closed.hal, 0
        02, ...
```

7.1.4 Pass0

The initial step in processing is to match up the individual mirror event packets with their corresponding GPS time-stamp in the time packets. The "hma" program adds the millisecond and minute counter time-stamp values from the EVENT packet to the time-stamp in the START packet. This gives the absolute time (to millisecond precision) of the event hold-off signal. The time is then matched to the telescope number and GPS time-stamp from the TIME packet to achieve sub-hundred-nanosecond precision for the event hold-off time. Based on this absolute time, consecutive packet timing information is then compared. If two or more packets have telescope triggers within 100 μs of each other, they are combined into a single "event." Events are primarily single-telescopes,

but in each event the information from the TIME and EVENT packets of all telescope triggers are then assembled into a single HRAW1 bank, and written into a .ps0.dst file.

7.1.5 Pass1

This is the first step of real data processing in which the hraw1 data are converted into physical values. The raw TDC values are converted into microseconds and then subtracted from the event hold-off time relative to the GPS time-stamp for the earliest triggered telescope in the event. The raw QDC values are converted into a number of photo-electrons per square-millimeter from which the pedestal is subtracted. The "hpass1" program performs this using the .hcal1.dst and .hped1.dst offsets from the individual night along with the appropriate RXF values and HNPE information. The output is written to an HBAR bank and updates the HRAW1 bank in .ps1.dst files.

7.1.6 Pass2

Starting in this pass, events are sorted according to their likelihood to be a cosmic-ray shower. Using the "hpass2" program, Pass2 starts by calculating the probability that the geometrical and true progression of the triggered tubes (hits) in an entire event can arise from a seemingly random-walk process. A unit vector is drawn between nearest-neighbor hits with sufficient time separation (between 0.02 and 8.00 μs) and angle separation (between 0.0 and 1.5 degrees) for reliable ordering. This vector is drawn from the earlier to the later hit. In the case of random noise, the vector sum of all these segments, known as a Rayleigh vector, has an expected distribution in (normalized) length given by the "random-walk" formula [82]

$$f(r) = \frac{r}{\sigma^2} e^{-\frac{r^2}{2\sigma^2}} dr \tag{7.1}$$

where $\sigma^2 = N$, the number of pairs of triggered phototubes included in the calculation. A value known as "PLog" is calculated to determine if the event could have had a Rayleigh vector with the calculated magnitude or larger based on the number of triggered tubes in the event. This is found by taking the negative of the natural log of the probability density function (the integrated form of equation 7.1) such that an event is considered good if $\frac{r^2}{n} > \frac{R^2}{n}$, where r is the calculated value, n is the number of tubes, and R is the cut value. The larger the PLog, the more likely the event is not caused by noise. Events with a PLog greater than $R^2 = 2.0$ (1% probability) are considered good events.

After this, the Rayleigh vector is used to determine if the event is pointing upward, downward, or horizontally. Horizontal events are all of those pointing between 20° below

to 20° above the horizontal. The events are thus sorted into appropriate directional files (.ps2[d,h,u].dst, where [d,h,u] signify downward, horizontal and upward going events respectively) with the new bank, PASS2.

7.1.7 Pass3 (ab)

Pass3 uses the "hpln" program to perform a plane fit described in section 4.4. This is done in three stages and the cuts for each were optimized originally by Abu-Zayyad [6]. First the tubes in the event are collected into clusters of two or more tubes that are at most 1.2° away from and triggered within 2 μs of each other.

All of the tubes belonging to clusters of two or more tubes are then grouped together, from which a Rayleigh vector is calculated. The result is then forwarded into a routine which performs a chi-squared fit (see equation 4.19). This fitting procedure sometimes fails to converge to a minimum χ^2, in which case the process is repeated with clusters of 3 or more tubes.

Assuming a plane is found, tubes that are too far from the time-angle plane (> 3 root mean squared, RMS, deviation from the plane) are marked as noise tubes. The event is then subjected to a second-order polynomial fit of the trigger time, t_i, of each tube versus its χ_i angle (see Figure 4.15). From this fit, tubes that are not in time-correlation with the event tubes (> 3 RMS deviation in the time-angle plane) are removed. The sequence of plane and time fits is repeated, keeping only the remaining "good" tubes. The iteration is stopped if the number of good tubes remaining drops below 3, in which case the fit is deemed to have failed and the event rejected, or the fit successfully terminates when no "bad" tubes are rejected after a complete iteration.

The surviving events are subjected to the following selection criteria and rejected if any of the following criteria is met:

1. Plane fit - if the number of good tubes per degree is $< 0.85/^\circ$ or $> 4.0/^\circ$ there won't be enough slant depth for a reliable profile reconstruction.

2. Track-length - if there is less than 6° of track available there will not be enough range of slant depth for the profile reconstruction (see section 7.1.8).

3. Brightness - an average of 75 photons per good tube is the bare minimum signal needed to have a discernable shower profile.

4. Track width - tracks with a plane RMS deviation greater than 1° are considered noise since they are usually airplanes or Čerenkov light or are too close to the detector to have a sufficient fraction of the shower observed for analysis.

5. Inverse angular speed - events with track speeds slower than 0.175 $\mu s/^\circ$, corresponding to ~ 3 km, happen too close to the detector and are difficult to reconstruct.

The events that make it through the above cuts are processed again with an additional correlation coefficient, ρ. This is calculated from the t_i versus ψ_i distribution of good tubes. Those events with $\rho < 0.985$ are removed to eliminate remaining noise events [6]. Altogether, these fits and cuts are referred to as "pass3a".

As a second part to pass3, additional quality cuts are applied in order to remove events that have insufficient information for a reliable profile-constrained geometry fit. Pass3b rejects an event if:

1. the brightness is less than 200 photons per good tube
2. the angular speed is $3.33^\circ/\mu s$ ($\gtrsim 5$ km away)
3. the data is considered poor-weather in the on-time files created in the preprocessing 0 stage.

Pass3 inserts the PASS3 and HPLN1 banks into .ps3[d,h,u].dst files. Only downward-going events are considered to be real cosmic-ray showers and analyzed further.

7.1.8 Pass4

This is the final stage of processing in which the actual event reconstruction takes place. This was the primary work performed by Abu-Zayyad [6] and so only the salient points will be noted here. While traditionally the geometry of the air shower is reconstructed sequentially from a plane fit and a time fit (see equation 4.19), a single-ring ($3^\circ - 17^\circ$ elevation) fluorescence detector has limited elevation coverage and events are typically too short in angular extent for reliable timing fits. Kidd [56] showed that uncertainty in R_p and Ψ, respectively, rose as

$$\sigma_{R_p} = \frac{12\sqrt{5}\,(\sigma_t c)}{\rho^{\frac{1}{2}} L^{\frac{5}{2}}} \tag{7.2}$$

$$\sigma_\psi = \frac{12\sqrt{5}\,(\sigma_t c)}{R_P \rho^{\frac{1}{2}} L^{\frac{5}{2}}} \tag{7.3}$$

where σ_t is the uncertainty in the tube trigger time (~ 40 ns), c is the speed of light, L is the angular track-length in radians, and ρ is the tube density in tubes/radian. For HiRes-1 events, the peak of the calculated R_P and ψ uncertainties are ~ 1.5 km and 10°, respectively (see Figure 7.1(a), 7.1(b)).

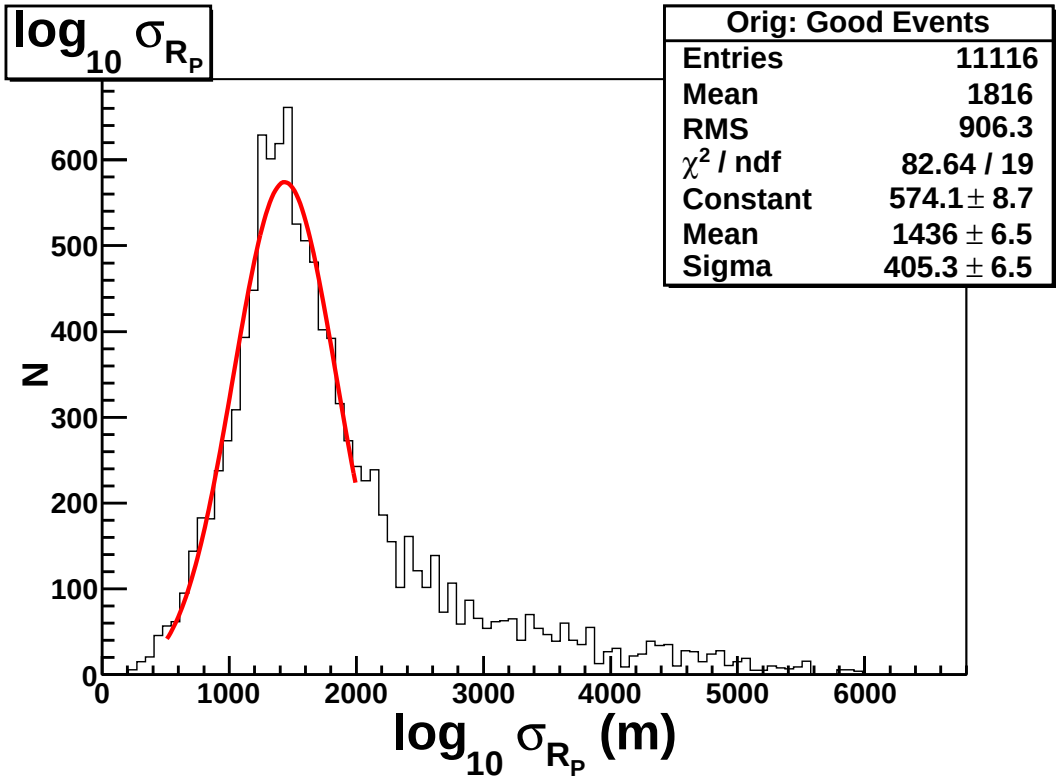

(a) R_P

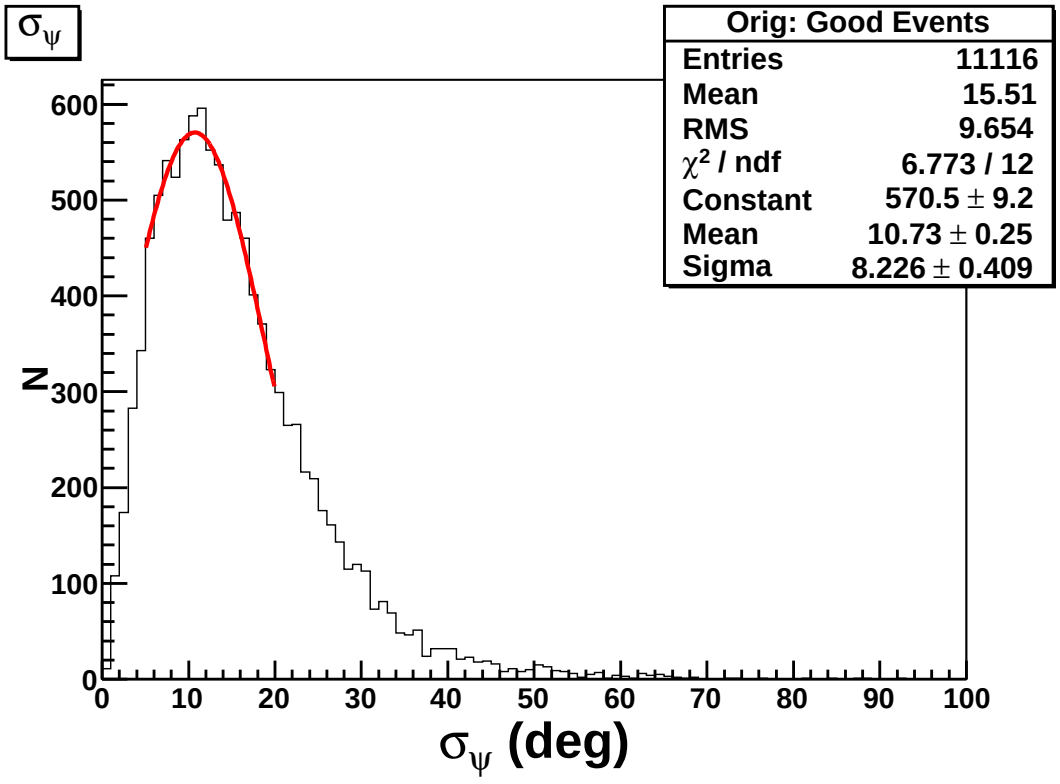

(b) Ψ

Figure 7.1: Calculated uncertainty in reconstructed R_P and ψ

Applied alone, the timing fit does not reconstruct the shower geometry well. Instead, Abu-Zayyad [6] showed that a combined shower profile-plus-timing fit gives a more accurate and robust reconstruction for the HiRes-1 detector configuration. A Gaisser-Hillas parameterization (see equation 4.11) is assumed for the shower profile (N_{ch} versus X), with X_{max} in a range between 600 and 900 g/cm^2. This range comfortably contains the mean X_{max} values for either protons or iron in the 10^{18-20} eV energy range. This fit also uses a fixed $X_0 = 40$ g/cm^2. For each assumed X_{max} value in the inverse Monte Carlo fit, the $\chi^2_{profile}$ is minimized according to the signal variations in the tubes (see section 4.4). To obtain a good fit in the geometry, the in-plane angle of approach, ψ, is varied by 1° steps between 0° and 180°. This determines R_p according to equation 4.18 from the relative tube trigger times. Once $\chi^2_{profile}$ is minimized for each tube, χ^2_{time} is minimized with the individual R_p and ψ values. All sets of χ^2 are then normalized to $\overline{\chi}^2 = \chi^2/\text{d.o.f.}$ and used in the equation

$$\overline{\chi}^2_{combined} = \overline{\chi}^2_{time} + \overline{\chi}^2_{profile}. \tag{7.4}$$

to determine the best combined fit parameters.

Quality cuts are performed on the fully reconstructed showers to remove any events that may have too much aberrant behavior. Events are considered good if all of the following conditions are met:

1. the angular tracks are $\geq 7.9°$
2. the depth of the first interaction in the atmosphere happens before 1000 g/cm^2
3. ψ is $< 120°$
4. Čerenkov radiation accounts for $\leq 25\%$ of the light in any one angular bin
5. the average correction factor (amount of fitted track away from the mirror edges) is > 0.9 m^2

Figure 7.2 shows an example of a reconstructed shower.

7.2 Stereo_TA Search Procedure

The HiRes-1 data and Middle Drum data can both be processed using a new combined code set known as "stereo_TA". This merger primarily enables the processing of Telescope Array data using the same programs that can process the HiRes data. The actual analysis algorithms in the code largely remained unchanged; the user interface and detector component integration were the primary adjustment. The separate HiRes-1 and HiRes-2 main programs were combined with an input parameter that would allow

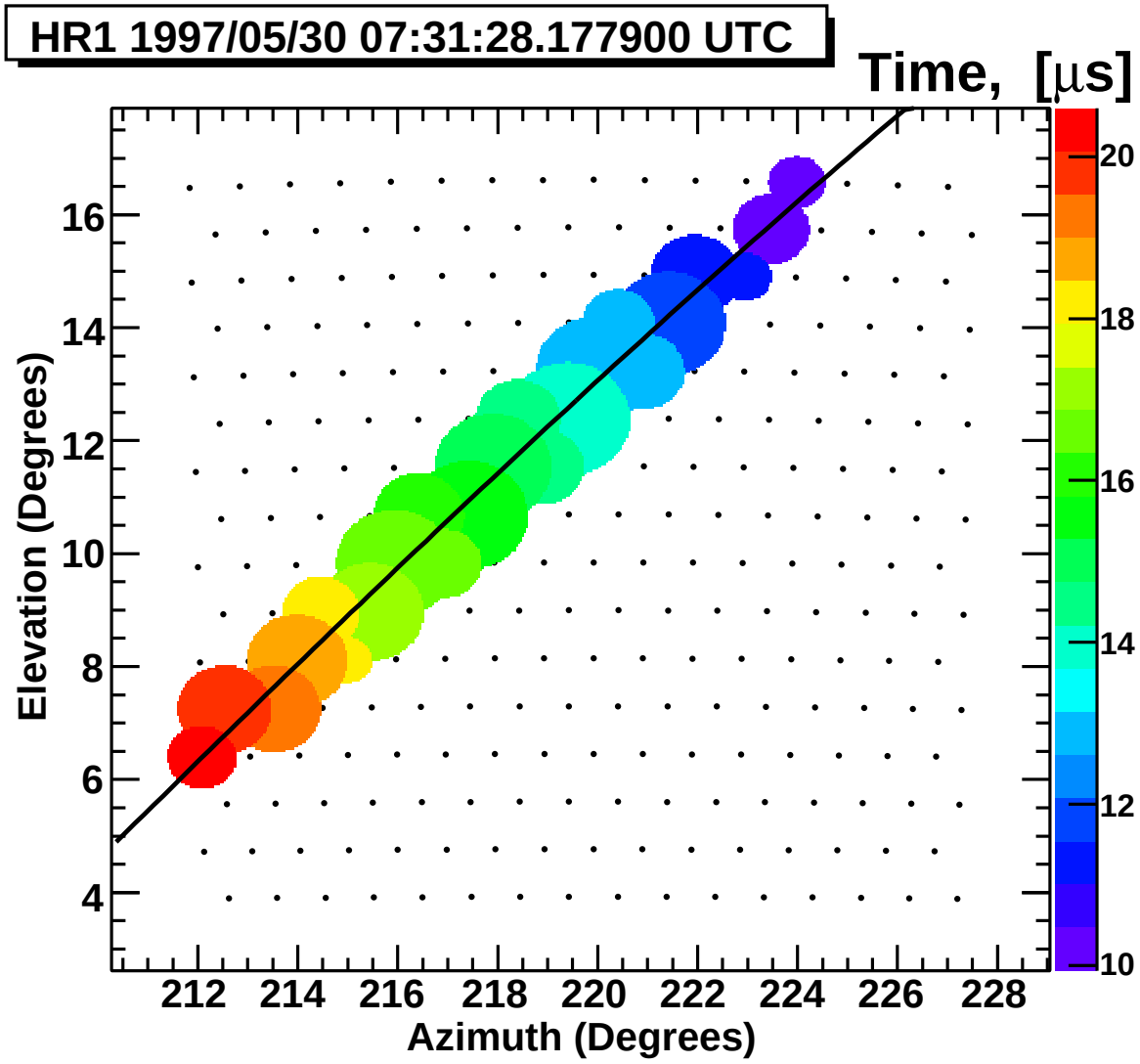

(a) Event Display

Figure 7.2: Observed air shower example.

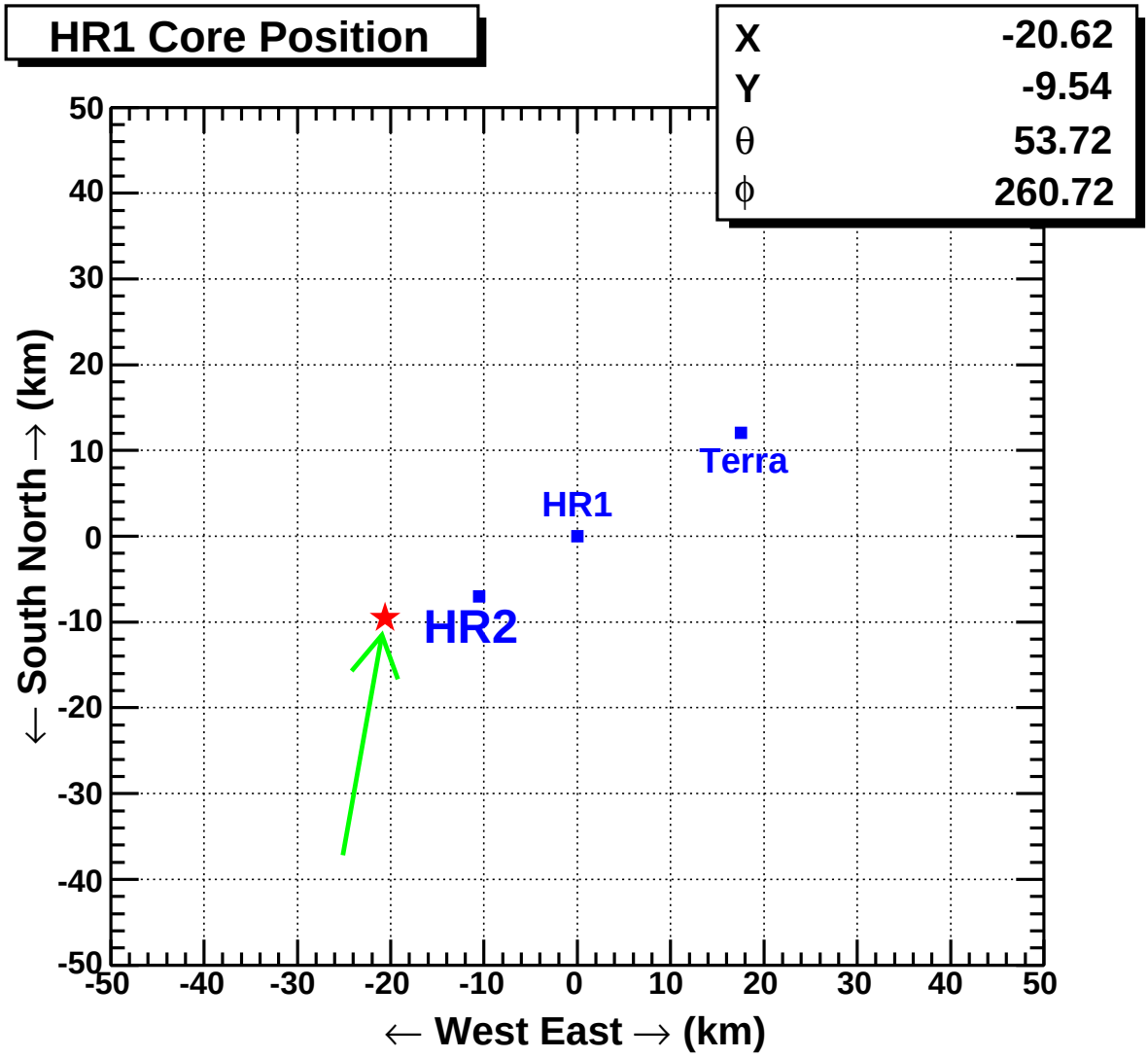

(b) Core Position

Figure 7.2: Continued.

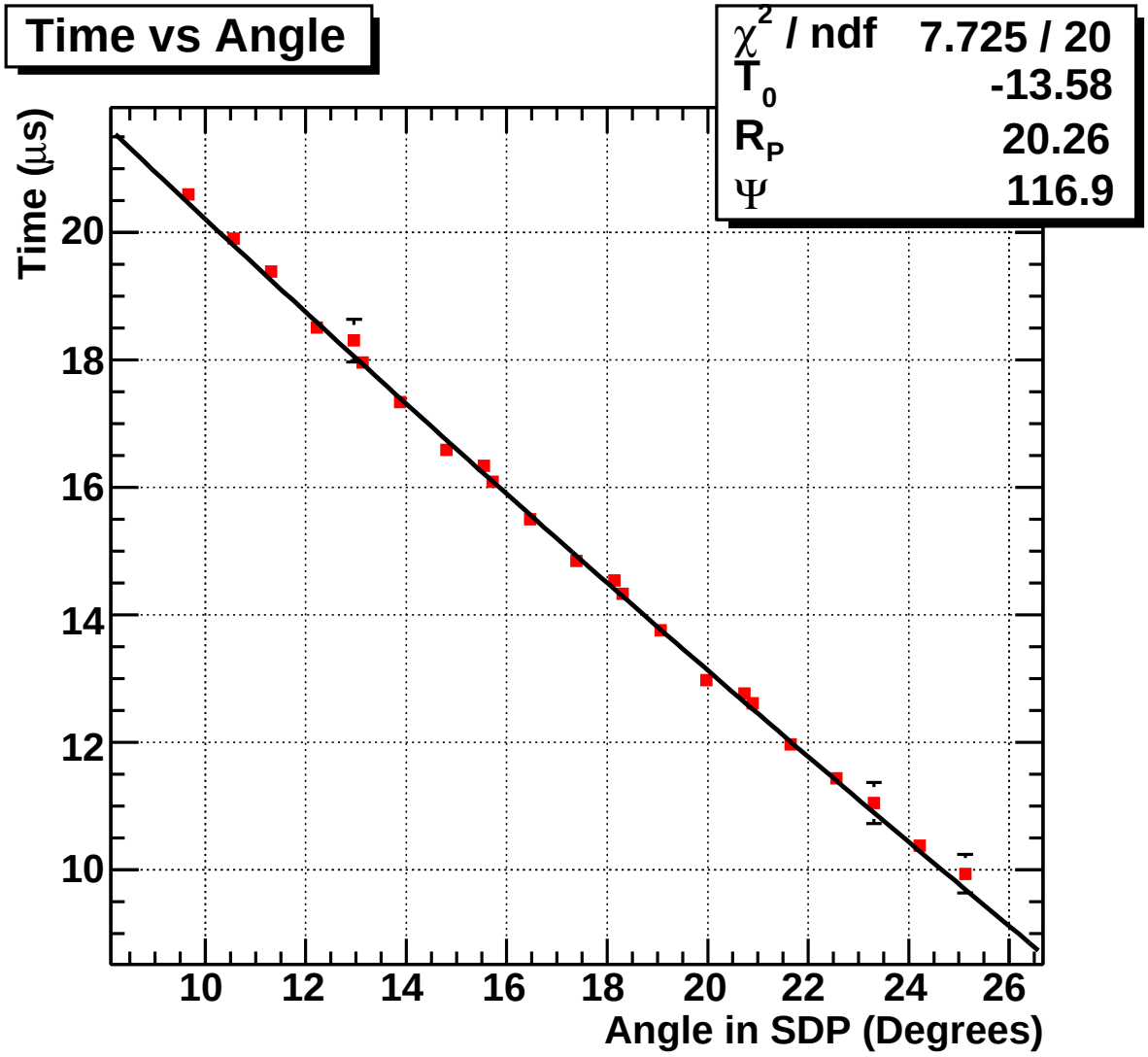

(c) Geometrical Fit

Figure 7.2: Continued.

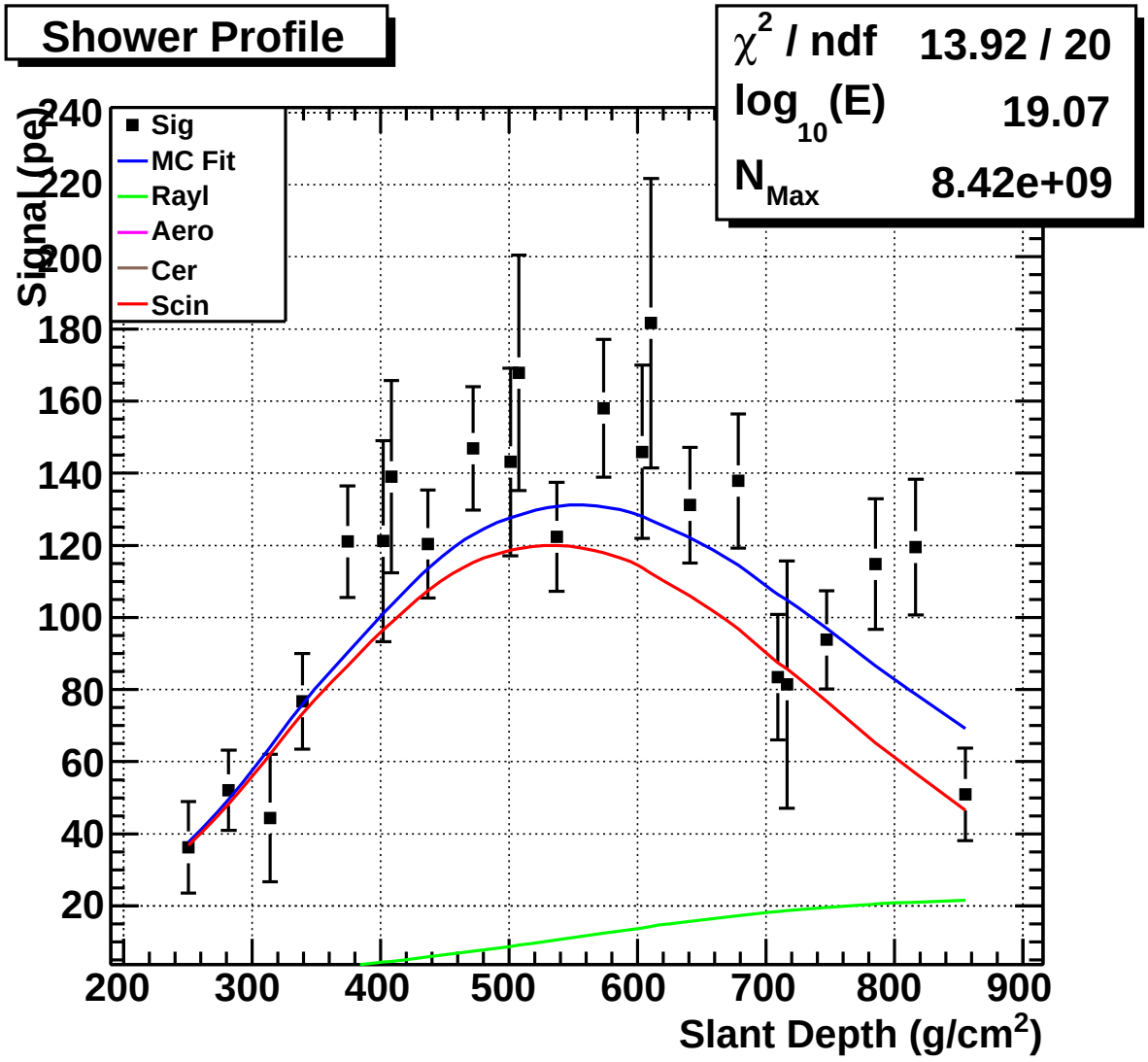

(d) Profile Fit

Figure 7.2: Continued.

the user to choose which detector's data were being analyzed. This allowed HiRes-1 monocular, HiRes-2 monocular or HiRes stereo reconstruction to be processed using one set of programs rather than three separate sets. Each telescope, including those of Telescope Array, can be analyzed in monocular mode or multiple telescopes can be run in stereo mode depending on the choice of input parameter (see Table 7.2). Pertaining to the work in this dissertation, the only differences between HiRes-1 and Middle Drum are in the geographical locations. Therefore, the only differences will show up in the tube pointing directions and the local detector coordinate origins. The most important goal of this dissertation is to make a direct comparison of the HiRes and TAMD spectra, as the same equipment is being used. Because of this, the Middle Drum data is processed initially using the same routines as HiRes-1, including the profile-constrained geometry fit and the final selection of events.

The stereo_TA programs are applied after Pass1 (see section 7.1); the programs used through Pass1 have remained exactly the same. Since this dissertation focuses on HiRes-1 and Middle Drum monocular analyses, this chapter will describe each of the programs listed in Table 7.3 used in these two analyses and compare their respective bank inputs and outputs in separate sections. In addition to combining the different code sets into a single set, a significant effort was made to fully automate the data processing (see Table 7.4). New scripts were written that handled not only each pass, but sequences of passes and lists of run nights. In this manner, an individual run night could be processed using a single script from hps0 all the way through stpfl. Alternatively, a list of run nights could be fully processed through each pass, which could also be consecutively processed from hps0 through stpfl. The list-script would run the individual passes for a list (multiple or single) of run nights. The from-script ran the consecutive list-scripts starting from the indicated pass for a list (multiple or single) of run nights. The stpfl pass performed the

Table 7.2: The detector choice can be any of these combinations from either HiRes or Telescope Array.

Choice	Telescope
1	HiRes (stereo)
11	HiRes-1
12	HiRes-2
30	TA (stereo)
31	TABR
32	TALR
33	TAMD
34	TALE4, TALR
40	TALE4
42	TALE2

Table 7.3: These are the programs used to process the HiRes-1 and Middle Drum data using the stereo_TA code set along with the input banks used by the program and the banks created by the program.

Program	Banks Used	Banks Created
stps2	HBAR, HRAW1/MCRAW	STPS2
stps2 -only	HBAR, HRAW1	STPS2
stpln	HBAR, HRAW1	STPLN
hrlsr	HBAR, HRAW1, STPLN	
stgeo	HBAR, HRAW1	HCTIM
stpfl	HBAR/HRAW1/FMC1/MC04, HCTIM	PRFC, HCTIM, HCBIN

Table 7.4: These are the appropriate scripts which handle the processing of the HiRes-1 and Middle Drum data using the stereo_TA code suite.

Program	Script	List-script	From-script
stps2	stps2	run_stps2	run_from_stps2
stps2 -only	stps2only	run_stps2only	run_from_stps2only
stpln	stpln	run_stpln	run_from_stpln
hrlsr	hrlsr	run_hrlsr	run_from_hrlsr
stgeo	stgeo	run_stgeo	run_from_stgeo
stpfl	stpfl	run_stpfl	

final reconstruction so there is no from-script.

7.2.1 Preprocessing, Pass0, and Pass1

The processing of the data through Pass1 is identical to the original routines (see sections 7.1.2 through 7.1.5). Both require the on-time to be determined, the .cal.hal files to be processed into .hcal1.dst files and the .noise-closed.hal files to be processed into .hped1.dst files. The RXF calibration is processed into .hnpe.dst files and the .pkt.hal files are run through the "hma" program to group mirror-triggers into events and renumber the tubes. The "hpass1" program converts the digitized time and charge information into physical values of time and number of photo-electrons.

7.2.2 STPS2

This is the first program of the new stereo_TA set. It incorporates the "hpass2" (HiRes-1) and "fpass2" (HiRes-2) programs and is also the first program in the processing chain that accesses the detector photomultiplier tube (PMT) pointing directions.

Therefore, TA/TALE detector configurations are also included in this program. For all detectors, the Rayleigh filter (see equation 7.1) is used to reject noise events. The same cuts are made as in "hpass2". The output is written to the STPS2 bank.

One additional feature of this program is the ability to keep only the downward-going events. As described in section 7.1.6, downward-going events are those with stps2 Rayleigh-vector directions 20° below horizontal. For the efforts of processing convenience, only downward-going events are chosen as potential extensive air showers and further processed for HiRes and TAMD spectral studies.

7.2.3 STPLN

This program determines the shower-detector (SD) plane. As discussed in section 7.1.7, noise tubes are removed if they are not within 3 RMS angle and time deviations from the plane (degrees or microseconds, respectively). The PMT pointing directions are taken into account to form the SD plane, so STPLN relies heavily on detector choice (see Table 7.2). For the HiRes data, if the upward and horizontal events from stps2 are processed, a preliminary laser cut is performed using the known HiRes laser positions (see sections 5.2.5 and 5.2.6). The cuts made in Pass3 (see section 7.1.7) were loosened slightly for TAMD, HiRes-2, and HiRes stereo since these configurations have better geometrical viewing capabilities. Summarized in Table 7.5, the "HiRes-1 mono" column is how the cuts appear in the "stpln" program for HiRes-1 monocular mode. The "HiRes-1 stereo" column are the configurations used only if the event is begin processed in stereo mode. The "HiRes-2 mono and stereo" and "TAMD" columns are used as stated. The following cuts are defined as: 1) PRMSDEV - the deviation in the plane angle; 2) TL - the track length viewed by all telescopes in the detector; 3) IAS - the inverse angular speed of the track as it traverses the viewing angle of the detector; 4) PPGT - the average number of photons per good tube; 5) GTPD - the number of good tubes per degree of the entire track.. The output bank is STPLN.

7.2.4 HRLSR

This is the only program of the stereo_TA code set that does not correspond to any program in the original processing routines. This program searches for events that are "most-likely laser" events. The first check looks for repetition of similar events. If a set of events occur within 9 seconds between consecutive member events, have three or more "good" tubes in common in the same mirror, the top six NPE (number of photo-electron) values are within 30% of each other, and they have plane-normals within

Table 7.5: These are the "stpln" cuts made on the events that resolve to have a plane. (See the text for details.)

Cut	HiRes-1 Mono	HiRes-1 Stereo	HiRes-2 Mono & Stereo	TAMD Mono
PRMSDEV (degrees)	1	1.2	2	1.2
TL (degrees)	6	4.5	4.5	4.5
IAS (degrees/μs)	0.2	0.1	0.04	0.05
PPGT (photons/good tube)	75	75	75	50
GTPD (min) (good tubes/degree)	0.85	0.75	0.75	0.75
GTPD (max) (good tubes/degree)	4.0	5.0	8.0	5.0

10° of each other, they are deemed to be from the same artificial light source. The second way "hrlsr" determines lasers is to look at the STPLN plane-normal. The known lasers (such as HR1sls, Intersite Flasher, etc. described in section 5.2.5) are all upward-going, so they are automatically deemed lasers and removed. As indicated in the STPS2 summary, only downward-going events were processed starting in this pass, so most upward- and horizontal-going artificial light sources were already removed. There is no additional output bank; events are only removed in this process. Previous to this, spurious laser events that were not fired by GPS timing had to be removed by hand-scanning.

7.2.5 STGEO

Since HiRes-1 is a single-ring detector, "stgeo" was unnecessary for the processing of that data and "stpfl" was performed on the "hrlsr" output files. This program performs a basic chi-squared timing fit to the tubes without any correction (see equation 4.19). The values R_p, ψ, ϕ and θ are found for a timing-only fit for the particular eye (detector). No events are cut since these are all supposed to be air-shower candidates. The banks produced are HCTIM and FCTIM, the same produced in hpass4 and fpass4 (see section 7.1.8).

7.2.6 STPFL

This is the final processing program of the stereo_TA code set. This performs the profile-constrained geometry reconstruction as was performed in htim_pfl (see section 7.1.8). The primary difference between the htim_pfl and stpfl programs lies in the adaptation made for the processing of Telescope Array detectors. Since there are more detectors at TA and every site consists of a two-ring configuration, the number of profile-constrained geometry fits was reduced from 12 to 6. Since there are half as many

steps for the user-defined X_{max} values, the step size was also increased from 35 g/cm^2 to 50 g/cm^2, as well as a decrease in the processing time. In addition, it can now perform a profile reconstruction to the Gaisser-Hillas (GH) function (see equation 4.11) on the good tubes after separately determining the geometry fit. This will be the next iteration of Middle Drum reconstruction, but is out of the scope of this dissertation. The banks produced are PRFC, HBIN and HCTIM.

7.2.7 STRZ5 and DST2RT_HR1

Two additional programs used in the analysis chain are "strz5" and "dst2rt_HR1". The "strz5" program converts the .dst files into .rz files readable by PAW [48]. No new banks are created in this pass, only ntuple files with the desired analysis parameters. The "dst2rt_HR1" program converts .dst files into .root TTree files readable by ROOT [99]. Again, no new banks are created. Instead each DST bank within the file is converted into a TBranch on the "HR1tree" TTree.

CHAPTER 8

ALPHAPROC SEARCH PROCEDURE

The HiRes group at Utah decided that an alternate monocular event selection process would be a good verification of our original process. The work to create this alternate processing routine and the various studies that could be performed using the results of this new process is one of the constituents of this thesis. Additionally, the PassA program has also become the basis for the design of the TAMD/TALE hybrid electronics trigger.

This process starts with the calibrated data from Pass1 and replaces Pass2 with PassA to remove most noise events. The events are then sorted according to their types (e.g., air shower or laser) in PassB after track information is identified in Pass3 and Pass3a. The "htim_pfl" program of Pass4 (see section 7.1.8) is used to reconstruct the events considered cosmic ray showers from PassB. The passes of the AlphaProc processing series are summarized in Table 8.1 and a comparison of each step is shown in Figure 8.1.

8.1 PassA

The first part of this process, PassA, uses a modified Hough transform, motivated by the work found in the Abbasi thesis [1]. Hough transforms are used in graphical analysis to look for one-dimensional structures in a two-dimensional bitmap dataset [32]. PassA performs a series of steps using the calibrated event information in order to find lines from the event information. While a pure Hough transform is applied to a static image, PassA is a modified Hough transform since timing information is used to order pairs of tubes along with the geometrical information: within a single telescope, the triggered PMTs from air shower and laser events appear as time-ordered lines. PassA removes noise events (primarily consisting of random tube firings and aircraft that are not time-ordered or linear) as well as determining the direction of the event. The process is performed on each individual telescope within an event.

Table 8.1: The AlphaProc programs used to process the data, along with the input banks used by the program and the banks created by the program.

Program	Banks Used	Banks Created
PassA	HRAW1	PASSA
PassB	HRAW1, PASS3, PASSA	

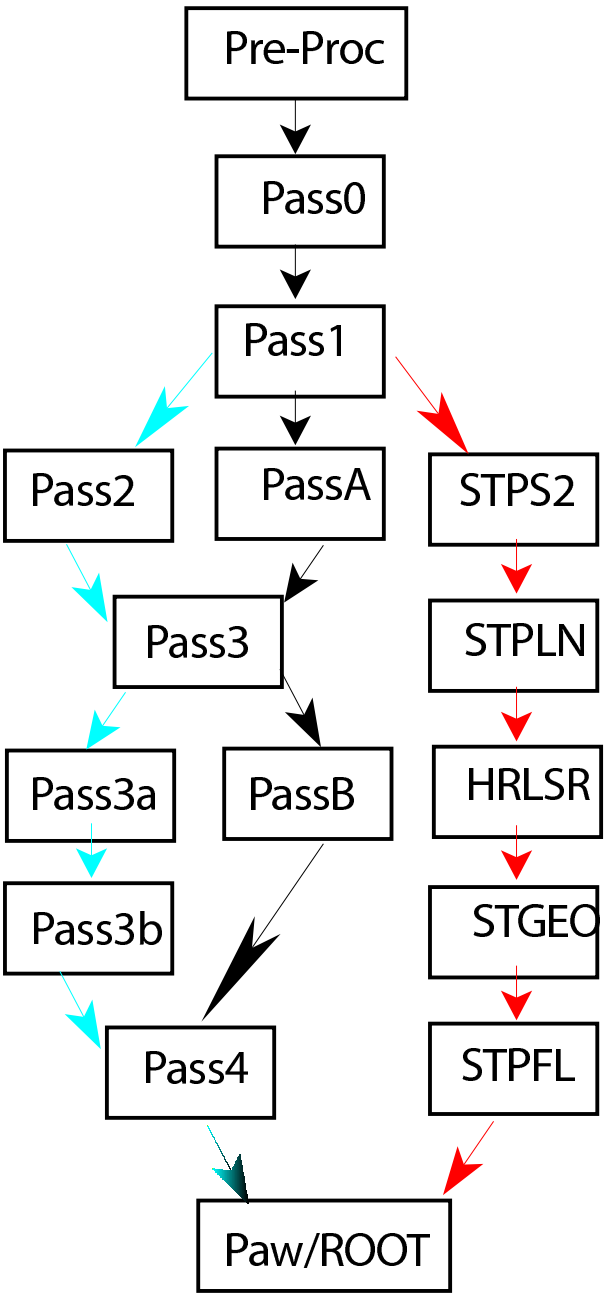

Figure 8.1: Sequence of steps for the original, stereo_TA, and AlphaProc processing code sets.

8.1.1 Transformation

For each telescope in the event, the first step takes each triggered tube and determines its x and y coordinate in the plane of the photomultiplier tube (PMT) camera face. The lower left corner is considered the origin of the x-y plane while the tube numbers, as defined in the hardware, start in the upper left corner (see Figure 8.2). Along with the tube number and the x- and y-coordinates (note, these are in inverted image space), the time each tube is triggered (with respect to the event time), and the telescope number for each tube are also recorded for further analysis.

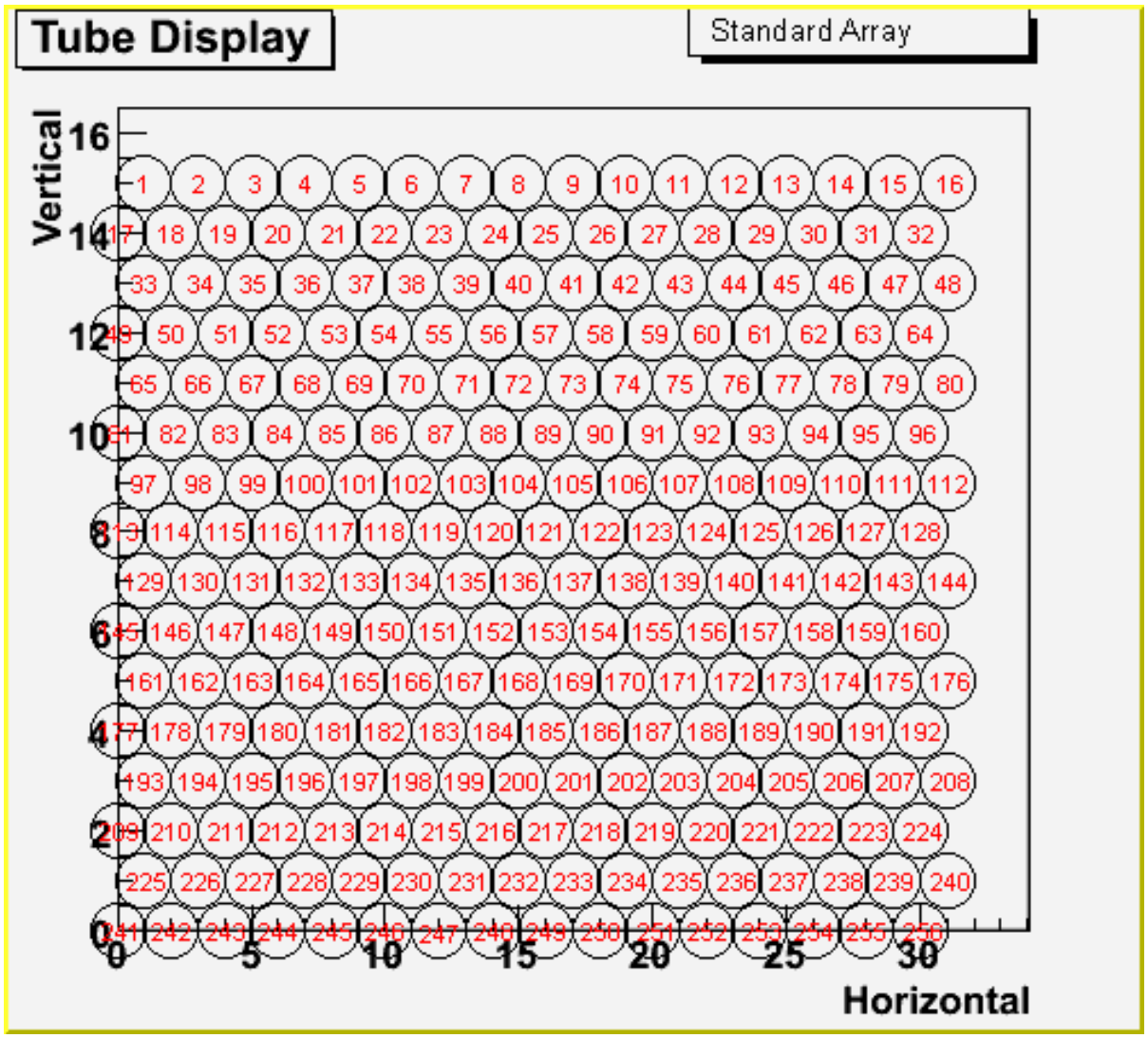

Figure 8.2: Tube numbering. This shows the standard array for a photomultiplier tube cluster in inverted image space. The numbering of the tubes is based off of revalued hardware distribution while the x-y plane is centered at the lower left hand side (tube 241).

8.1.2 Pairing

Each triggered tube is then paired with all other triggered tubes within each separate telescope in the event. Muons traveling through the PMT cameras are rejected since they are observed with crossing times less than $\sim$ 50 ns. Therefore, if the tube pair's trigger times are greater than 50 ns and less than 50 μs (determined from the mean time difference of known laser events) apart from each other, the following parameters are found, taking into account which tube was fired first (see Figure 8.3):

1. θ - the angle the pair-line makes counter-clockwise from the x-axis between $-\pi$ and π,
2. R - the distance from the origin to the point closest to the origin of that line
3. ϕ - the angle the r-vector makes with respect to the origin.

All of the tube pair-lines are considered good until the next step.

8.1.3 Best Fit

Still for individual telescopes within an event, the distribution of all pair-lines is examined. The mean and standard deviation of R and θ are determined along with the covariance between them:

$$\sigma^2_{r,\theta} = (\theta - \overline{\theta})(r - \overline{r}). \tag{8.1}$$

The uncertainty in the means of each parameter and the covariance between R and θ are also determined:

$$\sigma_{\overline{r},\overline{\theta}} = \sqrt{\frac{\sigma^2_{r,\theta}}{N-1}} \tag{8.2}$$

$$\rho_{r,\theta} = \frac{\sigma_{r,\theta}}{\sqrt{\sigma^2_r\ \sigma^2_\theta}} \tag{8.3}$$

where $\sigma_{r,\theta}$ is the standard deviation value of the given parameter and N is the number of pairs of tubes.

The probability that each pair-line is a good fit is then determined using the bivariate gaussian equation:

$$P_i = \exp\left[-\frac{1}{1-\rho^2_{r,\theta}}\right] \times \left[\frac{(r_i - \overline{r})^2}{2\sigma^2_r} + \frac{(\theta_i - \overline{\theta})^2}{2\sigma^2_\theta} - \rho_{r,\theta} \times \frac{(\theta_i - \overline{\theta})(r_i - \overline{r})}{\sigma_r \sigma_\theta}\right]. \tag{8.4}$$

This equation determines a relation between two correlated, normal-distributed variables. As can be seen in Figure 8.3, the initial values for $\overline{\theta}$, $\overline{r}$, σ_θ, σ_r, and $\rho_{r,\theta}$ are usually contaminated by pair-lines associated with noise hits. To remove noise tubes, those pairs

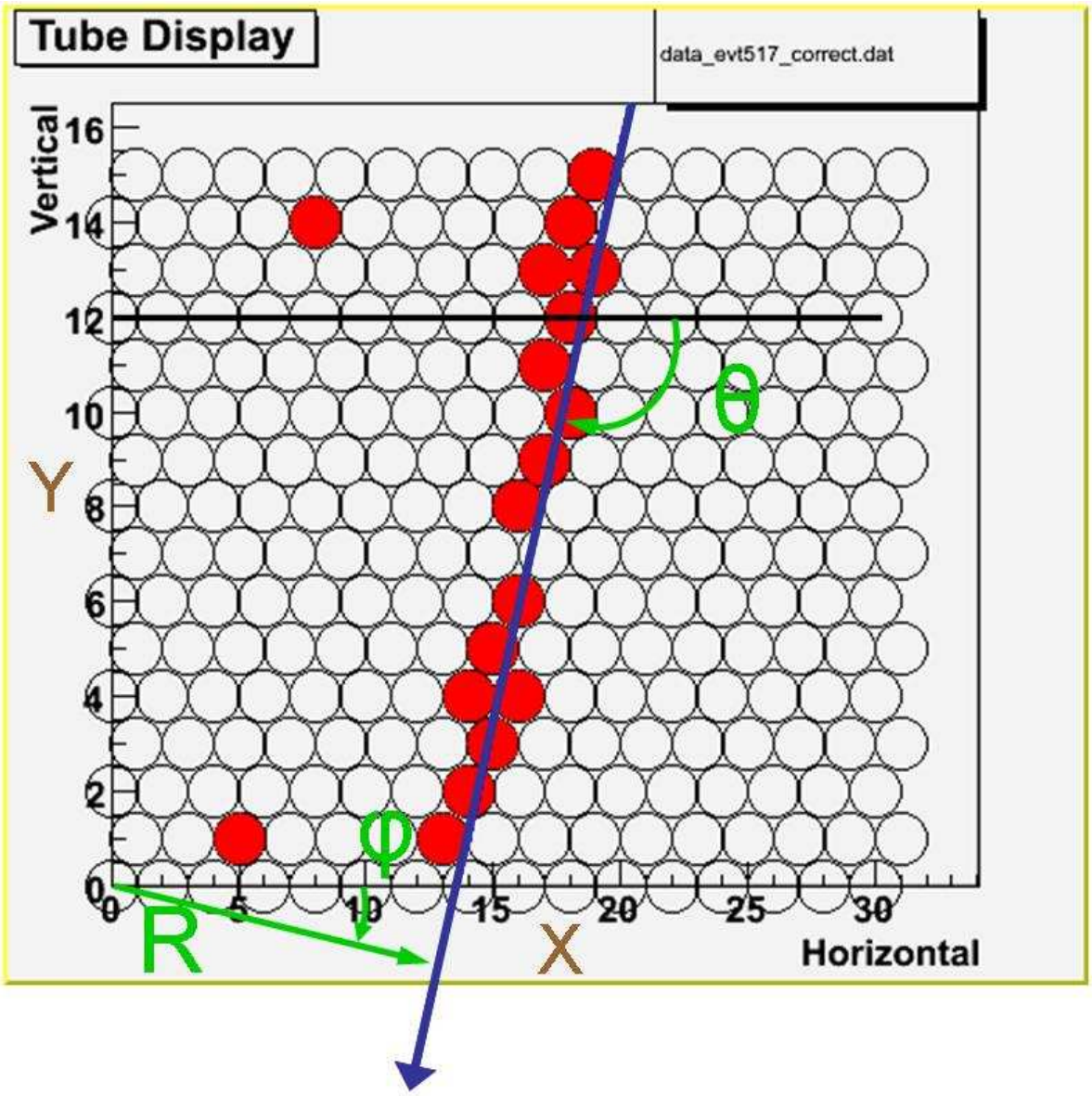

Figure 8.3: This figure shows an example of a cosmic ray shower found by the PassA program and the parameters of that test.

with calculated $P_i < 0.044$ (2.5σ) are removed. The means and covariance are then recalculated, followed by another round of noise removal. This process is iterated until either (a) fewer than 15 pairs (6 tubes) remain, or (b) no more tubes are removed.

8.1.4 Telescope Selection

If there are less than 15 pair-lines at the end of the iterative process above, the telescope is excluded because the reconstruction is not reliable on events with track-lengths of less than 6 tubes, or equivalently $\sim 6^\circ$. If there are more than 3,000 pair-lines the telescope is also excluded because there are too many tubes for a reconstructable cosmic ray shower track (see section 7.1.7). Lastly, if the telescope meets these tube criteria and has $\sigma_{\overline{\theta}} \leq 0.05$ radians ($\sim 3^\circ$) (see Figure 8.4) the telescope is considered good.

If there is at least one good telescope after the angle quality is determined, the event is considered good and a weighted $\sigma_{\overline{\theta}}$ is calculated for only the good telescopes:

$$\sigma_{\overline{\theta}} = \frac{\sum_i \frac{\sigma_{\overline{\theta_i}}}{\sigma_{\theta_i}}}{\sum_i \frac{1}{\sigma_{\theta_i}}} \tag{8.5}$$

The following event information is inserted into the PASSA bank:

- Weighted $\sigma_{\overline{\theta}}$ - the weighted average of all the good telescopes' $\sigma_{\overline{\theta_i}}$
- Telescope number - a list of all of the telescopes in the event with the rest of the information listed
- Good/bad - a flag for whether the telescope was considered good or bad
- $\overline{r}$, $\sigma_{\overline{r}}$, σ_r - the mean distance of closest approach to the origin, the uncertainty of the mean, and the standard deviation of the line defining the event
- $\overline{\theta}$, $\sigma_{\overline{\theta}}$, σ_θ - the mean angle with respect to the origin of the unit vector of the track, the uncertainty of the mean, and the standard deviation of the line defining the event
- $\overline{\phi}$, $\sigma_{\overline{\phi}}$, σ_ϕ - the mean angle, the uncertainty of the mean, and the standard deviation of the r-vector of the line defining the event
- Pairs - the number of good pair-lines in the telescope
- $\sigma^2_{r,\theta}$ - the covariance between r and θ in the telescope
- $\rho_{r,\theta}$ - the correlation between r and θ in the telescope.

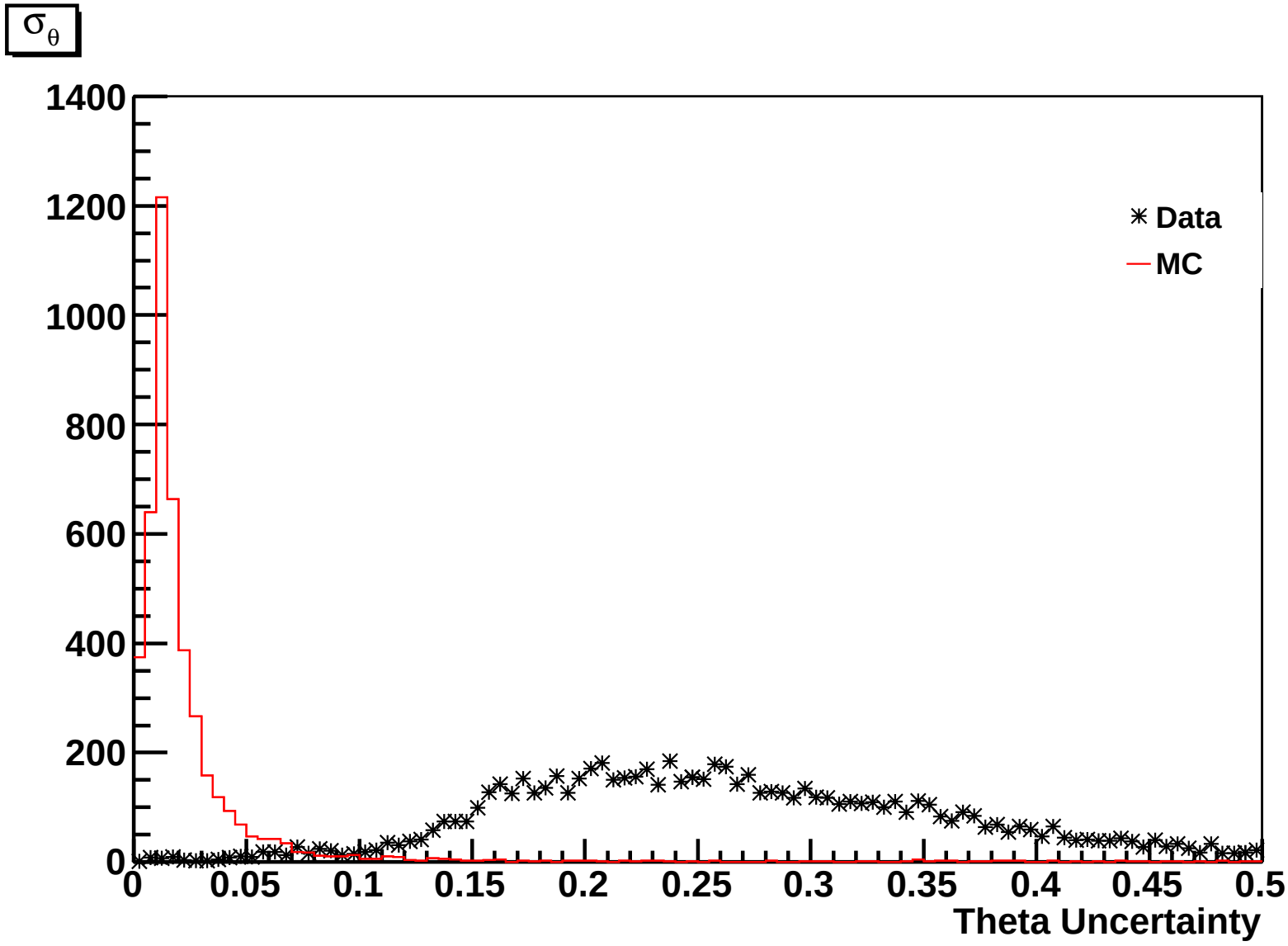

Figure 8.4: Uncertainty in the mean θ of HiRes-1 events for both real data (stars) and Monte Carlo data (solid line). The bulge peaking at ~ 0.25 radians is due to the randomness of noise events' pair-line direction.

8.2 PassB

After "hpln" (see section 7.1.7) is performed on the events kept in PassA to determine the event's shower plane, they are sent through PassB to be sorted into a type of event: shower, laser, noise, etc. This program uses a combination of track information (from Pass3) and telescope event information (from PassA) to sort the surviving data into seven types of events: HR1sls, HR2sls, HR3sls, flashers, intersite flasher (ISF), random lasers, and air showers. The HiRes-1 data stream filters out HR1sls events at the data acquisition level, because these shots trigger all tubes in the quadrant and cannot be analyzed. The other types of events will each be defined in the process described below.

8.2.1 Event Classification

The first step of the process performs a basic sort on each event in the file and counts the total number of events in that file (see Table 8.2). The event angle for each event is calculated from the weighted average $\overline{\theta}$ of the telescopes' PassA angle using a modification of equation 8.5. This is done by replacing $\sigma_{\overline{\theta_i}}$ for each telescope's good tubes with each telescope's $\overline{\theta_i}$ and using $\sigma_{\overline{\theta_i}}$ in place of σ_{θ_i}. By default, all of the events are considered to be air showers. Their classification can be changed if they meet certain criteria as explained below.

- Flasher events are selected by a combination of the telescope in which they were observed and the event angle. From the viewpoint of HiRes-1, telescopes 7, 8, 10, 11, and 12 were all able to see at least one flasher (see Figure 8.5). If the angle in that telescope was within 5.5° to either side of vertical the event was labeled "flasher".

- HiRes-2 steerable lasers (HR2sls) are visible between telescopes 2 and 21 (see Figures 5.5 and 8.6) azimuthally (facing HiRes-2). Additionally they are fired at precise milliseconds (section 5.2.5.1). If the event started within 2 ms of the firing time, the event was considered HR2sls. If the lasers were triggered to

Table 8.2: These PassB sorting parameters are used to make the initial determinations of the kind of event.

Source	$\overline{\theta}$ (deg)	Telescope range	Timing (ms)	Other
Flashers	90 ± 5.5	7, 8, 10, 11, 12	-	-
HR2sls	$>$ horizontal	4-14, 21, 24, 25	222 ± 0.002	Starts in M7, M8, or M12
HR3sls	90 ± 5.5	19	322 ± 0.002	-
ISF	$>$ horizontal	4-14, 21, 24, 25	-	Starts in M15, M20, or M22

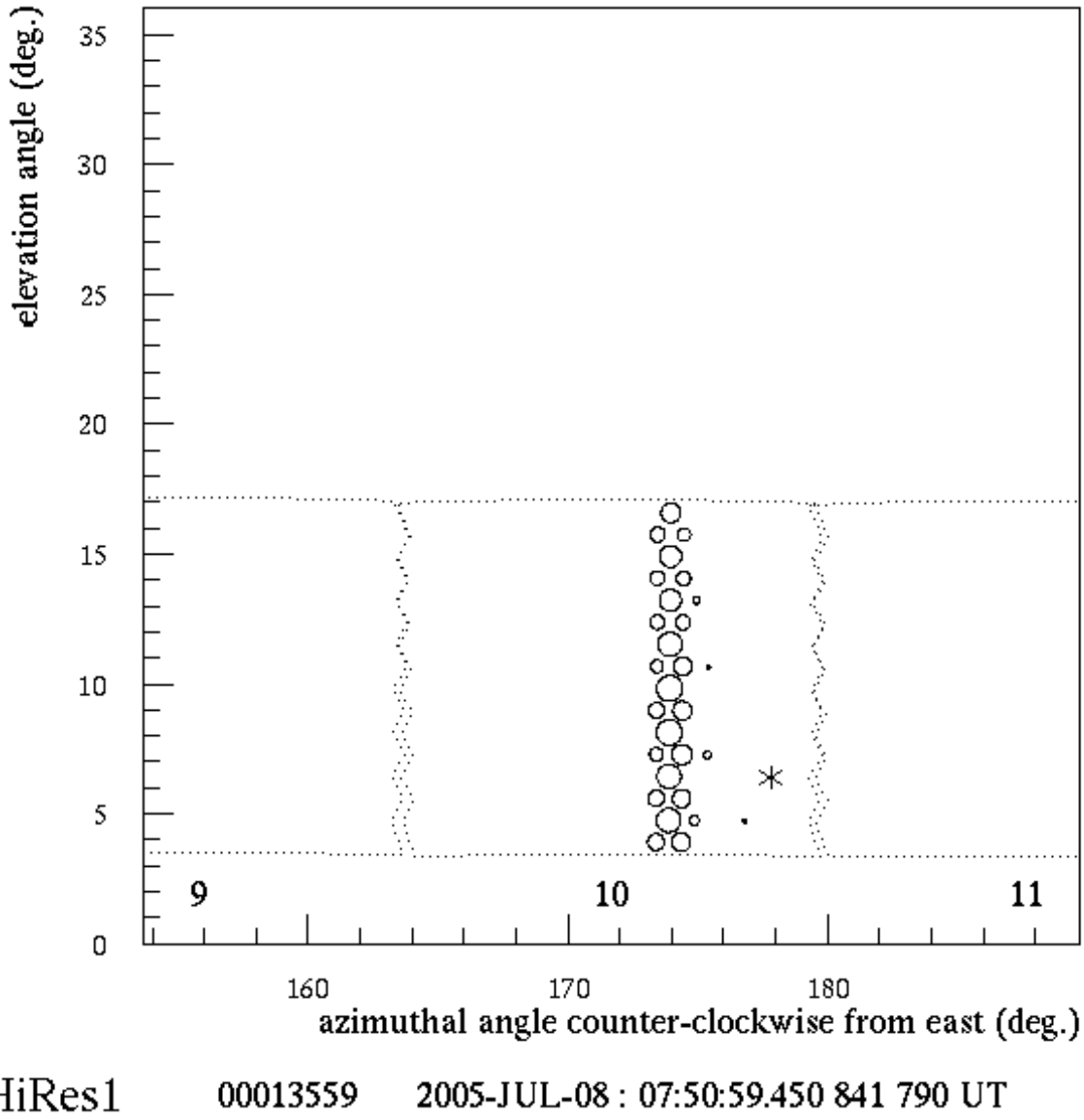

Figure 8.5: This display shows how a single flasher would have been observed by the detector and viewed by the operators.

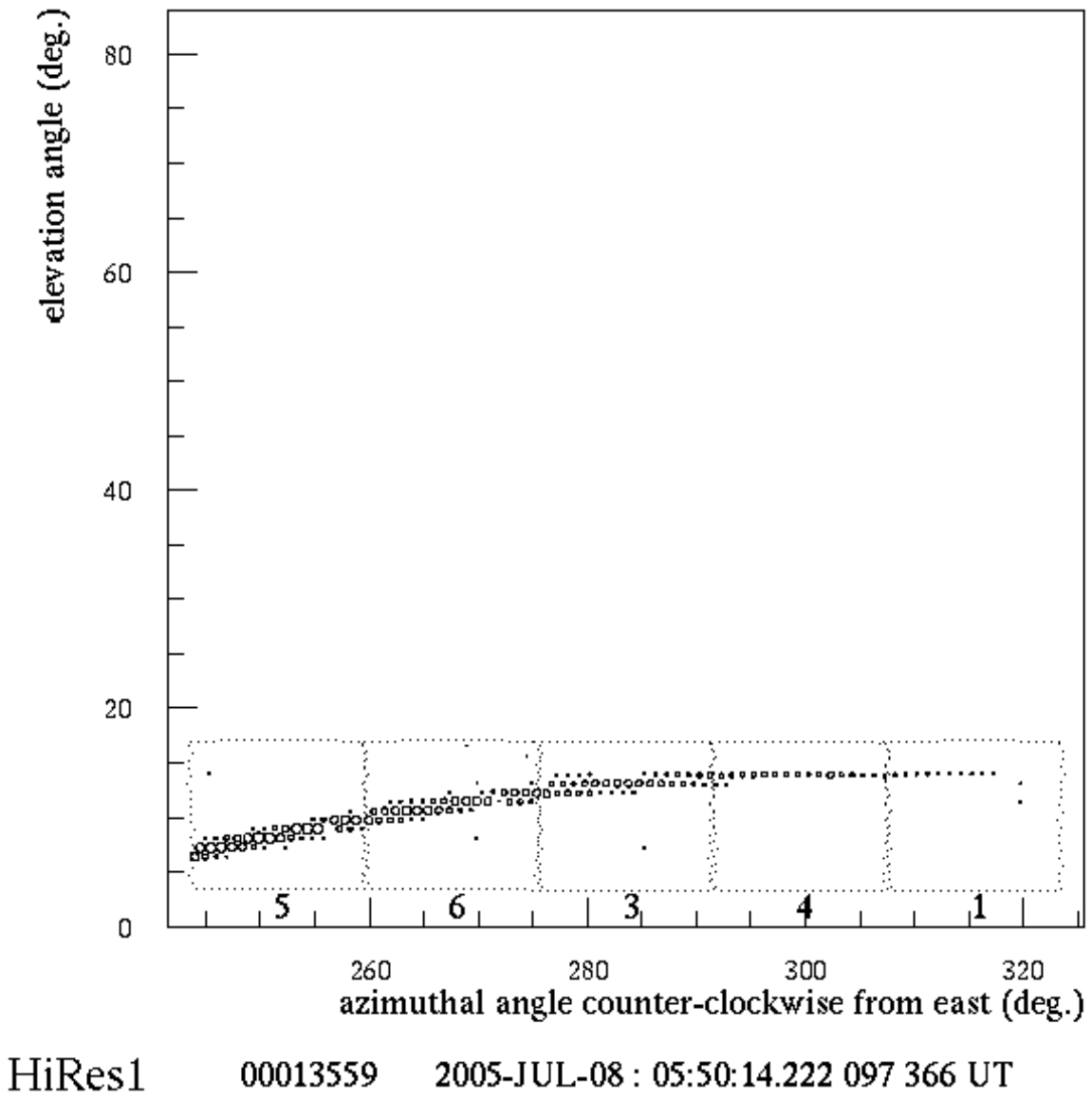

Figure 8.6: This display shows how the HR2sls laser would have been observed by the detector and viewed by the operators.

"shoot-the-shower", the laser would not have been fired at the aforementioned millisecond. A second check is performed on the events visible in this range of telescopes based on the spread of the event (see Table 8.2). Only these telescopes are able to view the HR2sls and the event angle is upward-tending (between 0 and π) starting in telescope 7, 8 or 12. If there are between five and eight telescopes, the event is automatically considered "HR2sls". If there are three or four telescopes, the beginning and ending telescopes are checked. If there are two telescopes, the beginning and ending telescopes along with the event angle is checked. If there is only one telescope, the event angle is checked.

- If the event starts in telescopes 15, 20, or 22, but has the same range of telescopes

as the HR2sls, the event is tested to be the intersite flasher (ISF) (see Figure 8.7 and section 5.2.6). If the event angle is upward-tending and there are at least three telescopes in the event, including bad-fit telescopes, or if the event is pointing straight up, the event is labeled as an ISF event. Otherwise, the event is still considered an air shower.

- HiRes-1 can only view the Terra laser, HR3sls (see section 5.2.5.2), in telescope 19 (see Figure 8.8). As with the other steerable lasers, HR3sls is fired at precise milliseconds, but it is always pointing straight up. These conditions are used to sort between HR3sls and a random laser event in that telescope.

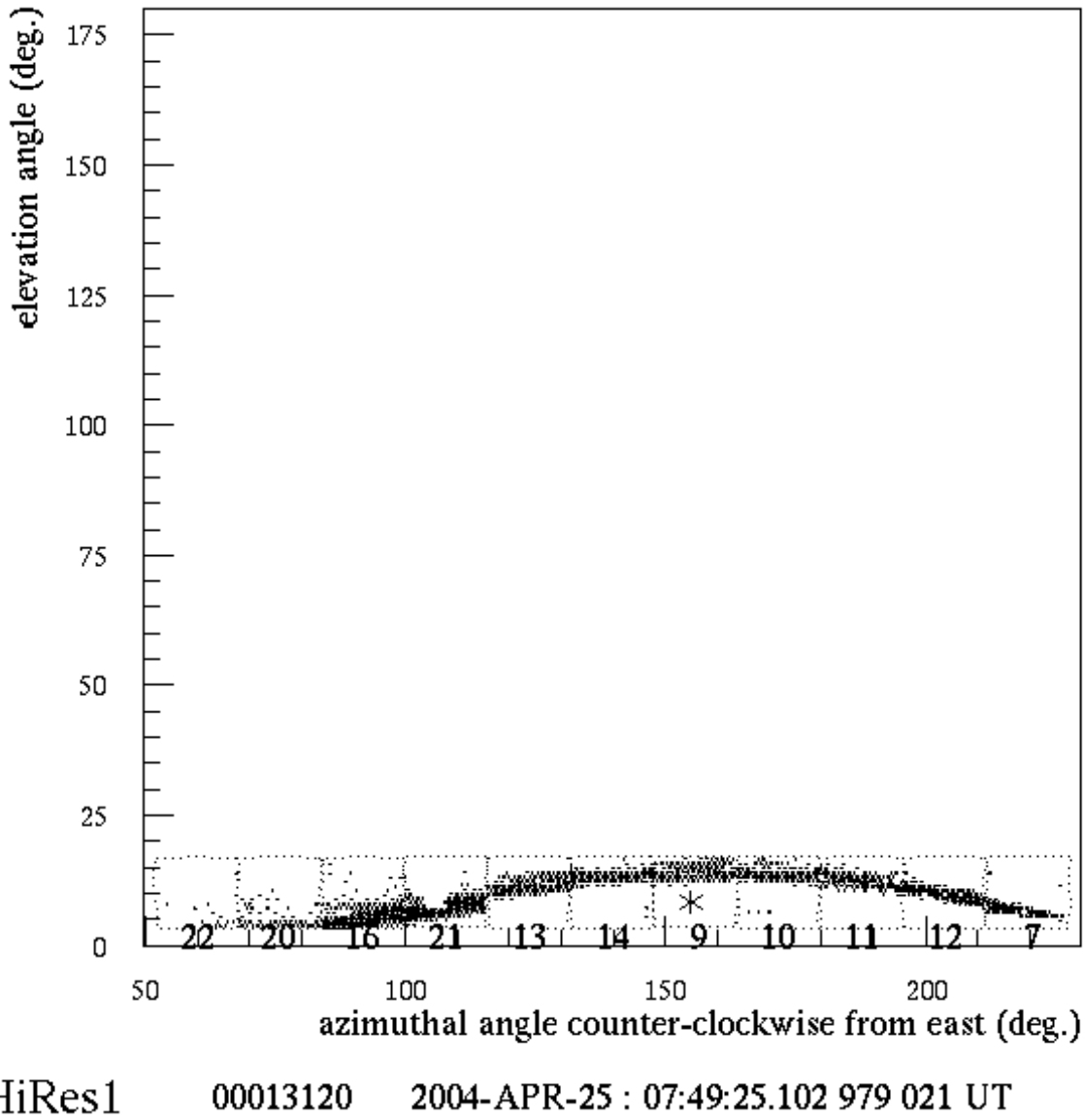

Figure 8.7: This display shows how the intersite flasher would have been observed by the detector and viewed by the operators.

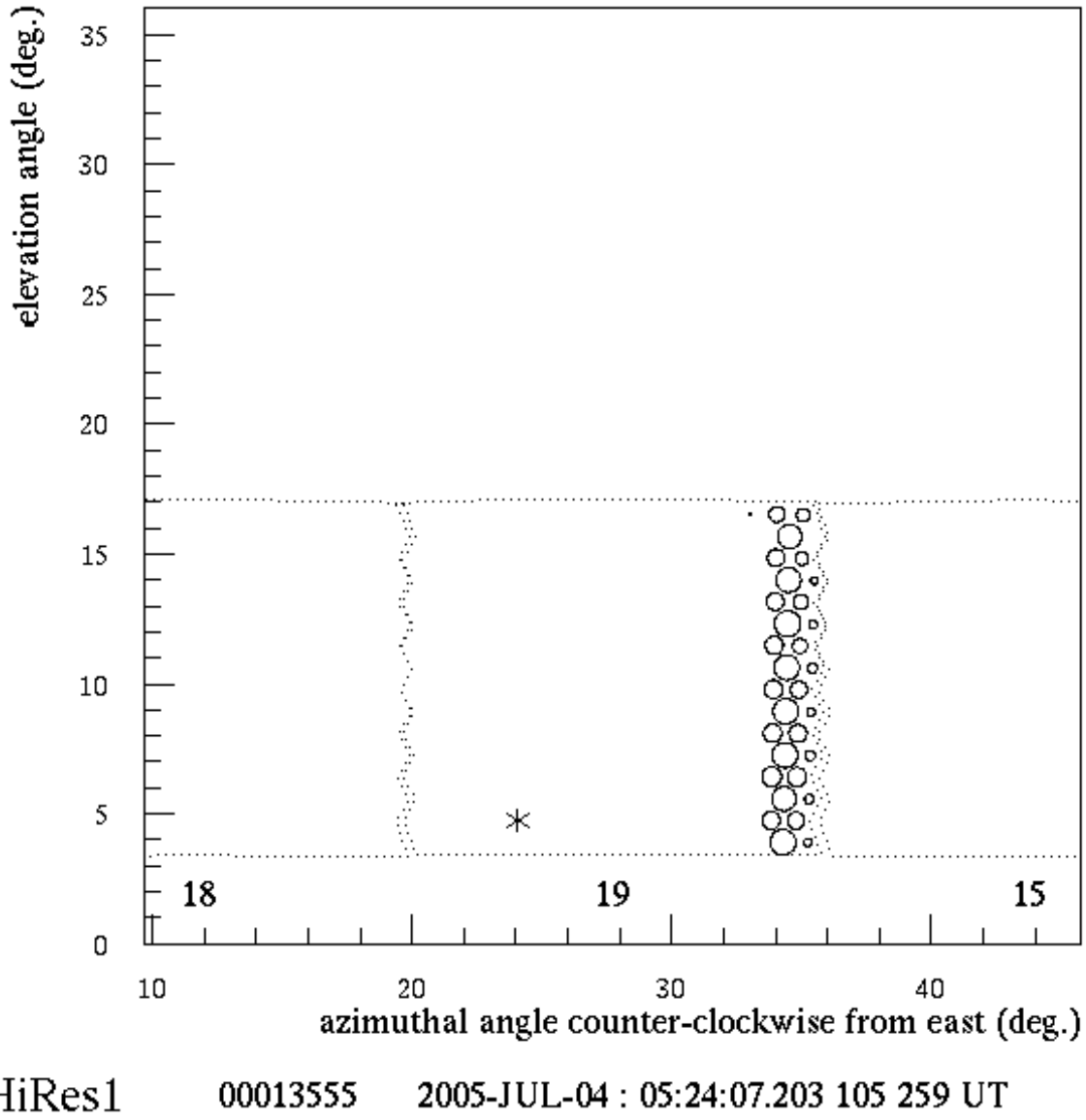

Figure 8.8: This display shows how the Terra Laser (HR3sls) would have been observed by the detector and viewed by the operators.

8.2.2 Identification of laser/flasher by repetition

Events that were not sorted to a specific laser classification in the previous check are then compared to all of the other events in the same file. This check is performed because occasionally a laser or flasher would not meet the above criteria. This process compares only good telescopes to the same good telescopes from sorted events in two passes.

In the first pass a test is done to make sure the unsorted events' $\overline{\theta}$'s and $\overline{\phi}$'s (from passA) are within 12° of each other and their $\overline{r}$'s are within a quarter of a tube width of each other (see Figure 8.9). If this is true, the unsorted event is classified as that of the laser to which it is compared.

A second test checks for matching tubes for each pair of events within a file. If the pair has matching good telescopes (PassA), the QDCB values are compared for each matching, good tube (hpln). If there are six or more tubes with QDCs within 50 volts of each other, the events are considered to be matching. If one of the events in the pair happens to already be classified as a laser, the unsorted event is considered to be from the same artificial light source.

Since each event in the file can have many classifications within each test, the prominent type must be determined. The classifications are tallied for each of the above tests, and the most prominent is chosen as the event-type (flasher, hr2sls, etc.) for that particular test. These two new types (from matching PassA and matching tubes) are then compared to the initial classification. If two of these three types match, the event is reclassified as that type. If all three types are distinct, the event is labeled "unknown". If there are more than four individual events that all match but are still unsorted by this step, each of those events is relabeled as a "random" laser (roving laser, military laser, etc.).

8.2.3 Event Distribution

Once classified, all of the events are distributed into separate files based on their label. Each event will only show up in one file and so the event reconstruction (section 7.1.8) can be performed on each type of event separately. All of those events that were not considered a laser or unknown are assumed to be air showers and reconstructed as such.

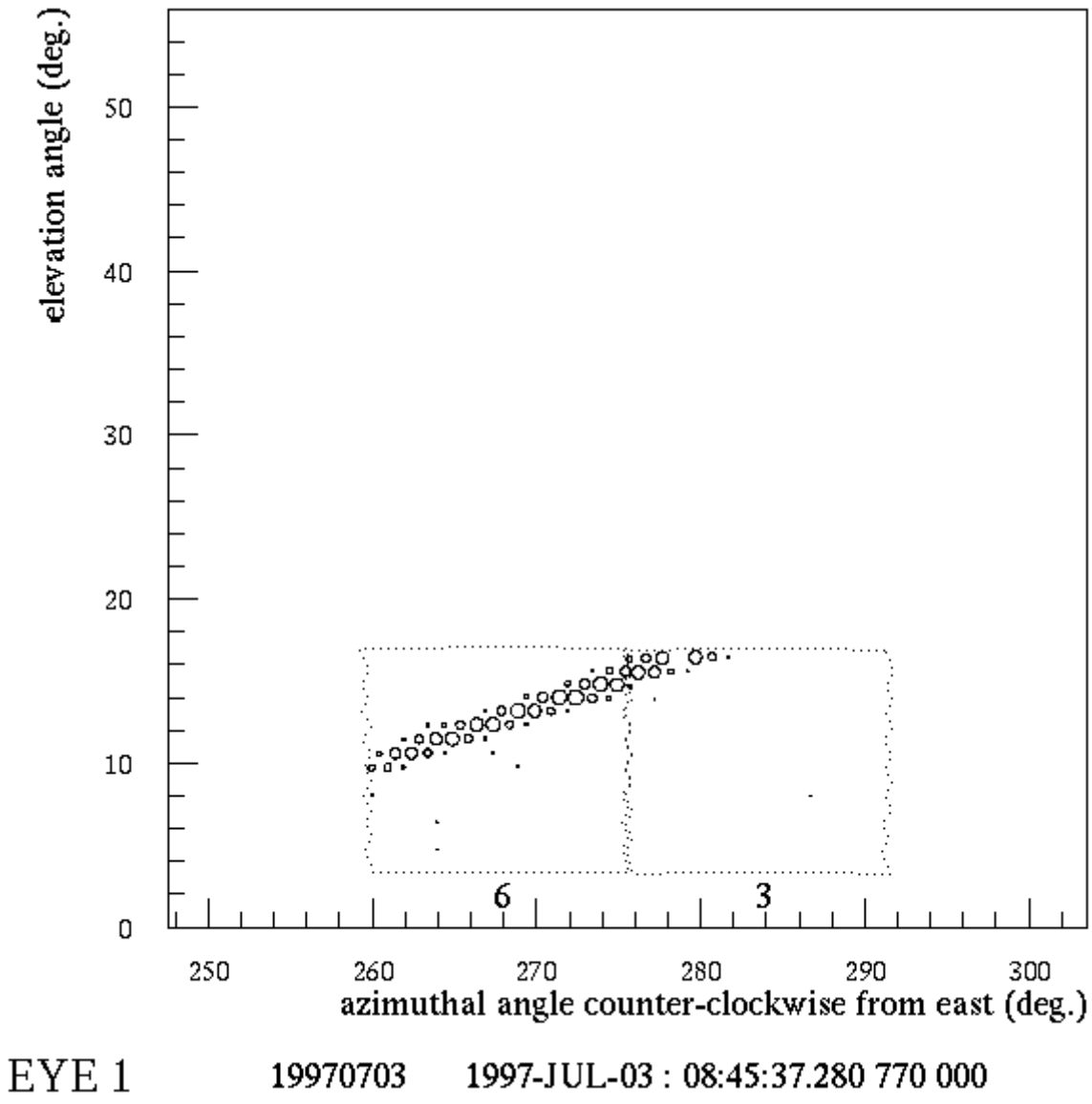

(a) Event 1

Figure 8.9: Two events compared in PassB and determined to be from the same laser source.

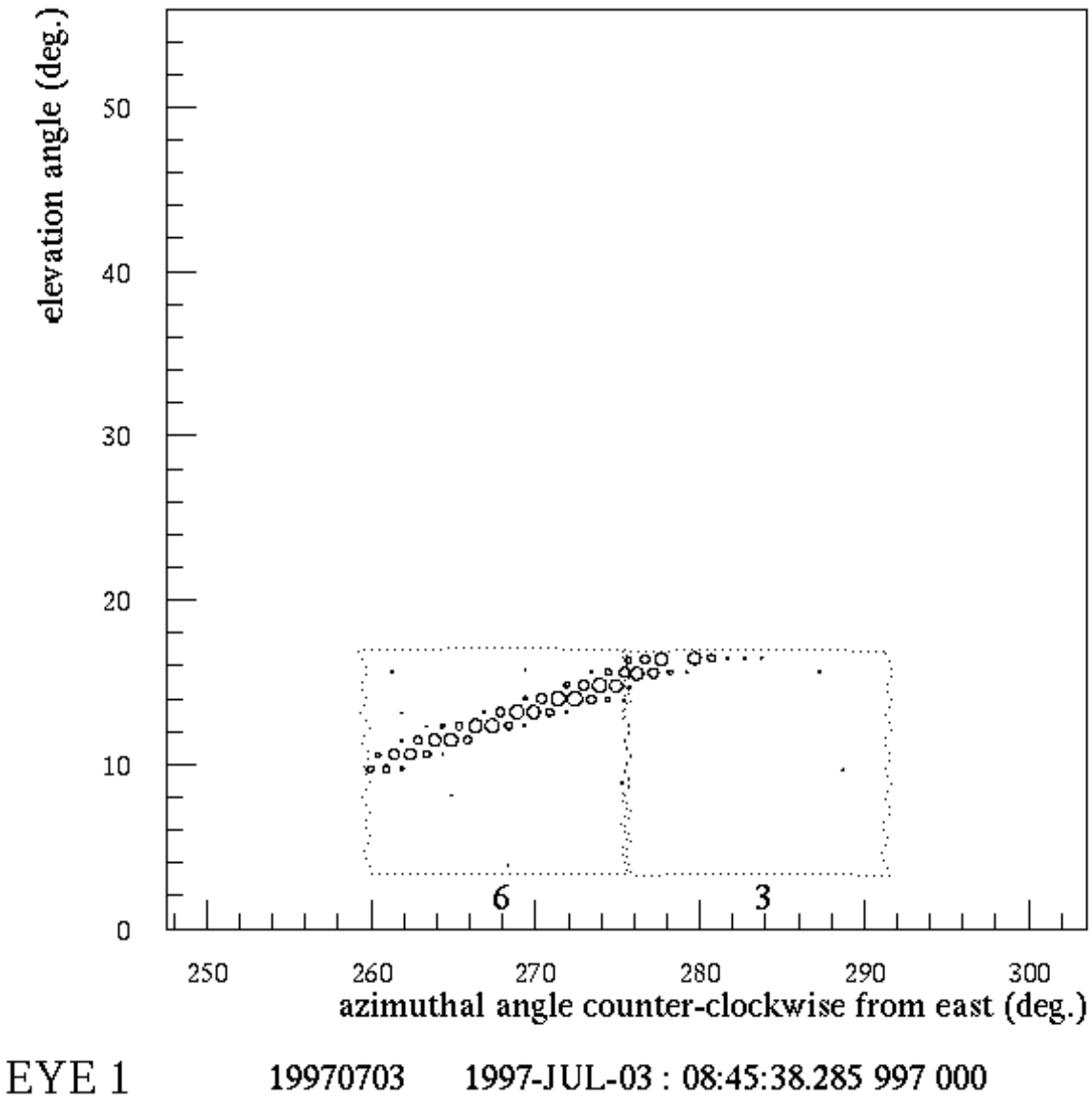

(b) Event 2

Figure 8.9: Continued.

CHAPTER 9

PROGRAM SET DIFFERENCES

This section describes the various differences between the three code sets of Chapters 7 and 8. Differences in geometry and energy reconstruction will be compared. The number of events in both the observed and simulated data will vary depending on the exact event processing chain and selection cuts.

9.1 Monte Carlo Shower Production

As described in section 4.3, the Monte Carlo simulations for HiRes-1 and Middle Drum were generated using the same standard code with the same parameters used in the 2008 publication [3]. This simulation package, like the rest of the stereo_TA code, is only different in the user interface. Since the original and, therefore, AlphaProc code sets were only applied to HiRes-1 data, Middle Drum results were not included in this comparison. The comparisons were made primarily on the simulated data where the "true" event information was known. Thus the comparison serves to highlight the few changes in the reconstruction code.

The Monte Carlo produced and used in this dissertation assumed a piece-wise power law fit to the High Resolution Fly's Eye spectrum [3] where the energy of the ankle break point (a change in the spectral index) was found at $10^{18.65}$ eV. Thus the events were generated in two regions: (A) from $10^{17.5-18.65}$ eV (energy region "1"), with a spectral index of $\gamma_1 = 3.25$; and (B) $10^{18.65-20.5}$ eV (energy region "2"), with a spectral index of $\gamma_2 = 2.81$. The number of showers thrown represents this change in the spectral index with the integrated numbers of events in the two regions matching at the $10^{18.65}$ eV break-point energy.

The number of events in a spectral range is calculated by the integral

$$N_i = \int_{E_{a_i}}^{E_{bi}} J_i(E)(A\Omega_0)(E)dE\Delta t \tag{9.1}$$

where N_i is the number of events in region i, E_{a_i} and E_{b_i} are the endpoints of the energy range, Δt $(A\Omega_0)(E)$ is the exposure, and $J_i(E) = B_n E^{-\gamma_i}$ is the flux of the events in the

region. We can assume the observation time for both regions will be the same, reducing the number of variables necessary to solve $J_1 = J_2$ at the break-point energy, $E_2 = 10^{18.65}$ eV. Since the two regions must have a matching flux of particles coming from both above and below, we know that

$$J_1(E_2) = J_2(E_2) \Rightarrow B_1 E_2^{-\gamma_1} = B_2 E_2^{-\gamma_2} \tag{9.2}$$

or

$$B_1 = B_2 E_2^{\gamma_1 - \gamma_2} \tag{9.3}$$

will fulfill this requirement. The ratio of these two values is calculated, and, after reducing,

$$\frac{N_1}{N_2} = E_2^{\gamma_1 - \gamma_2} \times \frac{\left[E_2^{1-\gamma_1} - E_1^{1-\gamma_1}\right]}{\left[E_3^{1-\gamma_2} - E_2^{1-\gamma_2}\right]} \times \frac{1-\gamma_2}{1-\gamma_1} \tag{9.4}$$

where N_1 goes from $E_1 = 10^{17.5}$ eV to $E_2 = 10^{18.65}$ eV with spectral index $\gamma_1 = 3.25$ and N_2 goes from E_2 to $E_3 = 10^{21.0}$ eV with spectral index $\gamma_2 = 2.81$.

The aperture into which the Monte Carlo events are thrown must contain all events which can trigger the detector. Therefore a safe upper limit for the thrown input parameter is set to 50 km for region 2 ($E \geq 10^{18.65}$ eV), and 25 km for region 1 ($10^{17.5}$eV $\geq$ E $< 10^{18.65}$eV). Both used a lower limit distance of 100 m. To compensate for the thrown aperture difference, the actual number of thrown events in region 1, N_1', is rescaled by

$$\frac{N_1'}{N_1} = \frac{\left(R_{1-upper}^2 - R_{1-lower}^2\right)}{\left(R_{2-upper}^2 - R_{2-lower}^2\right)} \tag{9.5}$$

where $R_{i-upper}$ is the upper limit of region i and $R_{i-lower}$ is the lower limit.

From this point, only the desired number of thrown events of one range needs to be decided in order to determine the number in the other. To produce $\sim 10\times$ the observed on-time, $N_2 = 31$ sets of 10,000 events each were produced for the upper energy range. Using the same number of events per set, it was calculated that there should be $N_1 = 2405$ sets for the lower energy range. Only one Monte Carlo set was generated for each of the HiRes-1 and, separately, the Middle Drum detector configurations. The single HiRes-1 Monte Carlo set was then processed using each of the three processing code routines to show the comparisons described here.

About 100,000 Monte Carlo events were collected that triggered the simulated detector and passed all of the cuts (see Table 9.1). The exact numbers varied between the different selection and reconstruction code sets since each made cuts in different ways and at different stages (see Figure 8.1 and Table 9.2). The "Triggered" row represents those thrown events that triggered the detector. The timing/profile reconstruction program did not remove any events; they only reconstructed those not removed as noise or lasers.

Table 9.1: These numbers represent the final number of events for both real data and Monte Carlo events that passed all of the applied quality cuts.

	Orig	Alpha	STA
Data	11116	14348	18130
MC	92174	149294	131692

Table 9.2: Average percentages of retained events from previous pass for each processing code set of the HiRes-1 Monte Carlo.

Pass (O/A/S)	Orig	Alpha	STA
Triggered	2.36	2.36	2.36
hpass2/passA/stps2	95.28	87.16	76.83
hpln/hpln/stps2 (d)	56.62	61.16	98.11
hpln -C/hpln -C/stpln	99.07	99.07	56.14
hpass3b/passB/hrlsr	49.73	99.98	99.29
htim_pfl/htim_pfl/stpfl	100.0	100.0	100.0
Quality	60.61	49.30	54.59
Final	16.11	25.92	22.94
Of Thrown	0.38	0.62	0.54

The "Quality" row shows the number of events which were reconstructed and passed the final quality cuts. The "Final" row shows the results of these percentages, showing that the AlphaProc code set retains the highest percent of generated events in Monte Carlo data.

The numbers in Tables 9.1 and 9.2 indicate that there is a discernible difference in the efficiency between the processing code sets and, potentially, actual numbers of real cosmic ray showers in the final data set. We note that the rejected events consist primarily of those that appear to consist of coincidences of multiple clusters of noise hits (sky noise was included in the simulation) or lack sufficient information such that they would reconstruct poorly (in timing, profile, or both). The numbers in the "Final" row of Table 9.2 show us that, of those that actually trigger the detector, $\sim 20\%$ are actually retained. Since all of the generated and real events were each processed using each code set, the only differences occur in selection cuts prior to reconstruction and in the changes in the reconstruction program itself.

9.2 Comparison of Reconstructed Events $\geq 10^{18.5}$ eV

The three processing code sets use only two reconstruction codes; the AlphaProc processing code set uses the original processing code set's reconstruction program. Because

of this, we would expect the AlphaProc and original reconstructed values for the same events to be the same. Additionally, from the original analysis, there is a known bias in the reconstructed geometry. With this current set of Monte Carlo it can be seen that the htim_pfl reconstruction program reconstructs the impact parameter, R_P, $\sim 5-11\%$ too low (see Figures 9.1 and 9.2) and the stpfl program reconstructs $R_P \sim 12\%$ too high (see Figure 9.3).

Since R_P and ψ, the in-plane angle, are related by equation 4.18, the error in ψ will be correlated to the error in R_P. The correlations between $\Delta R_P/R_P$ and $\Delta\psi$ are clearly demonstrated for all three reconstructions in Figures 9.4, 9.5, and 9.6. Correspondingly, we see biases for reconstructed ψ in Figures 9.7, 9.8, and 9.9.

Due to the nature of the detector and the reconstruction programs, HiRes-1 energy reconstruction is highly dependent upon the geometry to give the slant depth of the shower viewed by each photo-multiplier tube. Therefore, there should be a bias in the energy reconstruction based on the geometry reconstruction, which we do observe (see Figures 9.10, 9.11, and 9.12).

Over different energy ranges the reconstruction bias also shifts (see Figures 9.13, 9.14, and 9.15). This bias can be corrected by fitting for the mean difference as a function of the reconstructed energy (see Figure 9.16). To first order, these details do not affect the shape of the spectrum since the same bias correction is applied to both the data and the Monte Carlo (which determines the aperture). The primary reason for applying the correction is to obtain reconstructed energies that are as close to the "true" value for the event as possible. Before the correction there is a clear bias in comparing the reconstructed values to the thrown values (see Figures 9.17, 9.18, and 9.19), but this is clearly removed after applying the correction (see Figures 9.20, 9.21, and 9.22). Again, the correction for each code set was applied to the data from the appropriate code set and the same shift can be seen (see Figures 9.23, and 9.24). As was mentioned in Chapter 7, the stereo_TA reconstruction is quicker since there are fewer/wider X_{max} steps available. Slightly worse resolutions were expected, but this was allowable since this change was made in anticipation of the two-ring configuration at Middle Drum which will improve the resolution and reduce the bias. However, the number of events in each tenth-decade energy bin should still agree to within the percentage of events retained (see Tables 9.2 and 9.3).

9.3 HiRes-1 Reconstruction Comparisons

To validate our results, we made comparisons of the data and Monte Carlo distributions. Specifically, we see good agreement in those quantities related to the aperture,

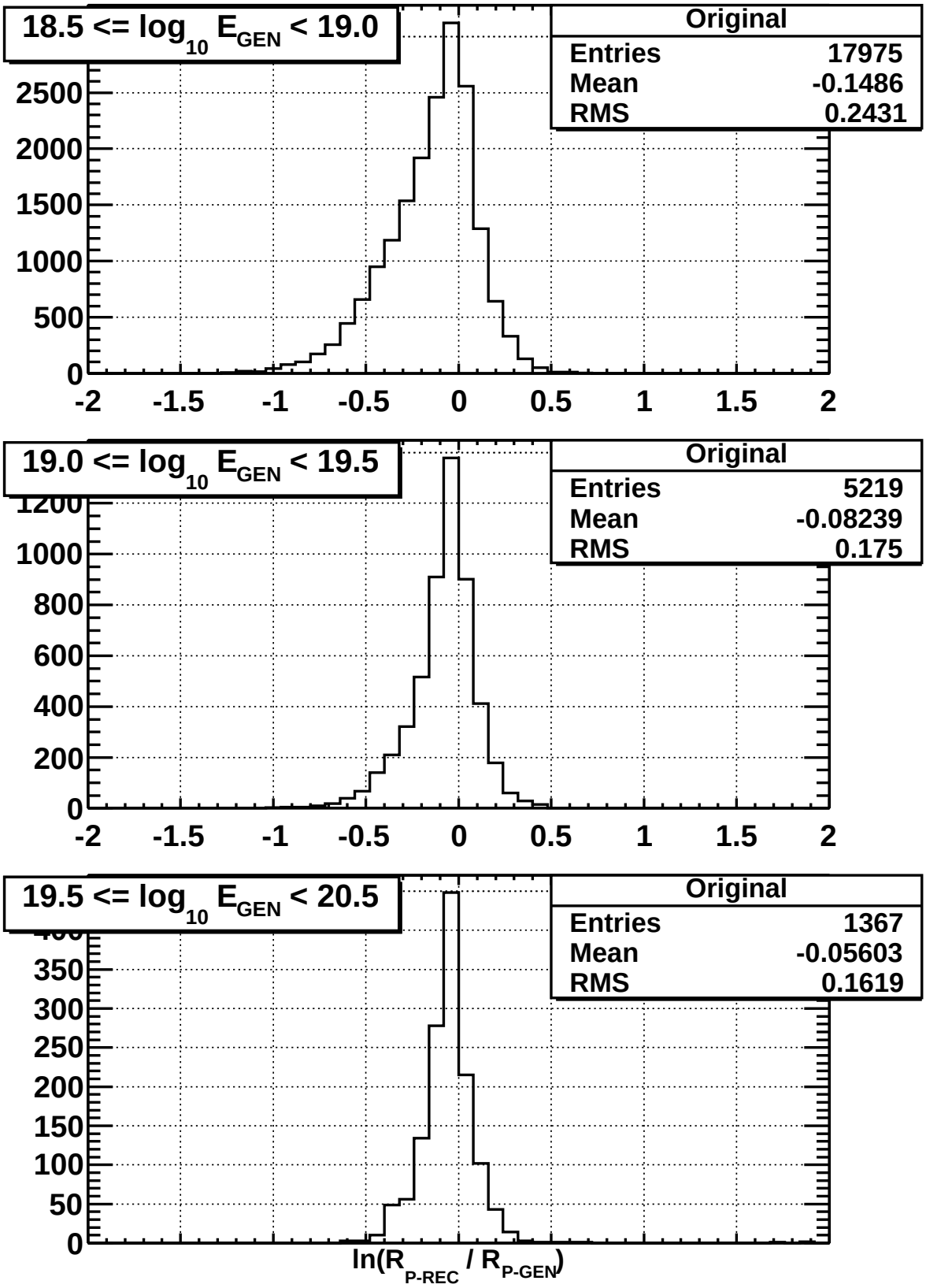

Figure 9.1: Monte Carlo R_P resolution for the original processing code over different energy ranges.

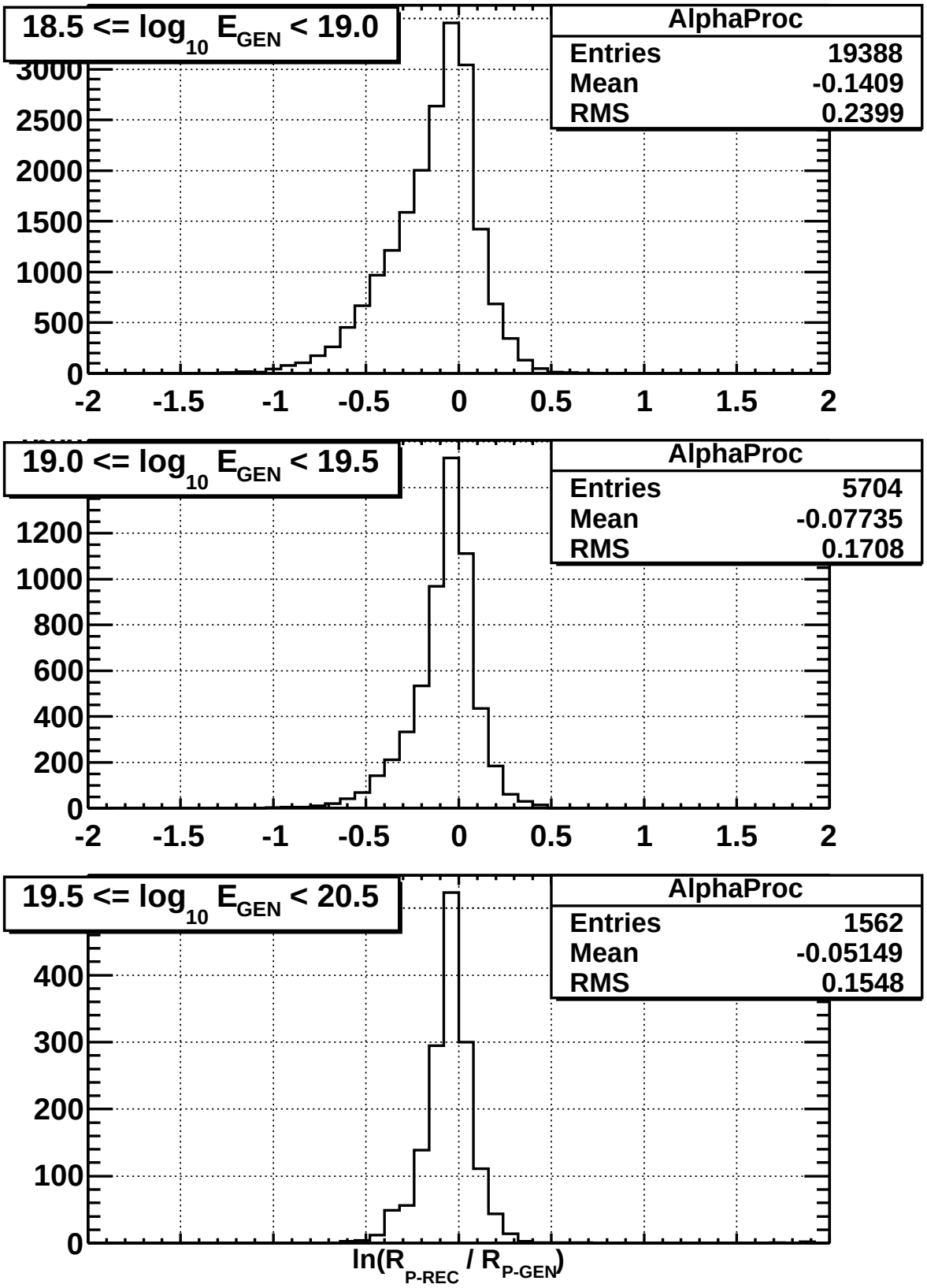

Figure 9.2: Monte Carlo R_P resolution for the AlphaProc processing code over different energy ranges.

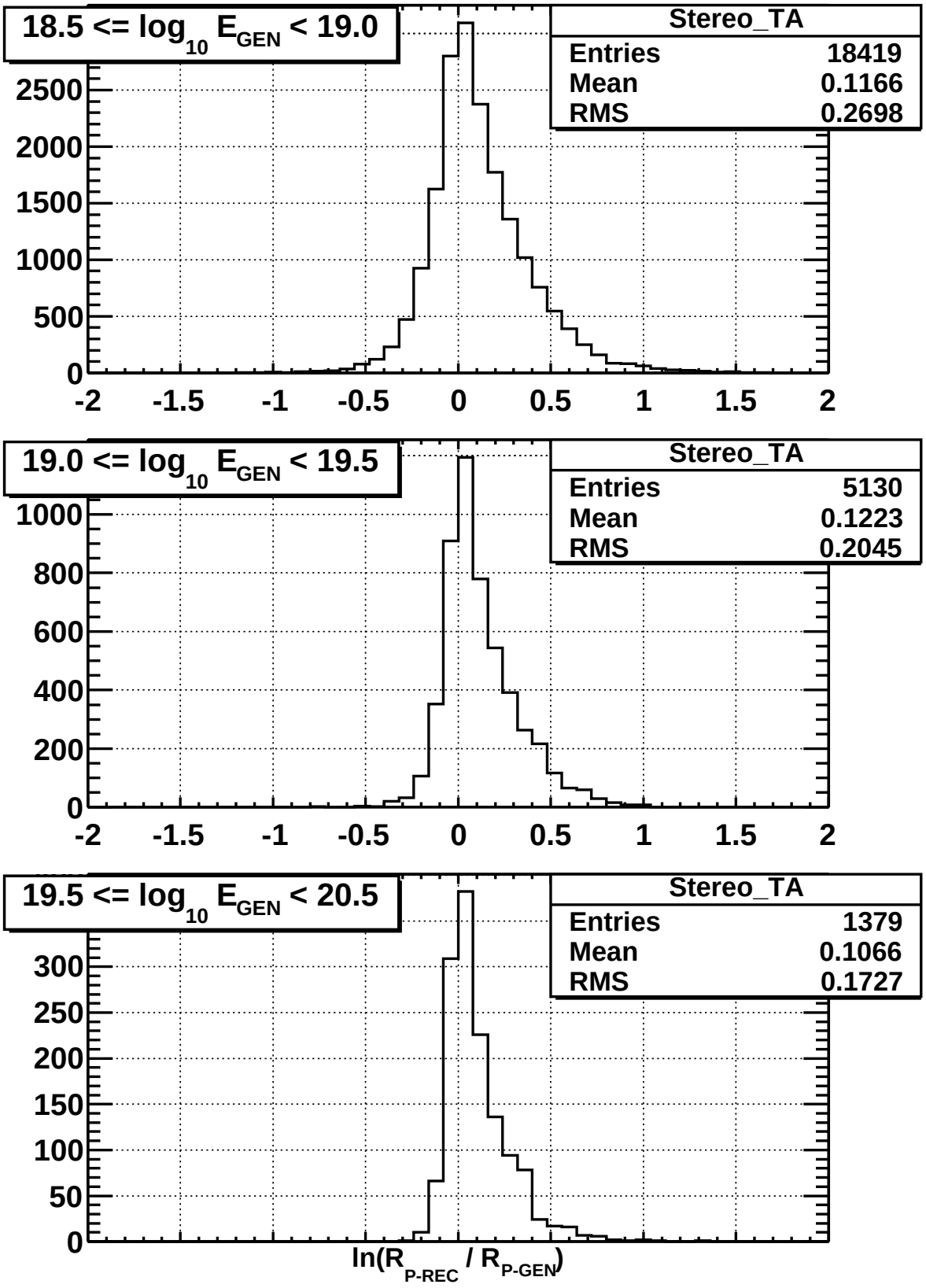

Figure 9.3: Monte Carlo R_P resolution for the stereo_TA processing code over different energy ranges.

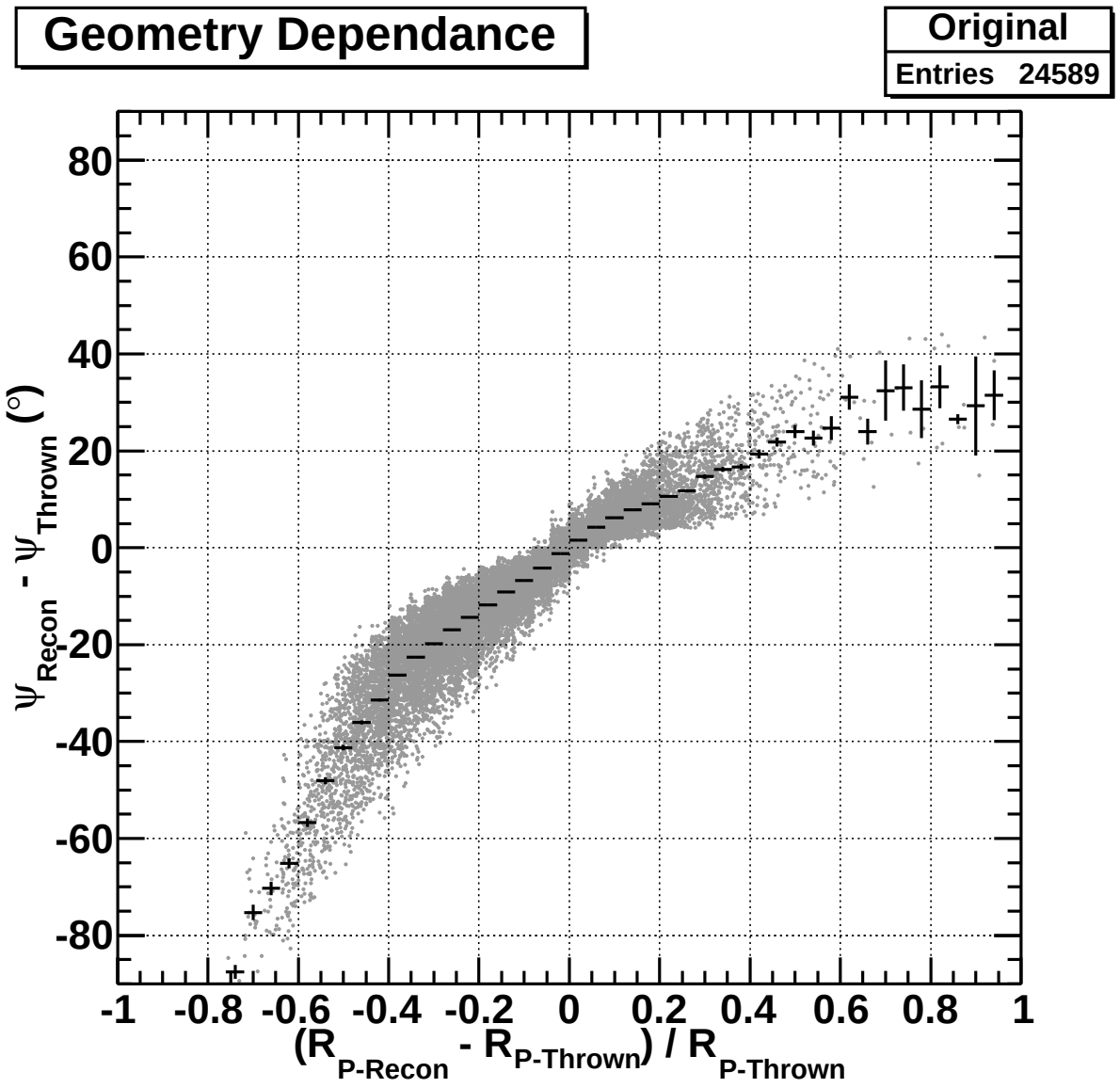

Figure 9.4: Monte Carlo error in ψ compared to the error in R_P for the original processing code.

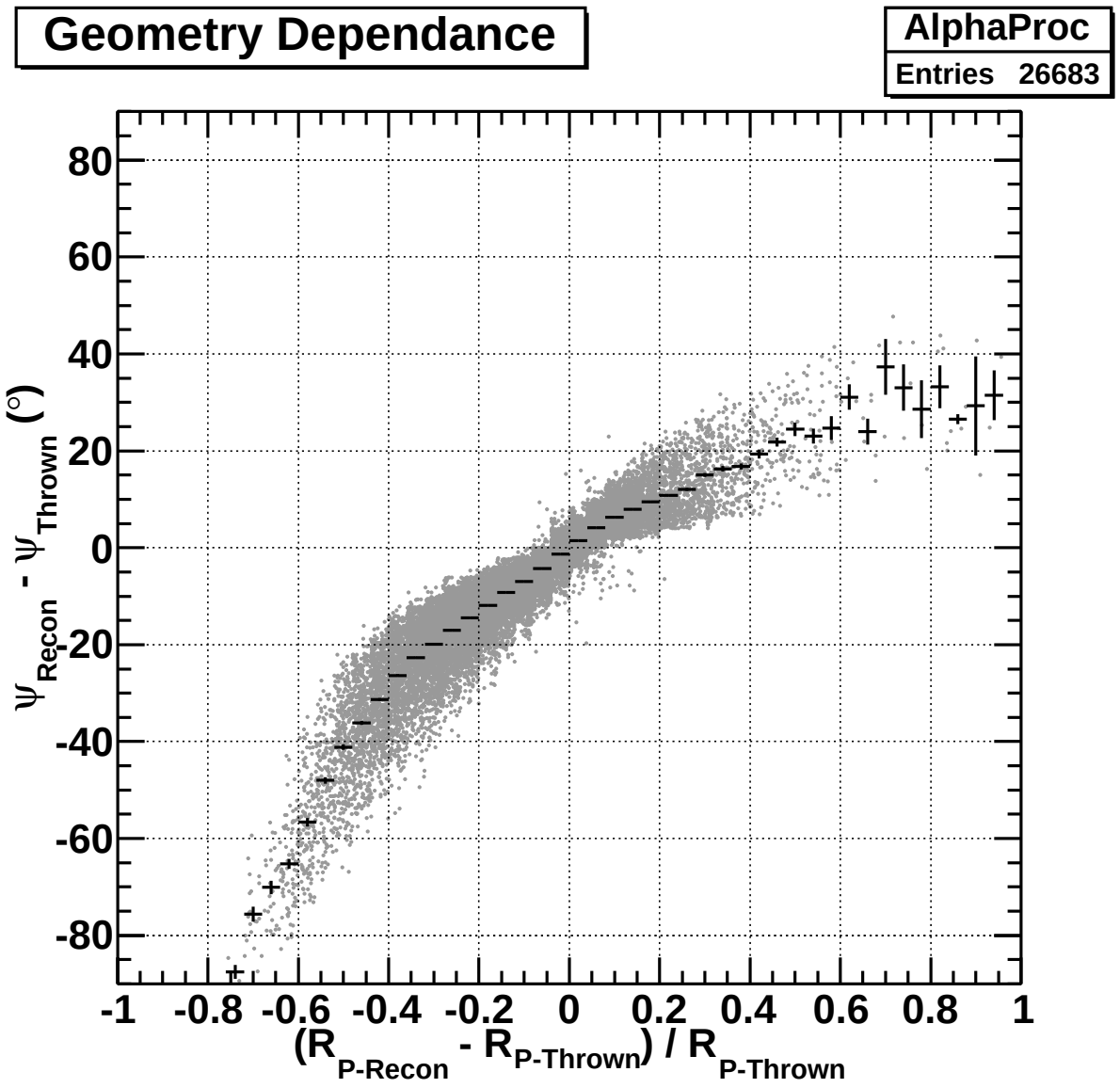

Figure 9.5: Monte Carlo error in ψ compared to the error in R_P for the AlphaProc processing code.

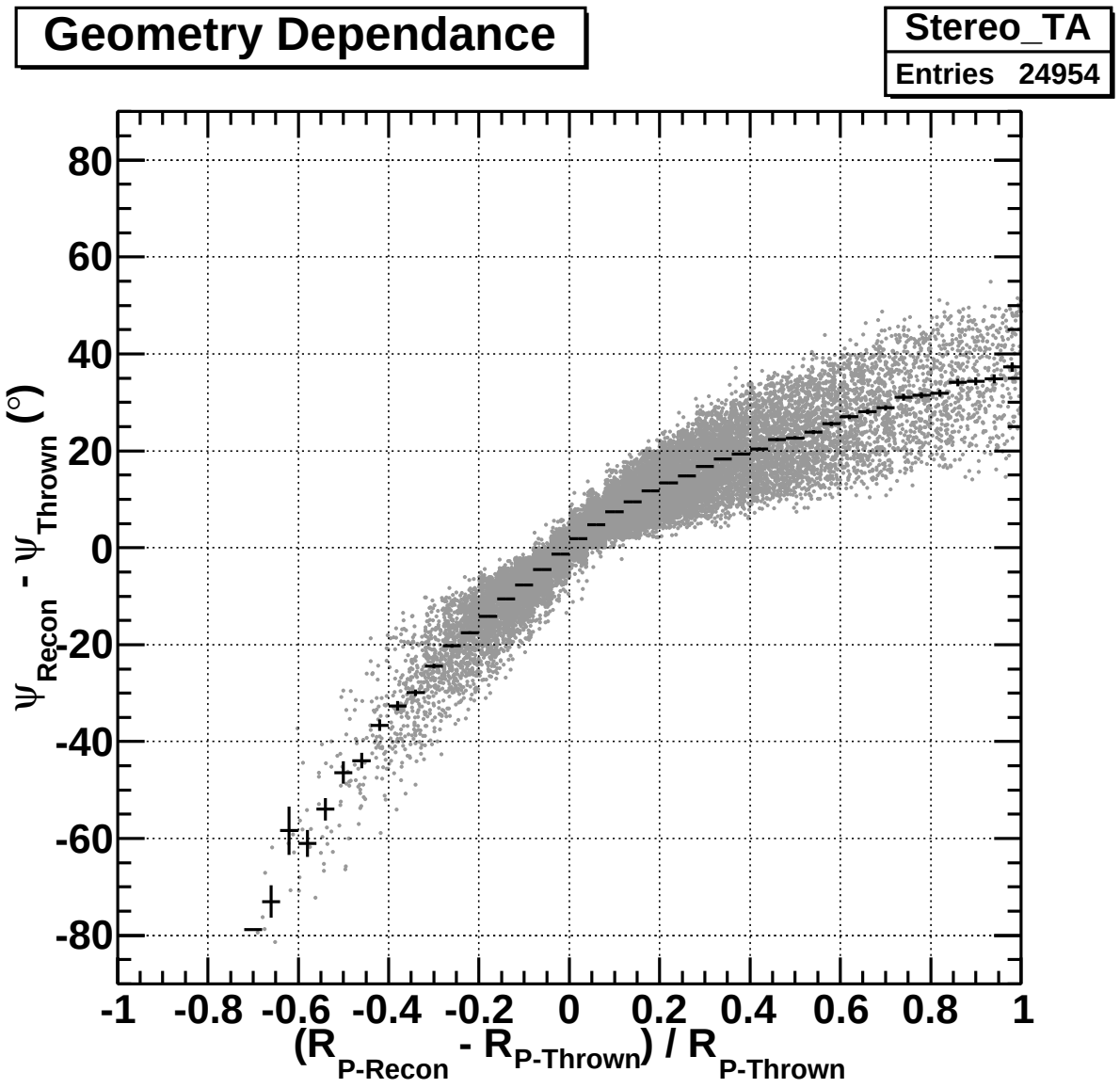

Figure 9.6: Monte Carlo error in ψ compared to the error in R_P for the stereo_TA processing code.

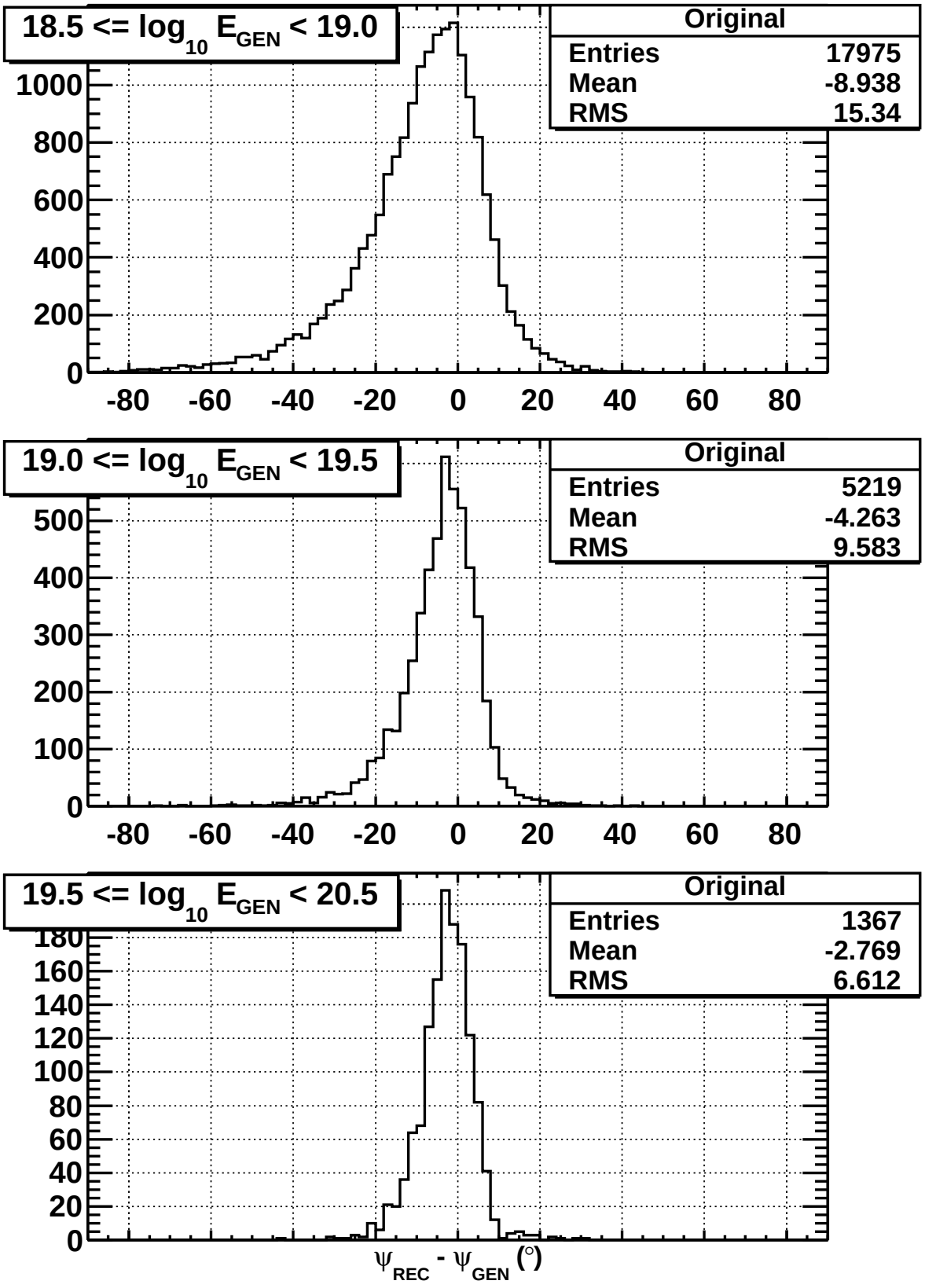

Figure 9.7: Monte Carlo ψ resolution for the original processing code over different energy ranges.

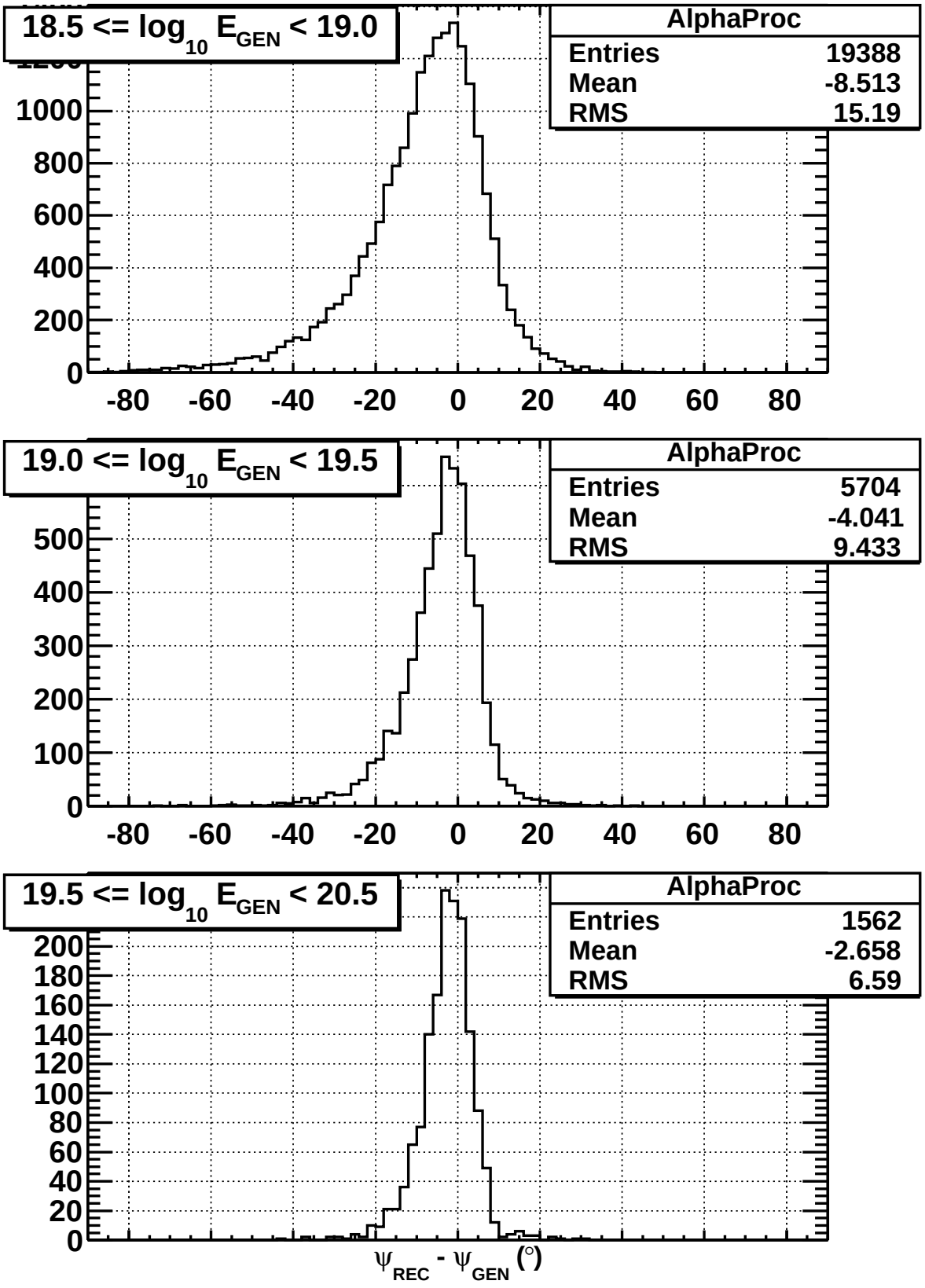

Figure 9.8: Monte Carlo ψ resolution for the AlphaProc processing code over different energy ranges.

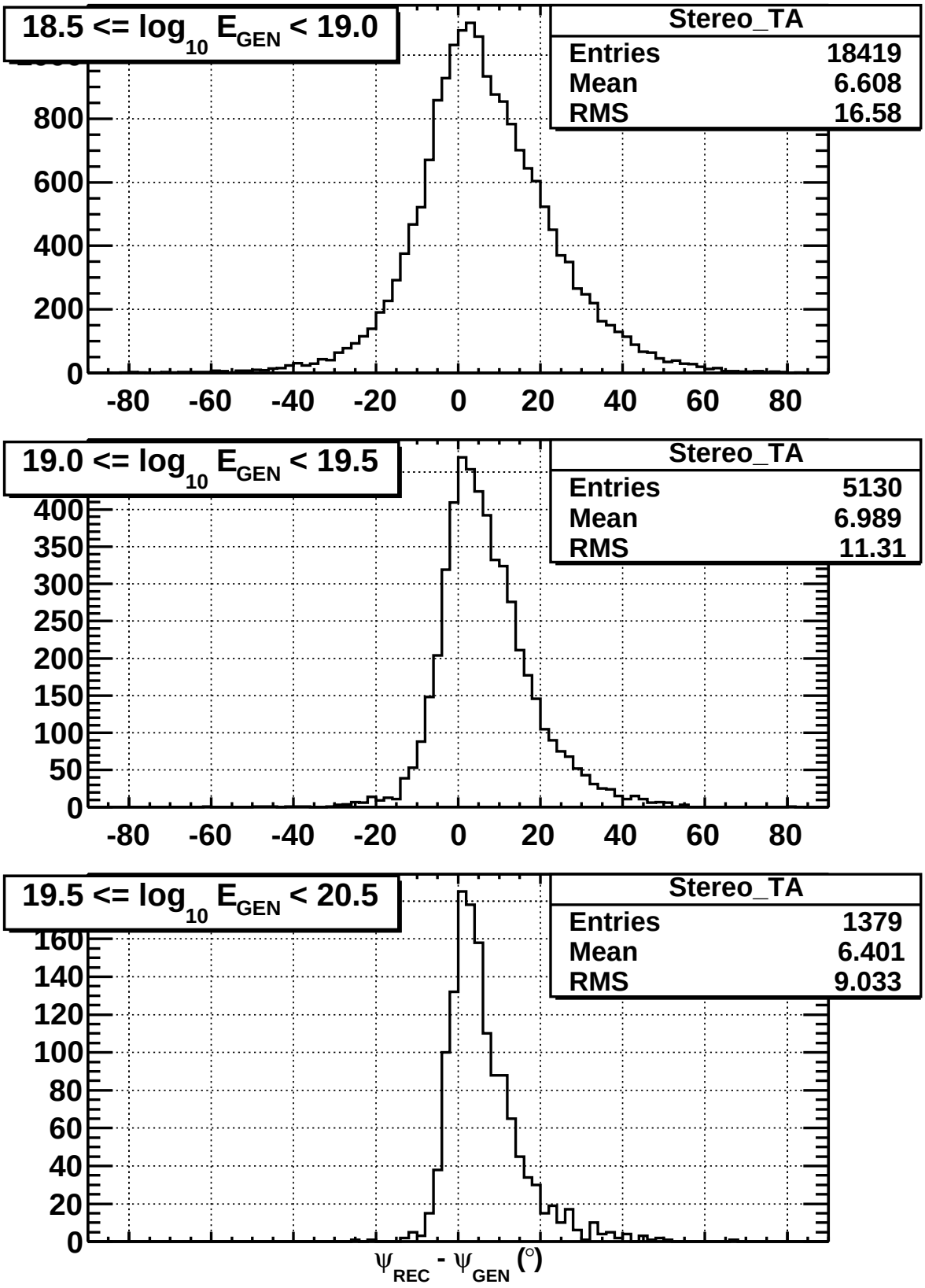

Figure 9.9: Monte Carlo ψ resolution for the stereo_TA processing code over different energy ranges.

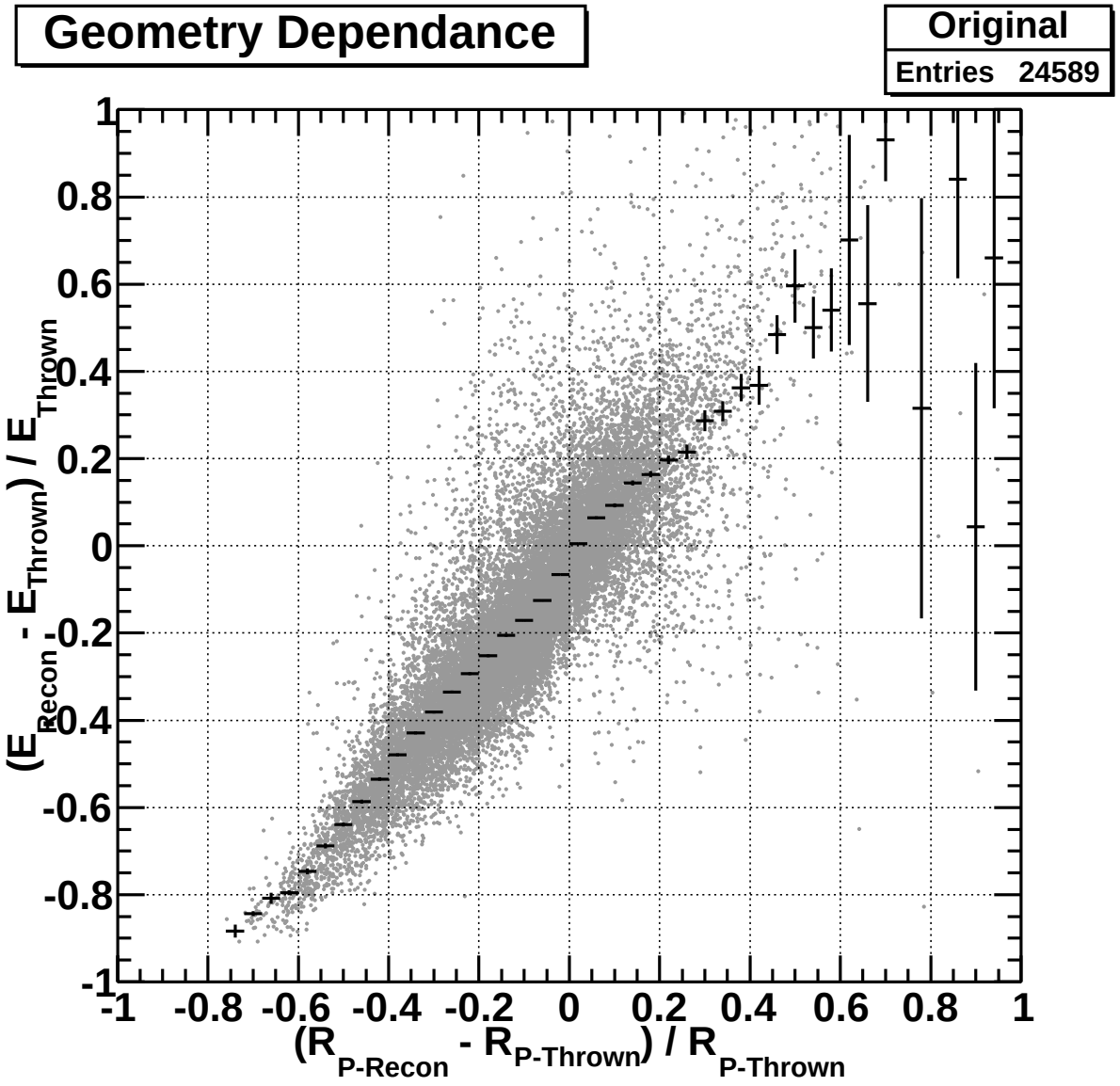

Figure 9.10: Monte Carlo error in energy compared to the error in R_P for the original processing code.

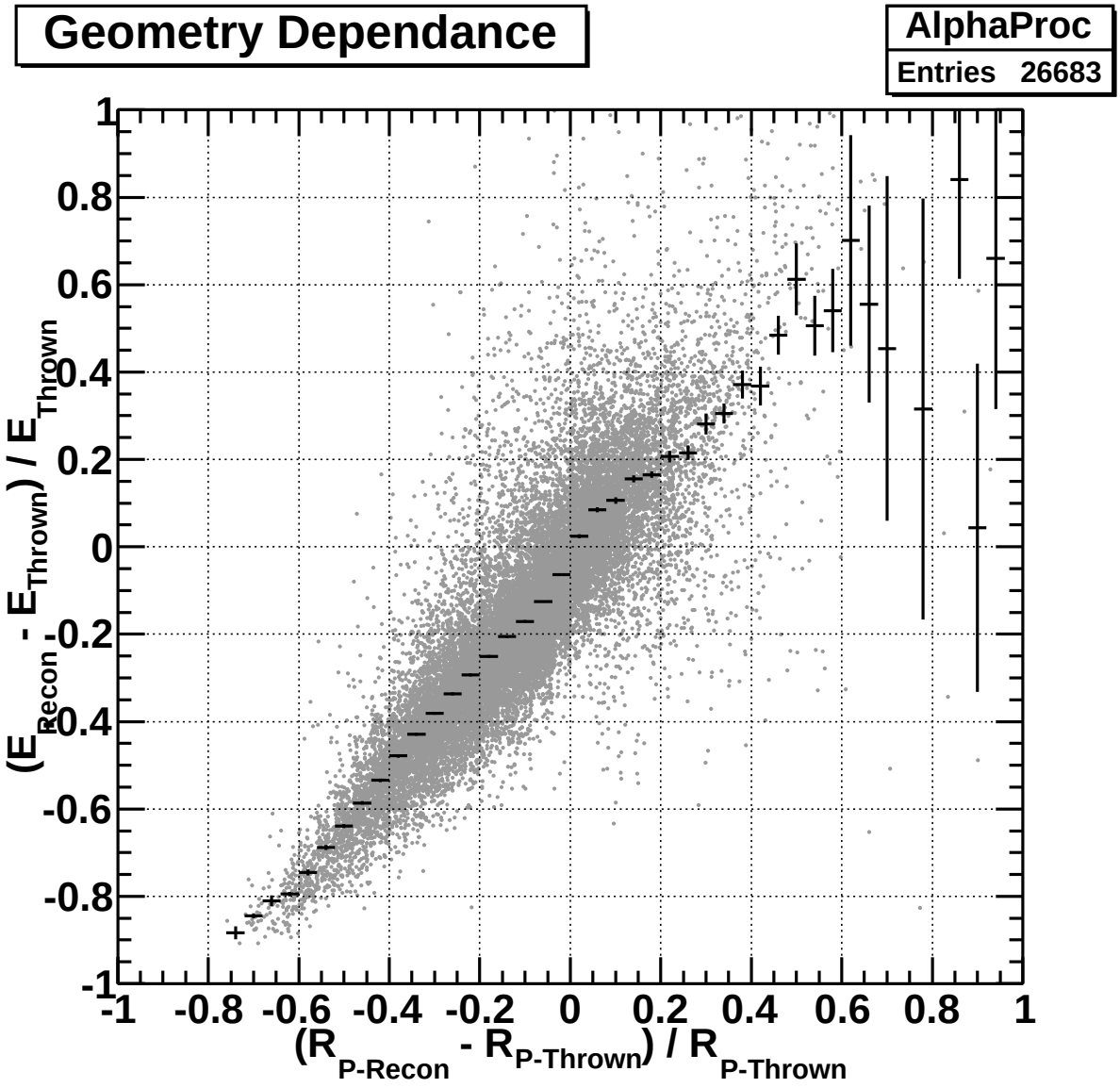

Figure 9.11: Monte Carlo error in energy compared to the error in R_P for the AlphaProc processing code.

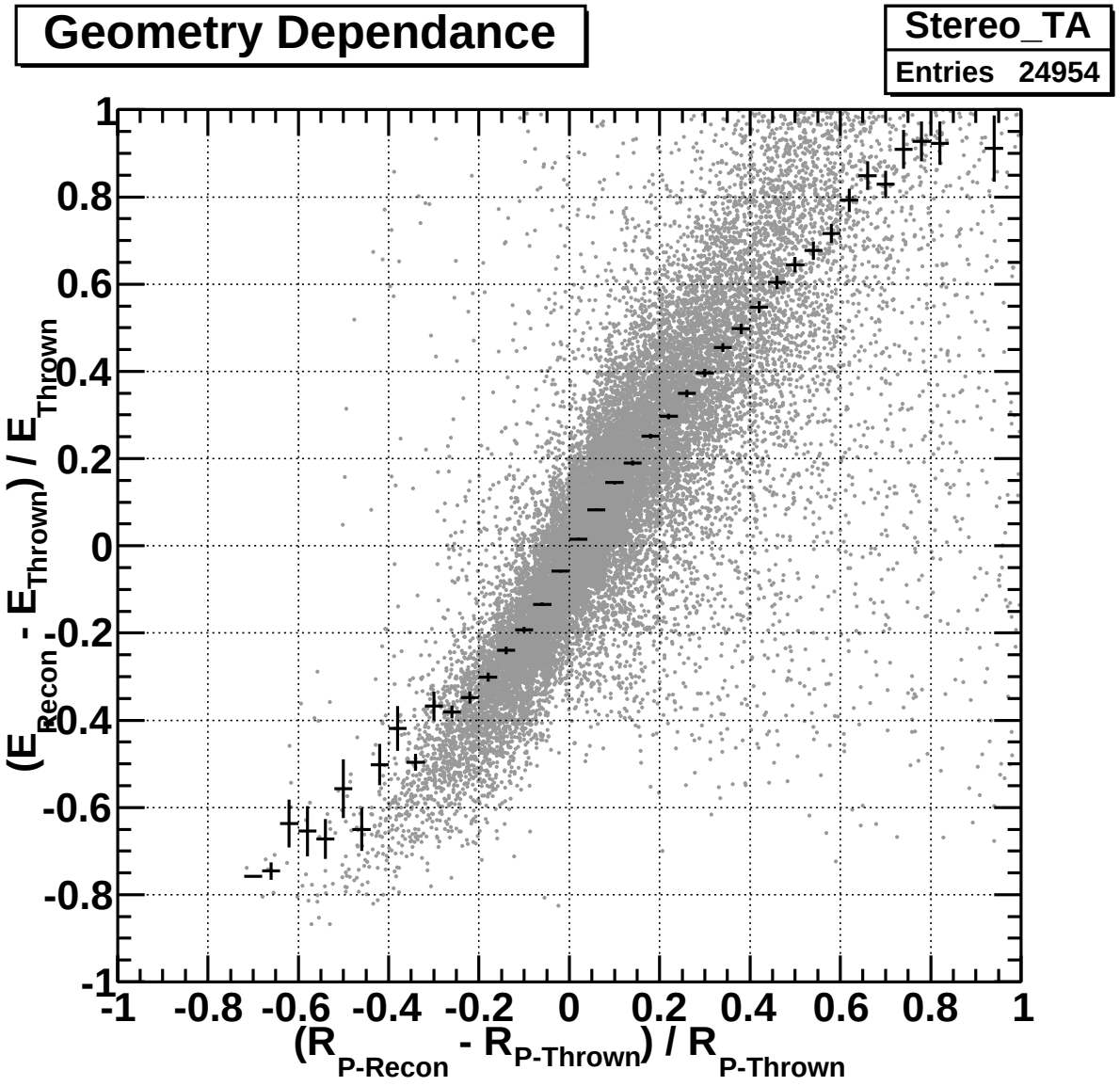

Figure 9.12: Monte Carlo error in energy compared to the error in R_P for the stereo_TA processing code.

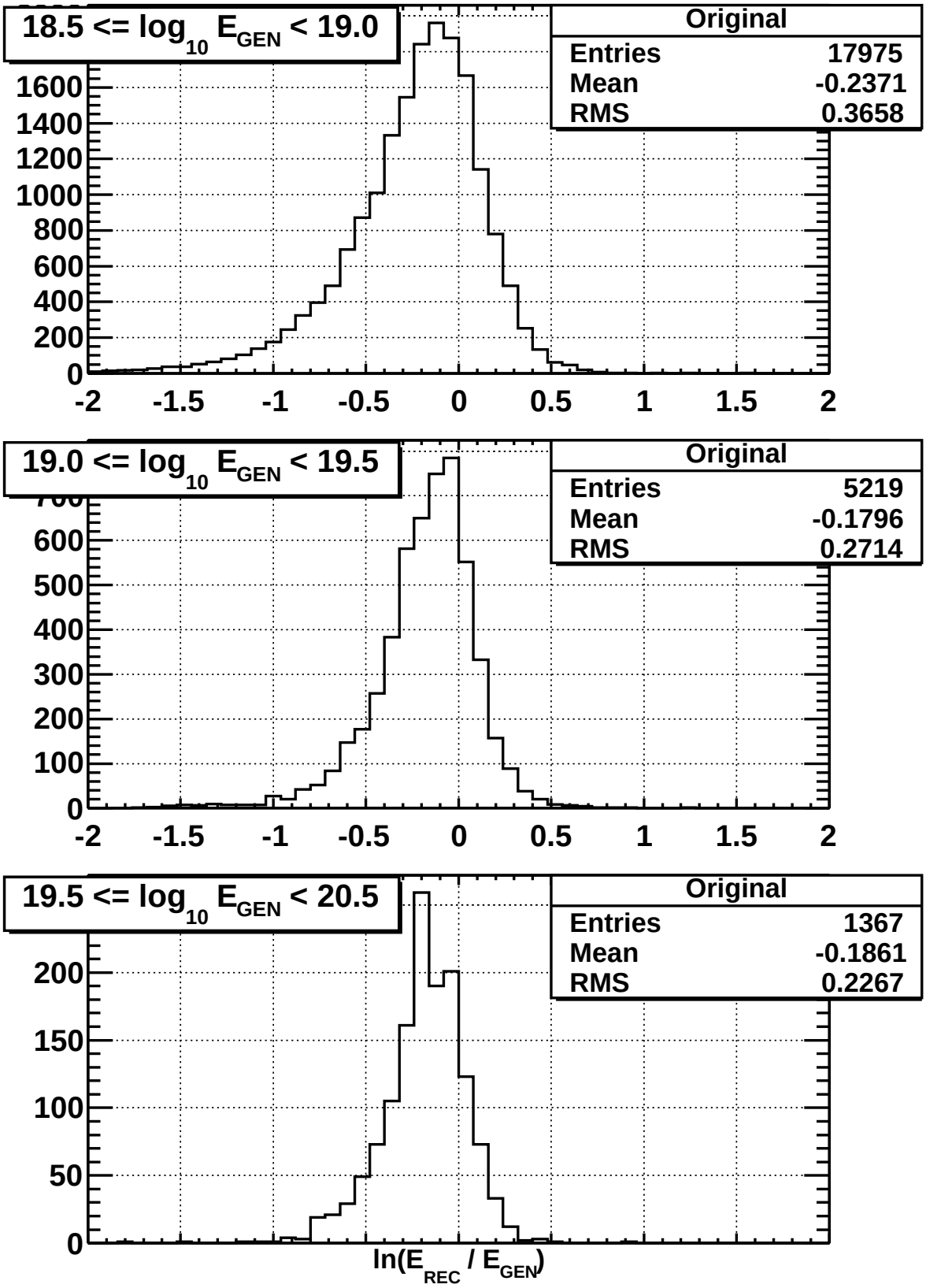

Figure 9.13: Monte Carlo energy resolution for the original processing code over different energy ranges.

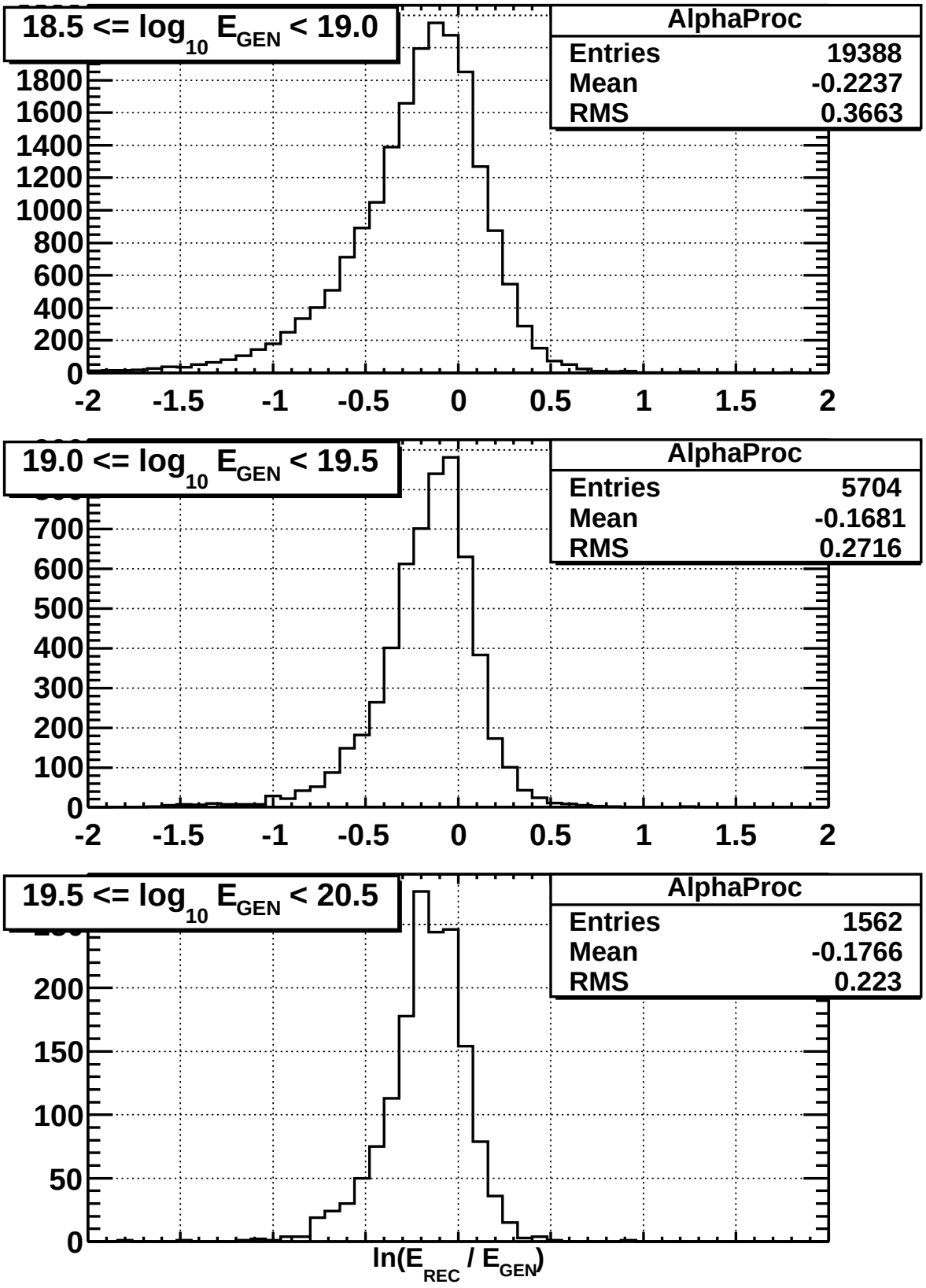

Figure 9.14: Monte Carlo energy resolution for the AlphaProc processing code over different energy ranges.

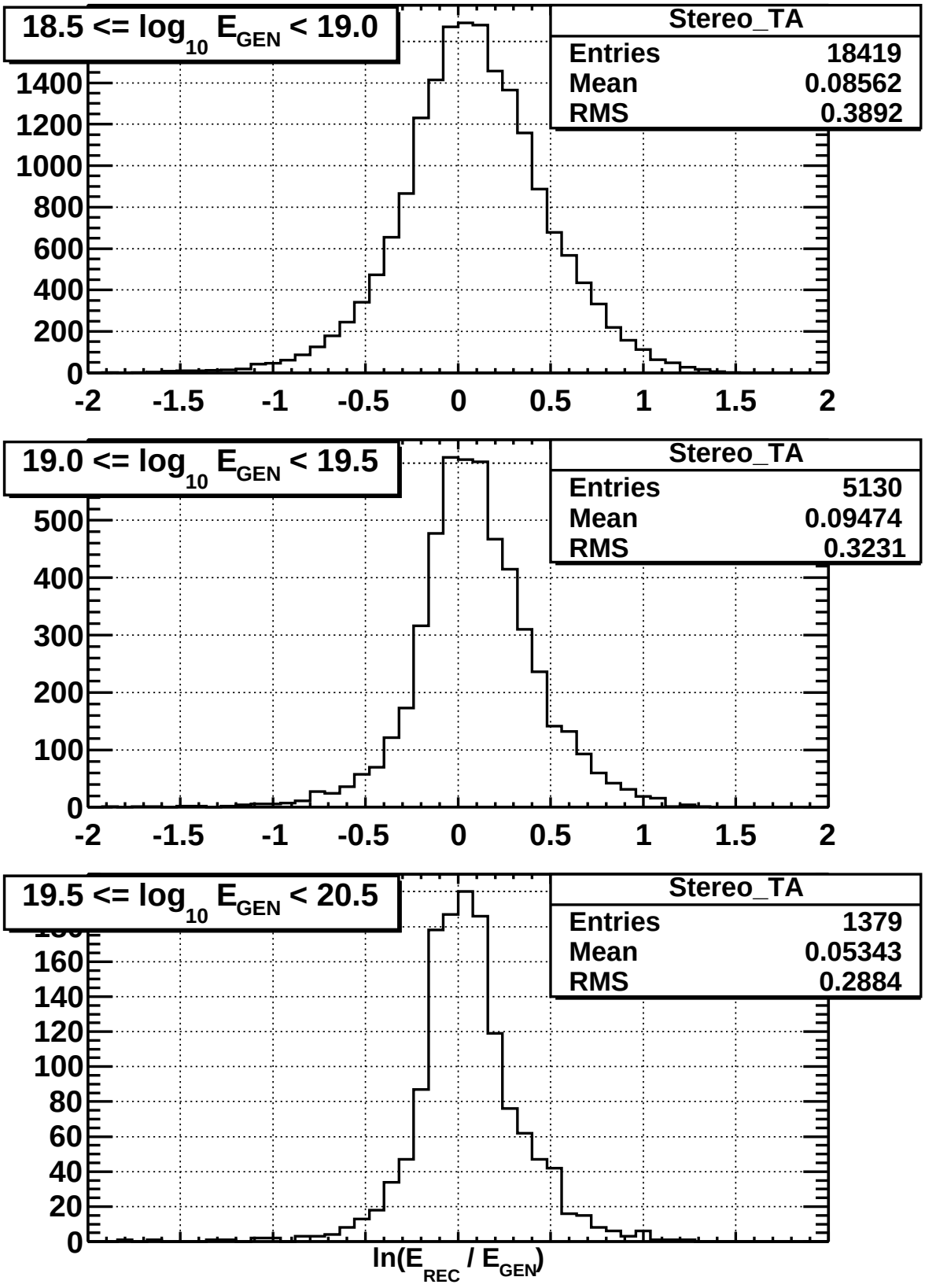

Figure 9.15: Monte Carlo energy resolution for the stereo_TA processing code over different energy ranges.

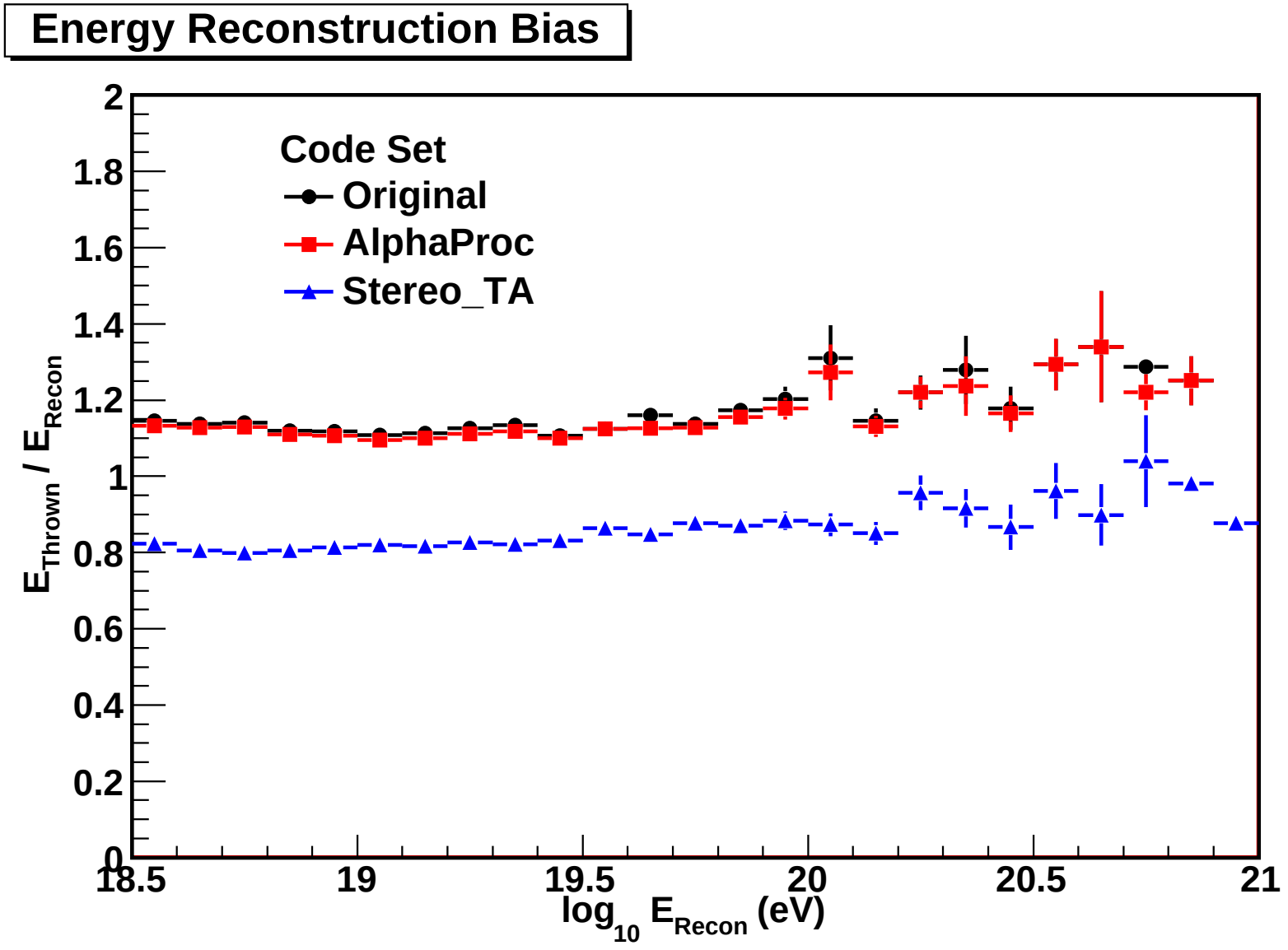

Figure 9.16: Monte Carlo reconstructed energy bias for each processing code.

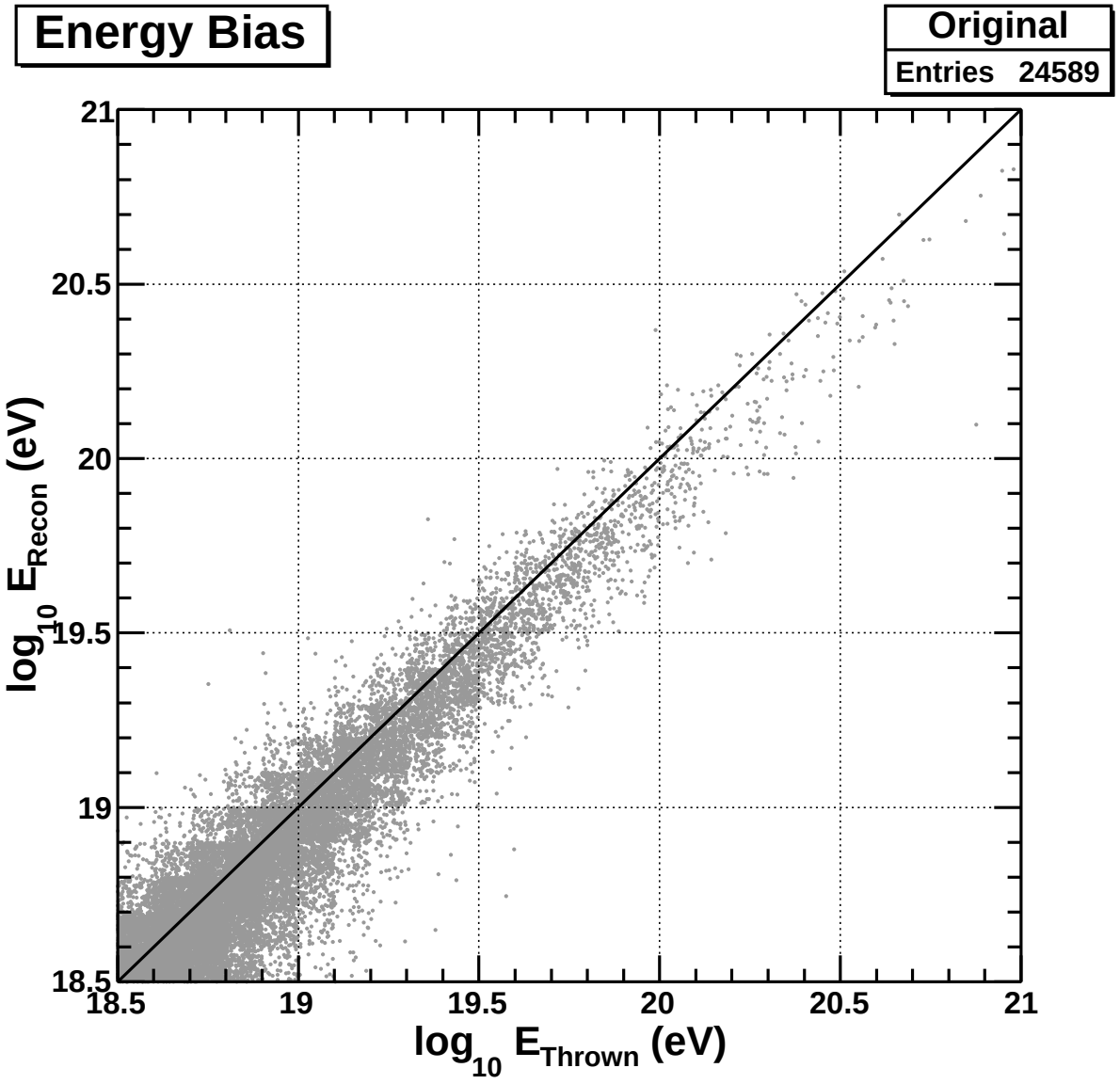

Figure 9.17: Monte Carlo reconstructed energy versus thrown energy for the original processing code.

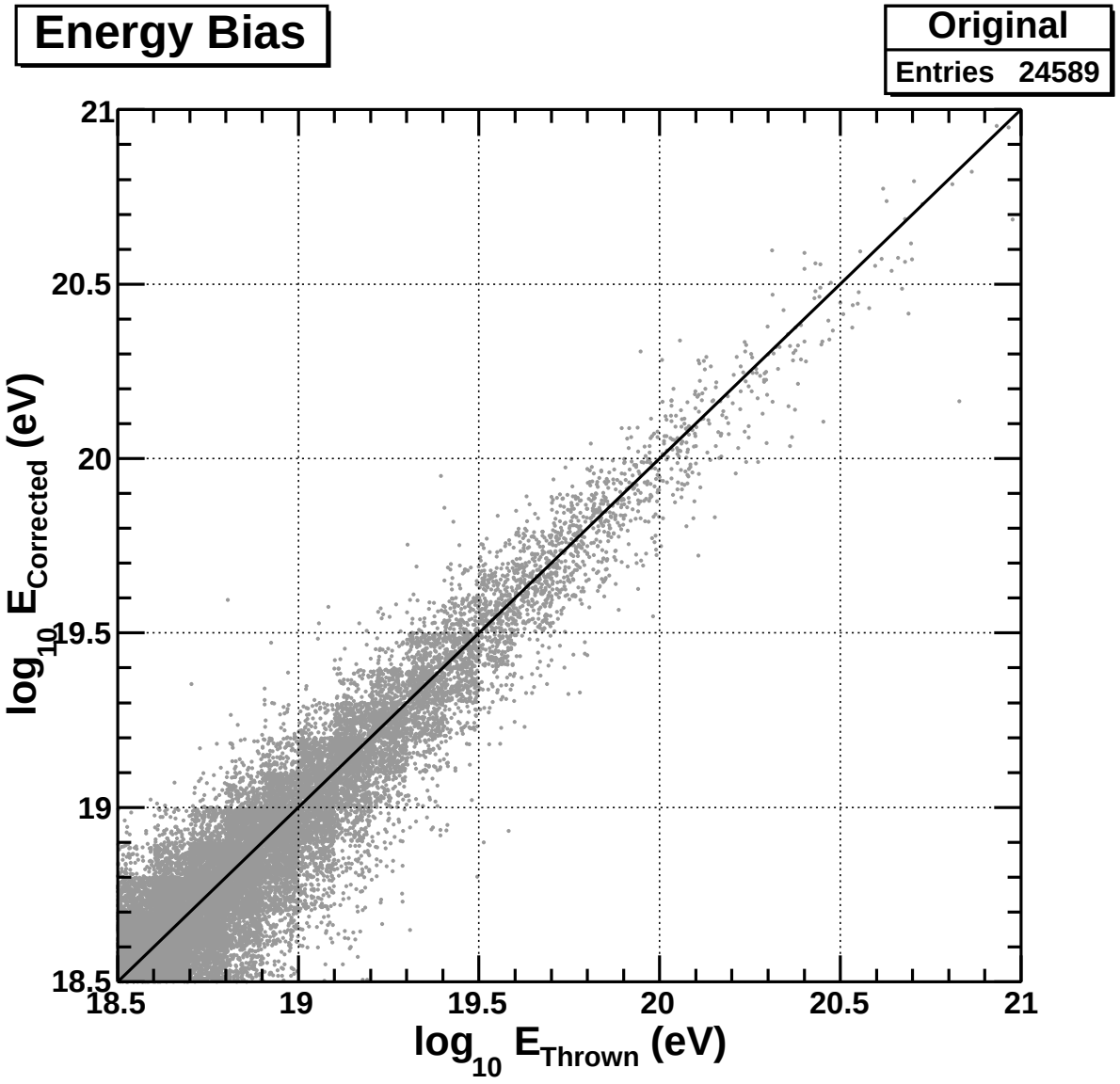

Figure 9.18: Monte Carlo corrected energy versus thrown energy for the original processing code.

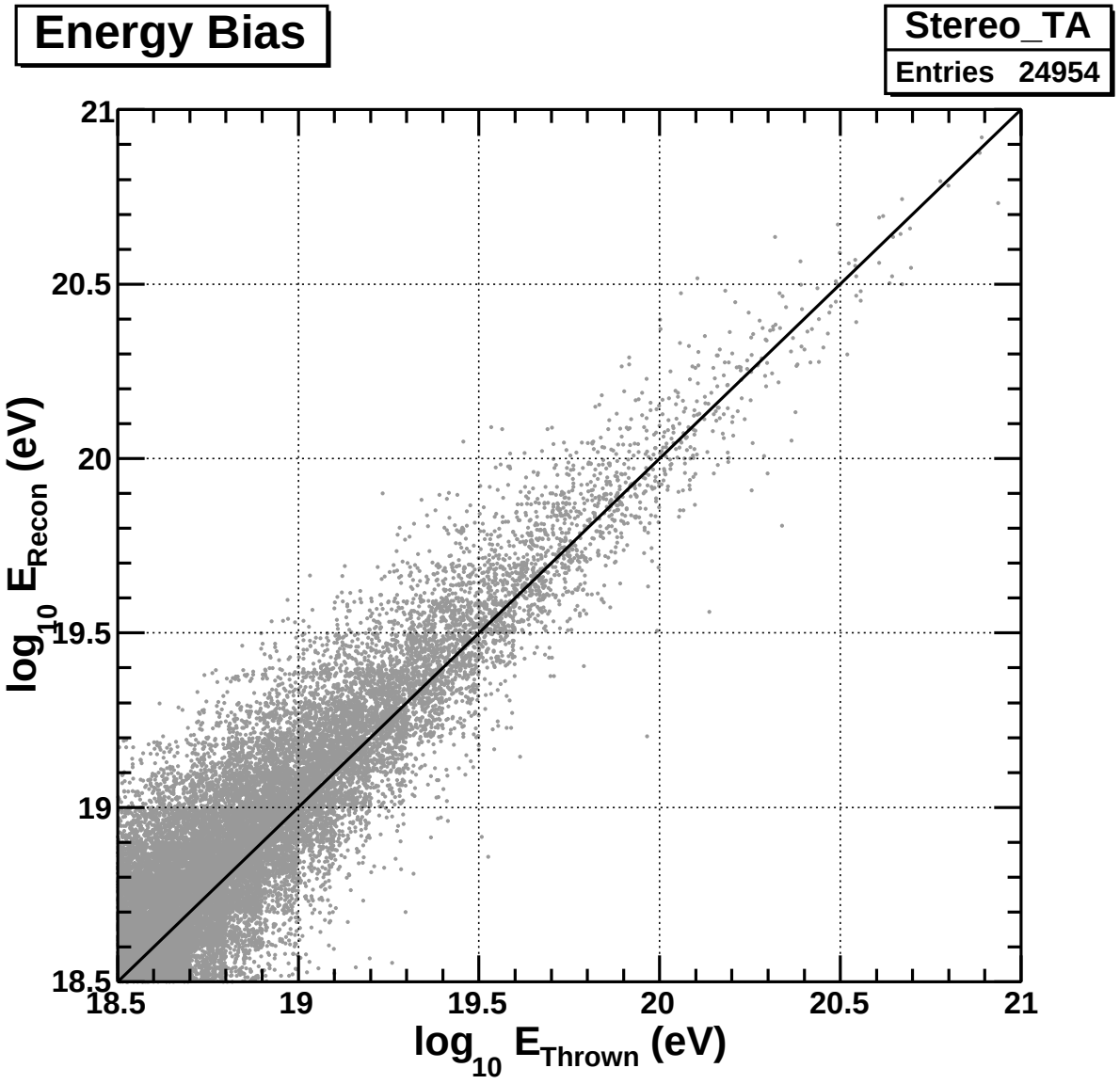

Figure 9.19: Monte Carlo reconstructed energy versus thrown energy for the AlphaProc processing code.

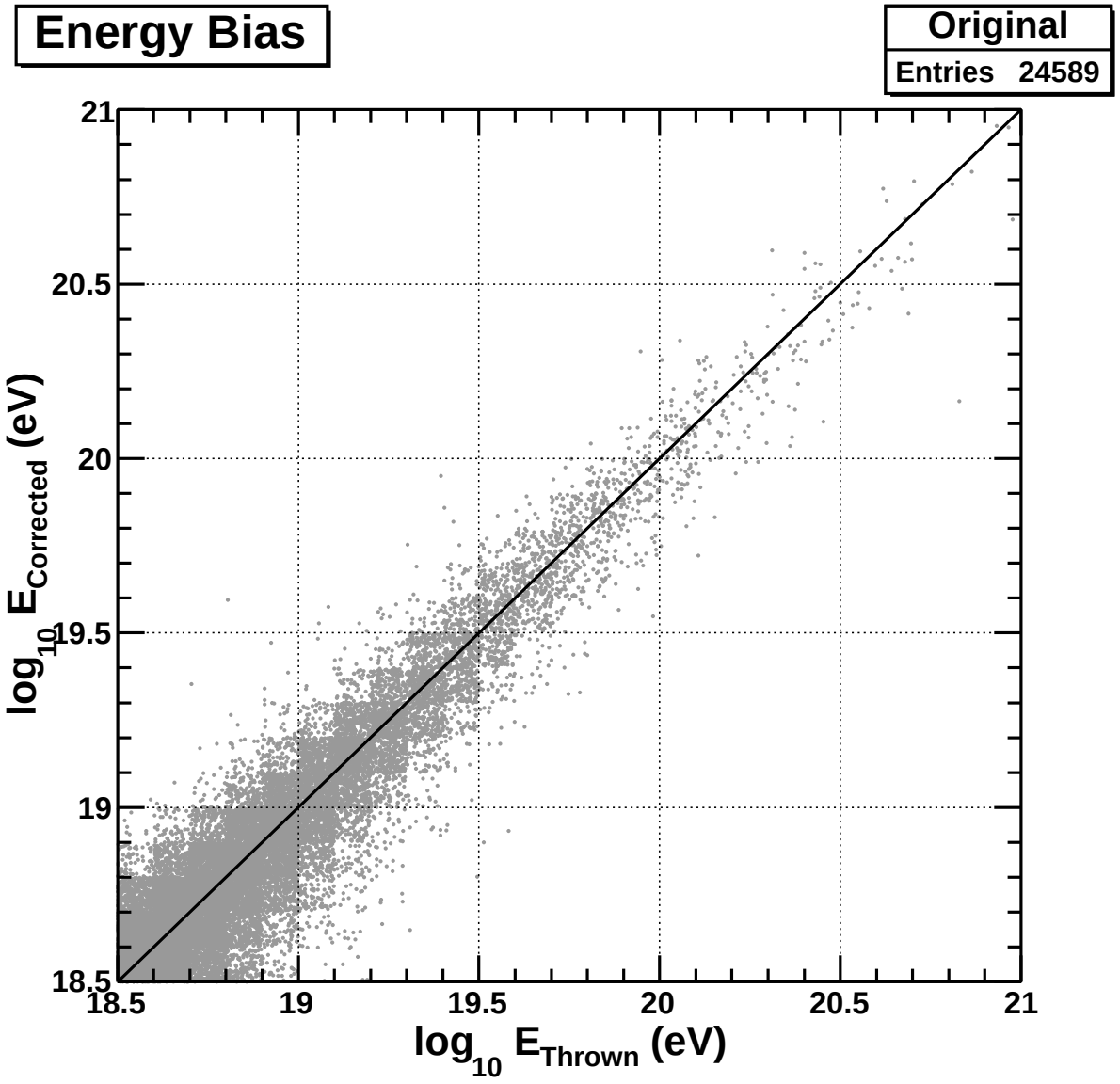

Figure 9.20: Monte Carlo corrected energy versus thrown energy for the AlphaProc processing code.

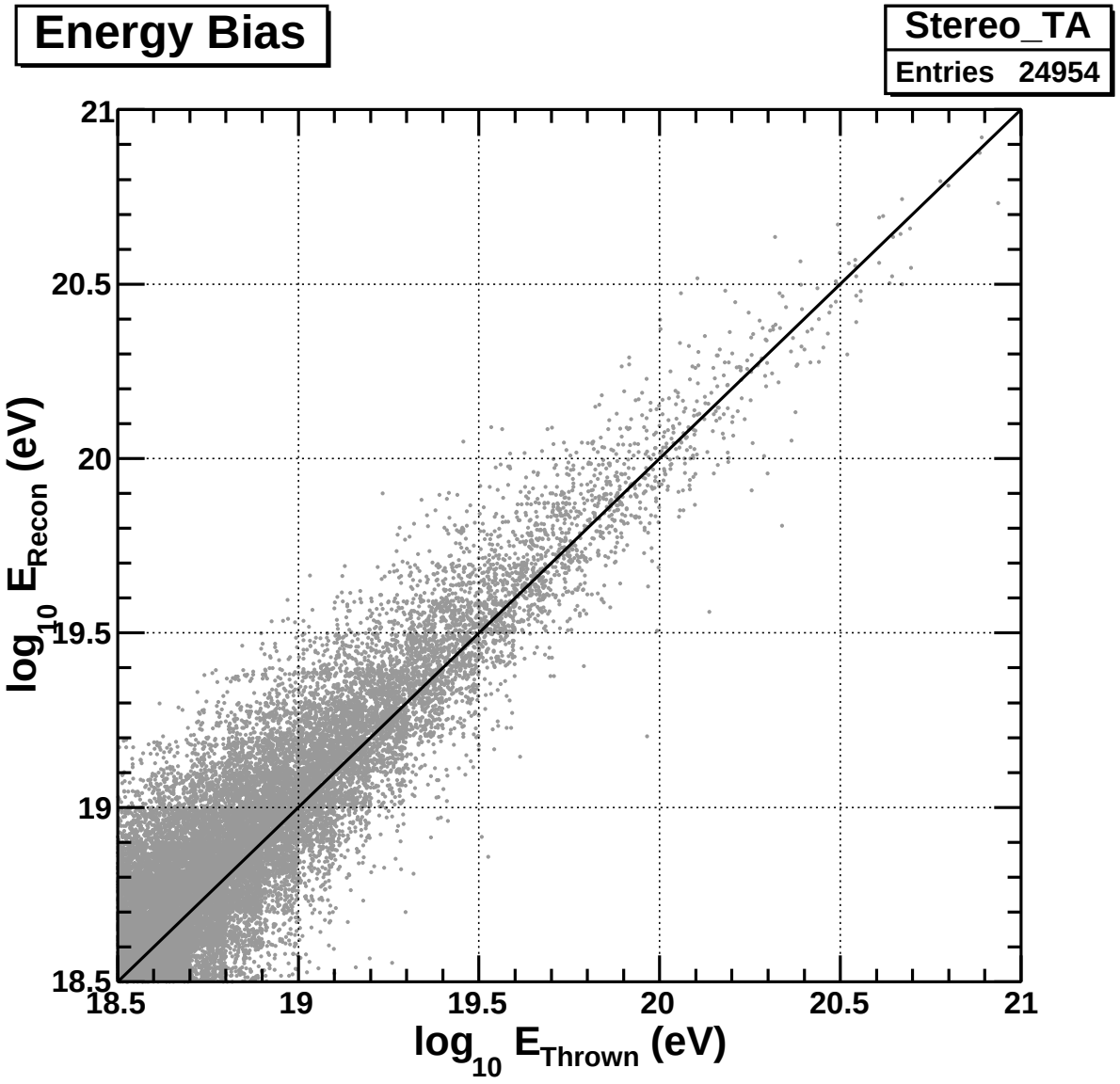

Figure 9.21: Monte Carlo reconstructed energy versus thrown energy for the stereo_TA processing code.

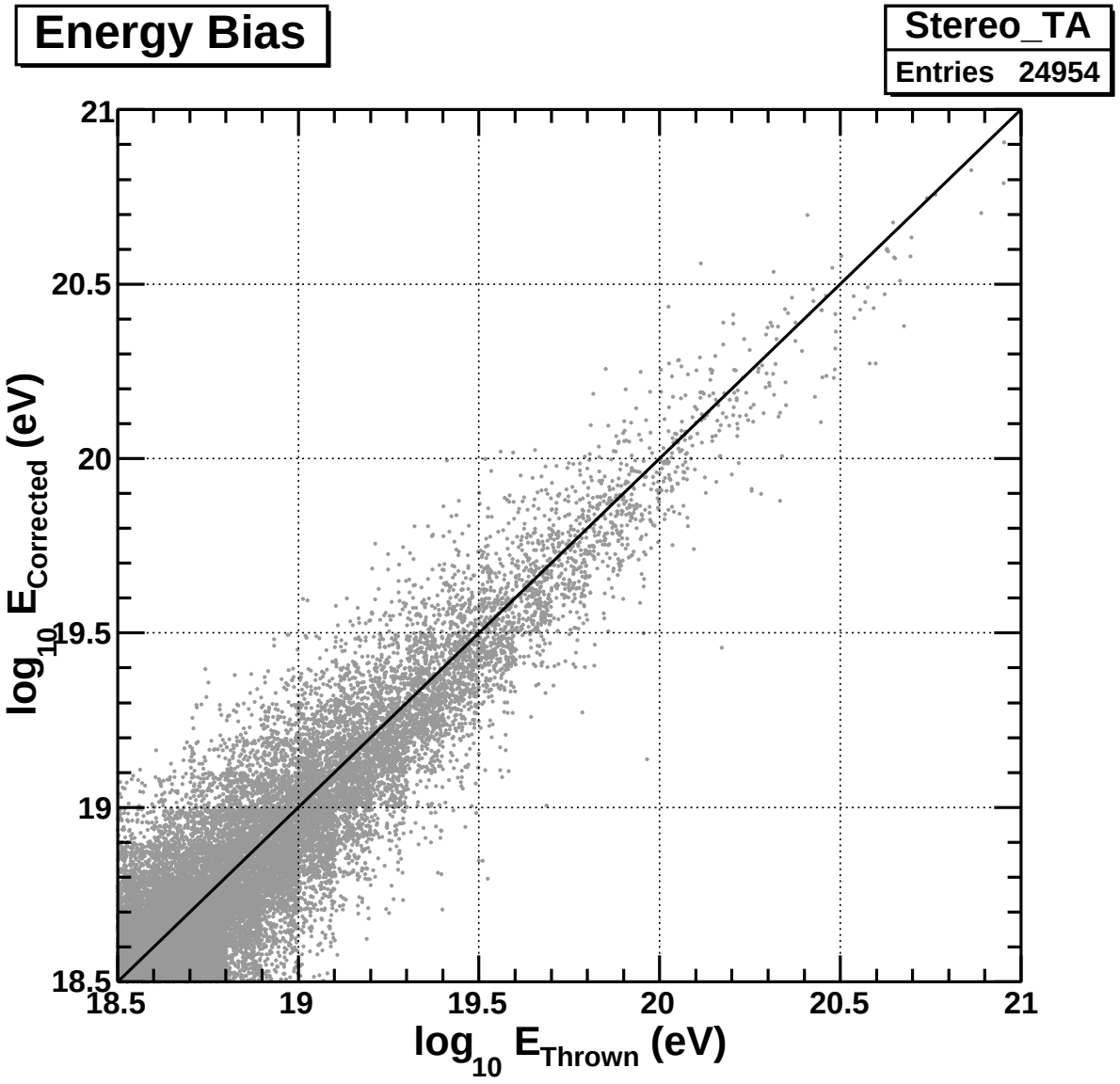

Figure 9.22: Monte Carlo corrected energy versus thrown energy for the stereo_TA processing code.

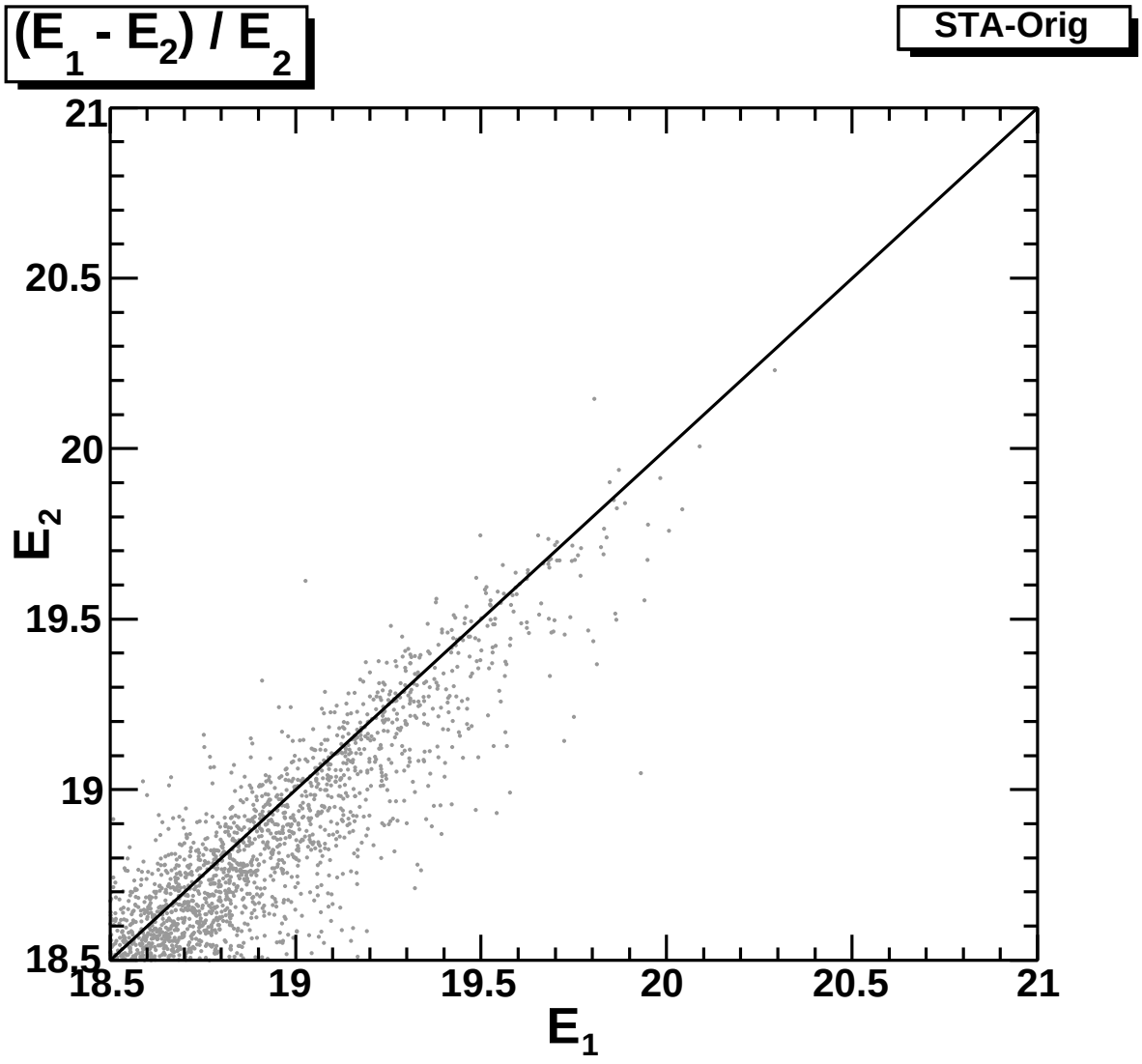

Figure 9.23: Data reconstructed energy comparison between the stereo_TA (E1) and original (E2) processing code sets.

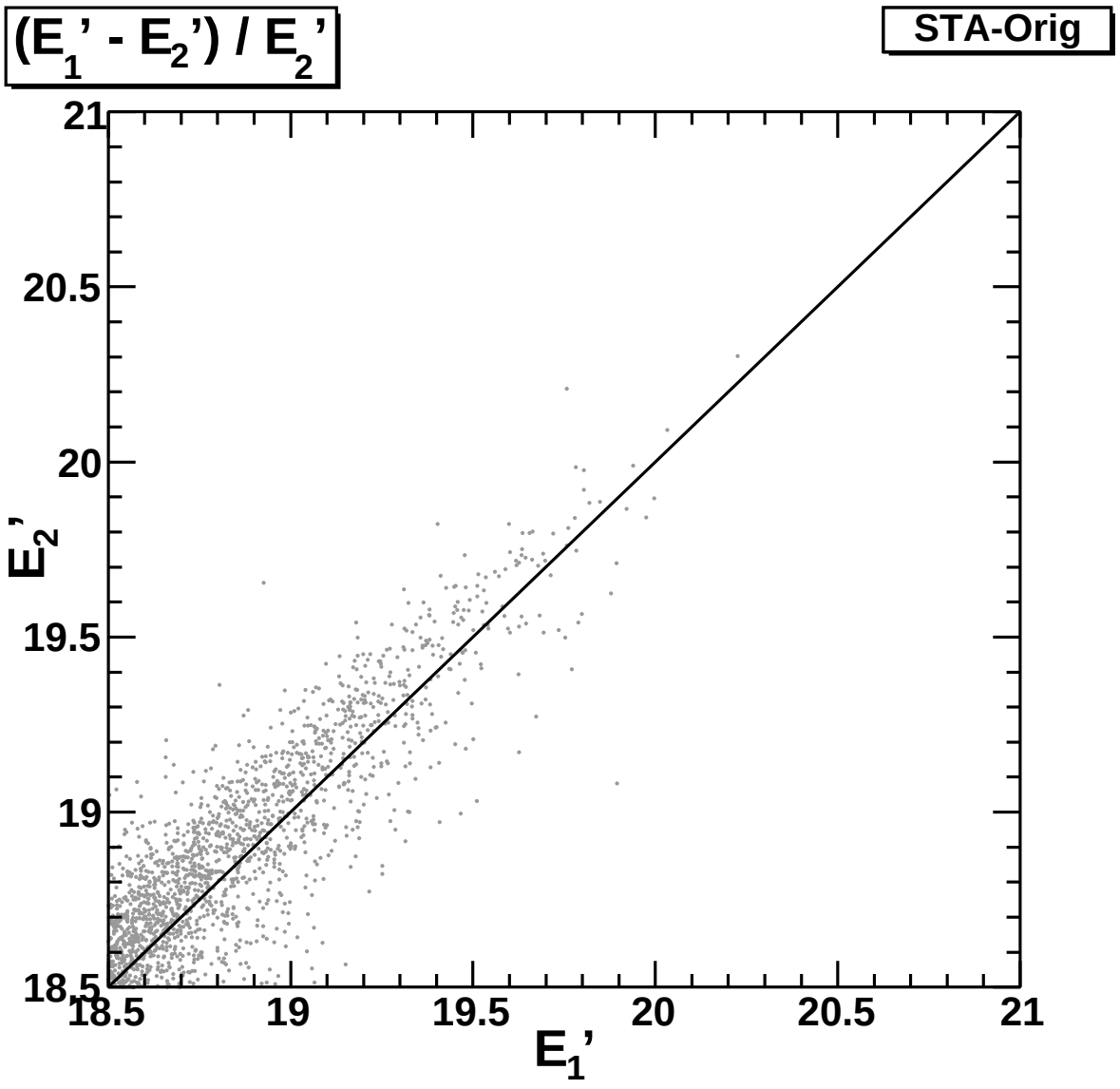

Figure 9.24: Data corrected energy comparison between the stereo_TA (E1') and original (E2') processing code sets.

Table 9.3: Final numbers of events for each tenth-decade energy bin. The two lowest ranges are adjusted for R_{P-max} differences.

Energy Range (log_{10} eV)	Thrown	Original	AlphaProc	Stereo_TA
18.45 - 18.55	283640	6174	6587	6820
18.55 - 18.65	169060	4762	5140	5266
18.65 - 18.75	105908	3807	4090	3839
18.75 - 18.85	70040	2930	3119	2946
18.85 - 18.95	45627	2302	2490	2203
18.95 - 19.05	30267	1805	1939	1808
19.05 - 19.15	19792	1391	1562	1337
19.15 - 19.25	13258	1178	1253	1075
19.25 - 19.35	8564	772	864	797
19.35 - 19.45	5658	656	725	614
19.45 - 19.55	3670	419	475	463
19.55 - 19.65	2428	365	393	347
19.65 - 19.75	1641	240	295	215
19.75 - 19.85	1087	206	227	204
19.85 - 19.95	732	123	138	133
19.95 - 20.05	472	84	101	95
20.05 - 20.15	300	59	70	52
20.15 - 20.25	185	46	50	42
20.25 - 20.35	137	26	30	29
20.35 - 20.45	84	13	19	19
20.45 - 20.55	58	18	19	14
20.55 - 20.65	37	8	8	7
20.65 - 20.75	24	6	6	4
20.75 - 20.85	13	1	3	1
20.85 - 20.95	11	1	0	1
20.95 - 21.05	7	2	2	1

such as the number of photo-electrons per good tube, R_P, ψ, θ, ϕ (see Appendices A, B, C, and D). But for the spectrum, the most important parameter is a comparison in the energy distribution of events to ensure that spill-down and resolution smearing are simulated as accurately as possible (see Figures 9.25, 9.26, 9.27, and 9.28). For all figures, the data points are represented with markers and error bars, and the Monte Carlo is given as a solid line histogram. As can be seen, there is a consistency between the data and the Monte Carlo for all energy bins quoted in the spectrum. One point of note is that, even before calculating a flux spectrum, the GZK suppression [39] [105] is quite obvious in each of these plots with a lack of data points above $10^{19.8}$ eV compared to the smooth reduction in the Monte Carlo distribution.

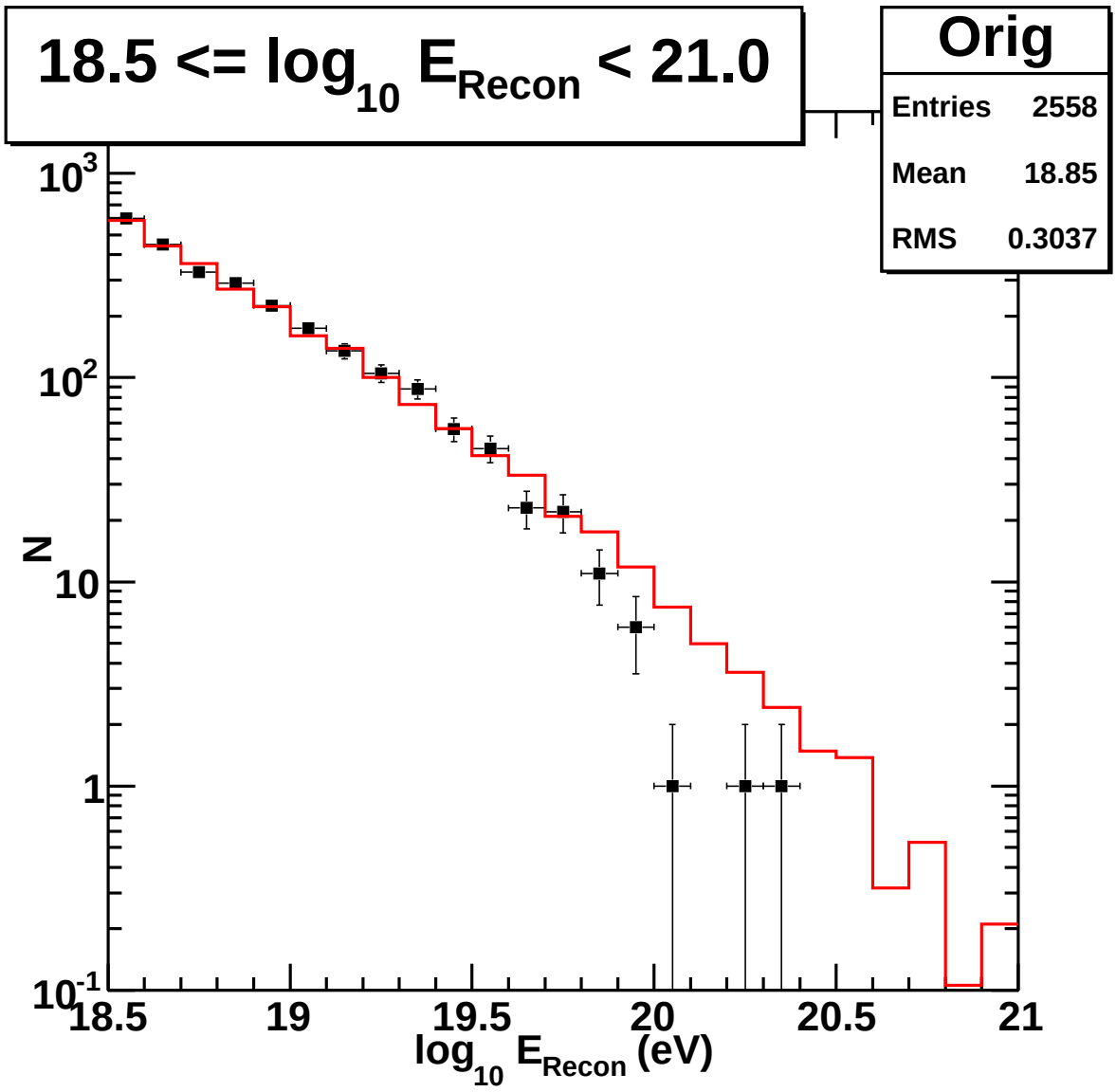

Figure 9.25: Data-Monte Carlo comparison of events determined in the original processing code set within the spectrum energy range.

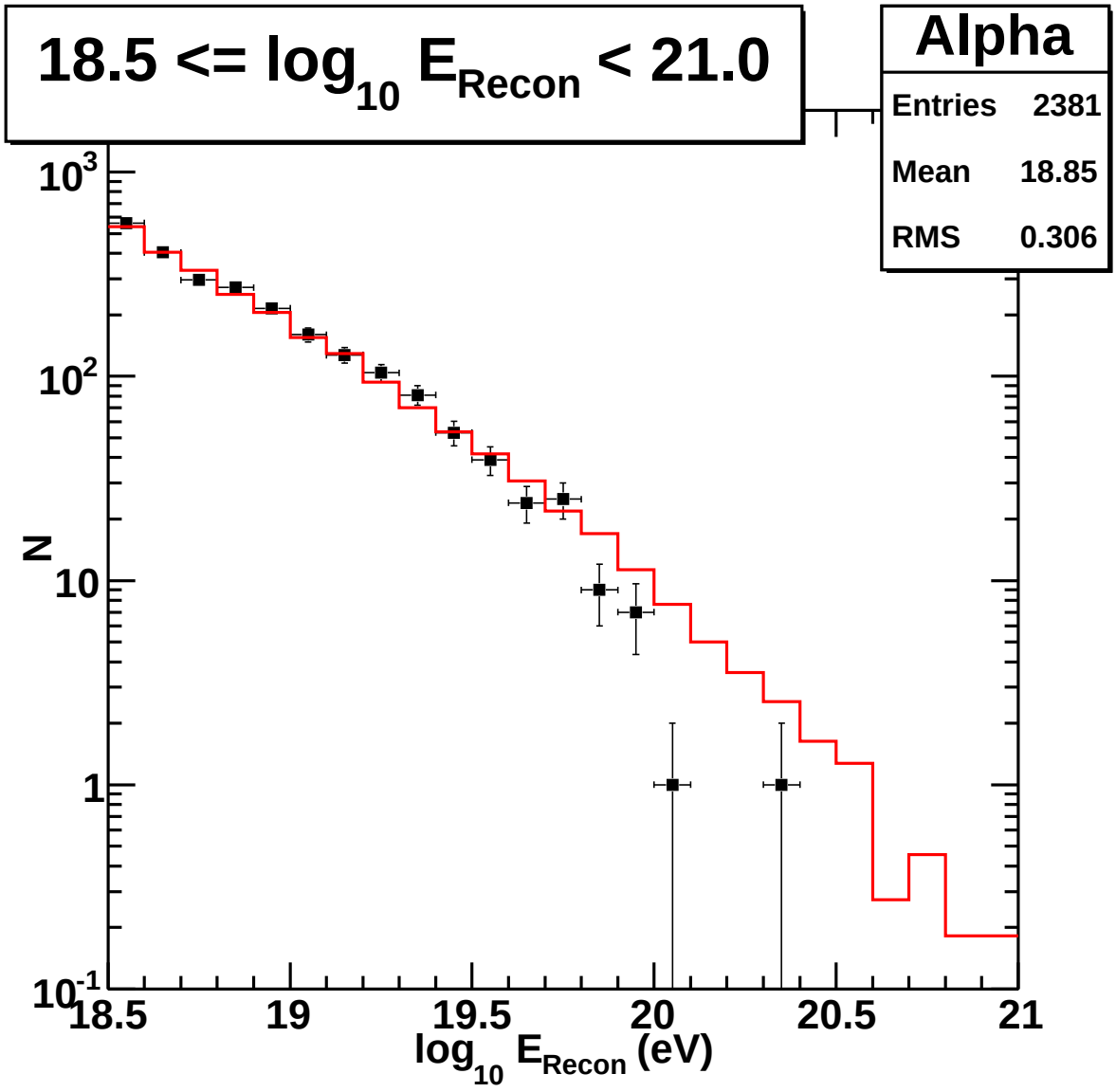

Figure 9.26: Data-Monte Carlo comparison of events determined in the AlphaProc processing code set within the spectrum energy range.

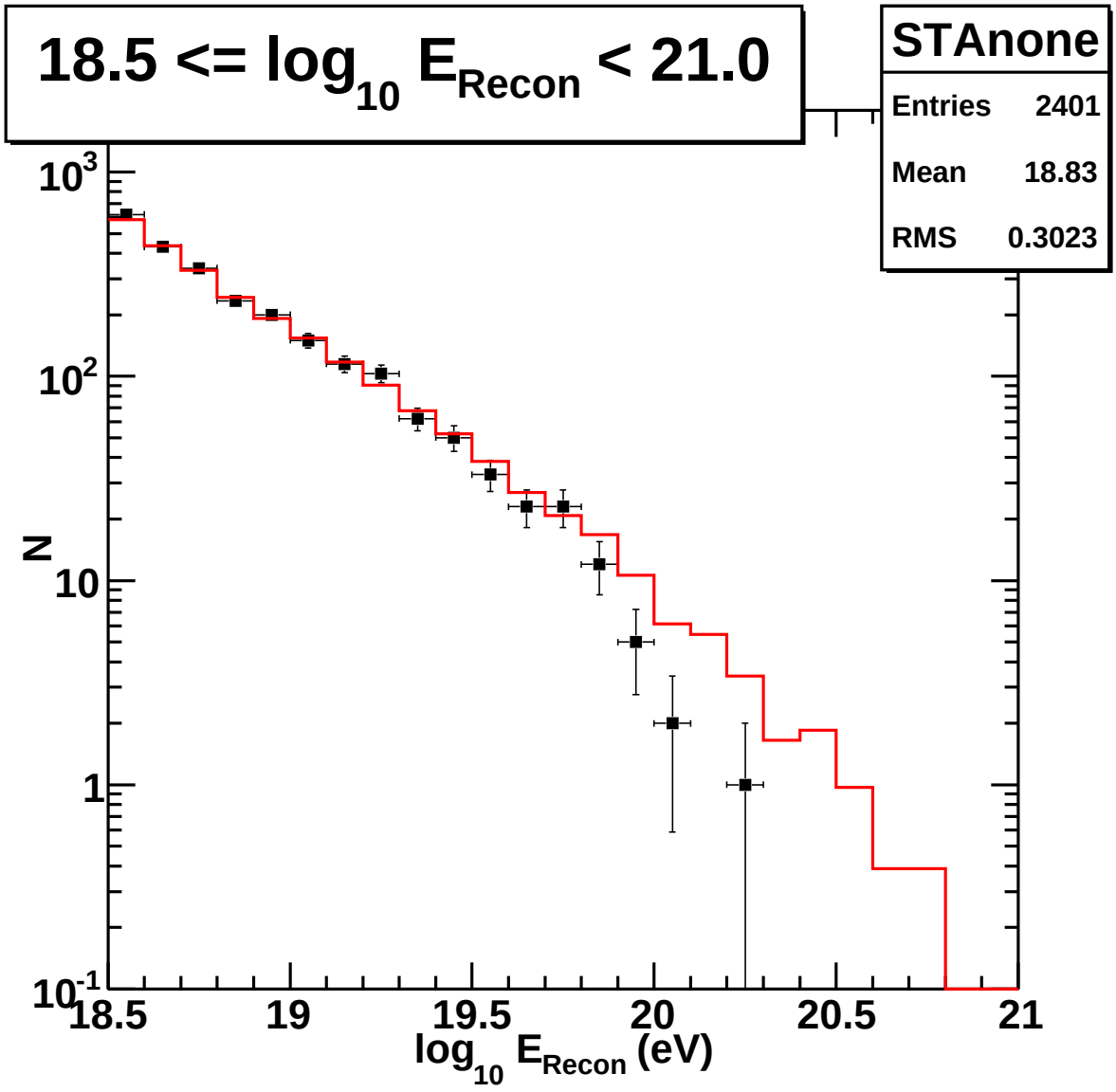

Figure 9.27: Data-Monte Carlo comparison of events determined using the stereo_TA processing code set without databases for the spectrum energy range.

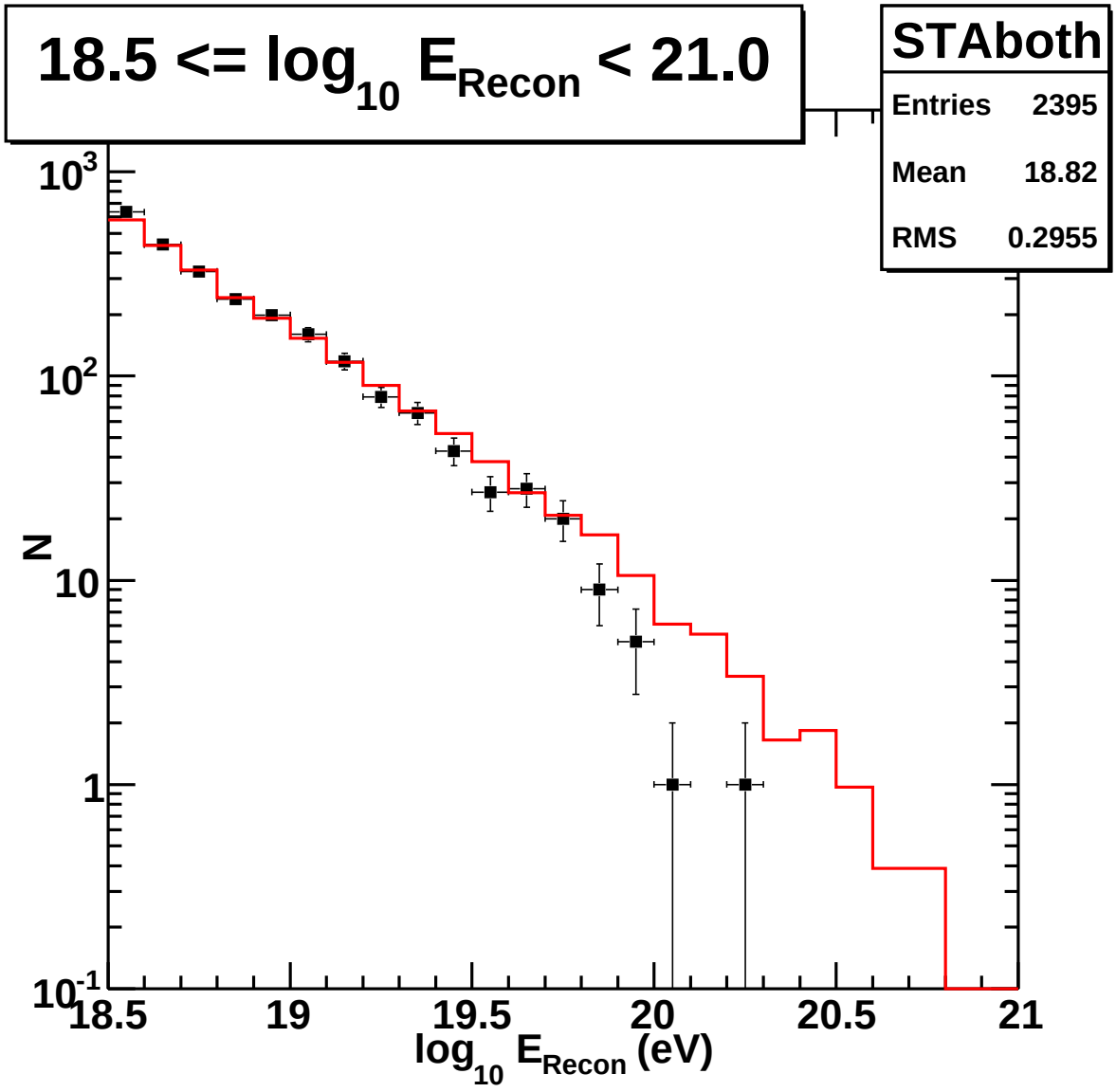

Figure 9.28: Data-Monte Carlo comparisons of events determined using the stereo_TA processing code set with calibration and good atmospheric databases for the spectrum energy range.

CHAPTER 10

FINAL HIRES-1 MONOCULAR SPECTRUM

The previous HiRes-1 monocular spectrum, published in 2008 [3], used the original processing routines (see section 7.1). The data were reprocessed with updated calibration values and a new spectrum has been obtained using the original processing code set with minor bug fixes that had minimal impact on the results. The details in this chapter will also describe the spectrum using the stereo_TA processing code set for a direct comparison to the Middle Drum spectrum. We also present a spectrum made using the AlphaProc results for a justification of the routines used in that code set for the simultaneous shower search. Finally, since the 2008 publication used a standard atmosphere (see section 4.2), a study was made to determine the difference in the energy spectrum if a calibration database and an atmospheric database were applied.

10.1 Measuring the Exposure

If it was possible to watch the entire universe, we would be able to easily count the number of high-energy cosmic rays that exist and to trace them back to where they were accelerated. However, we are limited to only those events that are observable by the detectors we have here on Earth. These can be measured only within the volume that the detector is observing and with the time period that we let the detector perform these observations. The combination of these is known as the exposure of the experiment.

10.1.1 On-time

As described in Chapter 5, the HiRes-1 detector collected data between May, 1997 and May, 2006. During this period, data collection was restricted theoretically to moonless nights. In practice, we only opened the garage doors on those nights where there was neither actual occurrence nor threat of precipitation. Of the data collected, we further

selected only those time intervals during which there was no lingering cloud cover, based on operator observation weather codes (see Table 5.2).

Over the course of the experiment, an integrated on-time (see Figure 10.1) is calculated from the amount of time that each telescope was operating. The HiRes-1 energy spectrum accounts for 9.74×10^4 telescope-hours. The actual on-time used in the exposure calculation is approximated by dividing by the number of telescope. This approximation is accurate to better than 1% since the appropriate telescope efficiencies are all $> 90\%$ (see Table 10.1). Therefore, the on-time used in this analysis was 4.868×10^3 hours (1.7525×10^7 seconds).

10.1.2 Aperture

As can be seen in Figure 5.3, the areas (and solid angle) that a detector can view are dependent on the energy of the particles. The more energetic the primary cosmic-ray, the more energy is deposited into the atmosphere and observed through fluorescence light. The more light available, the farther away a shower can be seen. To calculate the effective area $\times$ solid-angle (i.e., aperture) that can be viewed at each energy, Monte Carlo simulations are used.

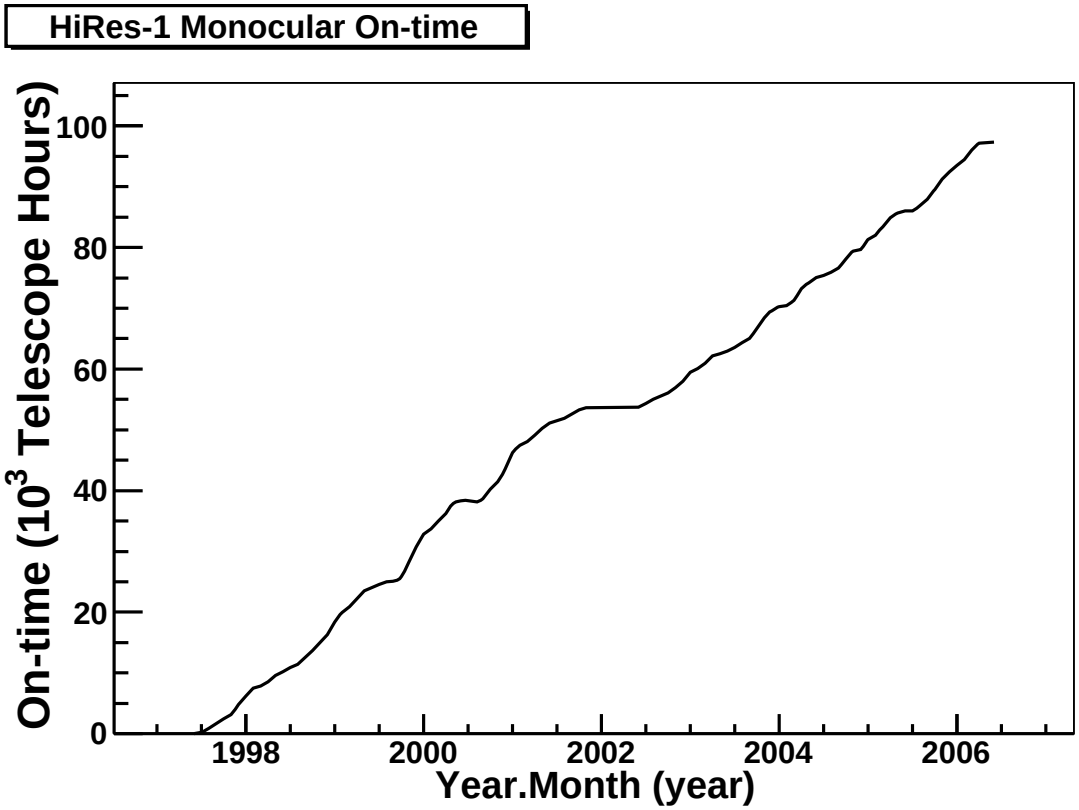

Figure 10.1: Integrated on-time of HiRes-1.

Table 10.1: The average telescope efficiencies over the entire experiment's lifetime.

Mirror	Eff. (%)	Mirror	Eff. (%)
01	0.972648	12	0.952637
02	0.959641	13	0.975216
03	0.951768	14	0.973233
04	0.968784	15	0.948802
05	0.961832	16	0.920566
06	0.962882	17	0.874359
07	0.953664	18	0
08	0.967672	19	0.973301
09	0.972826	20	0.950549
10	0.973147	21	0.957179
11	0.965702	22	0.969021

There are two ways to determine the effective aperture of the detector. The first way to do this is to produce a set of monoenergetic showers at each half-decade of energy (10^{17} eV, $10^{17.5}$ eV, etc.) and to fit this to a curve to determine the intermediate energies. The second way to do this is to simulate showers using a spectral index energy continuum, as described in Chapter 9. Values taken from this spectrum then give the number of events for each energy bin. HiRes found that the spectral index changes around $10^{18.65}$ eV [3] from -3.25 below this energy to -2.81 above (until the GZK suppression begins at $\sim 10^{19.8}$ eV). The spectral Monte Carlo described in chapter 9 is used for the aperture measurement and data-Monte Carlo comparisons found in this chapter.

Whereas the original HiRes spectrum was made using an exposure that included a mixed proton-iron composition measured by the Fly's Eye stereo data [21], the current study assumes 100% proton, consistent with published HiRes results [92]. In either case, the composition above $10^{18.5}$ eV is proton-dominated.

After the Monte Carlo data is produced, it must then be run through all of the same processing routines and analysis and quality cuts applied to the data. The HiRes-1 data used in this analysis was processed using three different code sets: the original program set (see section 7.1), the stereo_TA program set (see section 7.2), and the AlphaProc program set (see Chapter 8). The percentage of events kept at each pass can seen in Table 9.1.

Since we are throwing events with a known set of geometrical parameters, we can calculate our thrown aperture as

$$(A\Omega)_0(m^2 ster) = 2\pi^2 \left(R_{p\ max}^2 - R_{p\ min}^2\right) \times (1 - \cos\theta_{max}) \tag{10.1}$$

given in terms of area-solid angle (m^2 steradians), where R_p is the impact parameter (or distance of closest approach), and θ_{max} is the maximum zenith angle at which the

showers are thrown. The showers were thrown in a range of impact parameters which varied between $R_{P-min} = 100$ m and $R_{P-max} = 25$ km for the lower spectral range or $R_{P-max} = 50$ km for the upper spectral range. A maximum zenith angle of 80° is chosen since the downward shower selection effectively cuts the aperture at about $\theta \leq 75°$. The final number of events that pass all of the reconstruction steps and the final cuts for those that are best observed (see Table 9.3) is then used to calculate the detector aperture using the equation

$$A\Omega = (A\Omega)_0 \frac{N_{recon}(E_{MC-thrown})}{N_{thrown}(E_{MC-thrown})} \tag{10.2}$$

where $(A\Omega)_0$ is the maximum aperture available, and the ratio describes the true aperture of the detector for that energy bin. This essentially describes a complex multidimensional convolution integral of detector and analysis acceptance performed using the "rejection" Monte Carlo method. However, since only the reconstructed energy is known for the data we need to calculate the effective aperture which incorporates resolution smearing. Since there is "spill-down" from the $\sim E^{-3}$ spectral index, the first order corrected aperture is calculated by

$$A\Omega = (A\Omega)_0 \frac{N_{recon}(E_{MC-recon})}{N_{thrown}(E_{MC-thrown})} \tag{10.3}$$

where the numerator is dependent on the number of events reconstructed, rather than the thrown, within a given energy bin and the Monte Carlo events are generated with a spectrum similar to the measured flux spectrum.

If the showers are simulated using a continuum, the values obtained can be used as such for each bin, but significant fluctuations can arise in the highest energies where few events are actually produced. The shape of the aperture can then be compared using the smooth function

$$\log(A\Omega) = b \times \left(1 - e^{\frac{c-\log(E)}{d}}\right) \tag{10.4}$$

where this fit is made for the $\log_{10}$ of both the aperture, $(A\Omega)$, and the energy, E, for each energy bin (see Figures 10.2, 10.3, and 10.4). The fit parameters (b, c, and d) have no physical meaning; they just describe the rate of the increase of the aperture. As expected, the three different processing codes produce very similar apertures.

As can be seen, there is an obvious reduction in the aperture as the energy decreases. This is a known effect due to the fact that the less energetic the shower, the closer it must be to the detector for the ultraviolet light to reach the detector. In order to observe enough of the shower to reconstruct it, the detector must look at higher elevations, but HiRes-1 cannot observe enough of these close showers.

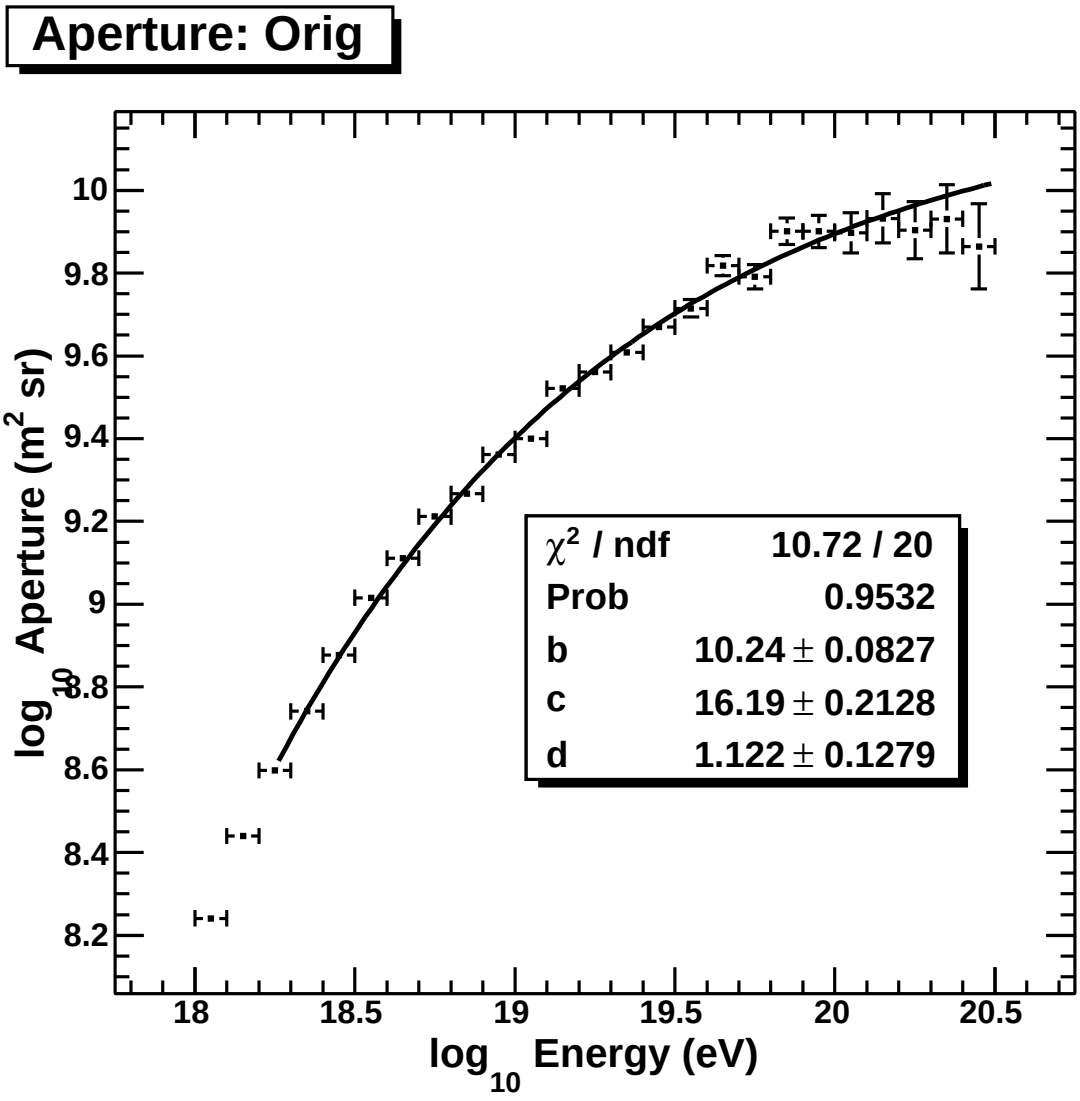

Figure 10.2: HiRes-1 aperture measured from events determined using the original processing routines.

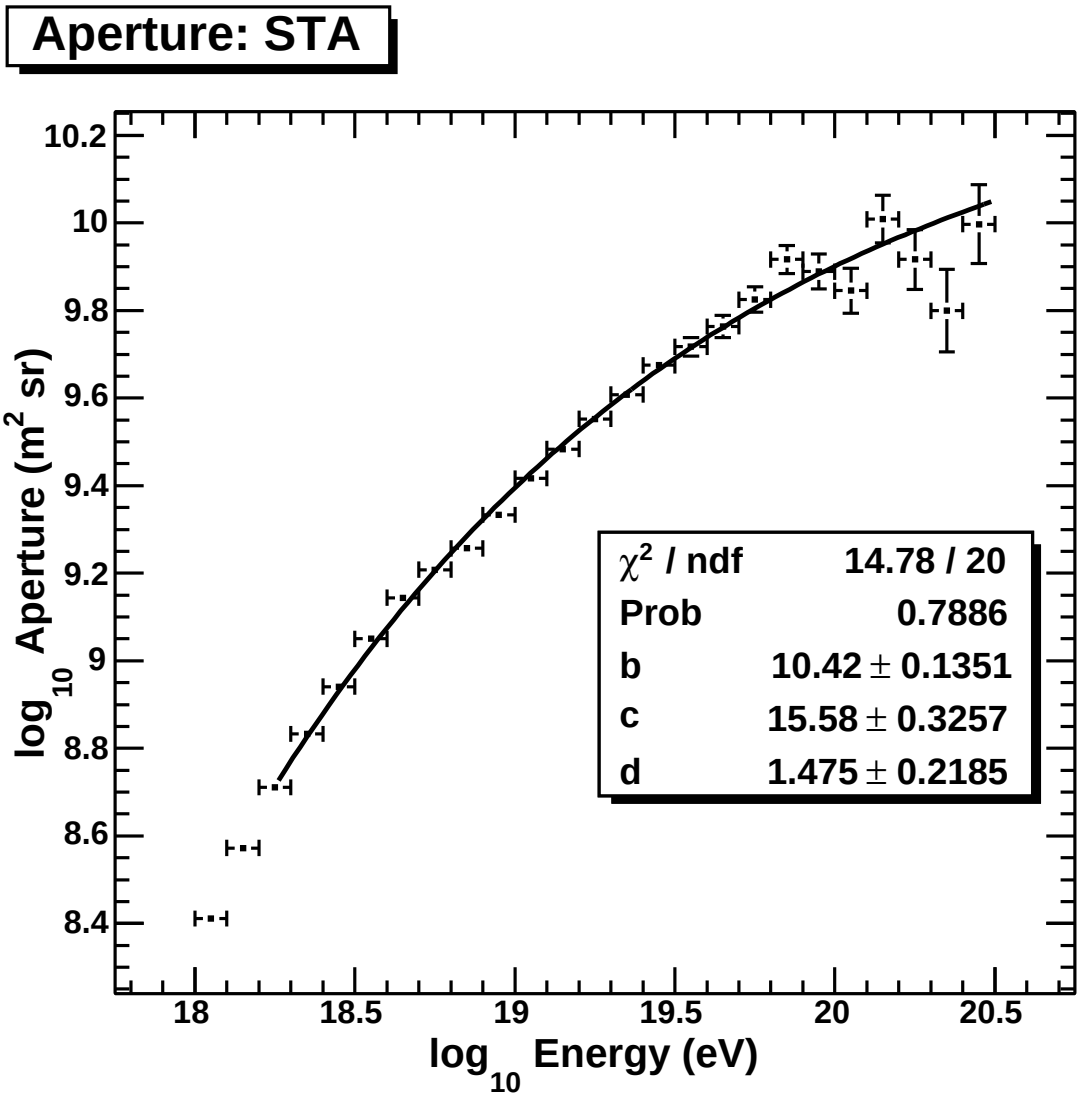

Figure 10.3: HiRes-1 aperture measured from events determined using the stereo_TA processing routines.

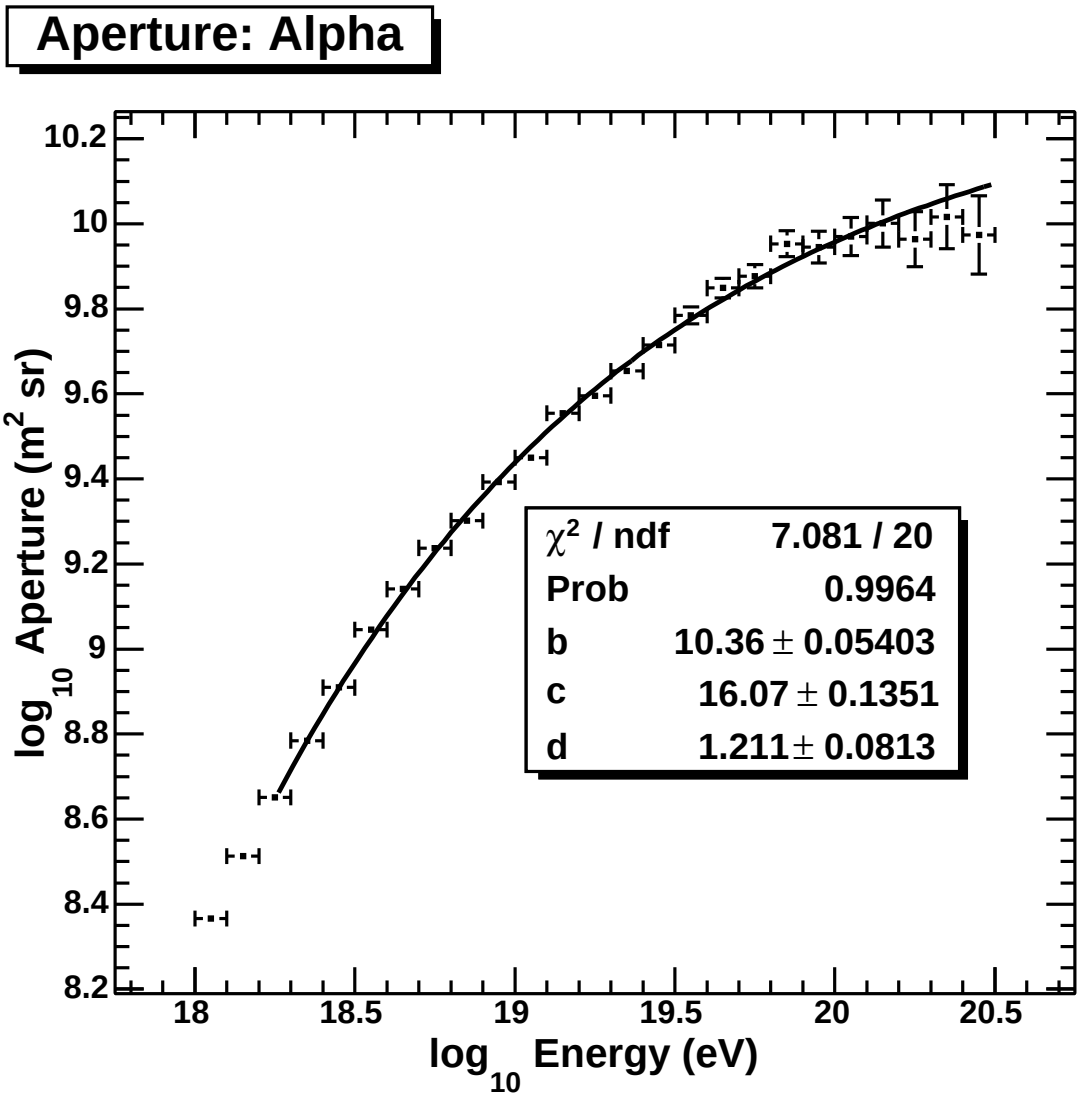

Figure 10.4: HiRes-1 aperture measured from events determined using the AlphaProc processing routines.

10.1.3 Data-Monte Carlo Exposure Calculation

In order to generate 10× the amount of exposure in the Monte Carlo simulation as compared to the actual data, we assume that they both have the same aperture, found by the process described in section 9.1. We know the amount of time the detector was running (see section 10.1.1). Then we must only find the Monte Carlo simulated on-time in order to determine the exposure ratio. To do this, equation 9.1 is rewritten to find Δt

$$\Delta t = \frac{N_i}{(A\Omega_0) \int_{E_1}^{E_2} J_i(E)\, dE} \tag{10.5}$$

where $J_i(E)$ is equated to $B_i E^{\gamma_i}$ and γ_i is the spectral index at which the simulated showers were thrown.

The only value not known from the values described in section 9.1 is the coefficient, B_i. This can be found by taking a previous spectrum and estimating it. Calculations made in the HiRes GZK publication [3] found the $10^{19.35}$ eV energy bin to have $B = 2.07 \times 10^{24}$, with the ankle taken to be at $10^{18.65}$ eV. Using the relationships

$$E^3 J_{upper} = B_{upper} E^{-\gamma_{upper}} E^3 \tag{10.6}$$

and

$$B_{lower} = B_{upper} E_{breakpoint}^{\left(\gamma_{lower} - \gamma_{higher}\right)} \tag{10.7}$$

we find that $B_{upper} = 4.36 \times 10^{20}$ and $B_{lower} = 7.01 \times 10^{28}$. Applying these numbers, equation 10.5 calculates to $\Delta t_{upper} = 1.80 \times 10^8$. These values were used to find the number of sets to throw declared in section 9.1: $N_{upper} = 31$ sets and $N_{lower} = 2405$ sets with each set containing 10,000 events each.

10.2 Finding Event Energies

The one other piece of information measured to determine the flux of cosmic rays is the number of particles that fall within each reconstructed energy range. This is done by processing the data as described in Chapters 7 and 8. As was noted in Chapter 9, there were slight differences in the number of events considered to be actual extensive air showers. Since there were modifications to the calibration of the detector, a spectrum produced from performing the original processing code set will show minor variations in the spectrum published in 2008 [3]. In order to show clear comparisons between the Telescope Array's Middle Drum energy spectrum, it was necessary to reconstruct the HiRes-1 data without any databases using the stereo_TA processing code set, the only code that can process Middle Drum data. Additionally, to justify the simultaneous

shower search using the AlphaProc processing code, a spectrum is also made using the AlphaProc results. Finally, since calibration and atmospheric databases exist for the HiRes-1 detector, a spectrum produced using either or both of these will show an applied energy scale. Each of these are compared to the published spectrum.

As has been discussed by Abu-Zayyad [6], there were some additional cuts performed on the reconstructed set of events considered to be extensive air showers. Occasionally an event would pass all of the cuts mentioned in Chapters 7 and 8, but are too poor to reconstruct well. In order to remove these events a final set of quality cuts was placed on both the reconstructed data and Monte Carlo (see Table 10.2). After these were applied, the final set of events were sorted into tenth-decade energy bins (see Table 10.3) and combined with the exposure values to determine the energy spectrum.

10.3 HiRes1 Monocular Spectrum

The final step of this procedure is to put everything together in order to obtain the actual energy spectrum. The flux is measured according to the equation

$$J(E) = \frac{n(E)}{A\Omega(E) \times \Delta t_{on} \times \Delta E} \tag{10.8}$$

where $n(e)$ is the number of events in the energy bin with bin center E. The aperture, $A\Omega(E)$, and on-time, Δt_{on}, are the values described in section 10.1 and ΔE is the (linear) width of the energy bin. In order to make the slopes easier to see, the flux is shown in $E^3 J = J(E) \times E^3$. The resulting spectrum for each of the desired spectra compared to the published spectrum is shown in Figures 10.5, 10.6, 10.7, and 10.8.

The two spectra produced by the stereo_TA processing codes sets are different only in the usage of atmospheric and calibration databases. To determine if there is an energy scale difference, the number of events were compared using the equation

$$R = \ln\left(\frac{N_{databases}}{N_{none}}\right) \tag{10.9}$$

Table 10.2: Postreconstruction, quality cut parameters.

Rejection Cut	Purpose
Failed PCF Fit	Want a convergent fit
Track-length $< 7.9°$	Shorter lengths do not fit well
$X_{First} < 1000$ g/cm^2	Ensuring $X_{first} < X_{max}$
$\langle CFC \rangle > 0.9$	Most of the light should be seen away from mirror/tube edges
In-Plane $\theta > 120°$	Remove events with too much Čerenkov light

Table 10.3: Final numbers of events for each tenth-decade energy bin.

Energy Bin Center (log_{10} eV)	AlphaProc Events (no databases)	Original Events (no databases)	Stereo_TA Events (no databases)	Stereo_TA Events (both good DBs)
18.55	563	600	617	638
18.65	404	447	429	441
18.75	296	328	338	324
18.85	272	290	234	238
18.95	215	225	199	199
19.05	160	174	150	161
19.15	127	135	115	119
19.25	104	105	103	79
19.35	81	88	61	66
19.45	53	56	50	44
19.55	39	45	32	27
19.65	24	23	23	28
19.75	25	22	23	20
19.85	9	11	12	9
19.95	7	6	5	5
20.05	1	1	2	3
20.15	0	0	0	0
20.25	0	0	1	1
20.35	1	1	0	0

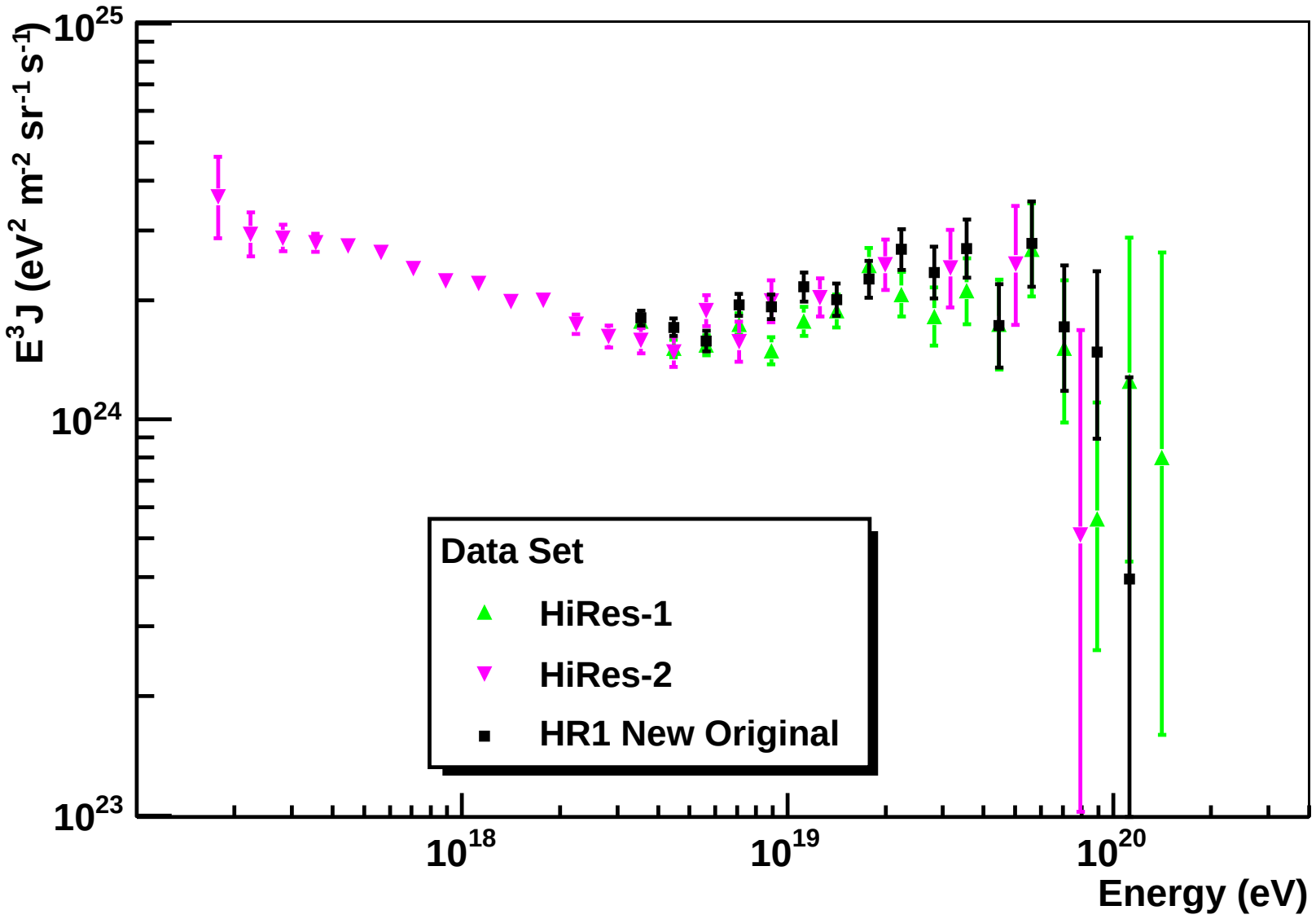

Figure 10.5: The HiRes-1 monocular spectrum processed using the original reconstruction compared to the publication [3].

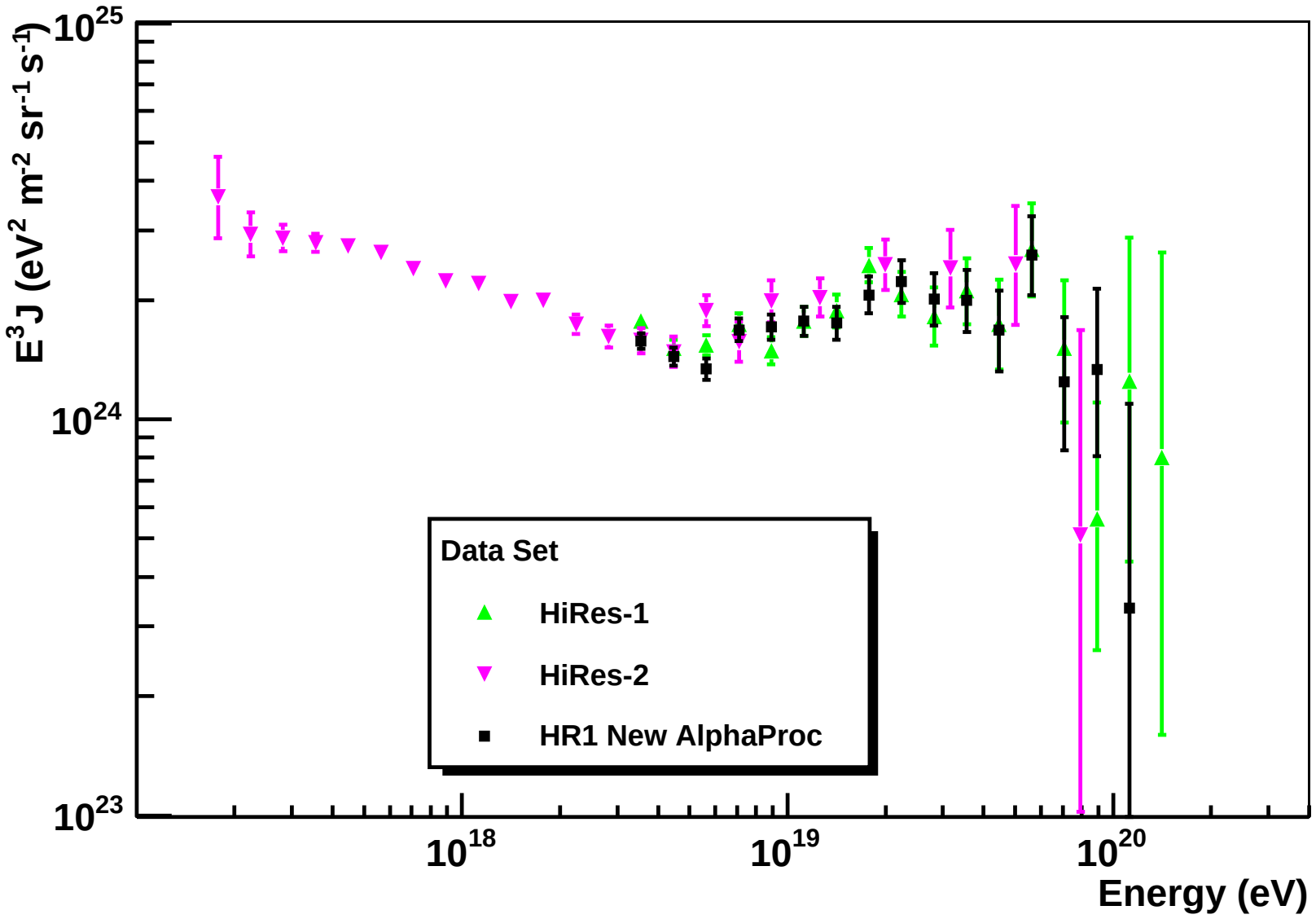

Figure 10.6: The HiRes-1 monocular spectrum processed using the AlphaProc reconstruction compared to the publication [3].

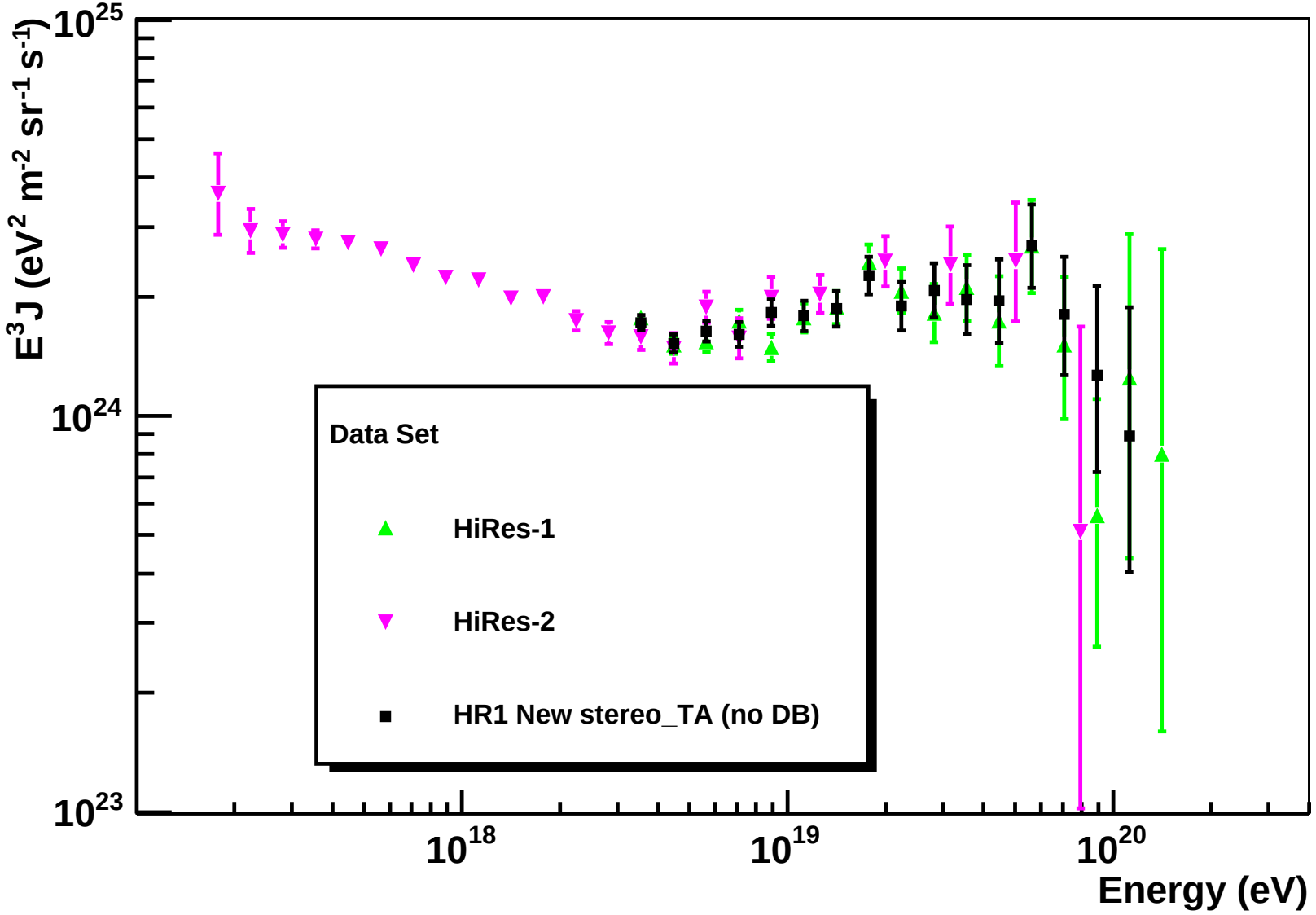

Figure 10.7: The HiRes-1 monocular spectrum processed using the stereo_TA reconstruction without databases compared to the publication [3].

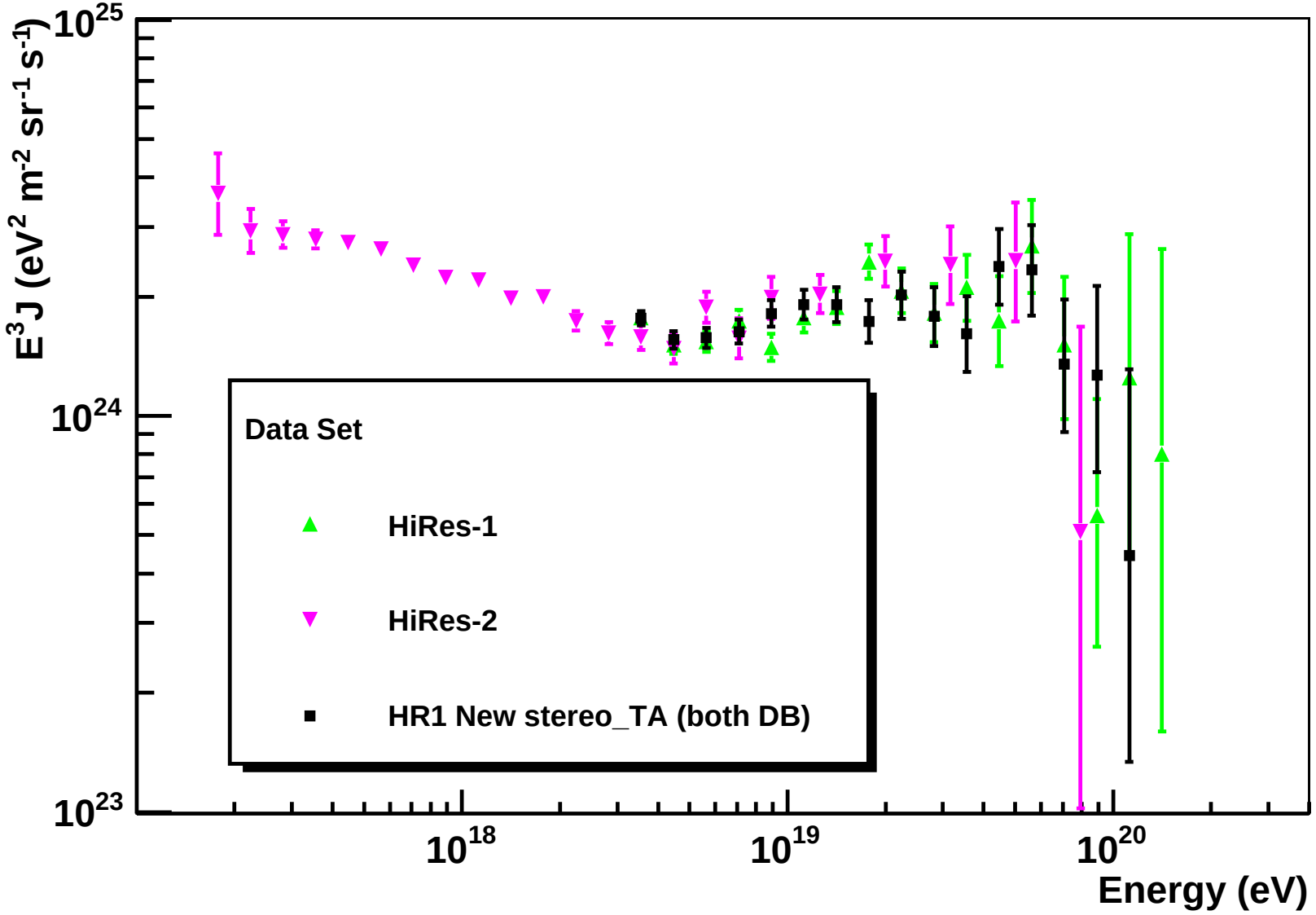

Figure 10.8: The HiRes-1 monocular spectrum processed using the stereo_TA reconstruction with good calibration and atmospheric databases compared to the publication [3].

where $N_{databases}$ and N_{none} are the number of events in each energy bin for those found using the two databases and neither, respectively. The uncertainty in each bin was calculated as

$$\delta R = \sqrt{\frac{1}{N_{databases}} + \frac{1}{N_{none}}}. \tag{10.10}$$

The ratio, R, of each energy bin was calculated for those energy bins with more than seven data events (see Table 10.3) and were fit to lines (see Figure 10.9). Fitting the points to a flat line, there is no significant bias in the energy scale. Fitting the points to a sloped line, the uncertainty in the slope is equivalent to the slope, showing there is still no significant bias in the energy scale.

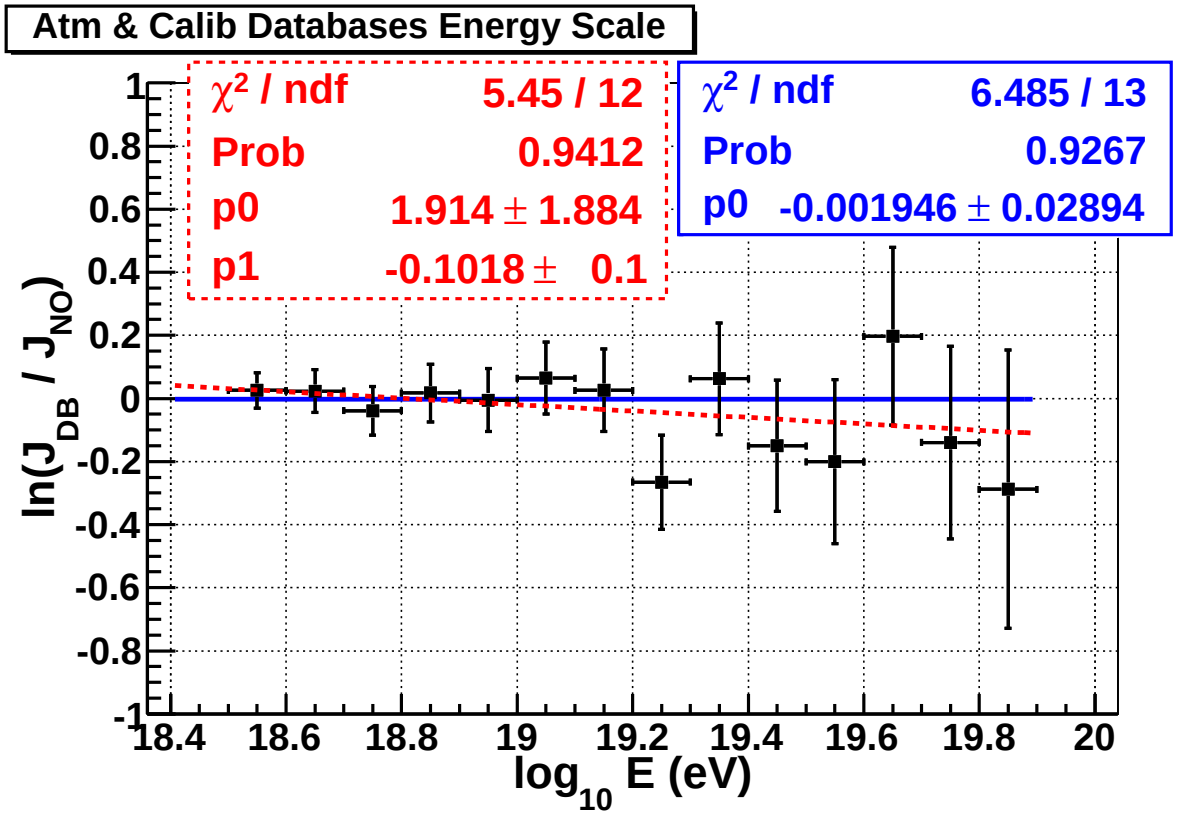

Figure 10.9: The natural log of the ratio between the number of events in the stereo_TA processed data with the atmospheric and calibration databases included over the stereo_TA processed data with neither database.

CHAPTER 11

PRELIMINARY MIDDLE DRUM MONOCULAR SPECTRUM

Since the Middle Drum detector was refurbished from the HiRes sites, it is now possible to compare the energy scale between the two experiments. This is easily performed by comparing the energy spectrum of each experiment after processing the data and Monte Carlo in the same way. This chapter will describe the process that was performed in order to produce the three-year spectrum of the Middle Drum detector and how it compares to the result of the previous chapter and the published HiRes spectrum [3].

11.1 Measuring the Flux

The Middle Drum flux is measured the same way as the HiRes-1 data (see Chapter 10). The only difference is the specific values obtained in the process.

11.1.1 On-time

As described in Chapter 6, the Middle Drum detector site of the Telescope Array experiment began collecting data on December 16, 2007. This spectrum for the Middle Drum detector accounts for the first three years of data collection, through December 16, 2010. As with HiRes, there is a limited amount of time that the doors can be opened in order to collect data: full-dark periods of at least three hours. We are further restricted to periods which have cloud cover defined by the nightly detector operator (see Table 5.2) which are considered clear (defined as no significant, stationary, cloud masses in the field of view) (see Table 6.4). This time is then used as the final on-time value. Over the course of the first three years, an integrated amount of time accounted for 33,686.11 mirror-hours (see Figure 11.1) from which the actual on-time is then approximated by dividing by the number of mirrors (14 in this case).

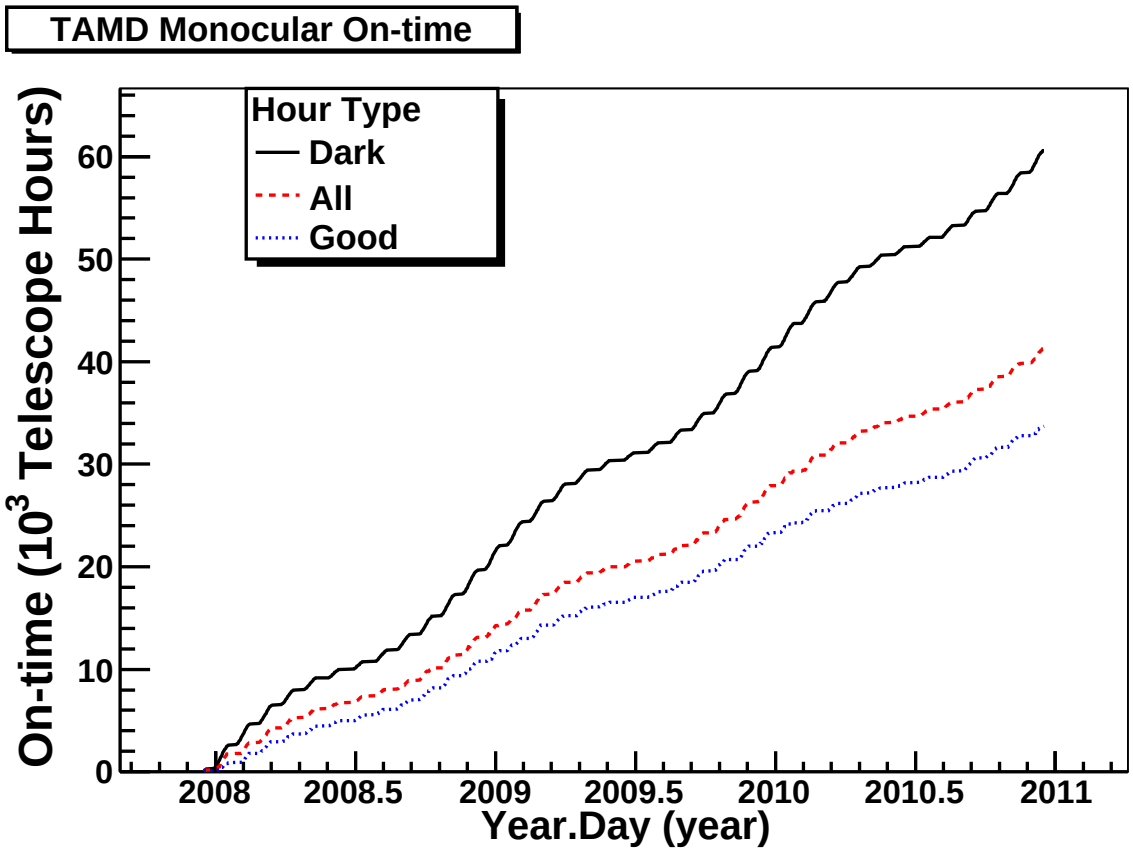

Figure 11.1: Integrated three-year on-time of Middle Drum.

11.1.2 Aperture

As can be seen in Figure 6.9, the areas that the detector can view are limited by the energy of the particles. Similar to the HiRes-1 aperture calculated in the previous chapter, the Middle Drum aperture calculation used a spectral index energy continuum. Results from the published HiRes spectrum [3] were used to generate the Monte Carlo, as described in chapter 9. To reiterate, above $10^{17.5}$ eV and below $10^{18.65}$ eV, the flux drops with increasing energy as a power law $J \propto E^{-\gamma}$ where $\gamma = 3.25$ and above $10^{18.65}$ eV the spectral index hardens to $\gamma = 2.81$. For the purposes of the aperture calculation we extend the "thrown" spectrum beyond the GZK threshold up to $10^{21.0}$ eV.

After the Monte Carlo data were produced, it was then run through all of the same processing routines and quality and analysis cuts applied to the real data. The Middle Drum data were processed using the stereo_TA (see section 7.2) program set. The relative percentage of triggered events is comparable to HiRes-1 (see Table 11.1 and Table 9.2). However, since there are two rings which view higher in elevation, more of the lower energy events are retained, effectively doubling the number of final events used in the spectrum.

The minimum energy of this new spectrum was fixed at $10^{18.0}$ eV primarily because HiRes composition results [92] appear to be unchanging and light (proton) above this energy (see Figure 2.4). Additionally, with only one "ring" of telescopes, the original HiRes-1 spectrum measured only to $10^{18.5}$ eV, so a conservative lower cut was chosen for this analysis with two rings. As such, all of the Monte Carlo showers thrown to determine the Middle Drum aperture were based off of proton-induced showers. This lower limit not only allows us to make a direct comparison to the HiRes-1 spectrum, but also gives us a check on the ankle region against HiRes-2 monocular results.

Table 11.1: Average percentages of retained events from previous pass for each processing code set of the Middle Drum Monte Carlo.

Pass	STA
Triggered	2.51
stps2	91.42
stps2 (d)	85.56
stpln	96.02
hrlsr	99.61
stgeo	100.0
stpfl	100.0
Quality	64.73
Final	48.42
Of Thrown	1.22

The Monte Carlo was thrown with the same input parameters that were used to generate the HiRes-1 Monte Carlo (see Chapter 9). The aperture is then calculated according to equations 10.1 and 10.3 where $R_{P-min} = 100$ m and $R_{P-max} = 25$ km for the $10^{17.5-18.65}$ eV energy range and $R_{P-max} = 50$ km for the $10^{18.65-21.0}$ eV energy range. In both ranges, the maximum zenith angle is $\theta = 80°$. As with HiRes-1, the aperture data points are fit to equation 10.4 to show the shape of the aperture (see Figure 11.2). As with HiRes-1, there is an intrinsic detector reconstruction bias over different energy ranges (see Figure 11.3). This is found as the mean ratio between the reconstructed energy and the thrown energy over the energy range of interest. This is applied to both the Monte Carlo and data to bring the observed events closer to the "true" value without significantly affecting the shape of the spectrum.

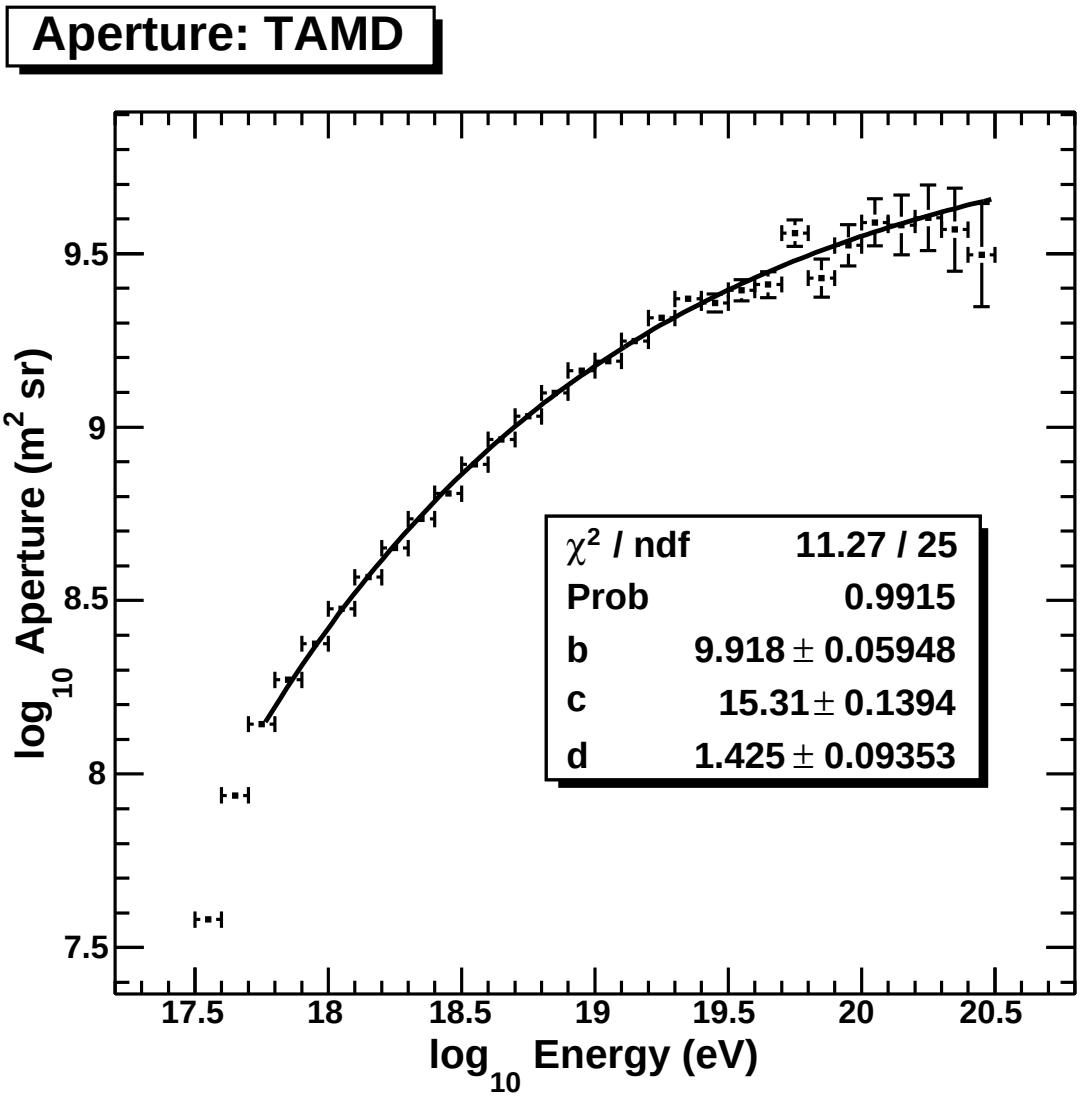

Figure 11.2: Middle Drum aperture in tenth-decade bins.

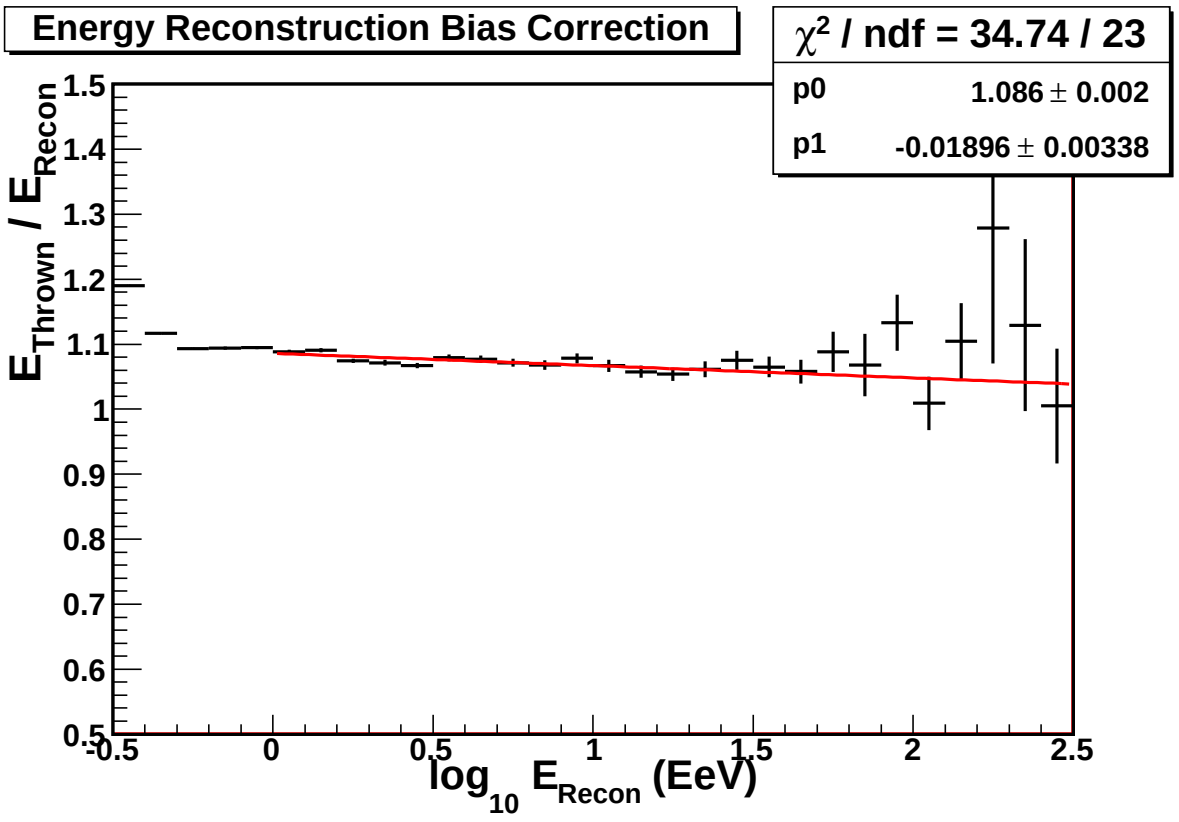

Figure 11.3: Monte Carlo reconstruction bias for the Middle Drum results.

11.1.3 Adjustments For Darker Sky

During the early processing of the Middle Drum data, it was discovered that there was a $\sim 15\%$ offset to the spectral result. The first Monte Carlo set was generated using the HiRes vertical aerosol optical depth (VAOD) and gain/threshold ratios, but with the Middle Drum geometry. Initially it was thought that the result was due to aerosol content in the atmosphere so a study was made (see section 12.2). This study ruled out this hypothesis that the effect of varying VAOD parameters greatly affects the energy scale.

As indicated in Chapter 6, the PMT camera types have distinct gain-voltage parameterizations. At HiRes-1, these cameras were distributed randomly over the mountain which allowed the HiRes-1 Monte Carlo to easily use an average gain-to-threshold ratio setting. By grouping the camera types at Middle Drum, the observation of the sky was more dependent on the PMT type. Using the same gain-to-threshold ratio as HiRes-1 showed a bimodal distribution in the number of photo-electrons per event-related PMT in the Middle Drum Monte Carlo (see Figure 11.4). In fact, the data showed that the ambient light was significantly less bright at Middle Drum that HiRes-1, and that the detector thresholds run $\sim$ 20% lower. The lower threshold had the effect of increasing our aperture since the floating thresholds would automatically decrease,

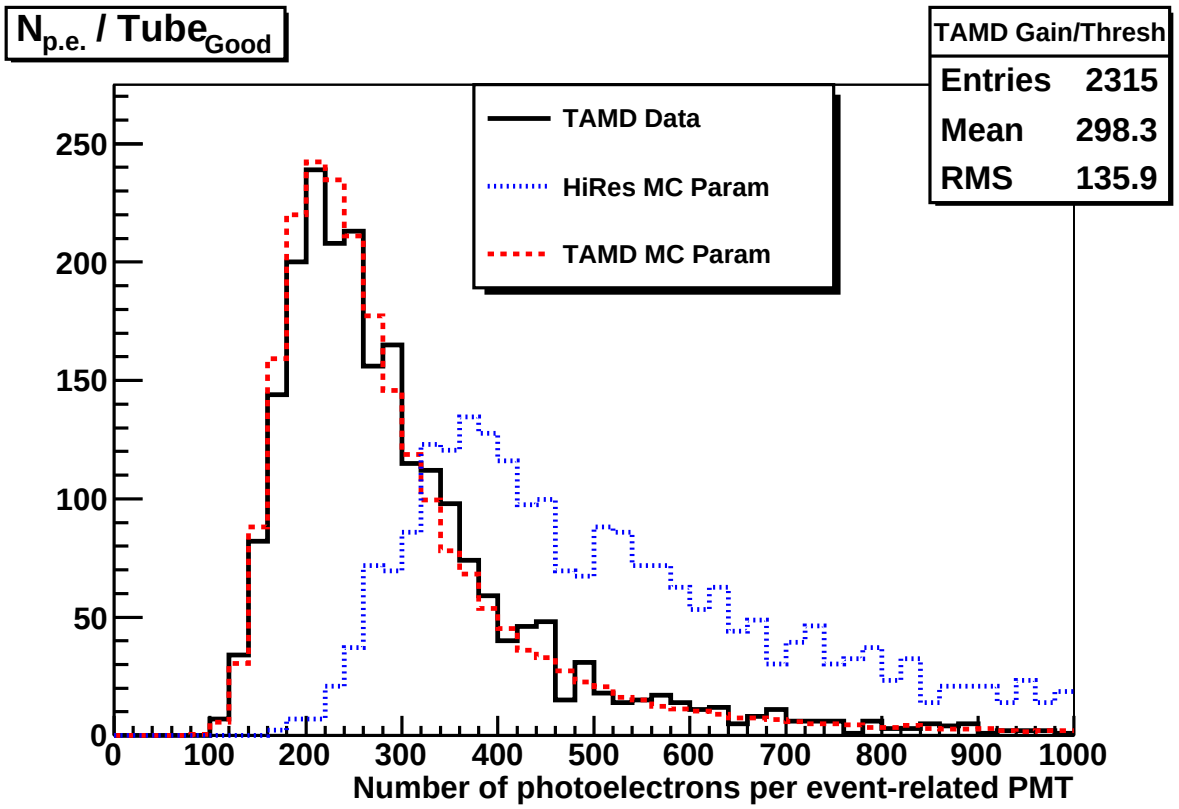

Figure 11.4: The number of photo-electrons per event-related photo-multiplier tube showing the Middle Drum Monte Carlo simulations before ("HiRes MC Param") and after ("TAMD MC Param") the gain-versus-threshold adjustment.

allowing farther-away, lower-energy showers to be observable which increases our number of retained events. These lower threshold-to-gain ratios are used for all of the Middle Drum Monte Carlo simulations. Applying these new gain-to-threshold ratios reduced the number of photo-electrons per event-related PMT, which is now more consistent with the observed data (see Figure 11.4).

11.1.4 TAMD Resolution

By comparing the reconstructed parameters to those that were thrown in the simulated set the resolution of the Middle Drum detector can be determined. The distribution of the differences in energy and N_{max} from the profile reconstruction and R_P, Ψ, θ, and ϕ from the geometrical reconstruction of the Monte Carlo set show how much intrinsic uncertainty there is in the reconstructed results (see Figures 11.5, 11.6, 11.7, 11.8, 11.9, and 11.10). For each parameter, the events are shown for energy ranges between $10^{18.0}$ and $10^{18.5}$ eV, between $10^{18.5}$ and $10^{19.0}$ eV, and between $10^{19.0}$ and $10^{20.5}$ eV. It can be seen that not only is there a trend of better resolution for increasing energy ranges, but

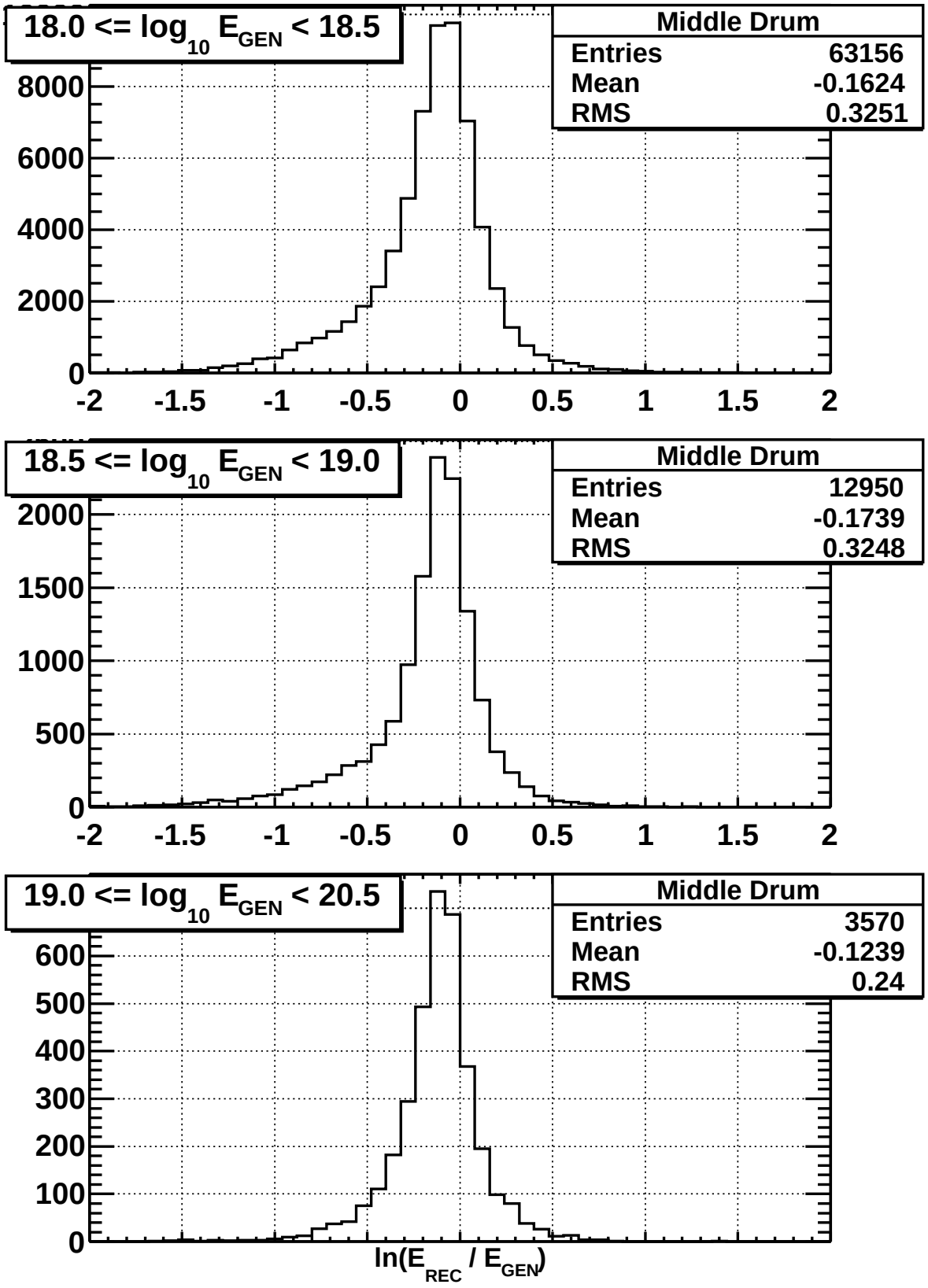

Figure 11.5: TAMD Monte Carlo reconstructed versus thrown comparisons for the energy.

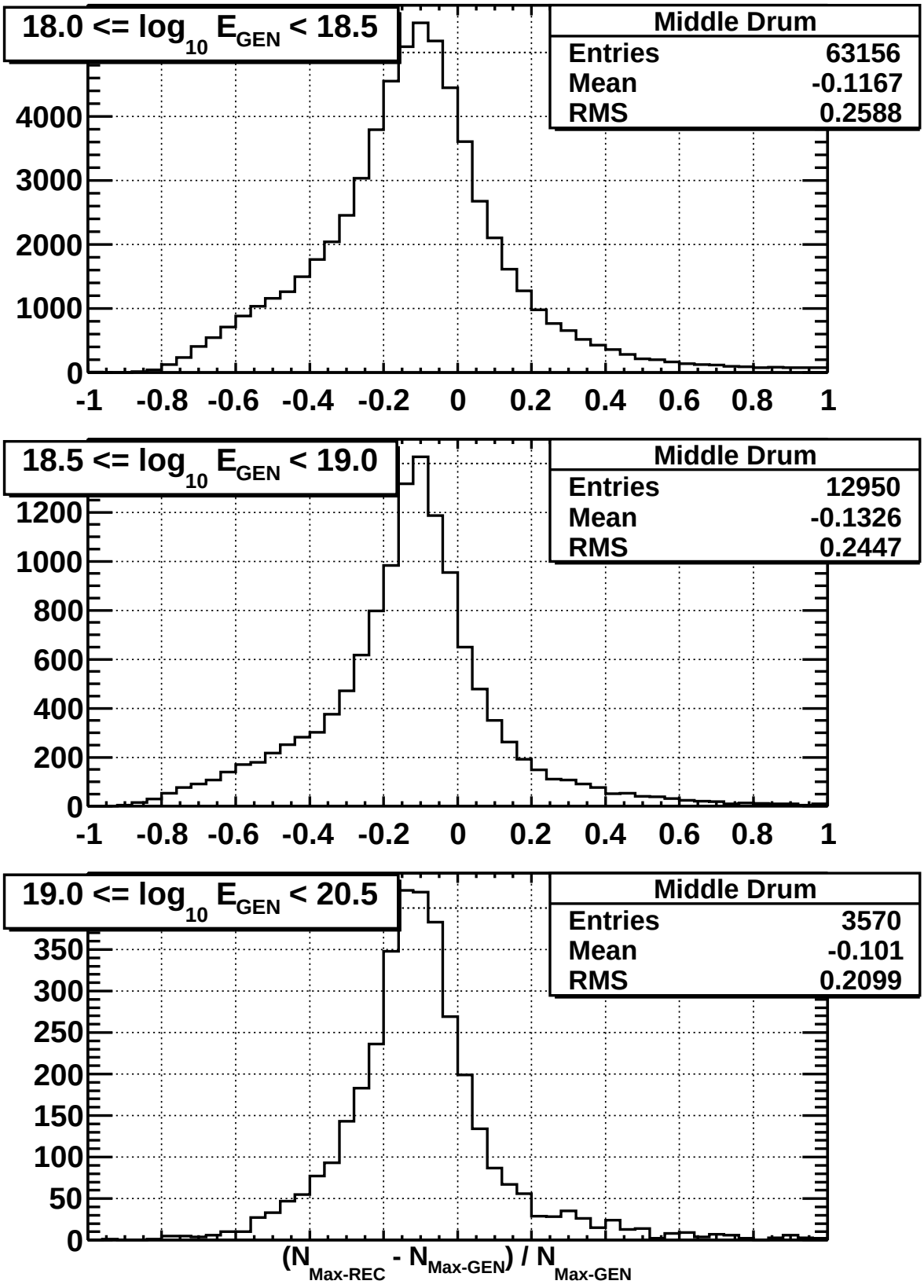

Figure 11.6: TAMD Monte Carlo reconstructed versus thrown comparisons for the maximum number of particles, N_{max}.

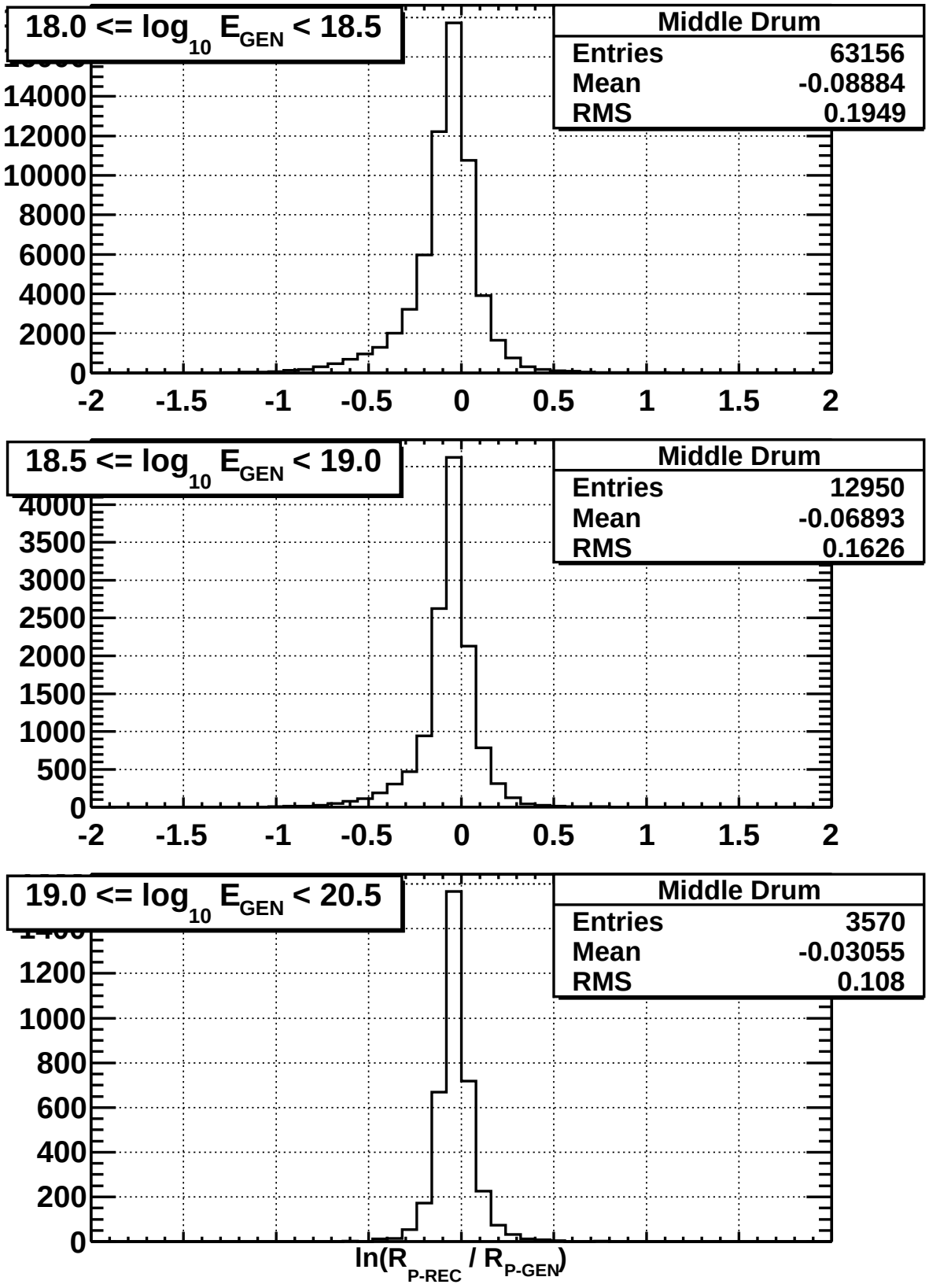

Figure 11.7: TAMD Monte Carlo reconstructed versus thrown comparisons for the impact parameter, R_p.

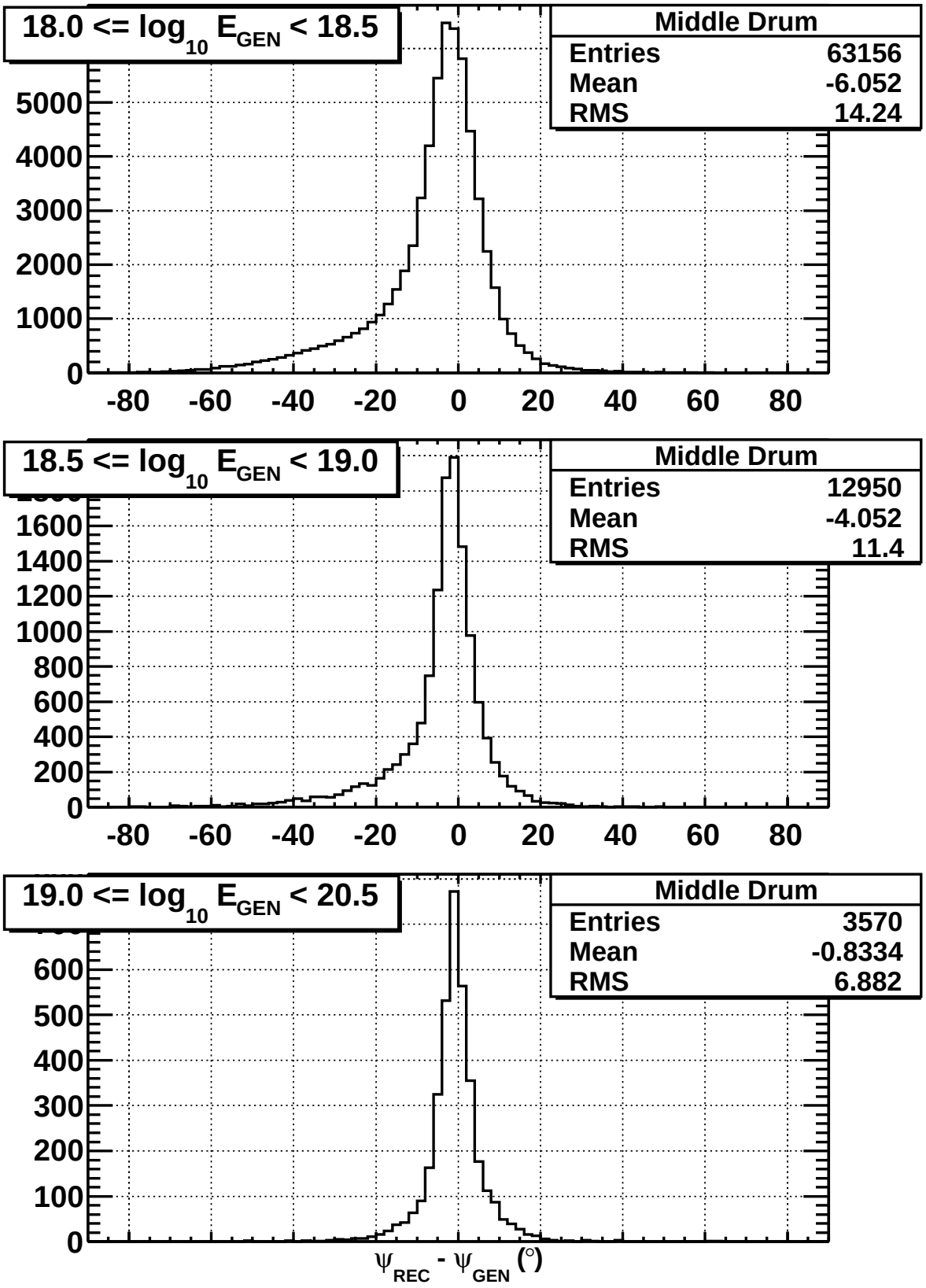

Figure 11.8: TAMD Monte Carlo reconstructed versus thrown comparisons for the in-plane angle, *Psi*.

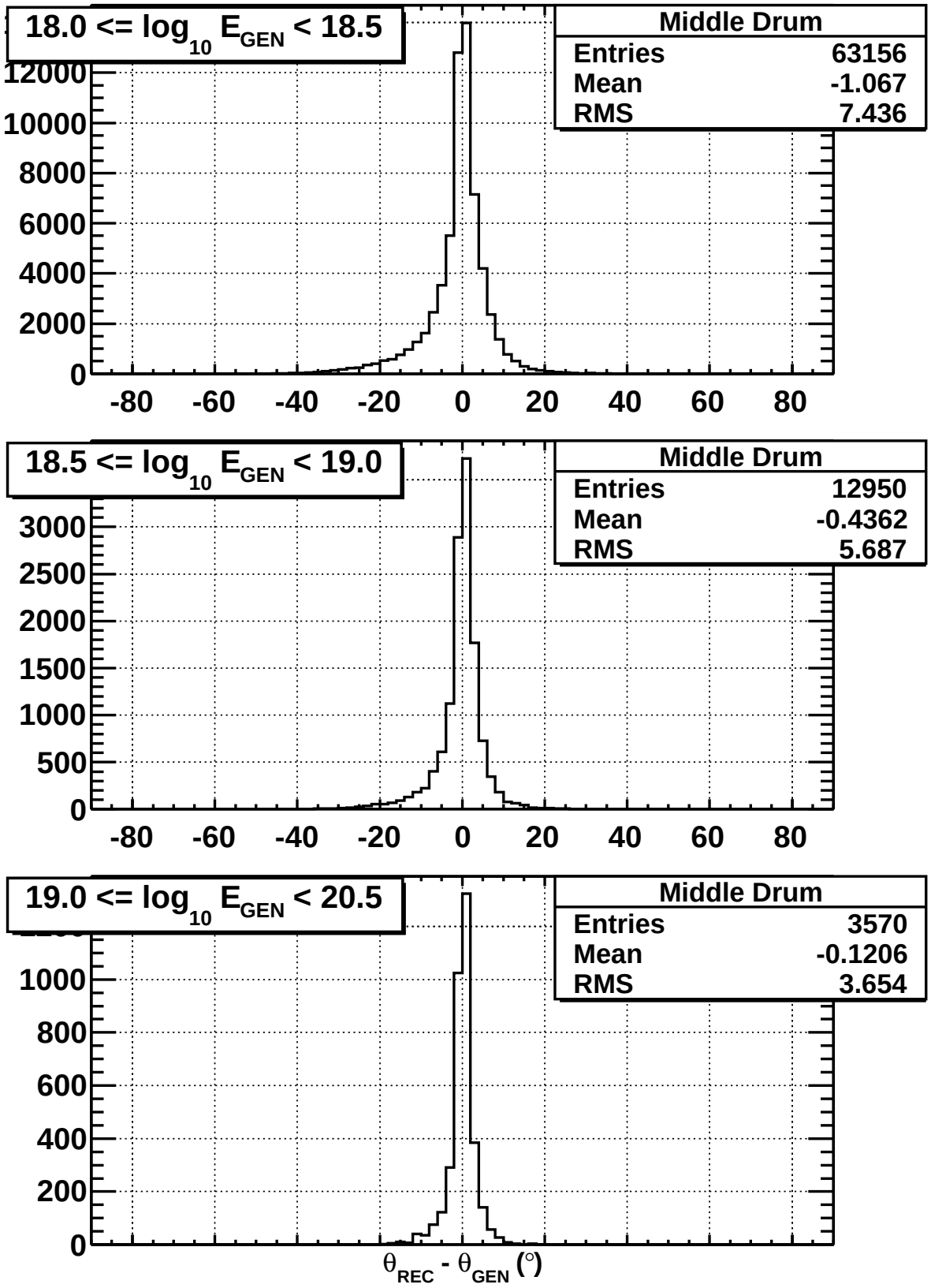

Figure 11.9: TAMD Monte Carlo reconstructed versus thrown comparisons for the zenith angle, θ.

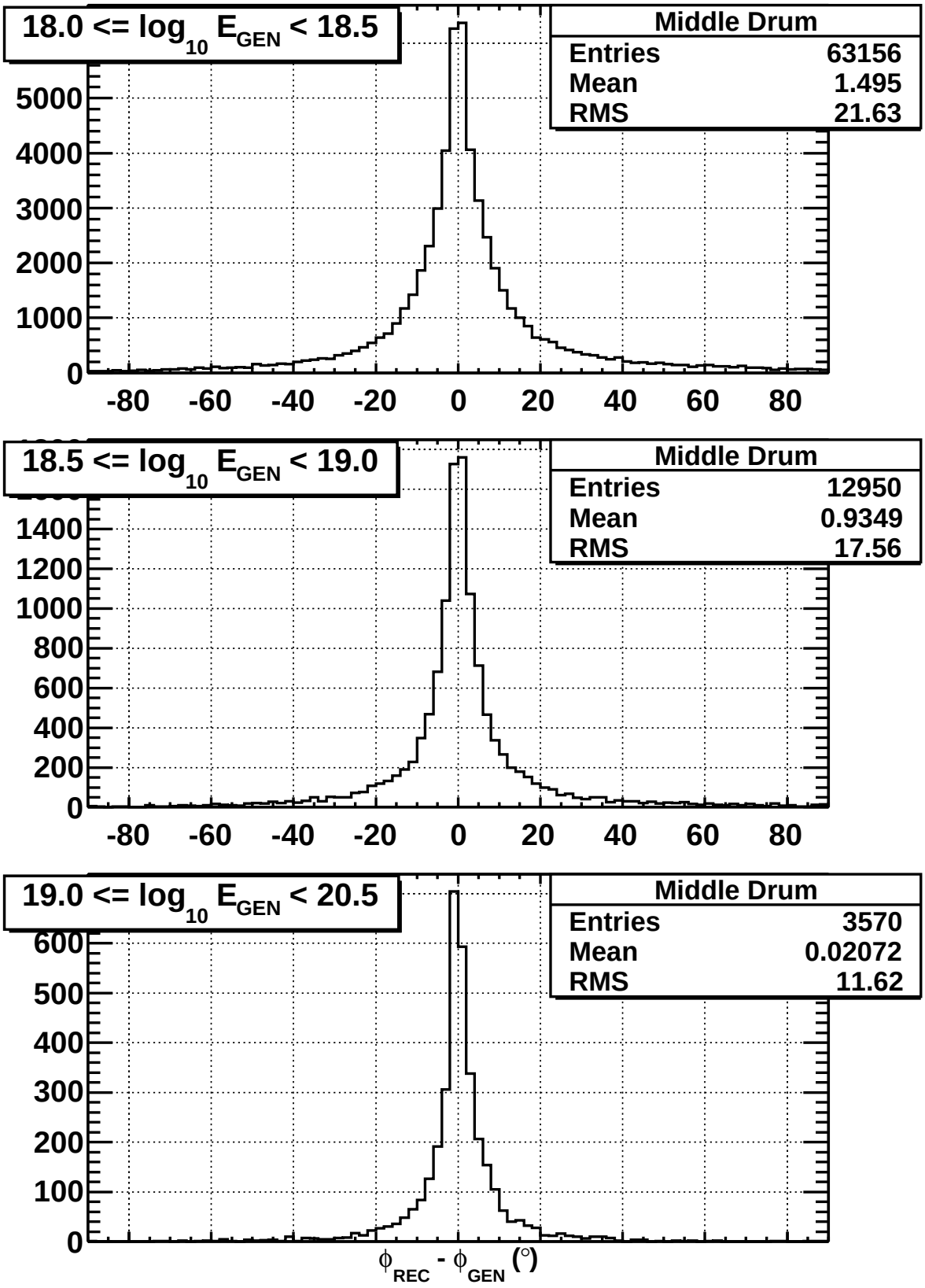

Figure 11.10: TAMD Monte Carlo reconstructed versus thrown comparisons for the azimuthal angle, ϕ.

the resolutions are significantly better than those for HiRes-1 processed using the same stereo_TA processing code.

11.2 Data-Monte Carlo Comparisons

Comparisons are made between the reconstructed data and Monte Carlo distributions to show how well the simulated showers compare to the observed events. Comparisons are made in the parameters pertinent to the aperture calculation (see appendix E): the number of photo-electrons per good tube ; the impact parameter, R_P ; the in-plane angle, ψ ; the zenith angle, θ ; and the azimuthal angle, ϕ . We make this check in order to assure ourselves that the Monte Carlo gives a good description of the detector response and thus validates our aperture calculation. A direct comparison is made in the energy distribution to show the quality of the spectrum (see Figure 11.11). The data points are represented with markers and error bars, the Monte Carlo is given as a solid line histogram. At this time there is not enough data to indicate the GZK threshold using only these distributions.

11.3 Energy Spectrum

In order to make a truly direct comparison of HiRes and Middle Drum energy scales, the same stereo_TA processing code (see section section 7.2) used for the HiRes-1 analysis in the previous chapter was applied to TAMD. The same final quality cuts described by Abu-Zayyad [6] were also performed on the final selection of extensive air showers (see Table 10.2). The surviving events were sorted into tenth-decade energy bins (see Table 11.2) and combined with the calculated exposure values to determine the flux. There was one event observed above $10^{20.0}$ eV in the first three years of Middle Drum observation. The flux is measured according to equation 10.8. The spectral values obtained are compared to the published HiRes spectrum [3] (see Figure 11.12 and Table 11.3). The Middle Drum spectrum agrees quite well with the HiRes monocular observations.

11.3.1 Most Energetic Events

In looking for the energy limit that cosmic rays can possess, it is helpful to look at the highest events observed by the experiment. As a final set of events, there are five of events with energy greater than $10^{19.7}$ eV (see Figures 11.13, 11.14, 11.15, 11.16, and 11.17). Each is shown in four separate images: a) the analyzed, triggered tubes with

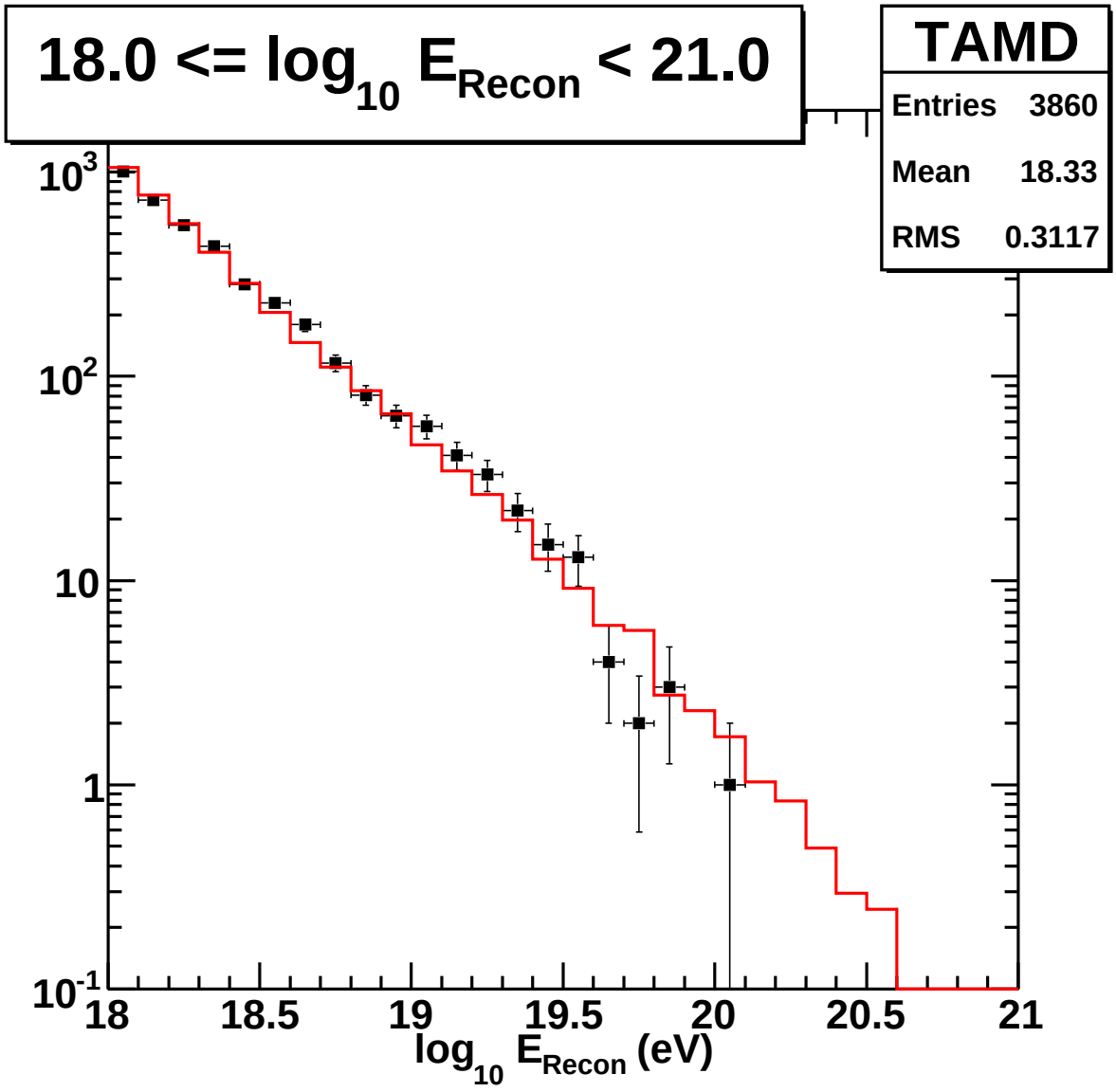

Figure 11.11: TAMD data-Monte Carlo comparisons for the energy in the range of interest.

Table 11.2: Middle Drum numbers of events for each tenth-decade energy bin for the first three years of observation.

Energy Bin Center (log_{10} eV)	Thrown MC Events	Reconstructed MC Events	TAMD Events
18.05	731316	21470	1007
18.15	434962	15752	730
18.25	259637	11404	548
18.35	154848	8251	433
18.45	92262	5822	282
18.55	54523	4174	229
18.65	132152	2985	179
18.75	85716	2258	116
18.85	56409	1736	81
18.95	37351	1333	64
19.05	24666	938	57
19.15	16114	700	41
19.25	10609	537	33
19.35	7000	402	22
19.45	4636	259	15
19.55	3074	187	13
19.65	1947	123	4
19.75	1306	116	2
19.85	850	56	2
19.95	574	47	0
20.05	367	35	1
20.15	224	21	0
20.25	173	17	0
20.35	110	10	0
20.45	78	6	0
20.55	56	5	0
20.65	23	1	0
20.75	21	2	0
20.85	13	0	0
20.95	7	0	0

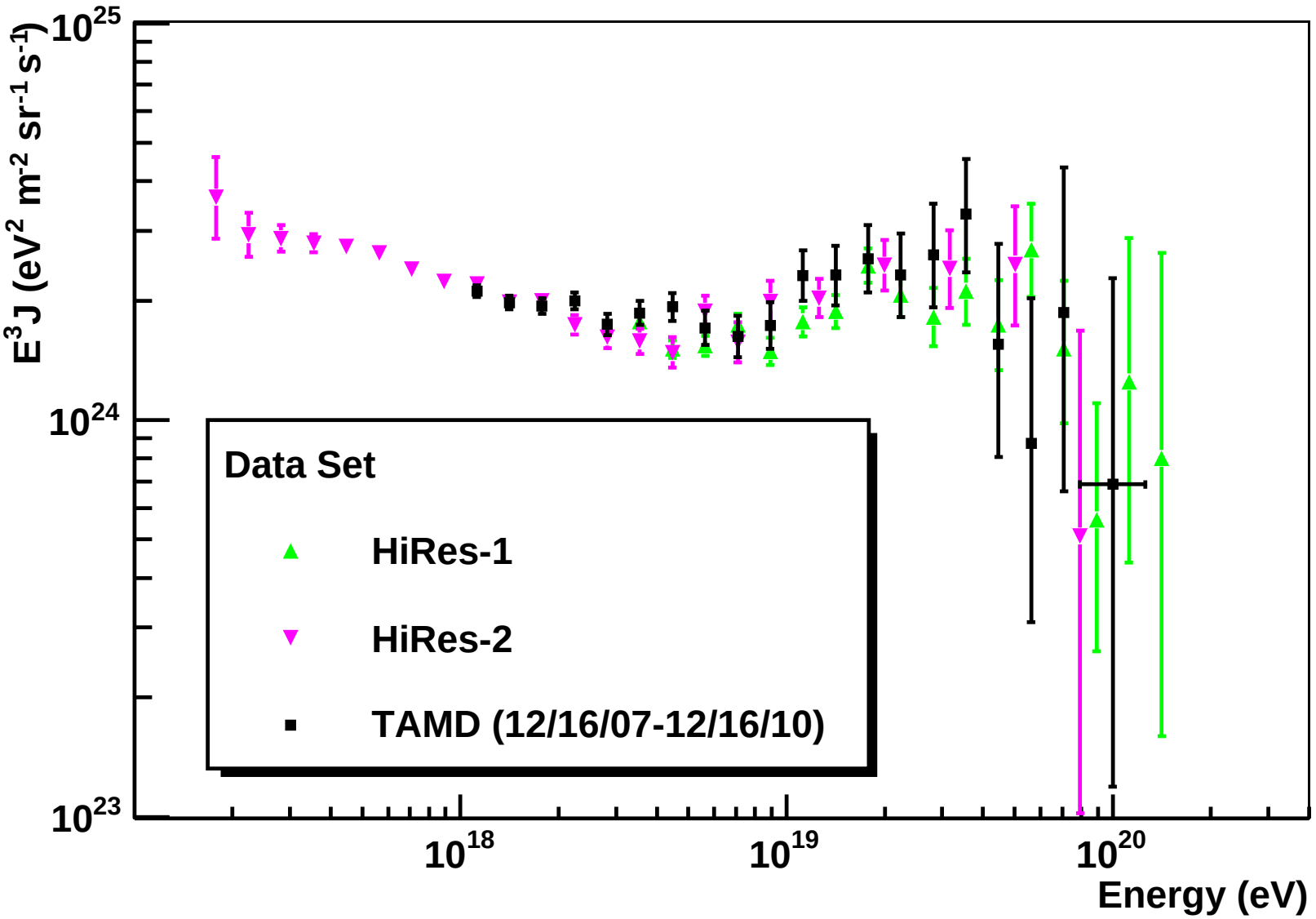

Figure 11.12: The Telescope Array Middle Drum three-year monocular spectrum.

Table 11.3: The three-year Middle Drum aperture and spectral data points.

log_{10} Energy (eV)	log_{10} Aperture (m^2 ster)	Flux / 10^{24} ($eV^2 km^{-2} ster^{-1} s^{-1}$)	$Err_{upper}/10^{23}$ ($eV^2 km^{-2} ster^{-1} s^{-1}$)	$Err_{upper}/10^{23}$ ($eV^2 km^{-2} ster^{-1} s^{-1}$)
18.05	8.48	2.12	0.68	0.70
18.15	8.57	1.98	0.75	0.77
18.25	8.65	1.94	0.85	0.89
18.35	8.73	2.00	0.99	1.04
18.45	8.81	1.74	1.06	1.13
18.55	8.89	1.86	1.26	1.35
18.65	8.96	1.93	1.48	1.60
18.75	9.03	1.71	1.63	1.79
18.85	9.10	1.62	1.85	2.07
18.95	9.16	1.73	2.22	2.52
19.05	9.19	2.31	3.14	3.60
19.15	9.25	2.31	3.70	4.34
19.25	9.31	2.55	4.56	5.46
19.35	9.37	2.32	5.03	6.26
19.45	9.36	2.61	6.90	9.02
19.55	9.39	3.30	9.40	12.55
19.65	9.41	1.55	7.42	12.26
19.75	9.56	0.74	5.64	11.53
19.85	9.43	1.87	12.06	24.63
19.95	9.52	1.62	13.40	37.26

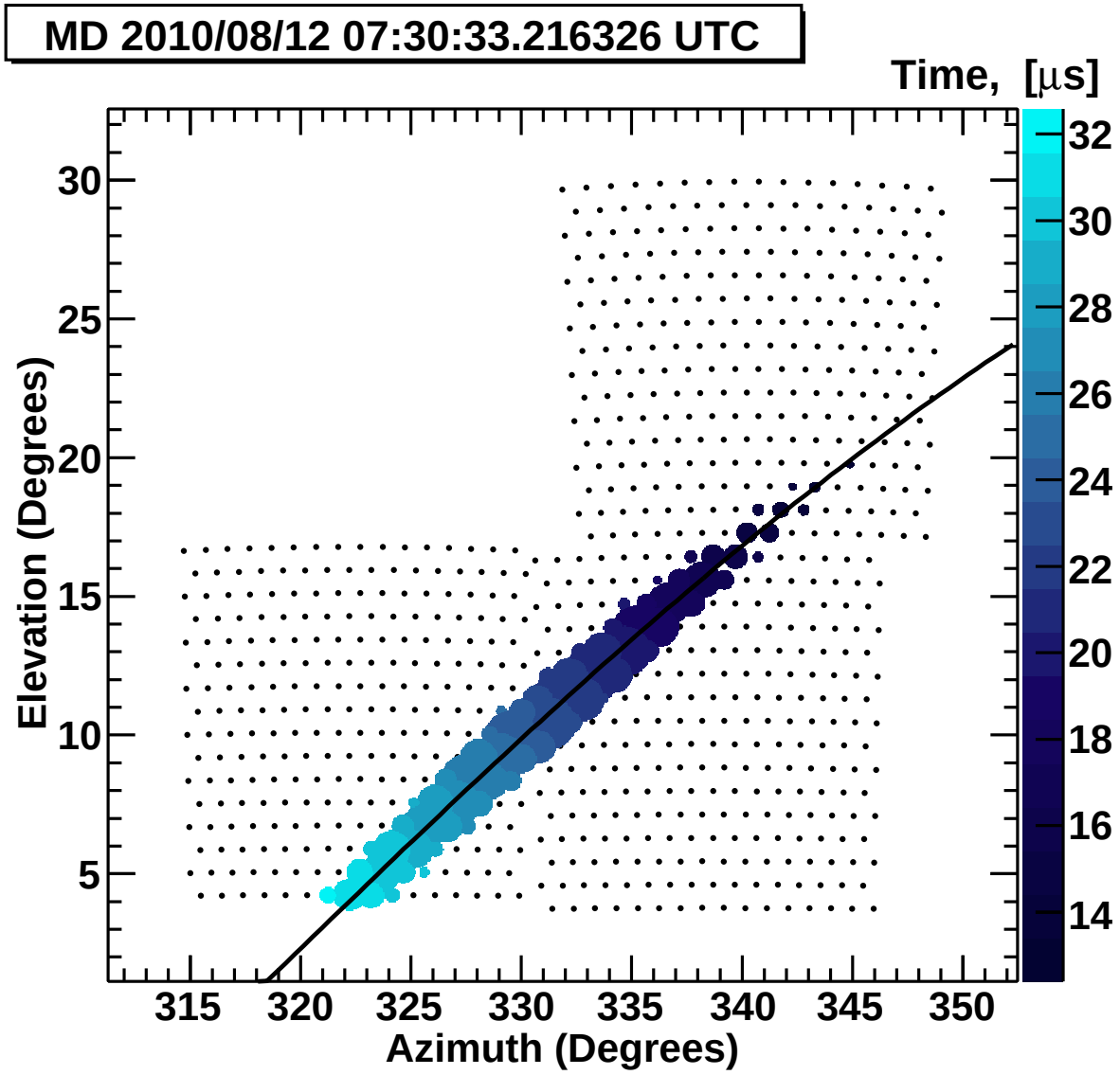

(a) Event Display

Figure 11.13: Event with $10^{20.08}$ eV energy.

grayscale indicating the time of triggering and radius indicating relative intensity; b) the core position (where the shower front was calculated to land on the surface of the earth) with respect to the HiRes experiment with the direction it was travelling in the azimuth shown by an arrow; c) the time-versus-angle graph that is used to obtain the geometrical-timing fit; and d) the profile fit split into relative amounts of various light sources.

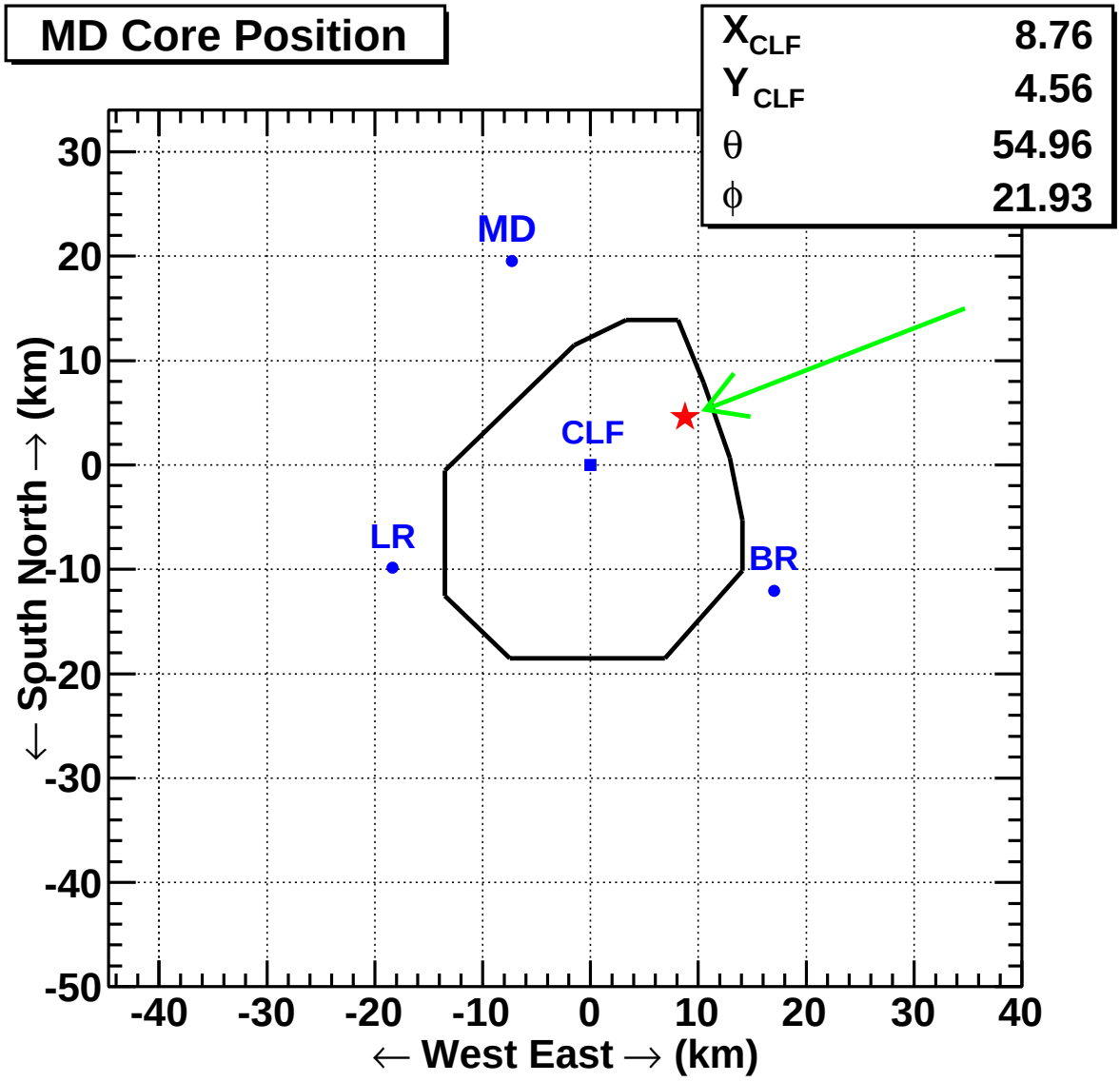

(b) Core Position

Figure 11.13: Continued.

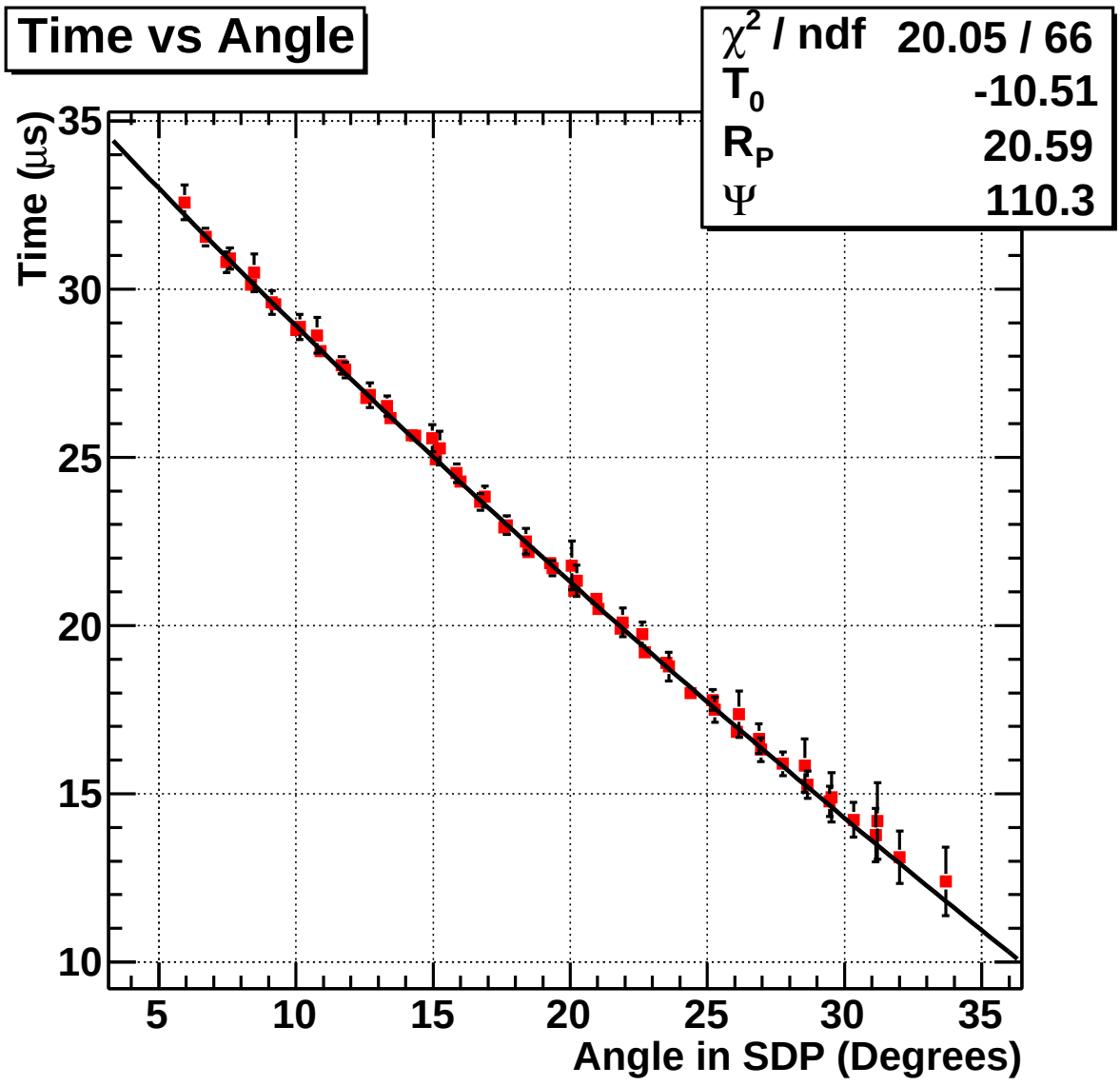

(c) Geometrical Fit

Figure 11.13: Continued.

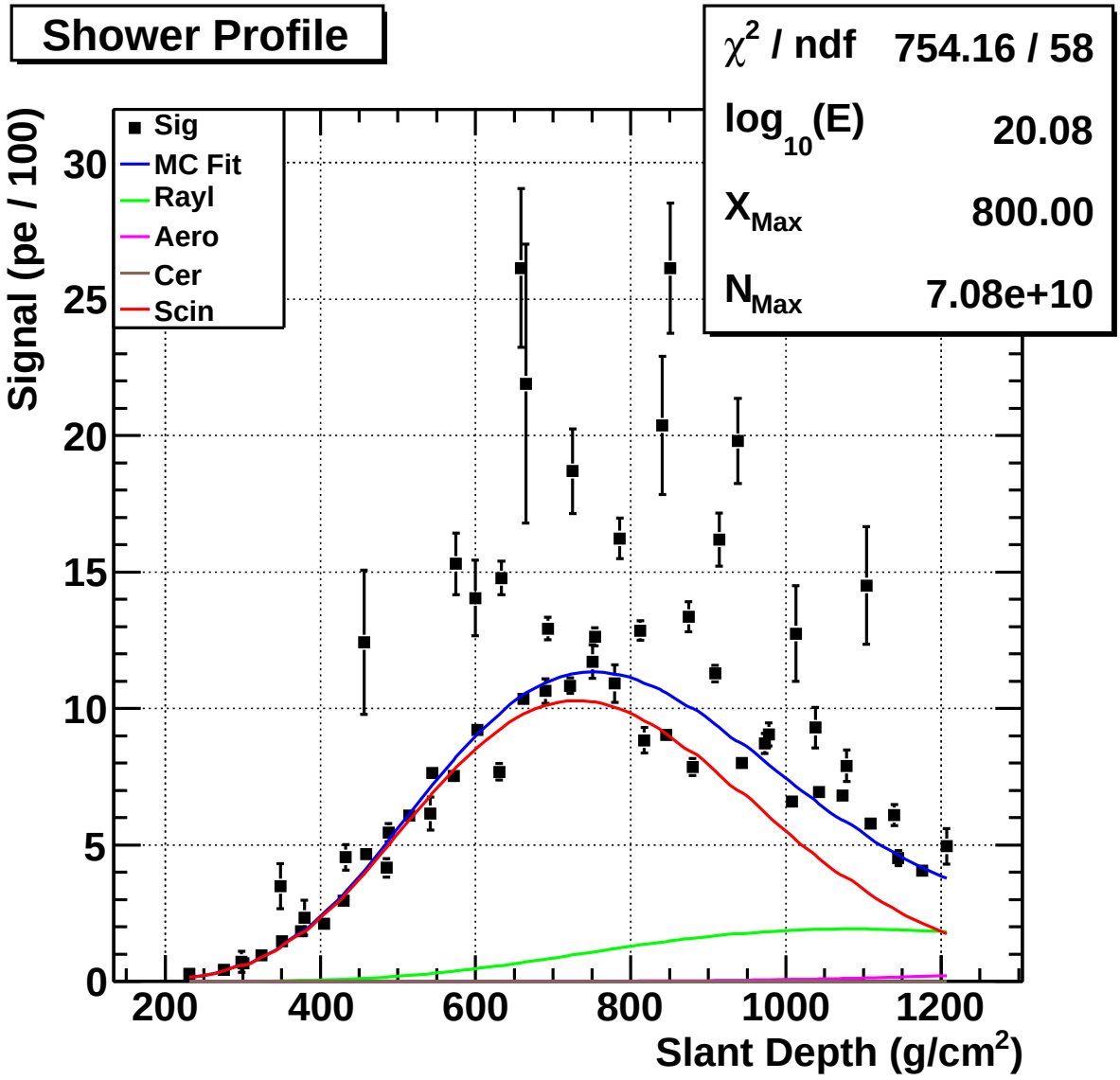

(d) Profile Fit

Figure 11.13: Continued.

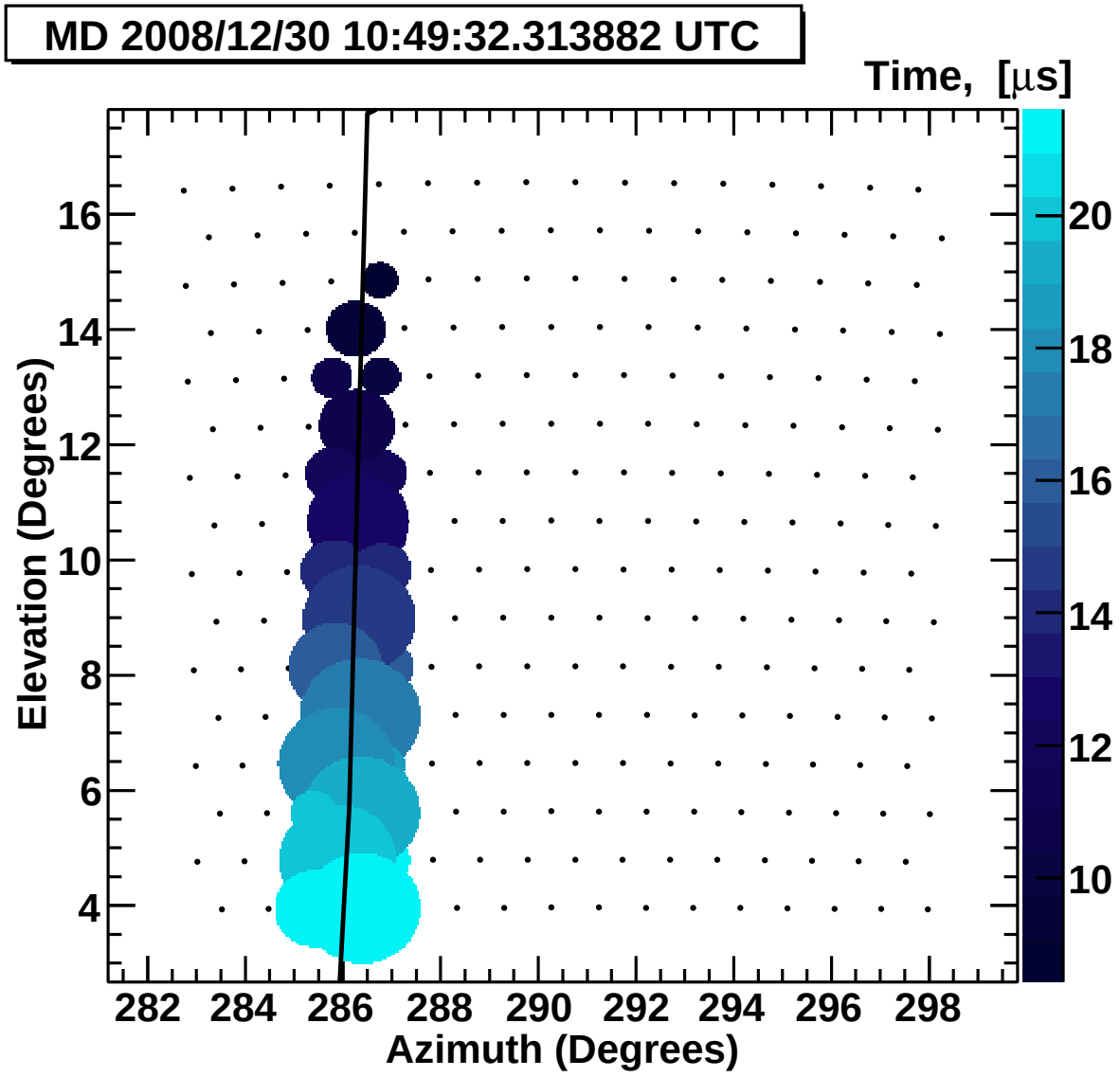

(a) Event Display

Figure 11.14: Event with $10^{19.86}$ eV energy.

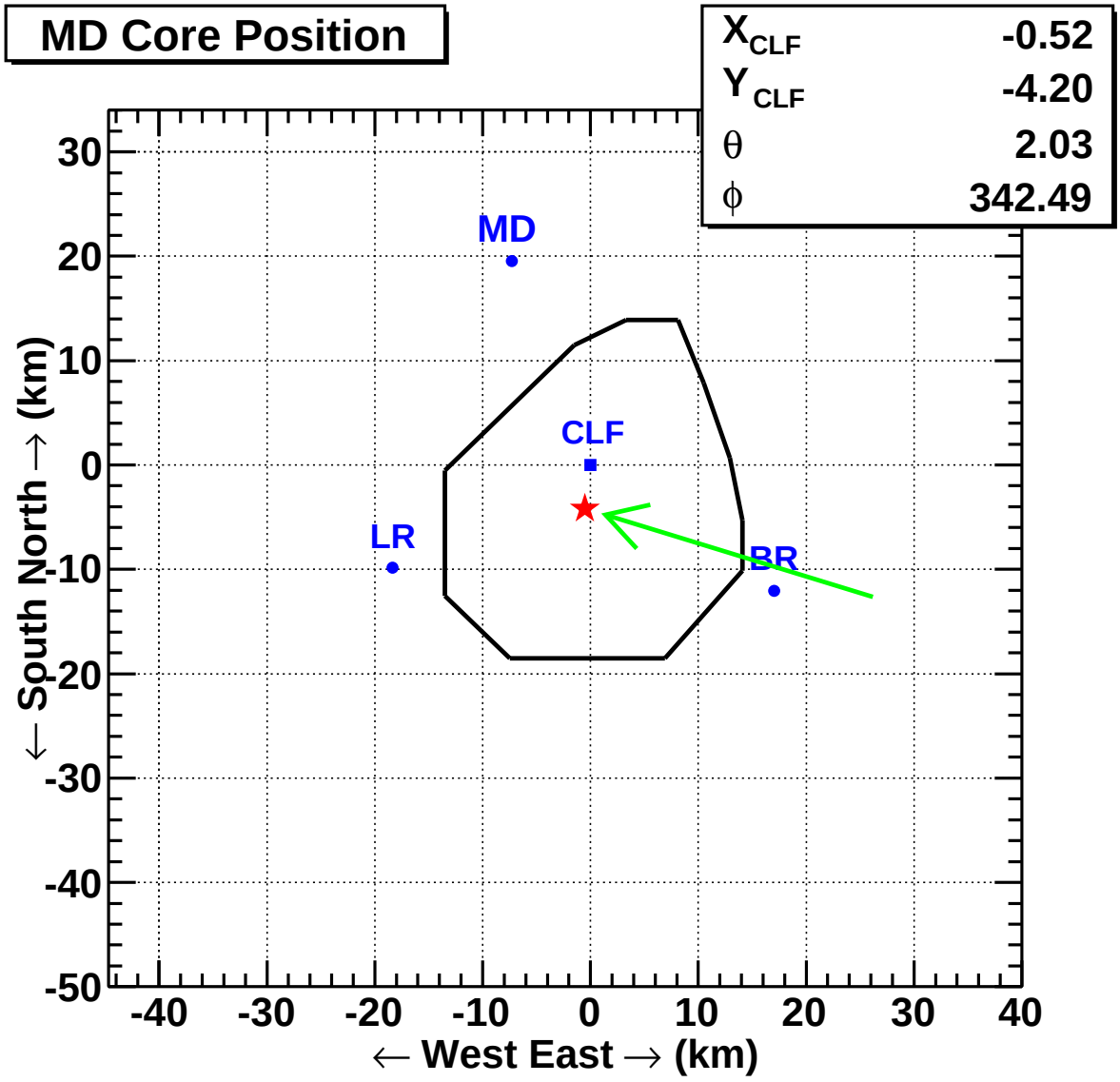

(b) Core Position

Figure 11.14: Continued.

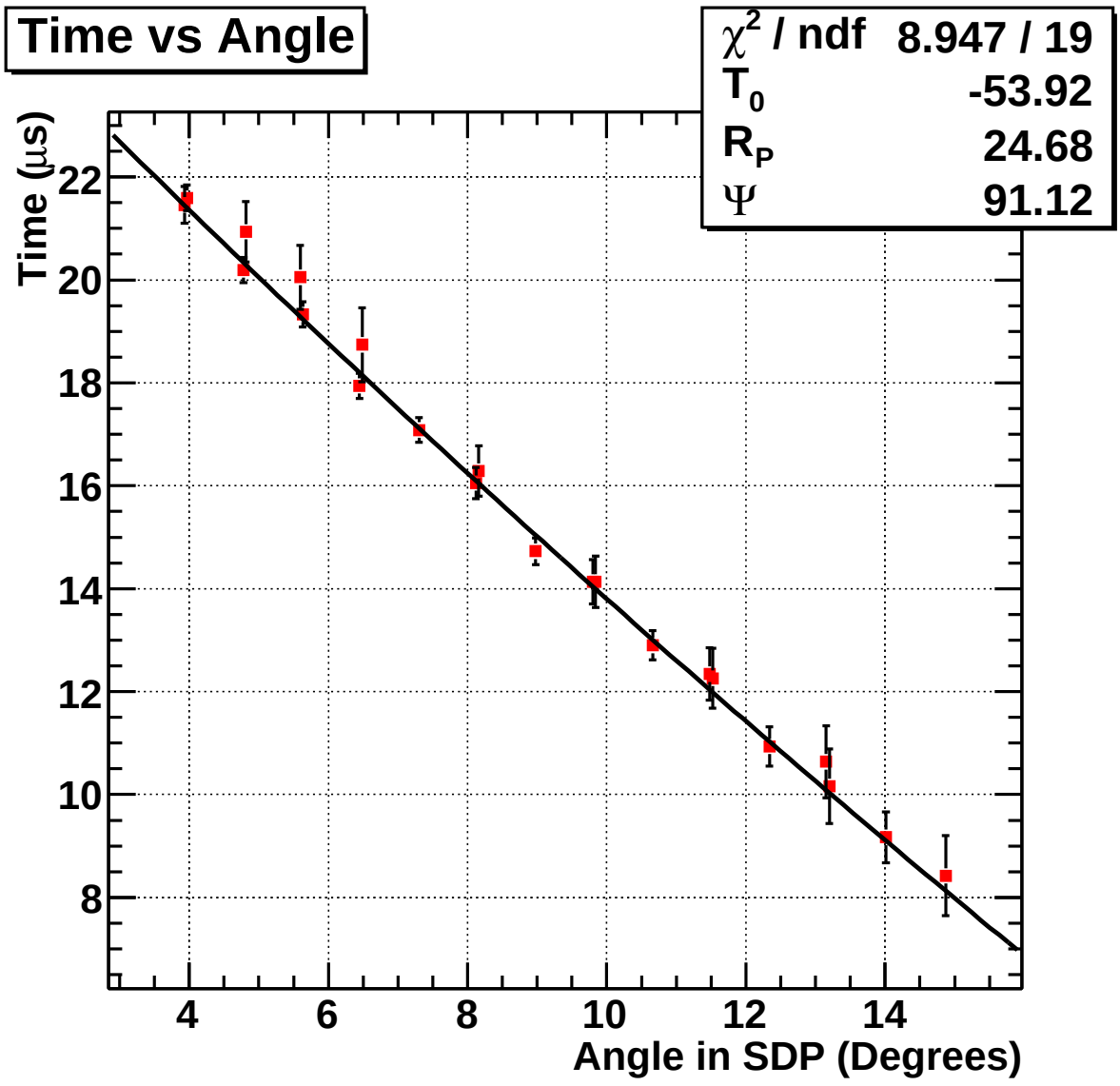

(c) Geometrical Fit

Figure 11.14: Continued.

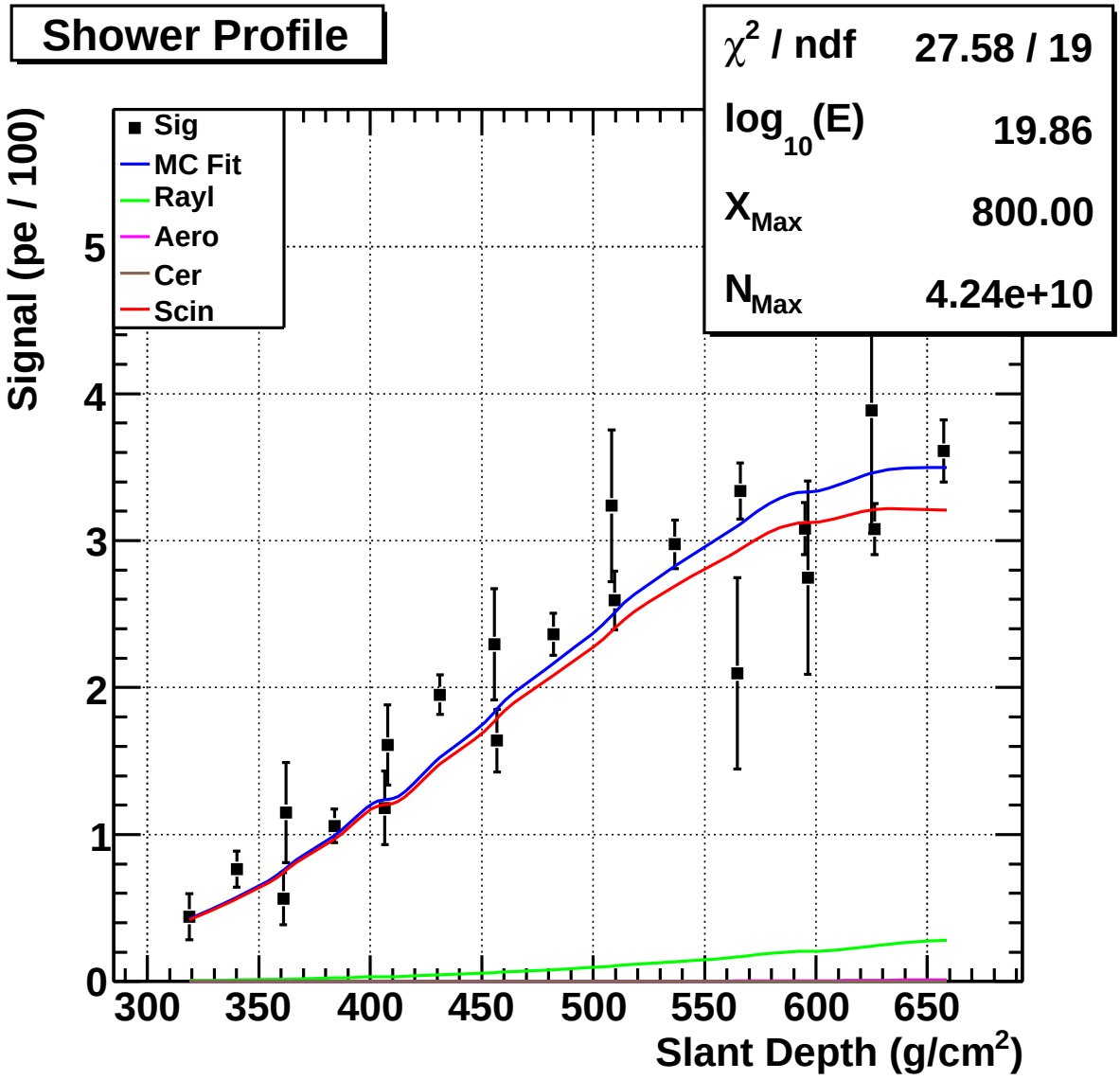

(d) Profile Fit

Figure 11.14: Continued.

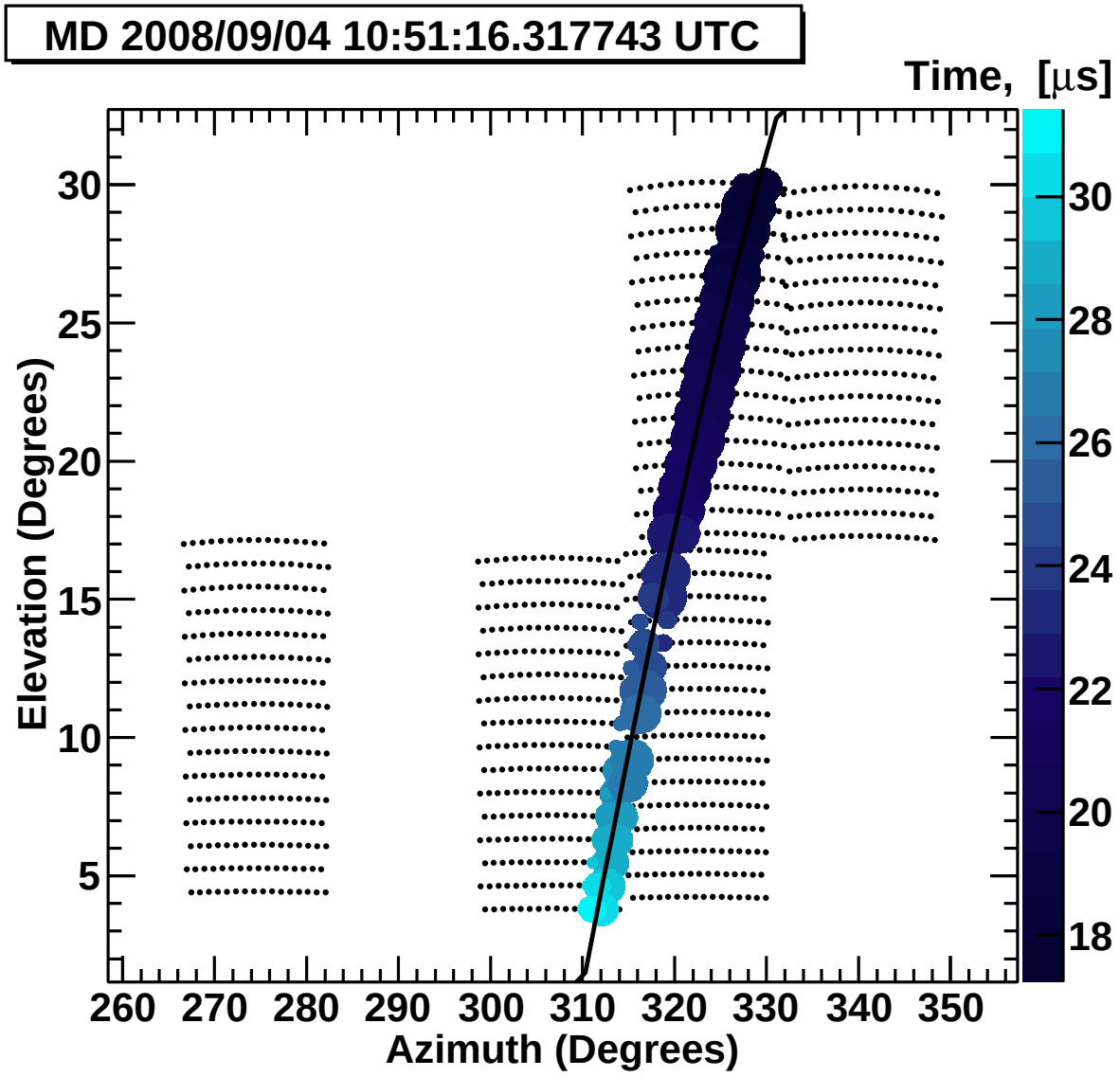

(a) Event Display

Figure 11.15: Event with $10^{19.84}$ eV energy.

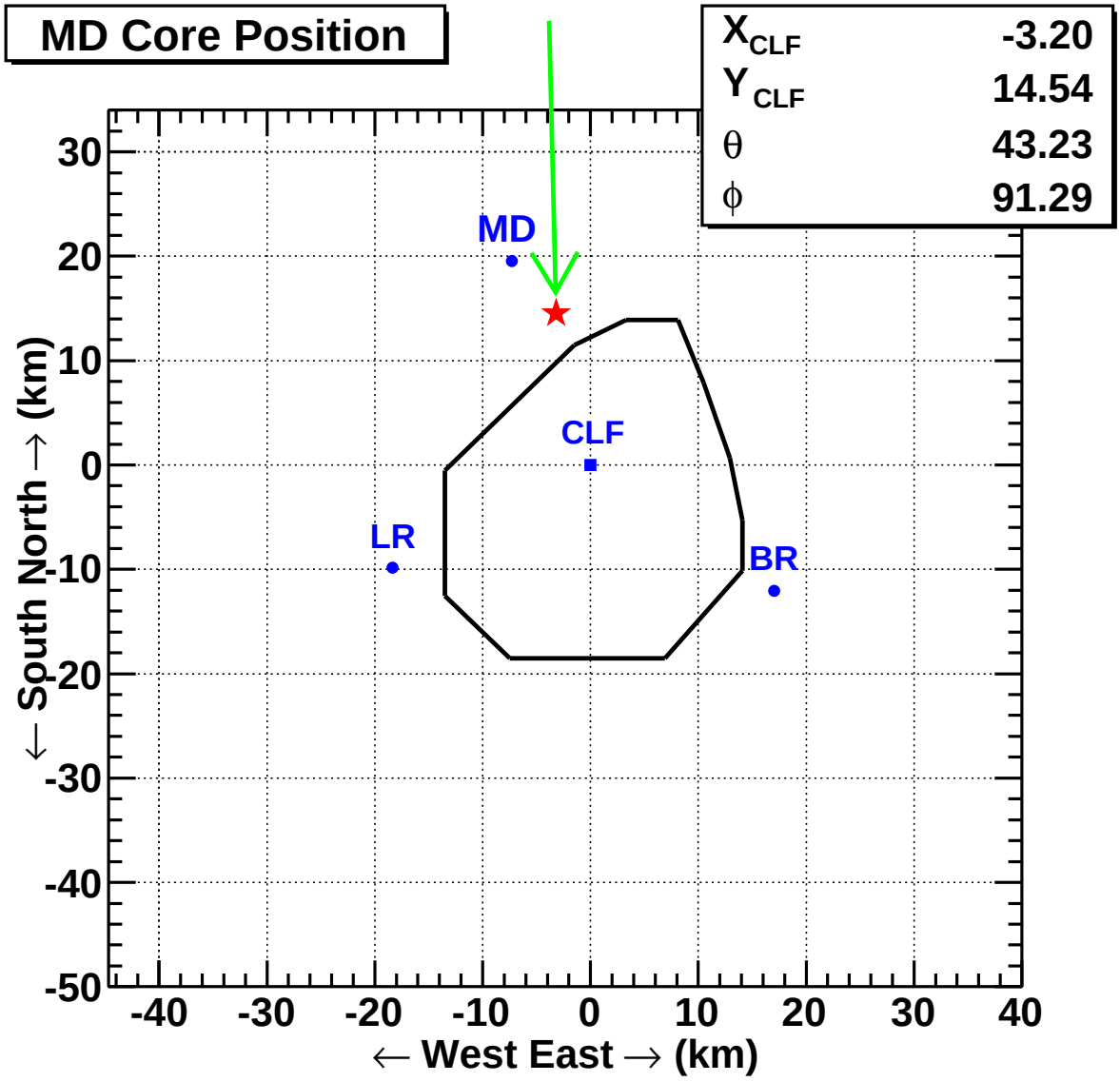

(b) Core Position

Figure 11.15: Continued.

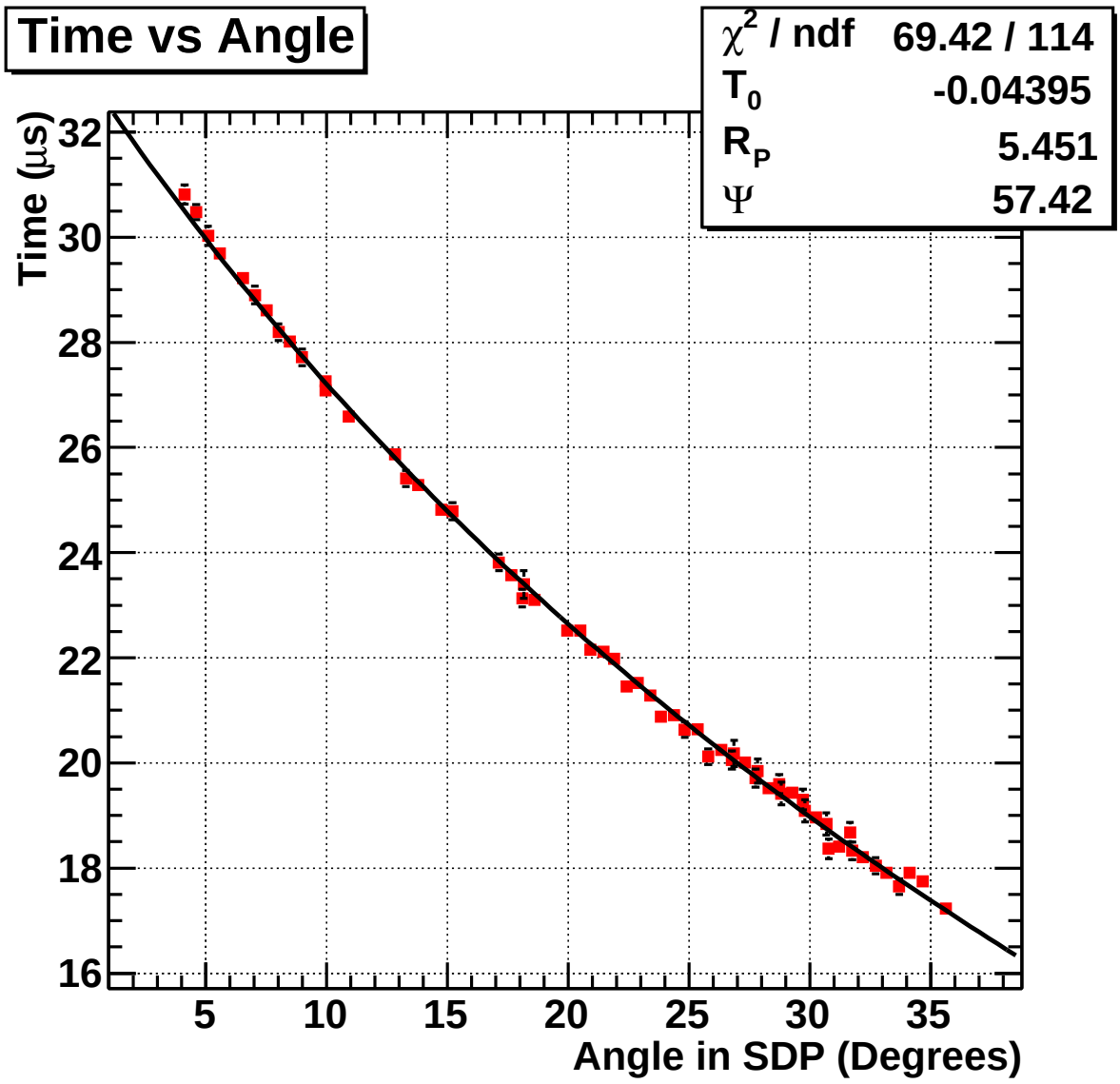

(c) Geometrical Fit

Figure 11.15: Continued.

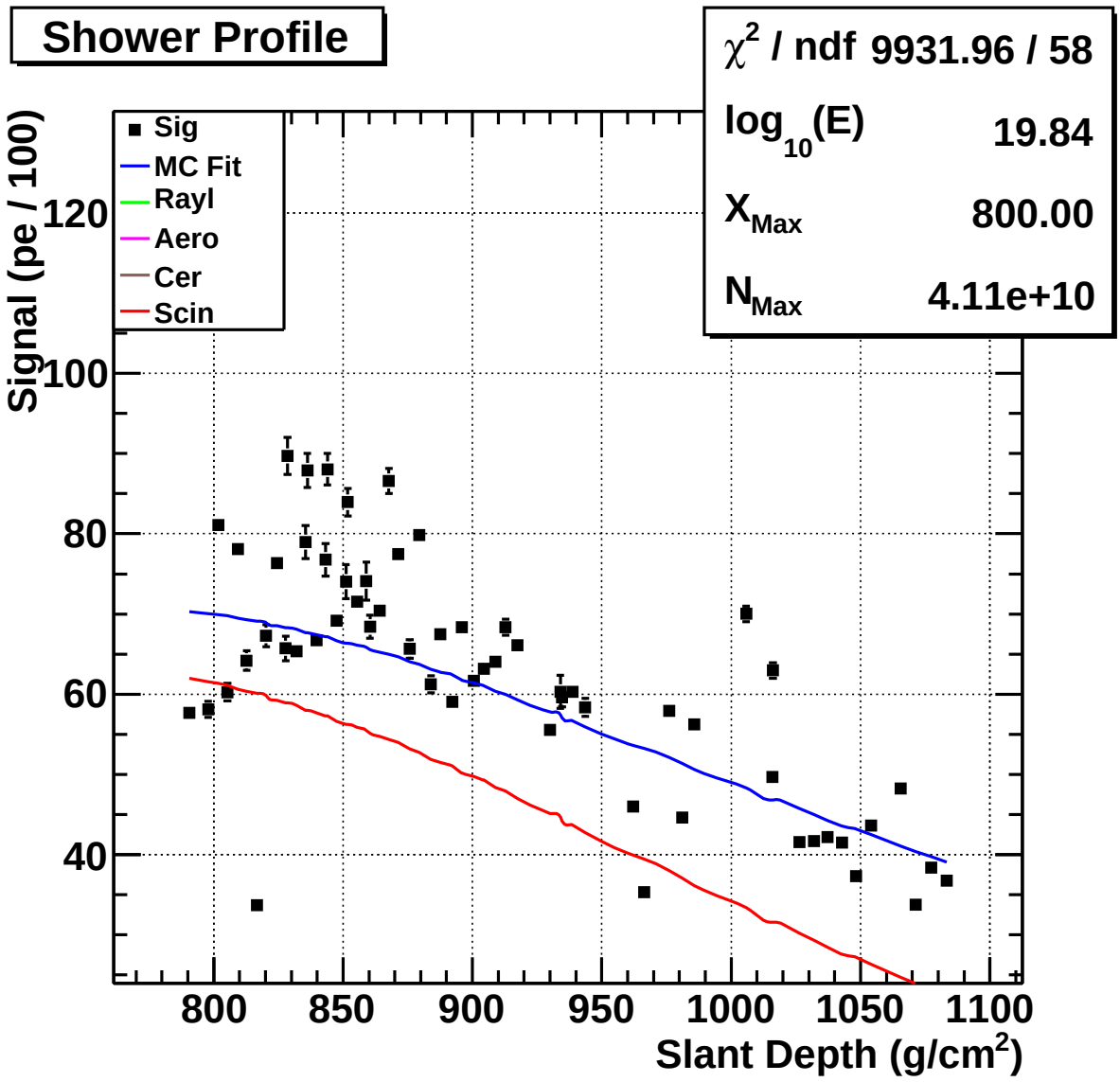

(d) Profile Fit

Figure 11.15: Continued.

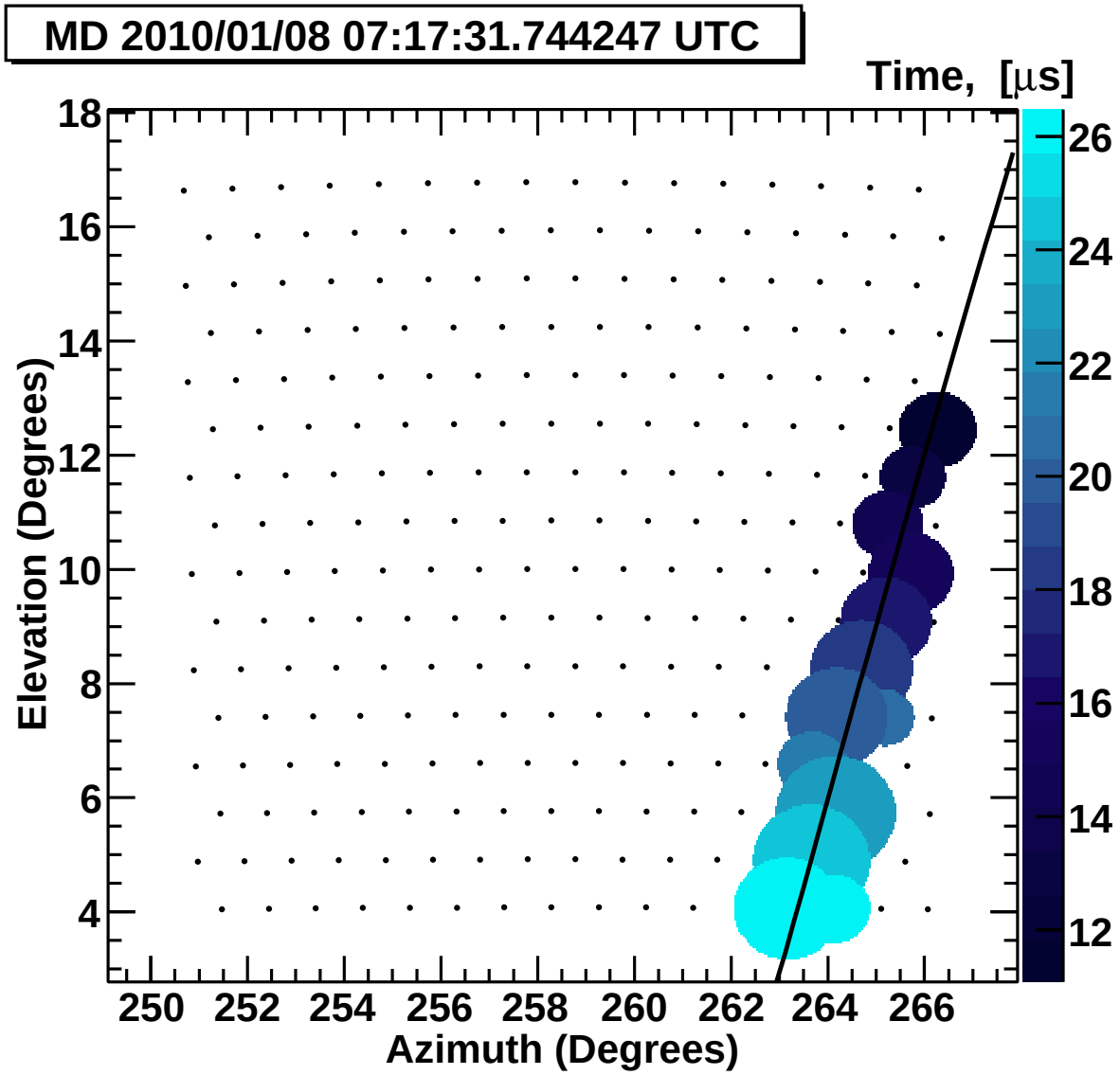

(a) Event Display

Figure 11.16: Event with $10^{19.74}$ eV energy.

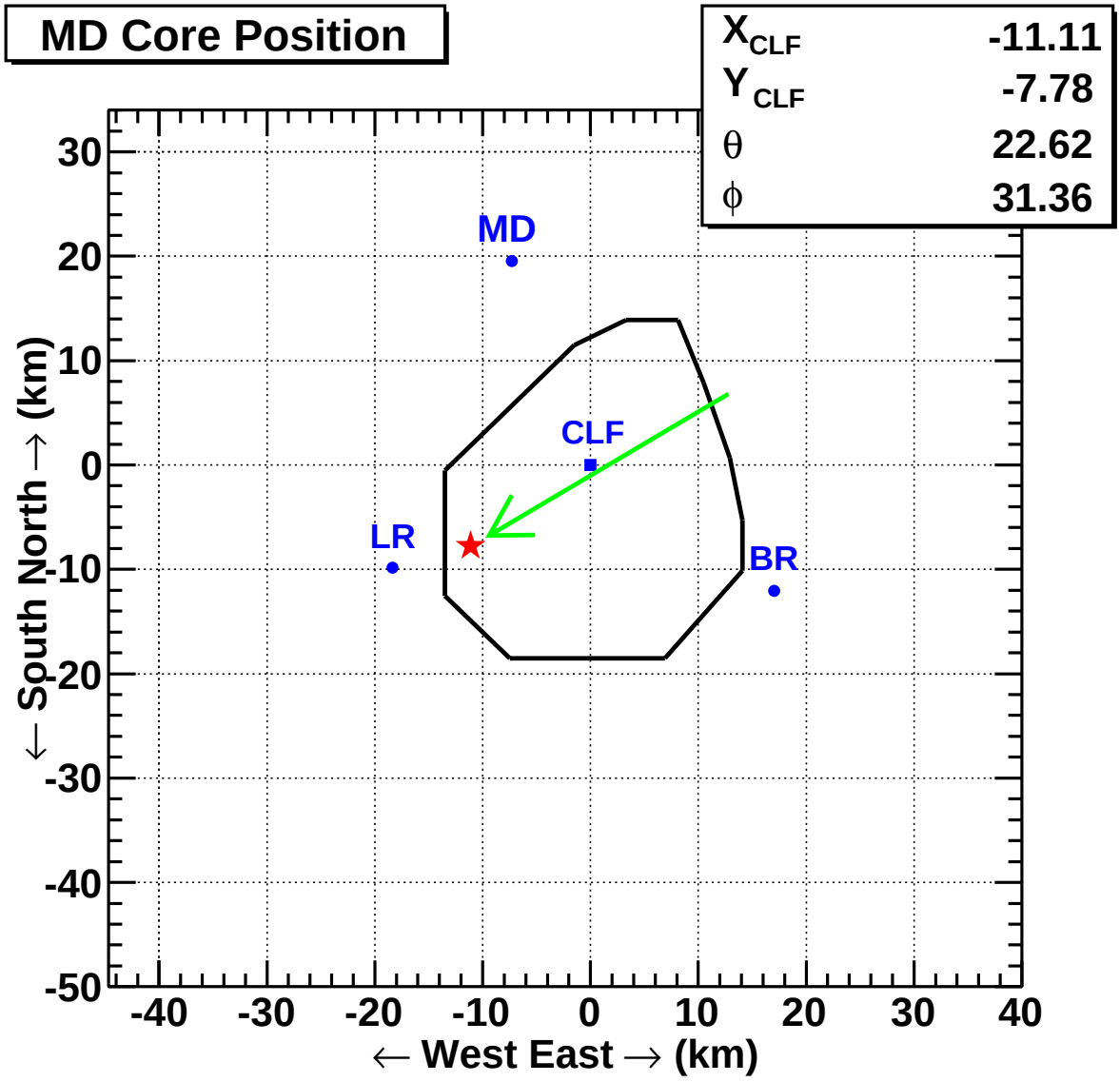

(b) Core Position

Figure 11.16: Continued.

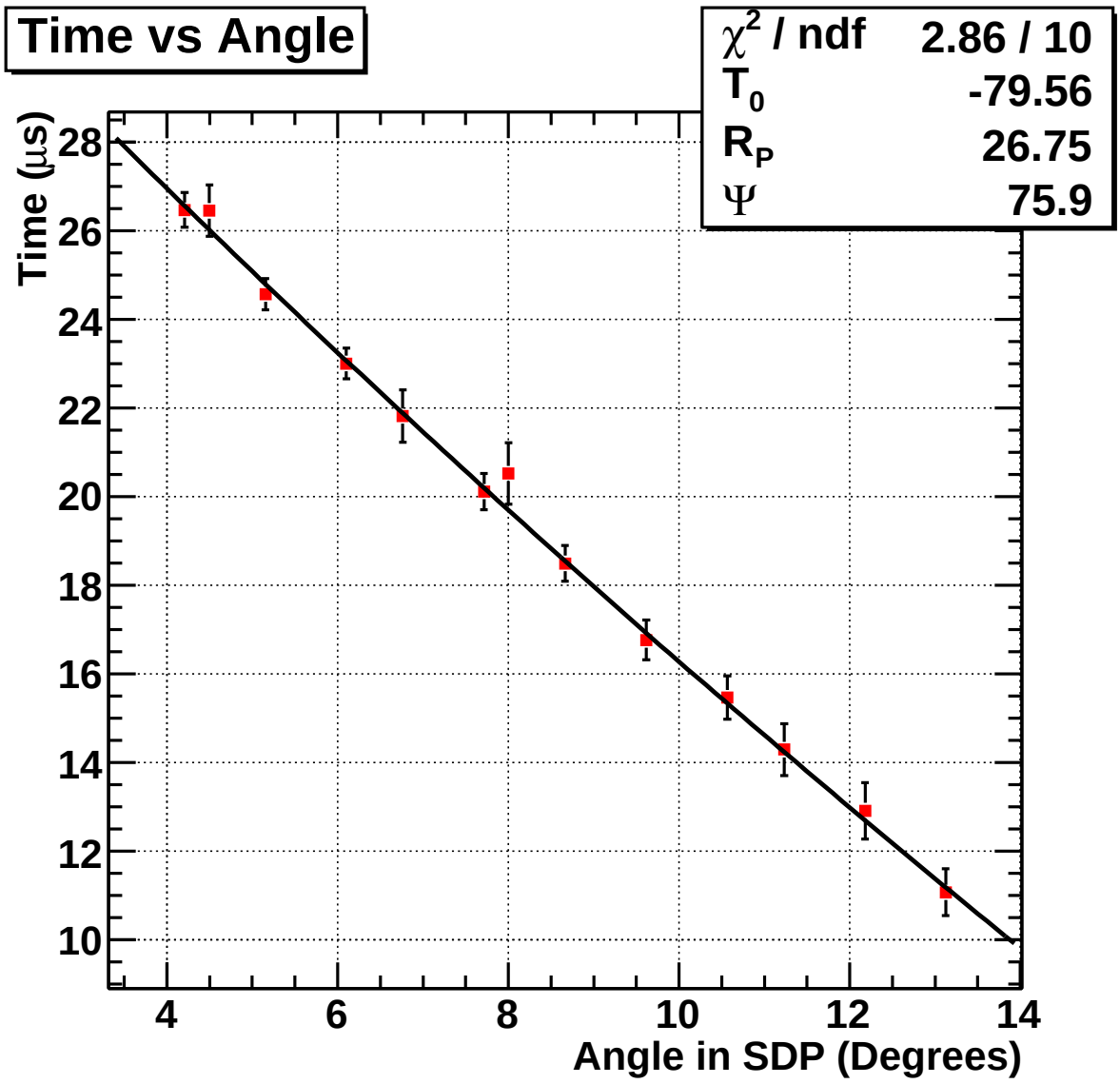

(c) Geometrical Fit

Figure 11.16: Continued.

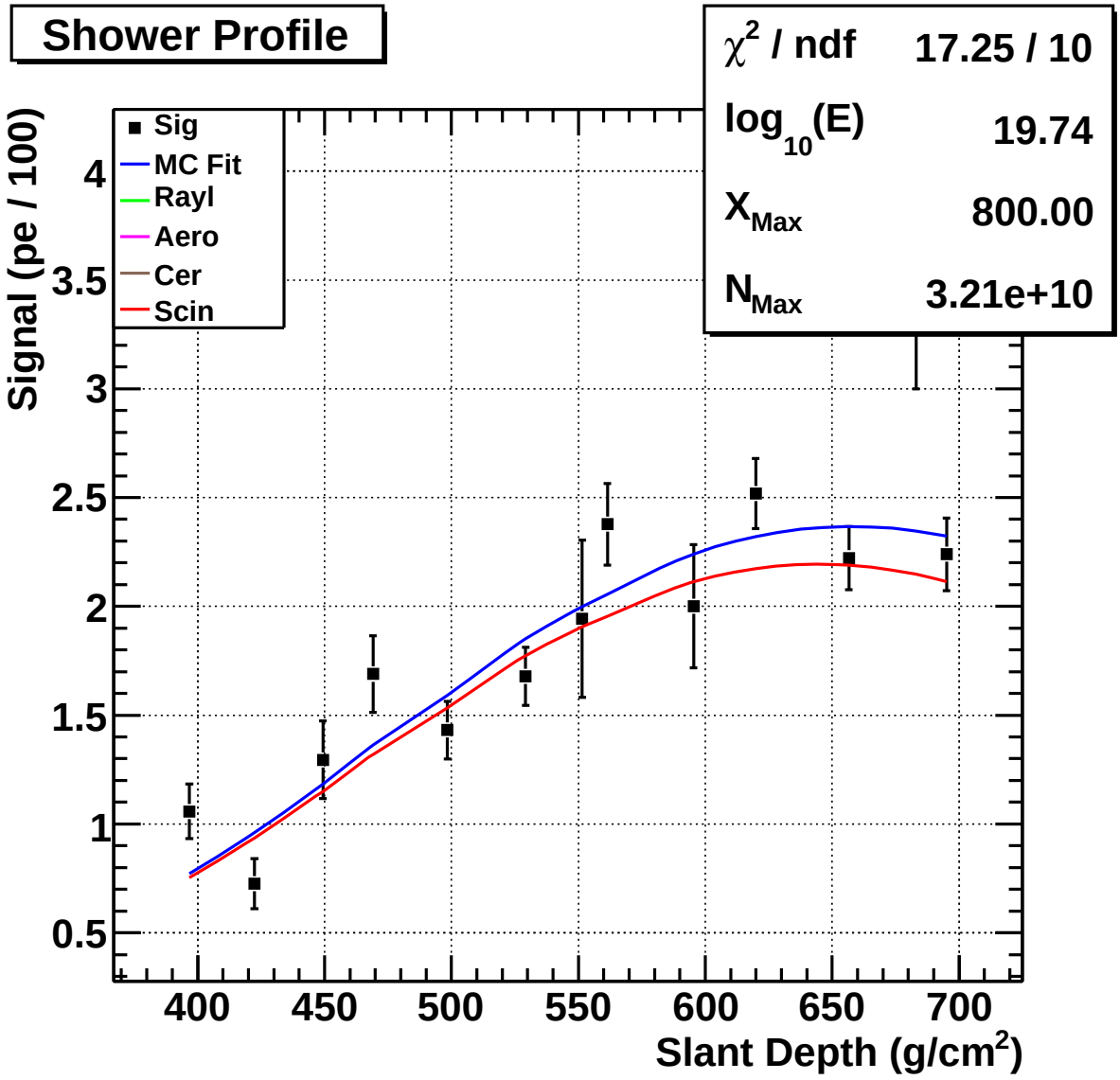

(d) Profile Fit

Figure 11.16: Continued.

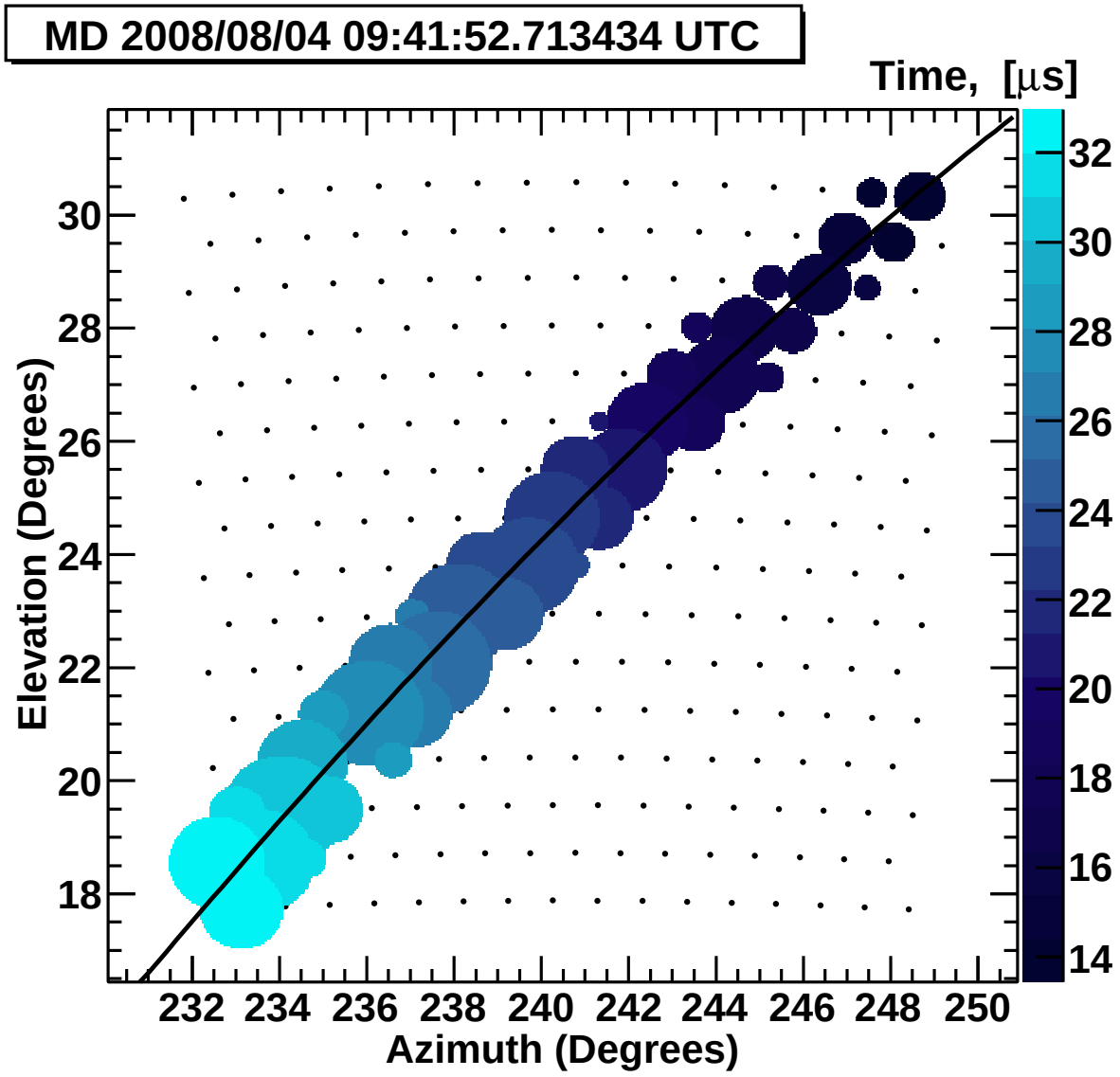

(a) Event Display

Figure 11.17: Event with $10^{19.72}$ eV energy.

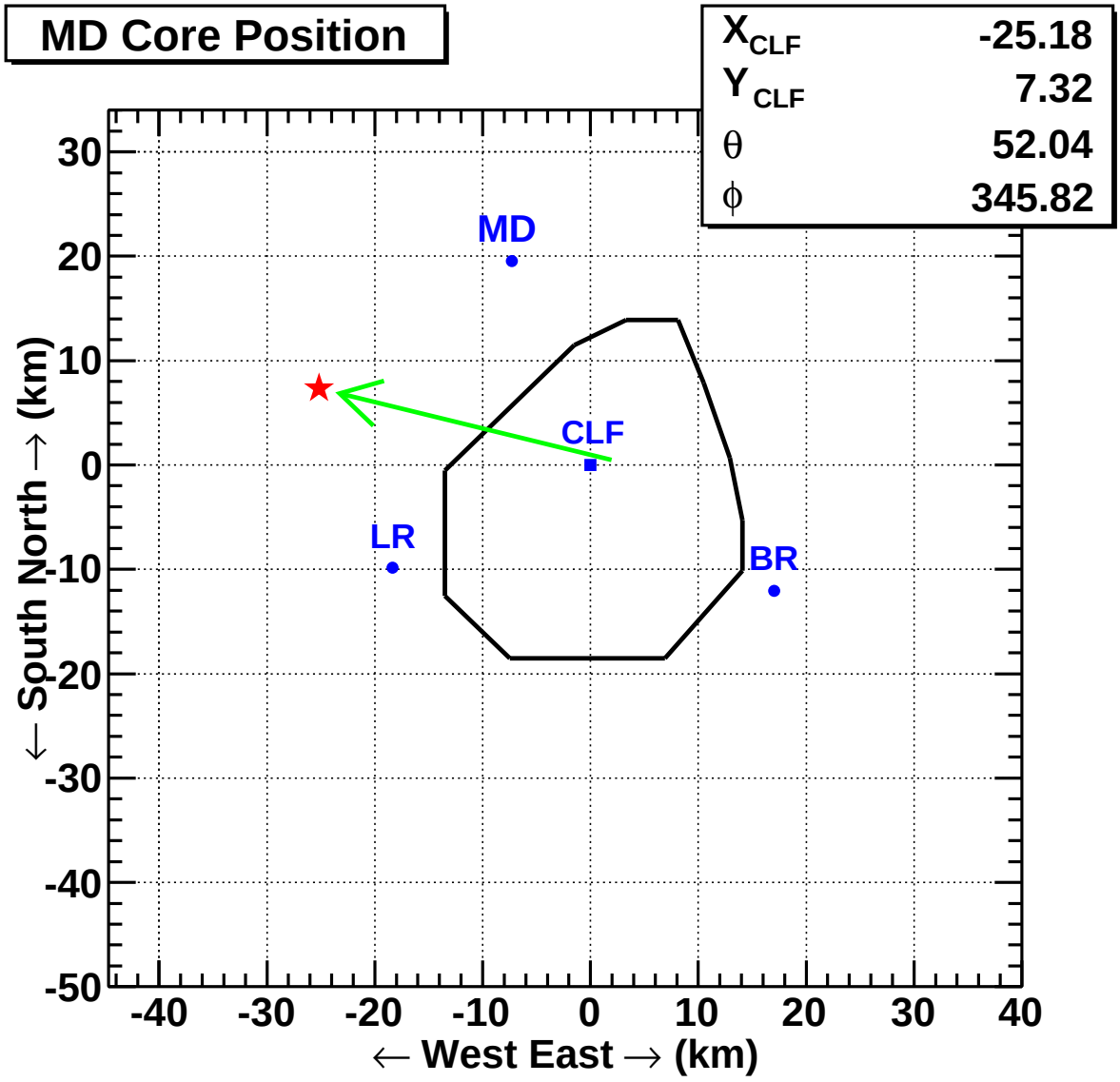

(b) Core Position

Figure 11.17: Continued.

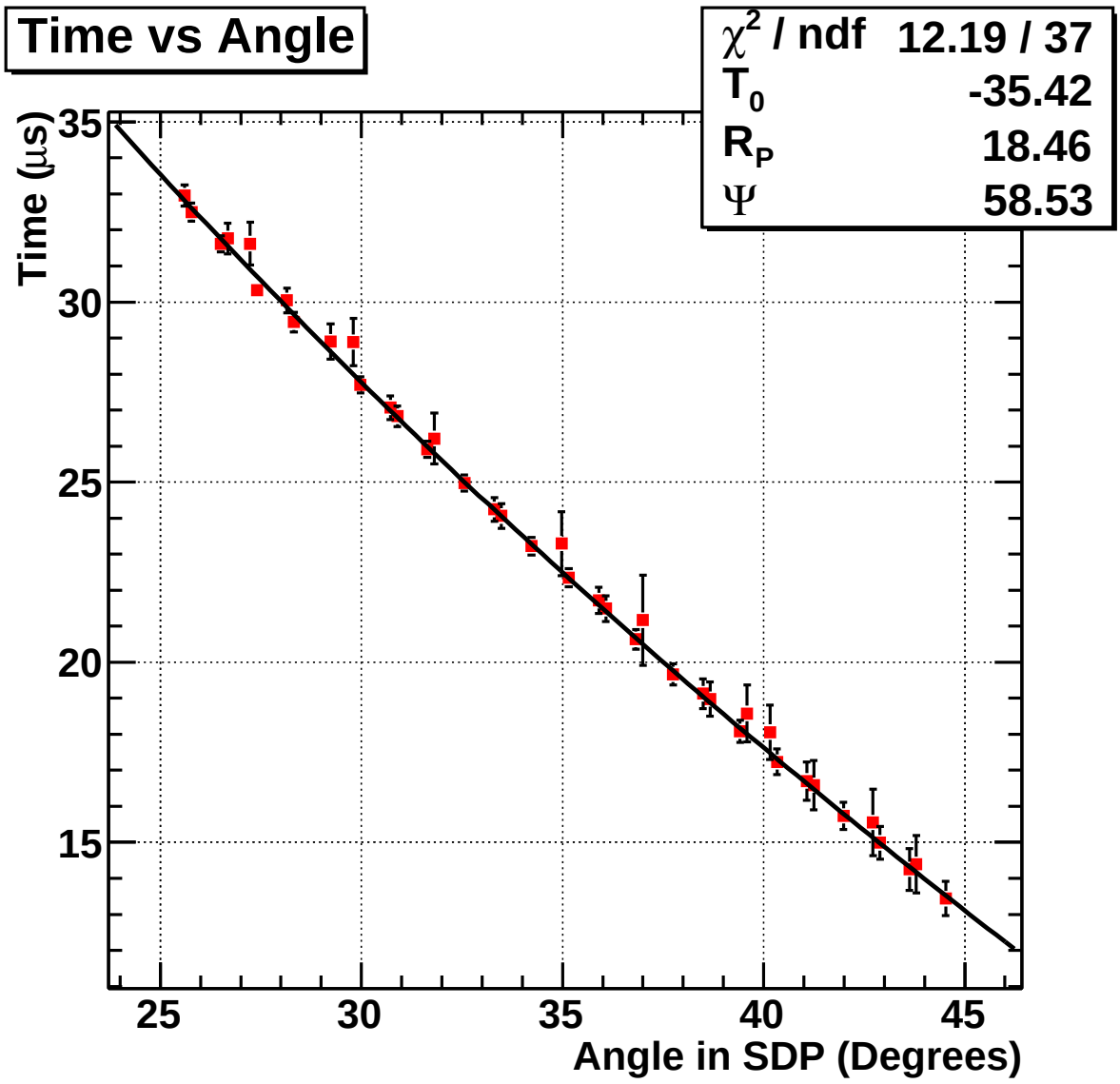

(c) Geometrical Fit

Figure 11.17: Continued.

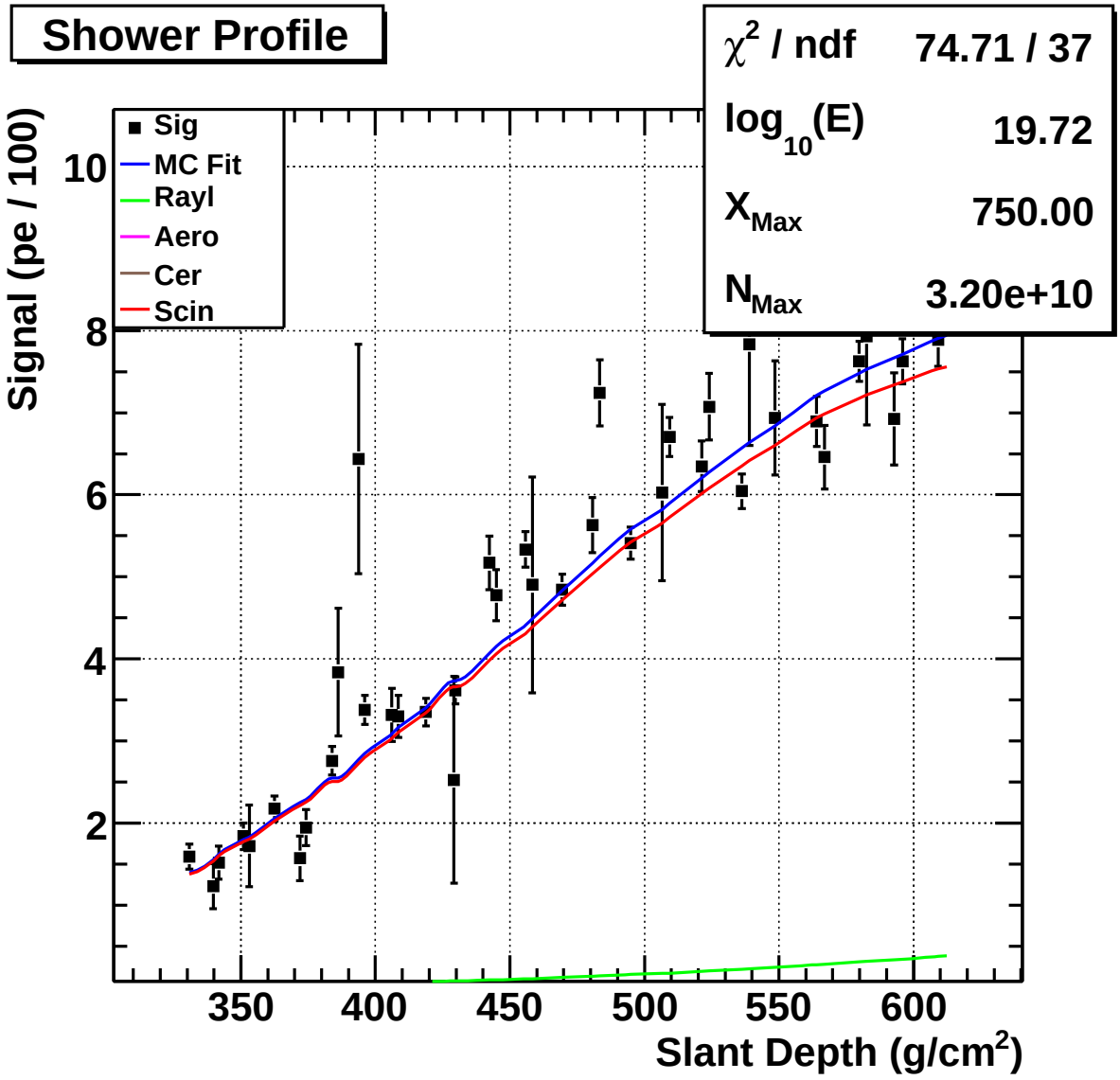

(d) Profile Fit

Figure 11.17: Continued.

CHAPTER 12

ATMOSPHERIC CORRELATIONS

As described in Chapter 4, fluorescence detectors work by observing photons emitted in the wake of ionizing particle interactions. There are two primary ways the atmosphere can attenuate the produced light: molecular scattering and aerosol scattering. The molecular scattering is nearly constant, but the amount of aerosol in the atmosphere can change over the course of an hour or two and requires real-time measurement. In an effort to understand the atmosphere, two studies were performed: aerosol correlations with the HiRes-1 data and the dependence of the energy scale of Middle Drum events on the aerosol concentration.

12.1 HiRes-1 Aerosol Correlations

Starting in October 1999, the HiRes experiment used two steerable laser systems (SLS) (see section 5.2.5.1) to monitor the atmosphere by sweeping over the fiducial volume of the detectors [69]. The light scattered from one laser (e.g., HiRes-2) was observed by the other fluorescence detector site (e.g., HiRes-1) in bistatic lidar mode. From these events a vertical aerosol optical depth (VAOD) is determined, which allows us to understand this factor in the overall attenuation by the atmosphere.

A study was performed on the HiRes-1 data in an attempt to determine whether or not the VAOD distribution can be correlated to observed air shower parameter distributions (e.g., the inverse angular speed). The motivation for this study was to see whether the night-by-night aerosol conditions could be recovered for the time periods prior to the installation of the steerable lasers or while they were down for repairs.

This chapter is the only documentation of this study and is included for the benefit of the HiRes and TA collaborations. This was a preliminary analysis with the intent to determine if a more thorough study is warranted.

12.1.1 VAOD Fitting

Proper energy calibration requires knowledge of the aerosol density and distribution in order to determine an accurate correction to the attenuation of the fluorescence light observed by the telescope. The measurable quantities include:

- Vertical Aerosol Optical Depth (VAOD): quantifies the vertical laser shot intensity at height z described by the equation

$$I(z) = I_0 e^{-z/VAOD}; \tag{12.1}$$

- Horizontal Attenuation Length (L): quantifies the light intensity of a horizontal laser shot at distance r and height $z = 0$ described by the equation

$$I(r) = I_0 e^{-r/L}; \tag{12.2}$$

- Vertical Scale Height (H): quantifies the aerosol density at height z described by the equation

$$\rho(z) = \rho_0 e^{-z/H}. \tag{12.3}$$

These three quantities are related by:

$$VAOD = \frac{H}{L}. \tag{12.4}$$

Shower track information was chosen from the final selection of AlphaProc events (see section 8.2). Track length (TL), inverse angular speed (IAS), number of photons per good tube (PPGT), and track length per good tube (TLPGT) were chosen as the most likely candidates to give a correlation.

The analysis was divided in three phases. First, the "VAODOP" program pulls out the shower parameter values (see Table 12.1) from the HPLN1 banks and organizes them according to their Julian date. Frequently, the VAOD was determined multiple times during the same night. In these cases a nightly mean and standard deviation was found. The "vaodanal" program brought all of the information together, giving output for every night that atmospheric calibration values existed. This program also incorporated the shower track parameters into the output (see Table 12.1).

12.1.2 Results

Comparisons were made between each aerosol parameter (e.g., VAOD, L, and H) and each track parameter. For a complete search, both the mean and the standard deviations

Table 12.1: Shower parameters used in the aerosol correlation study.

Shower Parameter	Bank
Julian date	HRAW1
Theta	PASSA
Track Length	PASS3
Inverse Angular Speed	PASS3
Photons Per Good Tube	PASS3
N Good Tubes	HPLN1
N Mirrors	HRAW1

of every shower parameter was plotted against the aerosol quantities and the resulting graph was fit to a straight line. To find a clear correlation between the aerosol parameter and the track parameter, the significance in the slope was determined according to

$$S = \frac{Slope}{\sigma_{Slope}}. \tag{12.5}$$

Only good weather nights, with minimal or no clouds, as determined by the operator observation codes (see Table 5.2), were used for the nightly track parameters. Additionally, only those aerosol bins that had more than six nights of track parameter entries were retained and included in the fit (see Tables 12.2, 12.3, and 12.4).

A significance of at least 5σ is considered sufficient correlation between the various combinations. Of these, four parameter combinations showed significant correlation (indicated by bold entries in Tables 12.2 and 12.3 and Figures 12.1, 12.2, 12.3, and 12.4).

The primary motivation for this study was to determine if a night-by-night correction could be applied to the aerosol content of the atmosphere for the data collected by the HiRes-1 detector prior to the onset of the steerable laser systems. A check was performed to determine the uncertainty in these parameters for those nightly values used in the correlation study for those nights with a VAOD of 0.02, 0.03, and 0.04 and, separately, a

Table 12.2: Final VAOD comparison candidates.

Parameters	Slope	Significance
TL	0.110 ± 0.531	0.208
σ_{TL}	-0.884 ± 0.533	1.659
IAS	-0.179 ± 0.078	2.291
$\boldsymbol{\sigma_{\mathbf{IAS}}}$	$\mathbf{-0.690 \pm 0.102}$	**6.770**
PPGT	$\mathbf{-300.295 \pm 50.125}$	**5.991**
$\boldsymbol{\sigma_{\mathbf{PPGT}}}$	$\mathbf{-612.177 \pm 99.118}$	**6.176**
TLPGT	-0.056 ± 0.044	1.269
σ_{TLPGT}	-0.017 ± 0.034	0.508

Table 12.3: Final H comparison candidates.

Parameters	Slope	Significance
TL	0.007 ± 0.017	0.441
σ_{TL}	-0.042 ± 0.018	2.353
IAS	-0.007 ± 0.002	3.005
σ_{IAS}	-0.012 ± 0.005	2.453
PPGT	$\mathbf{-10.119 \pm 1.680}$	**6.024**
σ_{PPGT}	-14.038 ± 4.047	3.469
TLPGT	0.001 ± 0.002	0.435
σ_{TLPGT}	0.002 ± 0.001	1.605

Table 12.4: Final L comparison candidates.

Parameters	Slope	Significance
TL	-0.001 ± 0.003	0.242
σ_{TL}	-0.003 ± 0.003	1.018
IAS	$6.311e-05 \pm 4.211e-04$	0.150
σ_{IAS}	$-3.437e-04 \pm 0.001$	0.465
PPGT	0.112 ± 0.390	0.288
σ_{PPGT}	0.345 ± 0.636	0.543
TLPGT	$2.914e-04 \pm 2.781e-04$	1.048
σ_{TLPGT}	$-5.653e-05 \pm 1.622e-04$	0.348

scale height of 500 m, 750 m, and 1 km. Each shower parameter was checked individually (see Figures 12.5, 12.6, 12.7, 12.8, 12.9, 12.10, 12.11, 12.12, 12.13, 12.14, 12.15, 12.16, and a summary in Table 12.5). As can be seen, the nightly number of photons per good tube is much larger than the uncertainty of the slope of the vertical scale height correlation. The uncertainty of the VAOD values is on the same order as the uncertainty in the slope of each correlation and is also infeasible to use as a parameterization. The aerosol content of the atmosphere changes too drastically on a nightly basis to parameterize with observed events.

12.2 Atmospheric Energy Scale of TAMD

An average vertical aerosol optical depth (VAOD) of 0.04 was found at Dugway Proving Grounds for the HiRes experiment (see Figure 4.6). Since the VAOD value had not been determined for the Telescope Array at the time of the original spectrum analysis, the same value was assumed for the preliminary reconstruction of the Middle Drum data. A test was performed to determine if the energy reconstructed with this assumption was robust by repeating the reconstruction of the Middle Drum data with

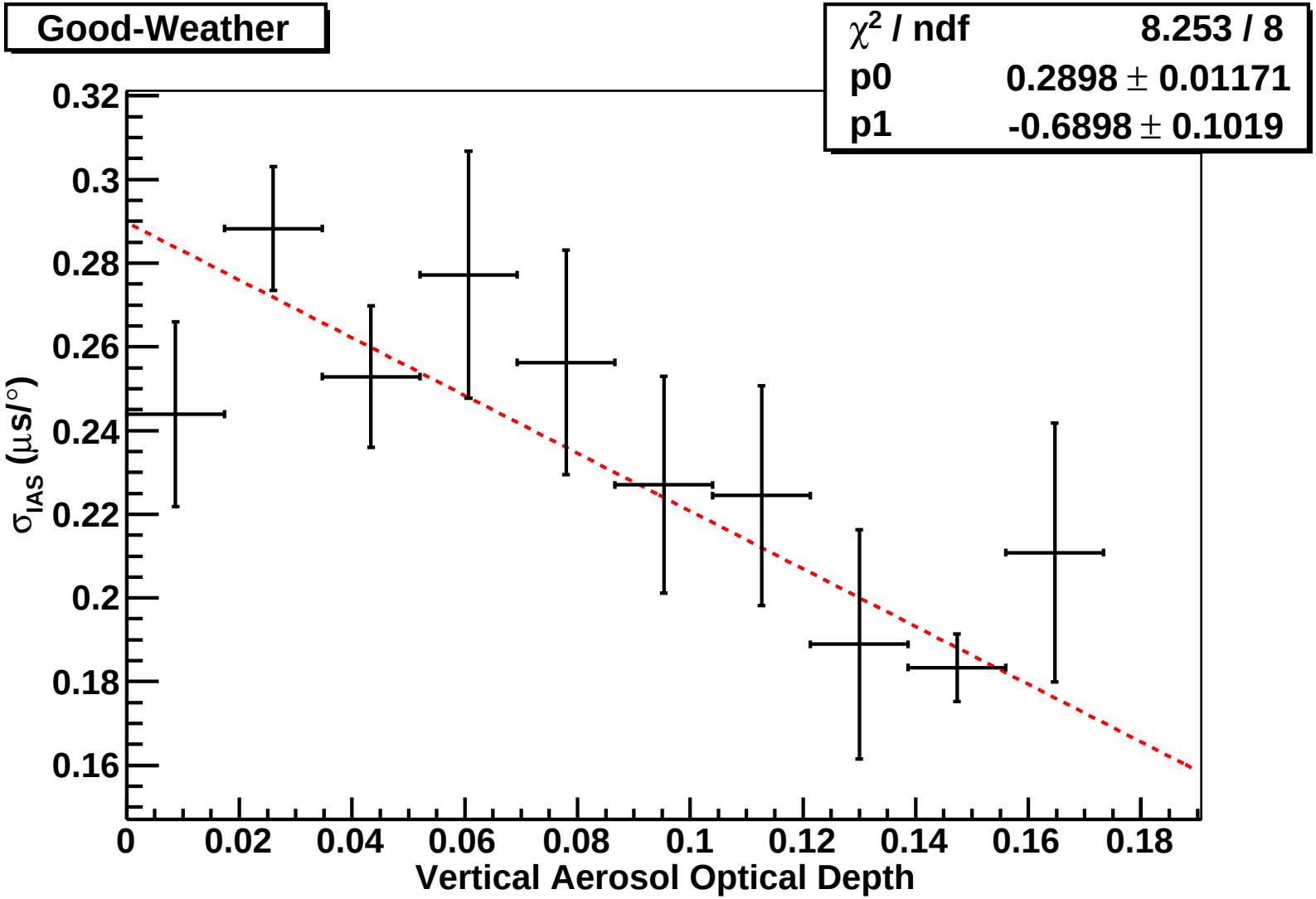

Figure 12.1: RMS in the inverse angular speed distribution as a function of VAOD.

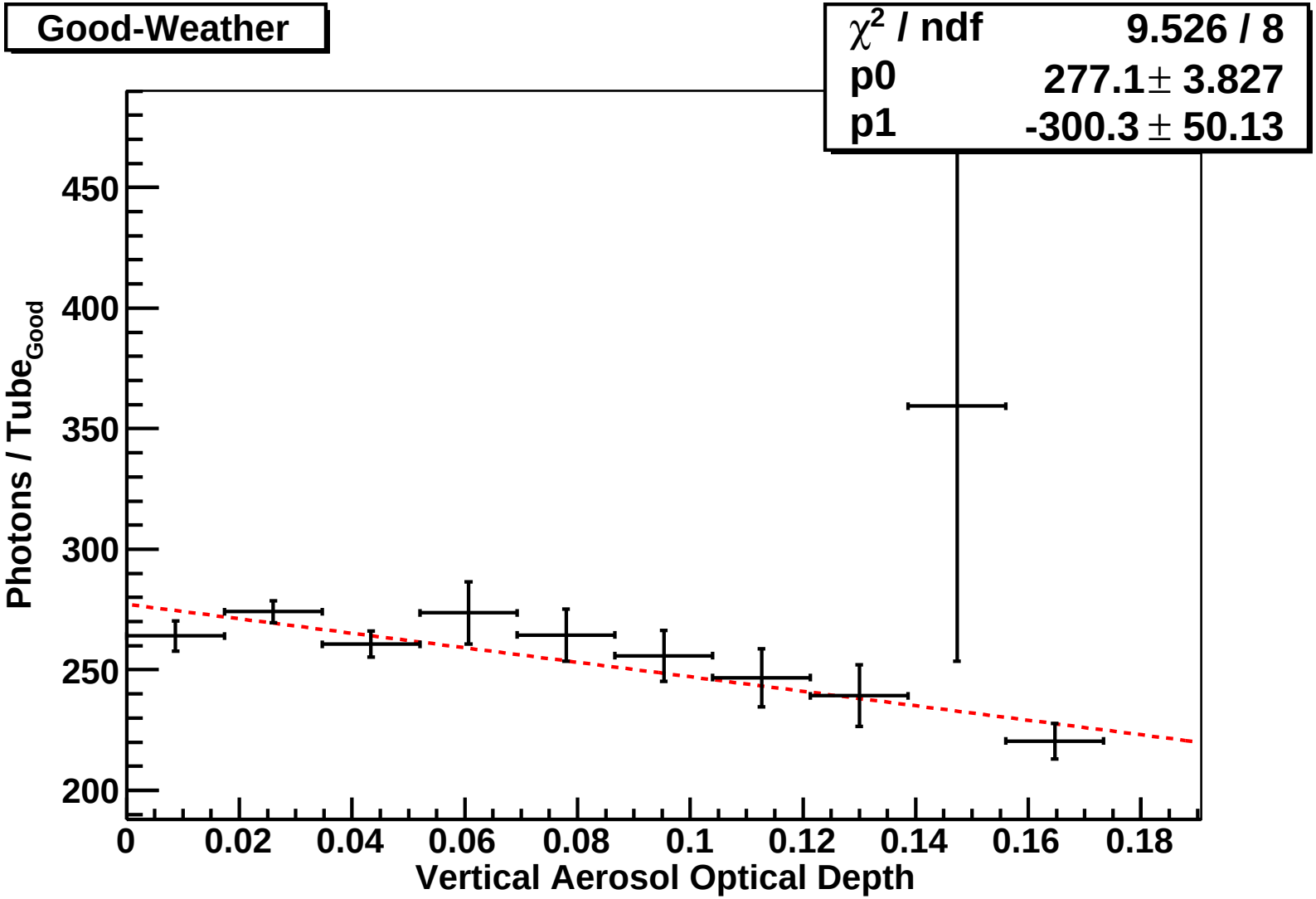

Figure 12.2: Average number of photons per track-related tube as a function of VAOD.

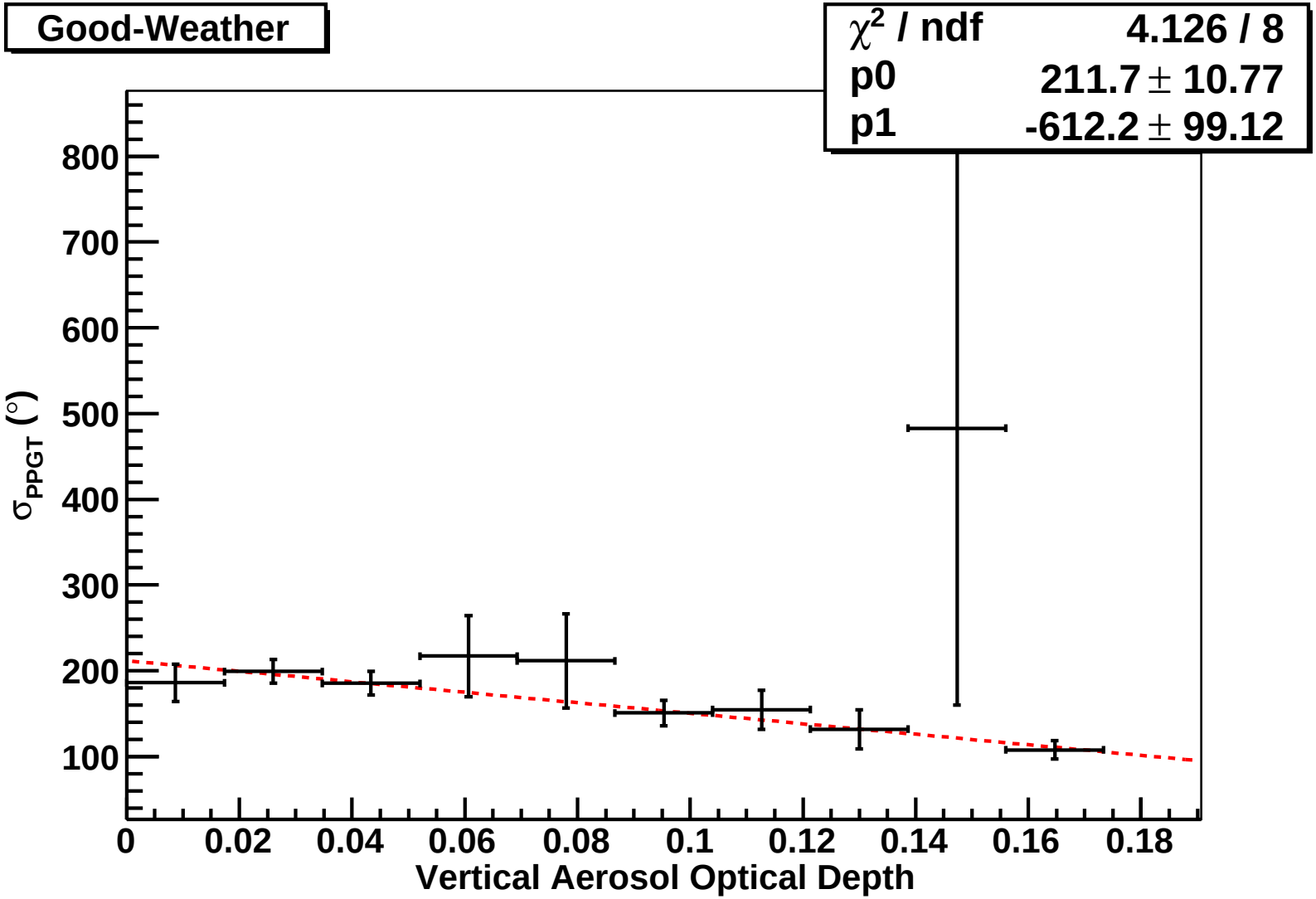

Figure 12.3: RMS of the number of photons per track-related tube distribution as a function of VAOD.

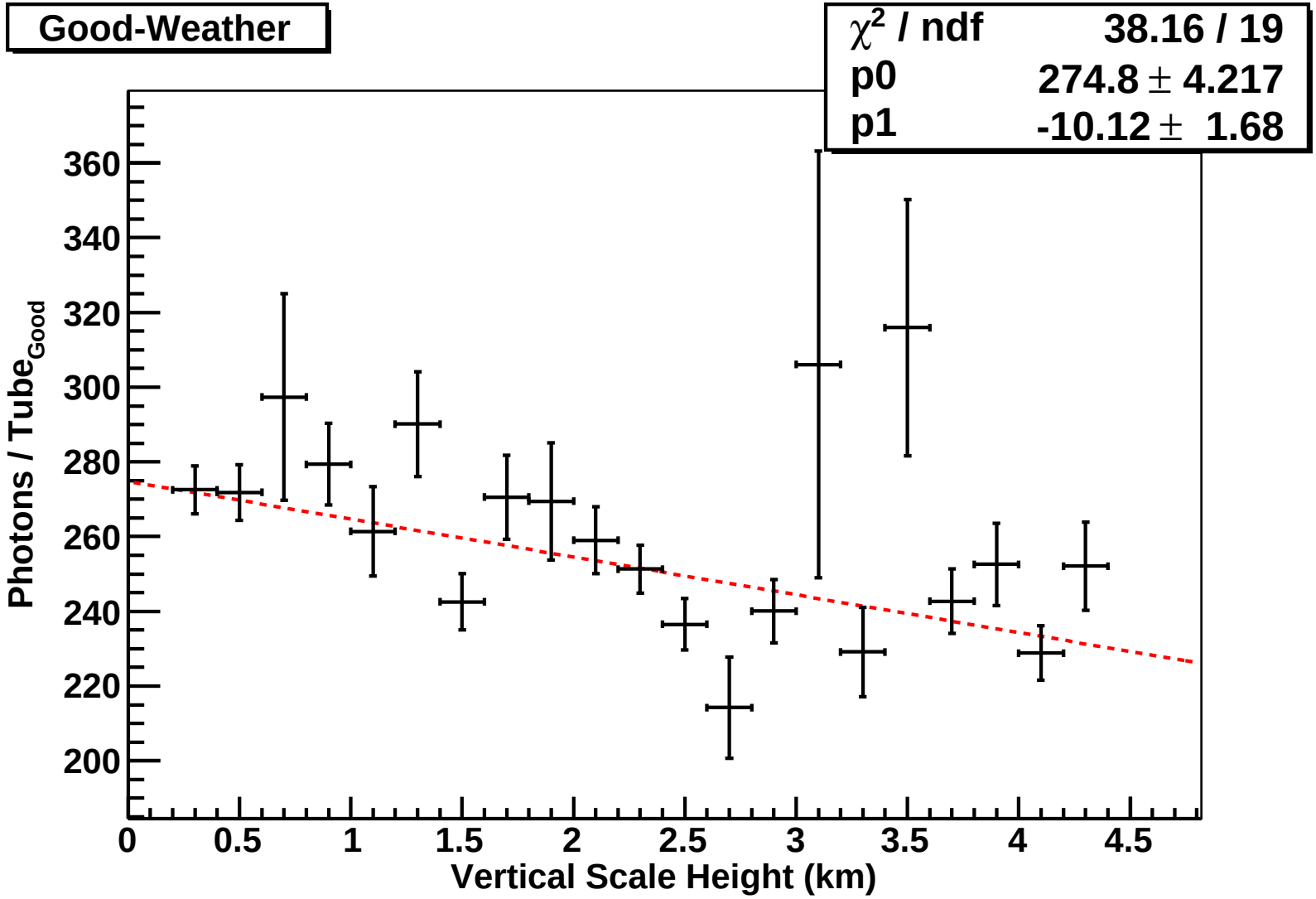

Figure 12.4: Average number of photons per track-related tube as a function of H.

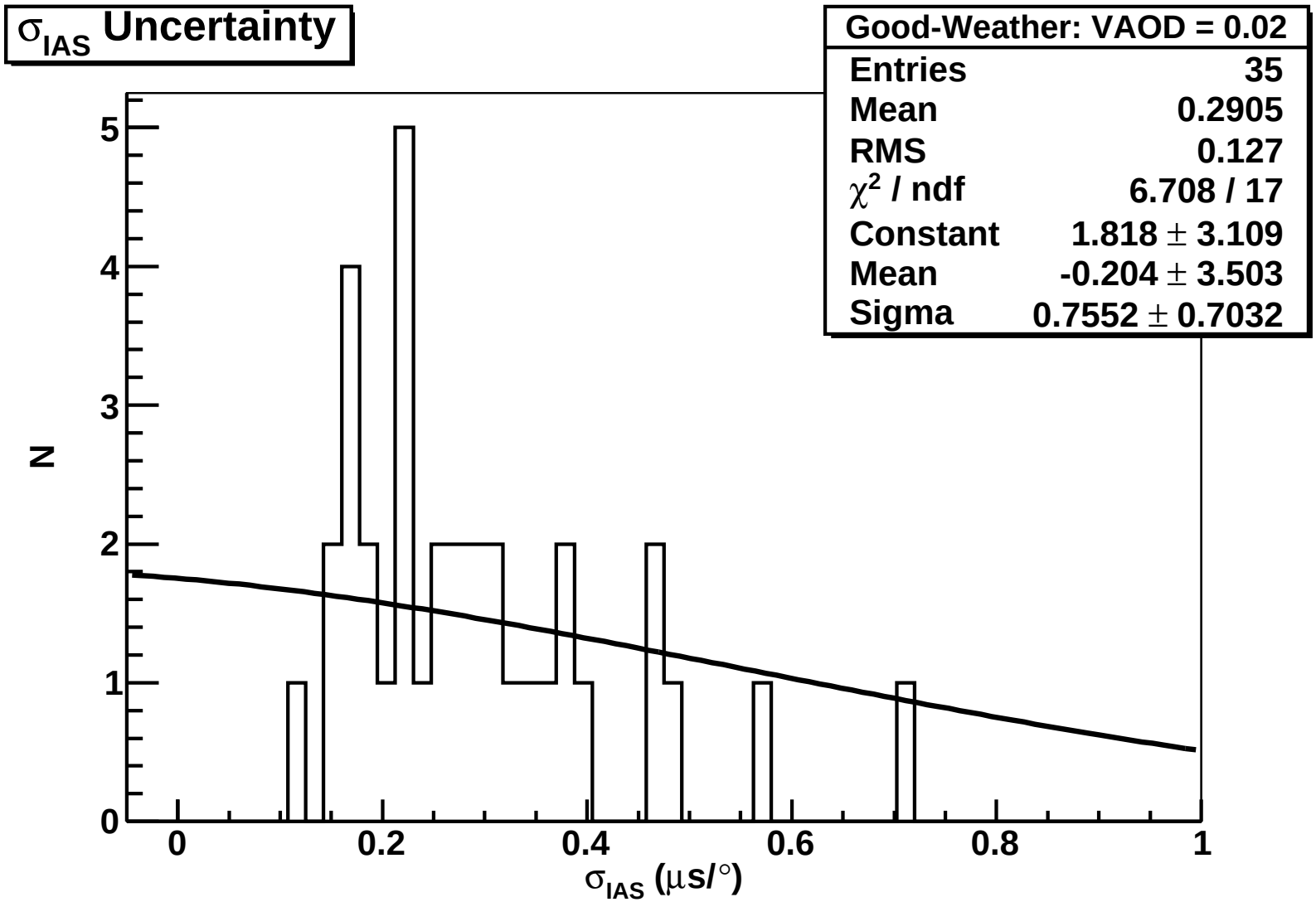

Figure 12.5: The nightly uncertainty in the standard deviation of the inverse angular speed of events correlated with a vertical aerosol optical depth of 0.02.

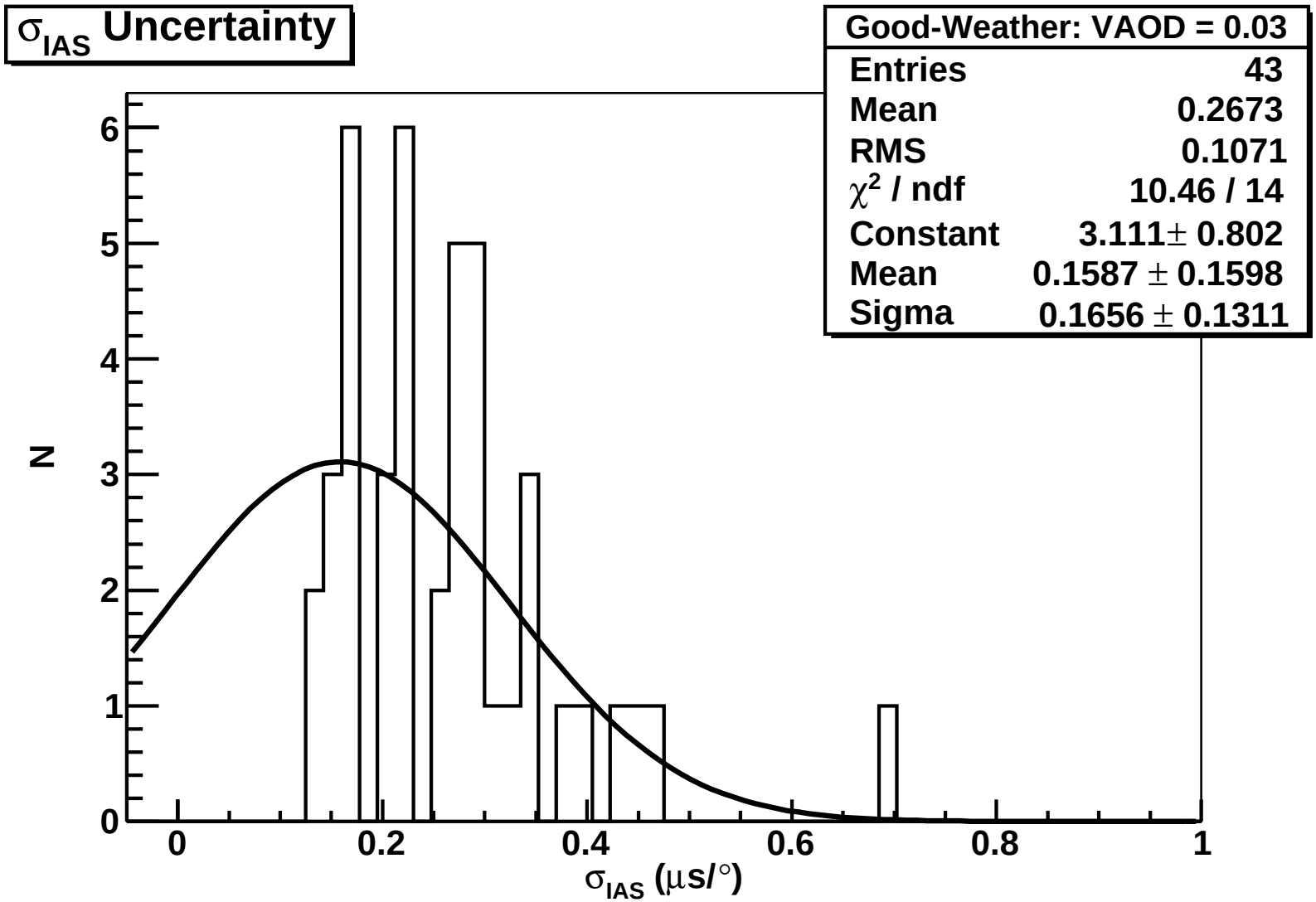

Figure 12.6: The nightly uncertainty in the standard deviation of the inverse angular speed of events correlated with a vertical aerosol optical depth of 0.03.

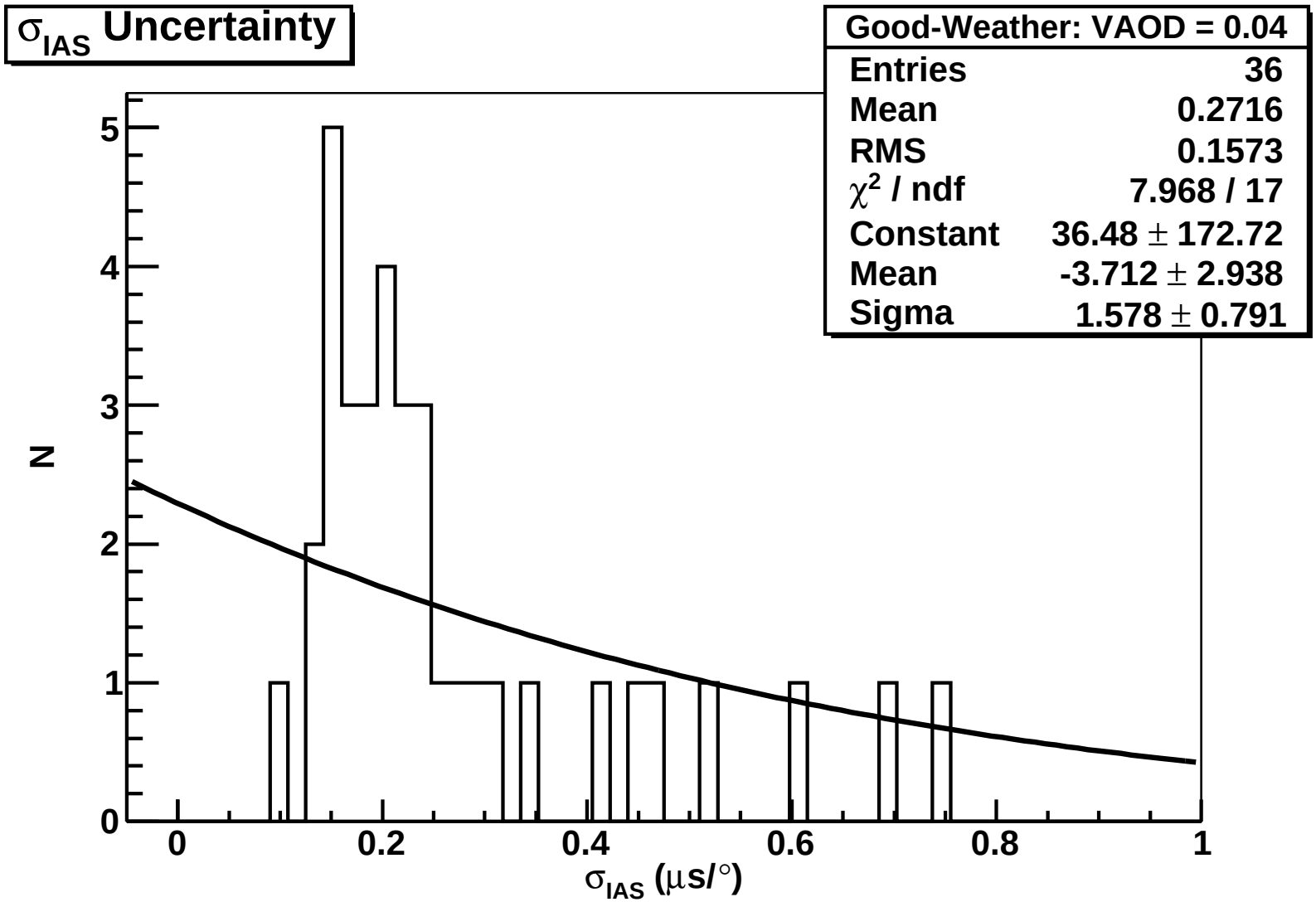

Figure 12.7: The nightly uncertainty in the standard deviation of the inverse angular speed of events correlated with a vertical aerosol optical depth of 0.04.

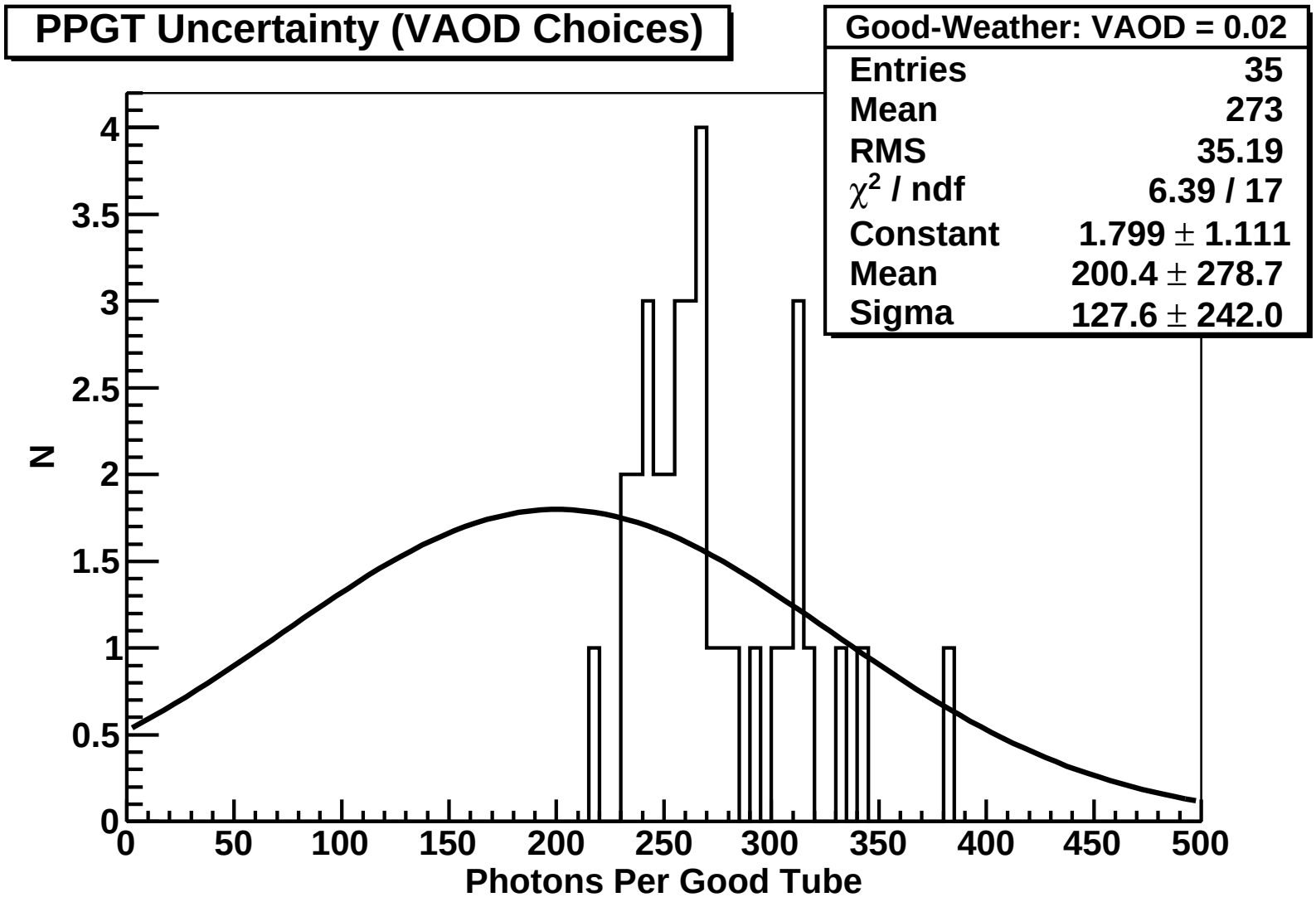

Figure 12.8: The nightly uncertainty in the number of photons per good tube of events correlated with a vertical aerosol optical depth of 0.02.

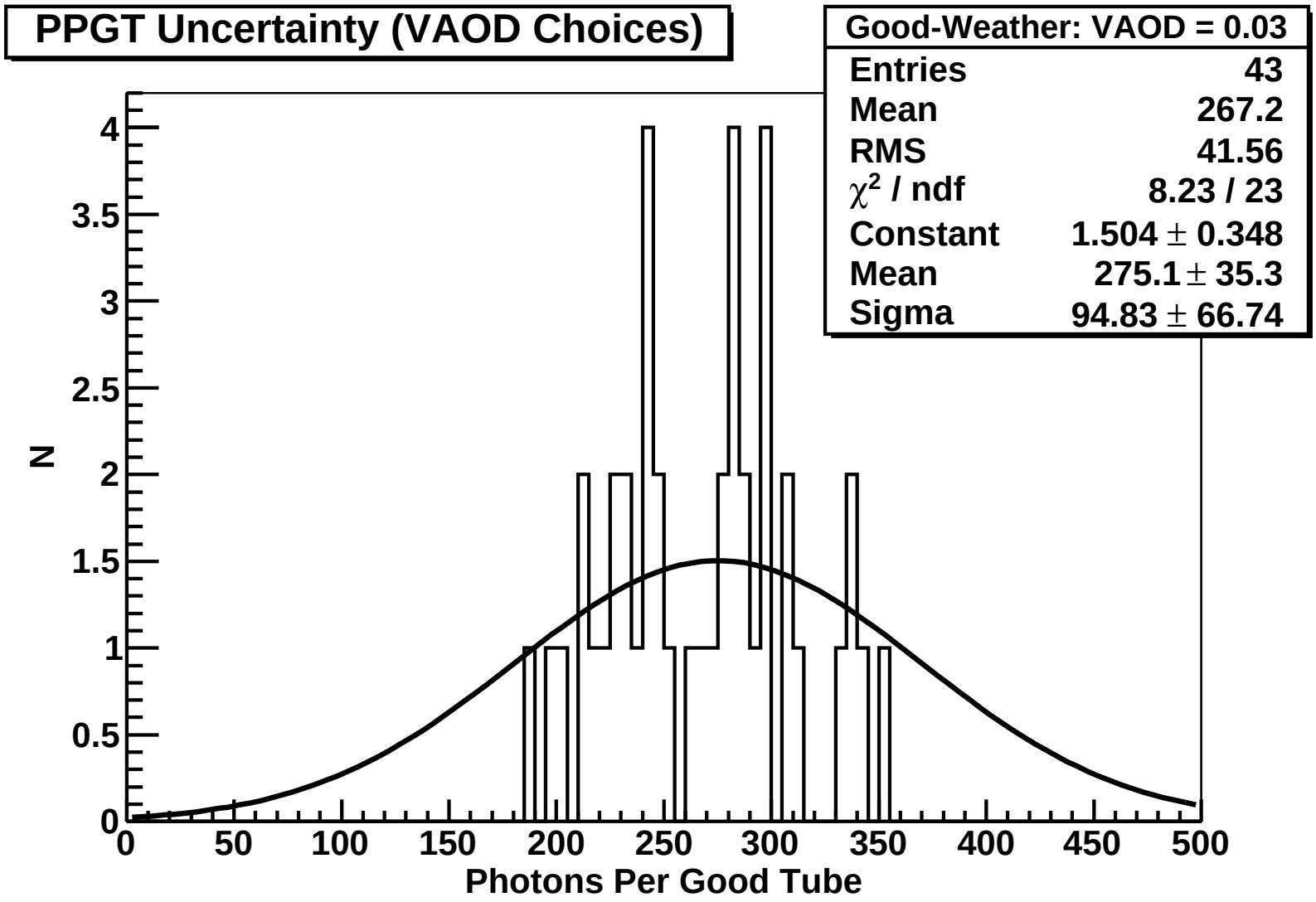

Figure 12.9: The nightly uncertainty in the number of photons per good tube of events correlated with a vertical aerosol optical depth of 0.03.

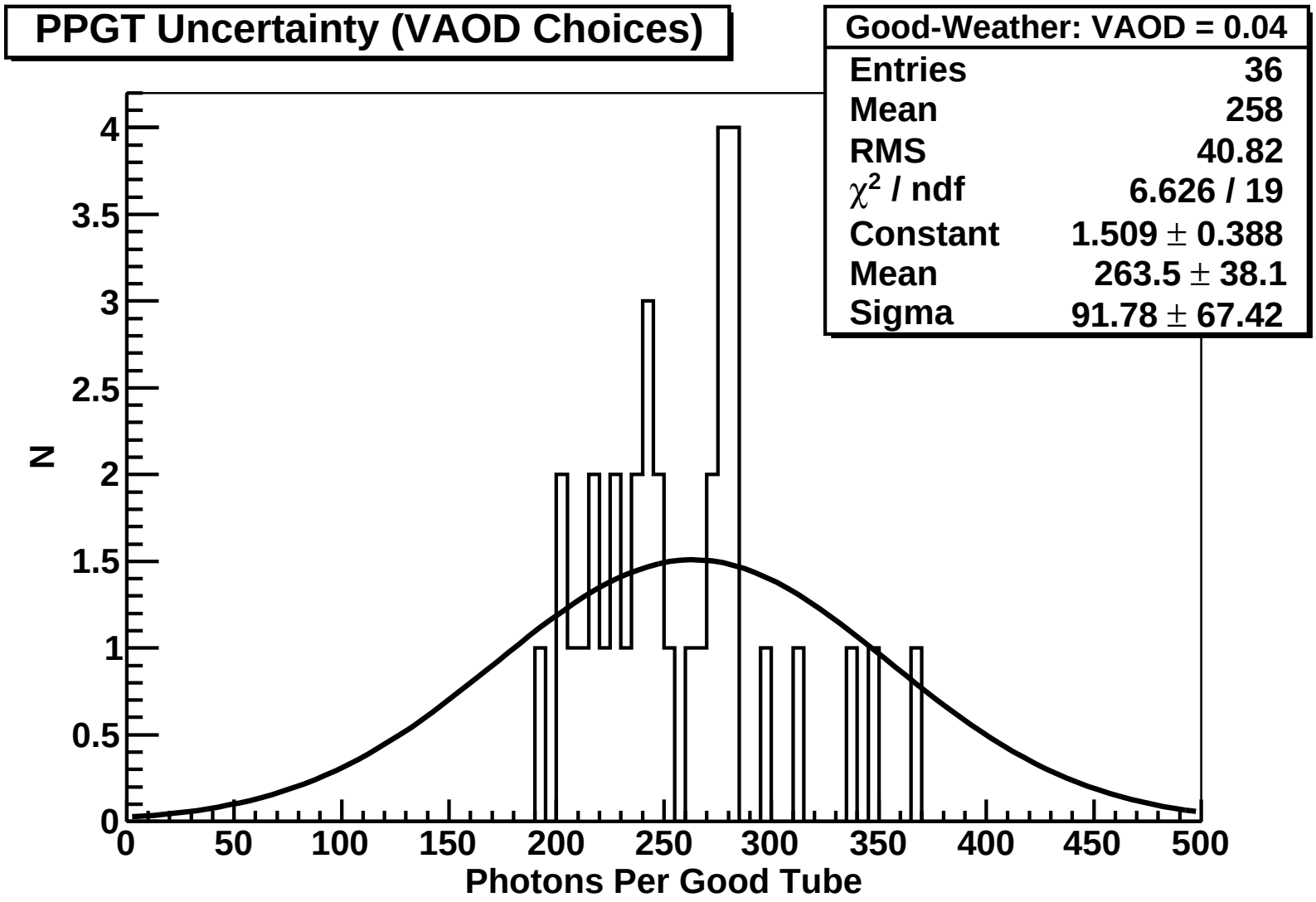

Figure 12.10: The nightly uncertainty in the number of photons per good tube of events correlated with a vertical aerosol optical depth of 0.04.

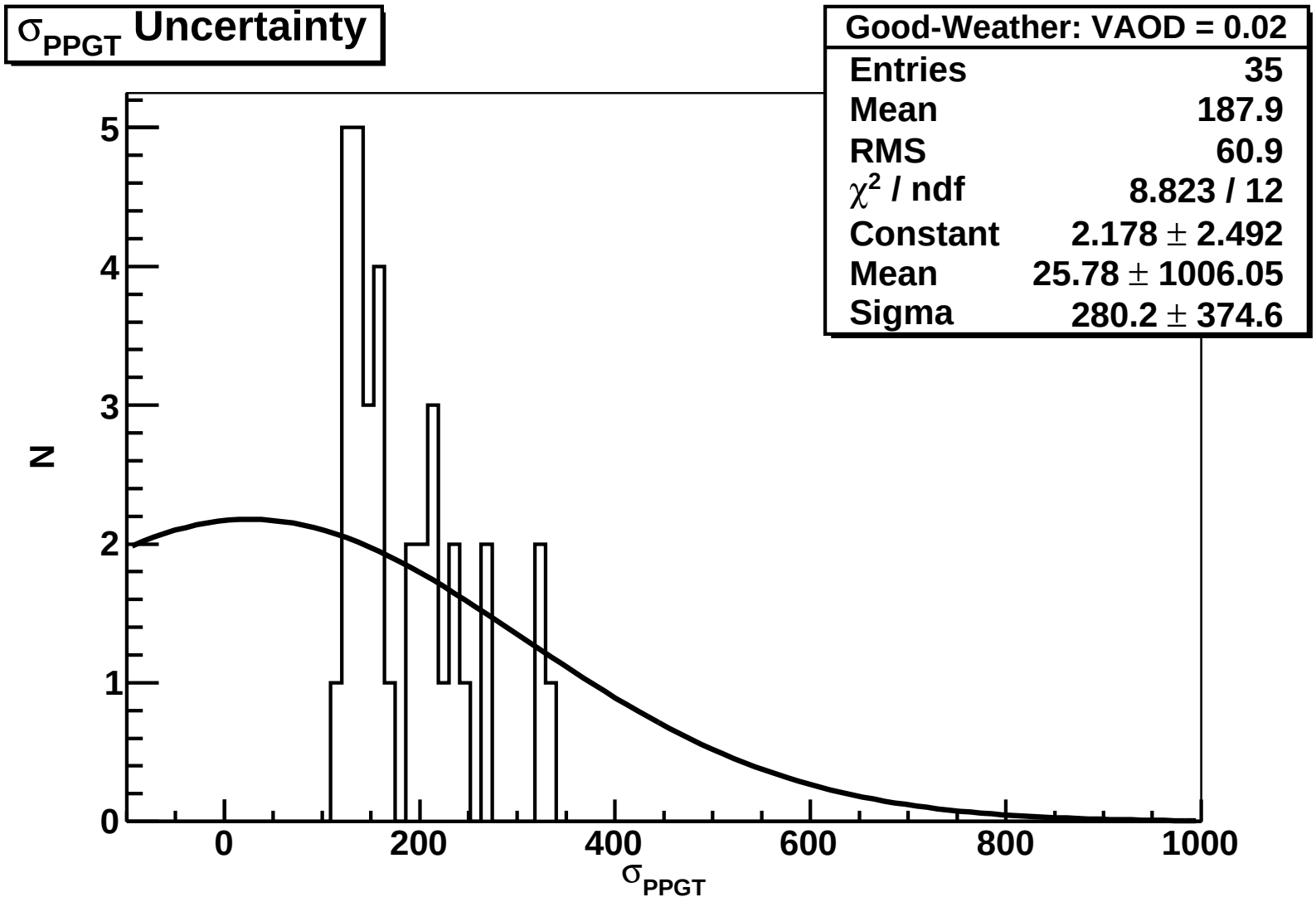

Figure 12.11: The nightly uncertainty in the standard deviation of the number of photons per good tube of events correlated with a vertical aerosol optical depth of 0.02.

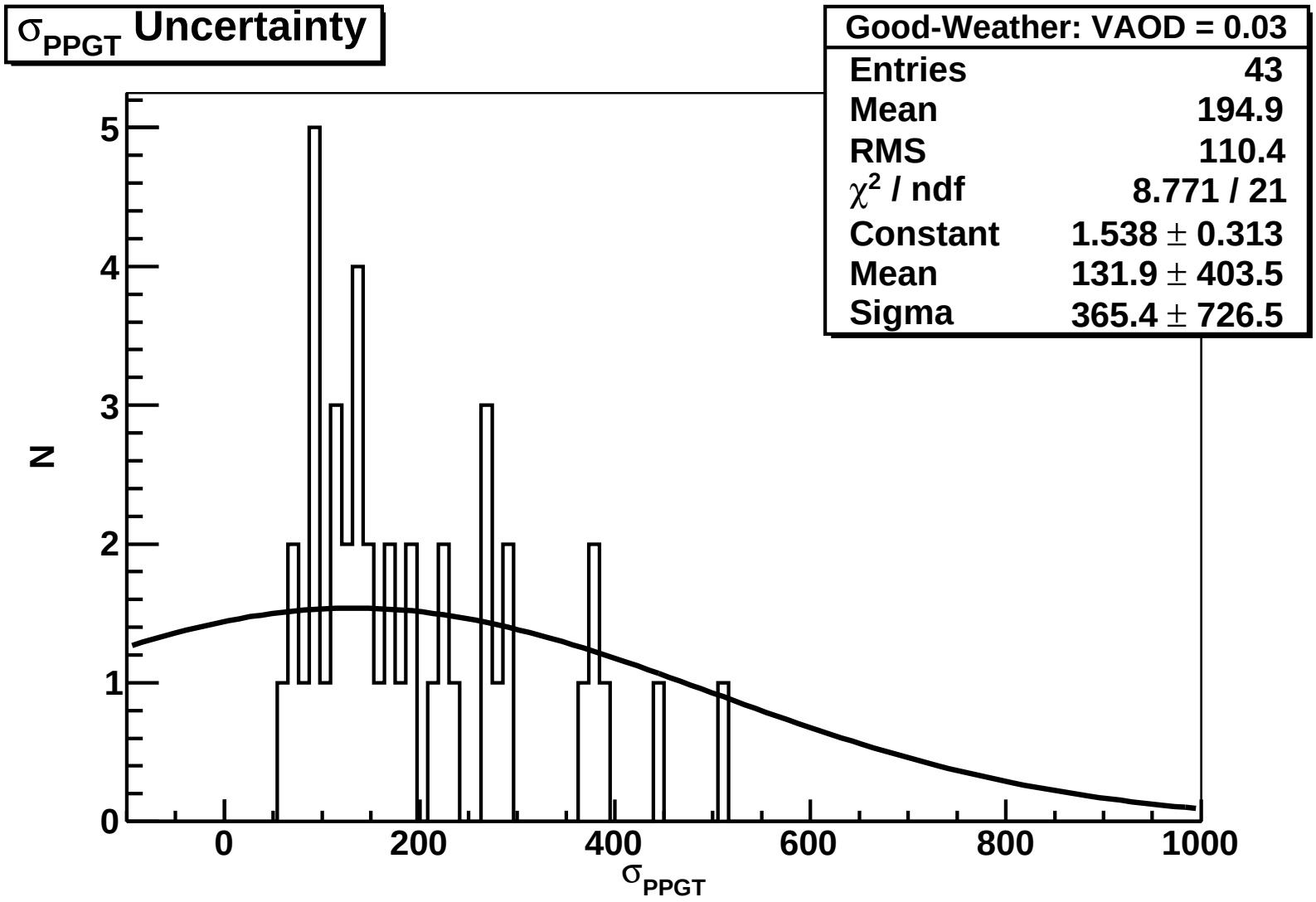

Figure 12.12: The nightly uncertainty in the standard deviation in the of the number of photons per good tube of events correlated with a vertical aerosol optical depth of 0.03.

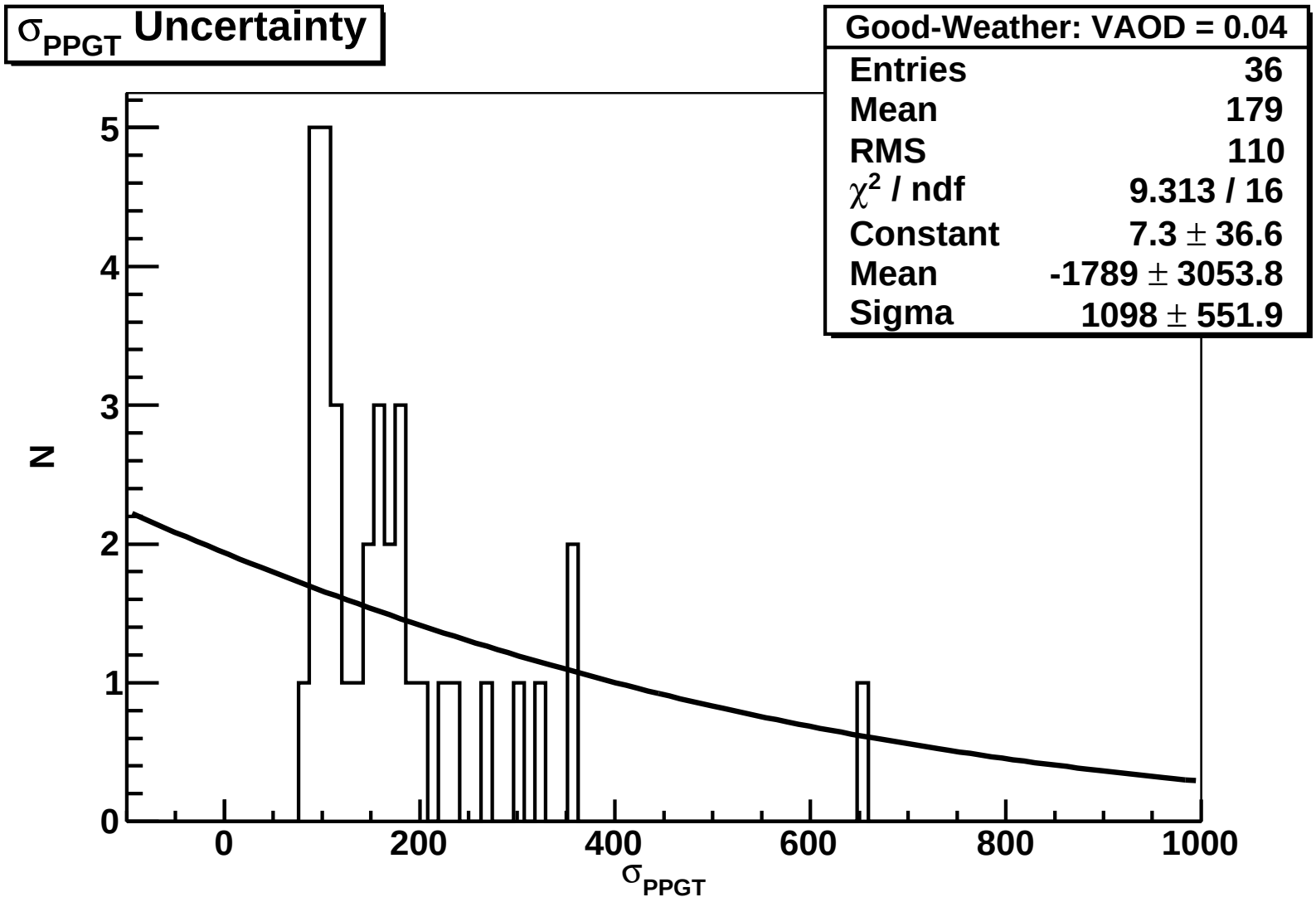

Figure 12.13: The nightly uncertainty in the standard deviation of the number of photons per good tube of events correlated with a vertical aerosol optical depth of 0.04.

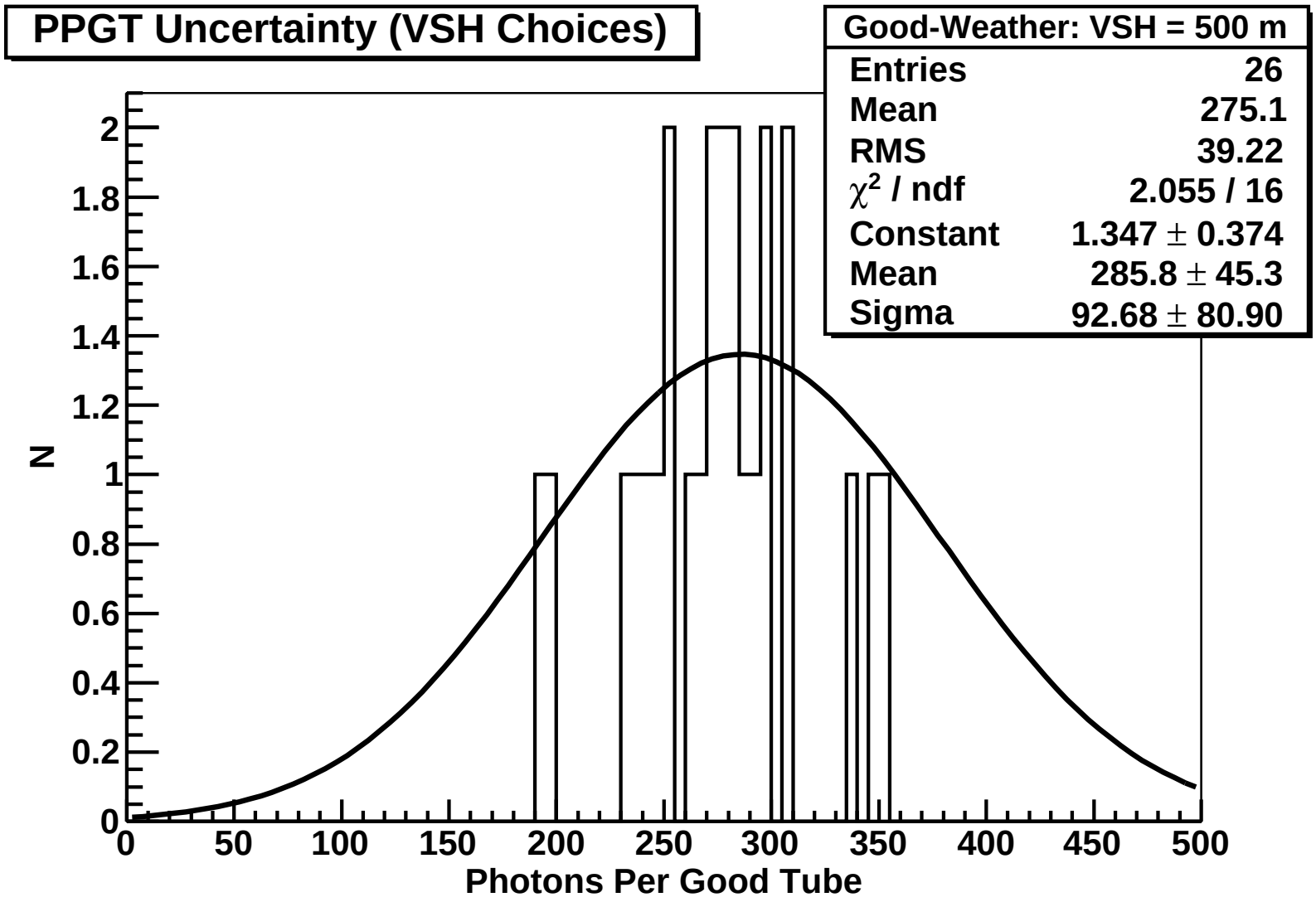

Figure 12.14: The nightly uncertainty in the number of photons per good tube of events correlated with a vertical scale height of 500 meters.

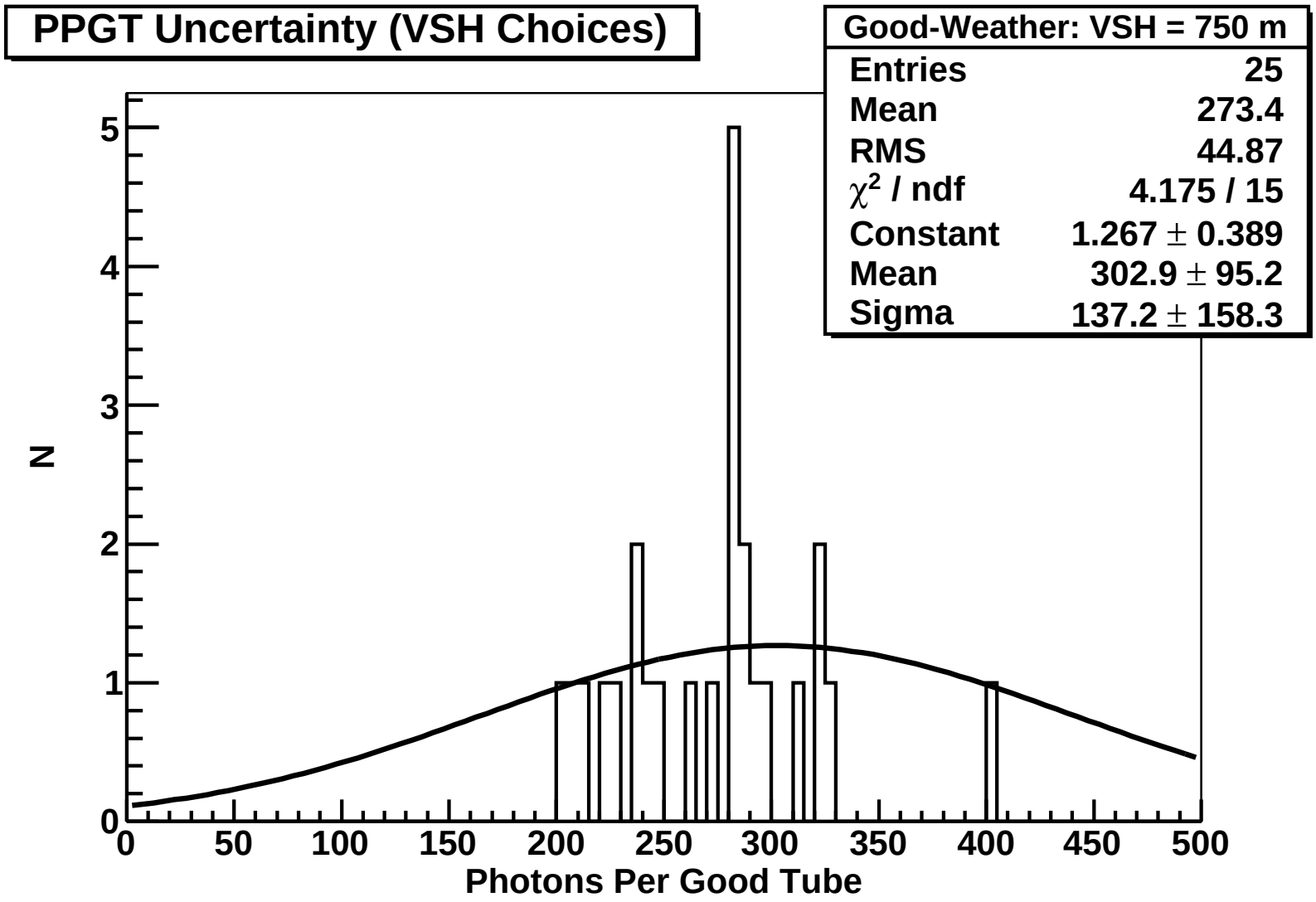

Figure 12.15: The nightly uncertainty in the number of photons per good tube of events correlated with a vertical scale height of 750 meters.

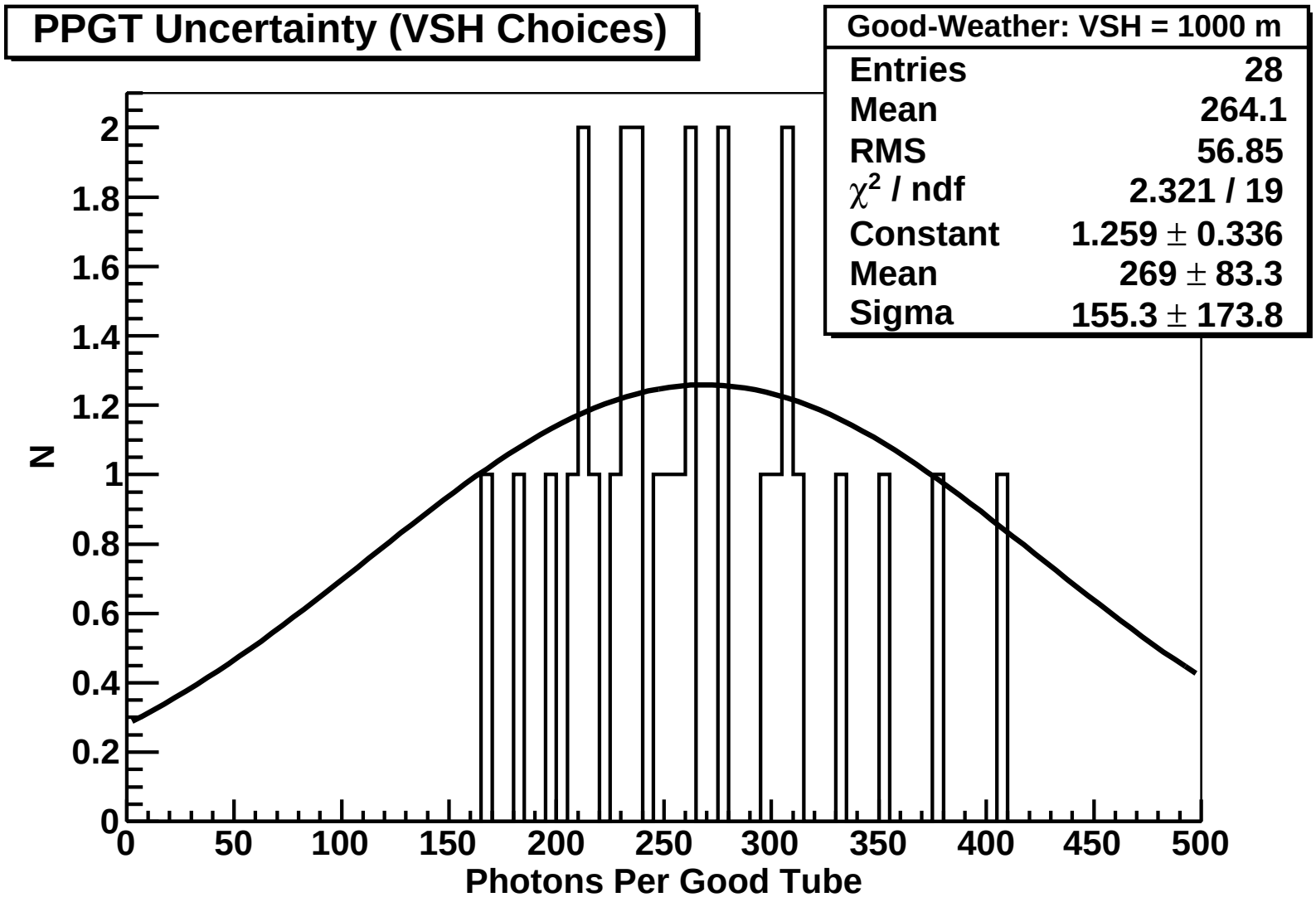

Figure 12.16: The nightly uncertainty in the number of photons per good tube of events correlated with a vertical scale height of 1 kilometer.

Table 12.5: Qualified shower-aerosol correlation selected bin uncertainty comparison.

Shower Parameter	Aerosol Parameter	Aerosol Bin RMS	Slope Uncertainty
$\sigma_{IAS}(\mu s/^{\circ})$	VAOD = 0.02	0.127	0.102
$\sigma_{IAS}(\mu s/^{\circ})$	VAOD = 0.03	0.107	0.102
$\sigma_{IAS}(\mu s/^{\circ})$	VAOD = 0.04	0.157	0.102
Photons / $Tube_{Good}$	VAOD = 0.02	35.19	50.13
Photons / $Tube_{Good}$	VAOD = 0.03	41.56	50.13
Photons / $Tube_{Good}$	VAOD = 0.04	40.82	50.13
σ_{PPGT}	VAOD = 0.02	60.9	99.12
σ_{PPGT}	VAOD = 0.03	110.4	99.12
σ_{PPGT}	VAOD = 0.04	110	99.12
Photons / $Tube_{Good}$	VSH = 500 m	39.22	1.68
Photons / $Tube_{Good}$	VSH = 750 m	44.87	1.68
Photons / $Tube_{Good}$	VSH = 1000 m	56.85	1.68

different VAOD values.

This study was performed using different values of vertical scale height (H) and horizontal attenuation length (L) combinations. By changing these values, the effective amount of aerosol scattering is changed. If the atmosphere is purely molecular, VSH is set to 0 and HAL is infinite. Equation 12.4 (along with Table 12.6) shows how different values of VSH and HAL can result in the same VAOD. The energy for the same event using the adjusted VAOD was compared to the energy given by the original 0.04 VAOD. The results of this are shown in Figures 12.17, 12.18, 12.19, 12.20, and 12.21.

As can be seen, the largest energy difference obtained on the low VAOD end is a decrease of $\sim 7\%$ if the atmosphere is molecular. Since our atmosphere is very rarely purely molecular, these results give us a very conservative estimate of the systematic uncertainties in the energy scale. By fitting the percent differences versus the VAOD values we can see a trend in the energy decrease (12.22). This trend is more linear than quadratic as indicated by the lines fit to the data. Based on these results, and the ± 0.02 RMS for the mean VAOD, we estimate the systematic uncertainty in the energy scale of the spectrum measurement at about 3%.

Table 12.6: VAOD adjustment values. Note the last item is molecular form.

H (km)	L (km)	VAOD	$\%\Delta_E$
0.5	25.0	0.02	-3.8
0.7	25.0	0.03	-1.9
1.0	33.0	0.03	-1.6
1.0	50.0	0.02	-3.3
0.1	99.0	0.001	-6.6

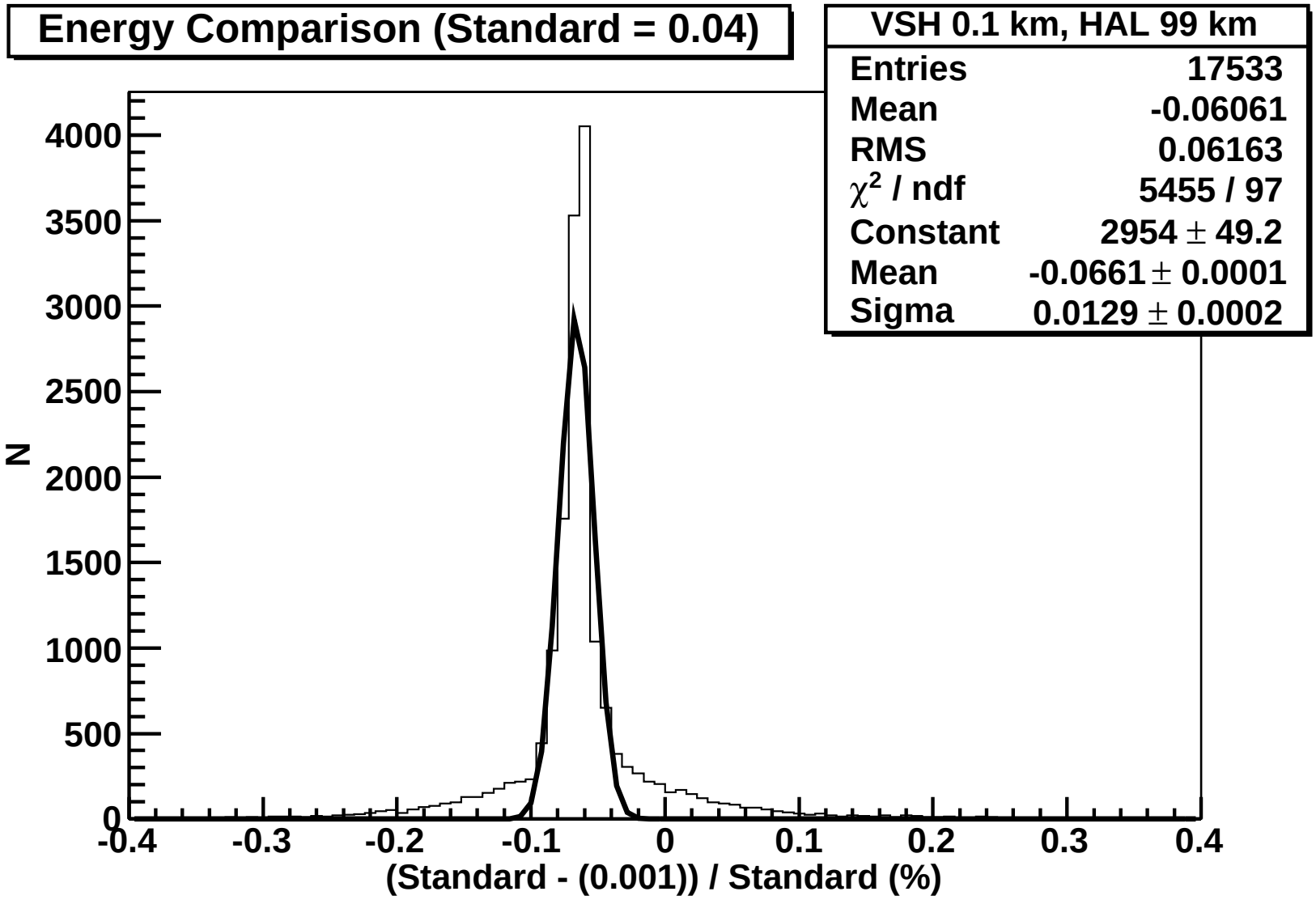

Figure 12.17: The comparison energy comes from the molecular $VAOD \approx 0.001$ values of $VSH = 0.1km$ and $HAL = 99km$.

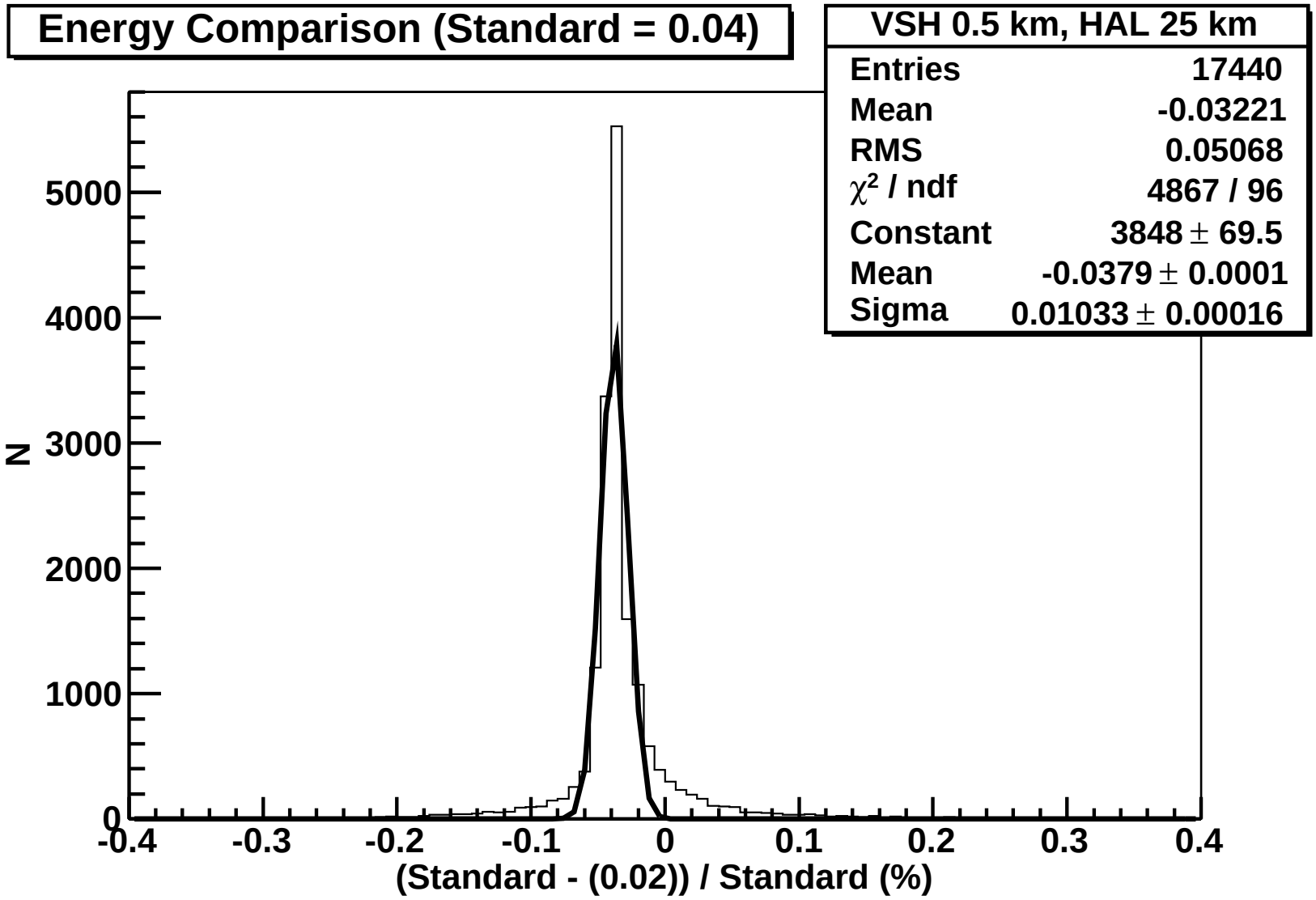

Figure 12.18: The comparison energy comes from the $VAOD \approx 0.02$ values of $VSH = 0.5km$ and $HAL = 25km$.

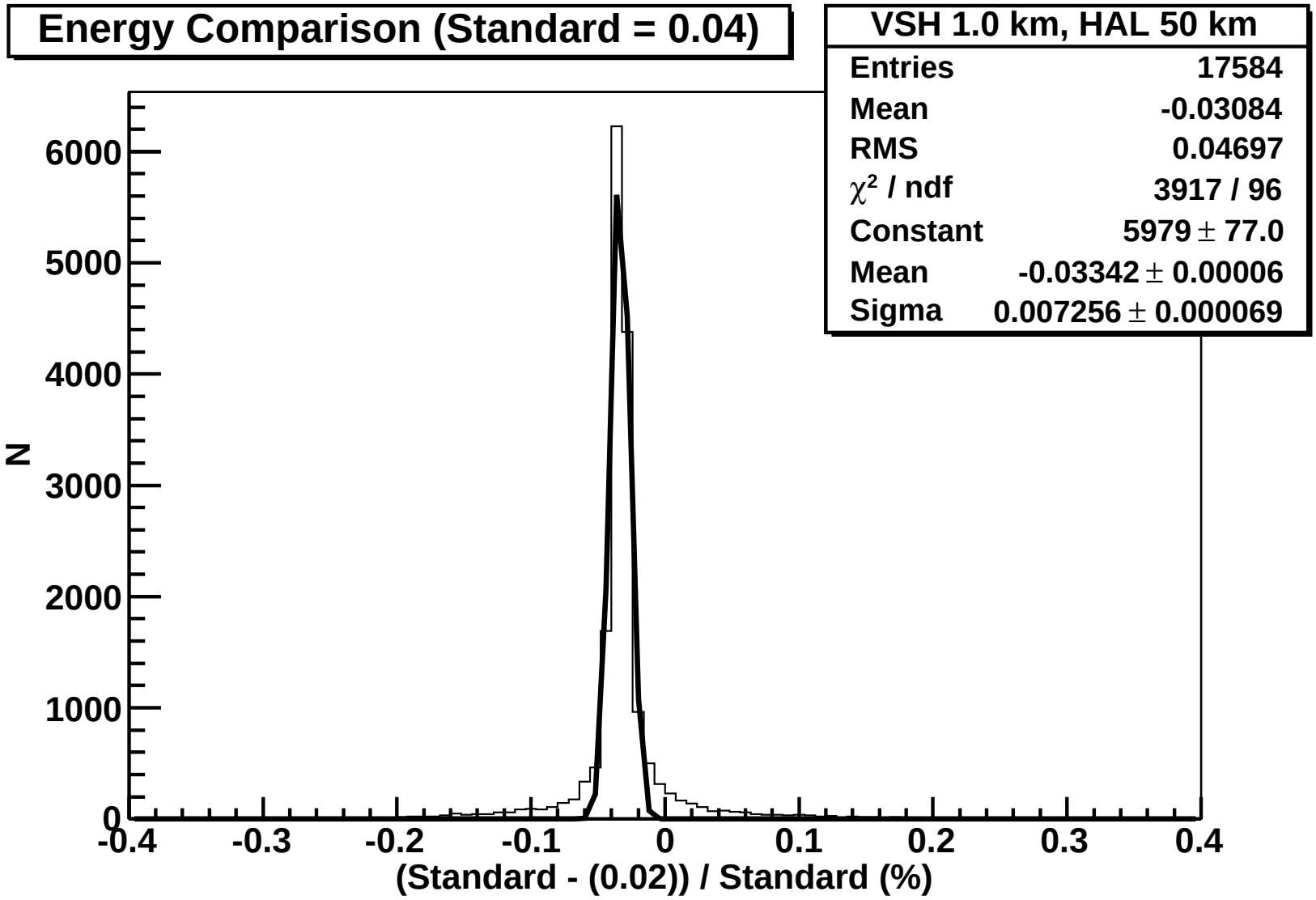

Figure 12.19: The comparison energy comes from the $VAOD \approx 0.02$ values of $VSH = 1.0km$ and $HAL = 50km$.

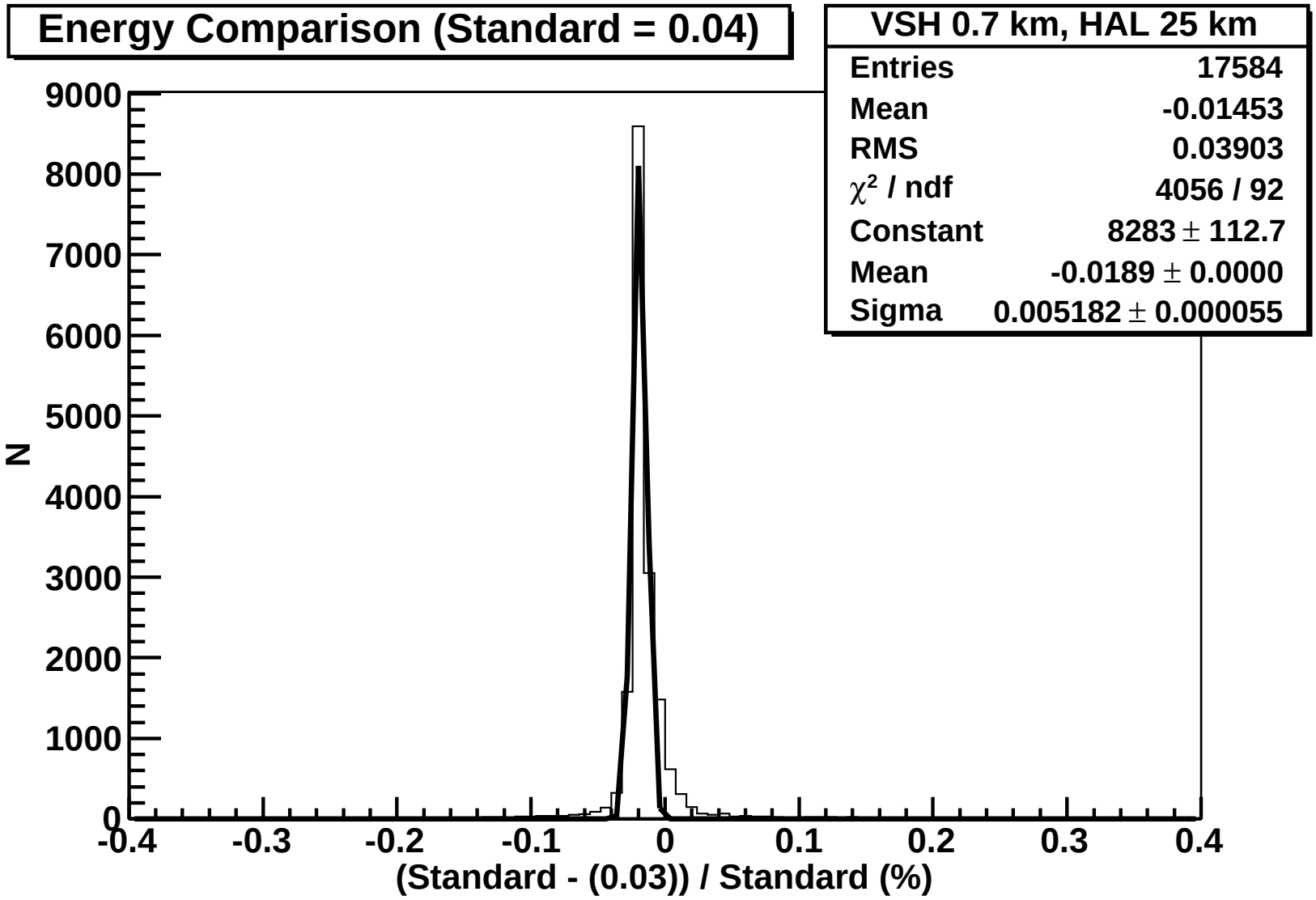

Figure 12.20: The comparison energy comes from the $VAOD \approx 0.03$ values of $VSH = 0.7km$ and $HAL = 25km$.

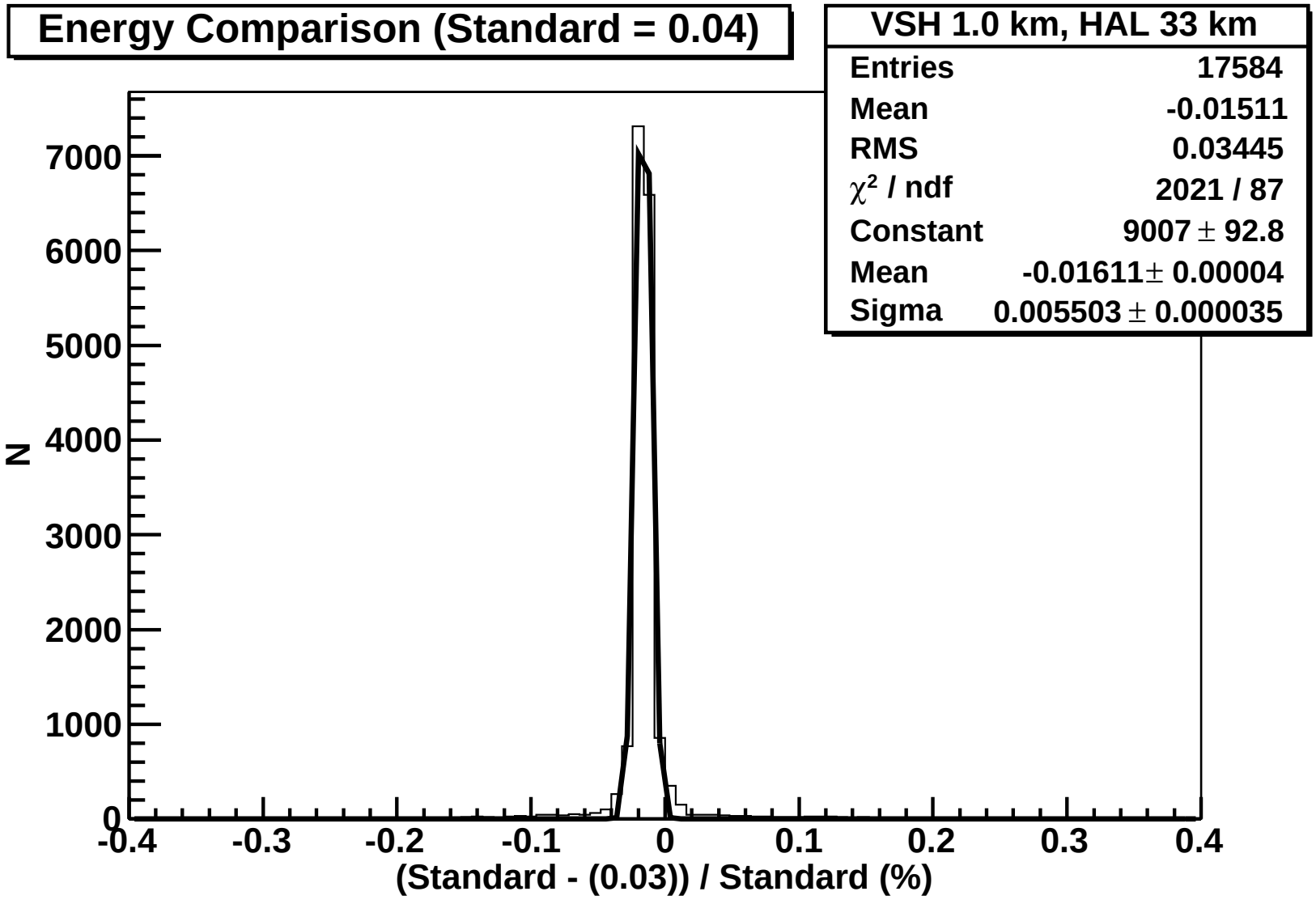

Figure 12.21: The comparison energy comes from the $VAOD \approx 0.03$ values of $VSH = 1.0km$ and $HAL = 33km$.

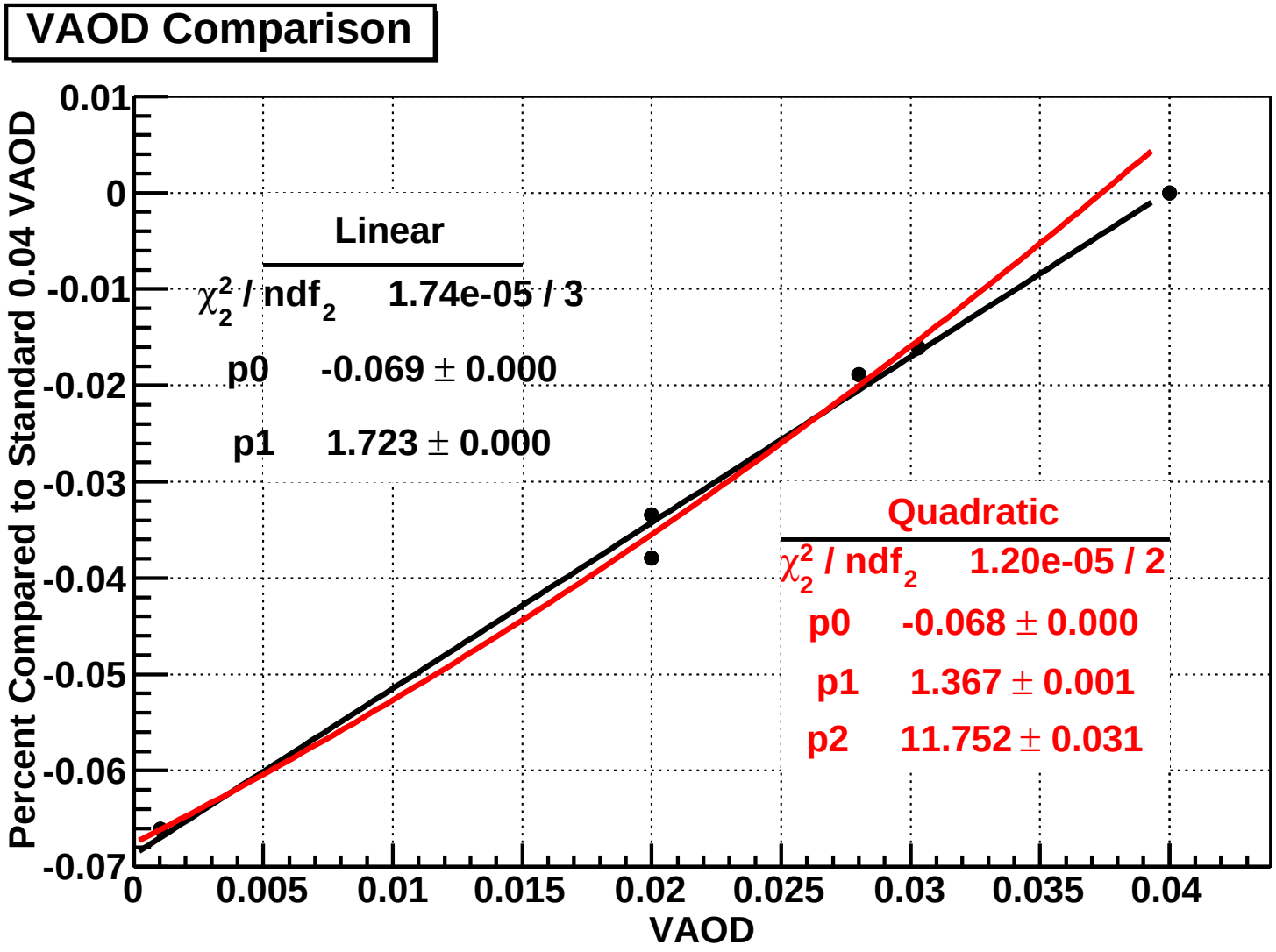

Figure 12.22: This graph shows a linear fit and a quadratic fit to the mean differences of the energy compared the 0.04 VAOD value used.

CHAPTER 13

COSMIC RAY INTERACTIONS IN THE HELIOSPHERE

As discussed in Chapter 2, a cosmic ray is a charged particle or nucleus accelerated to energies as high as $\sim 10^{20}$ eV. We know from Chapter 3 that when they arrive at the earth, they will interact with the atmosphere. The collision produces a hadronic and electromagnetic shower which fluorescence detectors can observe from the UV photons emitted along the track. It is possible, however, for interactions to occur before they reach the earth as discussed in section 2.3. One possibility is an interaction with the plasma of the heliosphere (see Figure 13.1).

If a cosmic ray does interact with the heliosphere, it will produce mostly pions (see section 3.1.1). The charged pions will decay into muons and neutrinos, of which the muons will be subjected to magnetic bending. The neutral pions will decay into a pair of photons and will travel almost directly along the initial pion's trajectory. Once the photons reach the earth they will act like ultrahigh energy gamma rays with energies close to the initial pion which can be within one to two orders of magnitude of the primary cosmic ray. One dramatic difference, however, is that they will produce a pair of simultaneous, nearly parallel showers.

13.1 Heliosphere

Solar physics has observed a region around the Sun that appears to be nearly a complete vacuum. The boundary, known as the heliosphere, is, however, denser than the rest of the interstellar medium [85]. Ionized atoms in the form of electrons and nuclei escape the Sun at ~ 400 km/s and travel away, modulated by the Sun's rotating magnetic field. This magnetic field produces a current sheet (see Figure 13.2) of varying speeds which have the characteristics of a gigantic magneto-bubble in the local interstellar medium. At the heliosphere edge the sheet smoothes out to just varying speeds and intensities. As the solar wind moves farther away it eventually interacts with the interstellar medium, which slows it down to ~ 100 km/s and produces large-scale structures at distances between

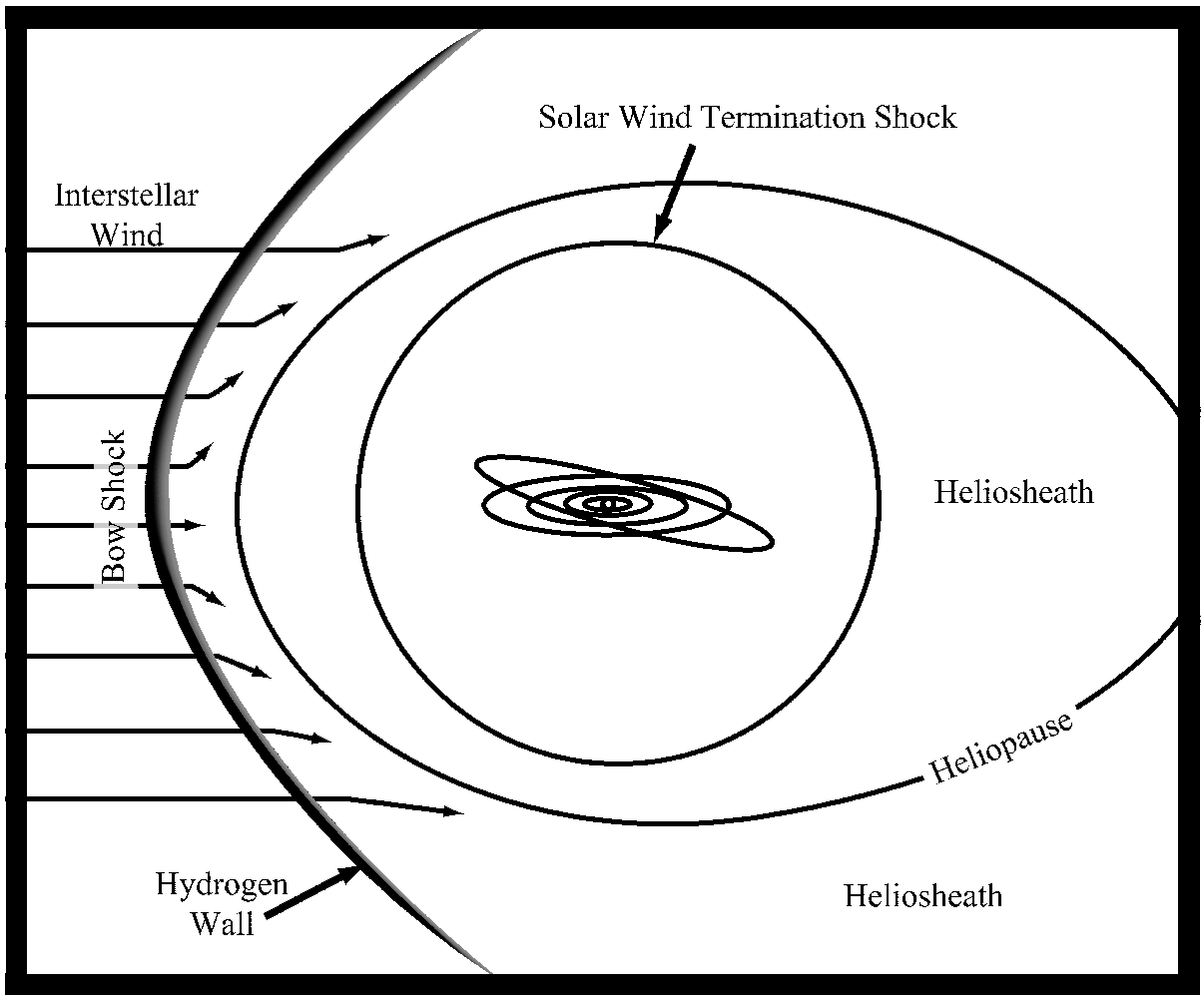

Figure 13.1: This schematic illustrates the general locations of the structures within the heliosphere. The innermost ring shown is the orbit of Jupiter.

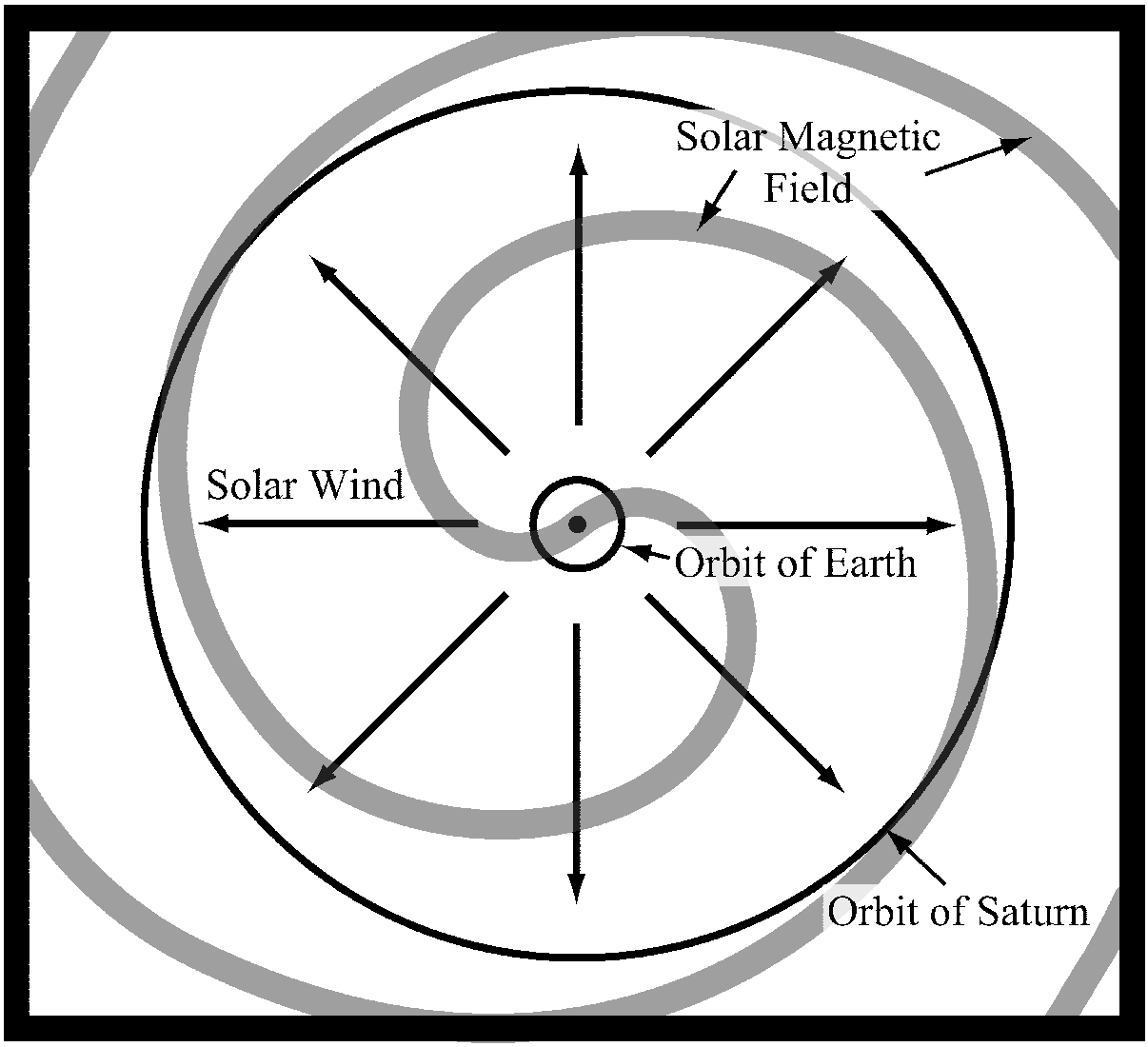

Figure 13.2: The peak amplitude of the magnetic field current sheet produced by the Sun is indicated by the spirals and shown out to the orbit of Saturn (~ 9.5 astronomical units).

75-200 astronomical units, or $1.12 - 2.99 \times 10^{10}$ km, from the known solar system. The heliosphere itself is divided into three general regions (see Figure 13.1): the termination shock, the heliopause, and the bow shock.

13.1.1 Termination Shock

The termination shock (TS) is produced when the solar winds suddenly drop to subsonic speeds of roughly 100 km/s. At distances between 70 and 100 astronomical units (AU) away from the Sun the persistent pressure from the interstellar medium compresses and heats up the solar wind particles to a density of ~ 0.1 particles/cm^3 [28].

Solar flare activity modulates this actual distance on an 11-year cycle [85]. The TS itself is not perfectly centered on the Sun due to a combination of the motion of the Sun around the Galactic center and an interstellar magnetic field which deflects the radiation $\sim 60^{\circ}$ away from the galactic plane [76]. In 2005 and 2007 the Voyager-I and -II spacecrafts successfully reached the TS at 94 AU and 84 AU respectively [75] (see Figure 13.3). This difference of arrival distances is due to the different spacecraft trajectories approaching the termination shock at different locations on the modified sphere.

13.1.2 Heliosheath

Just outside of the TS is a region of relatively slow turbulence known as the heliosheath. This starts at ~ 80 AU in the direction of the Sun's orbit through the galaxy and is ~ 10 AU thick. The heliosheath can extend 2-3 times that distance in the aft direction of the Sun's orbit, similar to a comet's tail (see Figure 13.1). In this region the particle density drops by about an order of magnitude [85]. The heliopause defines the external boundary of the heliosheath. It is created when the pressure from the solar wind and the interstellar medium reaches equilibrium.

13.1.3 Bow Shock

The outermost structure of the heliosphere is the bow shock. The Sun traverses the interstellar medium similar to a boat travelling through water. The bow shock is produced when the interstellar wind drops to subsonic speeds as it interacts with the solar wind. This type of phenomena was first observed in the forward path of the star R Hya [102] and is suspected to also be in front of the Sun in its galactic orbit at a distance as far away as ~ 230 AU (see Figure 13.3).

Due to the orbit of the Sun around the galaxy, more pressure builds up in the forward path producing a structure known as the hydrogen wall [49] (see Figure 13.3). The hydrogen wall has a density of ~ 0.3 particles/cm^3 and is ~ 150 AU away is in the direction of Vega in the Lyra constellation. Because of its high density, the hydrogen wall would be a good candidate location for interactions to occur.

13.2 Double-Photon Production

In the previous section we suggested that there are regions of the heliosphere with which a cosmic ray can potentially interact. The likelihood of an interaction will now be

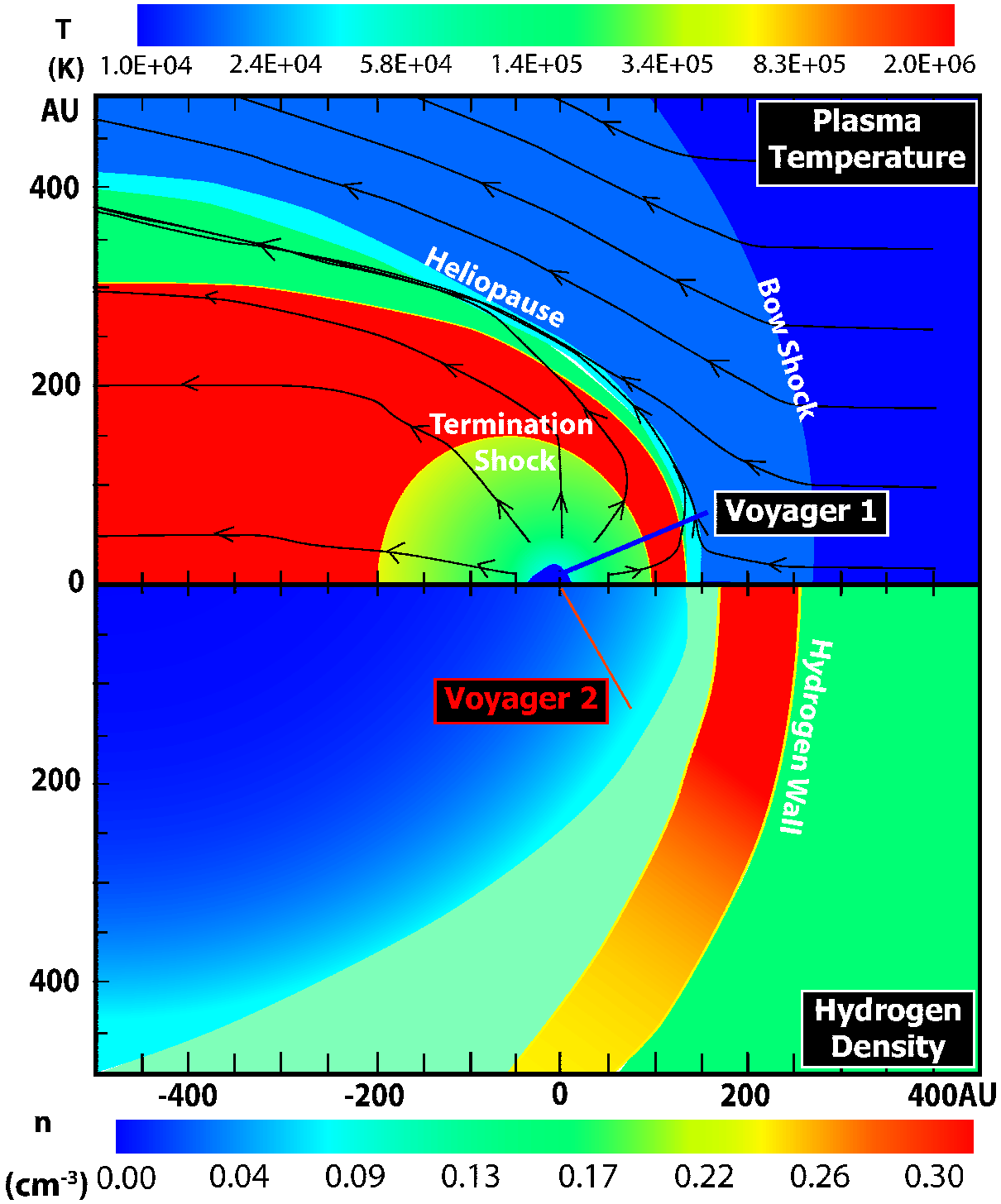

Figure 13.3: The heliosphere structures based on measured temperature and density. Adapted from [68].

discussed along with the physics of what would occur if an interaction did take place.

13.2.1 Cosmic Ray Interaction Probability

It is known that the density of the atmosphere is on the order of 1.2×10^{-3} g/cm^3 at standard temperature and pressure at sea level. As discussed in Chapters 3 and 4, high-energy protons and nuclei will produce hadronic showers when penetrating the atmosphere. The heliosphere is much closer to a vacuum and primarily consists of ionized particles with densities of $\lesssim 0.3$ protons/cm^3. The proton-proton inelastic cross section, σ_{pp}, can then be used to calculate the probability of an interaction between a cosmic ray and an ion in the heliosphere resulting in at least one neutral pion. There are no measurements of this value at the energy range of interest (above $\sim 10^{17.0}$ eV). However, there are studies that have calculated the total cross-section near these energies [25]. For an average energy of $\sim 10^{18.5}$ eV, the total cross-section is estimated to be approximately 120 mb from the HiRes experiment [16] (see Figure 13.4). A measurement of $\sigma_{p-air} \approx 450$ mb was made for proton-air interactions and converted into proton-proton interactions using Glauber theory in the center-of-mass frame [38].

The cross section and density of the region the CR passes through can give us the interaction length the cosmic ray would have to traverse in order to interact with a proton in the heliosphere. The equation to find this is

$$L_{int} = (\sigma_{pp}\rho)^{-1} \tag{13.1}$$

where ρ is the density of the plasma. Taking the thickness of the region and dividing by this value we can find the probability of an interaction occurring. The three most likely regions for interactions to occur are: the termination shock, the heliosheath, and the hydrogen wall (see Table 13.1). As can be seen, the hydrogen wall has the highest probability of having a cosmic ray interact with one of its protons. But, of the three, the hydrogen wall is also the farthest from the earth. In all cases, however, the likelihood of an interaction is vanishingly small. The rest of this chapter is a discussion of what would happen if an interaction did occur.

13.2.2 Photon Observation

In the standard model (SM) of particle physics, a proton-proton collision will result in mostly charged or neutral pions (see section 3.1). With the near vacuum of the heliosphere, pair-production and Compton scattering are negligible and were not considered in this study. Only the particle decay has any significance on the survival time. These

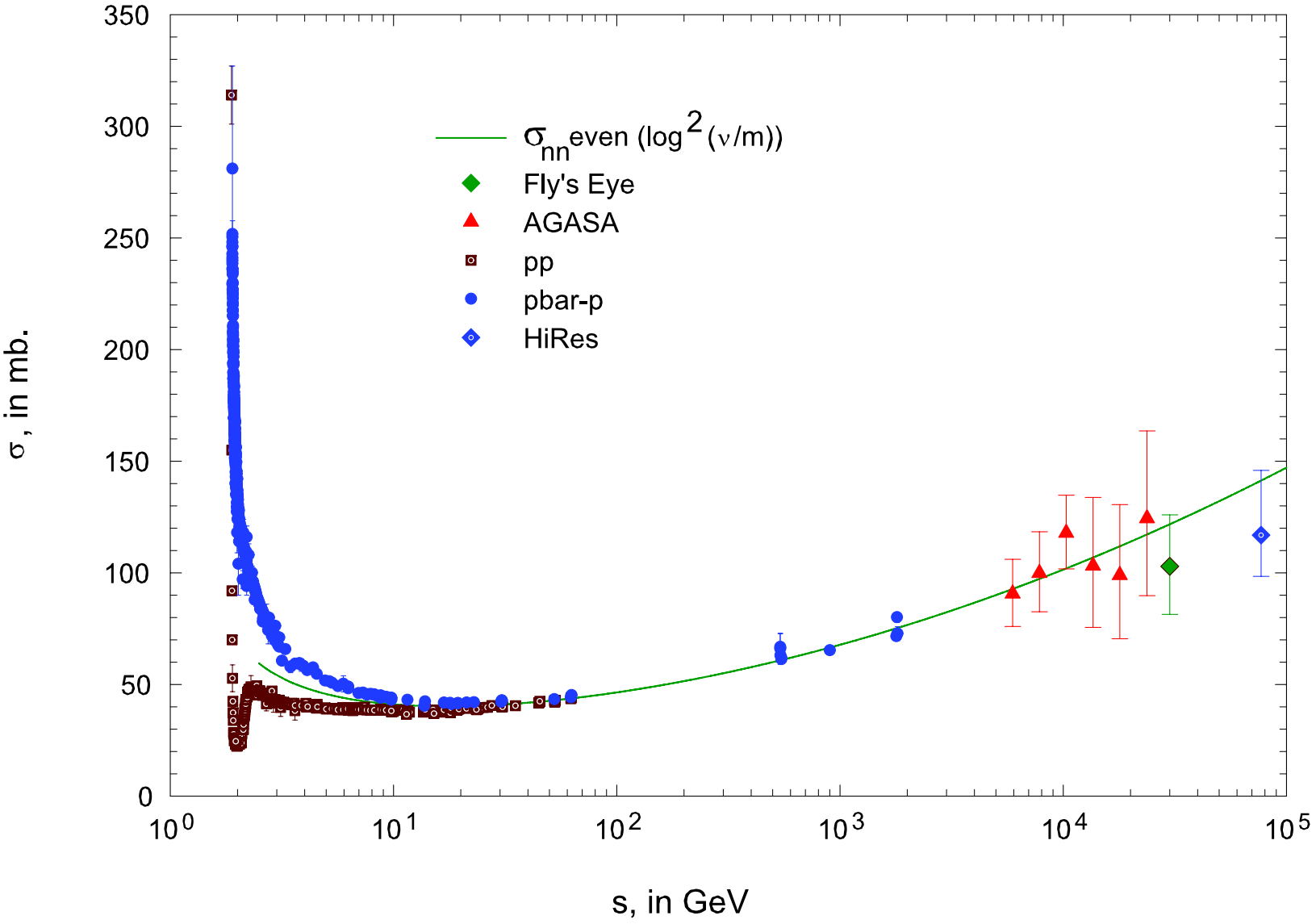

Figure 13.4: The estimated proton-proton total cross section as measured by HiRes in the center-of-mass rest frame and rescaled from a $\sigma_{p-air} \approx 450$ mb proton-air cross-section using Glauber theory [16] [38].

Table 13.1: Cosmic ray-Heliosphere interaction probabilities. The region thicknesses were found in [51] or estimated from Figure 13.3.

	Density (cm^{-3})	Interaction Length (AU)	Region Thickness (AU)	Interaction Probability
Termination Shock	0.1	1.45E+12	0.5	8.98×10^{-14}
Heliosheath	0.001	1.45E+14	59	1.06×10^{-13}
Hydrogen Wall	0.3	4.84E+11	20	1.08×10^{-11}

will then decay according to the charge of the pion. The charged particles, $\pi^{\pm}$, undergo leptonic decay after 2.6×10^{-8} seconds to produce muons and neutrinos. The magnetic fields of the earth, Sun, or even galaxy would then influence the muons and the final trajectory would be highly variable.

After 8.4×10^{-17} seconds, neutral pions will decay into two photons 98.8% of the time. In the rest frame of the π^0, the two photons would have trajectories directly away from each other in order to conserve momentum (see Figure 13.5) and each would carry half of the mass energy of the pion, M_{π^0}. First-order interactions between the two photons are unlikely to occur and, at these energies, the photons act more like particles than waves, so interference will not happen.

Starting with the pion's rest frame, four-vector relativistic mechanics can be used to describe how the photons would be observed by detectors on the earth. In the pion's rest frame, S', both the energy and momentum are split equally between the two photons:

$$E'_{\gamma i} = P'_{\gamma i} = \frac{m_{\pi^0}}{2} \tag{13.2}$$

where i is for photon 1 or photon 2 and m_{π^0} is the rest mass of the neutral pion. In the lab frame, S, all of the energy of both photons is contained fully in the momentum

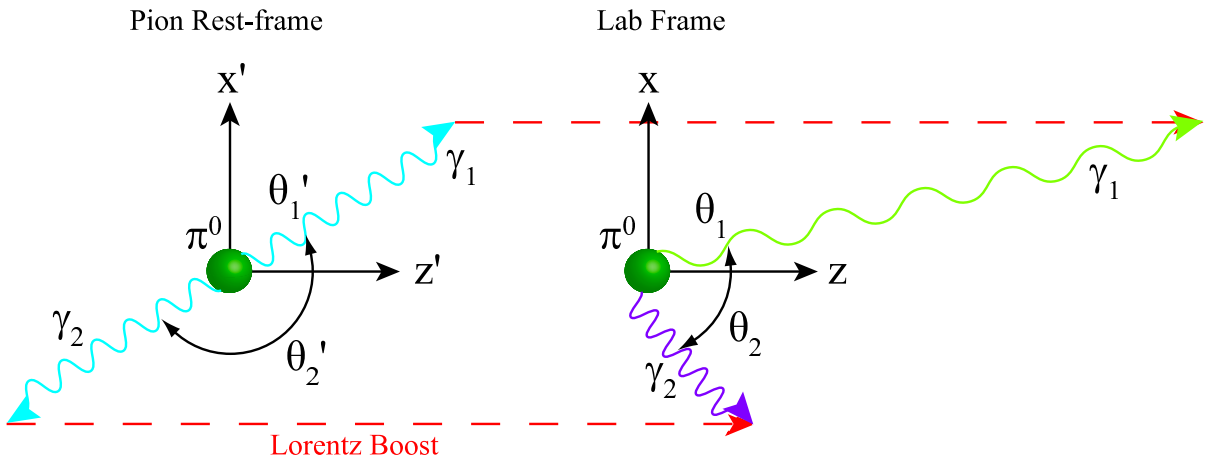

Figure 13.5: This figure shows the decay of a neutral pion in both its rest frame and the lab frame.

$$E_{\gamma i} = P_{\gamma i} \tag{13.3}$$

and the energy of of the pion is

$$E_{\pi^0}^2 = m_{\pi^0}^2 + p_{\pi^0}^2. \tag{13.4}$$

We are free to choose the initial direction of the pion before decay to be along the zz' direction. In the π^0 rest frame, we assume the two photons to be emitted within the x'z' plane, the photon-plane (see Figure 13.5). There is no way to distinguish the two photons, so one is arbitrarily labeled γ_1 and the other as γ_2. In the rest frame, γ_1 travels at an angle θ_1' away from the zz'-axis in the photon-plane; γ_2 travels at the angle $\cos\theta_2' = -\cos\theta_1'$. Note we have chosen θ_1', θ_2' to be positive polar angles measured from the +zz' axis.

The four-momentum vectors of the particles in the rest frame then become

$$q_1' = (E_1', P_{1x}', P_{1y}', P_{1z}') = \frac{m_{\pi^0}}{2}(1, \sin\theta_1', 0, \cos\theta_1'), \tag{13.5}$$

$$q_2' = (E_2', P_{2x}', P_{2y}', P_{2z}') = \frac{m_{\pi^0}}{2}(1, \sin\theta_2', 0, \cos\theta_2'), \tag{13.6}$$

and

$$q_{\pi^0}' = (E_{\pi^0}', 0, 0, 0) = m_{\pi^0}(1, 0, 0, 0) \tag{13.7}$$

where 1 and 2 represent the two photons. The (inverse) Lorentz boost from the rest frame to the lab frame is defined by the Lorentz matrix for the z-direction

$$\Lambda^{-1} = \begin{bmatrix} \gamma & 0 & 0 & \beta\gamma \\ 0 & 1 & 0 & 0 \\ 0 & 0 & 1 & 0 \\ \beta\gamma & 0 & 0 & \gamma \end{bmatrix} \tag{13.8}$$

where $\gamma = E_{\pi^0}/m_{\pi^0}$, $\vec{\beta} = \vec{P}_{\pi^0}/E_{\pi^0}$, and $\beta = (1-\gamma^{-2})^{1/2}$. In the lab-frame we have

$$q_1 = (E_1, P_{1x}, P_{1y}, P_{1z}) = E_1(1, \sin\theta_1, 0, \cos\theta_1), \tag{13.9}$$

$$q_2 = (E_2, P_{2x}, P_{2y}, P_{2z}) = E_2(1, \sin\theta_2, 0, \cos\theta_2), \tag{13.10}$$

and

$$q_{\pi^0} = (E_{\pi^0}, 0, 0, P_{\pi^0}) \tag{13.11}$$

where boosted photons are projected in the lab frame according to the equations

$$\tan\theta_1 = \frac{P_{1x}}{P_{1z}} = \frac{\sin\theta_1'}{\beta\gamma + \gamma\cos\theta_1'} \tag{13.12}$$

and

$$\tan\theta_2 = \frac{P_{2x}}{P_{2z}} = \frac{\sin\theta_2'}{\beta\gamma + \gamma\cos\theta_2'} \tag{13.13}$$

which results in an opening angle between the two photons of

$$\alpha = |\theta_1| + |\theta_2|. \tag{13.14}$$

Monte Carlo simulations were made using the above equations to determine observable properties of this process. These results showed that, except for the $\theta_1' = 0°$ case, the opening angle between the two photons will change based on the longitudinal momentum of the photon in the rest frame (see Figure 13.6). The more perpendicular the photons are projected away from the π^0 trajectory, the more narrow the opening angle between the two photons. This also translates into a smaller energy difference between the two photons (see Figure 13.7). Note that the ratio E_1/E_2 compared to the projection of γ_1 is independent of E_{π^0}. The sum of the energy of the two photons, however, will always be equal to the original pion's energy (see Figure 13.8) with the higher energy photon following closer to the original pion's trajectory.

As was discussed in section 13.1.1, the heliosphere has been estimated to be between 75 and 100 astronomical units away from the Sun (roughly the same to Earth). One astronomical unit is equal to $\sim 1.50 \times 10^8$ km. Presuming the photons are produced and arrive at the earth, the perpendicular separation between the shower axes, or spread, $D_\perp$, can be found by the equation

$$D_\perp = 2R \tan \frac{\alpha}{2} \simeq R\alpha \tag{13.15}$$

where R is the distance to the heliosphere and α is the opening angle between the photons. A comparison was made using four distances to the heliosphere: 75, 80, 85, and 90 AU. For a given pion energy, an increasing distance to the heliosphere results in at most a 20% increase in the spread between the two photons (see Figure 13.9). One additional feature in the spread between photons is that going one order of magnitude greater in pion energy, the spread will drop by an order of magnitude. Consequently, $\sim 99.5\%$ of the events in a single π^0 energy have spreads narrower than the smallest $D_\perp$ of the next lower energy decade (see Figure 13.10). For example, the minimum $D_\perp$ for a $10^{19.0}$ eV pion is 300 m and almost all of the $10^{19.0}$ eV photon-pairs will have spreads less than the 3 km minimum of $10^{18.0}$ eV pions.

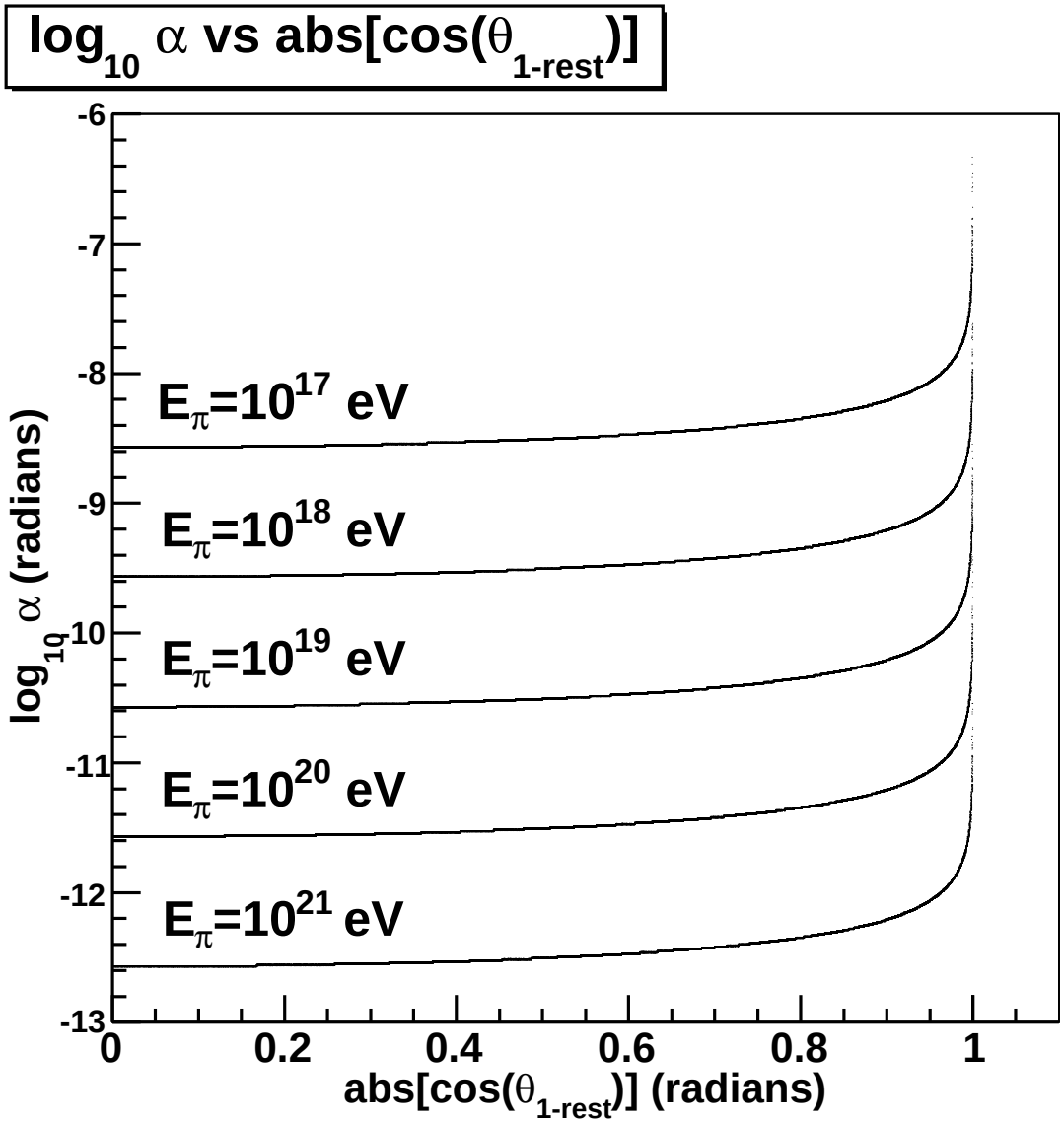

Figure 13.6: Opening angle, α, of the Monte Carlo pion decay in the lab frame compared to the projection of γ_1 along the z-axis.

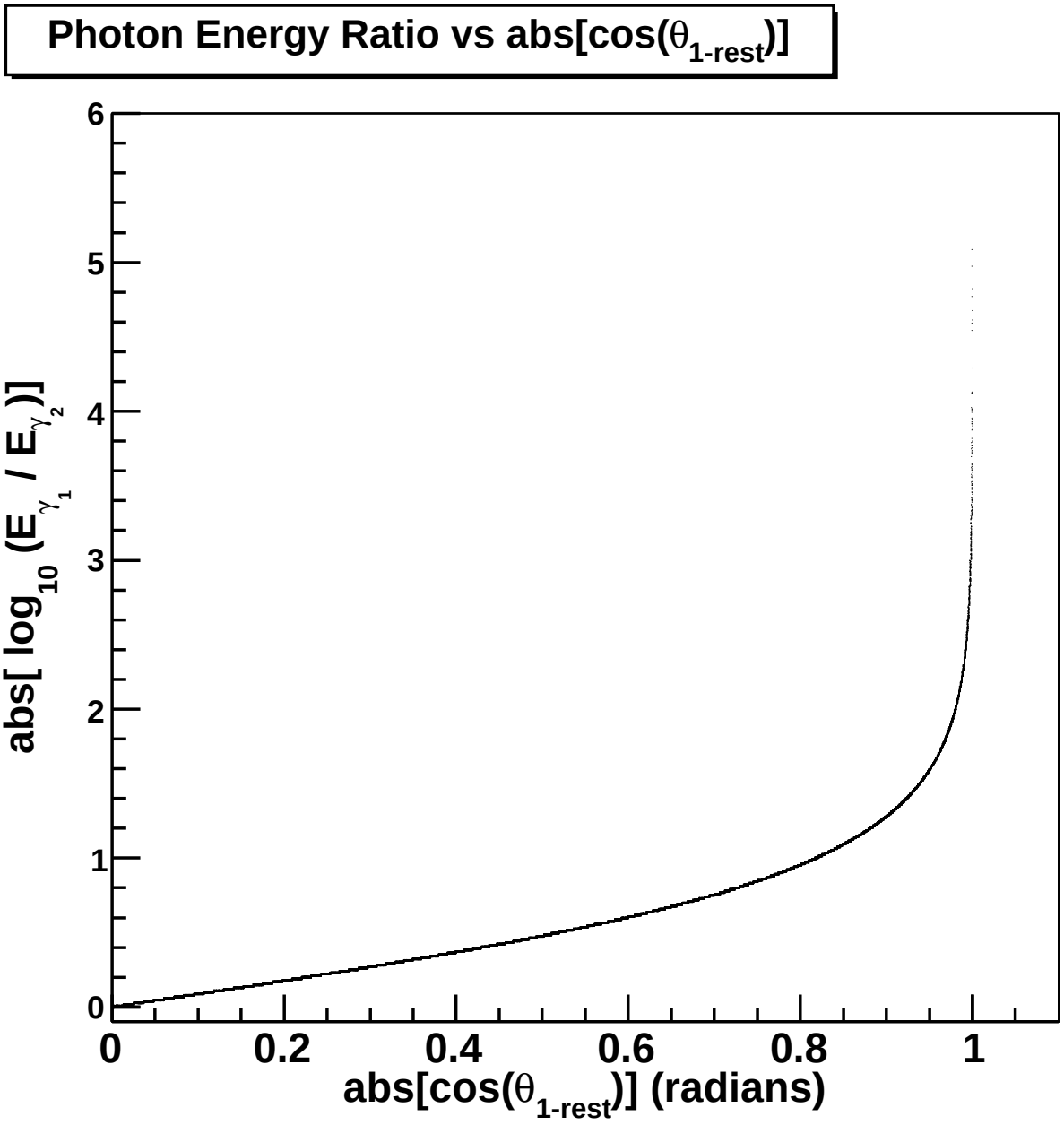

Figure 13.7: Energy difference between the Monte Carlo photons in the lab frame compared to the projection of γ_1 along the z-axis.

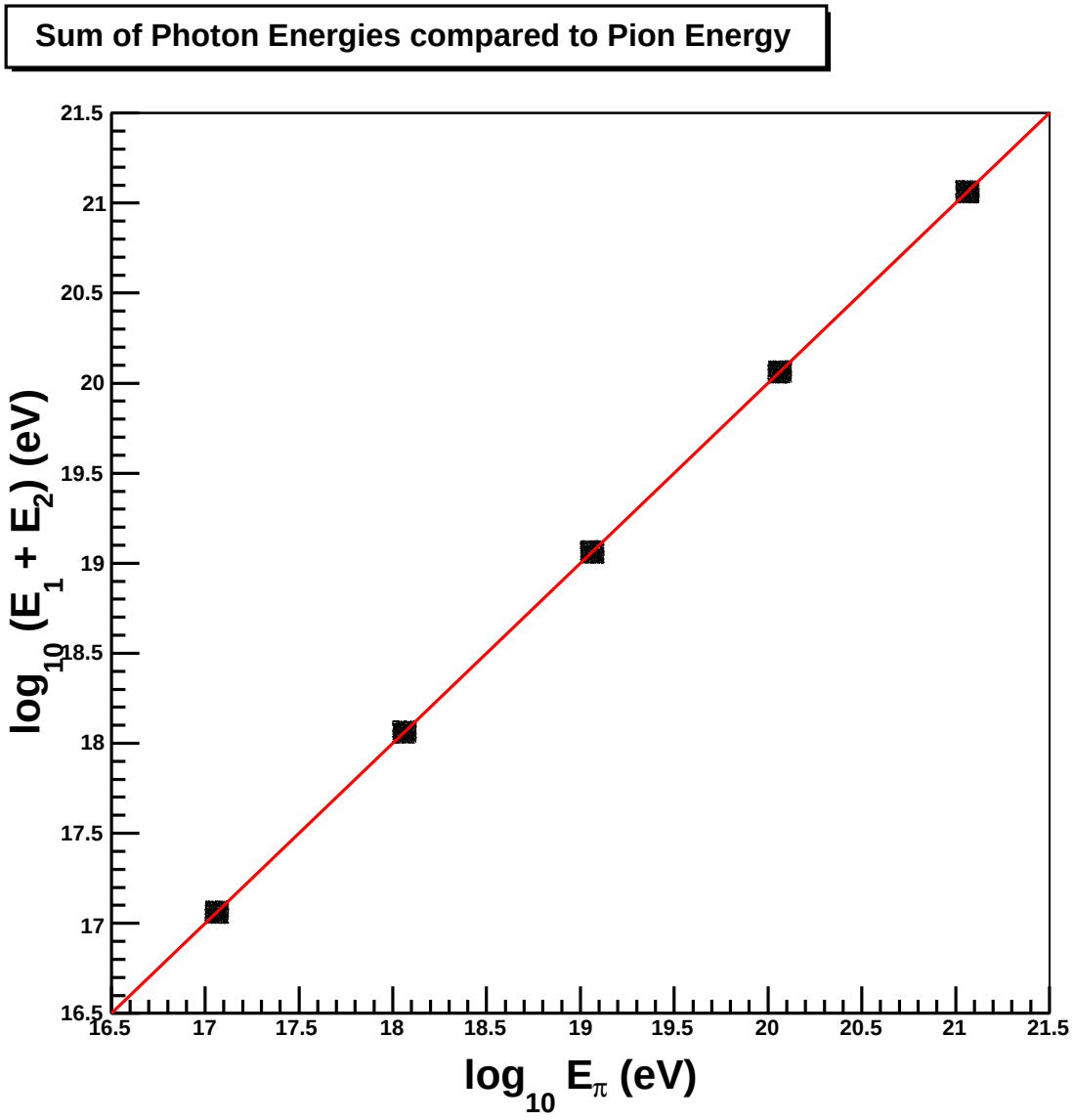

Figure 13.8: The sum of the two Monte Carlo photon energies is equal to the original simulated pion energy.

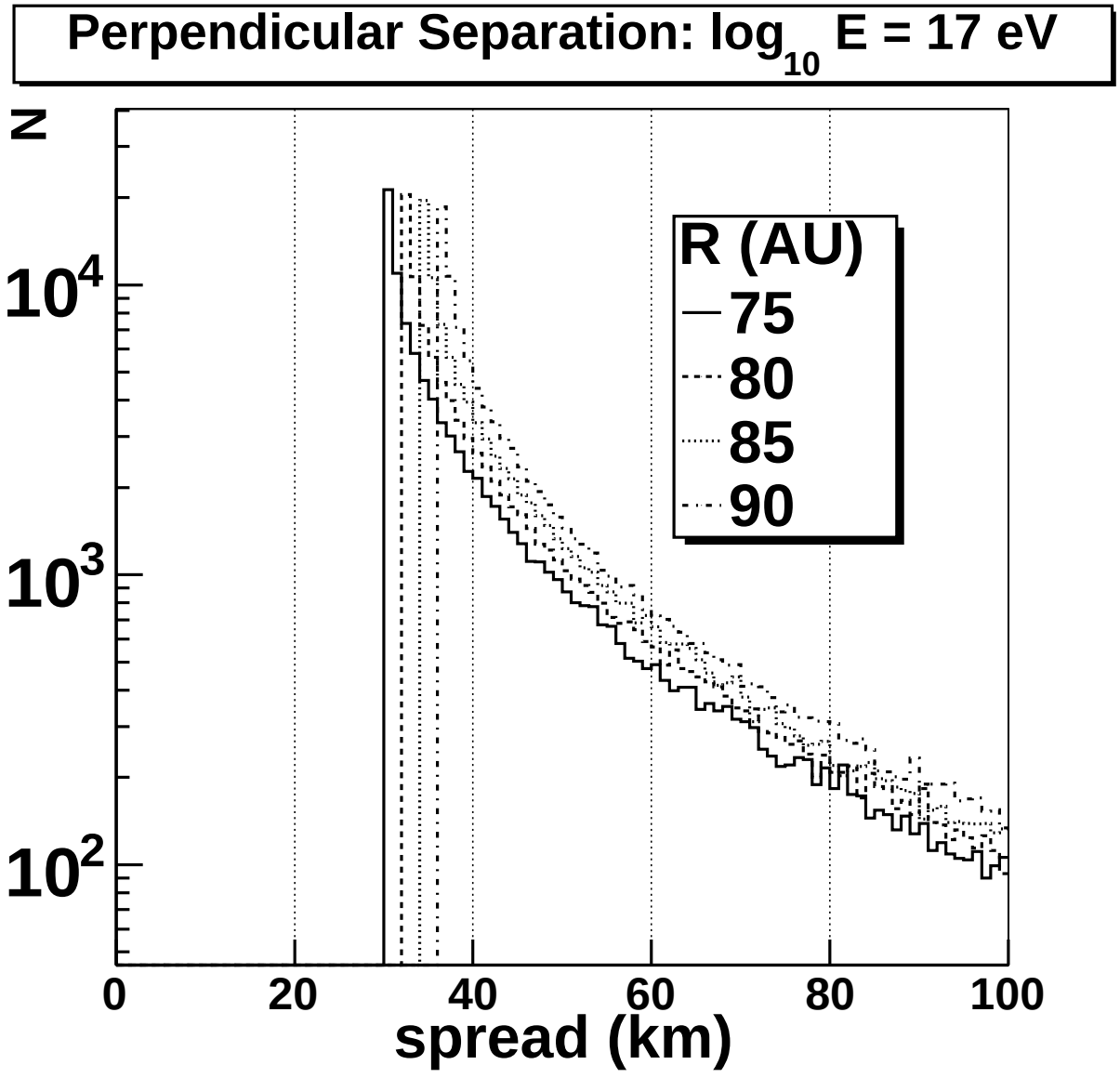

(a) $E_{\pi^0} = 10^{17.0}$ eV

Figure 13.9: The perpendicular separation between Monte Carlo photons after travelling from the heliosphere at the indicated distances (R).

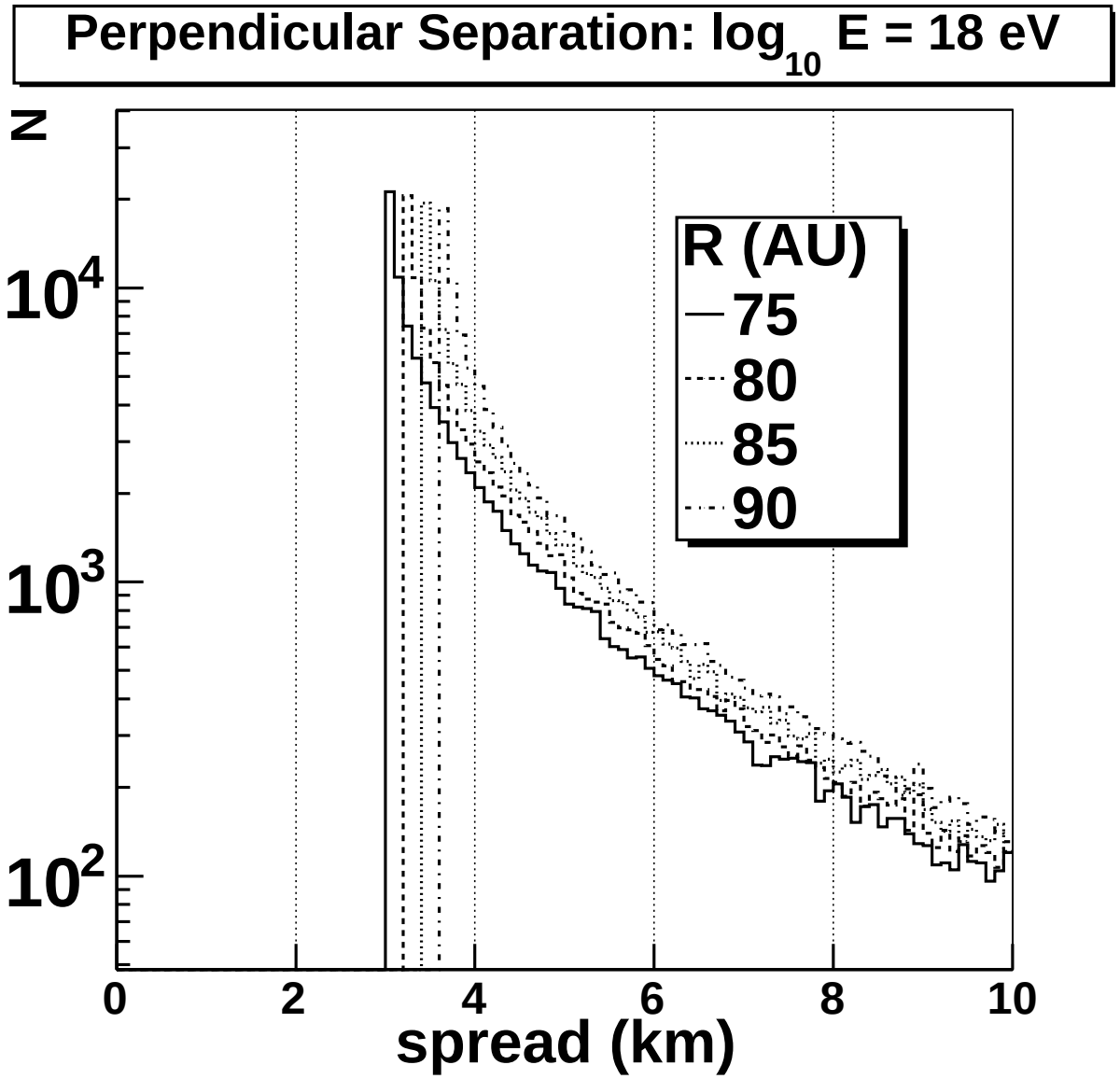

(b) $E_{\pi^0} = 10^{18.0}$ eV

Figure 13.9: Continued.

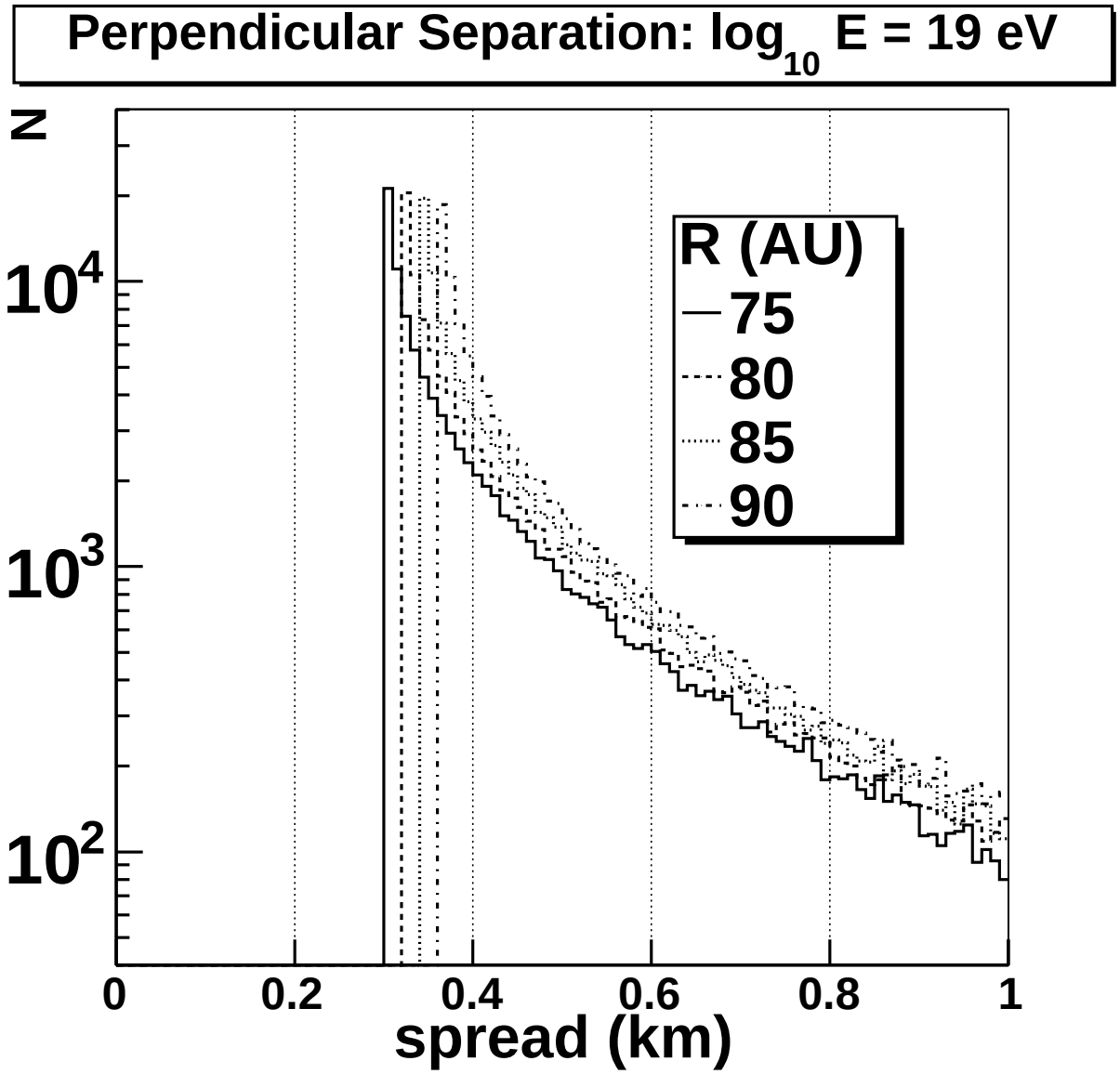

(c) $E_{\pi^0} = 10^{19.0}$ eV

Figure 13.9: Continued.

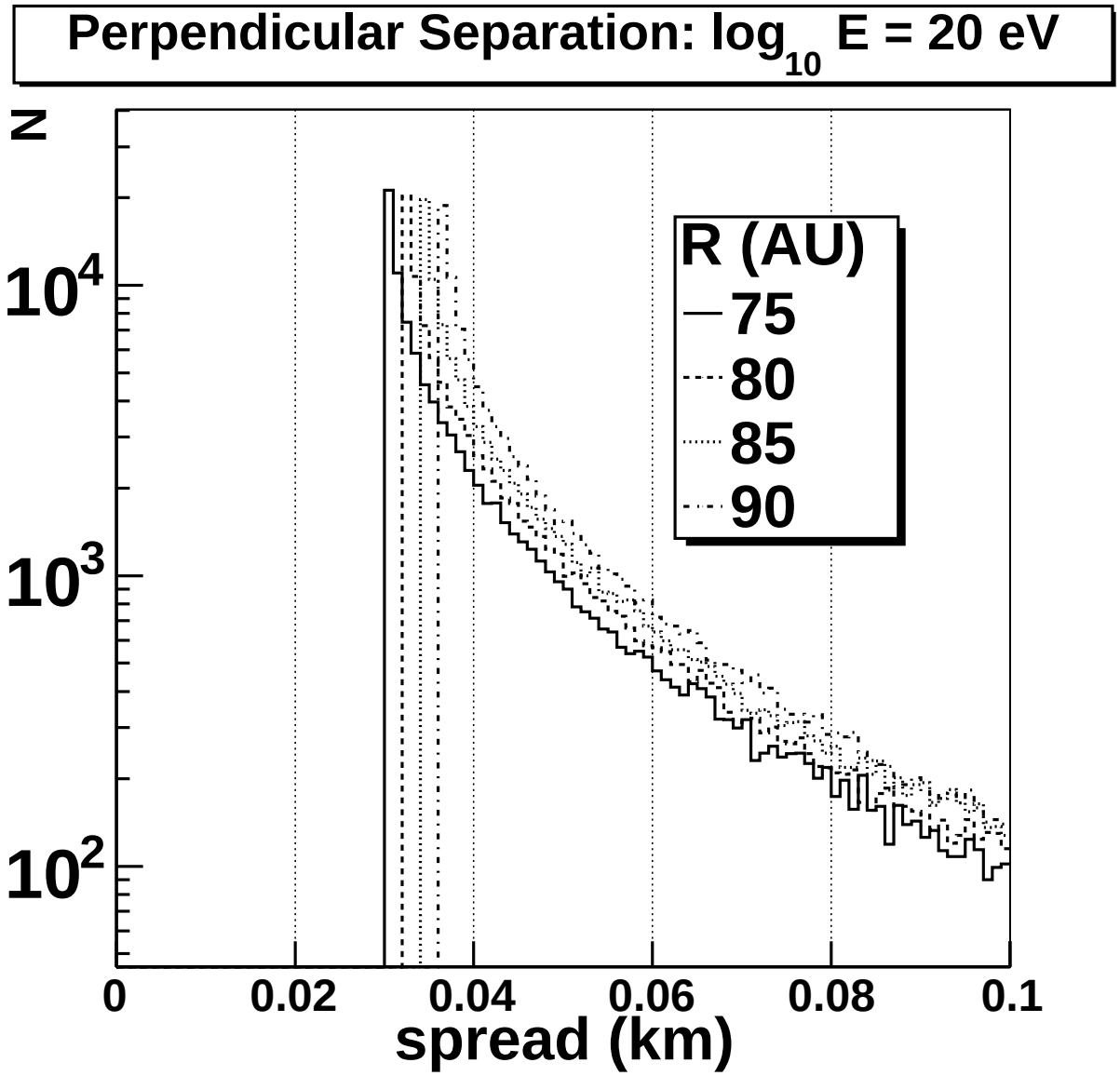

(d) $E_{\pi^0} = 10^{20.0}$ eV

Figure 13.9: Continued.

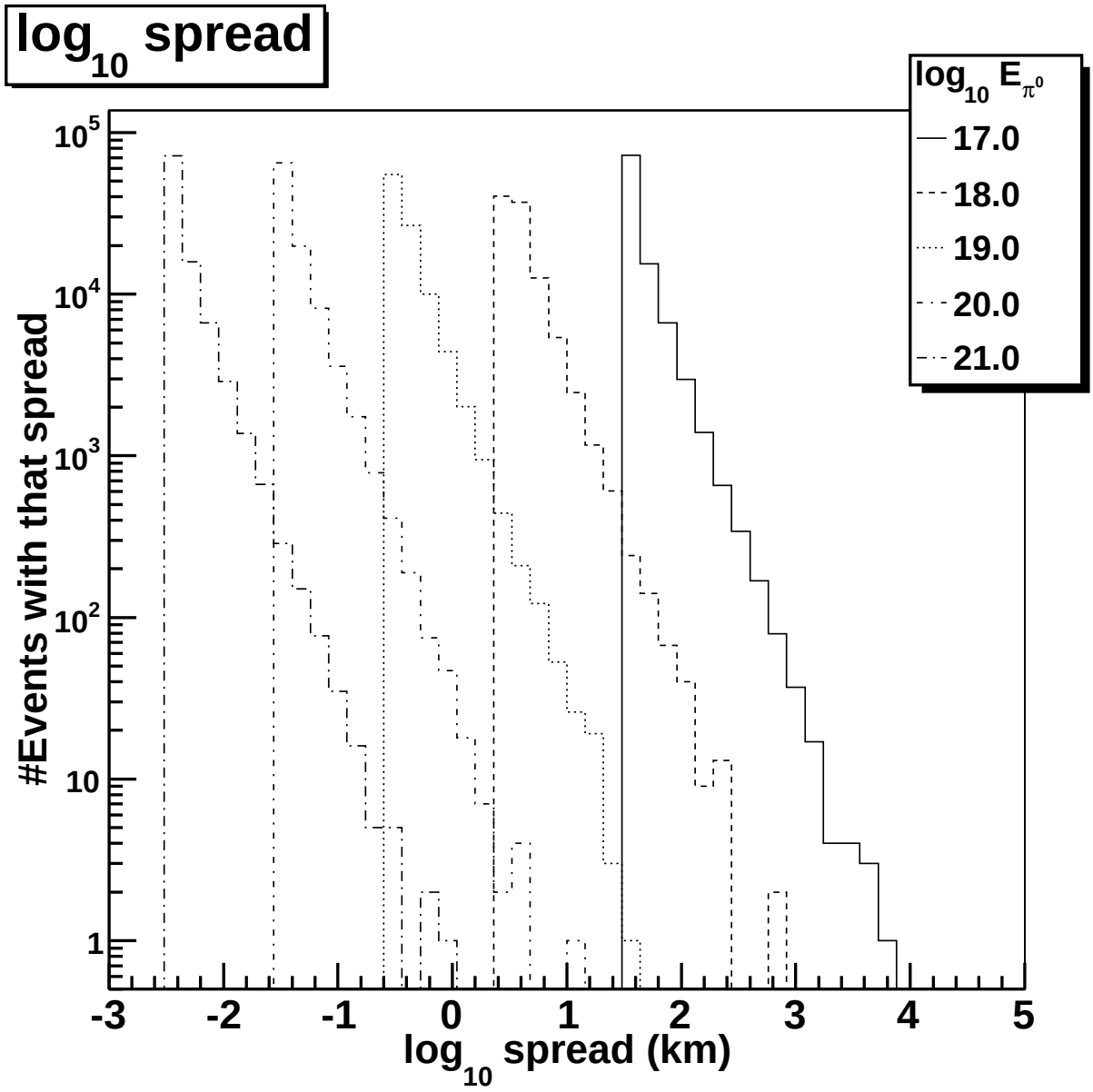

Figure 13.10: The perpendicular separation between Monte Carlo photons at various energies (R = 75 AU).

CHAPTER 14

MODELING DOUBLE PHOTON SHOWERS

In this chapter, we describe the Monte Carlo simulation of double-shower events from ultra-high energy π^0 decays. The simulated events are critical to the formulation of an event-selection strategy that optimizes the probability of observing actual π^0 double-photon showers while minimizing background. This preliminary Monte Carlo used the standard proton shower library for the Monte Carlo simulations since the spectra presented in previous chapters was deemed higher priority. The information presented in this chapter describes the steps taken to generate and fit photon showers using CORSIKA [44] as well as the double-shower Monte Carlo created to generate simultaneous showers. This search is considered preliminary and a more refined study is planned.

14.1 CORSIKA Shower Simulation

As high-energy photons (primaries) enter the atmosphere they produce purely electromagnetic extensive air showers (see section 3.2). In order to understand how ultra-high energy particles produce extensive air showers in the atmosphere, the CORSIKA simulation package [44] is used by the HiRes collaboration. Since most particles are known to be hadrons (see section 2.2) the standard HiRes-1 shower library is composed of mostly protons and iron. The entire simulated photon shower library generated previously consists of $\sim$ 5500 showers at $10^{18.0}$, $10^{18.5}$, $10^{18.7}$, $10^{19.0}$, $10^{19.5}$, $10^{19.7}$, and $10^{20.0}$ eV. These were all generated with a standard set of modeling techniques. In order to search for simultaneous photon showers, an extended CORSIKA shower library was generated down to energies of $10^{15.0}$ eV. In the follow-up searches, this new library will then allow for better modeling of π^0 decays with large perpendicular separations, $D_\perp$, where one photon will have more energy than the other (see Figures 13.9 and 13.10). By the time of this dissertation, the simulated CORSIKA showers have been generated and fit to the Gaisser-Hillas parameterization (see equation 4.11). This section will describe this process.

14.1.1 LPM Effect

In electromagnetic shower development, the Landau-Pomeranchuk-Migdal (LPM) effect can suppress photon production [58] [66]. When the electron passes through a region where bremsstrahlung can occur (see section 3.2.1), the radiation produced where the electron undergoes multiple scattering can destructively interfere, thereby reducing the probability of bremsstrahlung photon emission. This also occurs in the reverse process of pair-production. This effect becomes significant when

$$\frac{k}{E} < \frac{E}{E_{LPM}} \tag{14.1}$$

where k is the photon energy, E is the electron energy, and E_{LPM} is the material-dependent, LPM critical energy equal to

$$E_{LPM} = \frac{\alpha m^2 X_0}{4hc} \tag{14.2}$$

where α is the fine structure constant, m is the electron mass, h is Planck's constant, c is the speed of light, and X_0 is the radiation length of the material through which the electron is passing . This effect has been studied in cosmic ray extensive air showers [57] and is now a standard feature in the CORSIKA simulation package that can be turned on or off.

14.1.2 Magnetic Bremsstrahlung

Another effect that can influence UHE photon showers is preshowering, or magnetic bremsstrahlung [35] [65]. Cosmic ray photons of energy $\geq 2 \times 10^{19}$ eV can pair-produce in the Earth's magnetic field. The resulting electrons and positrons will then produce new photons through quantum synchrotron radiation. This process can then repeat and produce an early electromagnetic cascade which will interact with the Earth's atmosphere to produce the final extensive air shower. This effect has been studied on the effects of ultra-high energy photons [57]. This is also a standard option in the CORSIKA software that can be enabled of disabled.

14.1.3 CORSIKA Shower Generation

For the new shower library, three types of shower primaries were generated using CORSIKA: 1) preshowering photons, 2) nonpreshowering photons, and 3) protons. All three included the LPM effect and used QGSJET01 for the high-energy interactions and GHEISHA for the low-energy interactions. The shower size in these events was recorded

in 176, 7g/cm^2 bins in slant-depth (see section 4.2) [44]. Photon-primary sets were thrown at tenth-decade energies for individual energy bins between $10^{15.0} - 10^{20.9}$ eV, all with a 45° zenith angle, for both preshowering and nonpreshowering photons. Additional sets were thrown for protons and preshowering and nonpreshowering photons at multiple zenith angles (between 0° - 70°) at every half-decade in energy between $10^{15.0} - 10^{20.5}$ eV. This second set of simulated showers allowed for a combination of both a zenith angle and an azimuthal angle study. It also allowed for a comparison between the current reconstruction of photons and protons generated simultaneously, as well as a comparison of the current set of simulated proton showers to those in the HiRes-1 shower library. An example of a preshower input file is shown in Table 14.1. A nonpreshowering photon input file does not contain the "GCOORD" parameter [42] and the proton "PRMPAR" value [43] is 14 in the input file.

14.2 Photon Shower Library

After the generation of the CORSIKA showers, a ROOT [99] macro was used to fit the number of charged particles, as a function of slant depth, to the Gaisser-Hillas (GH) function (see equation 4.11). Since photons have very small cross sections at UHE energies and are therefore slow to increase in the number of charged particles in the shower, they tend to strike the surface of the earth before they reach X_{max}.

A number of checks were made to ensure that the GH fits were robust and accurate. First, for showers that reach ground before reaching maximum, the shower size drops discontinuously in the last few slant-depth, x, bins. As seen in Figure 14.1, the last data point is well below the expected value of a smooth curve and this Gaisser-Hillas fit, which includes all points, is obviously biased. To avoid this bias, the number of charged particles, n, of the last point was checked to be at most 1% of the largest recorded number of charged particles, N. If n_{last} was less than 1%, only data points with n above this lower limit were included in the GH fit. If n_{last} was greater than 1%, successive tests were then performed at $f_{last} = 2\%$, 3.5%, and 5% until $n_{last}/N > f_{last}$.

Occasionally n of the last few retained bins just before the last bin ($x_{last} \approx 1240$ g/cm^2) could be slightly discontinuous, but closer than x_{last}. As can be seen in Figure 14.2, where the last point has already been excluded, the few remaining end points bias the fit to peak early. To compensate for this bias, the last 10 bins (not including x_{last}) were averaged according to the equation

$$\langle n \rangle = \frac{\sum \frac{n_i}{n_{i-1}}}{10} \tag{14.3}$$

where n_i is the number of charged particles for slant depth i. Bins were then removed if

Table 14.1: A generic input file for a simulated preshowering photon.

RUNNR	RRRRRR	run number
EVTNR	NNNNN	number of first shower event
NSHOW	1	number of showers to generate
PRMPAR	1	particle type of prim. particle
ESLOPE	0.0	slope of primary energy spectrum
ERANGE	EEEEEEEE1 EEEEEEEE2	energy range of primary particle
THETAP	AAA1 AAA2	range of zenith angle (degree)
PHIP	0. 360.	range of azimuth angle (degree)
SEED	SSS11 0 0	seed for 1. random number sequence
SEED	SSS22 0 0	seed for 2. random number sequence
OBSLEV	1500.E2	observation level (in cm)
FIXCHI	0.	starting altitude (g/cm**2)
FIXHEI	0. 0	first interaction height & target
MAGNET	21.75 47.50	magnetic field:
		Dugway ave(CMB,MAAF,GATE)
GCOORD	-112.825 40.205 2005 1 0	preshowers centered at HR1
HADFLG	0 0 0 0 0 2	flags hadr.interact. & fragmentation
ECUTS	0.30 0.30 0.003 0.003	energy cuts for particles
MUADDI	T	additional info for muons
MUMULT	T	muon multiple scattering angle
ELMFLG	T T	em. interaction flags (NKG,EGS)
STEPFC	1.0	mult. scattering step length fact.
RADNKG	200.E2	outer radius for NKG lat.dens.distr.
ARRANG	0.	rotation of array to north
LONGI	T 7.07 T T	longit.distr. & step size & fit & out
ECTMAP	1.E3	cut on gamma factor for printout
MAXPRT	100	max. number of printed events
DATBAS	T	write .dbase file
USER	USERNAME	user
DEBUG	F 6 F 1000000	debug flag and log.unit for out
THIN	1.E-5 TTTT 0.E0	energy thinning options
PLOTSH	F	plot the shower

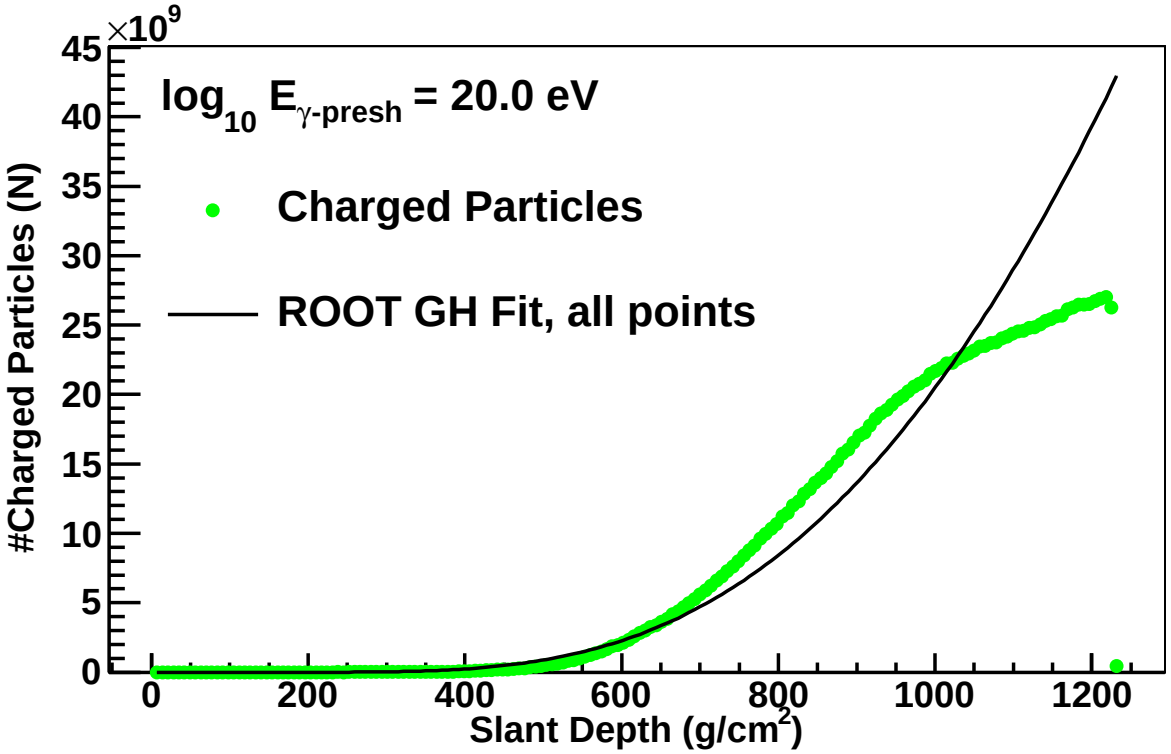

Figure 14.1: A CORSIKA-generated $10^{20.0}$ eV nonpreshowering photon extensive air shower profile with all bins included in the fits.

$$\frac{n_i}{\langle n \rangle} < 0.99 \tag{14.4}$$

to give a better fit to the GH parameterization.

The remaining data points are sent through an iterative series of fits initialized with idealized constants of both: A) $X_0 = -200.0$ g/cm^2, $\lambda = 50$ g/cm^2, and X_{max} and N_{max} obtained by finding the peak in the CORSIKA output; or B) the N_{max}, X_0, X_{max}, and λ_0 from the CORSIKA Hillas parameterization:

$$N_e(x) = N_{max} \times \left[\frac{x - X_0}{X_{max} - X_0}\right]^{\frac{X_{max}-X_0}{\lambda_0+\lambda_1 x+\lambda_2 x^2}} e^{\frac{X_{max}-x}{\lambda_0+\lambda_1 x+\lambda_2 x^2}}. \tag{14.5}$$

After an initial fit, the residuals were calculated for the shower size over the entire slant depth range that was considered. The ratio n_{calc}/n_{actual} was calculated for each bin and fit to both a linear and a cubic function (see Figure 14.3). Two values were defined

$$S = log_{10}(|L_1|) > -4 \tag{14.6}$$

and

$$R = log_{10}(\sigma_{L_1})/log_{10}(\sigma_{C_3}) \tag{14.7}$$

where L_1 is the 1^{st}-order polynomial constant of the linear fit, σ_{L_1} if the error in L_1, and σ_{C_3} is the error in the 3^{rd}-order polynomial constant of the cubic fit (see Figure 14.4).

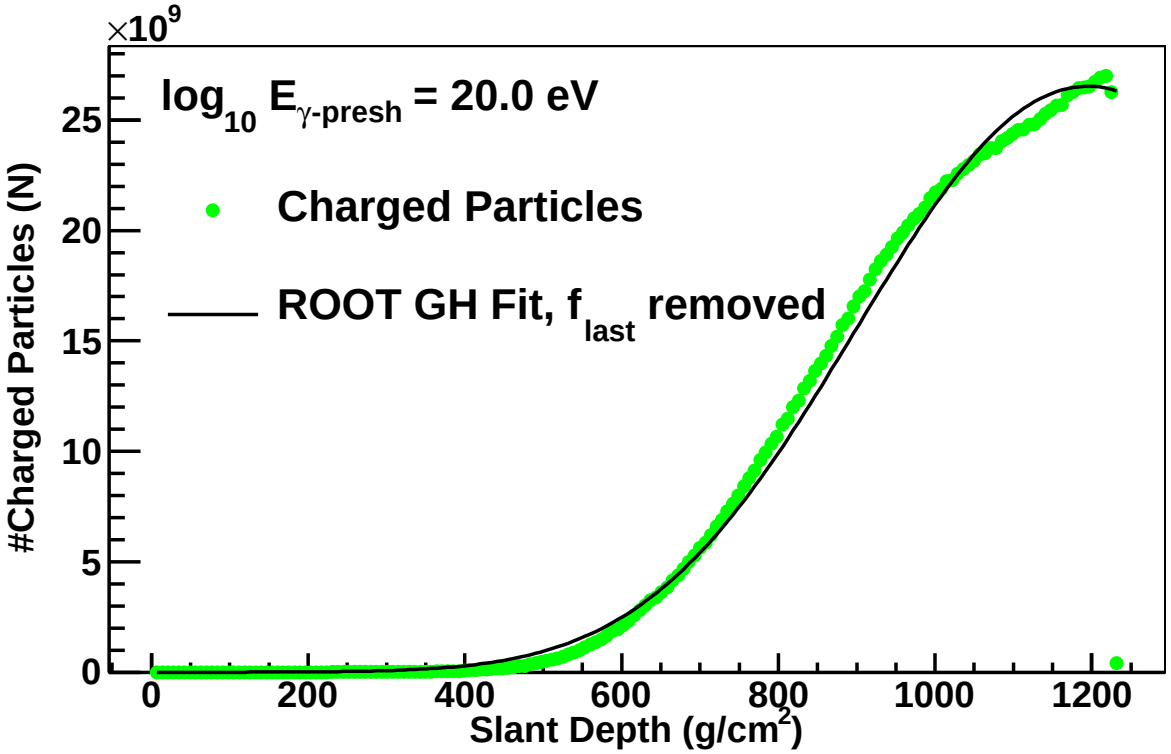

Figure 14.2: A CORSIKA-generated $10^{20.0}$ eV nonpreshowering photon extensive air shower profile with bins with $n > f_{last}$ included in the Gaisser-Hillas fit.

If either A) the combination of $S > -4$ and $R > 0.55$ or $R < 0.43$, or B) the X_0 and λ values did not change from the defined constants, the data were refit with a second initialization: the previous initialization values multiplied by the empirically-determined constants in Table 14.2.

At this point, there are two potential best fit parameterizations: CORSIKA Hillas initialized, or observed peak initialized. If only one fit passed the above quality cuts, it was retained. If both passed the cuts, their S and R were compared to see which was better (e.g., smaller) in both cases. The example event of Figures 14.1, 14.2, and 14.3 had the final good fit shown in Figure 14.5.

Elongation rate studies were made using the resulting fits. As expected, with increasing energy, the photon mean X_{max} shows an elongation rate well above that of protons (see Figure 14.6 and Table 14.3). For photons with energy above $\sim 10^{19.4}$ eV, preshowering usually happens and the mini-cascade entering the atmosphere will usually initiate the extensive air shower earlier. However, the arrival direction heavily influences the effects of the preshowering. Since the geomagnetic fields change depending upon the zenith and azimuthal directions of approach, the intensity of the fields will affect the photons differently (see Figures 14.7 and 14.8). The range of interest for double-showers lies within the photon region where preshowering and nonpreshowering elongation rates

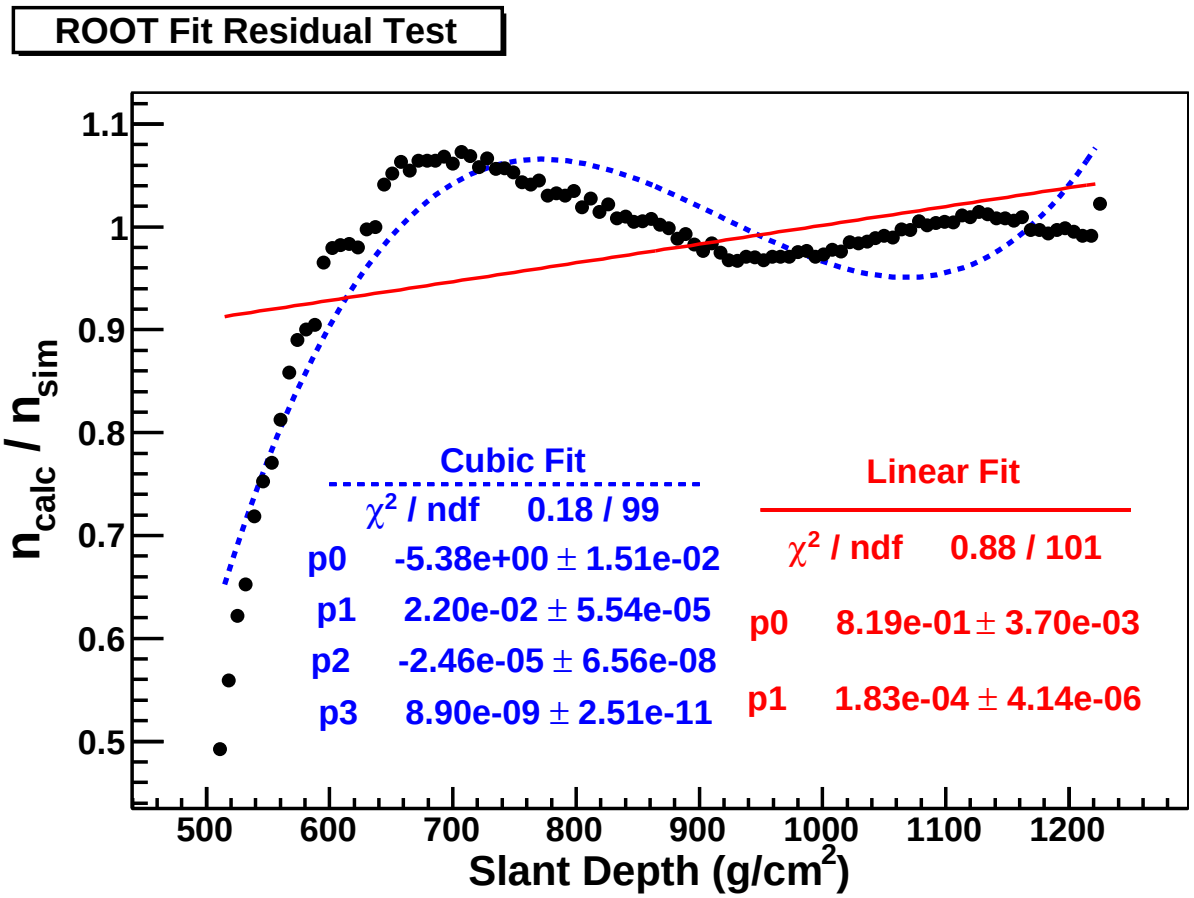

Figure 14.3: The residuals of the CORSIKA-generated $10^{20.0}$ eV non-preshowering photon extensive air shower profile of figures 14.2 and 14.1 for bins included in the fit. This fit passed the residual checks.

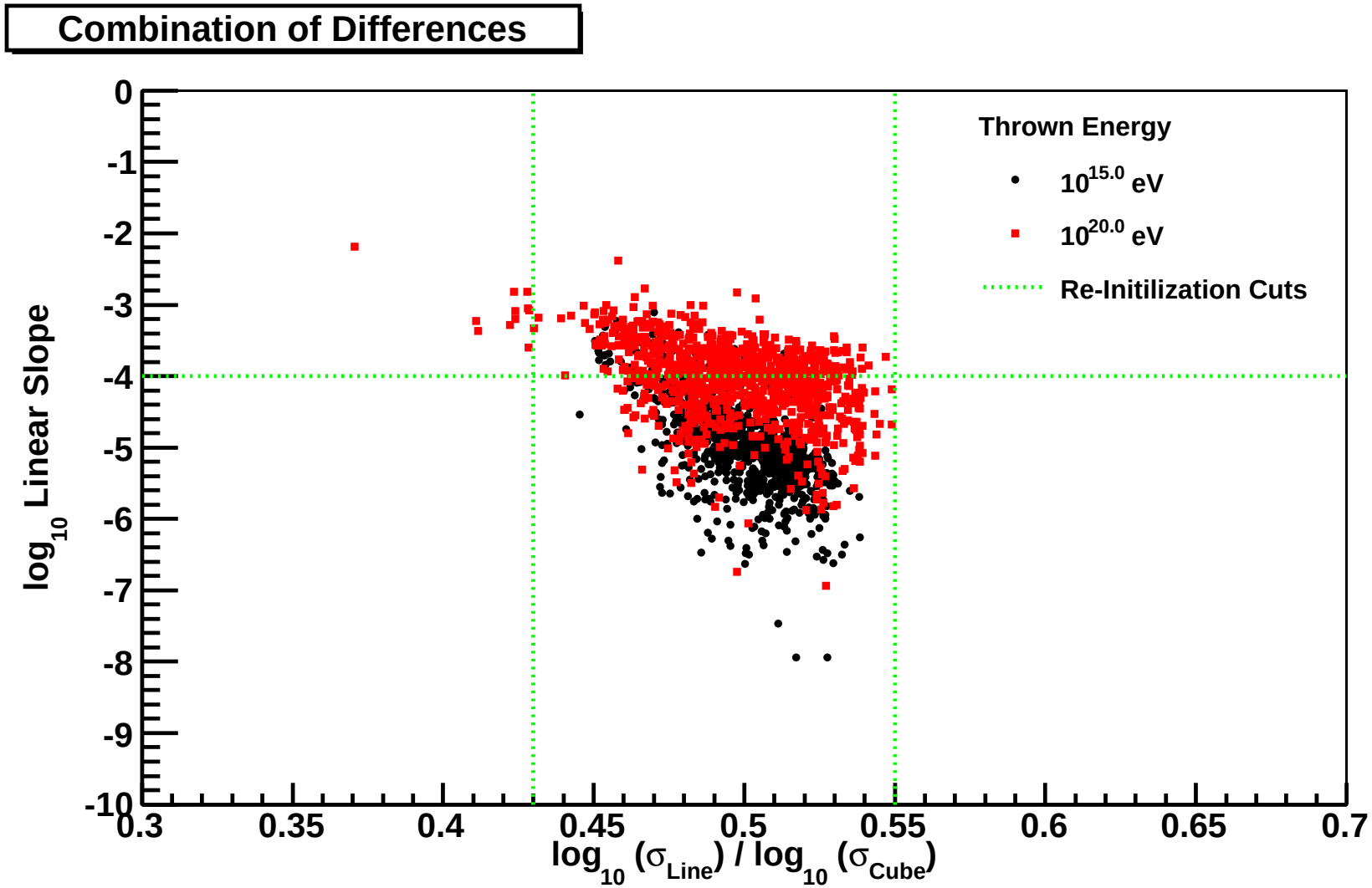

Figure 14.4: The residual cuts used to decide whether a reinitialization needed to be made to the cut parameters.

Table 14.2: These values were used as multipliers to the respective value for the input values of a secondary fit to the Gaisser-Hillas parameterization.

Parameter	Multiplier
X_0	-3
X_{max}	1.7
N_{max}	2.9
λ	6

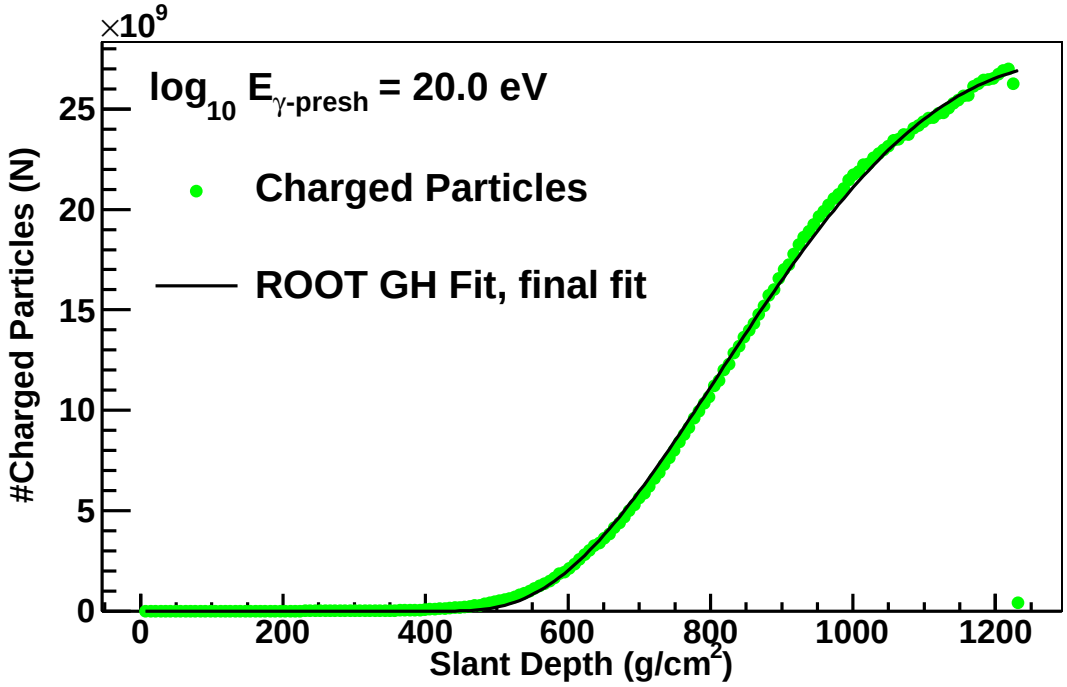

Figure 14.5: A CORSIKA-generated $10^{20.0}$ eV nonpreshowering photon extensive air shower profile with the final Gaisser-Hillas fit used in the library.

appear similar (between $\sim 10^{17.5} - 10^{18.8}$ eV). However, because the analysis for producing the Middle Drum spectrum was deemed higher priority the new shower library was not used in the double-shower search presented in this dissertation. Additional studies need to be performed on the events of the new library and were deemed beyond the scope of this dissertation.

14.3 Double Shower Monte Carlo

For this initial study, proton shower profiles were used in the generation of these double-shower Monte Carlo simulations using a modified version of the HiRes-1 Monte Carlo. The standard HiRes Monte Carlo could not be used since it only allowed a single

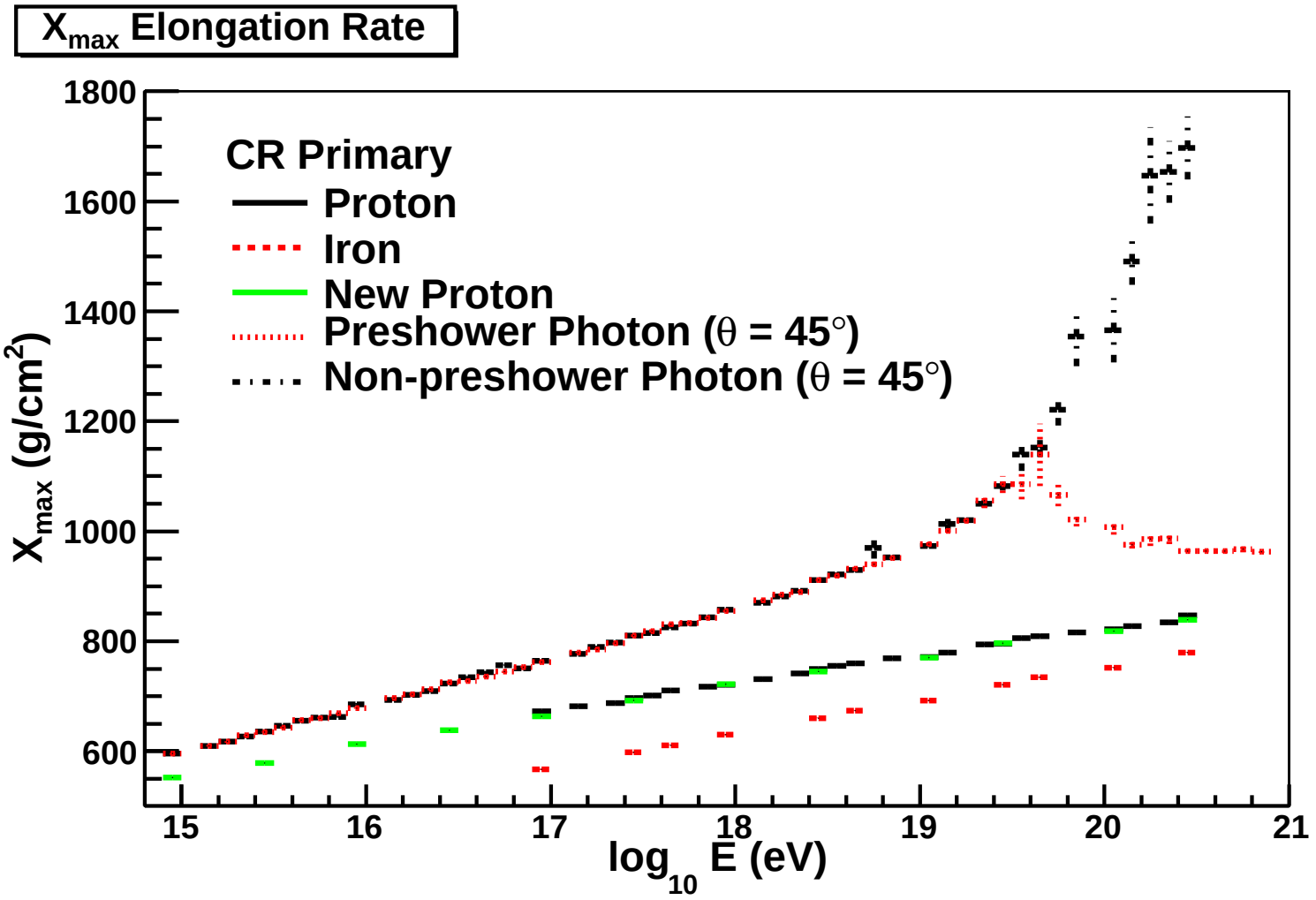

Figure 14.6: The elongation rates of photons, both preshowering and nonpreshowering, with respect to protons and iron. The divergence of the photon elongation rates above $\sim 10^{19.0}$ eV is due to the LPM effect; the split at $\sim 10^{19.5}$ eV is due to preshowering.

Table 14.3: The linear fit parameters of the elongation rates shown in Figure 14.6

Primary	Slope
Proton (standard)	49.04 ± 0.45
Iron (standard)	60.33 ± 0.22
Proton (new)	51.05 ± 0.24
Photon (preshowering)	89.05 ± 0.31
Photon (nonpreshowering)	88.89 ± 0.31

shower to be generated and observed. The normal Monte Carlo process is

1. randomly choose a trajectory and location for the shower
2. randomly choose a Gaisser-Hillas profile based on energy that follows the chosen trajectory
3. ray-trace the photo-electrons calculated at each slant depth based on the chosen Gaisser-Hillas profile to the detector
4. count the photoelectrons that hit a given photomultiplier tube
5. run the numbers through the electronic gains and filters
6. output the information.

The double-shower Monte Carlo takes advantage of the phenomenological observations that A) the $D_\perp$ spread between the shower axes is tightly correlated with the energy ratio between the two showers (see Figure 14.9), and that B) the energy ratio itself is well described by a simple Gaussian, independent of the π^0 energy, with a standard deviation of ~ 0.749 (see simulation results in Figures 14.10, 14.11, 14.12, 14.13, and 14.14). The simplest fit of the spread-energy correlation consists of two quadratics that intersect at the same 0.749 value (see Figure 14.15). The upper-range fit diverges from the simulation where the differences in the photon energies is greater than four orders of magnitude, but this difference would be, at most, a $\sim 10^{20}$ eV shower with a $\sim 10^{16}$ eV shower, of which the lower-energy shower would be nearly impossible to detect with the HiRes-1 detector. The only differences in the spreads for various pion energies arises in the intercept in the $\log_{10} D_\perp$ versus $|(\log_{10} E_1 - \log_{10} E_2)|$ plot of Figure 14.9 (see Figures 14.16, 14.17, 14.18). The linear and parallel nature of the polynomial-0 (P0) plot shows that the the only difference in the $D_\perp$ spreads is a scaling factor based on the initial pion energy. The parallel and flat nature of the polynomial-1 (P1) an polynomial-2 (P2) plots reflects our observation that the overall spread in $D_\perp$ depends only on the ratio E_1/E_2 and is independent of the pion energy.

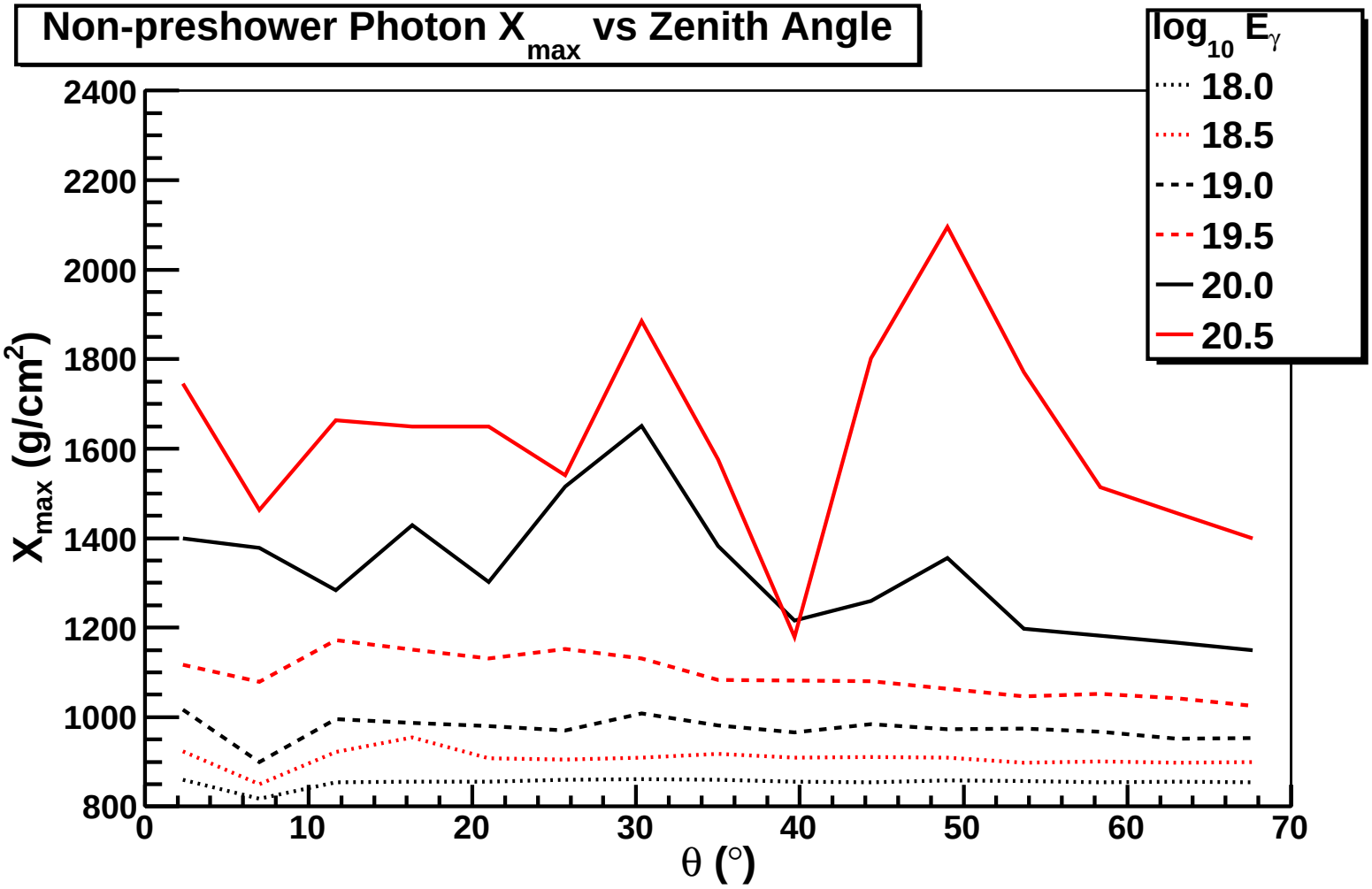

(a) Nonpreshowering

Figure 14.7: The zenith dependance on ultrahigh energy photons.

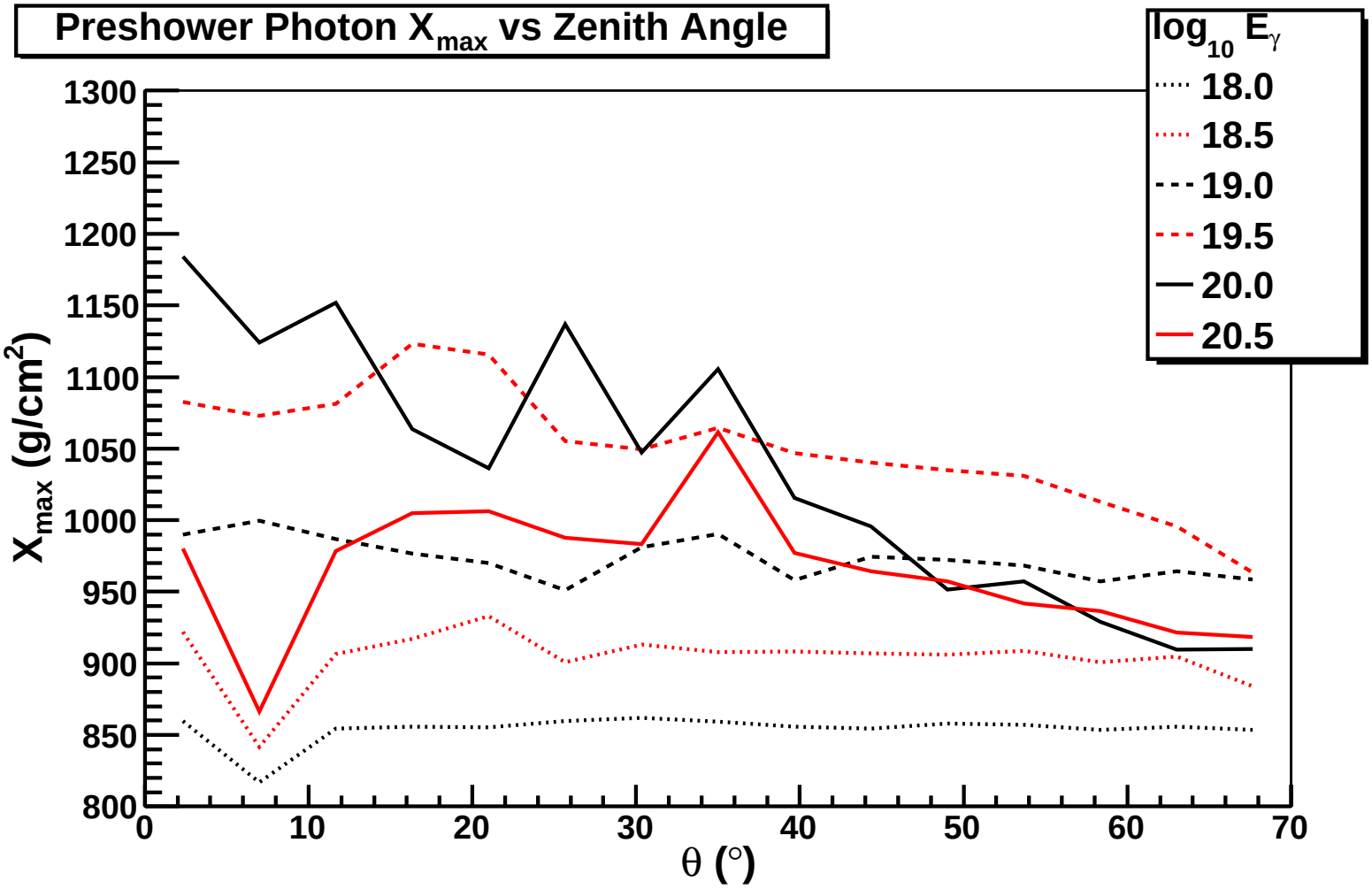

(b) Preshowering

Figure 14.7: Continued.

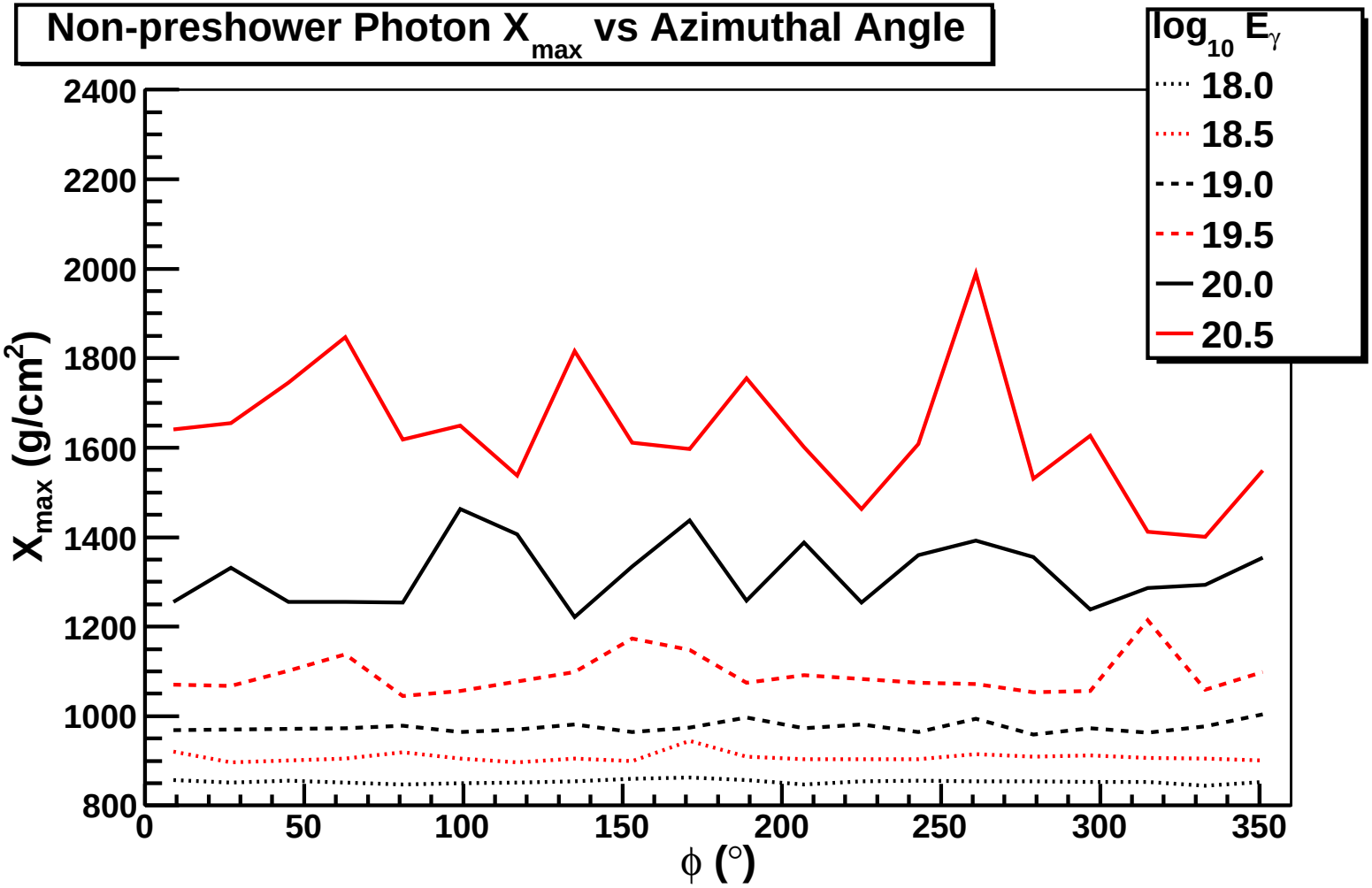

(b) Nonpreshowering

Figure 14.8: The azimuthal dependance on ultrahigh energy photons.

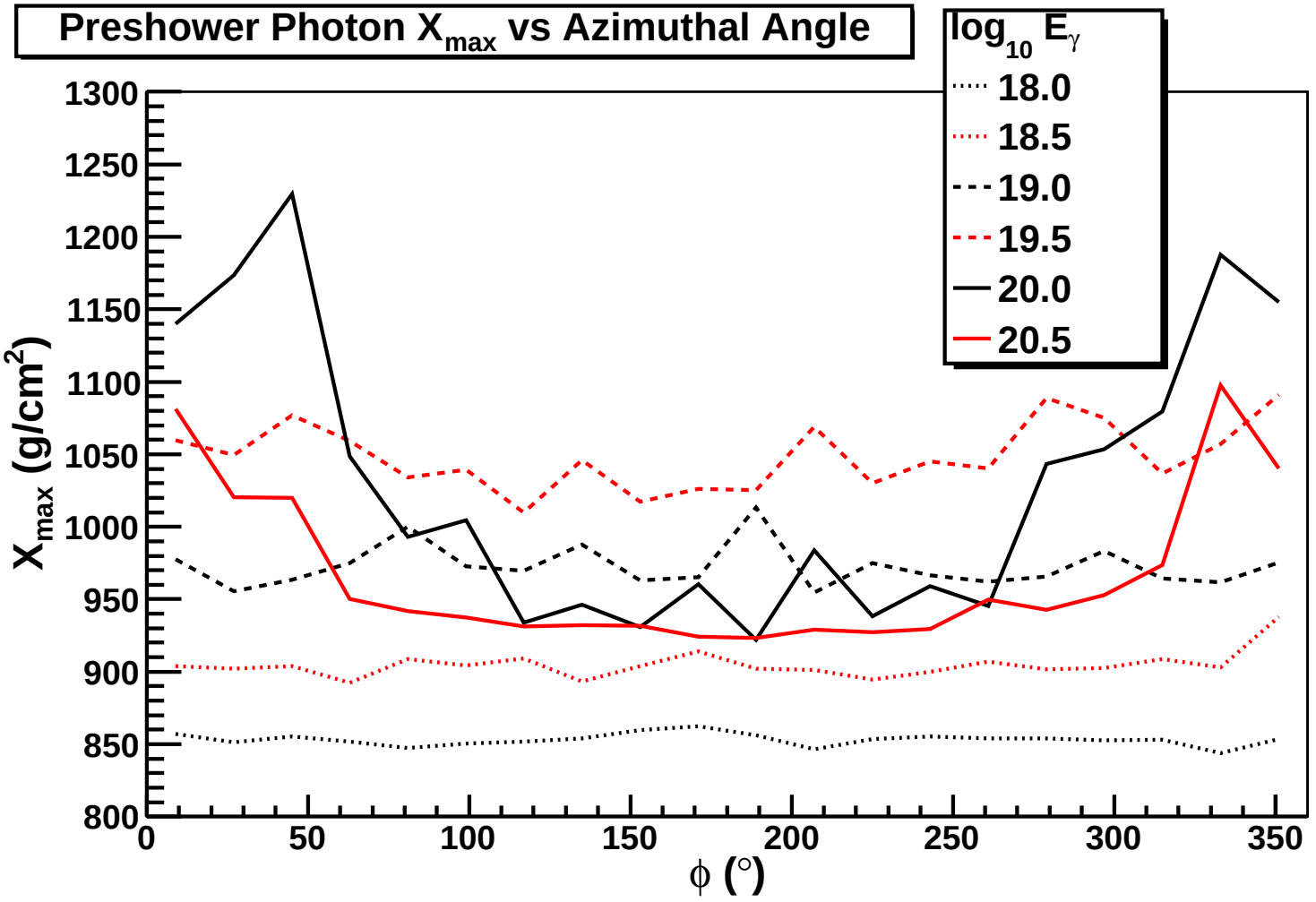

(b) Preshowering

Figure 14.8: Continued.

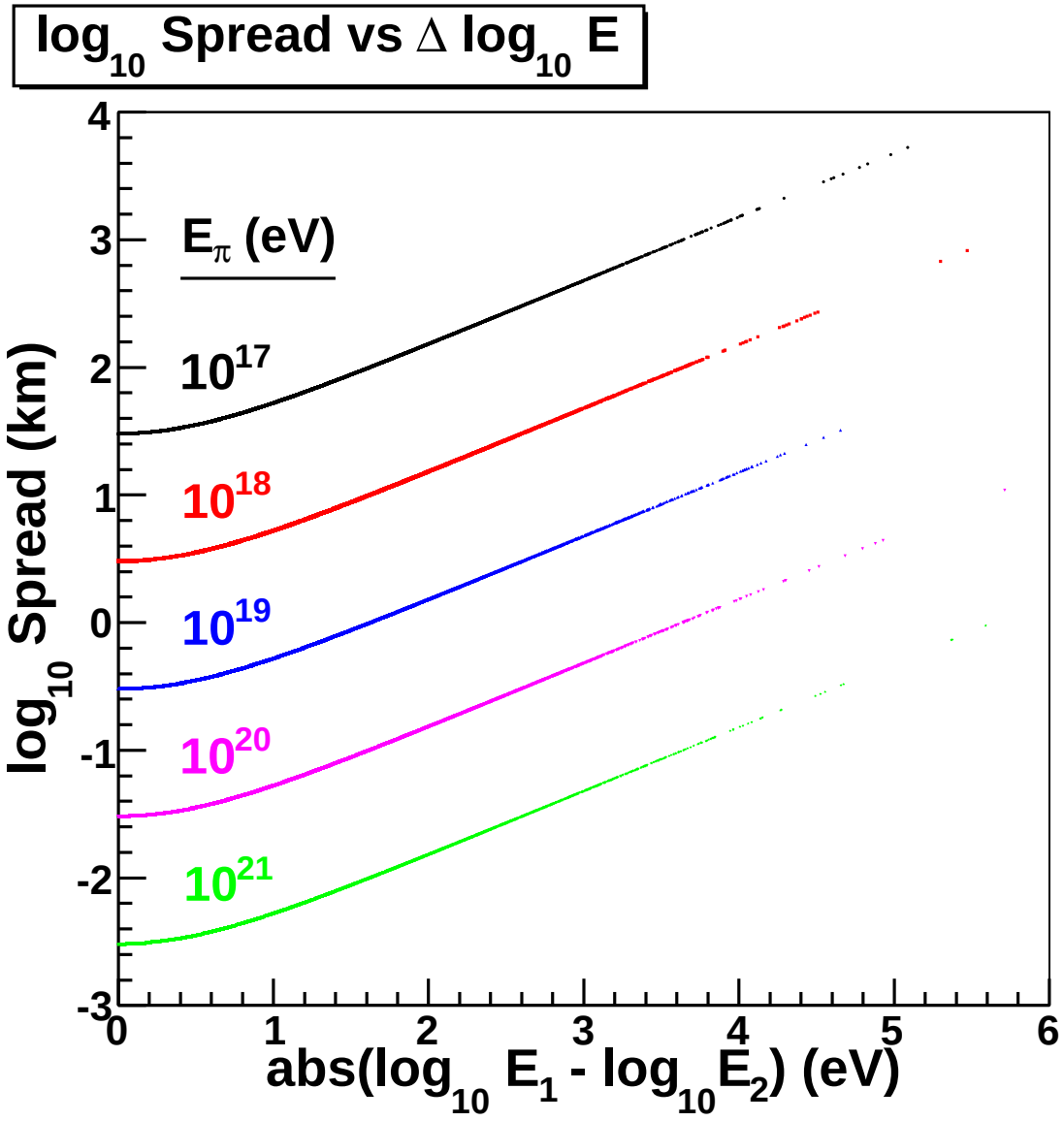

Figure 14.9: The spread between the simulated showers as a function of the difference in photon energy.

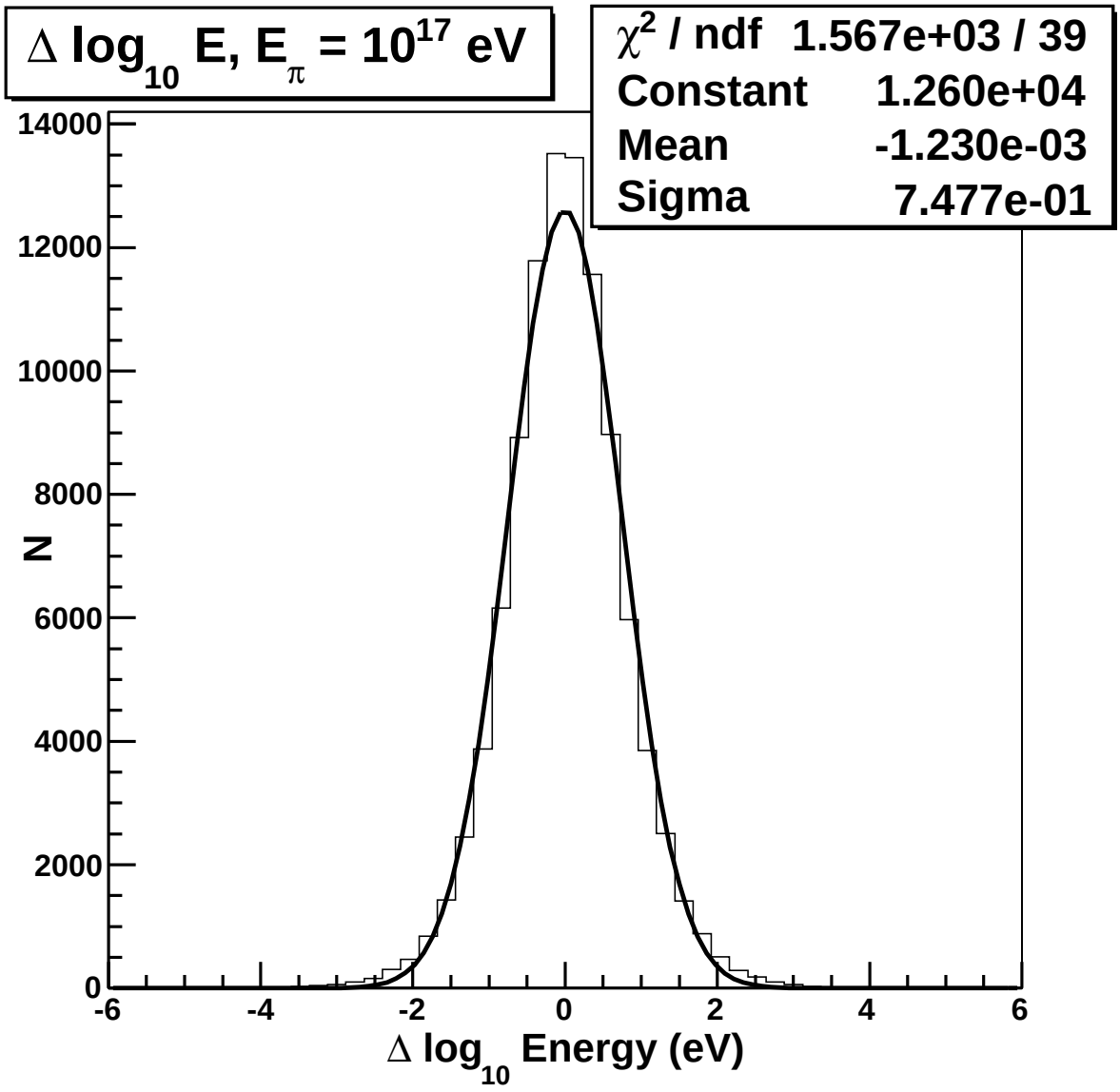

Figure 14.10: The difference between the two simulated photon energies produced 75 AU away with a π^0 energy of $10^{17.0}$ eV.

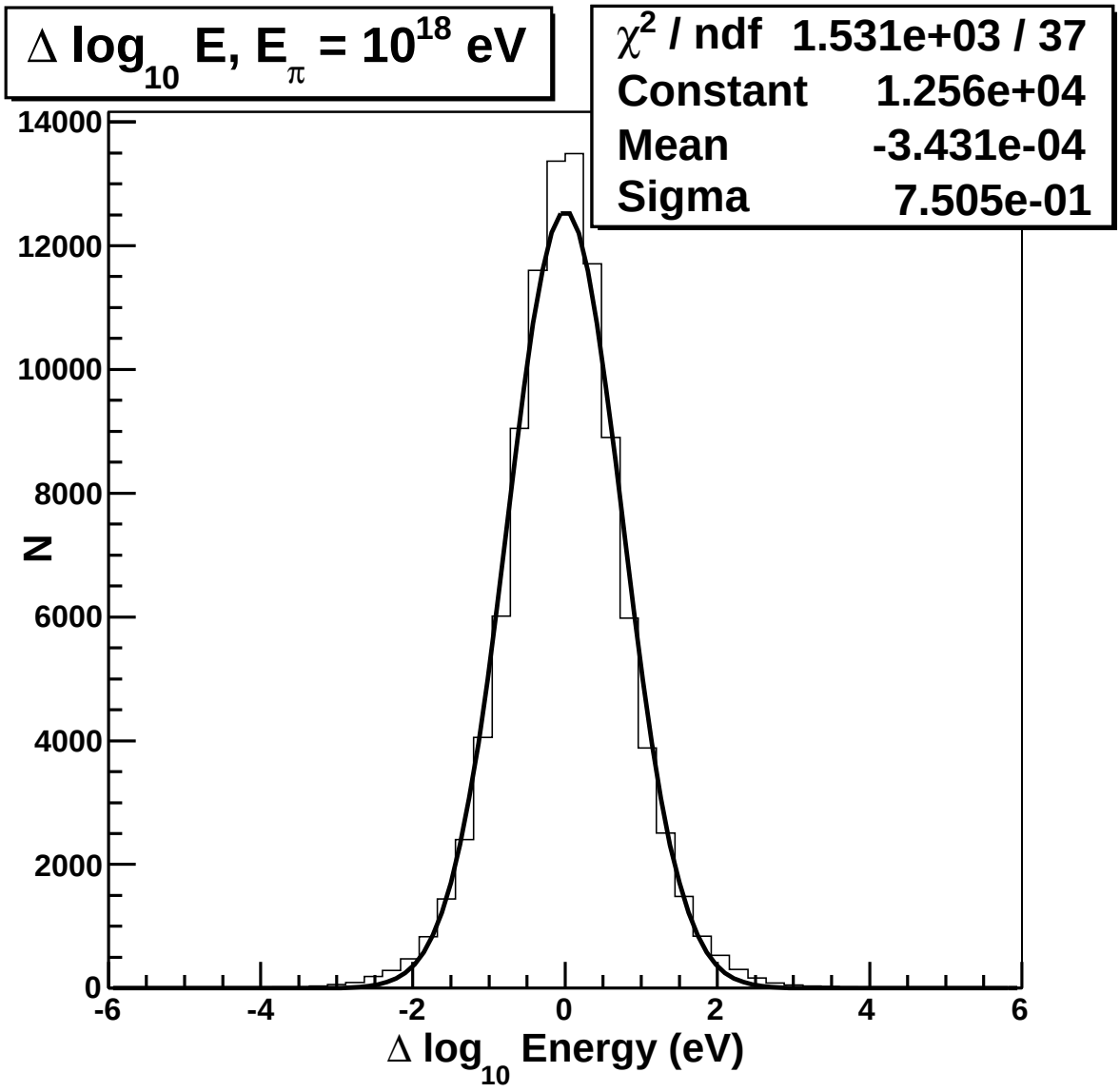

Figure 14.11: The difference between the two simulated photon energies produced 75 AU away with a π^0 energy of $10^{18.0}$ eV.

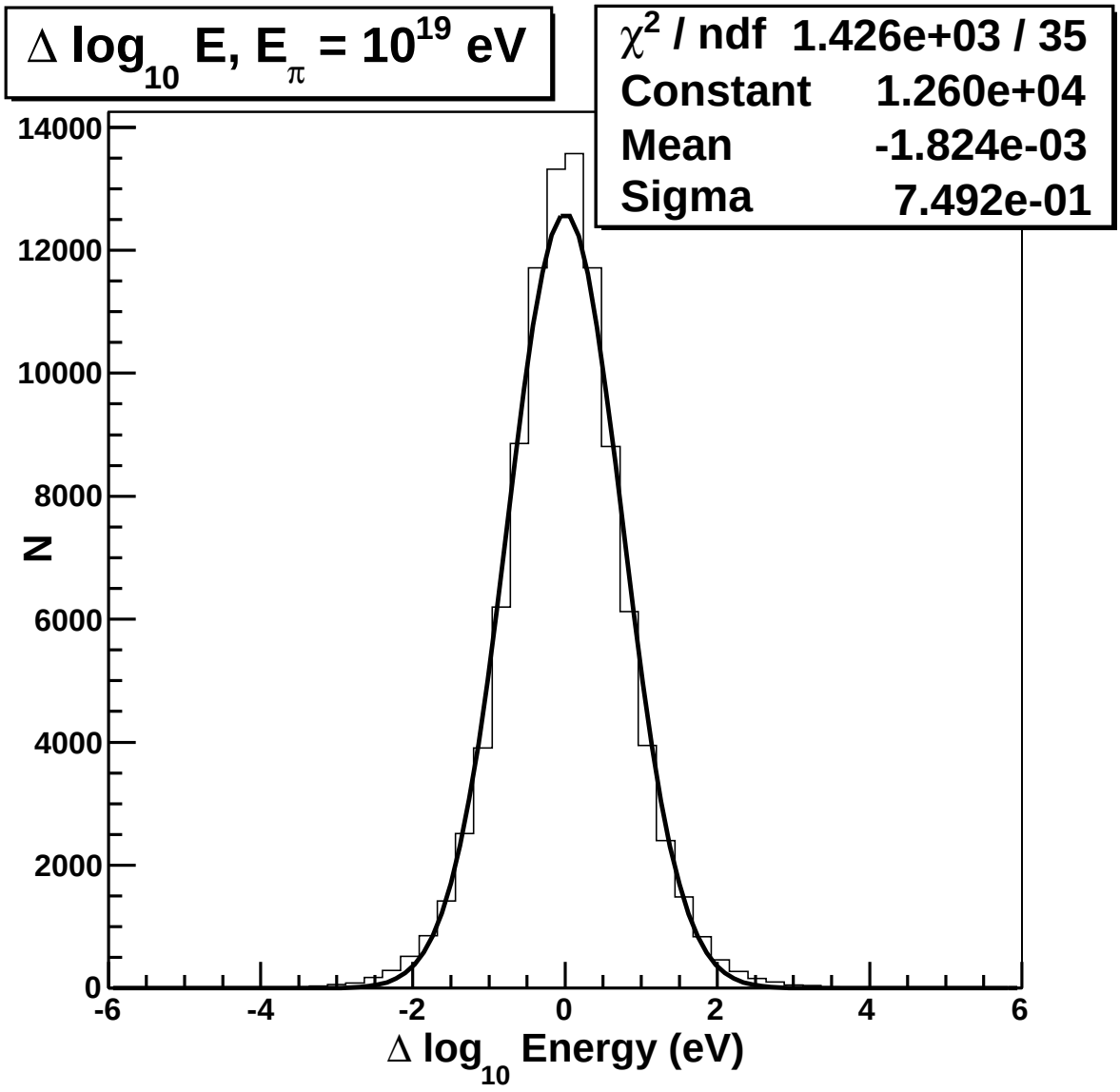

Figure 14.12: The difference between the two simulated photon energies produced 75 AU away with a π^0 energy of $10^{19.0}$ eV.

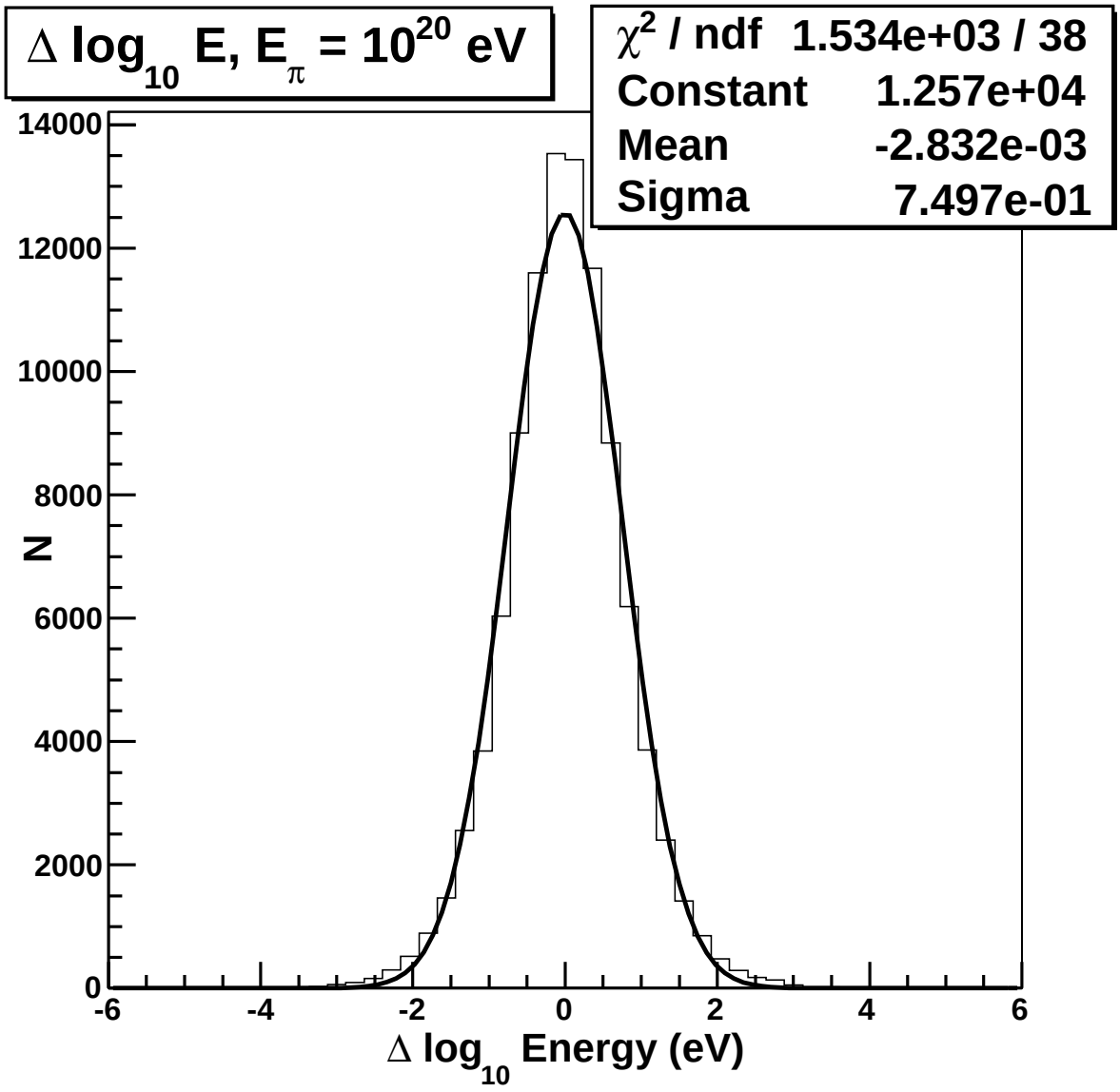

Figure 14.13: The difference between the two simulated photon energies produced 75 AU away with a π^0 energy of $10^{20.0}$ eV.

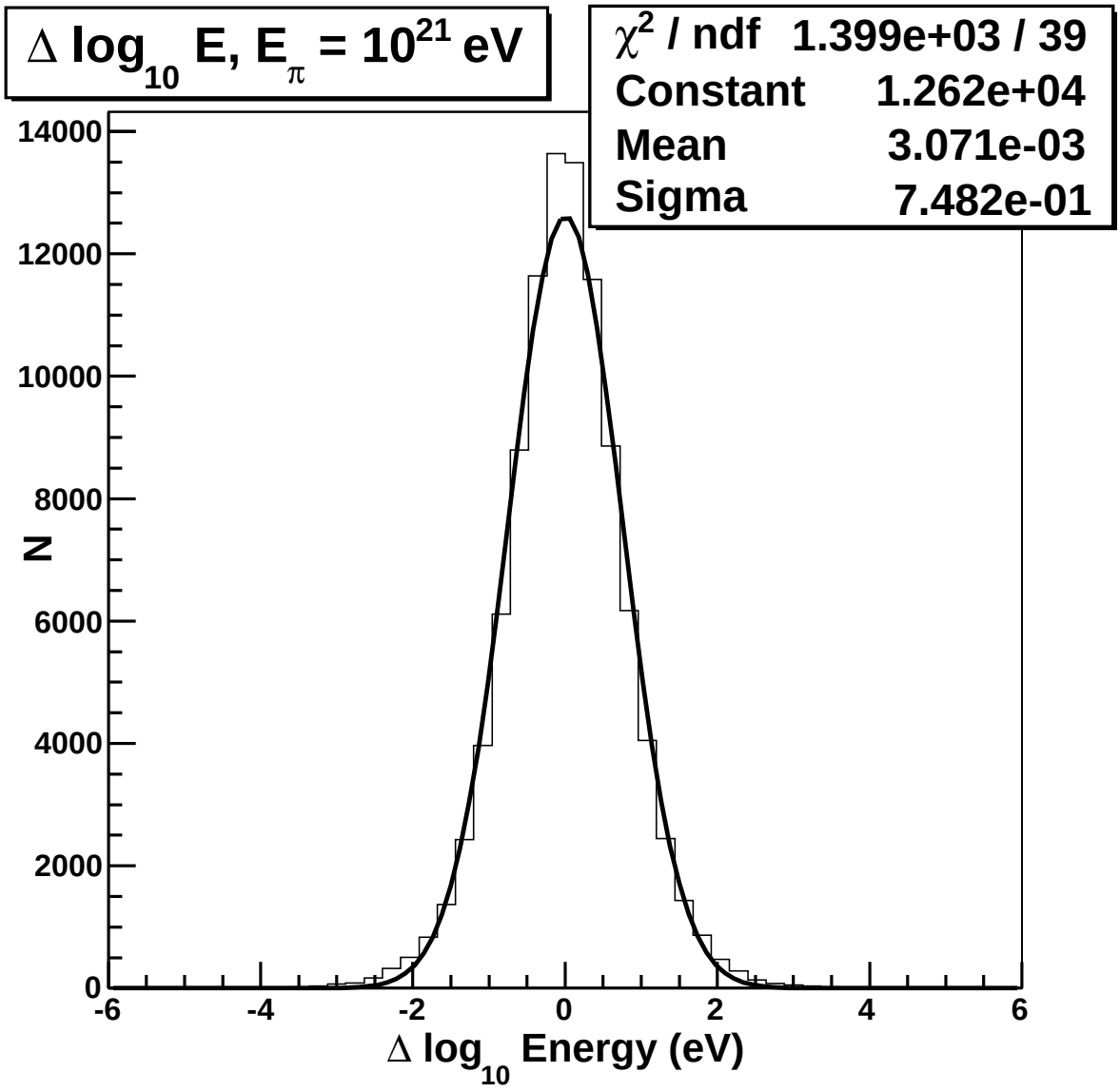

Figure 14.14: The difference between the two simulated photon energies produced 75 AU away with a π^0 energy of $10^{21.0}$ eV.

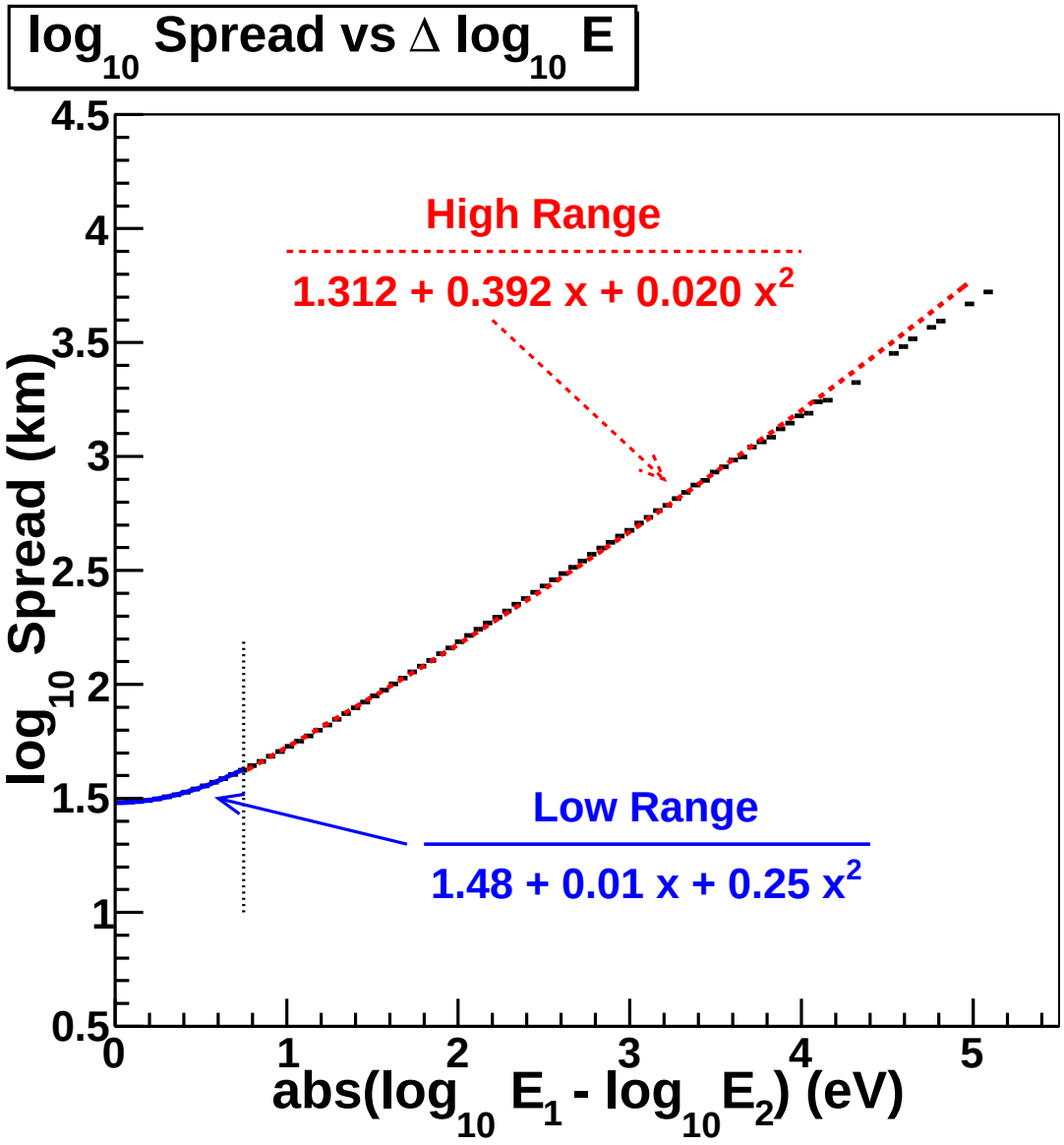

Figure 14.15: The fit of the 10^{17} eV pion energy for the upper and lower ranges. The other pion energies result similarly.

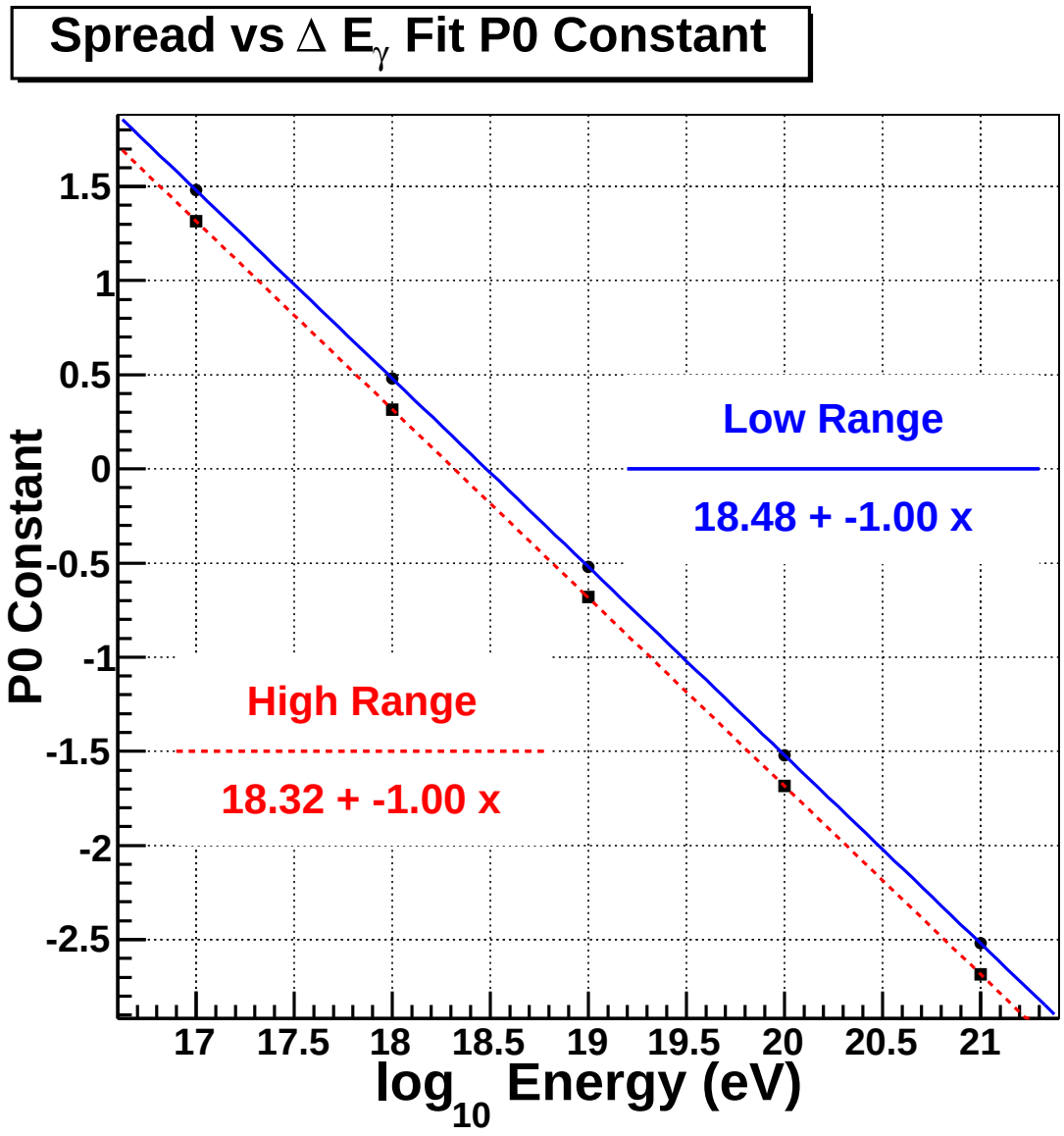

Figure 14.16: The difference in quadratic-fit P0 constant for the spread versus the difference in $\log_{10} E_{\pi^0}$ of the two simulated photons from Figure 14.15. The linearity and parallel nature of these lines indicates the $D_\perp$ spread is only dependent upon the pion energy.

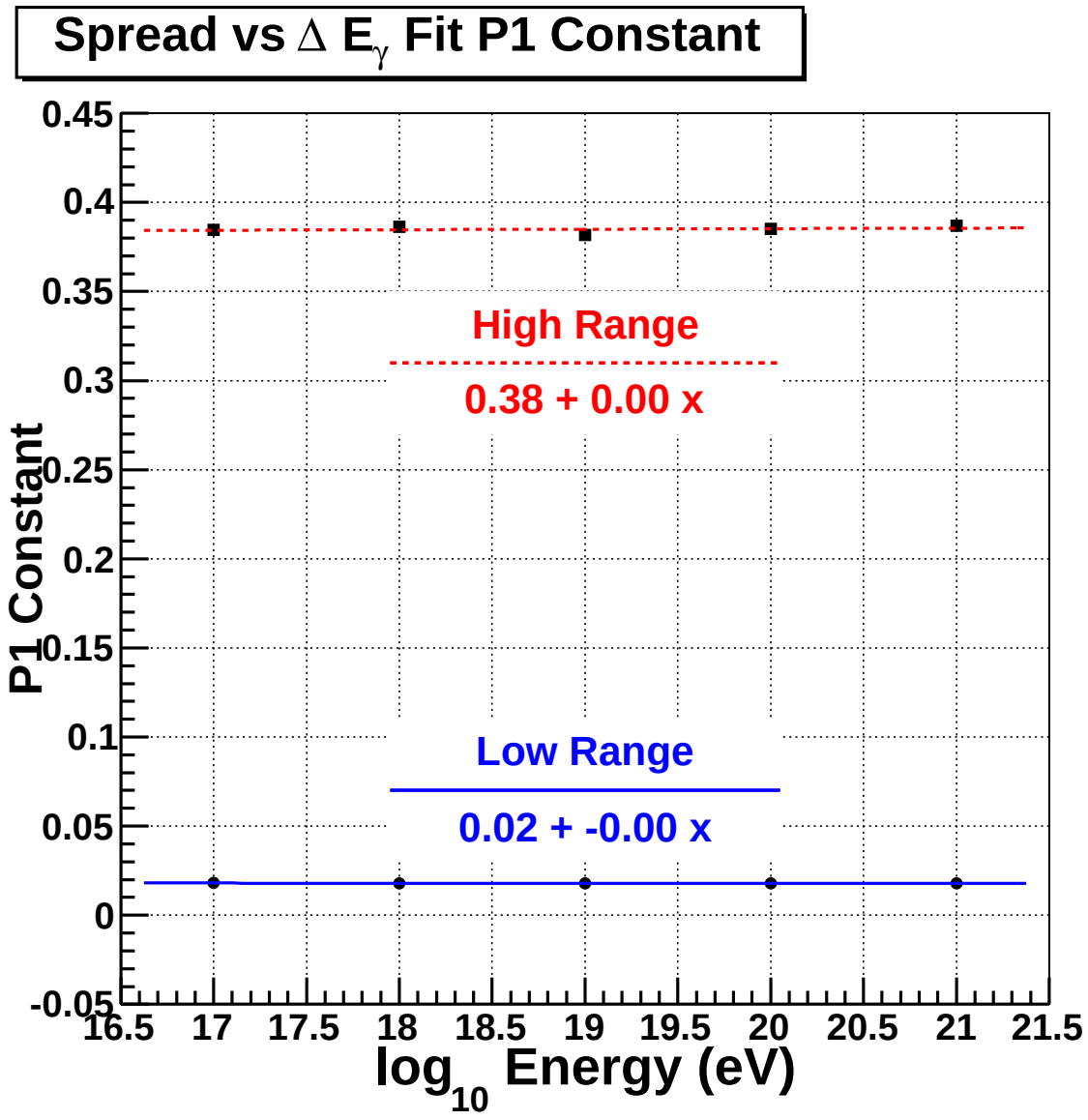

Figure 14.17: The difference in quadratic-fit P1 constant for the spread versus the difference in $\log_{10} E_{\pi^0}$ of the two simulated photons from Figure 14.15. The linearity and parallel nature of these lines indicates the $D_\perp$ spread is independent upon the pion energy.

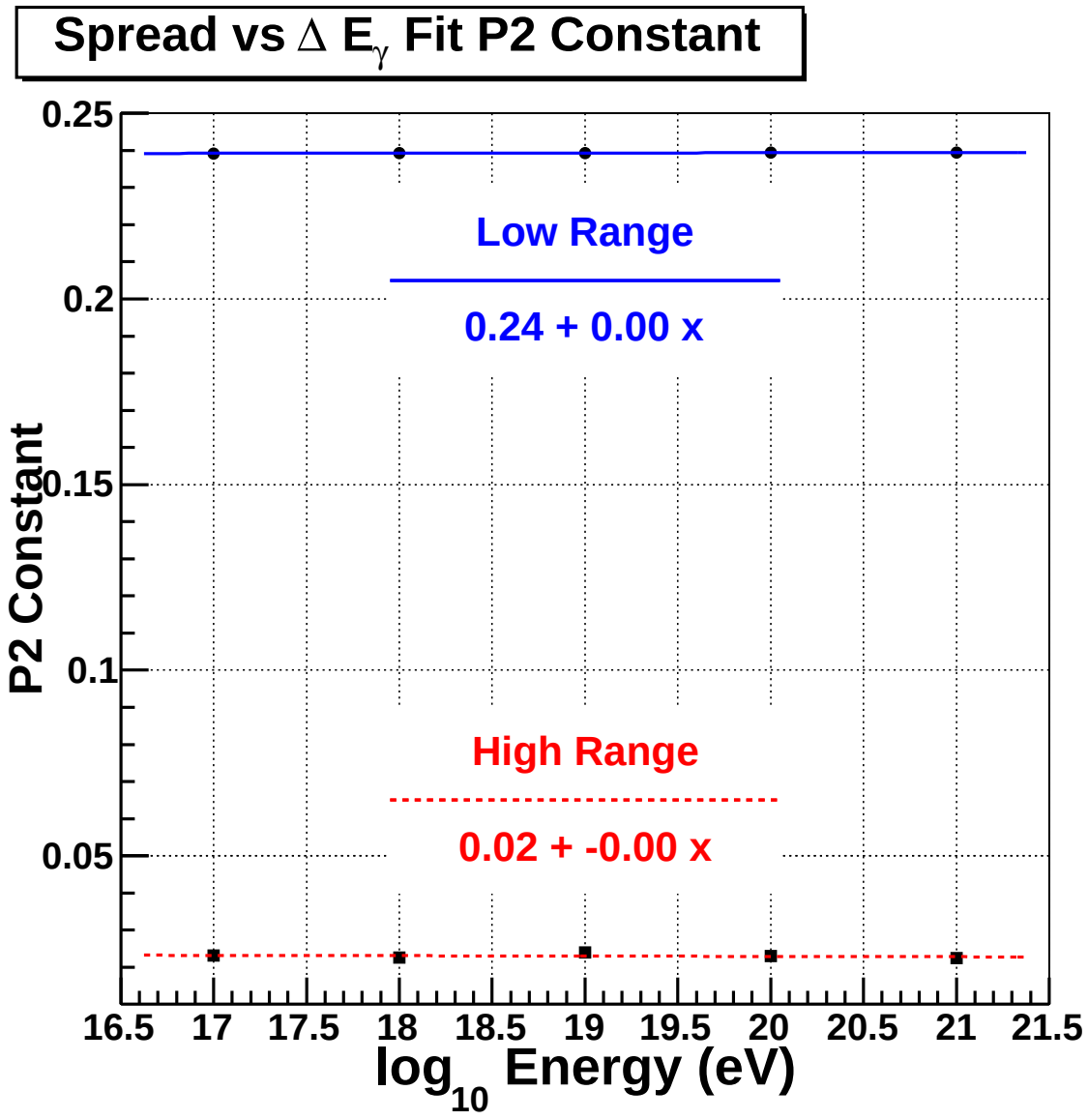

Figure 14.18: The difference in quadratic-fit P2 constant for the spread versus the difference in $\log_{10} E_{\pi^0}$ of the two simulated photons from Figure 14.15. The linearity and parallel nature of these lines indicates the $D_\perp$ spread is independent upon the pion energy.

A similar procedure to a single-shower event is followed for the first of the two simulated in the modified program, but before it is sent to the electronics, it instead stores the numbers and parameters of the first shower. A second shower is then generated with a randomly-chosen energy based on the 0.749 Gaussian standard deviation. The summation of these two shower energies then determines the simulated π^0 energy, and the difference between these two shower energies determines the perpendicular spread, $D_\perp$. Along with knowing the distance away from the first shower, the second shower is also thrown at a random angle, ϕ_{S2}, around the first shower, which will produce a different $\vec{R}_P$ to the observing detector. The second shower is thrown with the same trajectory as the first shower, but a new Gaisser-Hillas profile is randomly selected for this second shower and is projected to the detector. In summary, the procedure of the double-shower simulator is:

1. randomly choose a trajectory and energy of the first shower;
2. randomly choose a Gaisser-Hillas profile based on the energy that will follow the trajectory;
3. ray-trace to the detector the photoelectrons calculated at each slant depth based on the chosen Gaisser-Hillas profile;
4. count the photoelectrons that hit a given photomultiplier tube;
5. store the geometry, energy, and number of photoelectrons of the first shower;
6. randomly choose the energy of the second shower based on the 0.749 Gaussian standard deviation;
7. determine E_{π^0} and $D_\perp$ based on the correlation;
8. randomly choose the projection angle, ϕ_{S2}, about the first shower and the associated geometry to the detector (e.g., $\vec{R_P}$) using the same trajectory as the first shower;
9. randomly choose a Gaisser-Hillas profile based on the energy that will follow the trajectory;
10. ray-trace to the detector the photoelectrons calculated at each slant depth based on the chosen Gaisser-Hillas profile;
11. count the photoelectrons that hit a given photomultiplier tube.

After the numbers of photoelectrons (*npe*) observed by the photomultiplier tubes are determined for both showers, the electronics are allowed to trigger for 25 μs with

the intensity and the final tube trigger time of the two showers modulated for the time difference between the two showers to reach the cameras. Occasionally, one of the two showers is too far away to trigger within the gate window, so that shower is unobserved. As with the standard Monte Carlo, frequently both showers are unobserved and the event is recorded as empty. The final *npe* and timing values are then projected through the electronics to produce QDC and TDC values and the information is recorded.

Since a large number of shower pairs generated either fail to trigger or survive event selection and plane-fitting, many events were produced to allow for a reasonable number to be retained. Since the Monte Carlo generates one shower before choosing the other, the energy of the pion is dependent upon the summation of the two individual shower energies. The number of events generated for this study is listed by pion energy in Table 14.4.

For this preliminary study, two shortcuts were taken in the double-shower Monte Carlo simulation. First, all of the shower profiles were based on the proton shower library since the extensive photon shower library was being generated simultaneously. Second, these pairs of showers were generated with the preliminary shower following the Fly's Eye flux in two energy ranges [22]: $17.5 \leq log_{10}(E_{S1})(\text{eV}) < 18.5$, with a spectral index of $\gamma = -3.2$; and $18.5 \leq log_{10}(E_{S1})(\text{eV}) < 21.0$, with a spectral index of $\gamma = -2.8$. Both of these choices were made since many proton Monte Carlo event sets were being generated

Table 14.4: The number of Monte Carlo events generated in energy bins of 0.1 in $\log_{10} E_{\pi^0}$ shown with the center of each bin in the columns.

$log_{10}(E_{\pi^0})$ (eV)	Events	$log_{10}(E_{\pi^0})$ (eV)	Events	$log_{10}(E_{\pi^0})$ (eV)	Events
17.55	25328	19.15	8269	20.75	113
17.65	55519	19.25	6679	20.85	68
17.75	61839	19.35	5309	20.95	64
17.85	58615	19.45	4155	21.05	40
17.95	54474	19.55	3307	21.15	30
18.05	46131	19.65	2646	21.25	22
18.15	40077	19.75	2094	21.35	19
18.25	34258	19.85	1551	21.45	11
18.35	29358	19.95	1155	21.55	4
18.45	23940	20.05	914	21.65	6
18.55	21827	20.15	684	21.75	4
18.65	20603	20.25	502	21.85	3
18.75	17645	20.35	368	21.95	0
18.85	14836	20.45	285	22.05	1
18.95	12514	20.55	204	22.15	0
19.05	10016	20.65	150	22.25	0
				22.35	1

for the Middle Drum and HiRes spectral studies that was deemed higher priority for the computing resources available at that time.

CHAPTER 15

A SEARCH FOR COINCIDENT PARALLEL SHOWERS

This chapter describes the actual search for two coincident showers as the signature of a neutral pion decay in the heliosphere. Because of the very small probability of interactions between cosmic rays and heliospheric ions, this search for double-showers was performed using the HiRes-1 monocular dataset, which has the largest statistics. A modified version of the AlphaProc processing code set (see Chapter 8) is used to process the Monte Carlo and the data since the cuts are less restrictive than those of either the original or stereo_TA code sets (see Chapter 7).

Depending upon the opening angle between the photons and the energy of the initial pion, the perpendicular spread between the observed extensive air shower (EAS) axes will increase with the energy difference between the two photons. The light from the two showers will then arrive at the detector at different times (see Figure 15.1). There are three modes in which double-shower events can be observed. First, events can be close enough together to be observed as a single-event, single telescope event (see Figure 15.2). For example, the observation of two showers of equal energy from a $\geq 10^{19.0}$ eV pion decay with the photon-plane perpendicular to the mean shower-detector plane would be viewed within the same telescope. Secondly, the two showers could trigger the detector within the 100 μs "event" time window of Pass0 (see section 7.1.4) but separated far enough to be observed as a single-event, multiple telescope event (see Figure 15.3). For example, a $10^{17.0}$ eV pion decaying into two photons of equal energy could each arrive 15 km on either side of the detector. The light from these showers would reach the detector at about the same time, and would both be travelling in the same direction. Furthermore, the light would arrive in two different telescope viewing regions. Lastly, some showers can be spread by 30 km or more. Assuming the light from both showers can reach the detector and that one shower is directly in front of the other, light from the second shower could arrive outside of the 100 μs "event" time window of the first shower and so be separated into multiple events (see Figure 15.4). For example, if the closer, less energetic shower of a $10^{17.5}$ eV pion decay is in front of the detector and the other shower is 40 km away, this would result in the two showers triggering the detector 133 μs apart

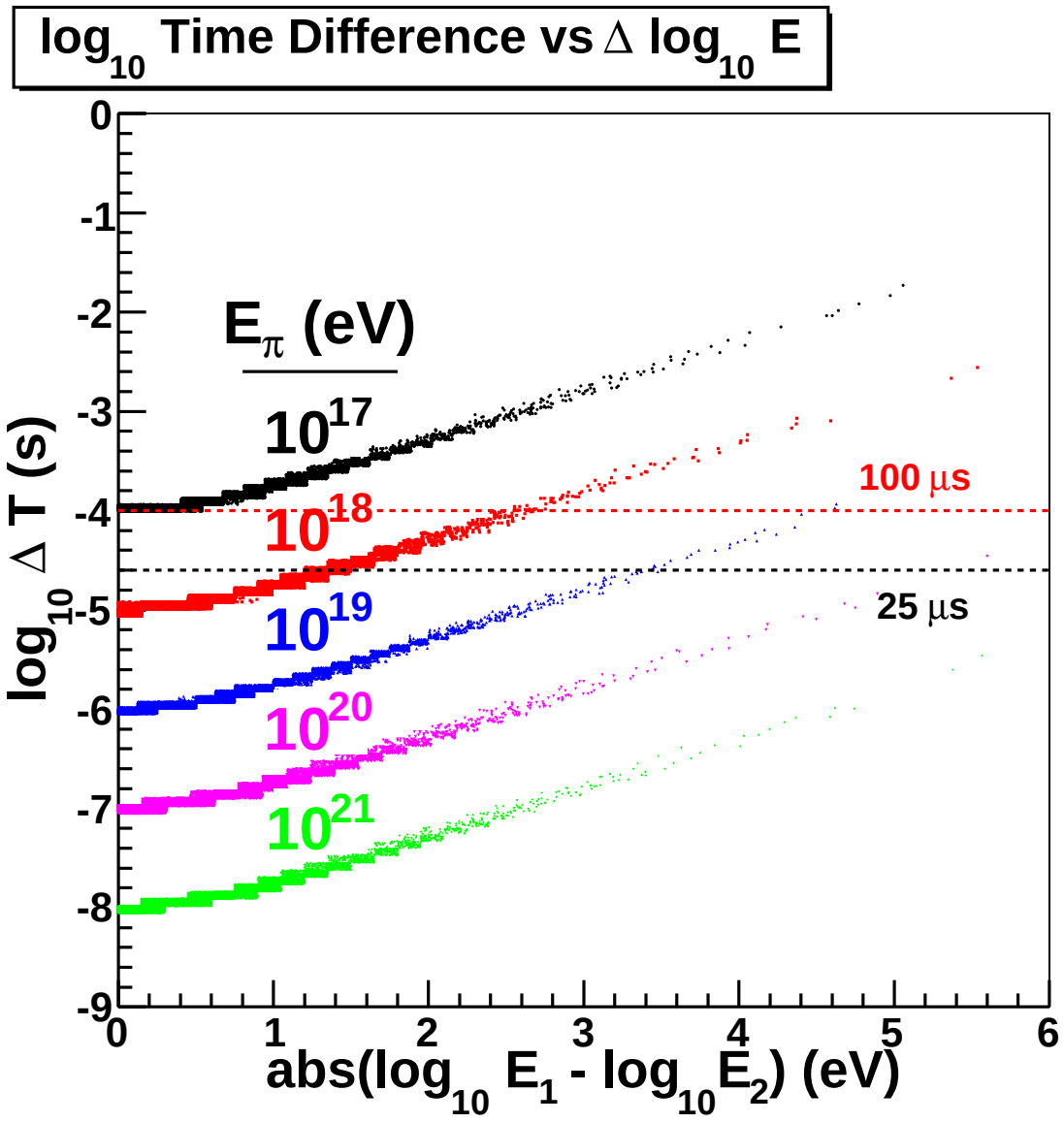

Figure 15.1: The difference in arrival time versus the difference in energy of Monte Carlo showers. Time is indicated by the shade.

and spread into two events. The "single-event" series of programs that will be described in this chapter assumes that most of the two photon showers are close enough to arrive within the 100 μs Pass0 event window.

15.1 Single-Event Double Shower Processing Codes

To determine if a double-shower is observed within a single event, a subset of the AlphaProc processing codes is used since it has the least restrictive cuts. Since this is primarily a search for candidates with a signature of unique shower trajectories, profile and geometry reconstruction is not performed. Only individual shower-detector planes

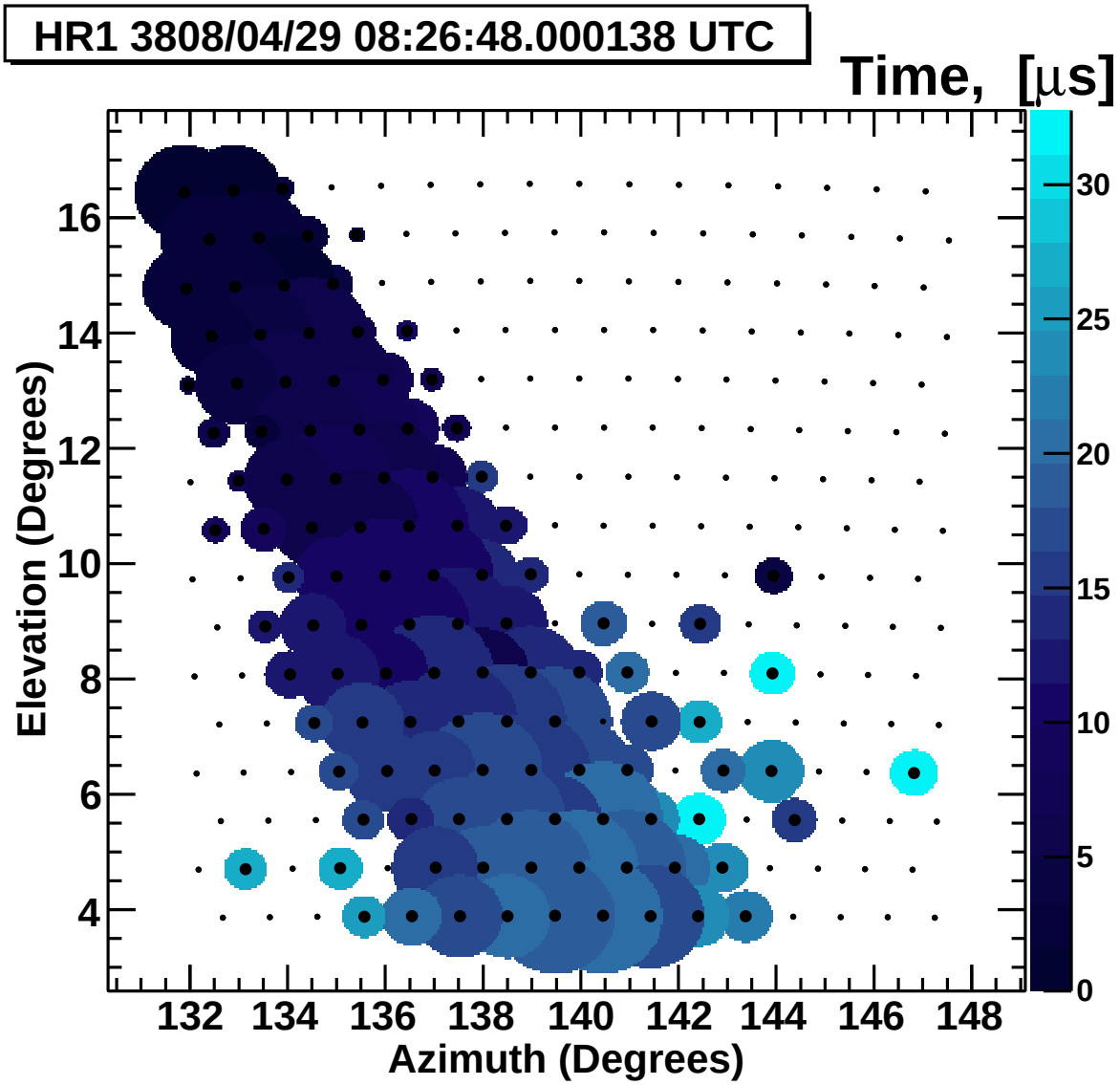

Figure 15.2: Two Monte Carlo showers observed in a single telescope in a single event. Time is indicated by the shade.

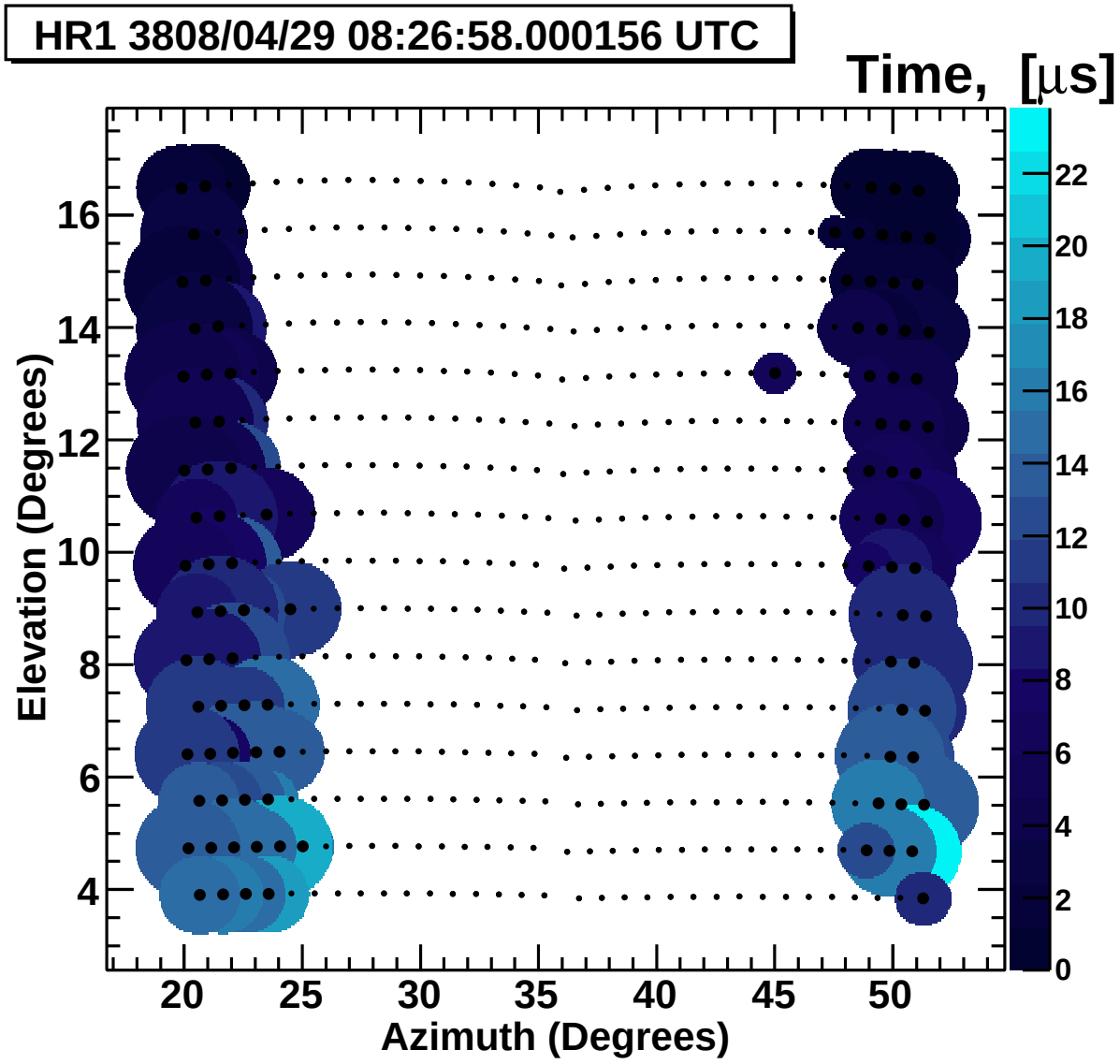

Figure 15.3: Two Monte Carlo showers observed in two telescopes in a single event. Time is indicated by the shade.

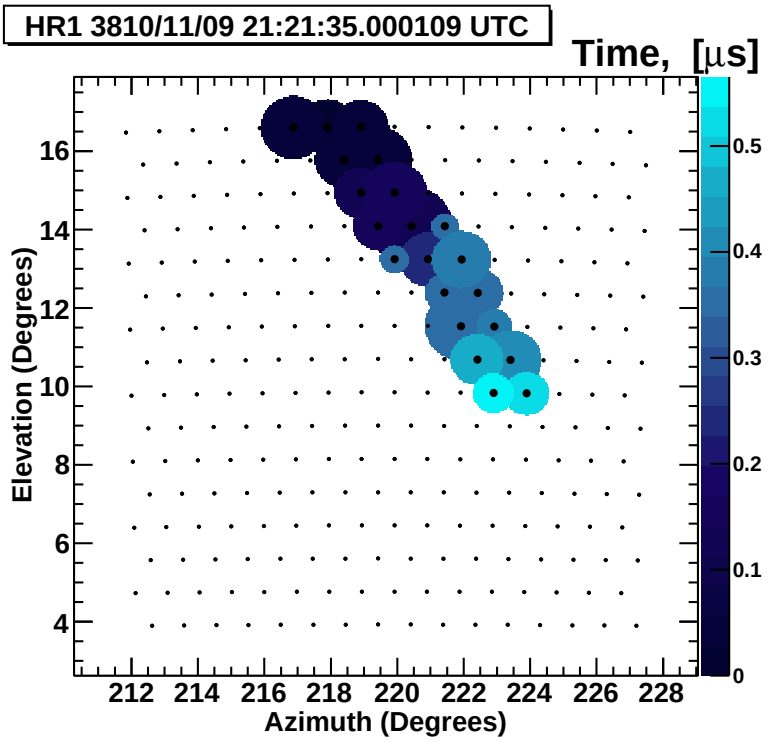

(a) Shower 1

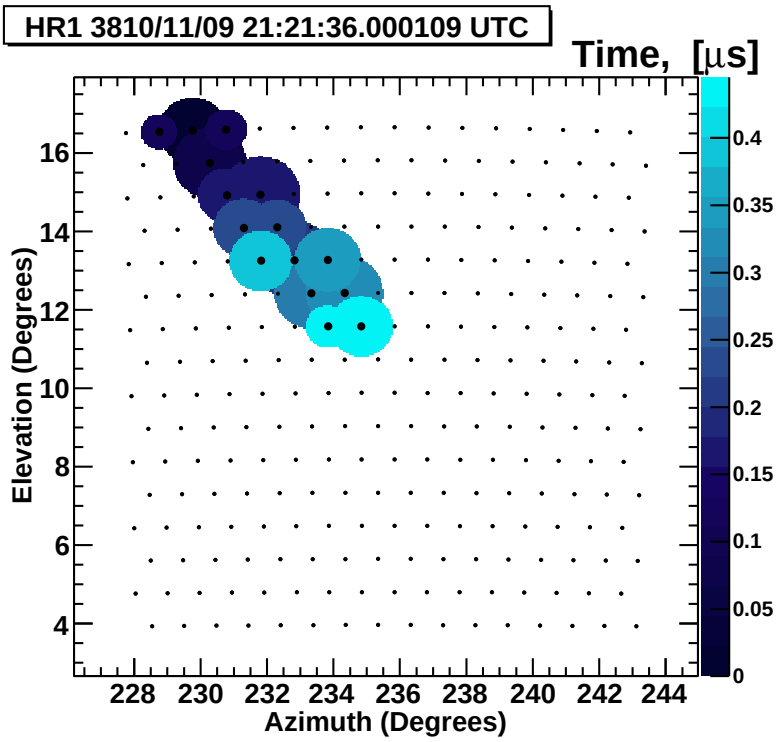

(b) Shower 2

Figure 15.4: Two Monte Carlo parallel showers separated across two events. Time is indicated by the shade.

are determined. This section will describe only those processing codes used to search for simultaneous showers within a single event.

15.1.1 PassA_dbsh

Data and Monte Carlo files are first sent through a modified version of the PassA program, where lines are determined in the set of triggered photomultiplier tubes (see section 8.1). In the standard code, the Hough transform cuts out triggered tubes that are 2.5 standard deviations away from a best fit line. In the modified program, "PassA_dbsh", those cut tubes are then assumed to be a new cluster of tube-vector lines and sent through another round of line finding. This process of cutting and determining a new line is repeated until no tubes are placed into a new cluster or there are at most seven lines found. These individual lines are then subjected to the same quality checks on $\sigma_{\overline{\theta}}$ of the standard PassA line (see section 8.1.4). With this process, only events that have multiple lines, whether in a single telescope or multiple, are retained (see Figure 8.3).

15.1.2 DBSH

After the events are determined to have linear patterns, the regular AlphaProc routines would run the events through the "hpln" (Pass3) processing code (see section 7.1.7). However, in that code, all triggered tubes that are deemed "good" based on angle and trigger-time difference are considered to be a single track. This program was modified to allow two or more tracks to be resolved in a single event. This new program code was named "dbsh_pln" (DBSH) to indicate that it is looking for two shower planes. This is applied to only those events with telescopes all having their passA θ values falling between -170° and -10° and less than three telescopes with $\sigma_{\overline{\theta}} \leq 0.05$ radians ($\sim 3^\circ$) (see section 8.1.4).

15.1.2.1 Fitting Cluster Shower-Detector Planes

The regular Pass3 first looks for clusters of tubes that fall within a 2.0 μs pair-wise trigger-time difference and a 1.2° pointing-angle difference. It then combines all of those tube-clusters into a single cluster and processes the event as a single track. The "dbsh_pln" program uses the same differences but assumes each tube-cluster to be an individual track within the event. Each tube-cluster (which will henceforth be referred to as "cluster") must have at least six tubes, otherwise the cluster, and each tube within it, is

excluded from further analysis. If there is only one cluster by the end of this process, the program breaks out of the double-search and proceeds with the regular Pass3 processing.

DBSH proceeds to ensure that each cluster can fit to a shower-detector plane individually. First, an angular plane is determined from the cluster's tubes. Tubes that lie at greater than three RMS deviations away from the plane are removed. If less than three tubes remain, the cluster is excluded. After that, a time-versus-angle (TvA) fit is made for each cluster. Tubes greater than three RMS deviations away in time residual of the fit line are removed. Again, if there are less than three tubes remaining, the cluster is considered bad and removed. Finally, after all extraneous tubes are removed, a check is made on the final cluster.

In order to ensure reasonable quality in the shower-detector plane, cuts were made on individual clusters. A distribution was made of the timing uncertainty of Monte Carlo clusters (see Figure 15.5). Events with an cluster time RMS of $2 \times HWHM$ (half-width at half-max), or $RMS_{Time} > 1.4$, from the plane's time fit were removed since these tended to be observed as wide, short clusters that resulted in uncertain timing (see Figure 15.6). A similar distribution was made on the plane uncertainty for Monte Carlo clusters (see Figure 15.7). Events with $RMS_{Plane} > 0.037$ were removed since they had unclear planes due to an abundance of many triggered tubes, as can be seen in Figure 15.8. The distribution of the number of good tubes per degree (GTPD) shows two peaks (see Figure 15.9) which generally correspond to long and short tracks (see Figure 15.10). However, clusters with $GTPD > 16/degree$ are considered bad since (A) they have too many tubes for the length of their track to be fit properly to a plane and (B) a camera is only 16° wide. These cuts and the reason for them are summarized in Table 15.1.

15.1.2.2 Buckshot Cut

The next cut to select reasonable double-showers was designed to remove entire events that had too many tubes, either from noise tube-triggers or from the shower being close to the detector and triggering many tubes. Both conditions can introduce many false-positive, multishower events. These "buckshot" cuts remove noise events with many tubes scattered over the camera face by determining the number of tubes triggered over the solid angle that they cover. A trapezoidal solid-angle is determined by

$$\Omega_{tubes} = |(\sin\theta_{m,i} - \sin\theta_{n,j})(\phi_{m,i} - \phi_{n,j})| \tag{15.1}$$

where θ is the zenith angle and ϕ is the azimuthal angle for tubes' pointing directions, i and j, in telescopes, m and n. For any given event, m and n can be the same telescope (single-telescope events) or different telescopes (multiple-telescope events). The program

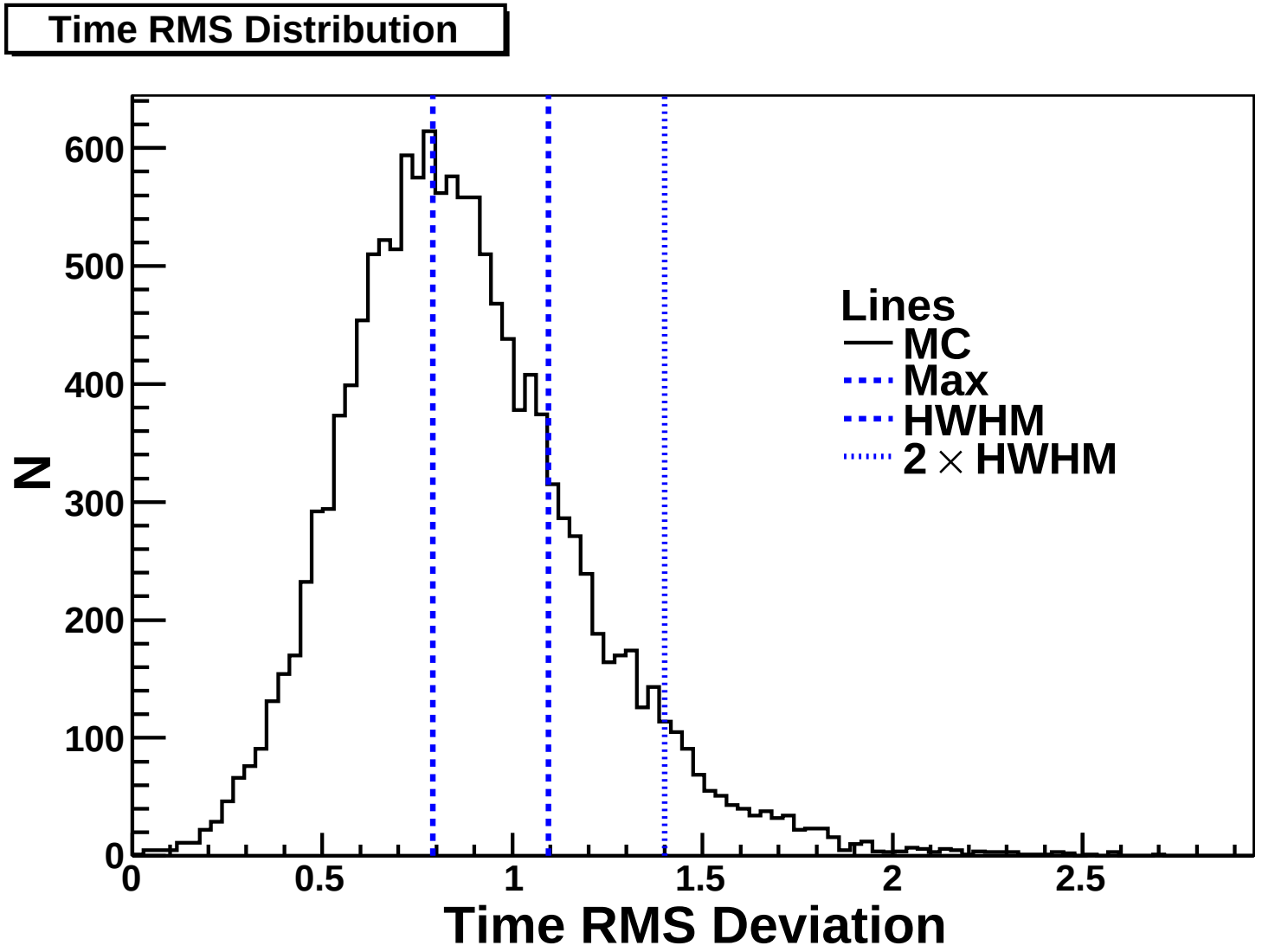

Figure 15.5: The distribution of the RMS time residuals of the timing fit of individual cluster in the pre-cut selection of double-shower Monte Carlo. The vertical lines show the max, the half-width at half-max, and the cut values.

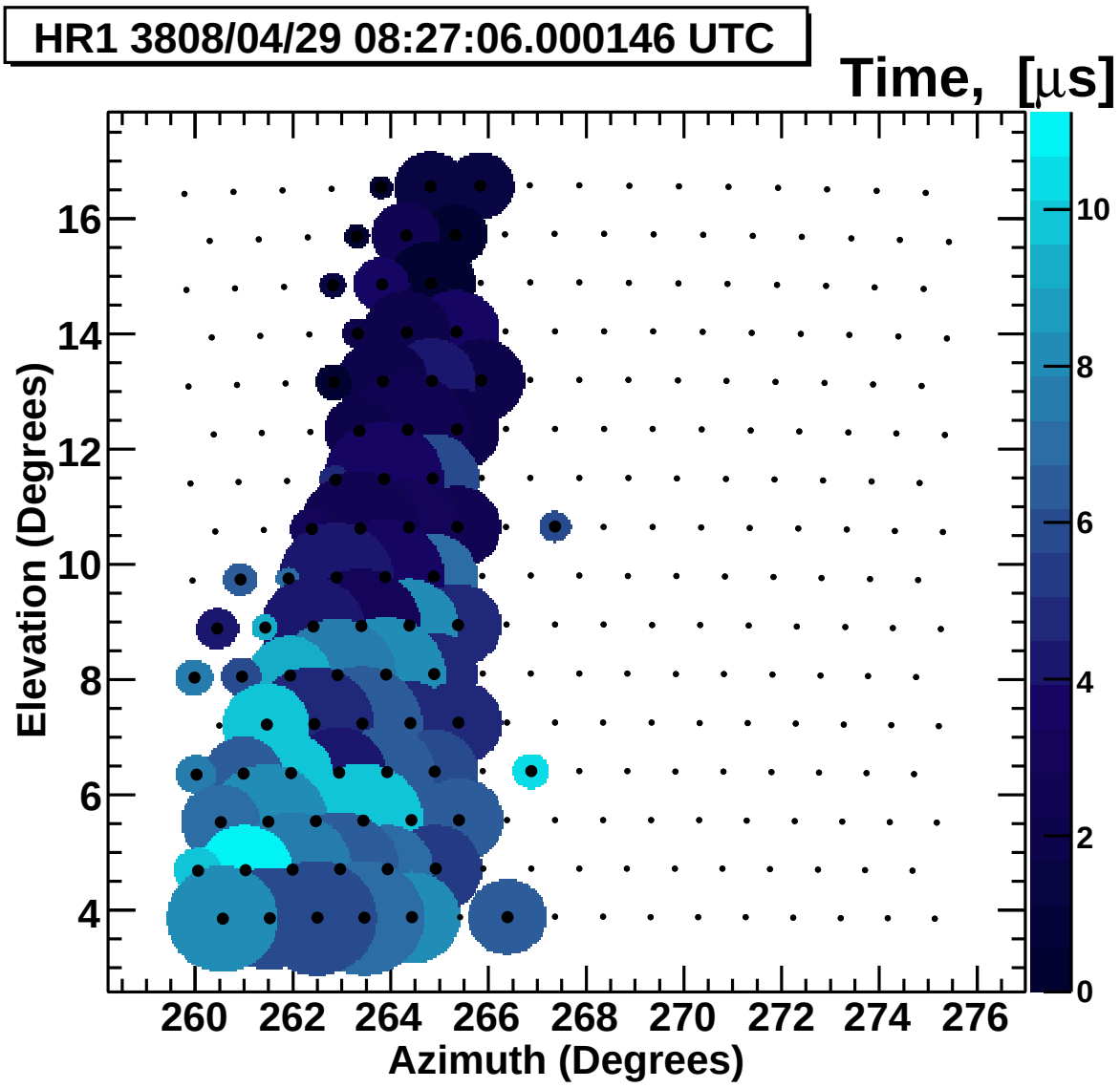

Figure 15.6: The later, lighter set of tubes of this Monte Carlo event was removed since it had an RMS residual of 1.65 in its time fit. It had a plane RMS residual of 0.02 and 9.90 good tubes per degree. Time is indicated by the shade.

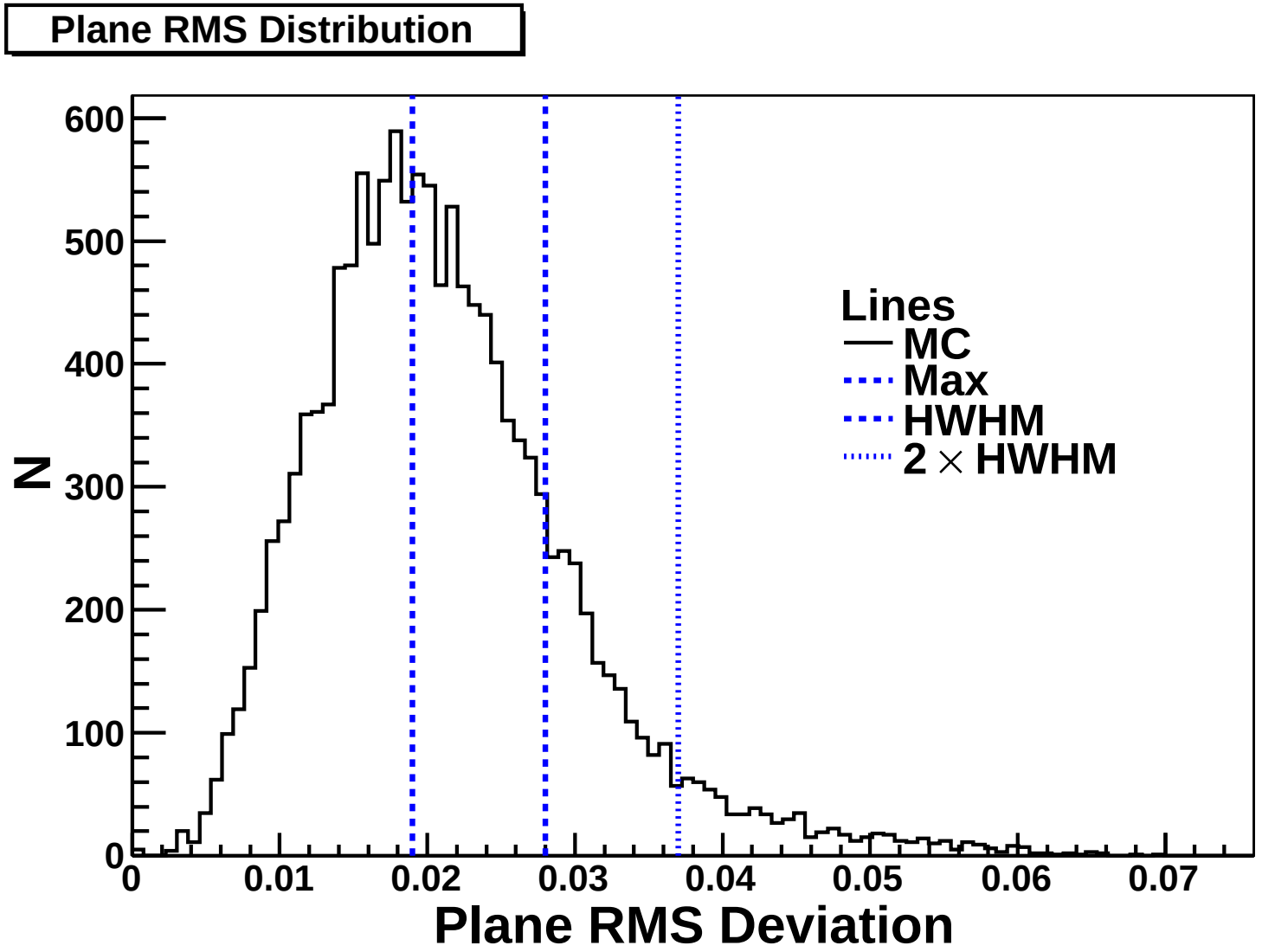

Figure 15.7: The distribution of the RMS plane residuals of the time-versus-angle fit of individual cluster in the pre-cut selection of double-shower Monte Carlo. The vertical lines show the max, the half-width at half-max, and the cut values.

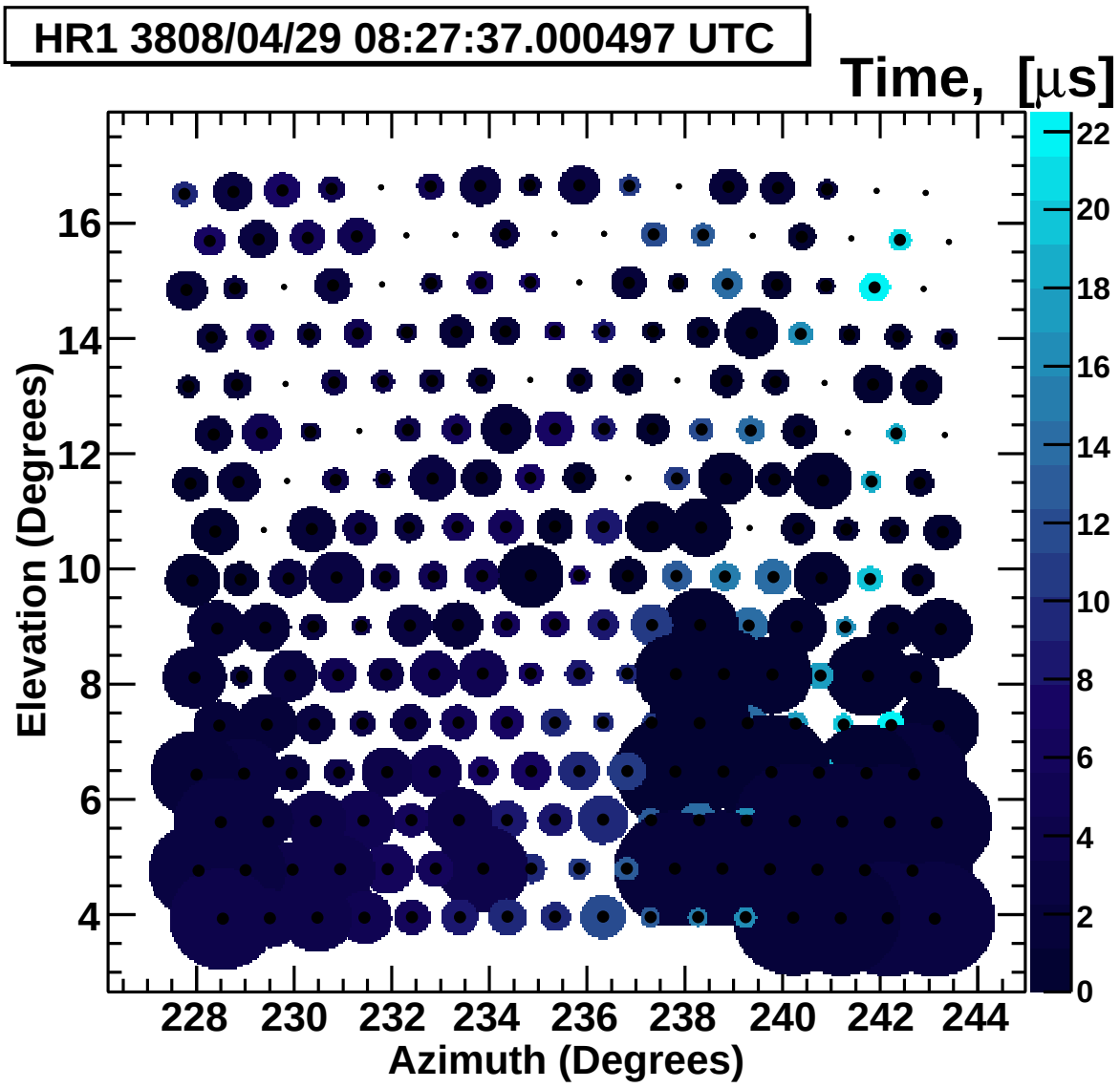

Figure 15.8: This Monte Carlo event was removed since it had an RMS residual of 0.054 in the plane fits. It had a time RMS residual of 1.29 and 12.07 good tubes per degree. Time is indicated by the shade.

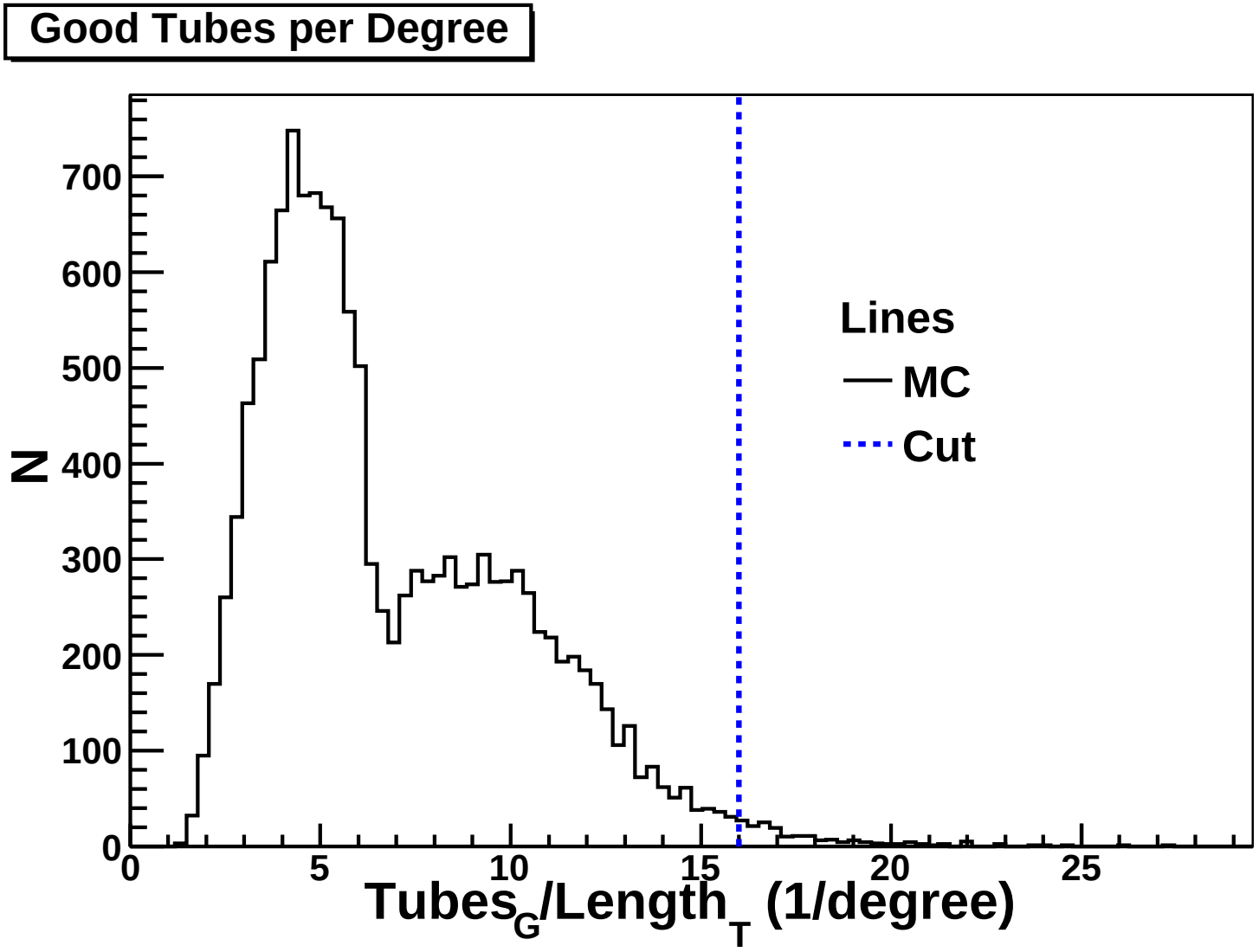

Figure 15.9: The distribution of the number of good tubes per track-length in single clusters of Monte Carlo events. The vertical line shows the cut value. The shorter peak is caused when the shorter track overlaps the longer one (see Figure F.3).

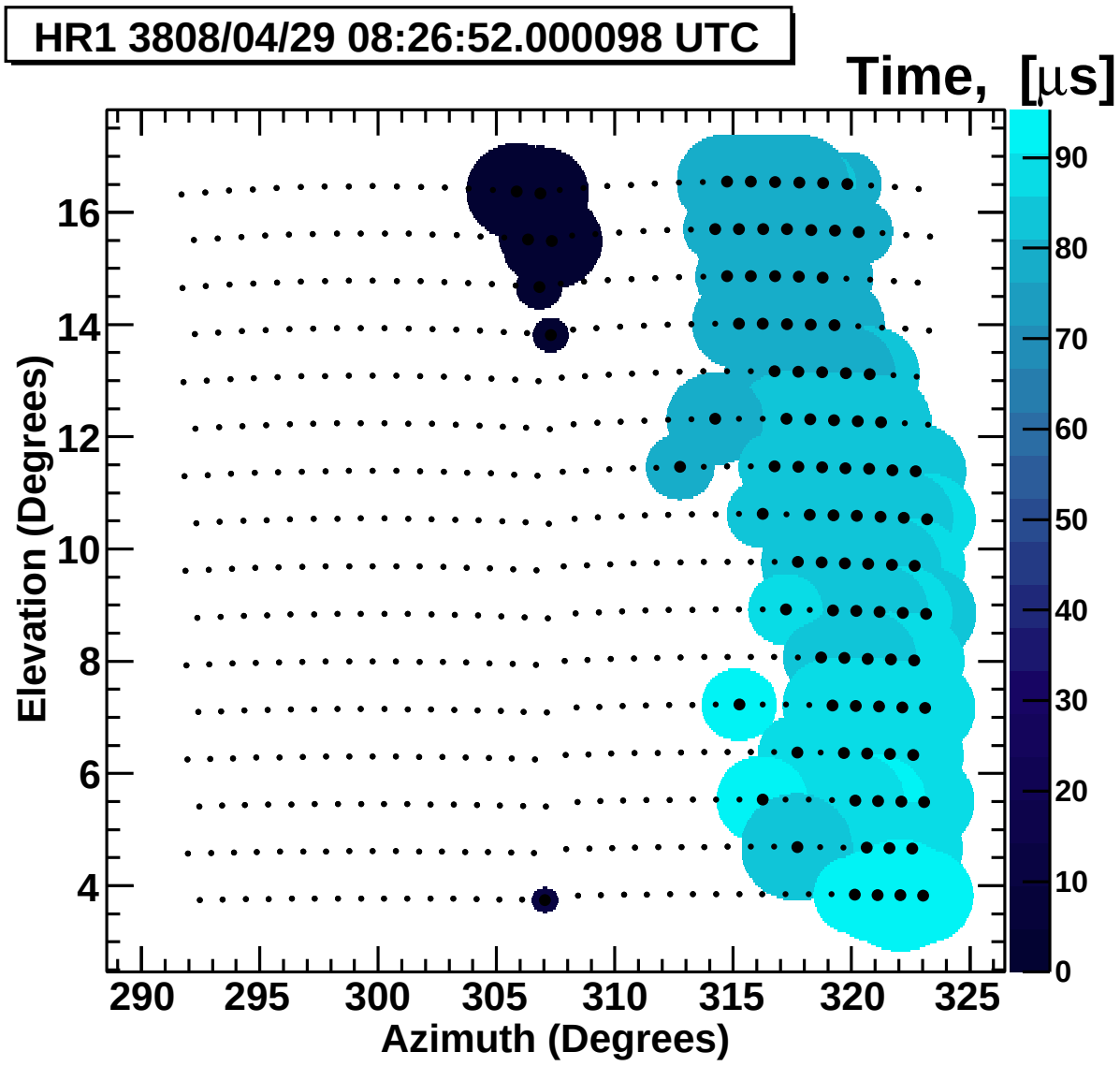

Figure 15.10: The small cluster of this Monte Carlo event was removed since it had 29.6 good tubes per degree. It had a time RMS residual of 0.16 and a plane RMS residual of 0.01. Time is indicated by the shade.

Table 15.1: Clusters are removed if these conditions applied in the first round of cuts of the "dbsh_pln" program are true.

Remove Cut	Value	Purpose
RMS_{Time}	> 1.4	wide, short tracks result in uncertain timing
RMS_{Plane}	> 0.037	many triggered tubes result in unclear planes
$N_{good-tubes}/degree$	$> 16/degree$	a camera is 16 tubes wide and many good short tracks reconstruct poorly

determines the maximum and minimum zenith and azimuthal values to determine the solid angle for good tubes.

By using only the good tubes, the solid angle of only the candidate tracks could be used to determine a quality solid angle. Many clusters in double-shower Monte Carlo are too close to be separated. It was also discovered that many lasers could be removed since they tend to be very narrow and long. If $\log_{10}\Omega_{good-tubes} < -4$ sterradians the solid angle that the event is viewed in is considered too small and is removed (see Figure 15.11). An example of a good solid angle is seen in Figure 15.12(a)); a bad one is seen in Figure 15.12(b).

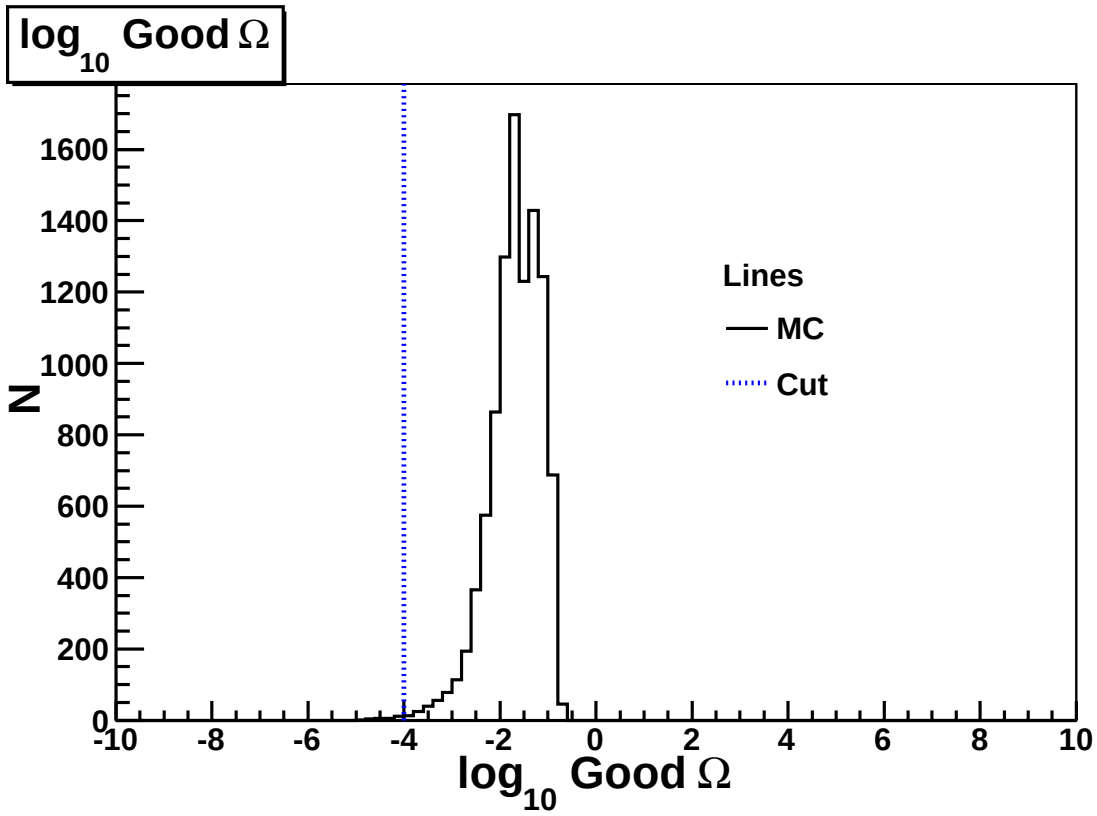

Figure 15.11: The distribution of $\log_{10}\Omega_{good-tubes}$, the solid angle of the event's good tubes, cover from Monte Carlo events.

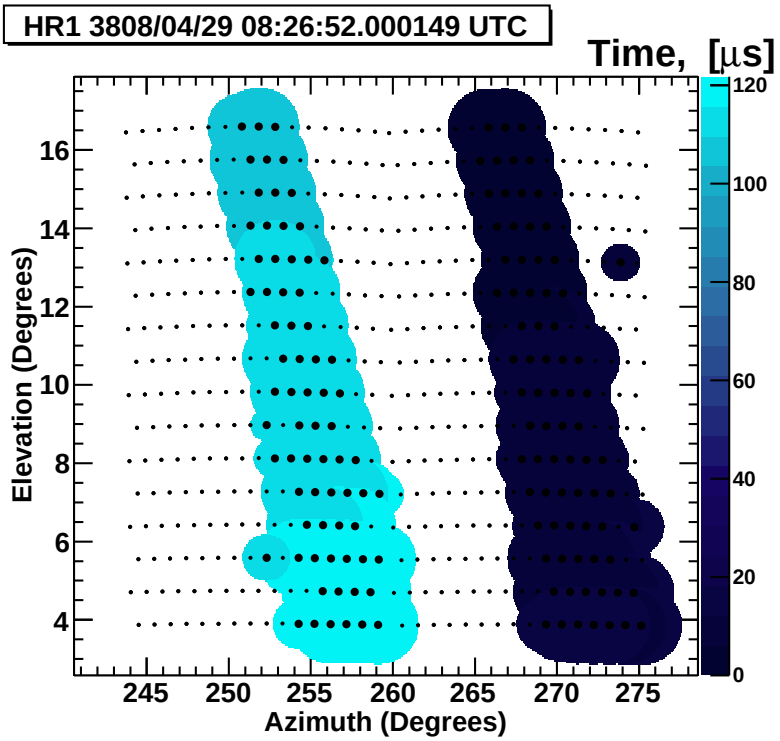

(a) $\log_{10}\Omega_{good} = -0.99$

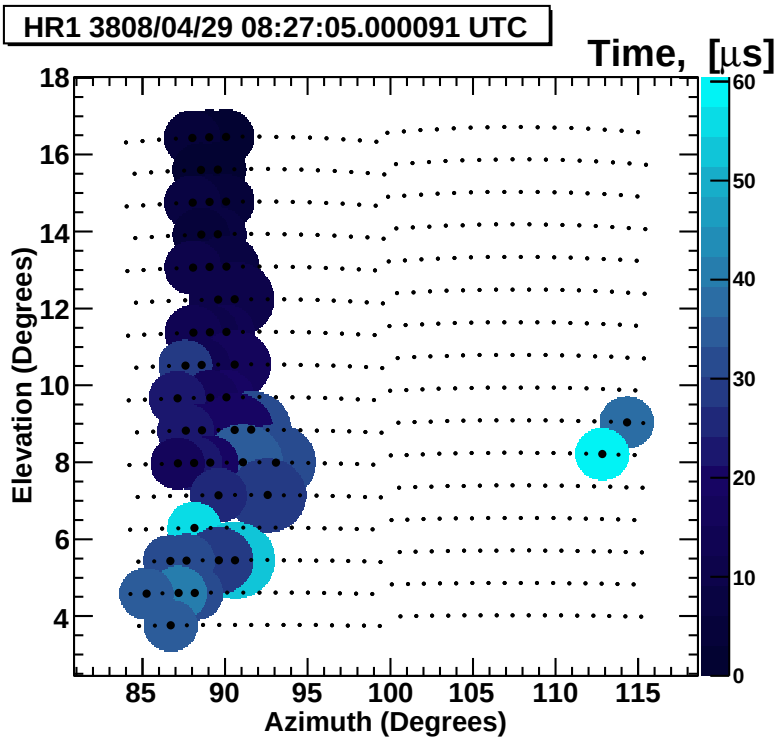

(b) $\log_{10}\Omega_{good} = -4.25$

Figure 15.12: The Monte Carlo event seen in Figure 15.12(a) has a good viewing solid angle of good tubes and was kept. The Monte Carlo event seen in Figure 15.12(b) had a bad viewing solid angle of good tubes and was removed.

The good tube population density is given by the ratio

$$R = \frac{N_{good-tubes}}{\Omega_{good-tubes}} \tag{15.2}$$

where $N_{good-tubes}$ is the number of good tubes in an event. This cut would remove those events with too many good tubes (e.g., aircraft flashers) or events that are too wide for the plane fit (e.g., close and without much light scatter). Only events with $\log_{10} R < 4.6$ are kept since they have the cleanest number of good tubes along the track (see Figure 15.13). A good Monte Carlo event is shown in Figure 15.14(a); a bad data event is shown in Figure 15.14(b).

Finally, a cut was made on the ratio of the number of triggered tubes divided by the number of triggered telescopes, $S = N_{tubes}/N_{telescopes}$. Only events with $S < 100$ were kept (see Figure 15.15). This limit was defined to remove those events with too many noise triggers (see Figure 15.16(a)). An example of a good event is shown in Figure 15.16(a). A summary of these buckshot cuts is shown in Table 15.2.

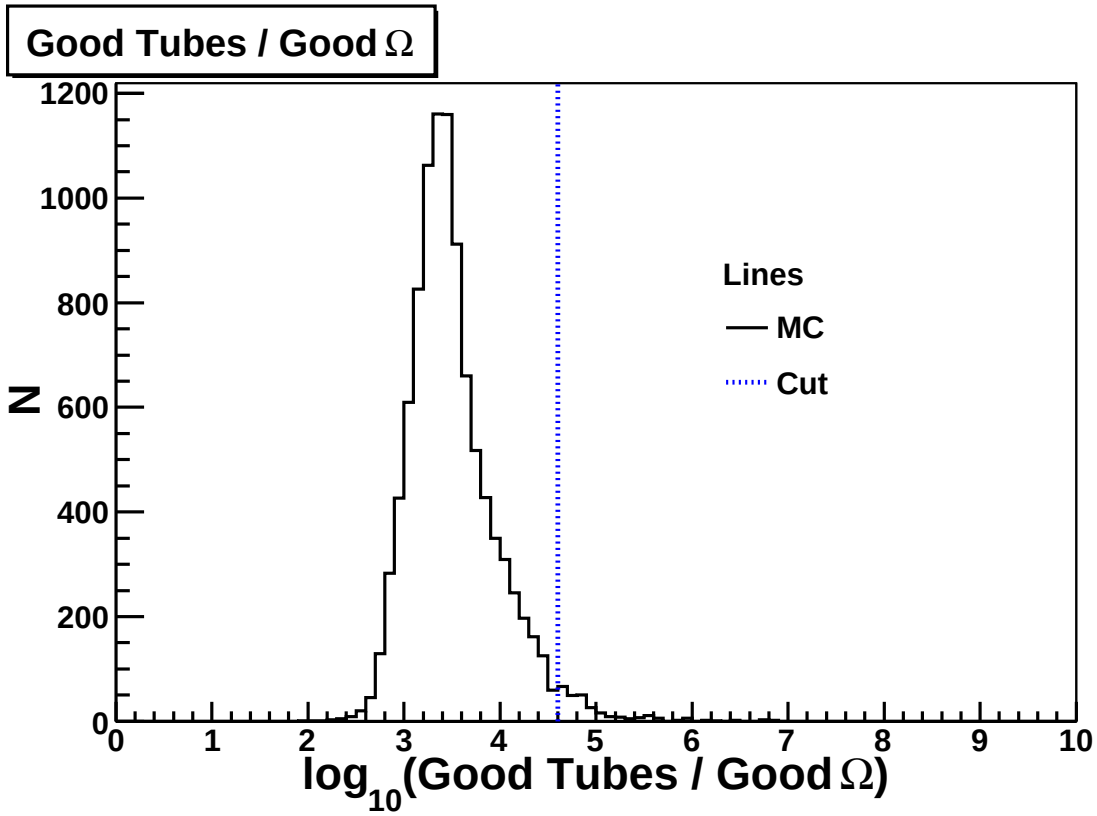

Figure 15.13: The $\log_{10}$ of the ratio of good tubes to the solid angle those tubes cover.

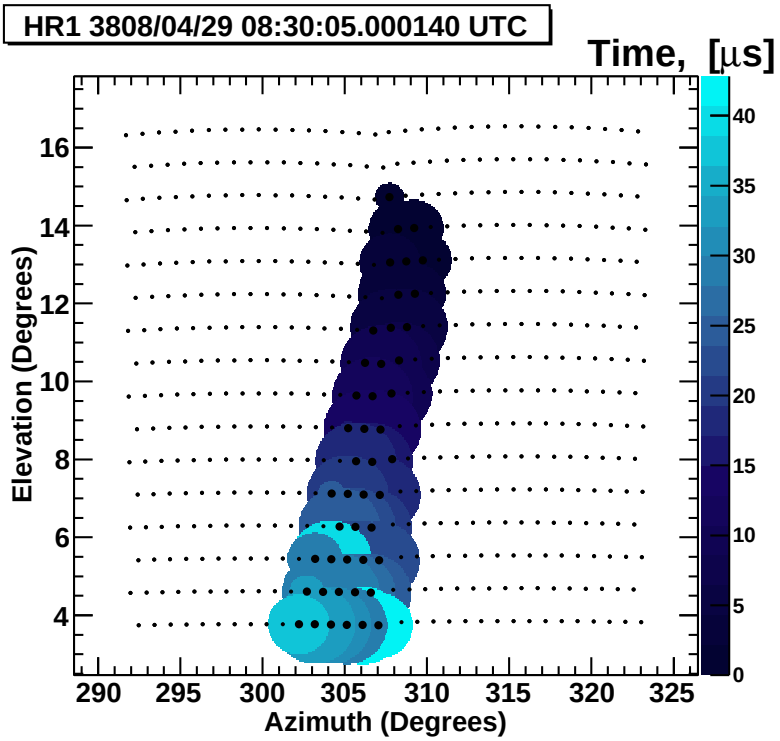

(a) $\log_{10} R = 3.41$ tubes/ster.

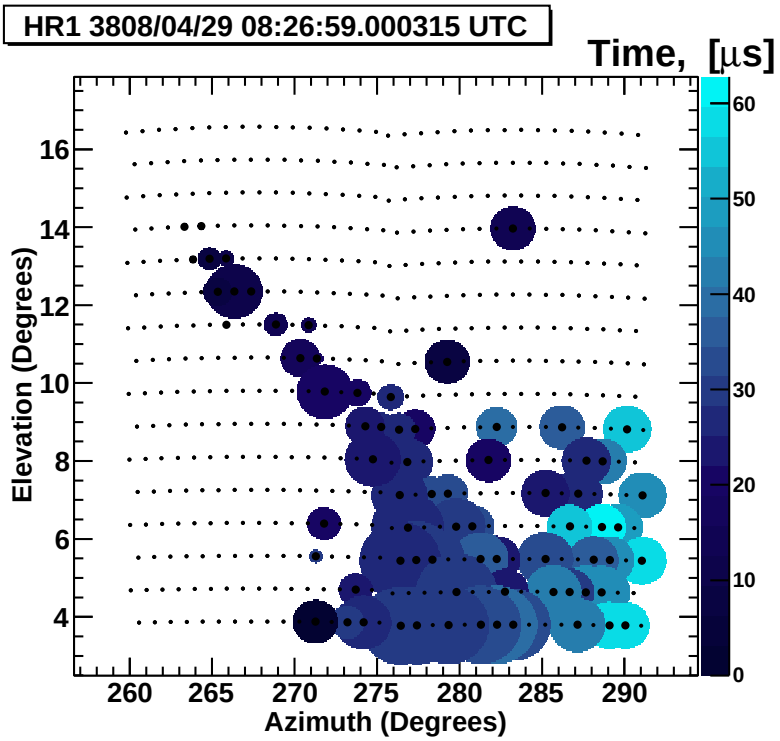

(b) $\log_{10} R = 4.88$ tubes/ster.

Figure 15.14: The Monte Carlo event seen in Figure 15.14(a) has a good population density of good tubes and was kept. The Monte Carlo event seen in Figure 15.14(b) had a bad population density of good tubes and was removed. Time is indicated by the shade.

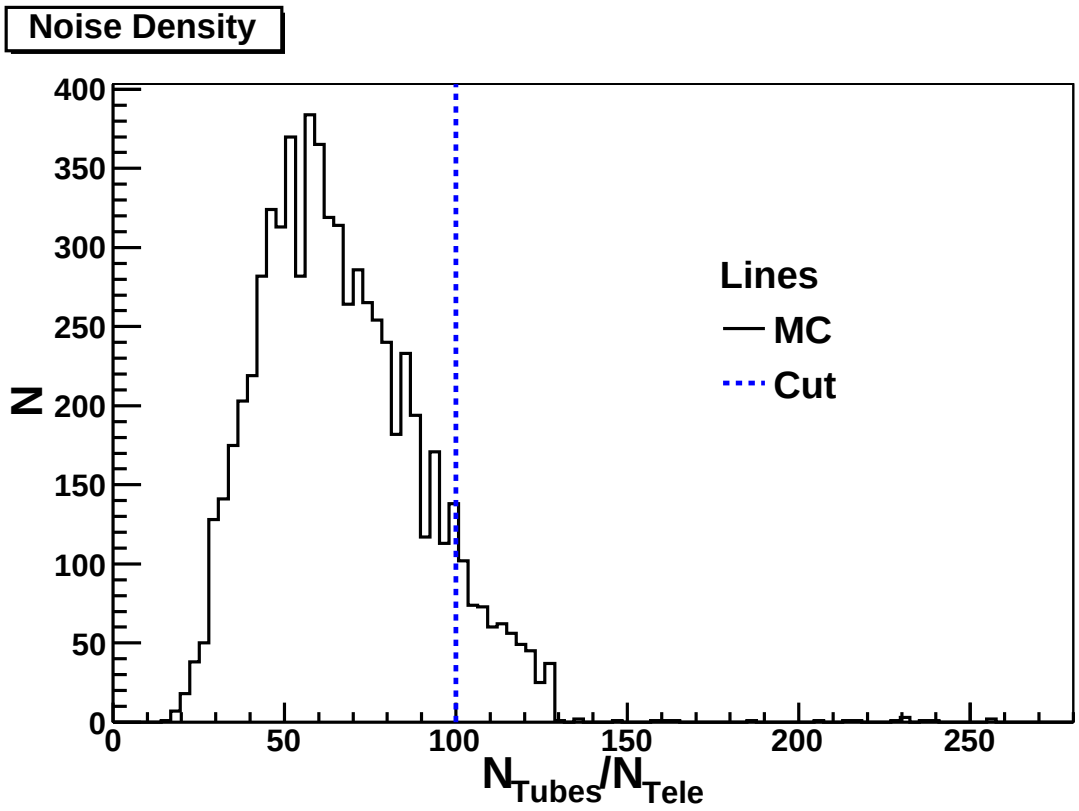

Figure 15.15: The number of triggered tubes per mirror.

15.1.2.3 Double-Cluster Selection

Occasionally, an event would show more than two cluster tracks. Since this is a search for double showers, only events with two good-quality tracks were considered. Additionally, most Monte Carlo showers would have track lengths greater than 12.5°, but could be as short as $\sim 2°$. HiRes-1, spectrum analysis considered showers with track lengths $> 7.9°$ to have reliable event reconstruction (see Table 10.2), but made plane fits to all events with track length $> 6°$. For this double-shower search, a choice was made to have the larger of the two tracks to be at least 8° and the shorter be at least 6°. This condition would allow for reliable reconstruction of the primary track with the secondary track being the minimum number of tubes retained as what is retained in the regular Pass3 program. If all of these cuts were passed (see Table 15.3), the event was written to a new file containing the "DBSH" dst bank information (see Table 15.4).

15.1.3 PassB_dbsh

After the potential double shower events are found, all of the .dbsh.dst files from a single night of data collection were combined into a single file and sent through a

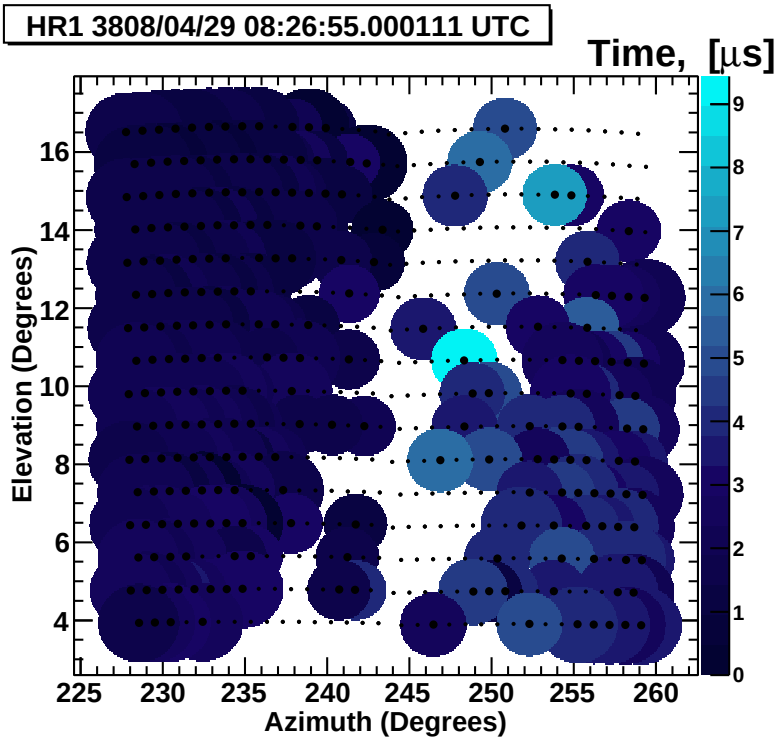

(a) 117.5 triggered tubes per telescope

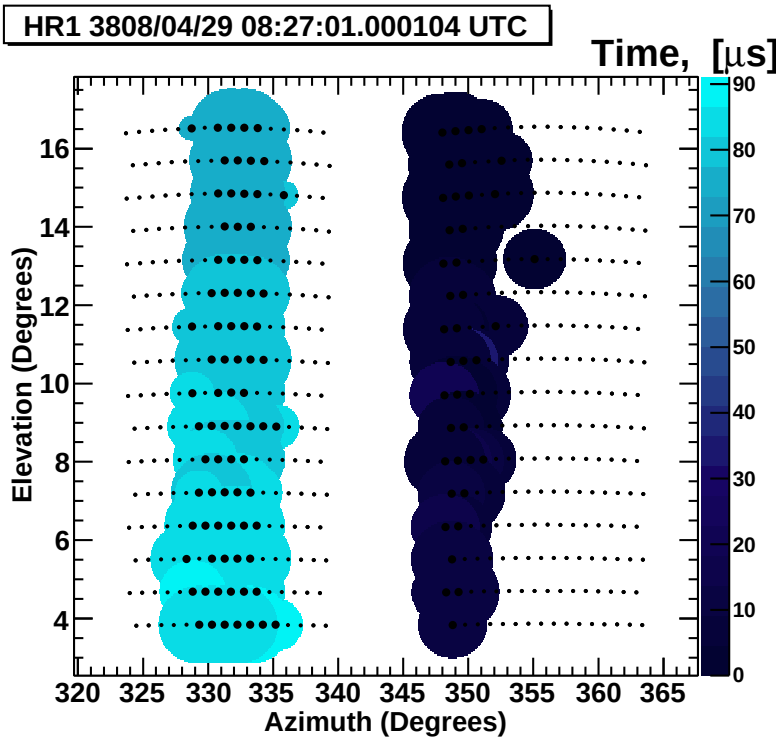

(b) 60.5 triggered tubes per telescope

Figure 15.16: The Monte Carlo event seen in Figure 15.16(a) had a bad noise density of triggered tubes per telescope and was removed. The Monte Carlo event seen in Figure 15.16(b) had a good noise density of triggered tubes per telescope and was kept. Time is indicated by the shade.

Table 15.2: Entire events are retained if these density study conditions applied in the second pass in the "dbsh_pln" program are true.

Remove Cut	Value	Purpose
$log_{10}\Omega_{g-tubes}$	> -4	provides a reasonable viewing of cluster tracks
$log_{10}(N_{g-tubes}/\Omega_{g-tubes})$	< 4.6	provides a good population density of good tubes
$N_{trig-tubes}/N_{Tele}$	< 100	removes events with large numbers of noise tubes

Table 15.3: Entire events are removed if these conditions applied in the third pass in the "dbsh_pln" program are true.

Remove Cut	Value	Purpose
Number of Clusters	$\neq 2$	looking for pairs of photon showers
Longer Cluster Track Length	$< 8°$	want a reliable primary shower
Shorter Cluster Track Length	$< 6°$	want a reasonable secondary shower

modified version of the PassB program (see section 8.2). Compared to the regular PassB, this version looked for time-stamps of lasers, a reduced selection on the spread of events across telescopes (3 or fewer telescopes), and the similarity of events through repetition. The Monte Carlo events were always placed into either the "psB" or "unkw" types (most-likely-showers or unknown-determination, respectively). As such, these event types were analyzed in both data and Monte Carlo.

15.2 Double-Shower Analysis Intermediate Results

15.2.1 DBSH: Single Events

After all of the processing, there were 3,393 events retained in the Monte Carlo and 5,141 events retained in the data. Plotting the plane-normal x- and y-components of these data and Monte Carlo events (see Figure 15.17), we see that most of the surviving data candidates looked to have laser event patterns. A small sample of prescaled laser events with known time-stamps were processed to look for characteristic patterns for analysis cuts. Plotting the plane-normal x- and y-components of these known lasers, the surviving data candidates showed consistency with the lasers as indicated in Figure 15.18.

These were then compared in zenith (Θ) and azimuthal (Φ) angles of the fit plane-normal to see if there were any additional patterns that could be found that to determine analysis cuts (see Figure 15.19). Shower-detector plane normals with $|\Theta| \approx 90°$ (1.5 radians) indicates the events would have a horizontal trajectory. The event seen in

Table 15.4: Information contained in the DBSH dst bank.

ntubes	the number of triggered tubes
ndbclu	the number of clusters in the event
trklen	the angular distance between the two most opposed "good" tubes along the fitted plane for each cluster in degrees
ppgt	the number of calibrated photons from the "HRAW1" dst bank per "good" tube for each cluster
prmsdev	the RMS off-plane angle of "good" tubes for each cluster in degrees
trmsdev	the RMS in tube trigger time of "good" tubes from the time fit to a quadratic for each cluster in degrees in microseconds
ias	the time it takes the track to cross one degree of its track-length for each cluster in microseconds per degree
gtpd	the number of "good" tubes per degree of its track-length for each cluster in inverse degrees
correl	the correlation of time and plane of all "good" tubes for each cluster
n_ampwt	the amplitude-weighted plane normal for each cluster
n_ampwterr	the error on the plane normal for each cluster
Timing fit parameters	the three quadratic constants of the time fit for each cluster
crstim	the time difference between the last and first "good" tube trigger time for each cluster in microseconds
azi	the azimuthal angle of the shower-detector plane normal for each cluster in radians
zen	the zenith angle of the shower-detector plane normal for each cluster in radians
Tube	the number of each tube
Mirror	the telescope to which each tube belongs for each tube
clust_no	the number of the cluster to which each tube belongs (-1 if not associated with a cluster)
goodness	the flag of whether the tube was considered good or bad for each tube

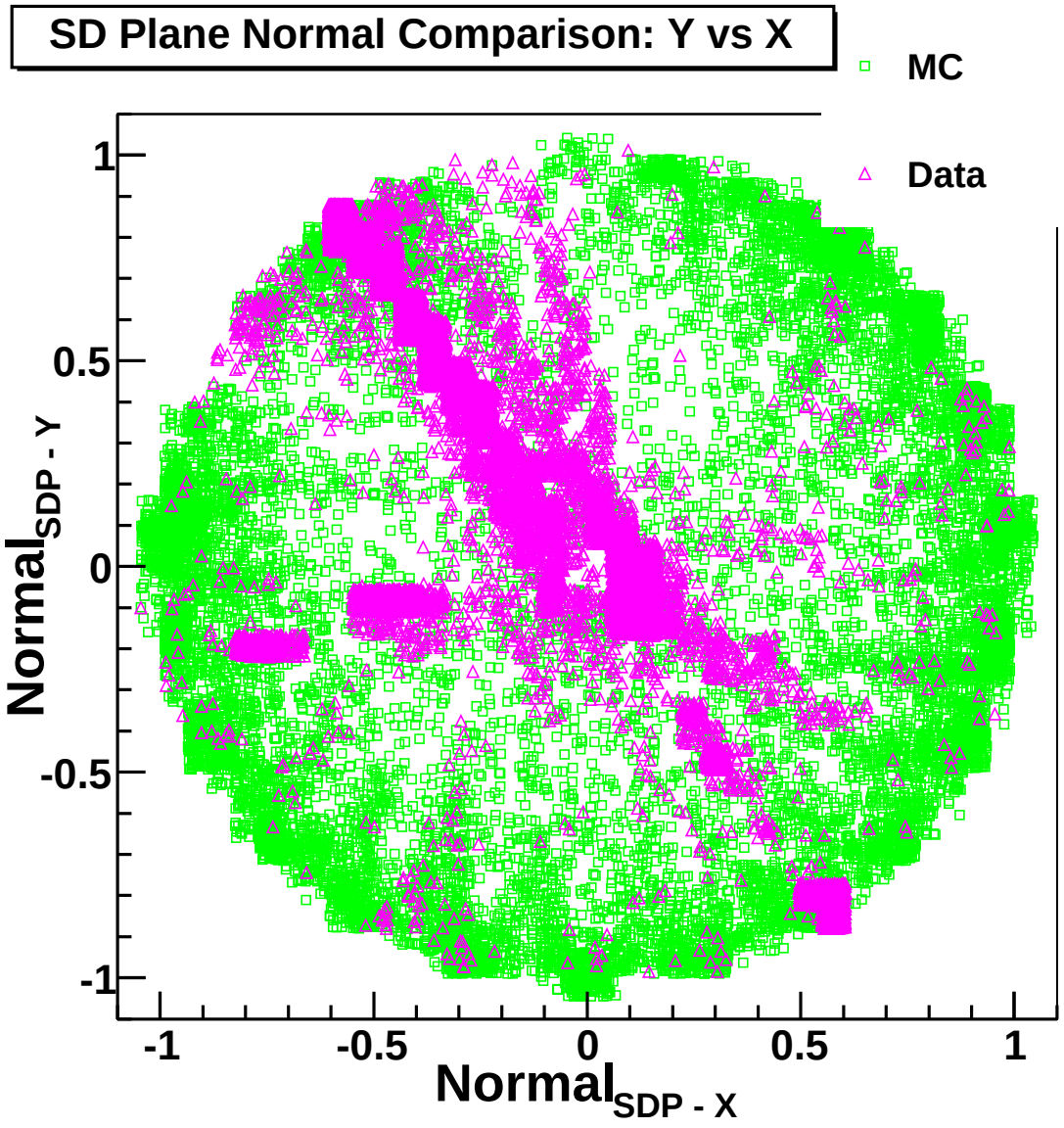

Figure 15.17: The shower detector plane normal x- and y-pointing directions of the processed data and Monte Carlo.

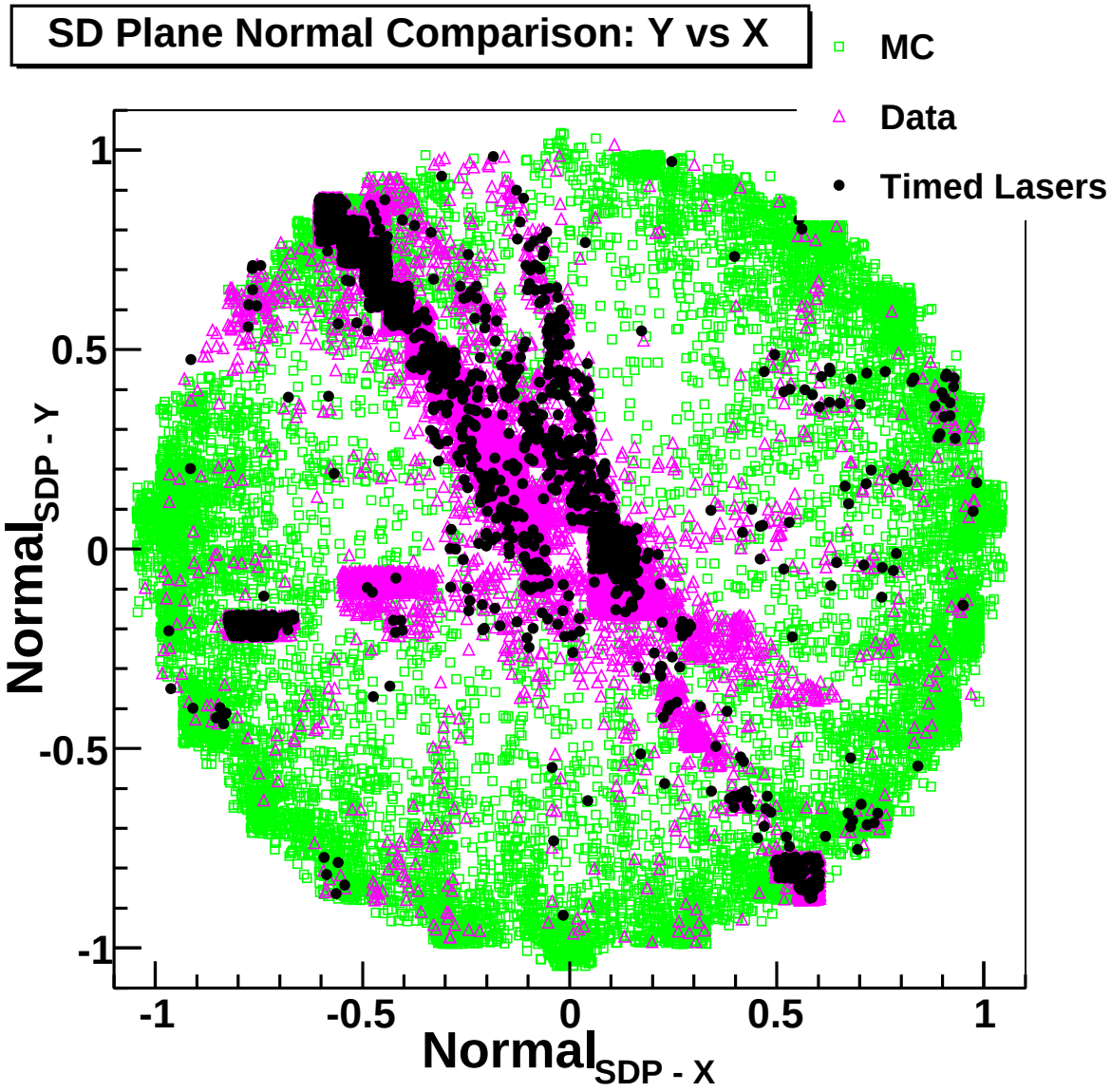

Figure 15.18: The shower detector plane normal x- and y-pointing directions of the processed data and Monte Carlo with lasers with known time-stamps indicated. The surviving candidate data events appear consistent with known laser events.

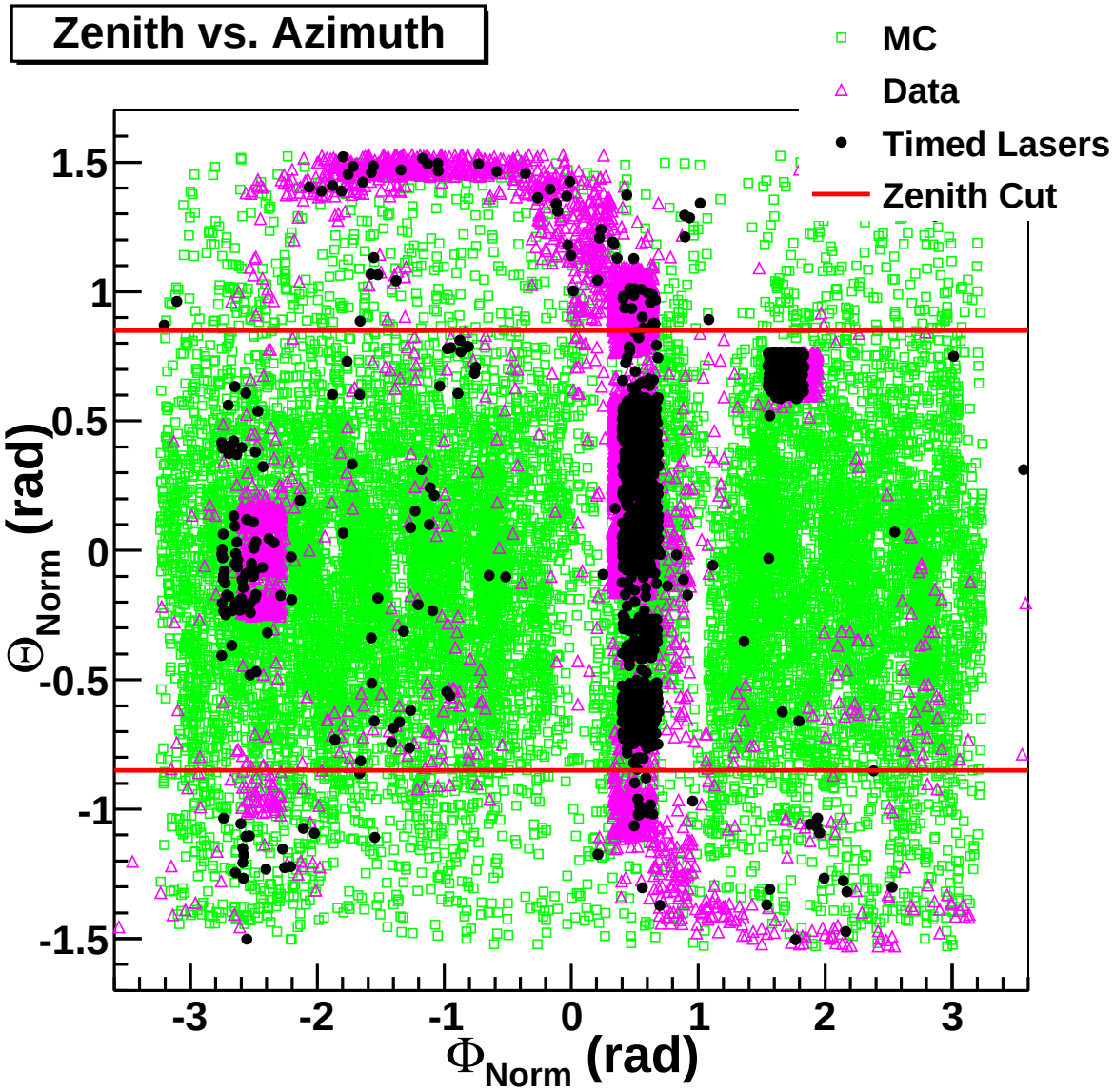

Figure 15.19: The shower detector plane normal zenith and azimuthal angles of the processed data and Monte Carlo with lasers with known time-stamps indicated.

Figure 15.20 falls into this pattern and was not flagged on a usual time stamp. It is either a flasher or the HR2SLS (see section 5.2.5) coming from the region viewed by telescope 7 but is heavily scattered because of ground fog. Because of this and the fact that most of the Monte Carlo had $|\Theta| < 0.85$ radians, only those events with both clusters having a zenith angle less than 0.85 radians were kept. Additionally, it was observed that most of the known lasers had an inverse angular speed (IAS) less than 0.3 $\mu s/degree$, as compared to the Monte Carlo (see Figure 15.21), so only events above this value were retained. The number of events retained after each of these events can be seen in Table 15.5.

If both clusters failed both the zenith and IAS cuts they were removed. For those

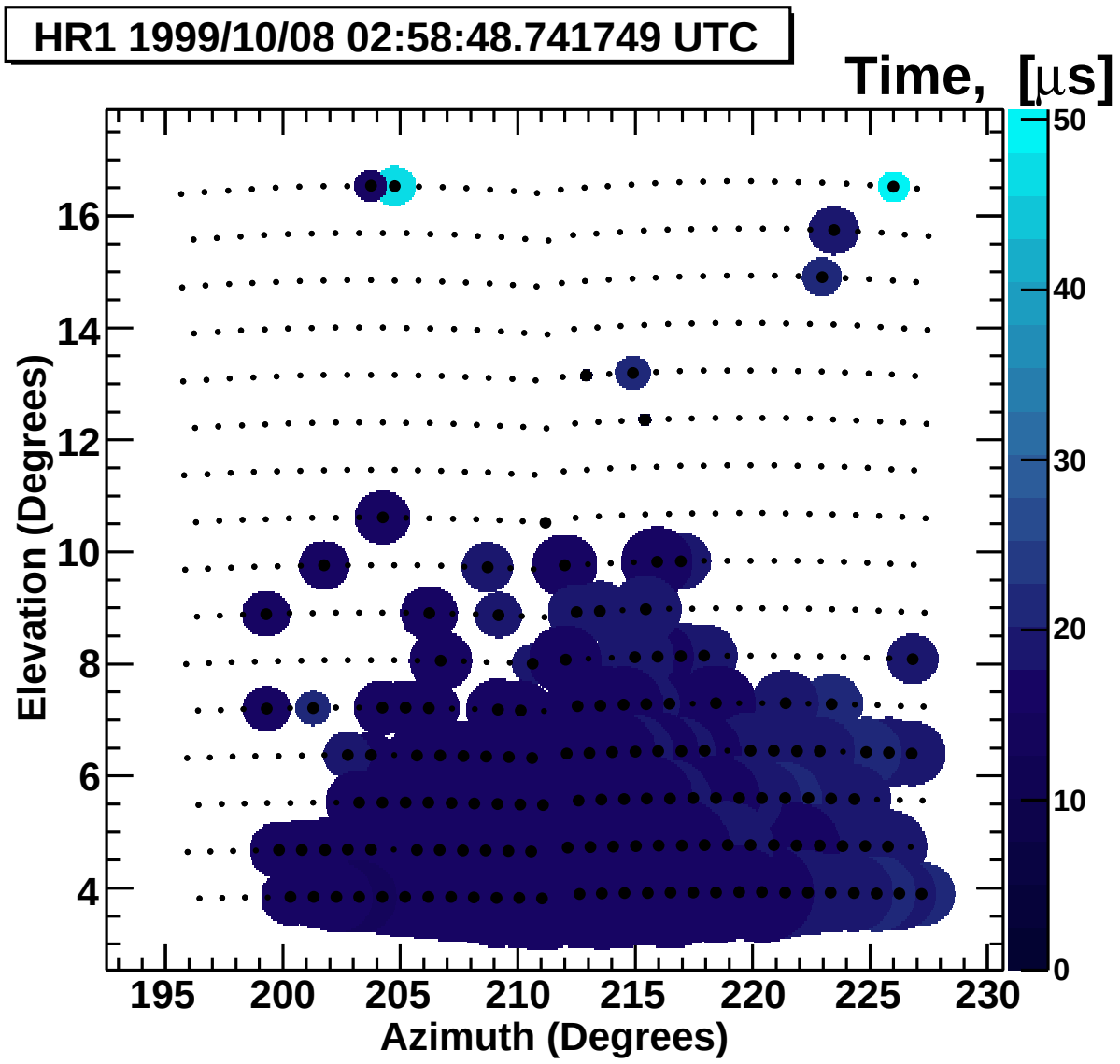

Figure 15.20: This event survived all of the processing cuts and was not fired on the usual time-stamp. It is either a flasher or the HR2SLS coming from the region viewed by telescope 7. Time is indicated by the shade.

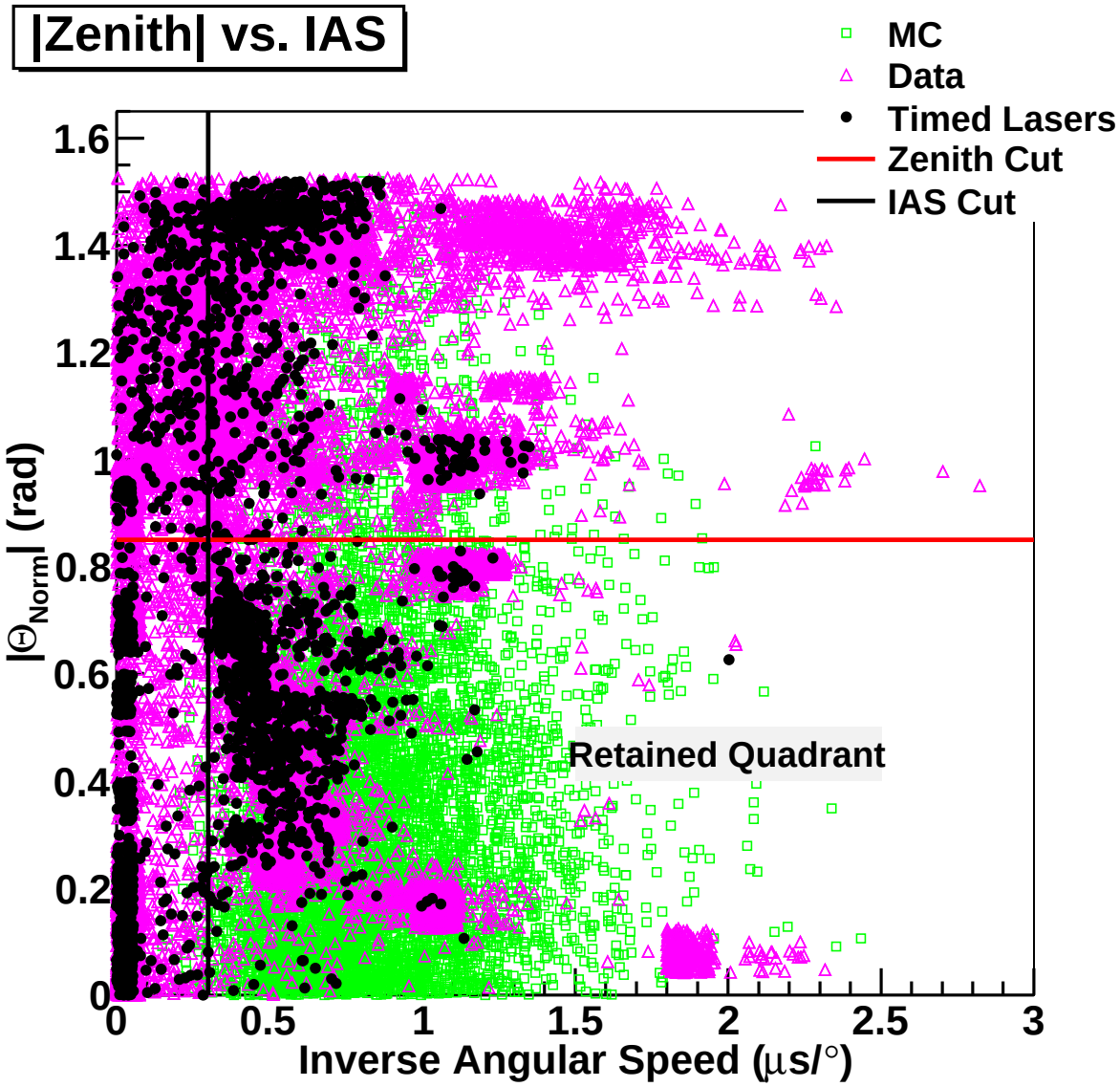

Figure 15.21: The shower detector plane normal Θ versus the inverse angular speed of the processed data and Monte Carlo with lasers with known time-stamps indicated.

Table 15.5: These are the number of events retained after each of the listed cuts.

Set	Cut	Remaining
MC	None	3393
MC	IAS	3319
MC	Zenith	2821
MC	Both	2796
Data	None	5141
Data	IAS	500
Data	Zenith	3270
Data	Both	187

that passed the cuts, 2,796 Monte Carlo and 187 data events remained. These were then sent through a program to check if there were similar, repetitive events that night in the raw data, presuming they could be lasers. This program located the Julian day, Julian second, and millisecond trigger time of the event in question and noted the tubes within the telescopes. The program then compared every other event on that night to the candidate event. If the checked event had over 50% matching telescope-tubes, it was recorded. Most of the candidate events resulted in either one (itself) or a few similar events; others resulted in thousands. A distribution of the number of similar events was made and it was decided that if there were eight or more similar events to the candidate, all events in the list were considered close enough to be considered lasers (see Figure 15.22). This resulted in over 300,000 previously untagged laser shots being found. Checking the list of data events and removing the found lasers dropped the number to 23 possible double-shower events. This same program was used in the HiRes-1 spectral studies.

It was noticed that 21 of the remaining data candidates were two-telescope events with one cluster being in one telescope and the second in another (see Figure 15.23). A test was made using the trigger time, t_i, and the in-plane angle, χ_i, to check if the two clusters could be from the same track. To do this, a Hough transform, similar to the PassA program (see section 8.1), was applied to the time-versus-angle (TvA) distribution. The details of how this was done can be found in Appendix F. Minimum difference cuts on $|X|$, determined from Monte Carlo generated with only one shower per event, were applied to the data (see Figure 15.24) and no single-event, double-showers were found in the HiRes-1 data.

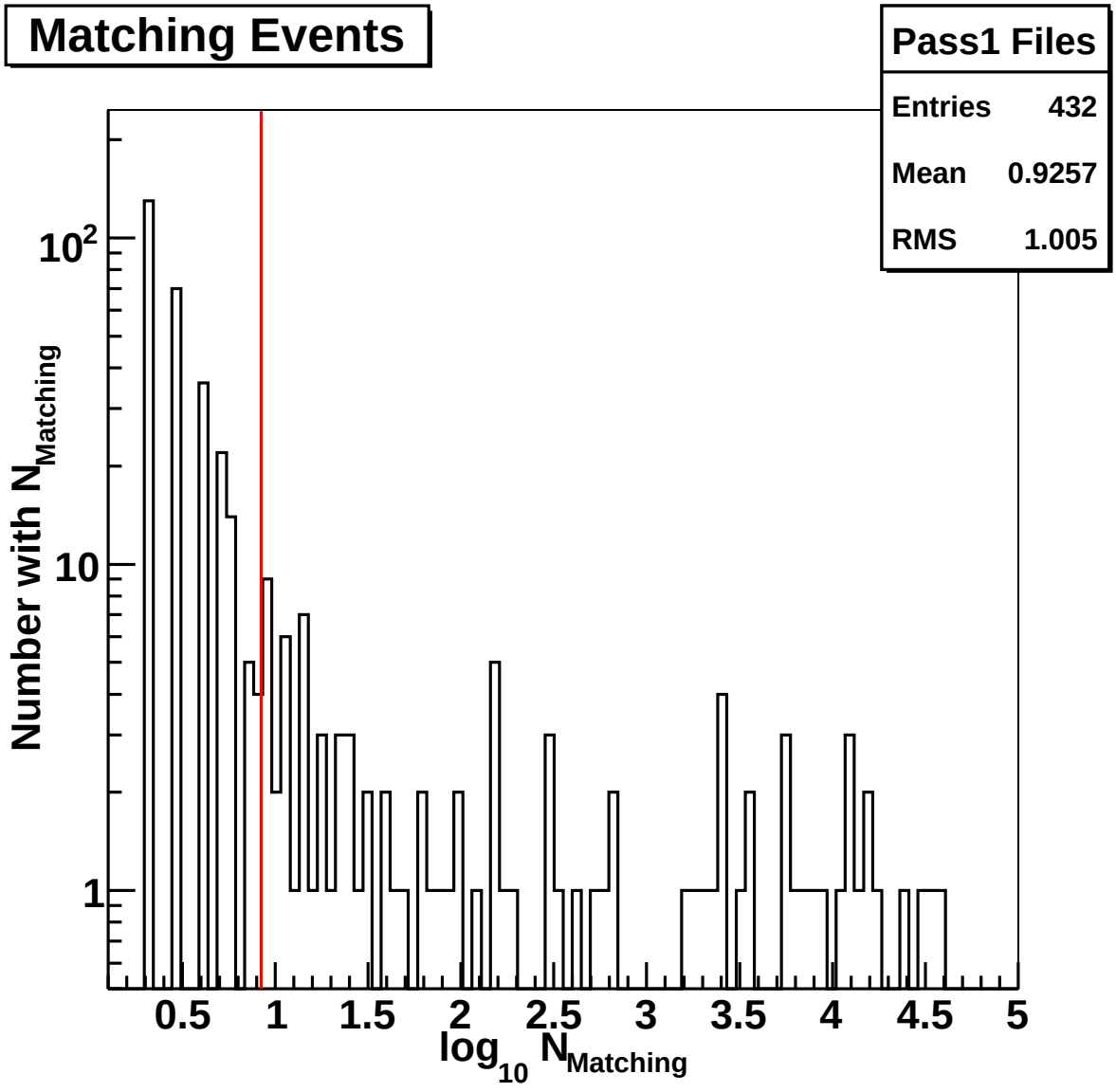

Figure 15.22: The distribution of the $\log_{10}$ of the number of events found to be similar to presumed lasers. The vertical line shows the minimum requirement to be considered a series of laser shots.

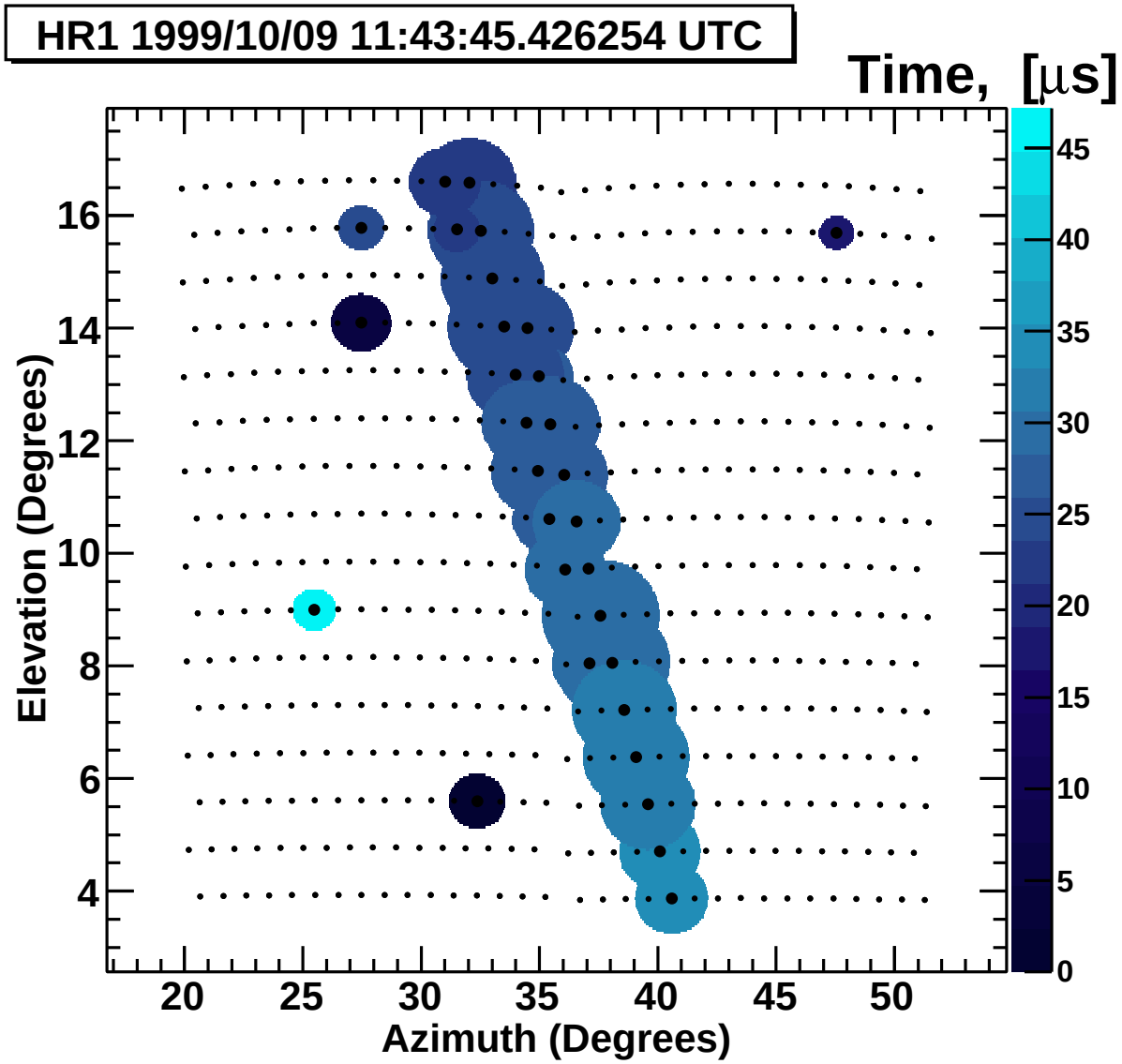

Figure 15.23: One candidate in the data with one cluster in each of the two telescope viewing angles. Time is indicated by the shade.

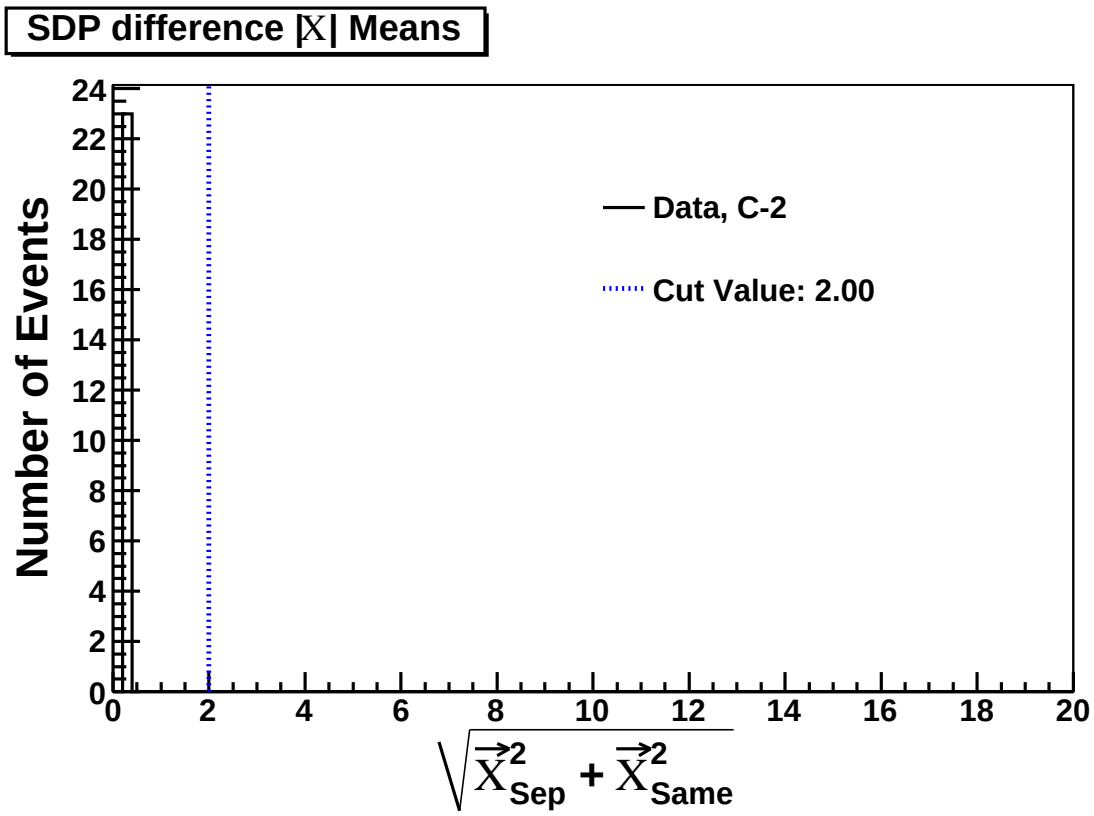

Figure 15.24: The distribution of $|\vec{X}|$ for the difference between the means of cluster-2 using individual, separate SDPs and cluster-2 using the same SDP of cluster 1 for data and single-shower Monte Carlo.

15.2.2 DBSH: Separate Events

Using the AlphaProc reconstructed data, it is possible to measure the time difference between events. Doing this has shown that the minimum time between reconstructed events is 101 ms (see Figure 15.25). As such, the combination of total energy ($E_{\pi^0} = \sum E_{showers}$), the energy difference ($\Delta E_{showers}$), and the time difference ($\Delta T_{showers}$) is inconsistent with π^0 double-showers. Comparing those event pairs with time differences of less than one second (see Table 15.6), it can be seen that all of the data candidates have combined energy differences and time differences inconsistent with the pion energy found by the summation of their individual energies (see Figure 15.26). No separate-event, double-shower candidates were observed using the AlphaProc processed HiRes-1 events.

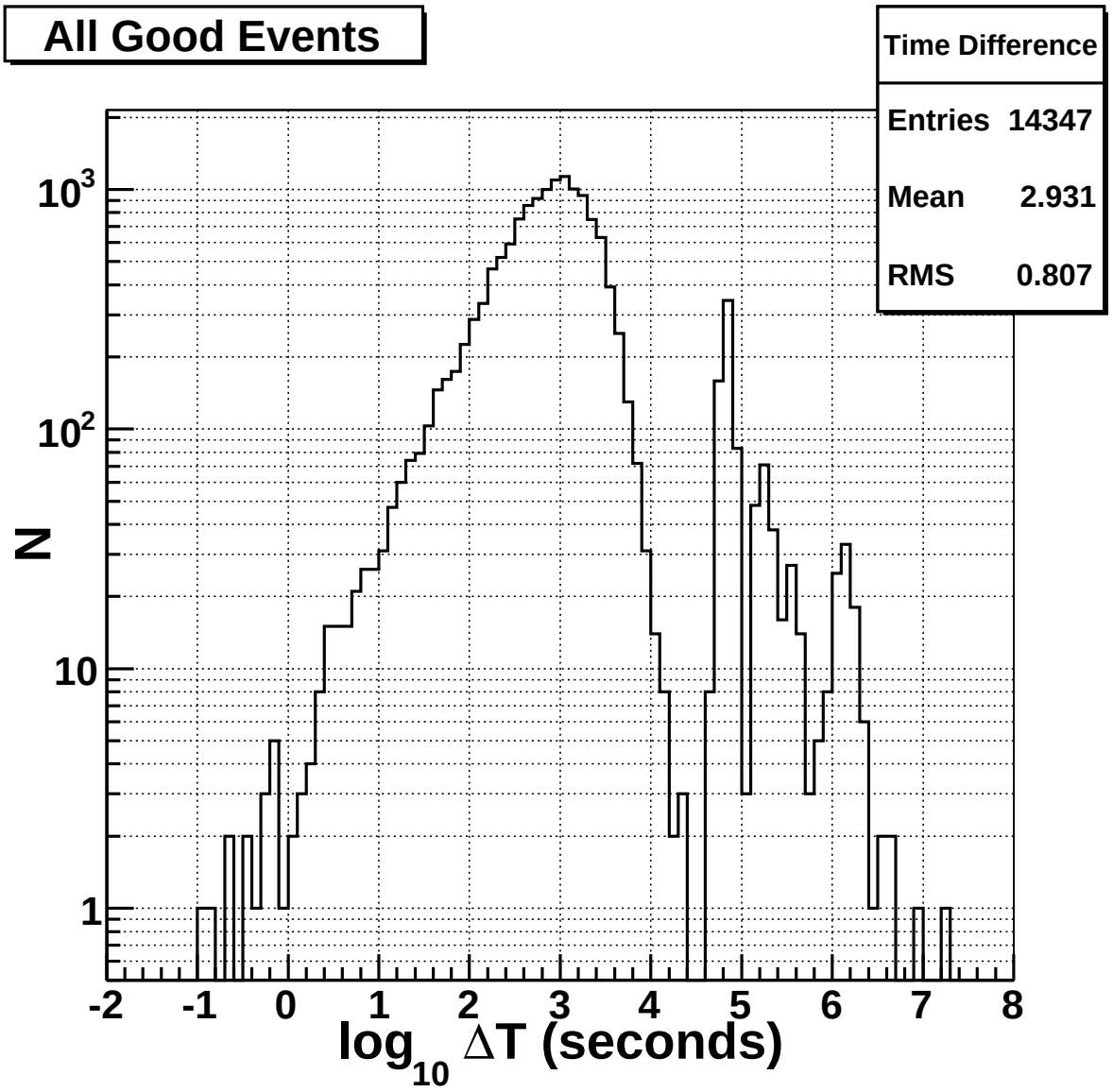

Figure 15.25: The difference in arrival time of observed events pairs in the data.

Table 15.6: Time and energy differences of the 16 event pairs shown in Figure 15.26.

Event-1 Time Stamp	Event-2 Time Stamp	$\sum E$ (E_π) (eV)	$\delta log_{10} E$ (eV)	$log_{10} \delta t$ (s)
1997/08/29 06:31:14.788	1997/08/29 06:31:14.889	18.21	0.220	-0.996
1998/02/01 07:19:37.916	1998/02/01 07:19:38.135	18.19	0.515	-0.660
1999/02/20 09:02:48.065	1999/02/20 09:02:49.054	18.35	0.584	-0.005
1999/02/24 11:30:31.274	1999/02/24 11:30:31.967	18.21	0.376	-0.159
2000/11/27 09:52:28.958	2000/11/27 09:52:29.710	18.73	0.298	-0.124
2001/01/21 07:24:28.685	2001/01/21 07:24:29.419	18.05	0.247	-0.134
2002/08/11 08:53:42.914	2002/08/11 08:53:43.307	18.13	0.423	-0.406
2002/11/07 04:55:35.663	2002/11/07 04:55:36.243	18.12	0.108	-0.237
2004/03/15 10:29:14.254	2004/03/15 10:29:15.018	18.19	0.103	-0.117
2004/04/20 07:57:13.811	2004/04/20 07:57:13.951	17.87	0.200	-0.854
2004/08/14 07:41:44.816	2004/08/14 07:41:45.427	17.86	0.025	-0.214
2005/01/07 03:06:56.104	2005/01/07 03:06:56.642	18.43	0.285	-0.269
2005/09/30 05:56:13.103	2005/09/30 05:56:13.435	19.26	0.182	-0.479
2005/10/31 07:25:26.011	2005/10/31 07:25:26.423	17.82	0.029	-0.385
2005/12/24 03:07:43.877	2005/12/24 03:07:44.651	18.09	0.707	-0.111
2006/02/03 12:14:28.420	2006/02/03 12:14:28.627	17.90	0.102	-0.684

15.2.3 Pion Decay Aperture

From the final selection of retained Monte Carlo events (see Table 15.7) a preliminary aperture for the π^0 decay double-showers could be determined using equations 10.1 and 10.2. Since the only signature of this type of event is the observation of two showers within time and distance constraints, the retention of these events is the only requirement of this determination. The energy of the individual showers was not calculated, so the corrected aperture based on reconstructed energy cannot be determined (see equation 10.3). The maximum zenith angle in which these events were thrown was $\theta_{max} = 80°$. The two subsets of thrown preliminary shower energy range had different maximum impact parameters: the $10^{17.5-18.5}$ eV range (range "2") was thrown to an $R_P = 25$ km, the $10^{18.5-21.0}$ eV range (range "1") was thrown to an $R_P = 50$ km. Both had a minimum R_P of 100 meters. This difference was taken into account by letting each event in the lower range to be multiplied by the ratio in equation 9.5 with the appropriate ranges indicated. The aperture is shown in Figure 15.27. It is interesting to note the pure accidental similarity in the shape of this aperture to the shape of the ultra-high energy cosmic-ray spectrum ($E^3 J$ vs. $\log_{10} E$). The energy region studied in this preliminary study did not go to low enough energies to observe a drop off below $10^{17.5}$ eV.

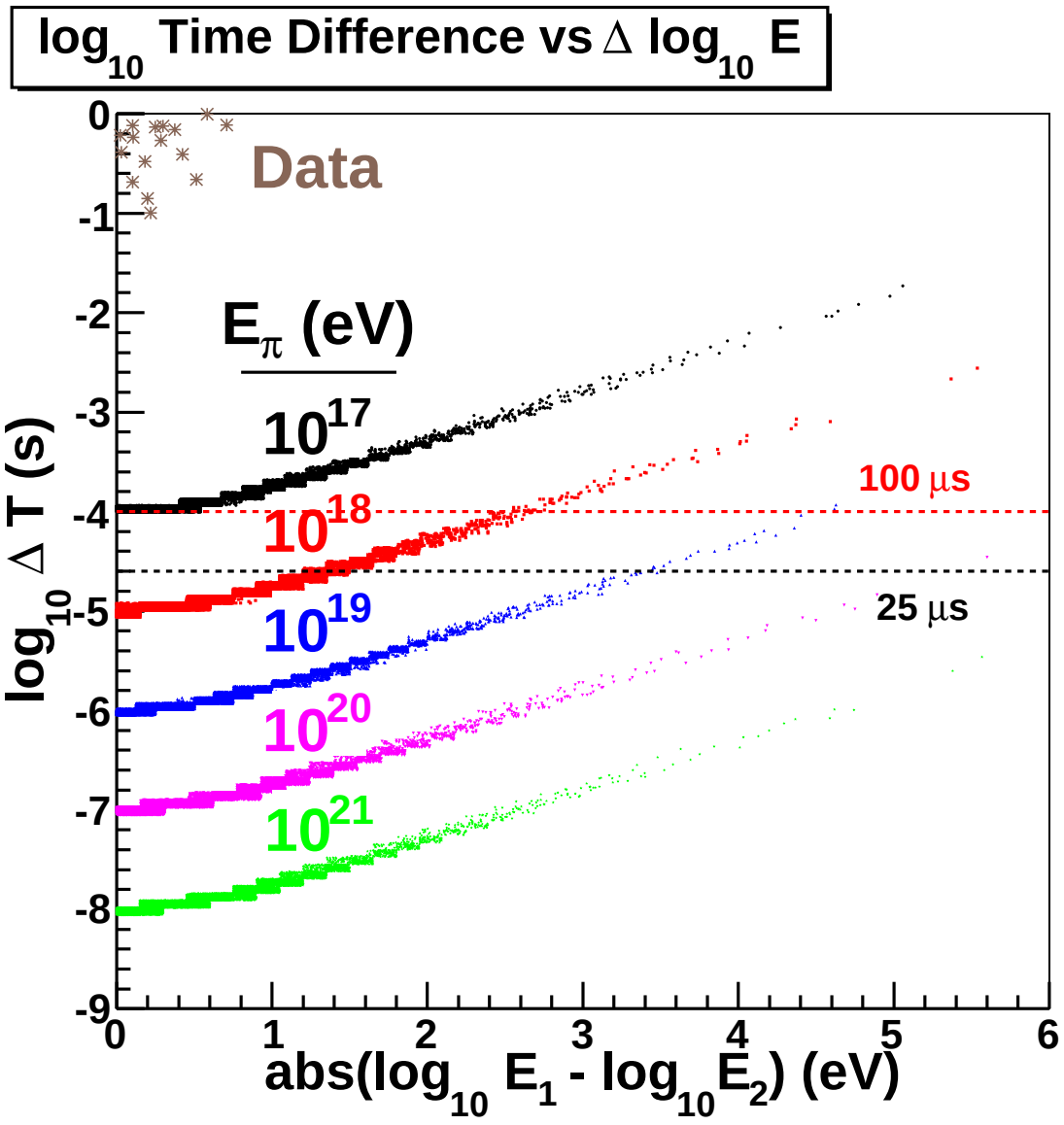

Figure 15.26: The difference in arrival time versus the difference in energy with observed event pairs. The Monte Carlo simulations are shown to have predictable patterns for which the data points have too small of energy difference for the time difference between when they were observed.

Table 15.7: These are the numbers of Monte Carlo events left after processing with combined pion energies indicated.

$log_{10}E_{\pi^0}$ (eV)	Events	$log_{10}E_{\pi^0}$ (eV)	Events	$log_{10}E_{\pi^0}$ (eV)	Events
17.55	105	19.15	10	20.75	0
17.65	193	19.25	11	20.85	0
17.75	231	19.35	8	20.95	0
17.85	217	19.45	1	21.05	0
17.95	164	19.55	1	21.15	0
18.05	145	19.65	3	21.25	0
18.15	97	19.75	0	21.35	0
18.25	90	19.85	1	21.45	0
18.35	62	19.95	0	21.55	0
18.45	48	20.05	1	21.65	0
18.55	41	20.15	0	21.75	0
18.65	39	20.25	1	21.85	0
18.75	16	20.35	1	21.95	0
18.85	14	20.45	0	22.05	0
18.95	12	20.55	0	22.15	0
19.05	8	20.65	0	22.25	0
				22.35	0

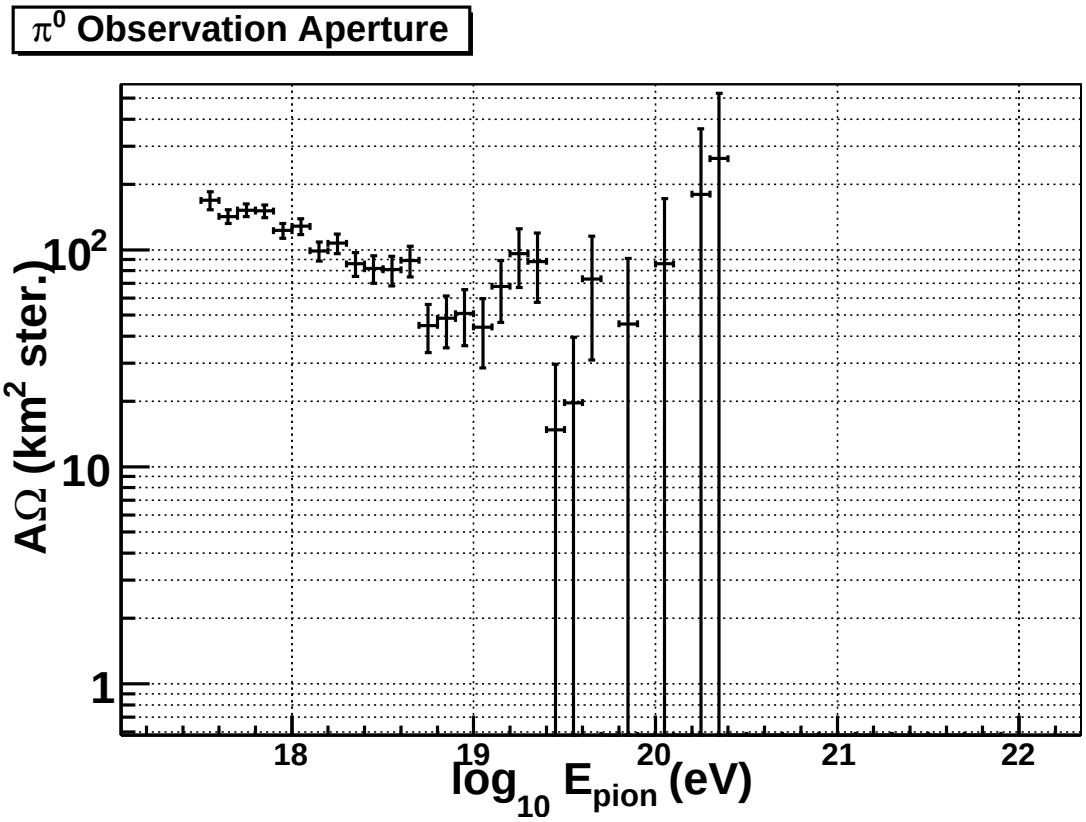

Figure 15.27: The true aperture of observing heliospheric π^0 decays calculated using the double-shower Monte Carlo.

CHAPTER 16

SUMMARY

This dissertation presented and discussed physics from two cosmic-ray experiments: the High Resolution Fly's Eye (HiRes) and Telescope Array (TA). These two experiments use the same telescopes in different configurations, which allows for an inherent bridge between their results. Chapter 5 discussed the HiRes experiment and the equipment used at the HiRes-1 and TA Middle Drum sites. Chapter 6 further discussed the TA experiment and the physics this new experiment would like to explore.

The HiRes-1 detector observed cosmic rays with energy above $10^{18.5}$ eV between May 29, 1997 and May 30, 2006. Middle Drum began collecting data on December 16, 2007 and will continue to observe cosmic rays for the foreseeable future to help resolve physics questions discussed in Chapter 2.

An important scientific sociology exploration discussed here is the rare experimental comparison using the same equipment to produce individual results. Both experiments observe extensive air showers (Chapter 3) using the fluorescence technique (Chapter 4). By using the same equipment and the same processing techniques on the data (programs described in Chapter 7), we are able to make a direct comparison of the two experiments and forge a bridge between the collected data sets.

With this rare opportunity, we made a comparison of the observed energy flux spectrum as measured by these two experiments. The Middle Drum measurements must either support the published HiRes-1 spectrum [3] or explain any differences that arise. A comparison of the data processing is made in Chapter 9. The HiRes-1 spectrum was generated using first the "Original" processing codes, which resulted in the published spectrum [3], and then by the "Stereo_TA" processing codes that were used to determine the Middle Drum spectrum. Both of these spectra are shown in Chapter 10. Comparing these to the published spectrum showed the consistency between the new HiRes-1 results and the published results. The Middle Drum spectrum, detailed in Chapter 11, is also consistent with the published spectrum. This provides the direct link between the two experiments and all future results.

A separate HiRes-1 spectrum measurement was obtained using data processed with the Stereo_TA code, but using both atmospheric and calibration databases. Comparing

the spectrum measured using the databases and the spectrum measured without using the databases, it was determined that the uncertainty in the energy spectrum based on this combined atmospheric and calibration database technique was less than 1% (Chapter 10).

In addition, a search was made for simultaneous showers as the signature of cosmic rays interacting with heliospheric ions. This interaction is expected to produce neutral pions that decay into two photons which could arrive at the earth as a potential double-shower. Although density studies show this to be an unlikely event, a search was made with the intent of extending cosmic-ray physics beyond standard explanations. The physics of this highly unlikely occurrence is discussed in Chapter 13. Photon showers and the Monte Carlo simulation of double showers was shown in Chapter 14.

This search was made using the HiRes-1 data set since it is the largest available to the author at the time of this study. New code was written to search for these coincident showers and is described in the "AlphaProc" Chapter, 8. The same HiRes-1 Monte Carlo generated for the Original and Stereo_TA spectra was also processed using these programs (Chapter 9) and an aperture and an energy spectrum was measured (Chapter 10). As with the other spectra produced for this dissertation, the AlphaProc spectrum is also consistent with the published HiRes spectrum.

No double showers were found in the data, so only an aperture based on double-shower Monte Carlo events was created. The details of the "DBSH" program set used to process these and the results of this search are shown in Chapter 15.

APPENDIX A

ORIGINAL PROCESSING CODE DATA-MONTE CARLO COMPARISONS

In order to justify our results, the reconstructed parameters of the Monte Carlo shower simulations must show a similarity to the data reconstructed in the same manner. Similar to resolution plots, this is done over separate energy ranges to show how the values change as energies increase: A) $10^{18.5-19.0}$ eV, B) $10^{19.0-19.5}$ eV, and C) $10^{19.5-20.5}$ eV. These figures show comparisons from the current Original processing results between: 1) the number of photoelectrons per degree (see Figure A.1); 2) the impact parameter, R_P (see Figure A.2); 3) the in-plane angle, ψ (see Figure A.3); 4) the zenith angle, θ (see Figure A.4); and 5) the azimuthal angle, ϕ (see Figure A.5). For all figures, the data points are represented with markers and error bars, and the Monte Carlo is given as a solid line histogram. As can be seen in the figures, there is a consistency between the data and the Monte Carlo for all of the energy ranges used in the spectrum.

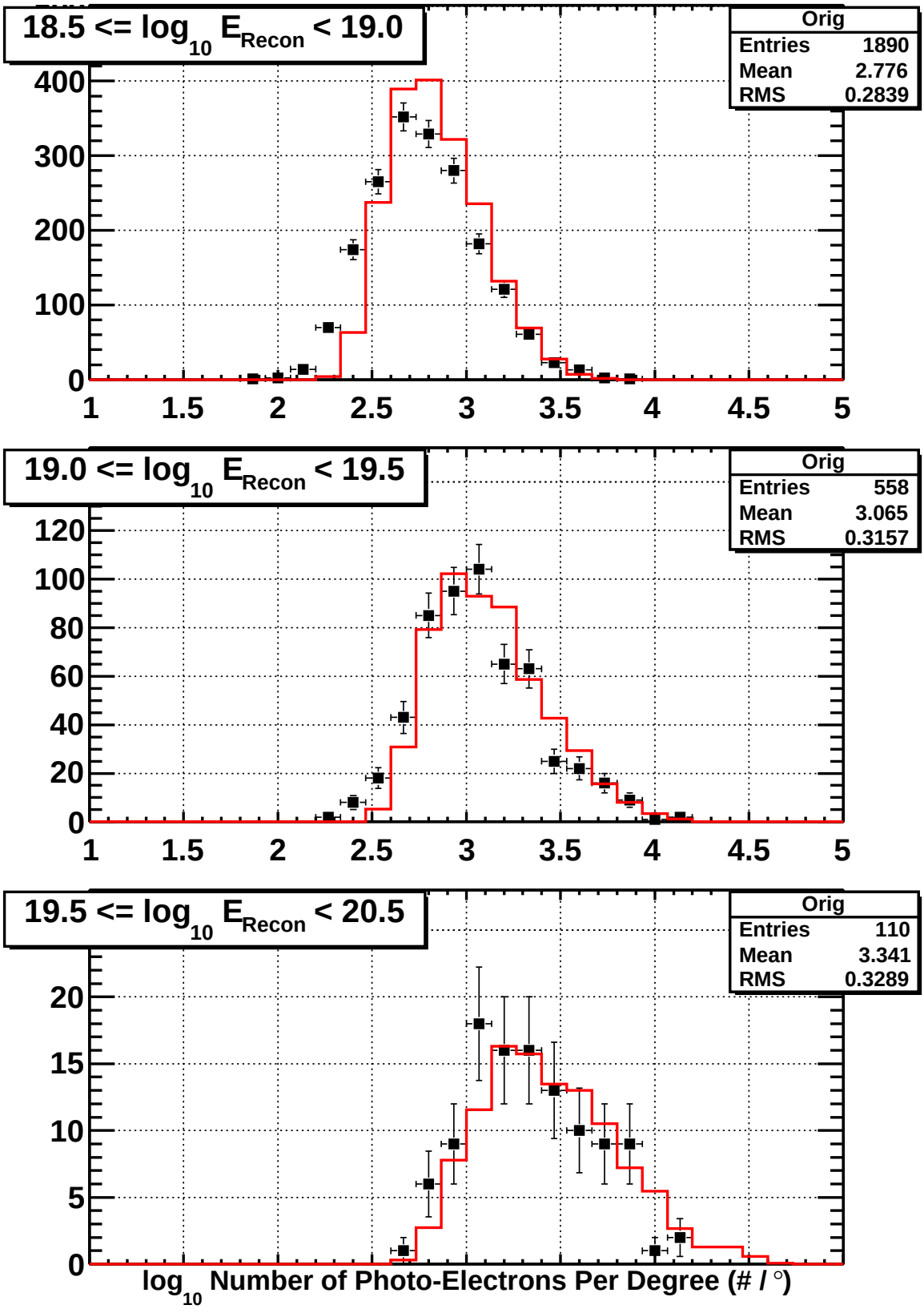

Figure A.1: Data-Monte Carlo comparisons for the number of photoelectrons per degree of events determined using the Original processing code set.

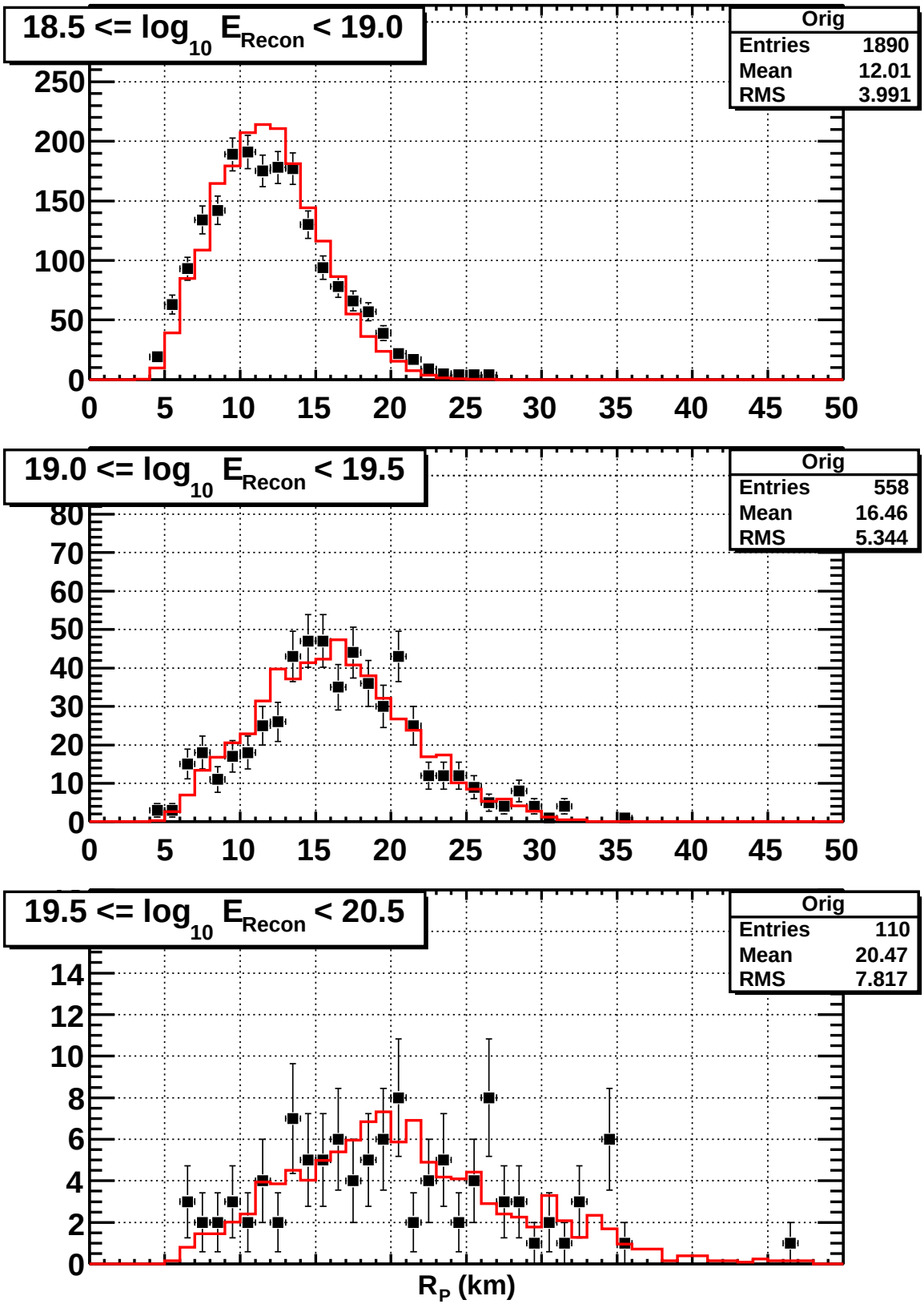

Figure A.2: Data-Monte Carlo comparisons for the impact parameter, R_P, of events determined using the Original processing code set.

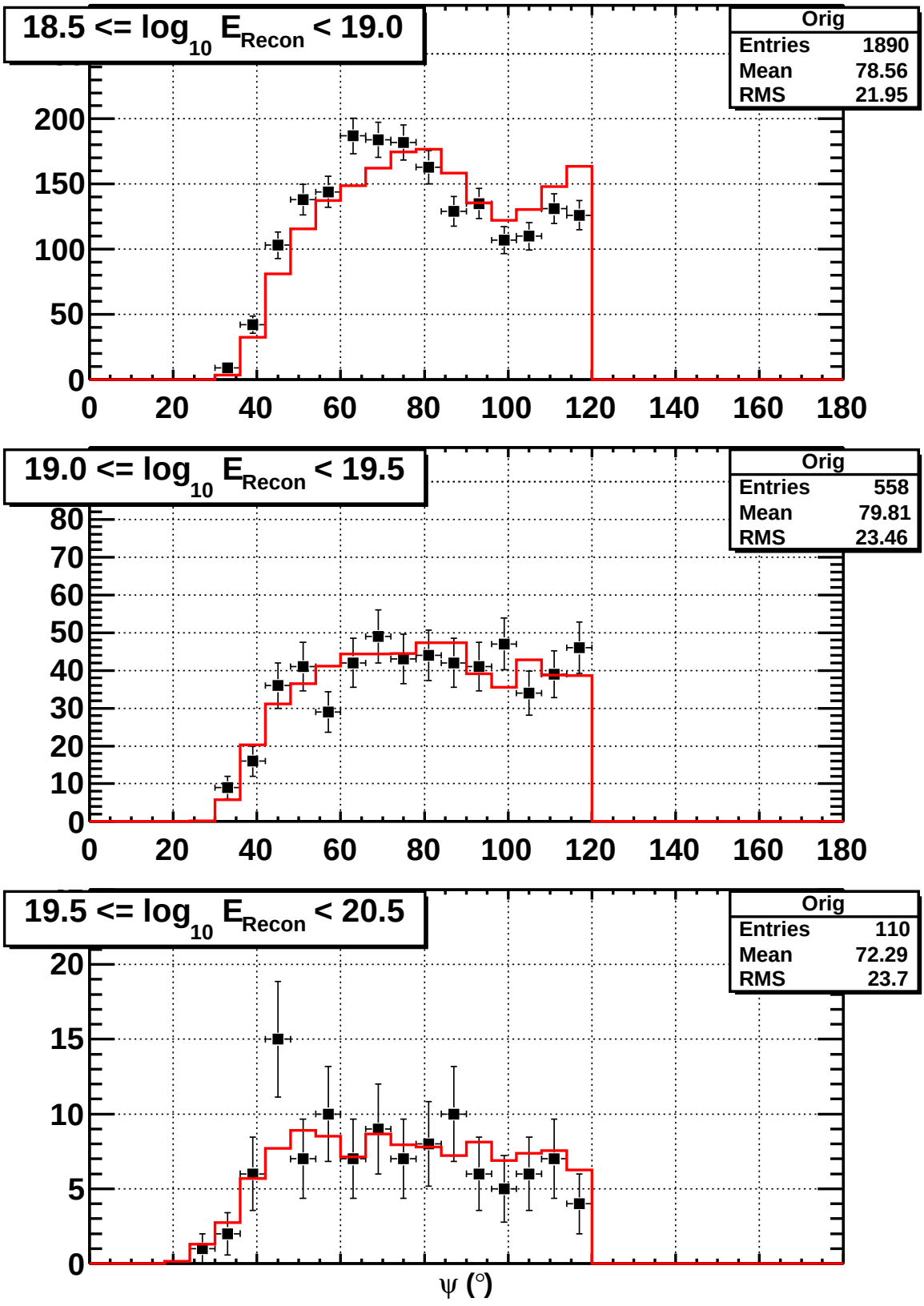

Figure A.3: Data-Monte Carlo comparisons for the in-plane angle, ψ, of events determined using the Original processing code set.

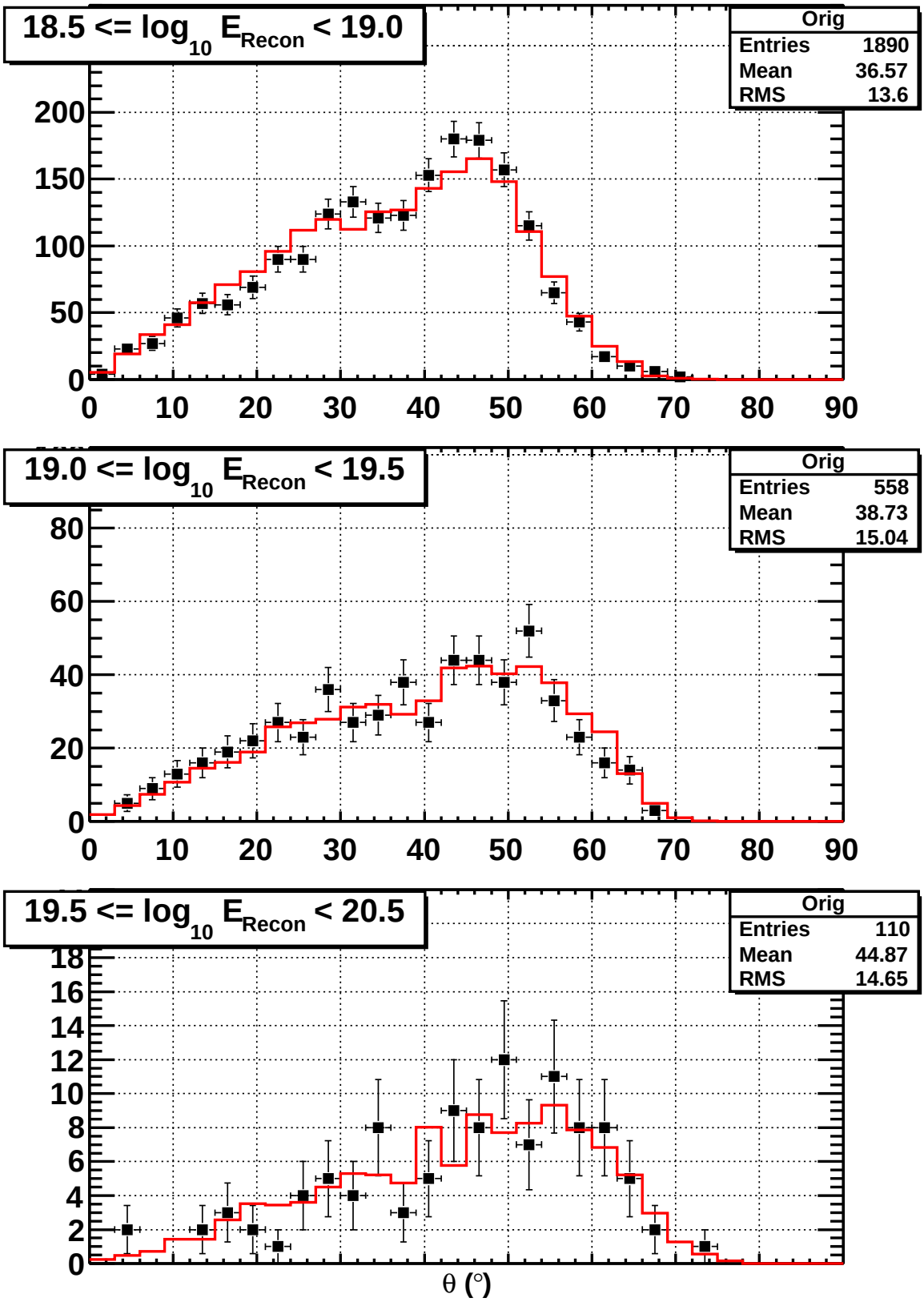

Figure A.4: Data-Monte Carlo comparisons for the zenith angle, θ, of events determined using the Original processing code set.

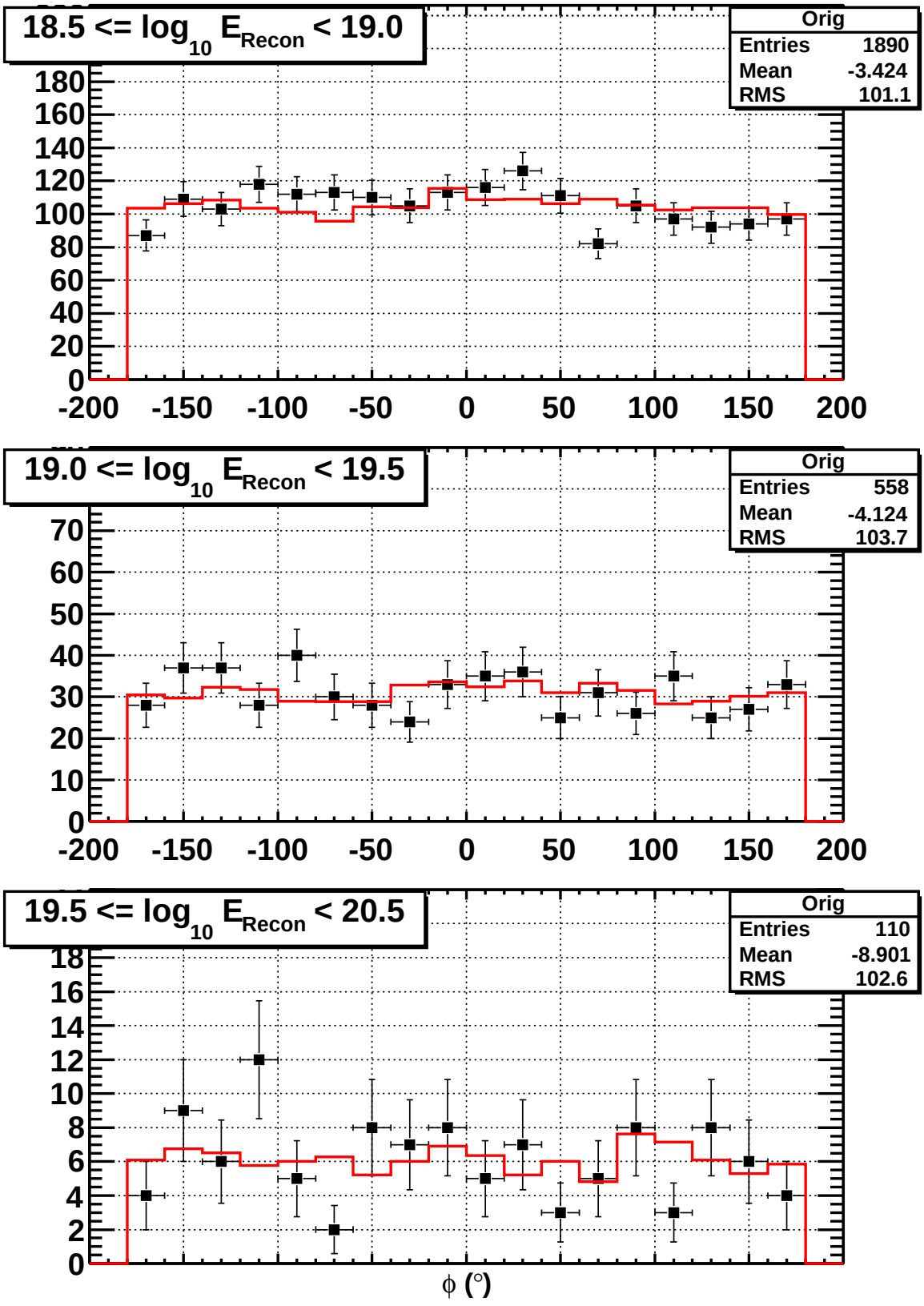

Figure A.5: Data-Monte Carlo comparisons for the azimuthal angle, ϕ, of events determined using the Original processing code set.

APPENDIX B

ALPHAPROC PROCESSING CODE DATA-MONTE CARLO COMPARISONS

In order to justify our results, the reconstructed parameters of the Monte Carlo shower simulations must show a similarity to the data reconstructed in the same manner. Similar to resolution plots, this is done over separate energy ranges to show how the values change as energies increase: A) $10^{18.5-19.0}$ eV, B) $10^{19.0-19.5}$ eV, and C) $10^{19.5-20.5}$ eV. These figures show comparisons from the current AlphaProc processing results between: 1) the number of photoelectrons per degree (see Figure B.1); 2) the impact parameter, R_P (see Figure B.2); 3) the in-plane angle, ψ (see Figure B.3); 4) the zenith angle, θ (see Figure B.4); and 5) the azimuthal angle, ϕ (see Figure B.5). For all figures, the data points are represented with markers and error bars, and the Monte Carlo is given as a solid line histogram. As can be seen in the figures, there is a consistency between the data and the Monte Carlo for all of the energy ranges used in the spectrum.

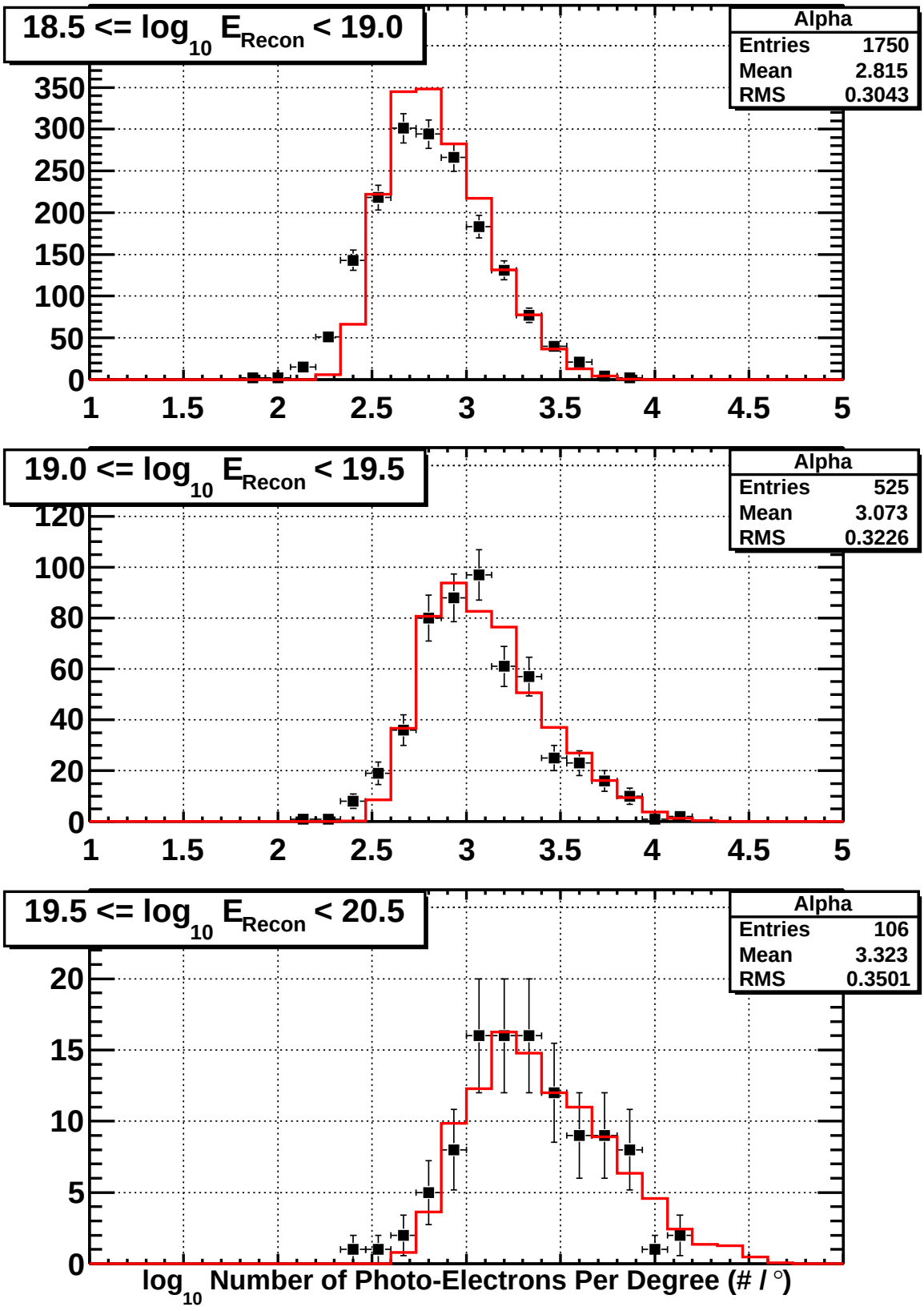

Figure B.1: Data-Monte Carlo comparisons for the number of photoelectrons per degree of events determined using the AlphaProc processing code set.

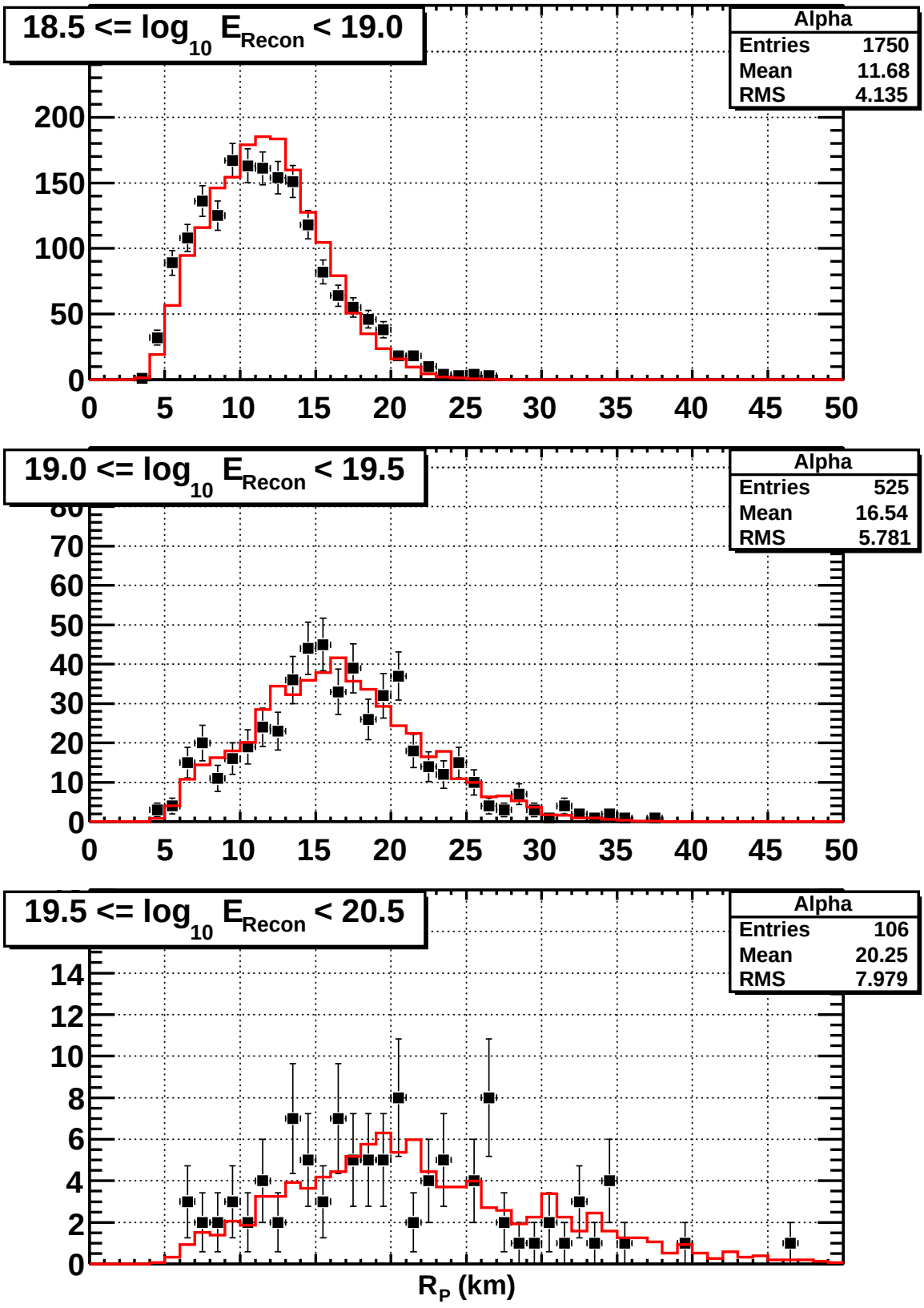

Figure B.2: Data-Monte Carlo comparisons for the impact parameter, R_P, of events determined using the AlphaProc processing code set.

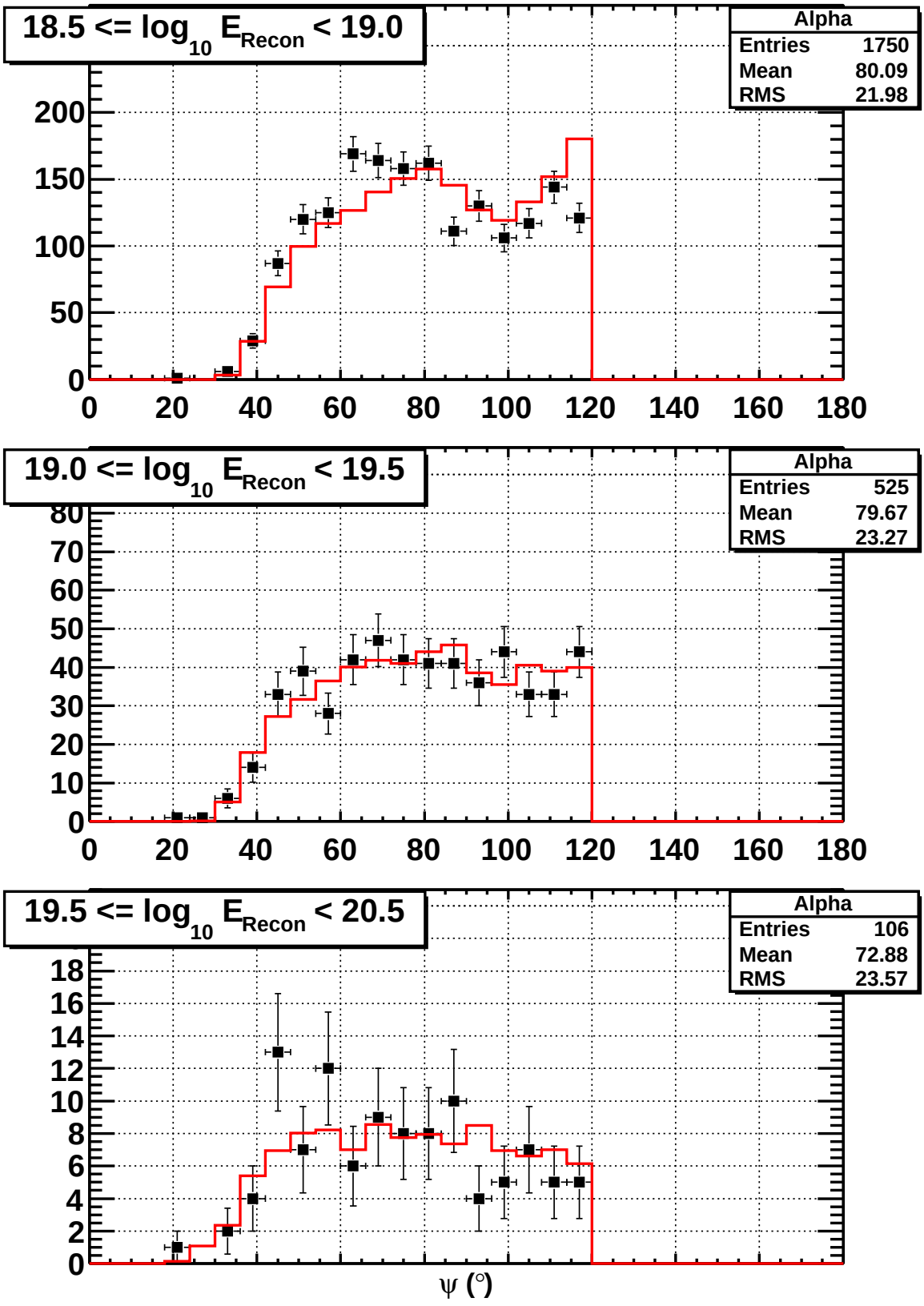

Figure B.3: Data-Monte Carlo comparisons for the in-plane angle, ψ, of events determined using the AlphaProc processing code set.

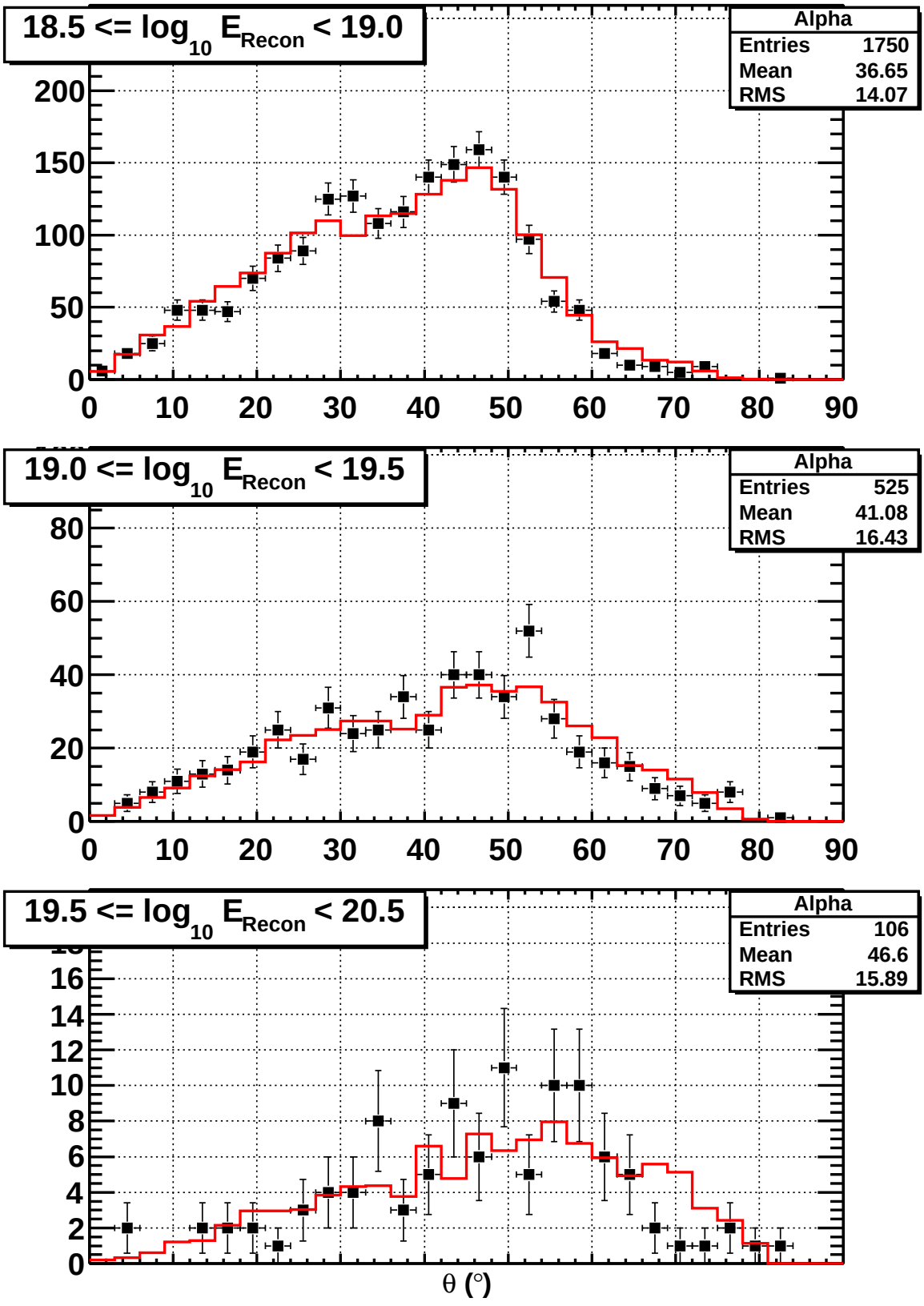

Figure B.4: Data-Monte Carlo comparisons for the zenith angle, θ, of events determined using the AlphaProc processing code set.

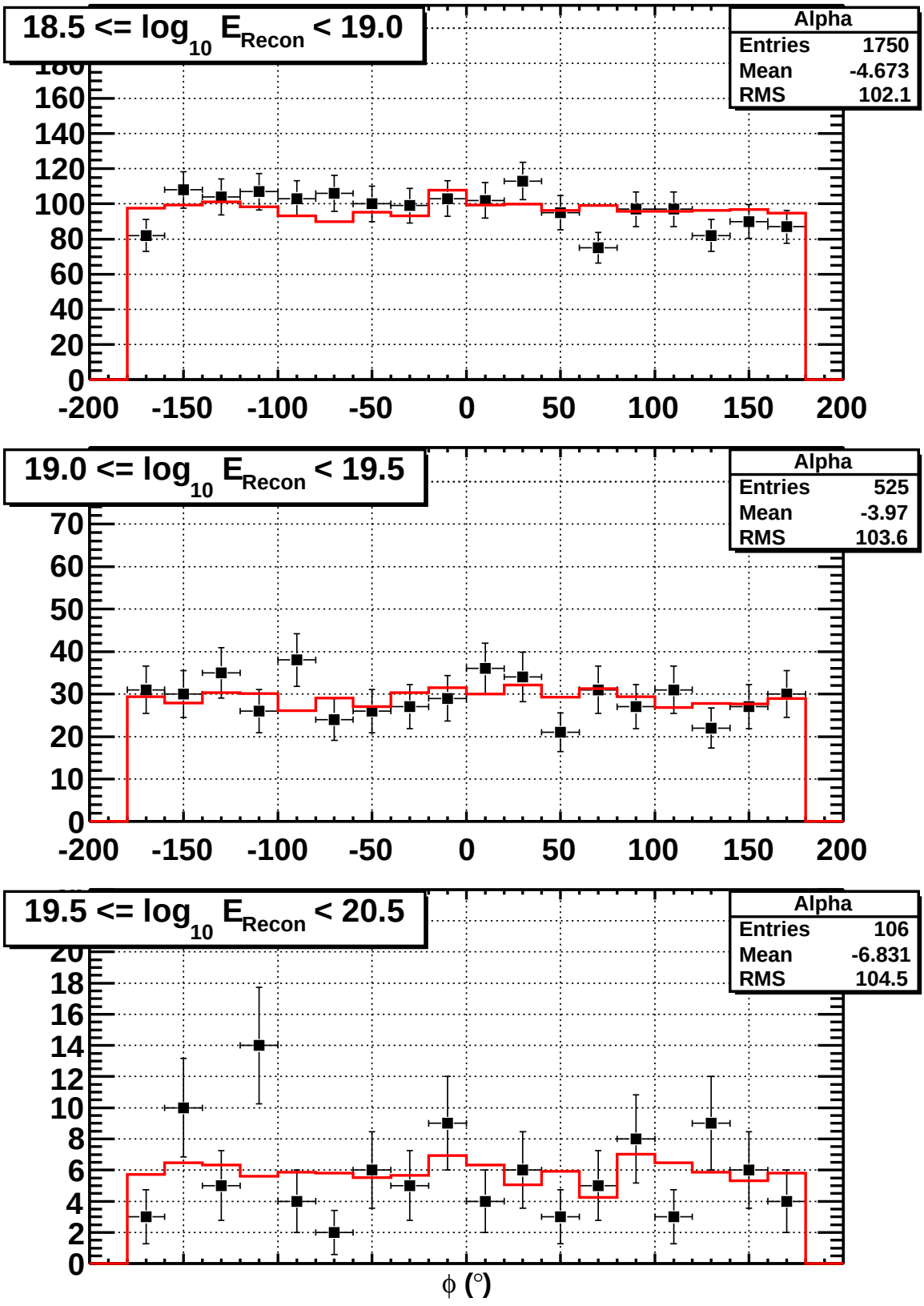

Figure B.5: Data-Monte Carlo comparisons for the azimuthal angle, ϕ, of events determined using the AlphaProc processing code set.

APPENDIX C

STEREO_TA PROCESSING CODE DATA-MONTE CARLO COMPARISONS (NO DATABASES)

In order to justify our results, the reconstructed parameters of the Monte Carlo shower simulations must show a similarity to the data reconstructed in the same manner. Similar to resolution plots, this is done over separate energy ranges to show how the values change as energies increase: A) $10^{18.5-19.0}$ eV, B) $10^{19.0-19.5}$ eV, and C) $10^{19.5-20.5}$ eV. These figures show comparisons from the no-database Stereo_TA processing results between: 1) the number of photoelectrons per degree (see Figure C.1); 2) the impact parameter, R_P (see Figure C.2); 3) the in-plane angle, ψ (see Figure C.3); 4) the zenith angle, θ (see Figure C.4); and 5) the azimuthal angle, ϕ (see Figure C.5). For all figures, the data points are represented with markers and error bars, and the Monte Carlo is given as a solid line histogram. As can be seen in the figures, there is a consistency between the data and the Monte Carlo for all of the energy ranges used in the spectrum.

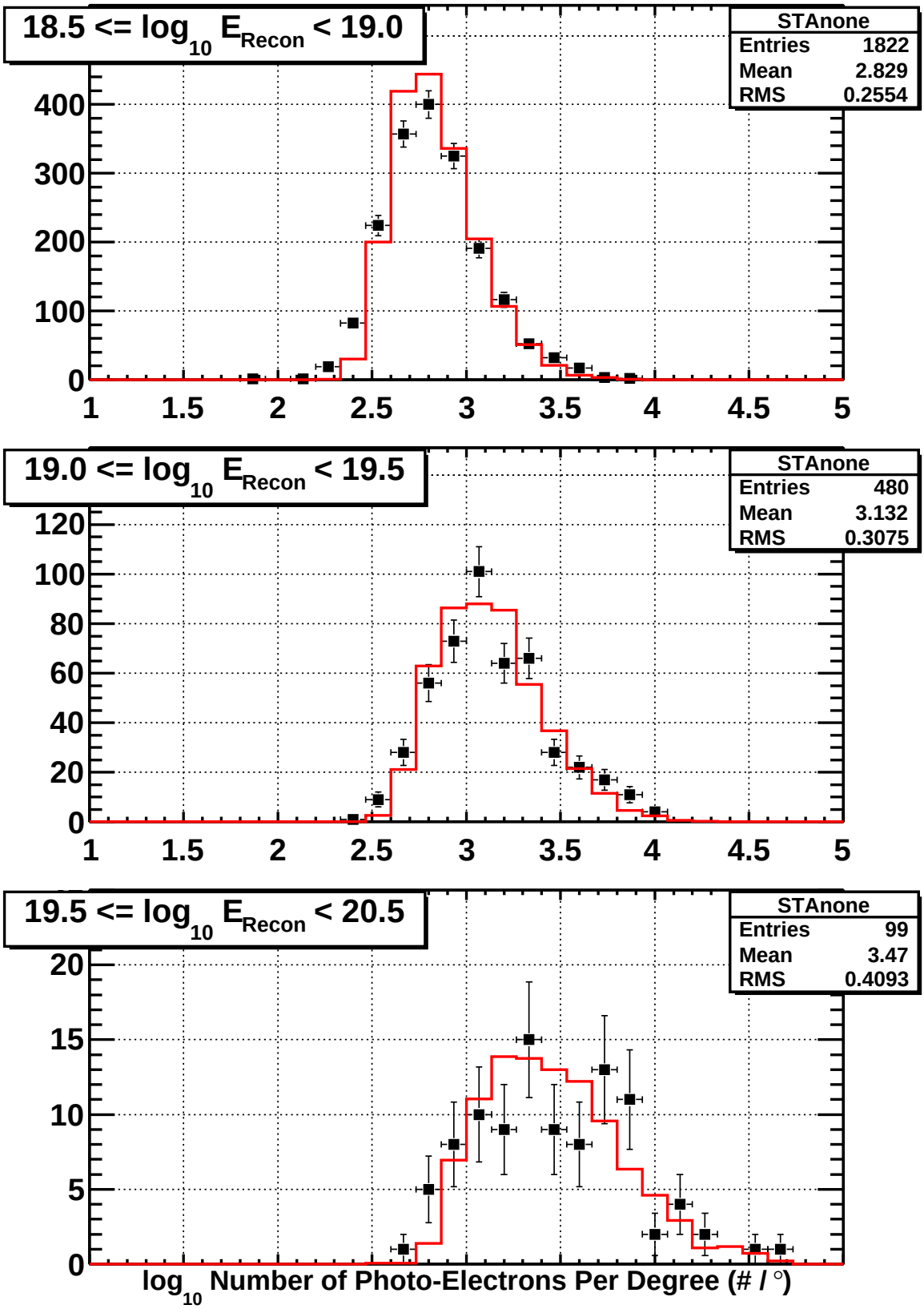

Figure C.1: Data-Monte Carlo comparisons for the number of photoelectrons per degree of events determined using the Stereo_TA processing code set without databases.

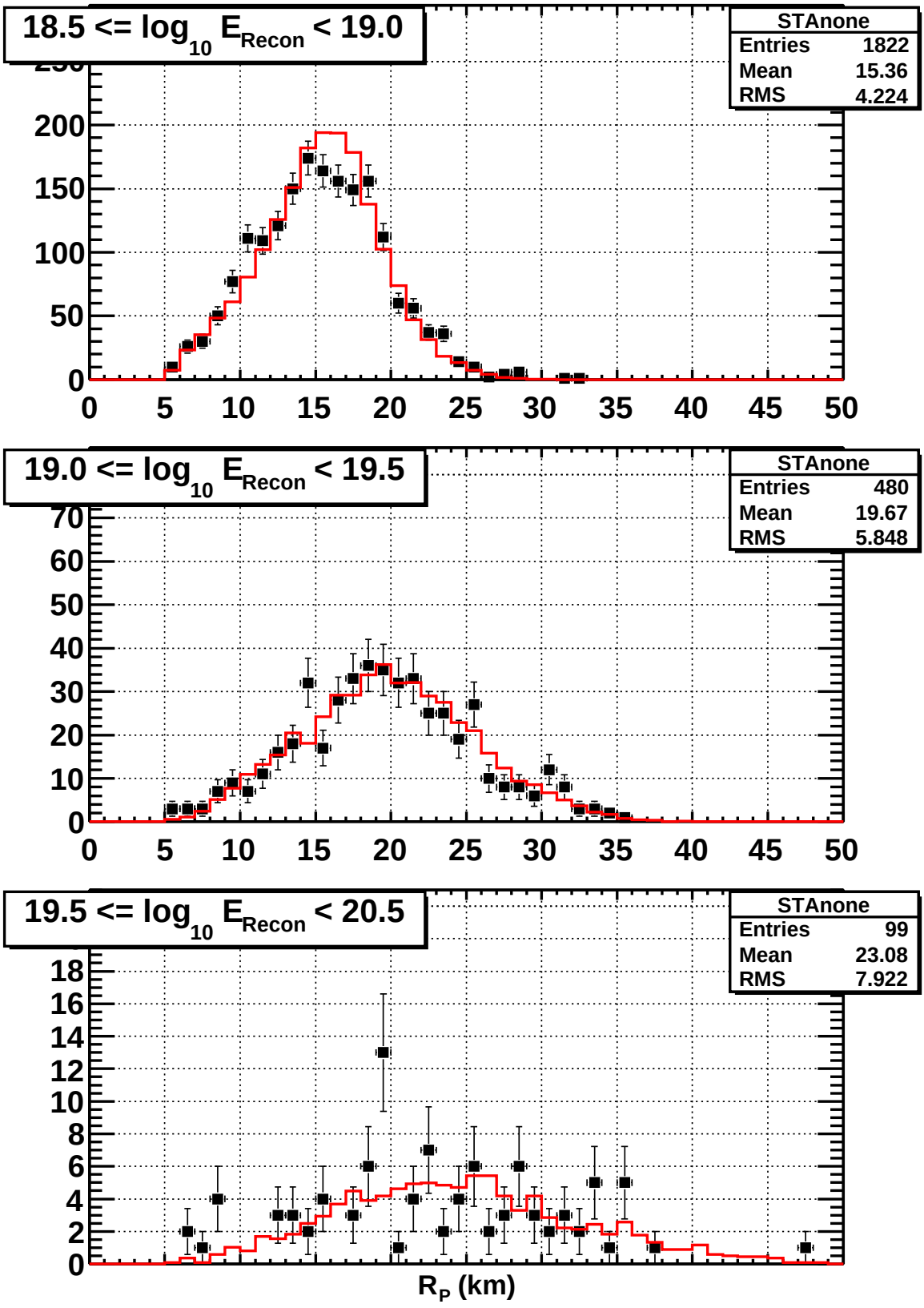

Figure C.2: Data-Monte Carlo comparisons for the impact parameter, R_P, of events determined using the Stereo_TA processing code set without databases.

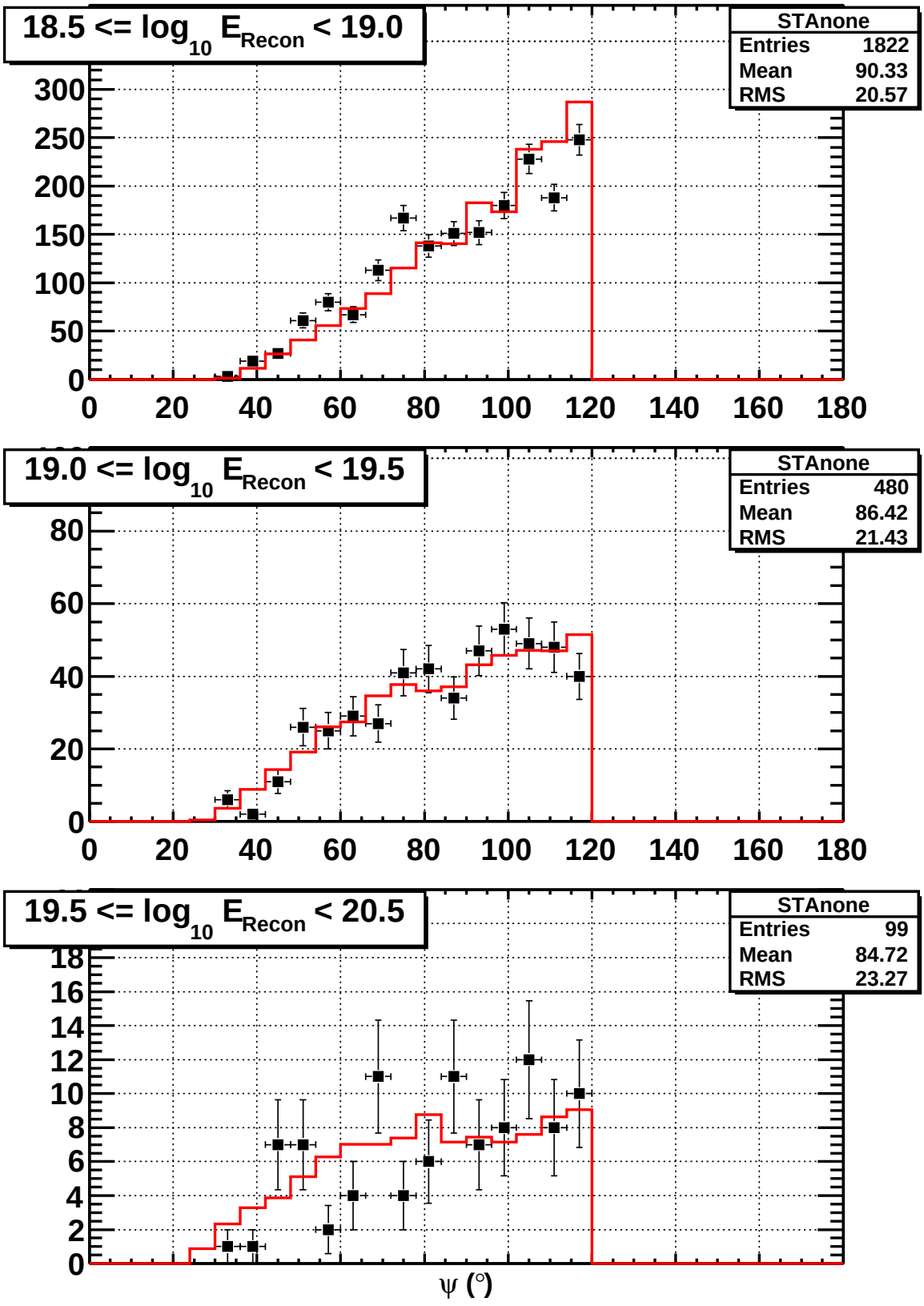

Figure C.3: Data-Monte Carlo comparisons for the in-plane angle, ψ, of events determined using the Stereo_TA processing code set without databases.

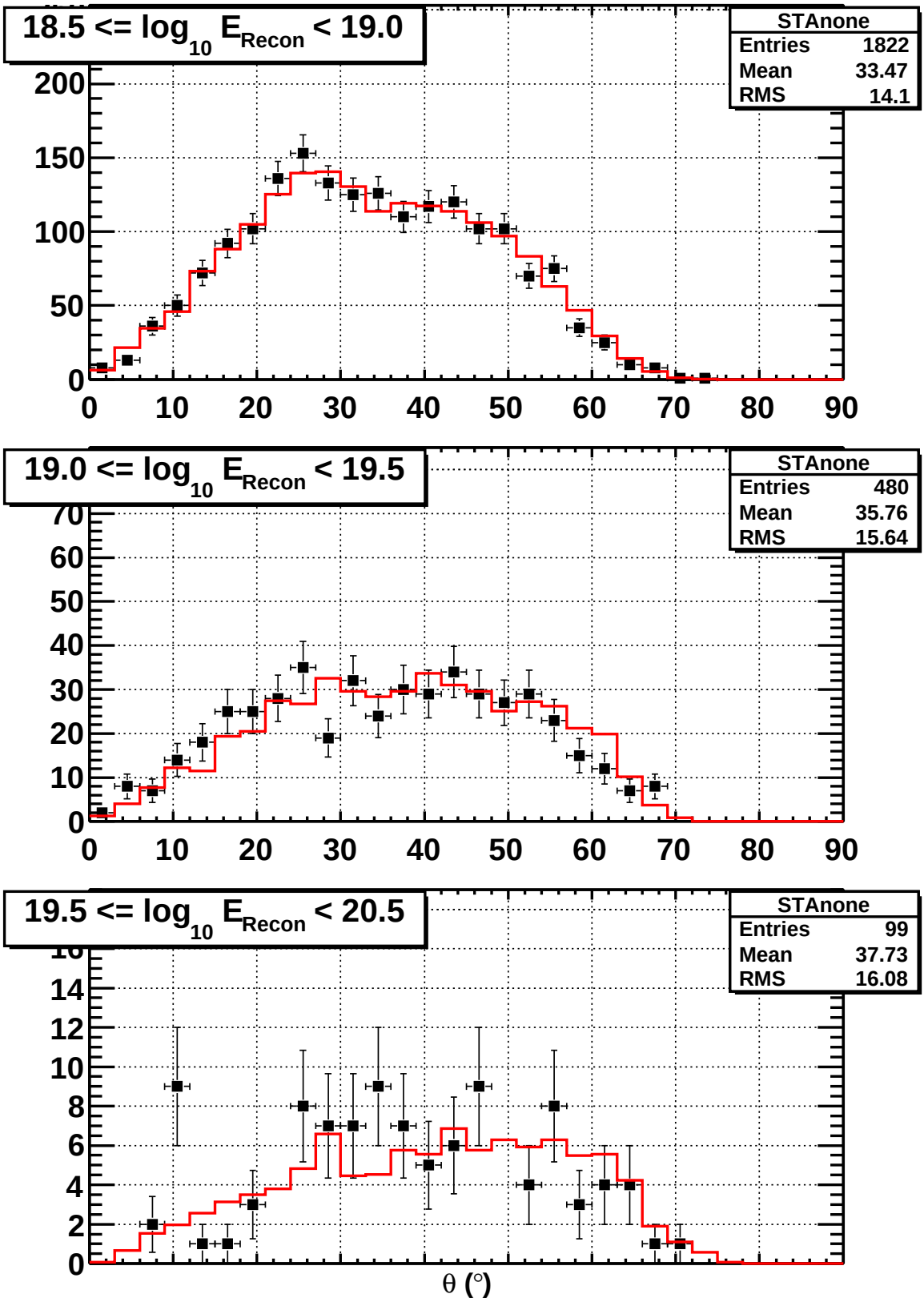

Figure C.4: Data-Monte Carlo comparisons for the zenith angle, θ, of events determined using the Stereo_TA processing code set without databases.

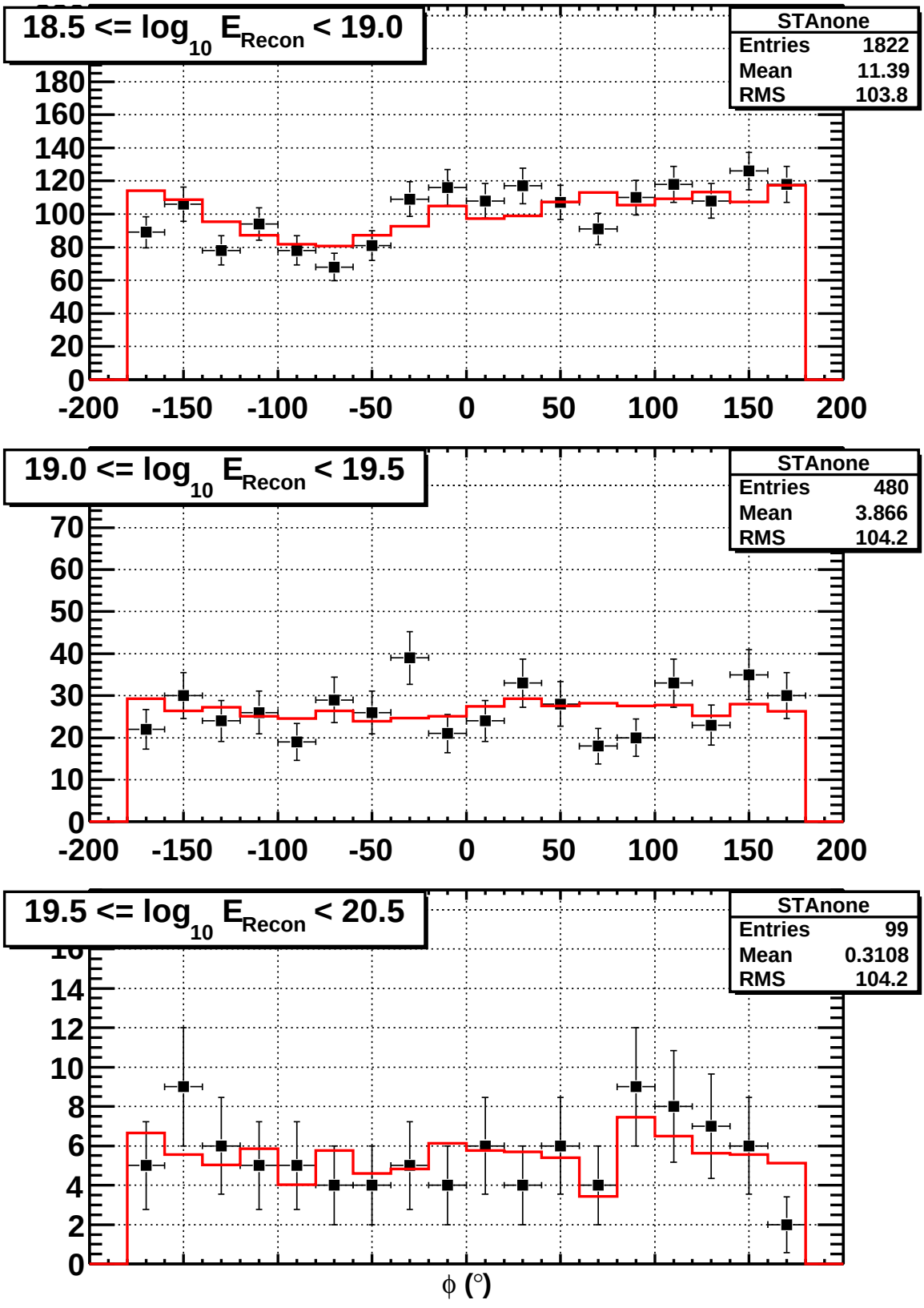

Figure C.5: Data-Monte Carlo comparisons for the azimuthal angle, ϕ, of events determined using the Stereo_TA processing code set without databases.

APPENDIX D

STEREO_TA PROCESSING CODE DATA-MONTE CARLO COMPARISONS (WITH DATABASES)

In order to justify our results, the reconstructed parameters of the Monte Carlo shower simulations must show a similarity to the data reconstructed in the same manner. Similar to resolution plots, this is done over separate energy ranges to show how the values change as energies increase: A) $10^{18.5-19.0}$ eV, B) $10^{19.0-19.5}$ eV, and C) $10^{19.5-20.5}$ eV. These figures show comparisons from the Stereo_TA processing results using both calibration and atmospheric databases between: 1) the number of photoelectrons per degree (see Figure D.1); 2) the impact parameter, R_P (see Figure D.2); 3) the in-plane angle, ψ (see Figure D.3); 4) the zenith angle, θ (see Figure D.4); and 5) the azimuthal angle, ϕ (see Figure D.5). For all figures, the data points are represented with markers and error bars, and the Monte Carlo is given as a solid line histogram. As can be seen in the figures, there is a consistency between the data and the Monte Carlo for all of the energy ranges used in the spectrum.

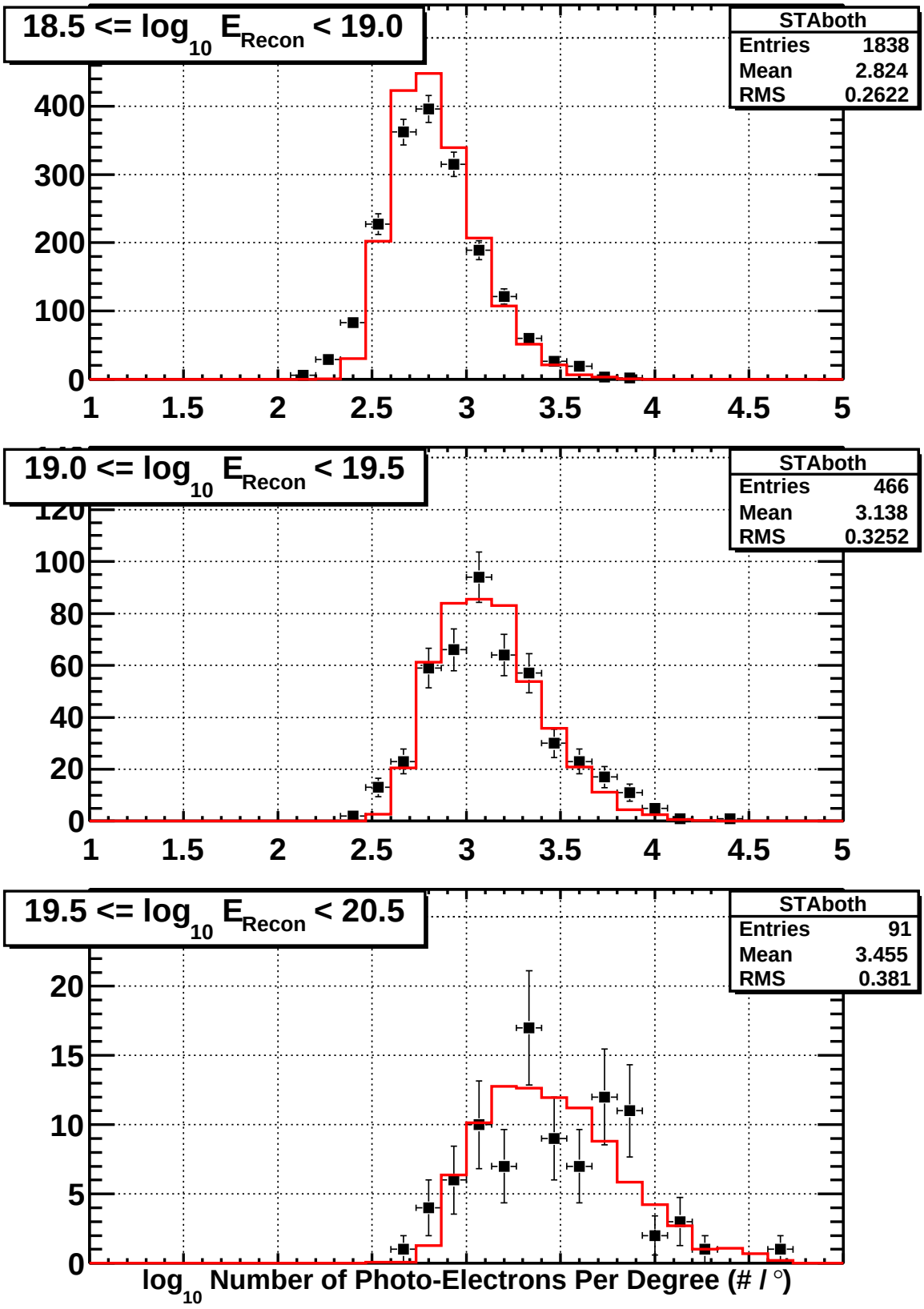

Figure D.1: Data-Monte Carlo comparisons for the number of photoelectrons per degree of events determined using the Stereo_TA processing code set with calibration and atmospheric databases.

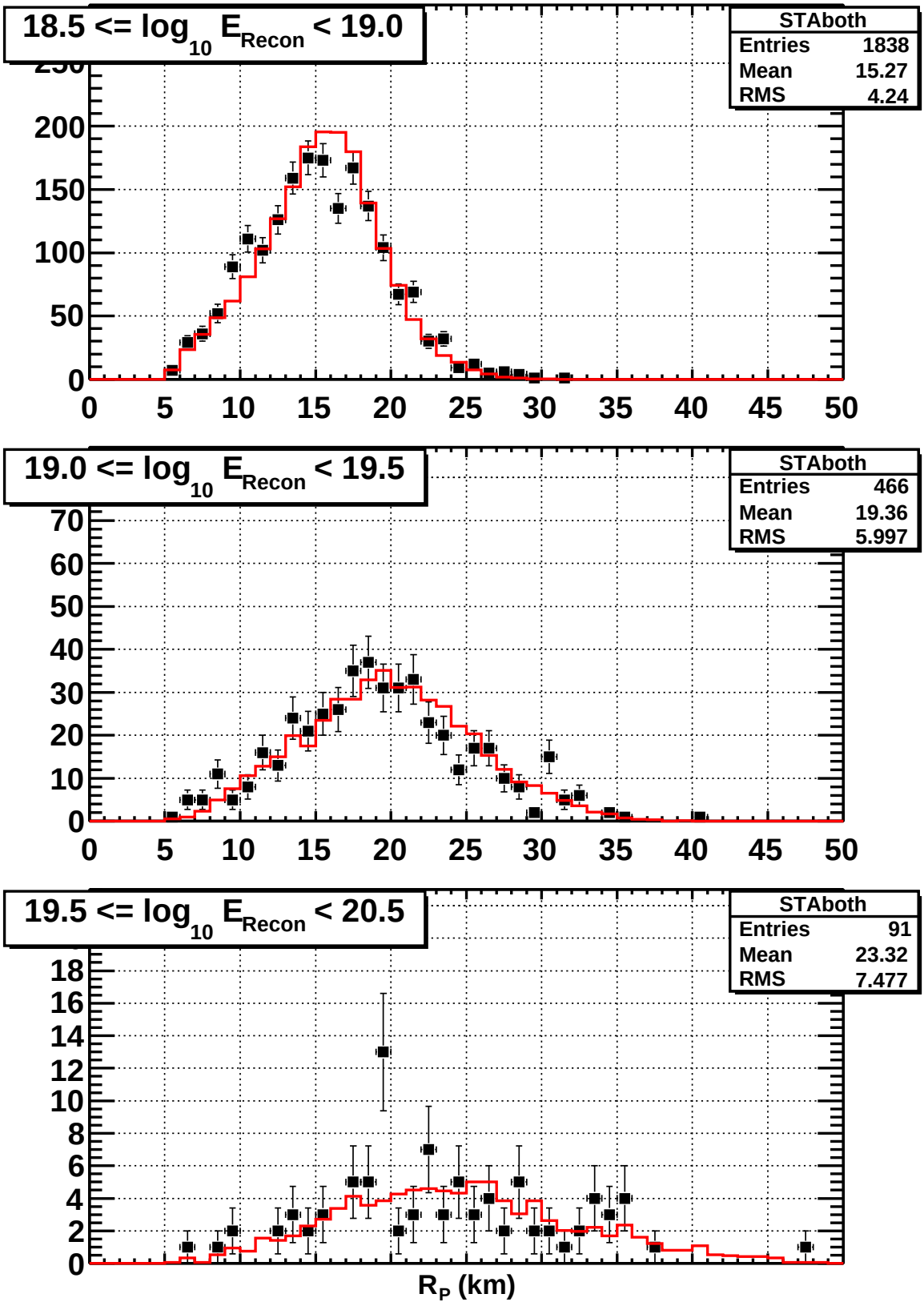

Figure D.2: Data-Monte Carlo comparisons for the impact parameter, R_P, of events determined using the Stereo_TA processing code set with calibration and atmospheric databases.

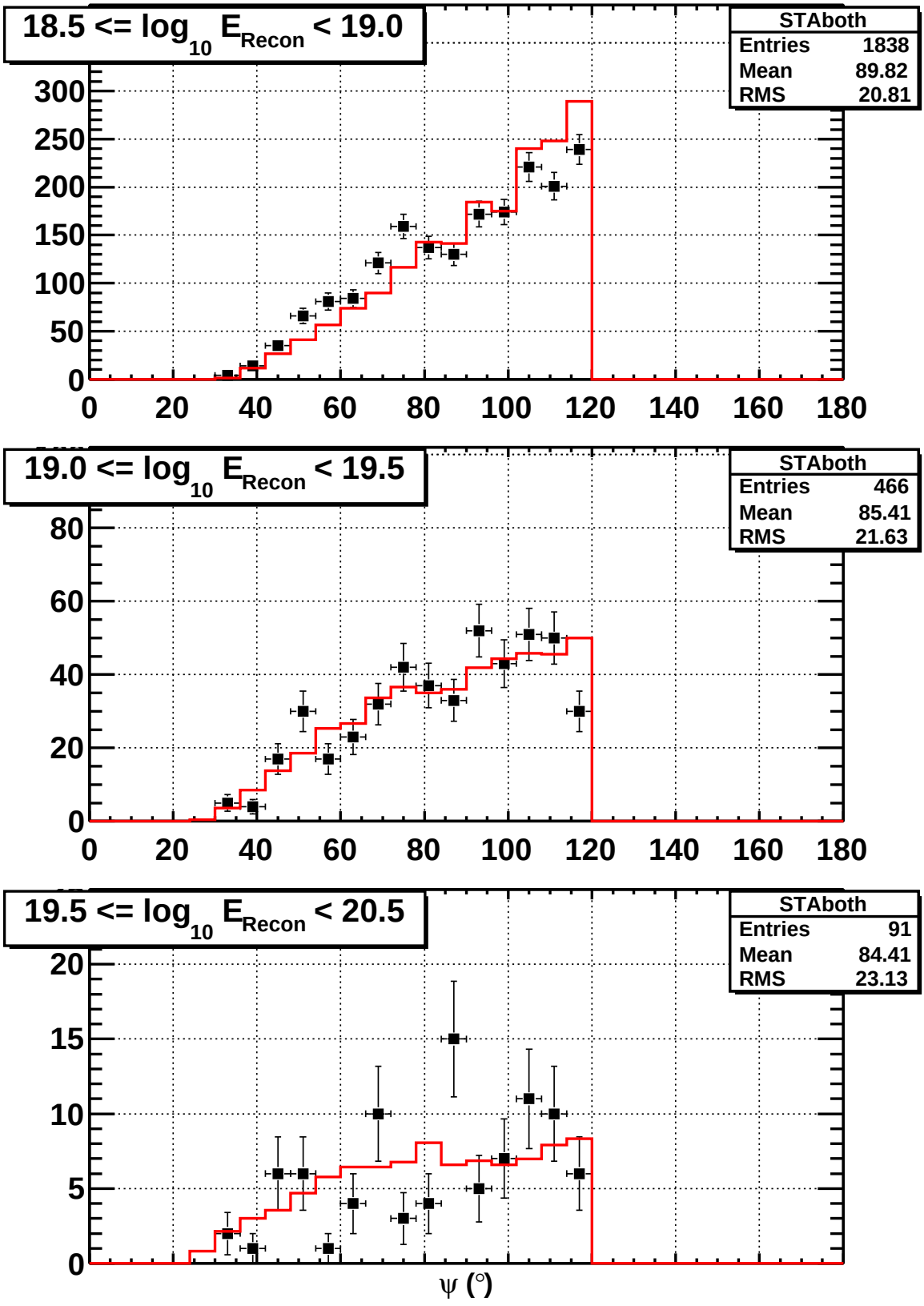

Figure D.3: Data-Monte Carlo comparisons for the in-plane angle, ψ, of events determined using the Stereo_TA processing code set with calibration and atmospheric databases.

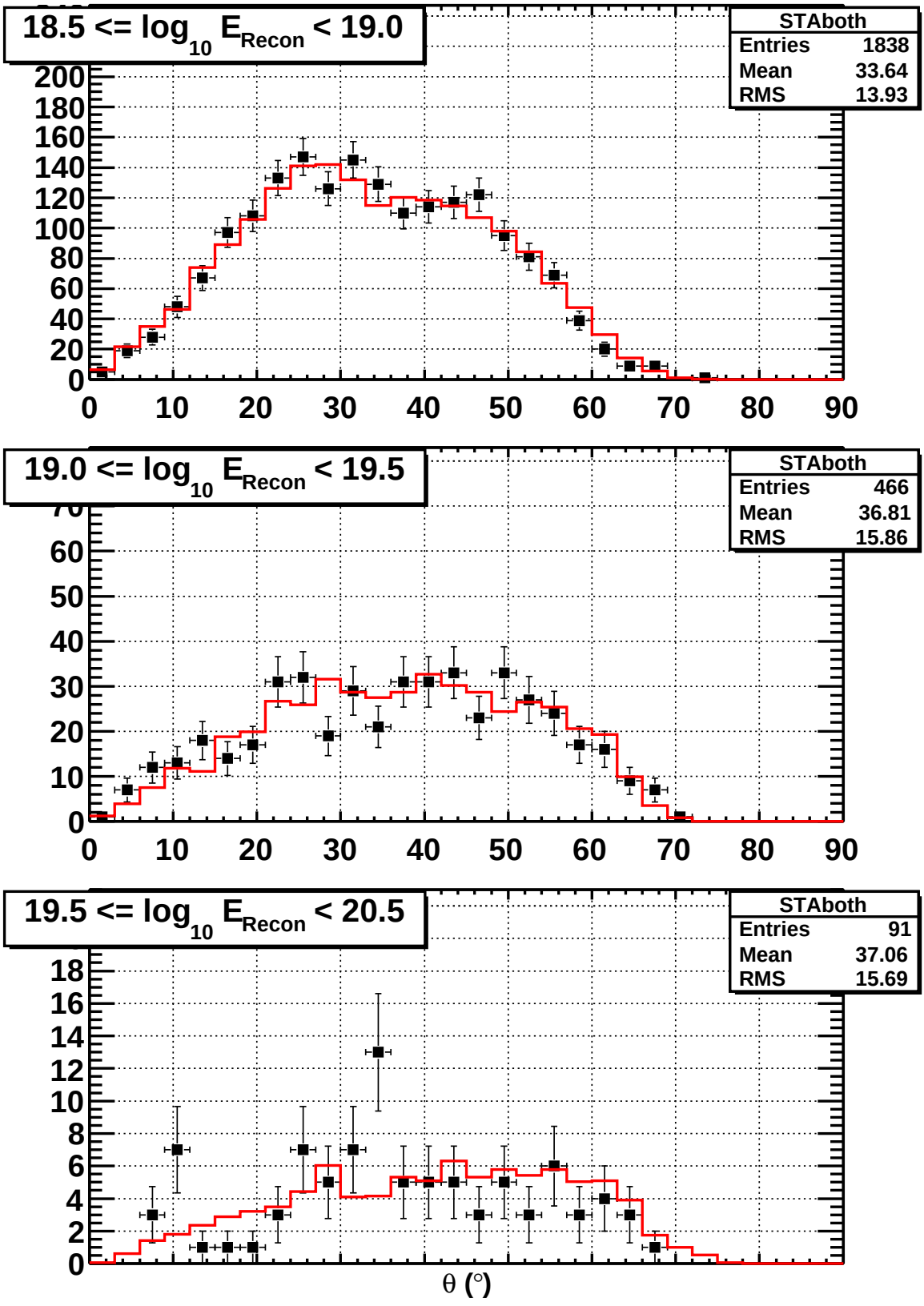

Figure D.4: Data-Monte Carlo comparisons for the zenith angle, θ, of events determined using the Stereo_TA processing code set with calibration and atmospheric databases.

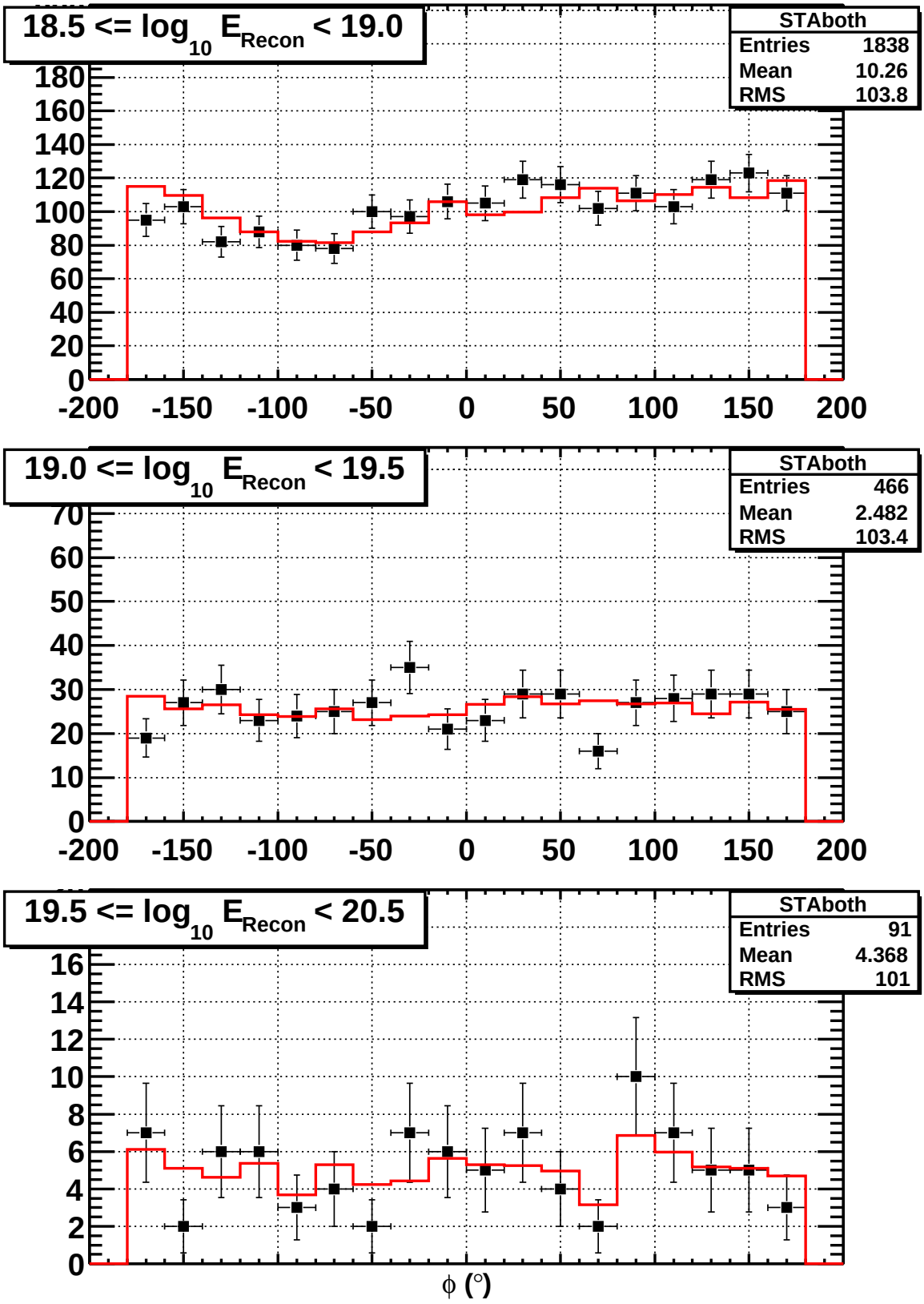

Figure D.5: Data-Monte Carlo comparisons for the azimuthal angle, ϕ, of events determined using the Stereo_TA processing code set with calibration and atmospheric databases.

APPENDIX E

TAMD PROCESSING CODE DATA-MONTE CARLO COMPARISONS

In order to justify our results, the reconstructed parameters of the Monte Carlo shower simulations must show a similarity to the data reconstructed in the same manner. Similar to resolution plots, this is done over separate energy ranges to show how the values change as energies increase: A) $10^{18.0-18.5}$ eV, B) $10^{18.5-19.0}$ eV, and C) $10^{19.0-20.5}$ eV. These figures show comparisons from the current TAMD processing results between: 1) the number of photoelectrons per degree (see Figure E.1); 2) the impact parameter, R_P (see Figure E.2); 3) the in-plane angle, ψ (see Figure E.3); 4) the zenith angle, θ (see Figure E.4); and 5) the azimuthal angle, ϕ (see Figure E.5). For all figures, the data points are represented with markers and error bars, and the Monte Carlo is given as a solid line histogram. As can be seen in the figures, there is a consistency between the data and the Monte Carlo for all of the energy ranges used in the spectrum.

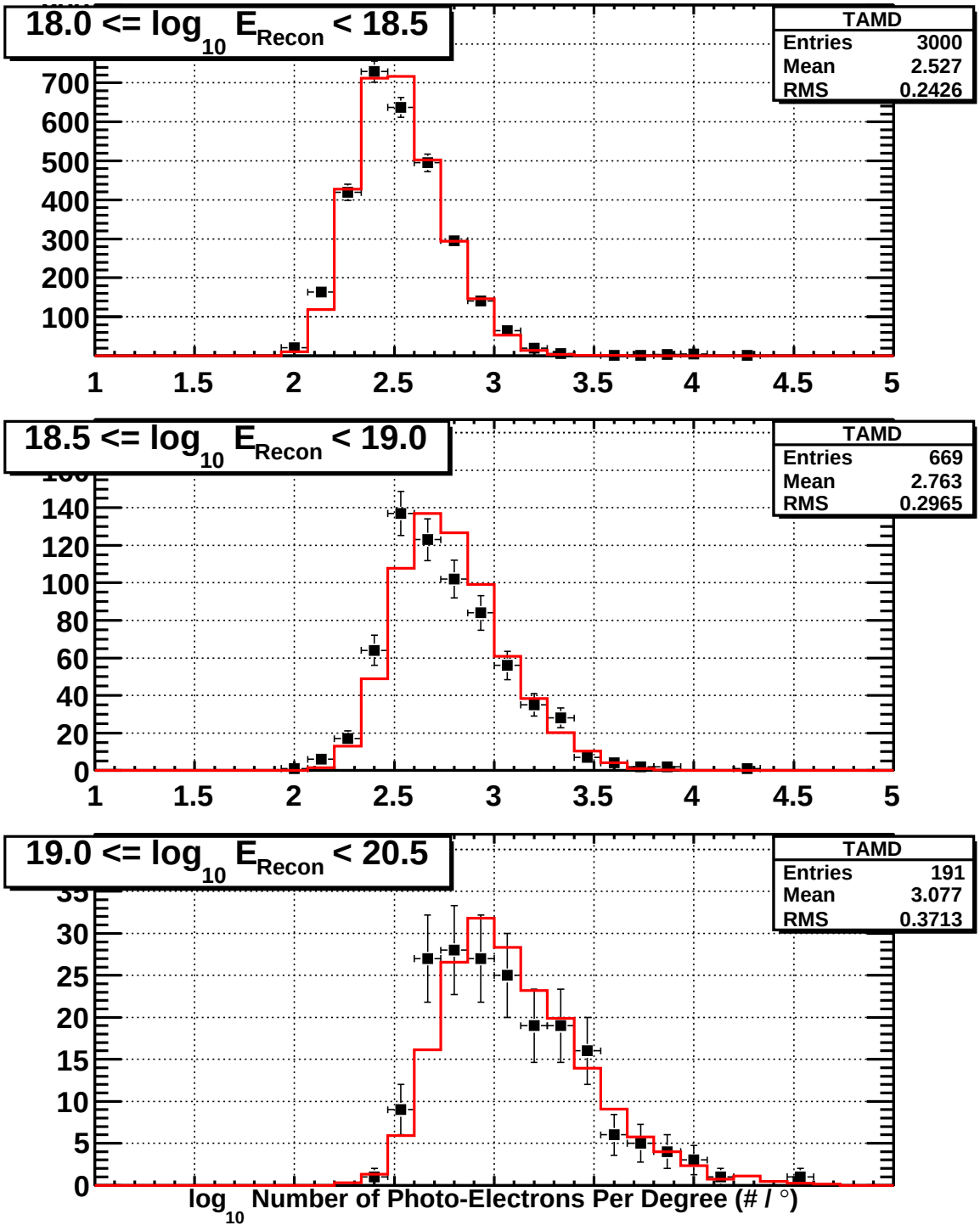

Figure E.1: Data-Monte Carlo comparisons for the number of photoelectrons per degree of events determined using the TAMD processing code set.

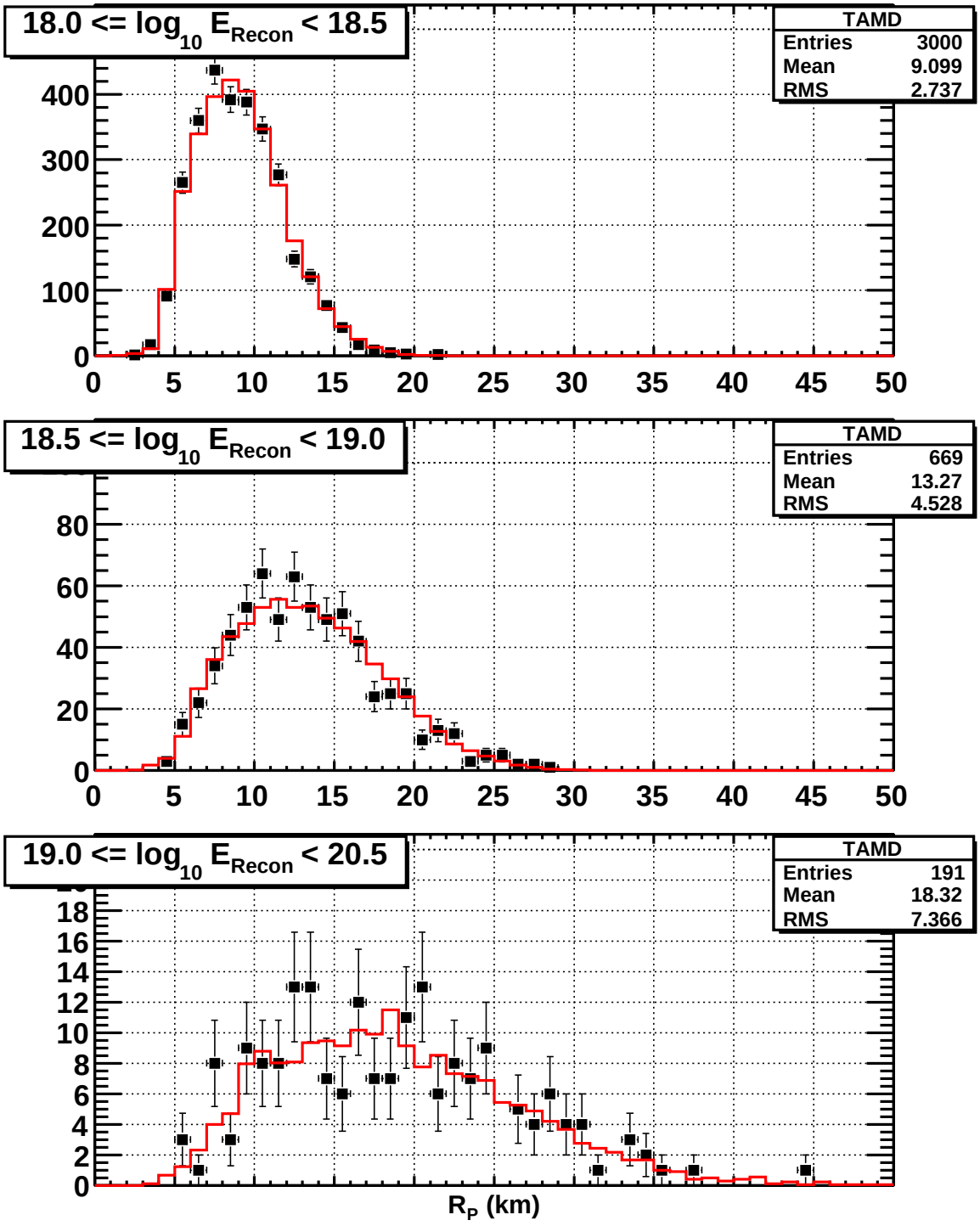

Figure E.2: Data-Monte Carlo comparisons for the impact parameter, R_P, of events determined using the TAMD processing code set.

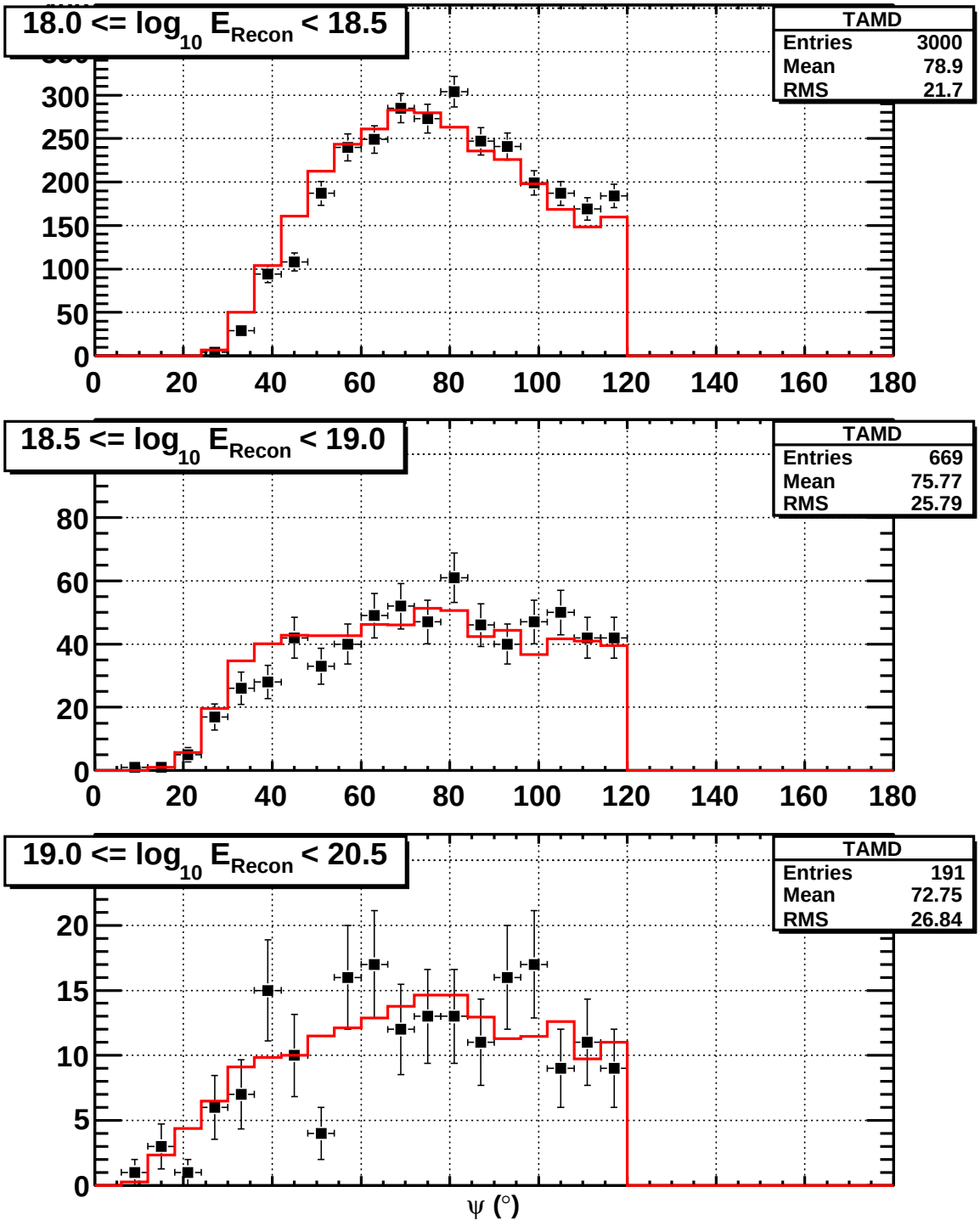

Figure E.3: Data-Monte Carlo comparisons for the in-plane angle, ψ, of events determined using the TAMD processing code set.

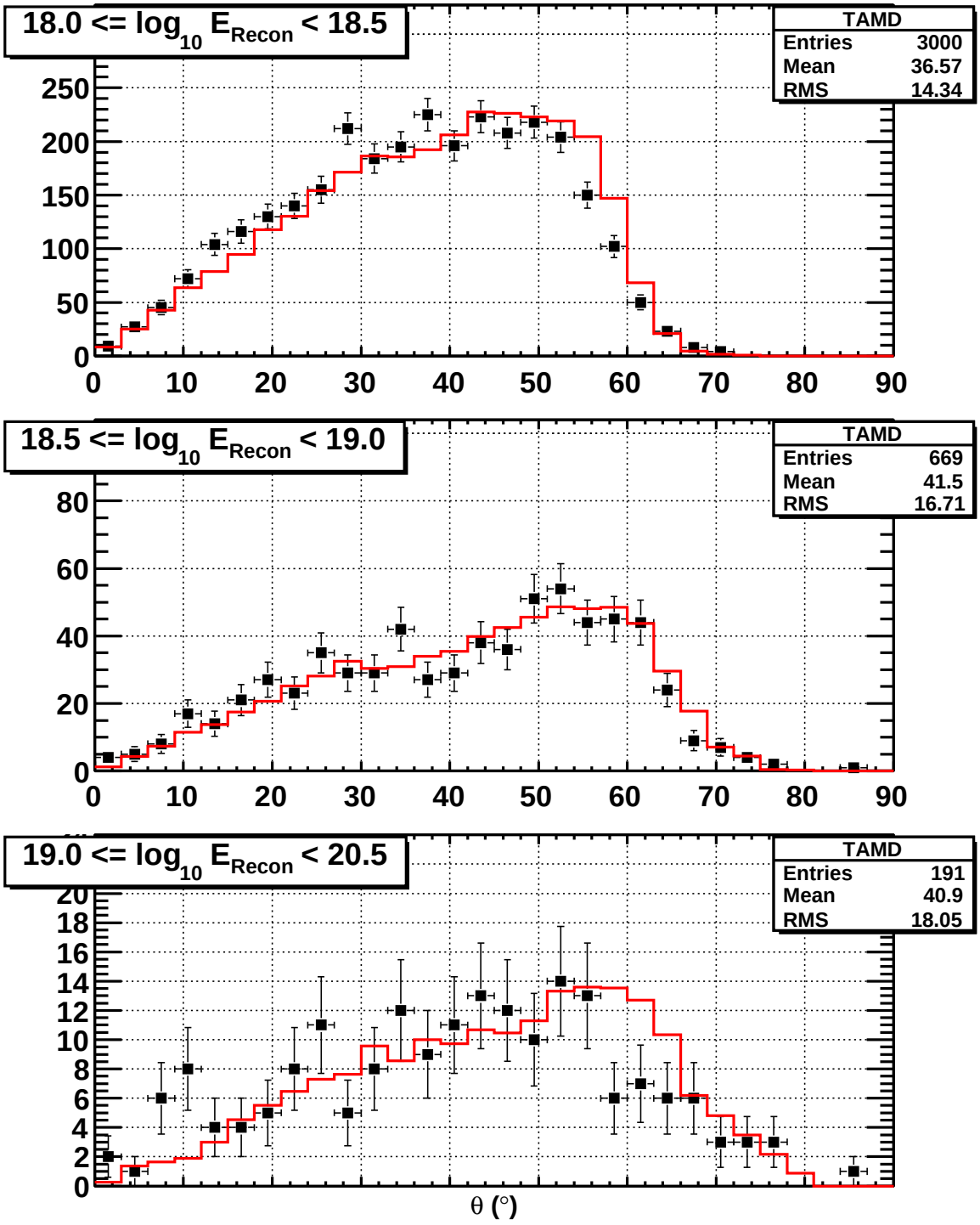

Figure E.4: Data-Monte Carlo comparisons for the zenith angle, θ, of events determined using the TAMD processing code set.

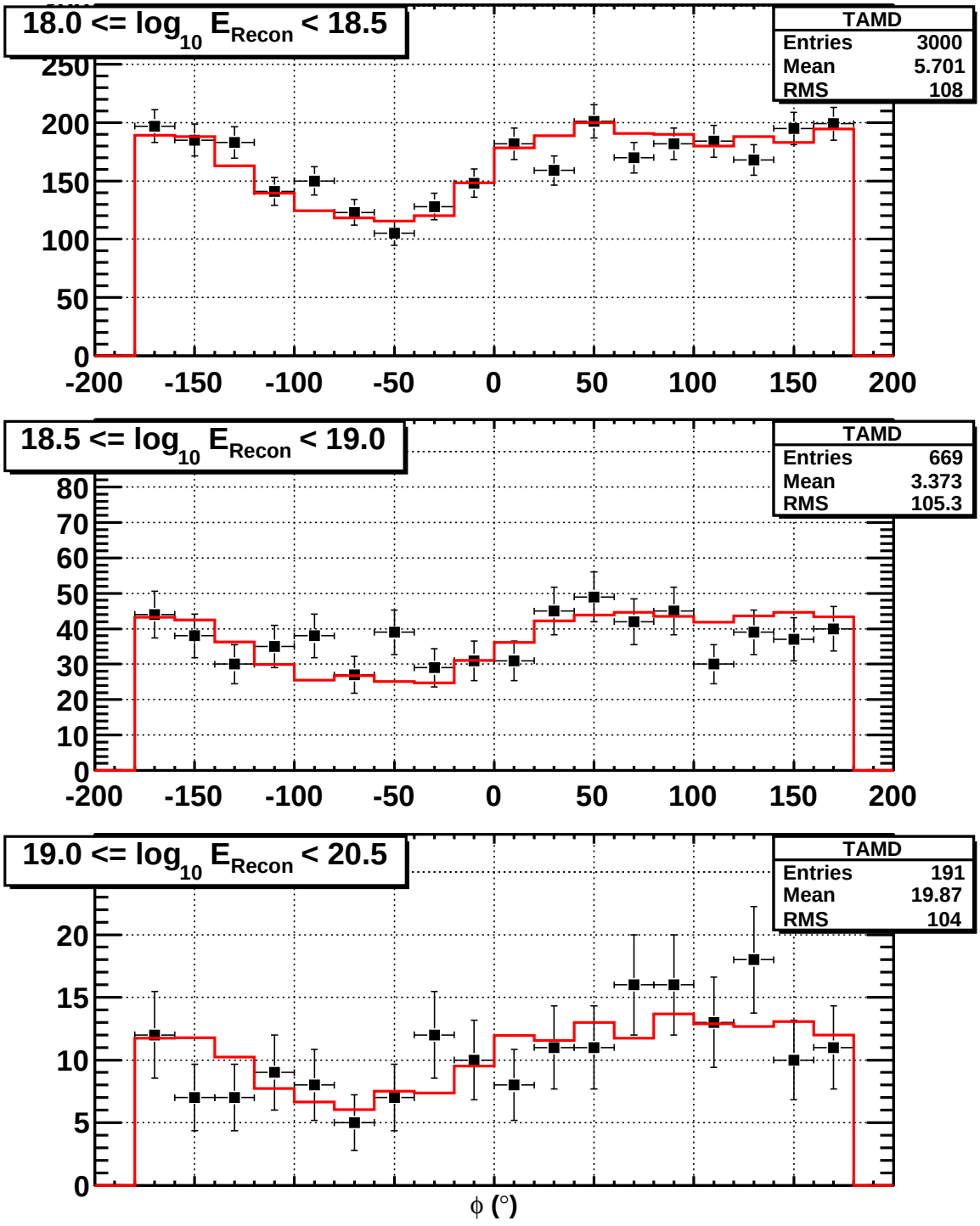

Figure E.5: Data-Monte Carlo comparisons for the azimuthal angle, ϕ, of events determined using the TAMD processing code set.

APPENDIX F

HOUGH TRANSFORM OF COINCIDENT PARALLEL SHOWERS

The process of converting the time-versus-angle (TvA) distribution of the double-shower Monte Carlo into a Hough transform and the subsequent application to the data is described in this appendix.

F.1 Double-Shower Patterns

There are also three ways double-shower Monte Carlo could be observed by the detector that affects the TvA and the corresponding Hough transform distributions. The first is a distinct double-shower pattern in the event display with the showers arriving at different times (see Figure F.1). The second pattern is where the two showers are approaching the detector in parallel and at the same time (see Figure F.2). The third pattern is where the two showers completely overlap since their perpendicular separation is very narrow (see Figure F.3). To distinguish these patterns, a series of three Hough transform calculations were performed: 1) using individual, separate cluster shower-detector planes, 2) using the shower detector plane of the first cluster for the second cluster, and 3) applying these processes to Monte Carlo events generated with only a single shower per event.

F.2 Calculating the Hough Transform Means - Individual Planes

The following process is used to calculate the mean angle of inclination, θ, and distance to the origin, d, of a time-versus-angle (TvA) distribution. First, the angle in the individual cluster's shower-detector plane, χ_i, was determined and plotted with the tube's trigger time, t_i. The clusters' TvA distribution for the Monte Carlo double-shower

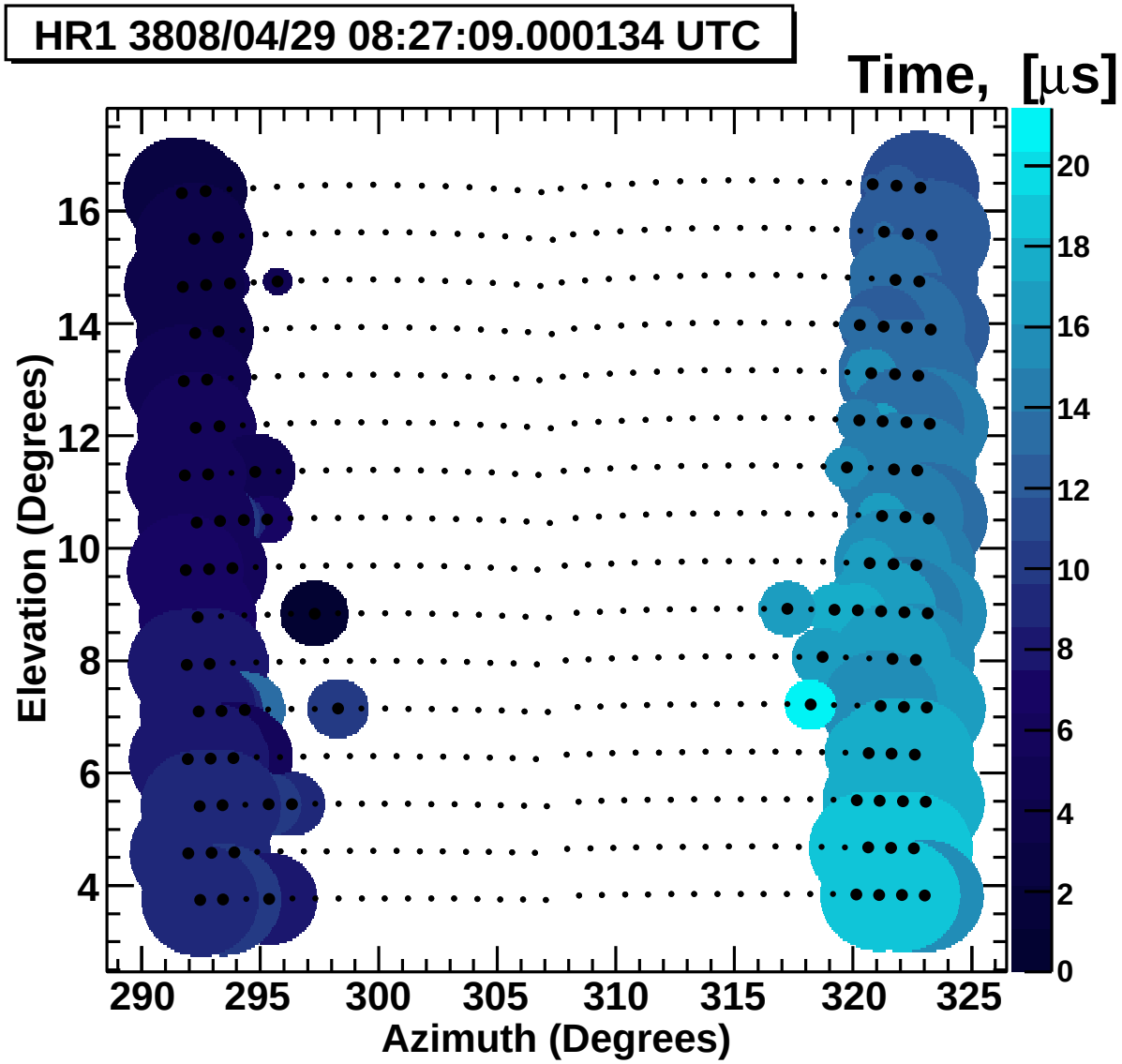

Figure F.1: A Monte Carlo double-shower event with distinct clusters as viewed by the detector arriving at different times. Time is indicated by the shade.

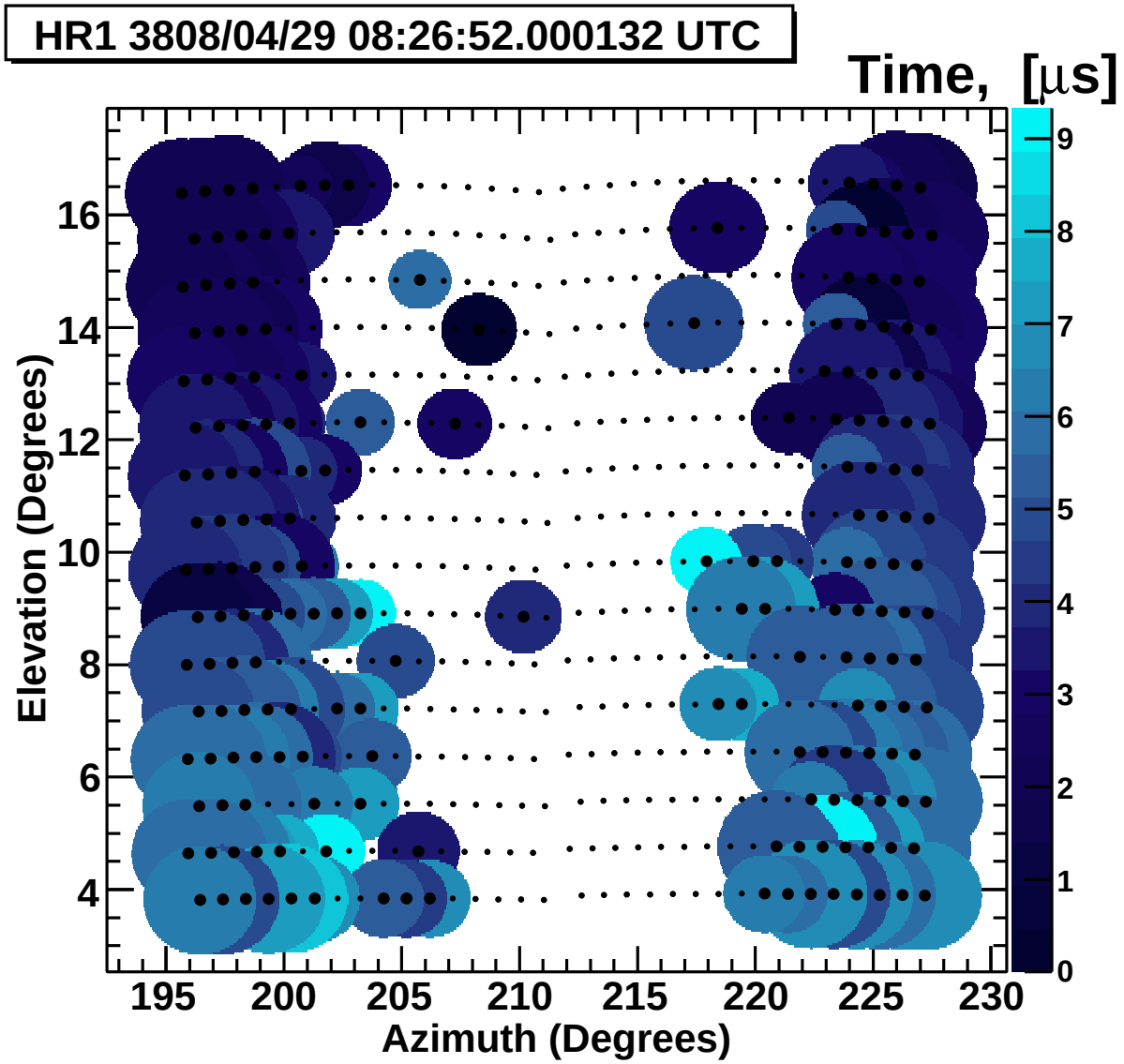

Figure F.2: A Monte Carlo double-shower event with similar time-trajectories as viewed by the detector. Time is indicated by the shade.

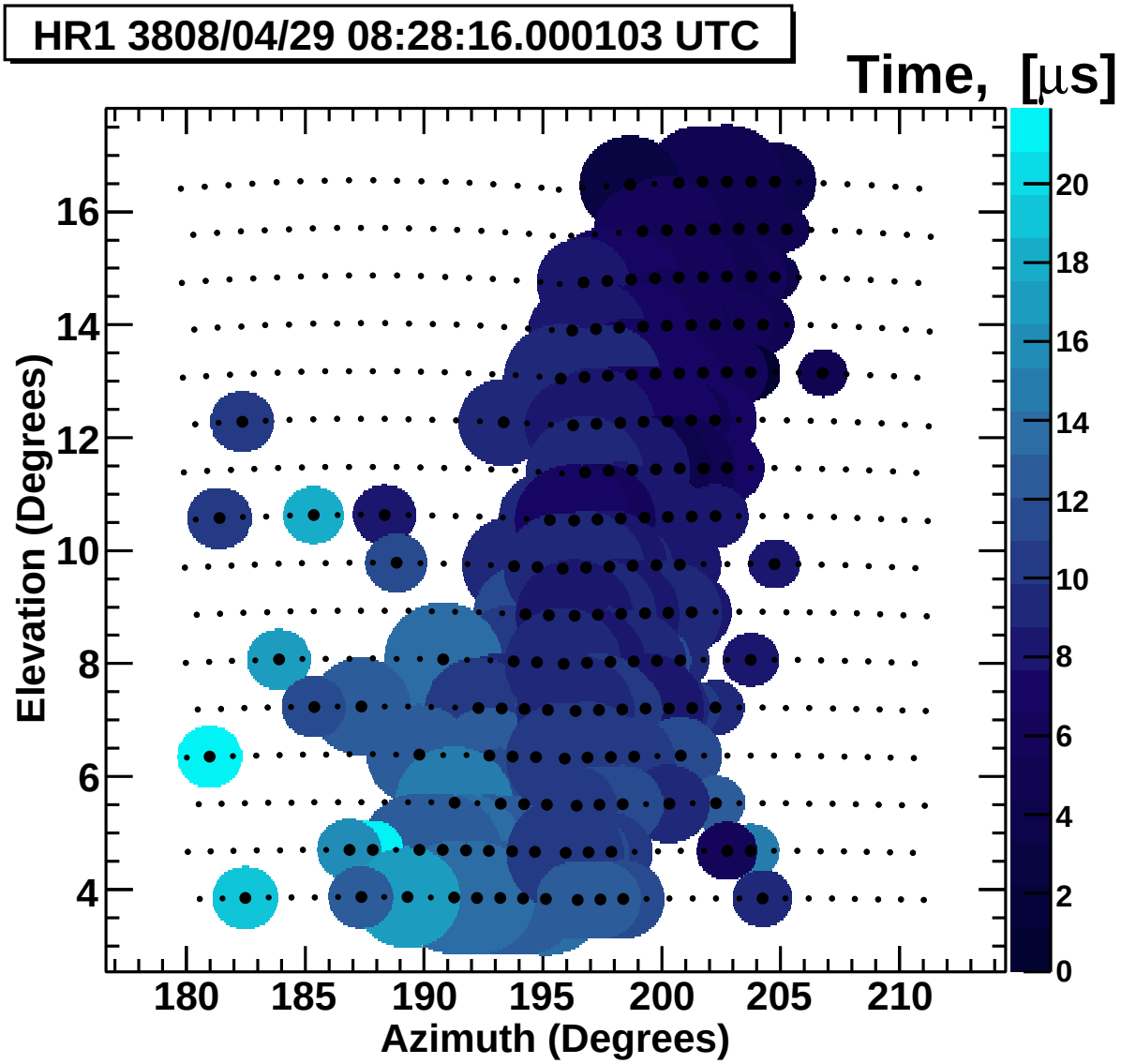

Figure F.3: A Monte Carlo double-shower event with overlapping time-trajectories as viewed by the detector. Time is indicated by the shade.

event shown in Figure F.1 is plotted in Figure F.4. For each pair of triggered tubes, the angle of inclination, θ, is calculated by the equation

$$\theta_{jk} = \tan^{-1}\left(\frac{t_j - t_k}{(\chi_j - \chi_k) \times IAS}\right) \tag{F.1}$$

where j and k are two tubes, time-ordered according to the same t_i values of the numerator (see Figure F.5). To maintain the same metric, the angle, χ_i, is converted from an angle into units of time by multiplying by the inverse angular speed, IAS, which has the units of $\mu s/degree$. The minimal perpendicular distance to the origin, r_{jk}, for each extended pair-line is calculated using

$$|r_{jk}| = |r_j| \sin(\alpha_{jk} + \beta_j) \tag{F.2}$$

where

$$\alpha_{jk} = \pi - \theta_{jk} \tag{F.3}$$

and

$$\beta_j = \tan^{-1}\left(\frac{t_j}{\chi_j \times IAS}\right) \tag{F.4}$$

with an angle of this r_{jk}-vector calculated by

$$\phi_{jk} = \frac{\pi}{2} - \alpha_{jk} \tag{F.5}$$

with the same time order taken into account.

These transformed values are then distributed in r-θ (see Figures F.6 and F.7). An initial mean and standard deviation is then determined for these inclination and distance parameters ($\overline{\theta}$, σ_θ, $\overline{r}$, and σ_r) that includes every pair-line. These mean values are then iteratively refined by determining the difference, $\vec{X}_{jk}$ between the individual r_{jk} and θ_{jk} positions and their means. They are calculated by

$$\Delta r_{jk} = r_{jk} - \overline{r} \tag{F.6}$$

and

$$\Delta\theta_{jk} = \theta_{jk} - \overline{\theta}. \tag{F.7}$$

These are then divided by the respective uncertainty to determine the r_{jk} and θ_{jk} directional vectors and combined to determine the normalized difference with the equations

$$X_{r_{jk}} = \frac{\Delta r_{jk}}{\sigma_r} \tag{F.8}$$

$$X_{\theta_{jk}} = \frac{\Delta\theta_{jk}}{\sigma_\theta} \tag{F.9}$$

and

$$|\vec{X_{jk}}| = \sqrt{X^2_{r_{jk}} + X^2_{\theta_{jk}}}. \tag{F.10}$$

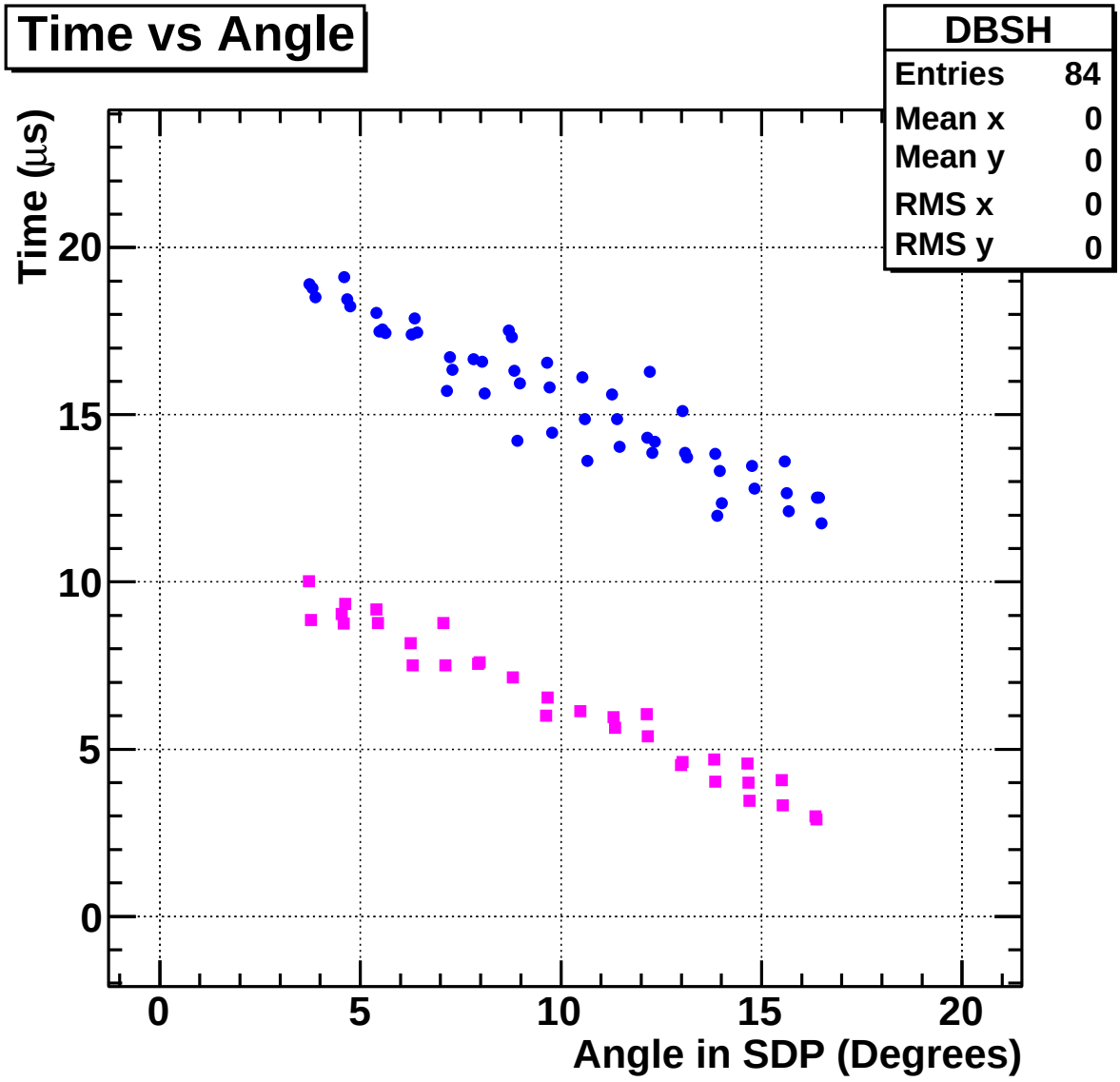

Figure F.4: The time-versus-angle distribution of the Monte Carlo double-shower event with distinct clusters from Figure F.1.

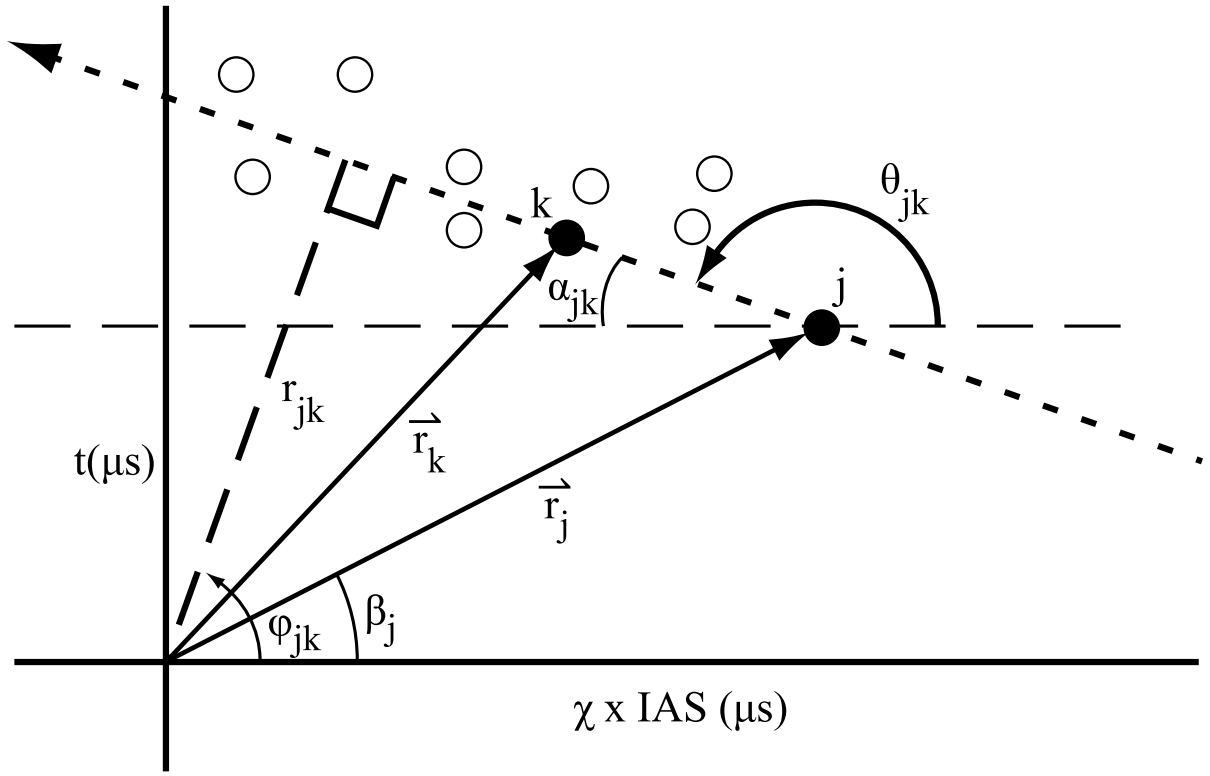

Figure F.5: This schematic shows how a pair of time-versus-angle distribution points is converted into θ and r parameters using the Hough transformation.

The mean $|\vec{X}_{jk}|$ represents a normalized RMS deviation. The distributions of each cluster for the above example is shown in Figures F.8 and F.9. As expected, almost every point is near to the mean ($|\vec{X}_{jk}| = 0$). However, as can be seen in Figures F.6 and F.7, many points can be far away from this mean due to remaining spurious noise hits, from tubes far off the shower axis, and from tubes that are occasionally assigned to the wrong cluster. To refine the mean, the spurious points are removed if $|\vec{X}_{jk}| > 2 \times \overline{|\vec{X}|}$. This process of determining the mean and standard deviation of the best-fit r_{jk} and θ_{jk} distributions and removing the distant points was repeated until no points were removed or the number of points was ≤ 15 (equivalently six tubes), as was done in the PassA program. This resulted in a refined mean and standard deviation for each cluster in the event. The refined θ_{jk}-r_{jk} distributions, with associated means and standard deviations, of the above example are shown in Figures F.10 and F.11.

F.3 Calculating the Hough Transform Means - Same Planes

As mentioned above, sometimes the two showers approach the detector in parallel and at the same time (see Figure F.2). This would cause their time-versus-angle distribution

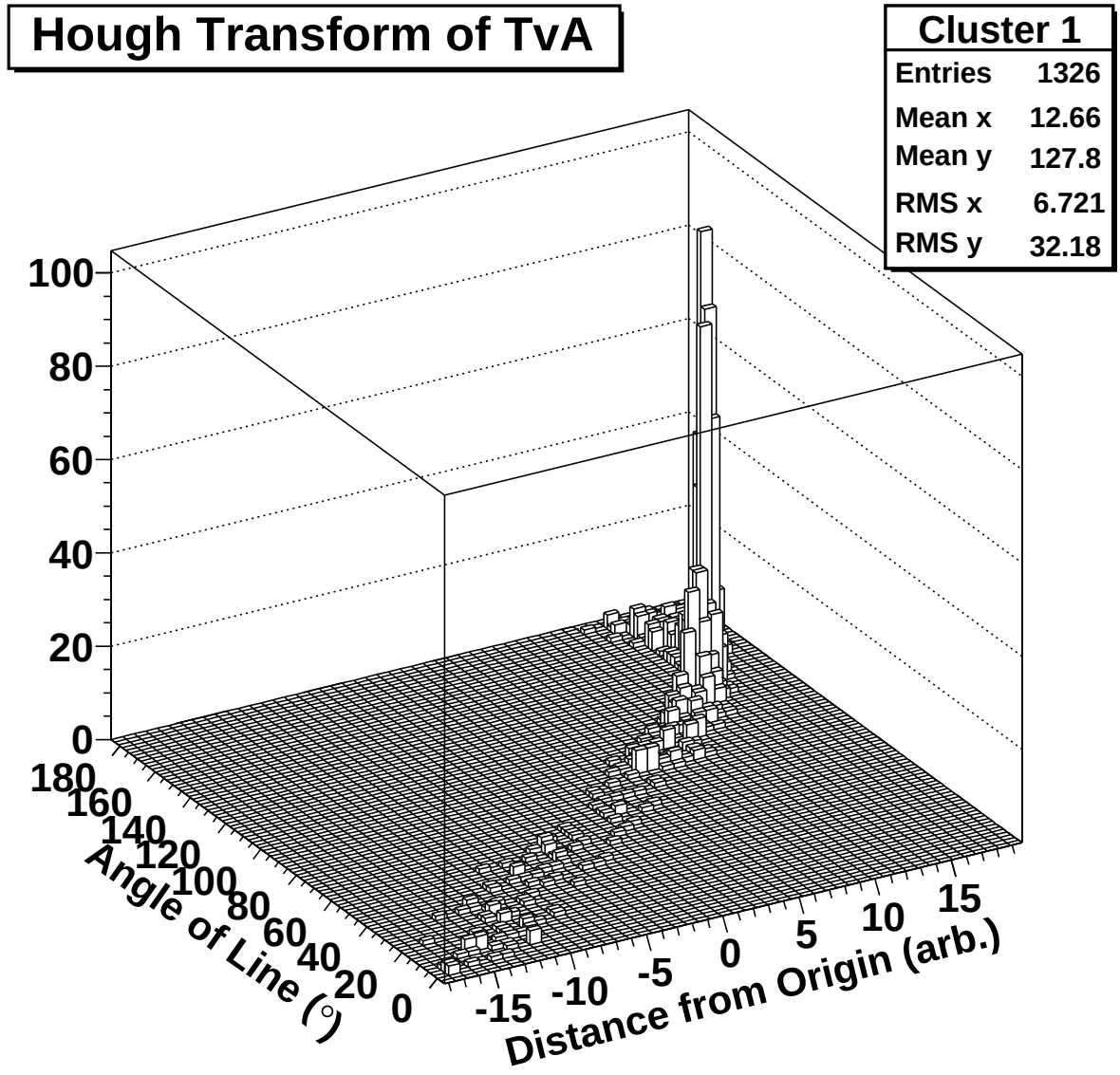

Figure F.6: The r_{jk} and θ_{jk} distribution of the first cluster (circles) of the Monte Carlo double-shower event determined from the time-versus-angle distribution of Figure F.4.

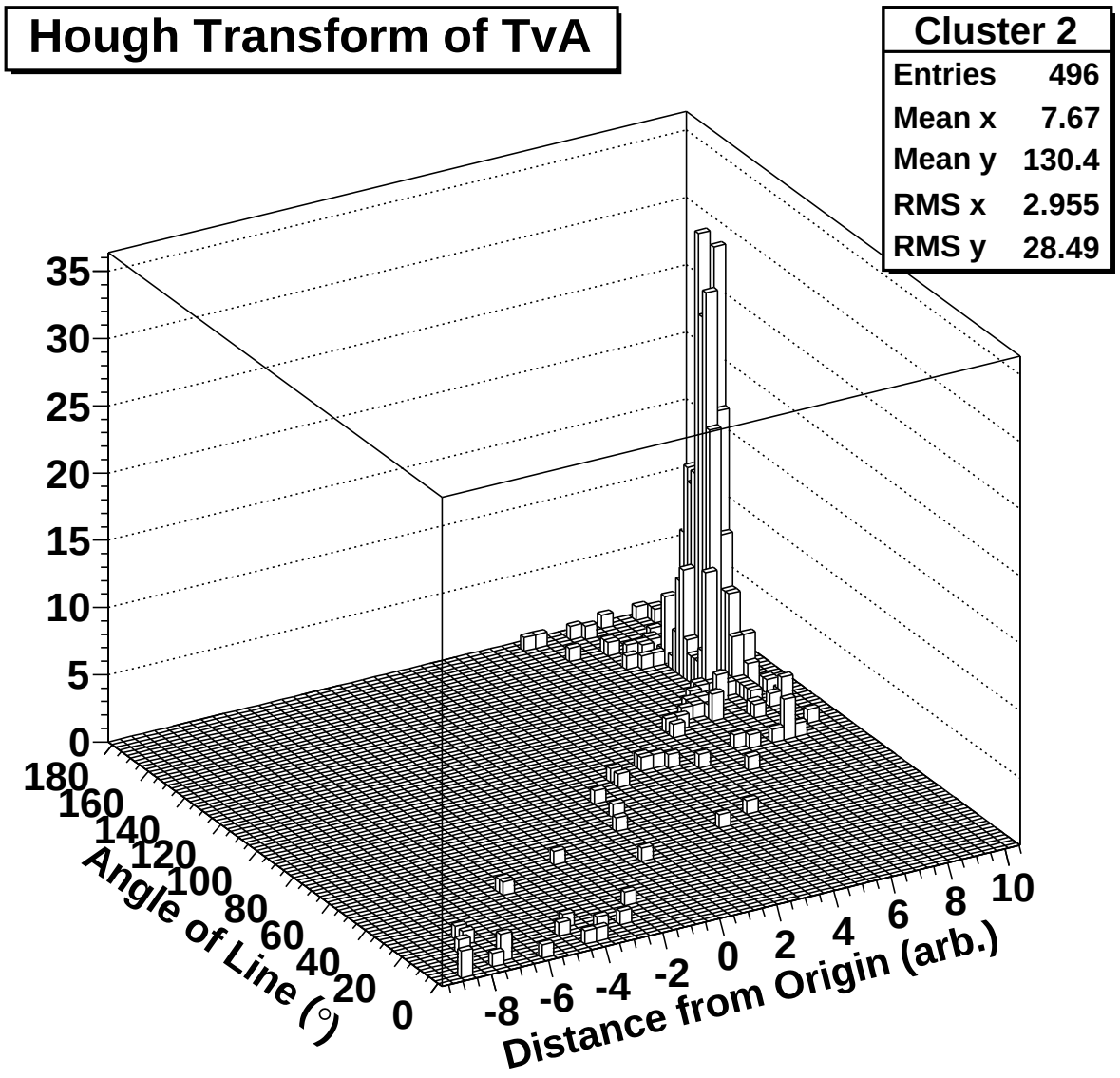

Figure F.7: The r_{jk} and θ_{jk} distribution of the second cluster (squares) of the Monte Carlo double-shower event determined from the time-versus-angle distribution of Figure F.4.

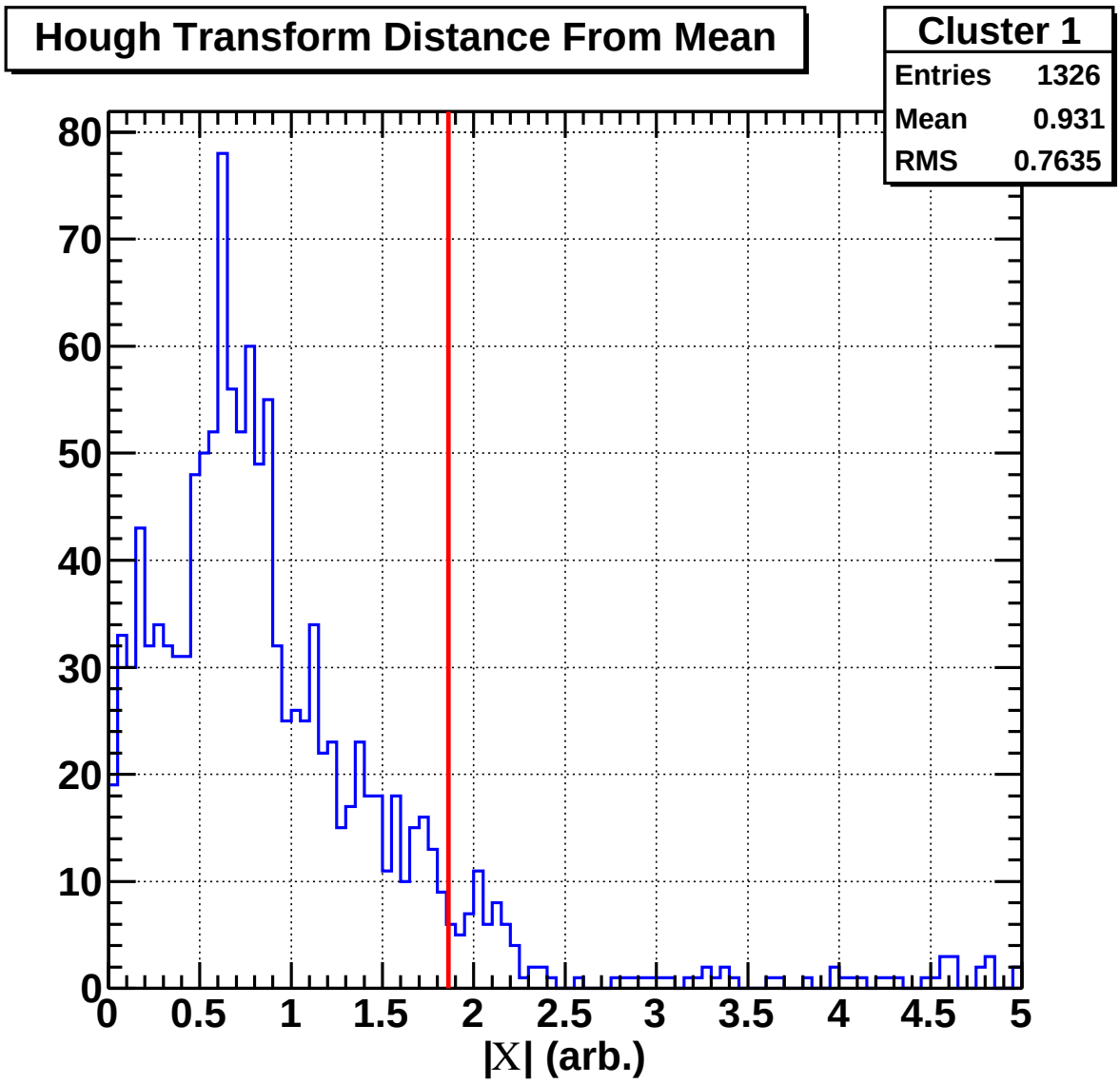

Figure F.8: The $|X_{jk}|$ distribution of the Hough transform of the first cluster of the Monte Carlo double-shower event determined from the r_{jk} and θ_{jk} distribution of Figure F.6.

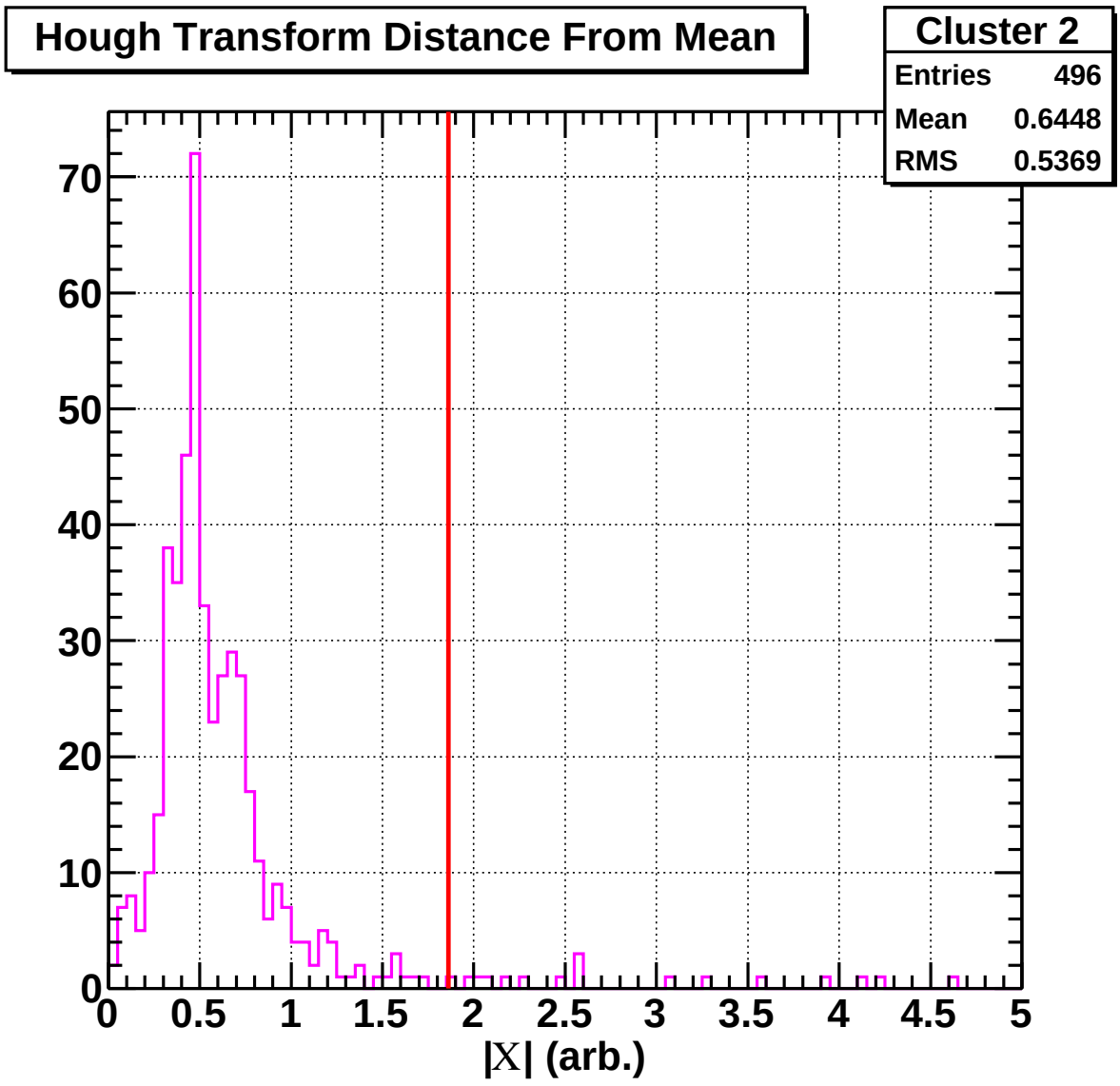

Figure F.9: The $|\vec{X_{jk}}|$ distribution of the Hough transform of the second cluster of the Monte Carlo double-shower event determined from the r_{jk} and θ_{jk} distribution of Figure F.7.

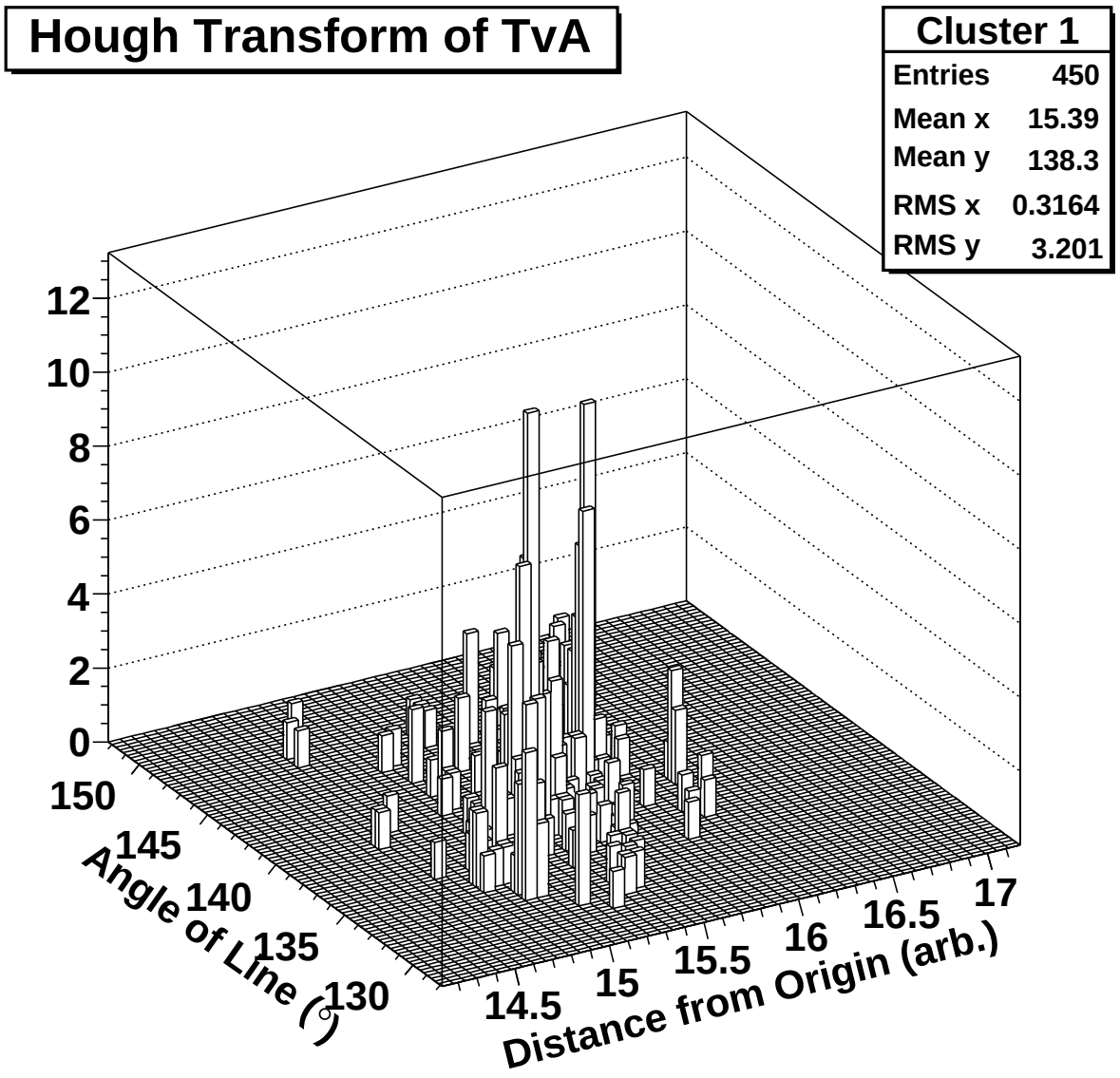

Figure F.10: The d_{jk} and θ_{jk} distribution of the first cluster (circles) of the Monte Carlo double-shower event determined from the time-versus-angle distribution of Figure F.4 after the spurious points are removed.

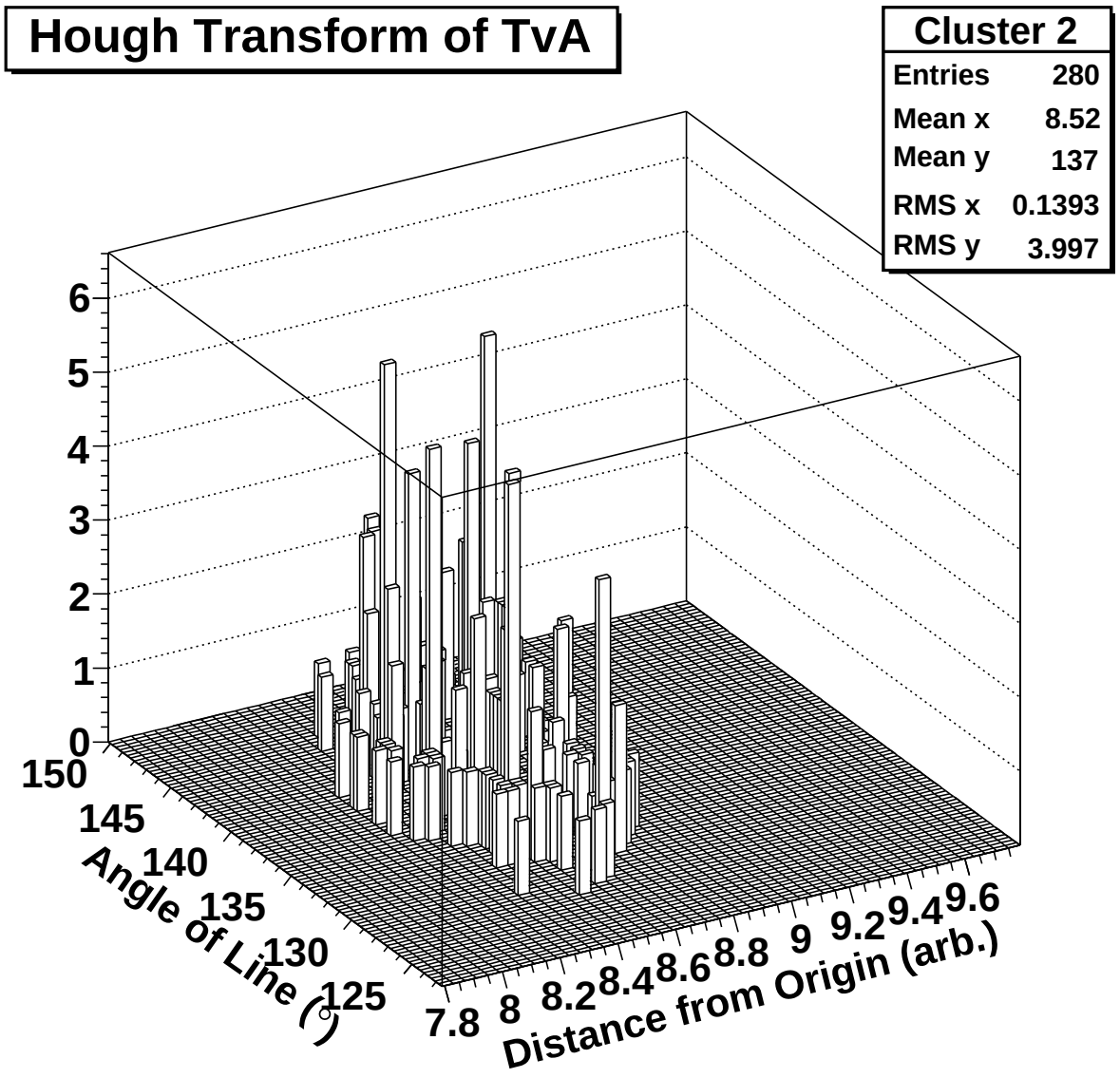

Figure F.11: The d_{jk} and θ_{jk} distribution of the second cluster (squares) of the Monte Carlo double-shower event determined from the time-versus-angle distribution of Figure F.4 after the spurious points are removed.

to overlap (see Figure F.12), even if the opening angle between the showers was wide enough to show two showers. The mean of their inclination-versus-distance distributions would also be refined to almost the exact same value (see Figures F.13 and F.14). A check was made for this by performing the same calculations for the individual-planes process but have both showers use the SDP of the first cluster. If the showers are distinct in space-time, this process would show in two ways: 1) the time-versus-angle distribution would separate (see Figure F.15), and 2) the second shower would have distinctly different means compared to using its own SDP (see Figures F.16 and F.17). The different $|X|$ values are shown in Table F.1 to show that this process can distinguish the pattern. Even though the event display shows the user that there is a distinct separation between the two clusters, this process was performed to quantify the cuts made to the data and Monte Carlo.

F.4 Double-Shower Cuts Determination

The question that must be answered is: what is the limit in order to distinguish the two showers? If the two showers overlap in their trajectories (e.g., two equal-energy photons from a 10^{20} eV π^0 decay with a perpendicular spread of 30 meters), it becomes difficult to distinguish these showers in the event display (see Figure F.3). The clusters' time-versus-angle distribution and their Hough transforms of this example can be seen in Figures F.18, F.19, and F.20.

To resolve these double showers, a test was made on the likelihood of Monte Carlo events that were thrown as single-shower events to be retained as double showers. A number of events comparable to the double-shower Monte Carlo was chosen from the Monte Carlo used for the HiRes-1 spectral studies performed for this dissertation: 530,000 of the $10^{17.5-18.65}$ eV energy range, and 50,000 of the $10^{18.65-21.0}$ eV energy range. These were processed in all of the same ways as the double-shower Monte Carlo events (e.g., PassA_dbsh, DBSH, PassB_dbsh, and the same analysis cuts and time-versus-angle comparisons). Since there is uniquely one shower per event, the detection of two clusters quantified the cuts to be applied on both the data and the double-shower Monte Carlo.

Using the single-shower Monte Carlo events that resulted in the calculation of two clusters, cuts were able to be made by comparing the difference between the different uses of shower-detector planes (SDPs). These comparison were made using equations F.8, F.9, and F.10, but with the cluster's mean $\overline{r}$ and $\overline{\theta}$ values instead of the individual r_{jk} and θ_{jk} points and

$$\sigma_{r_{mn}} = \sqrt{\sigma_{r_m}^2 + \sigma_{r_n}^2} \tag{F.11}$$

and

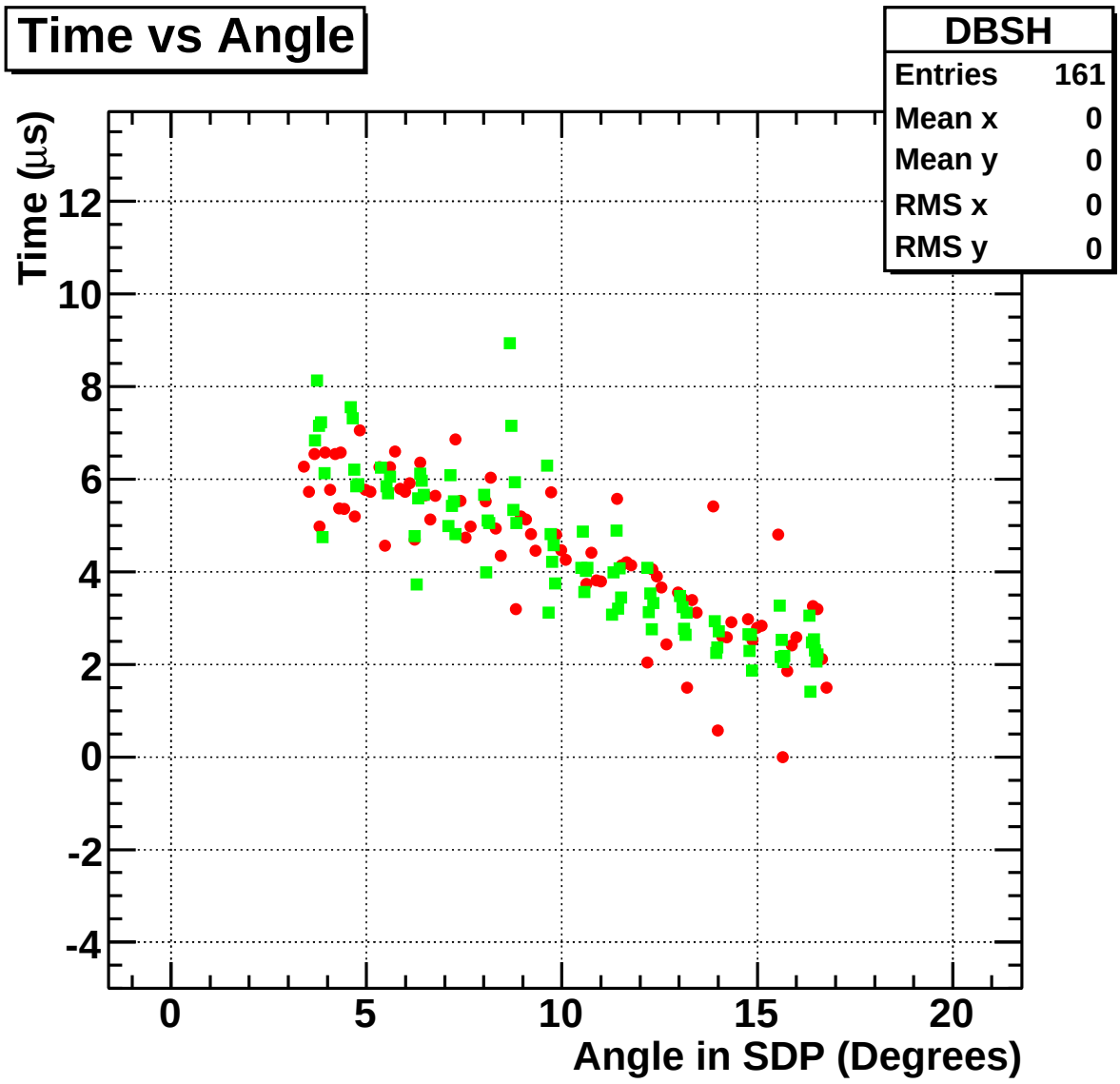

Figure F.12: The time-versus-angle distribution of the Monte Carlo double-shower event with similar time-trajectories from Figure F.2 using individual shower-detector planes and after the spurious points are removed.

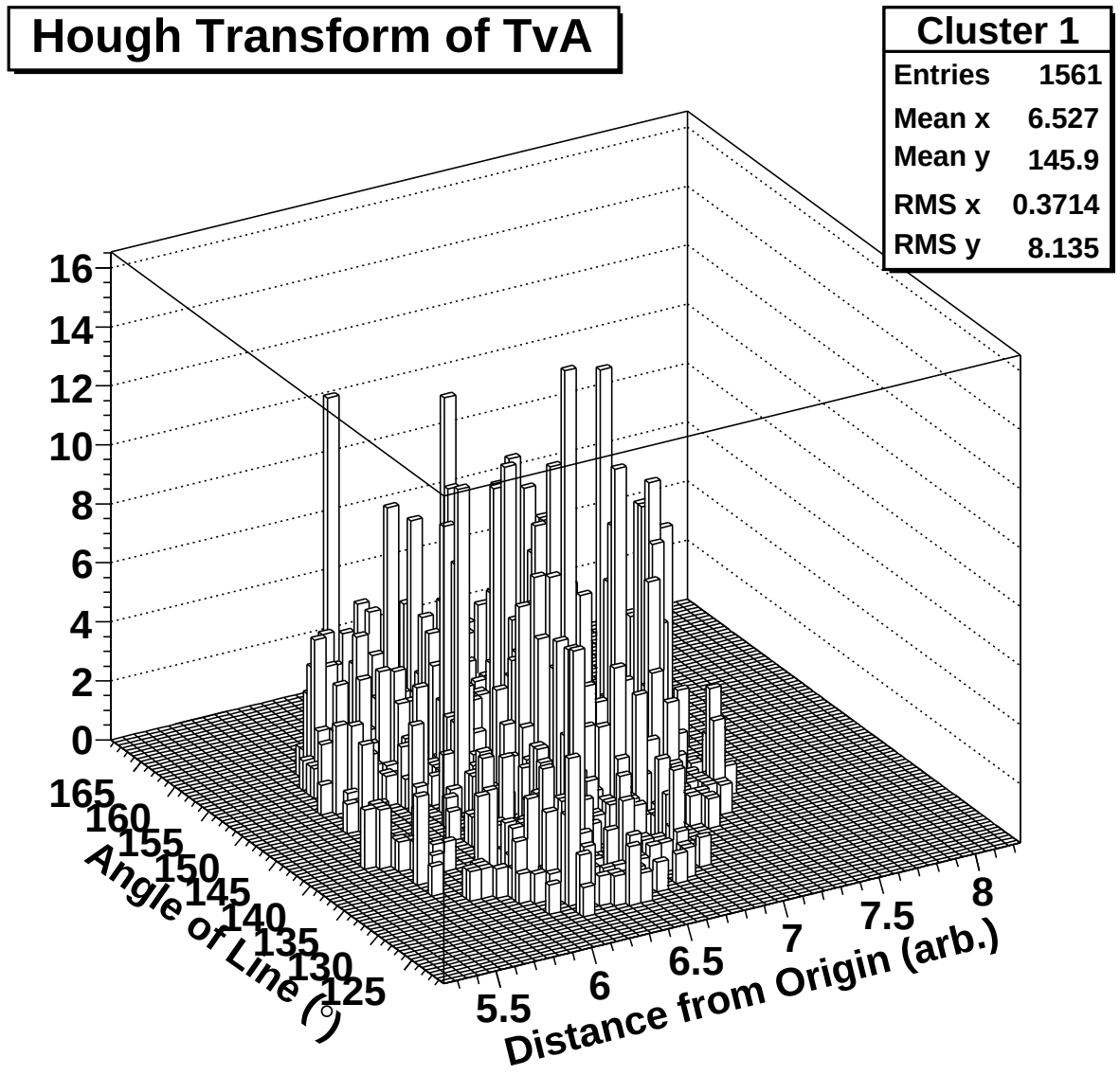

Figure F.13: The d_{jk} and θ_{jk} distribution of the first cluster (circles) of the Monte Carlo double-shower event determined from the time-versus-angle distribution of Figure F.12 after the spurious points are removed.

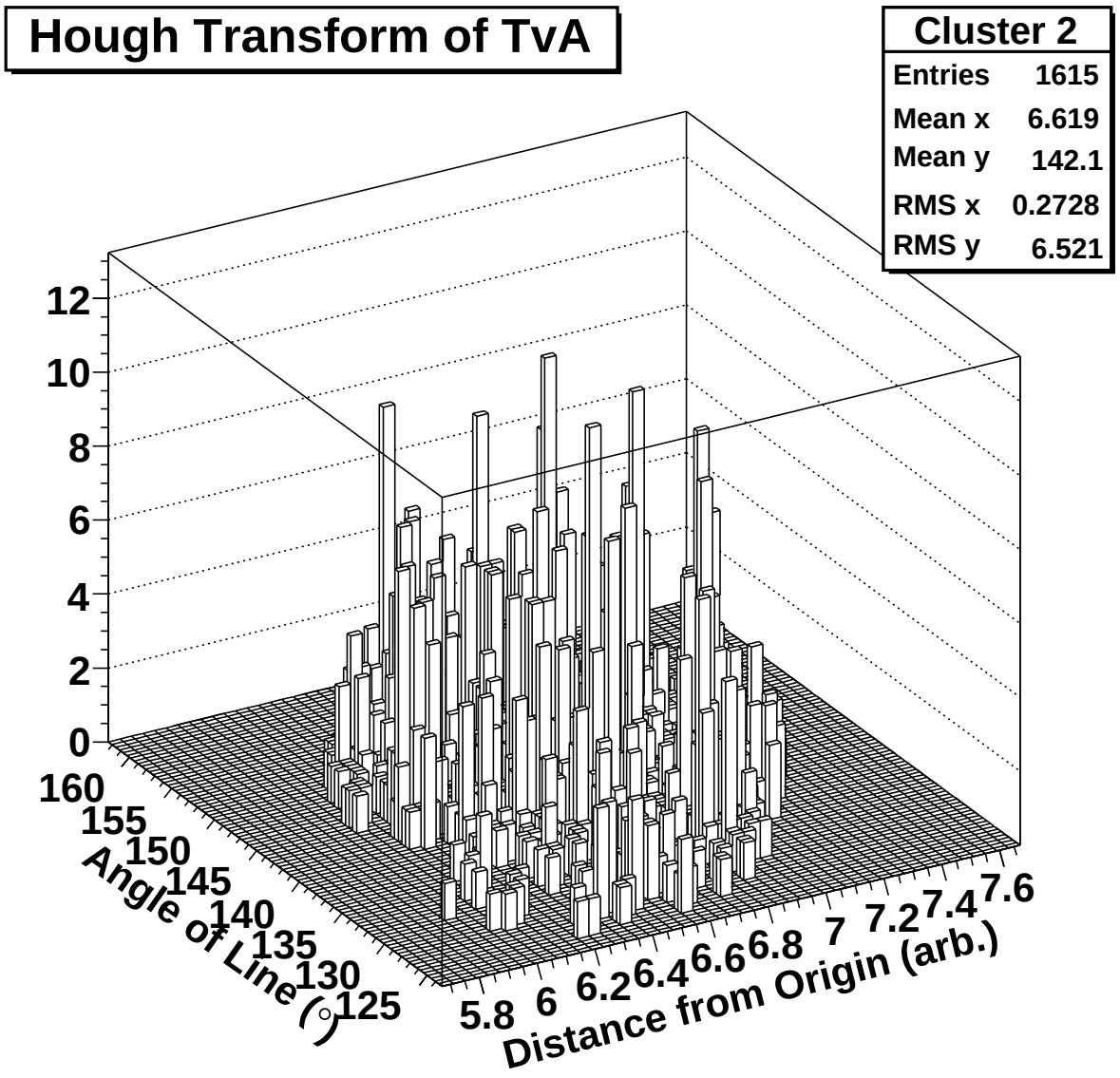

Figure F.14: The d_{jk} and θ_{jk} distribution of the second cluster (squares) of the Monte Carlo double-shower event determined from the time-versus-angle distribution of Figure F.12 after the spurious points are removed.

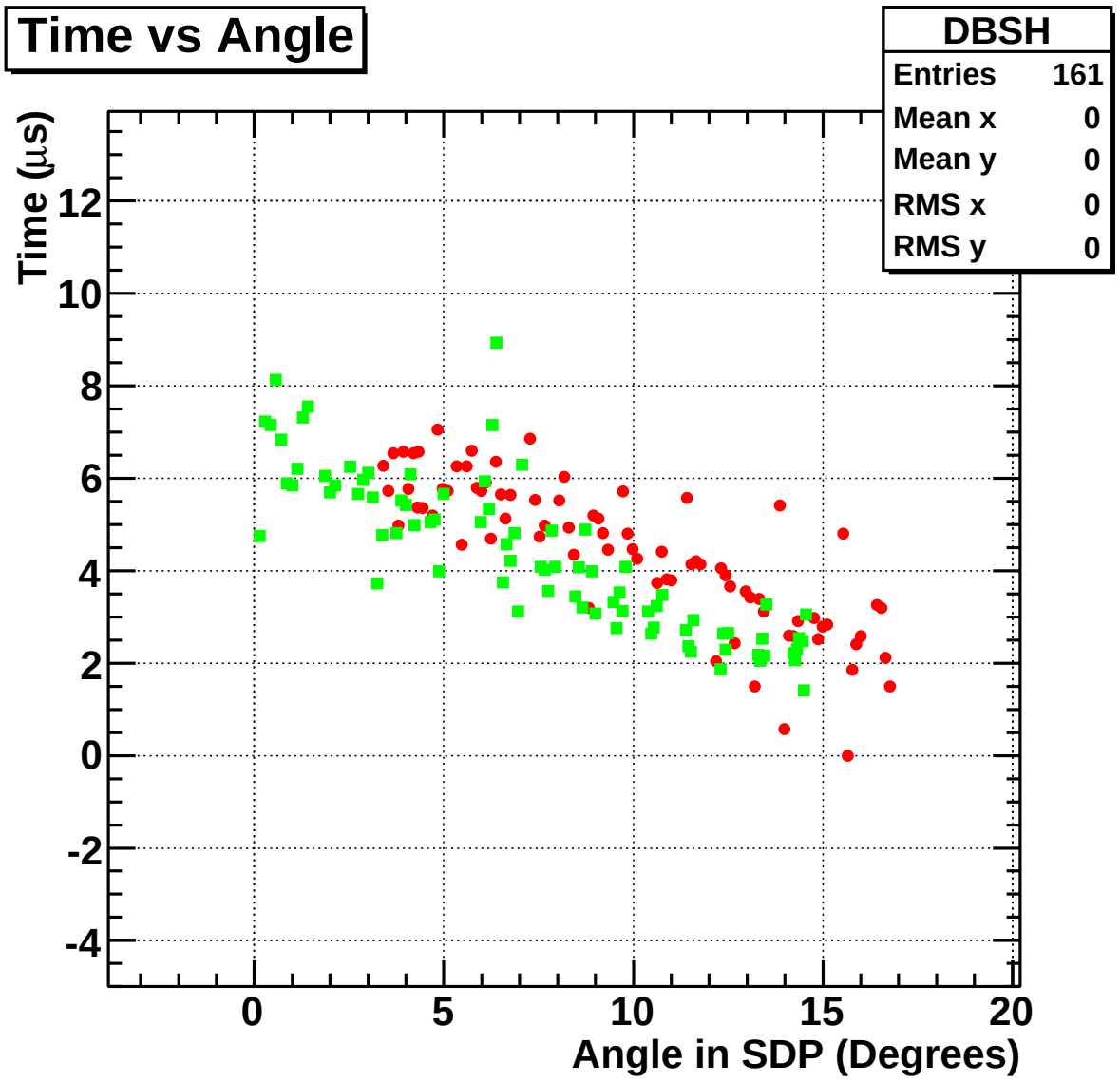

Figure F.15: The time-versus-angle distribution of the Monte Carlo double-shower event with similar time-trajectories from Figure F.2 with both showers using the shower-detector plane determined for the first shower.

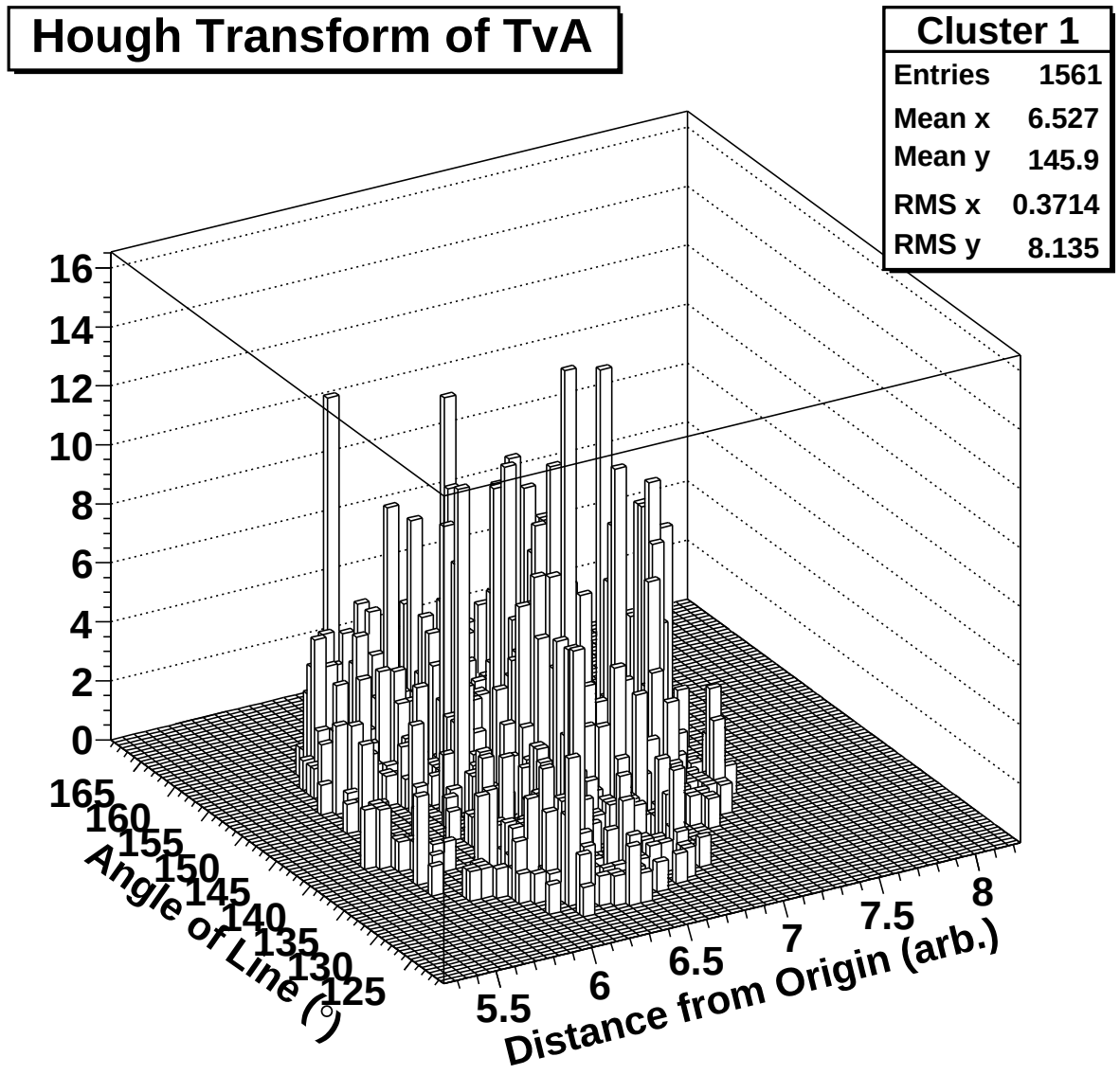

Figure F.16: The d_{jk} and θ_{jk} distribution of the first cluster (circles) of the Monte Carlo double-shower event determined from the time-versus-angle distribution of Figure F.15 after the spurious points are removed.

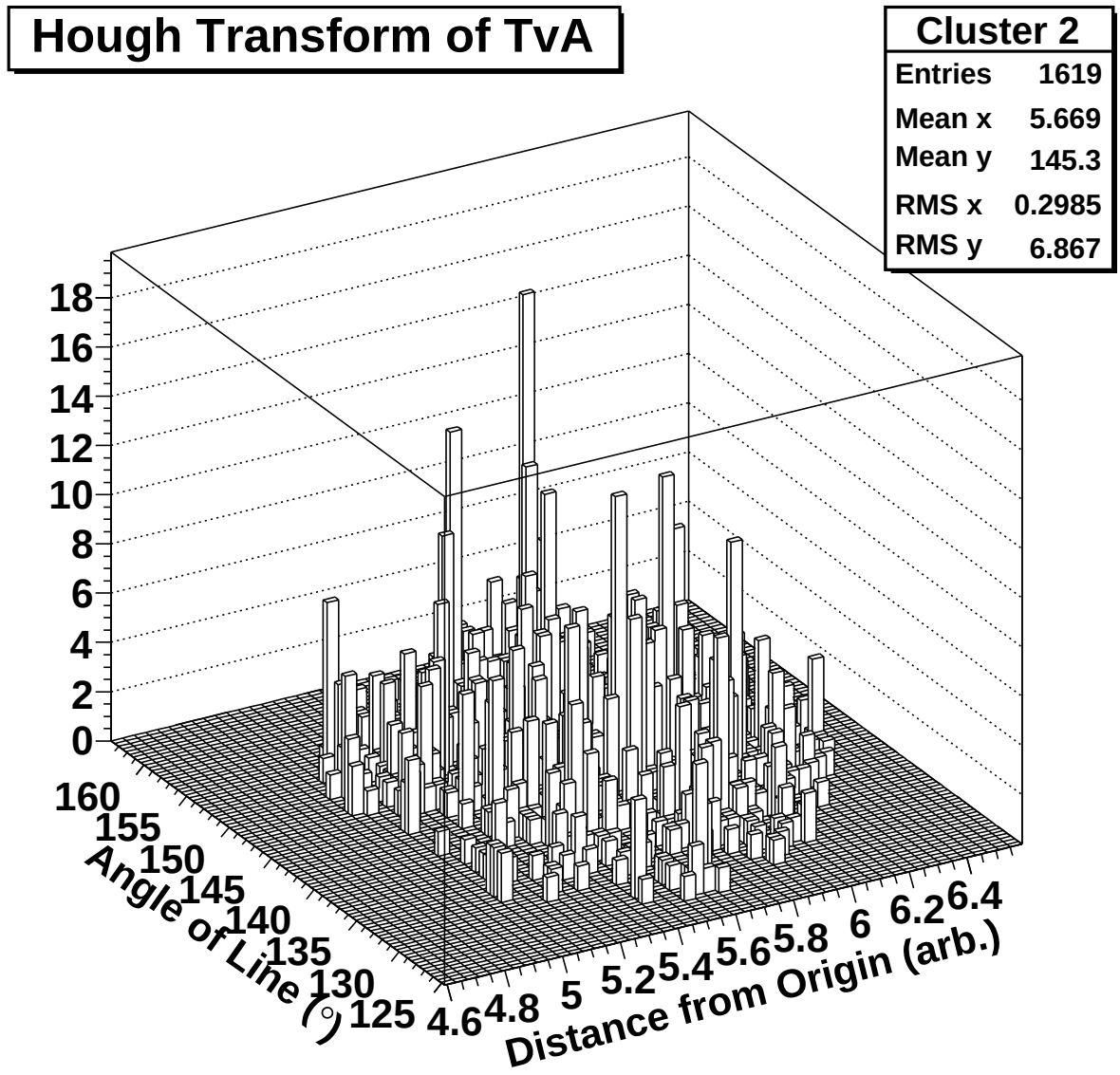

Figure F.17: The d_{jk} and θ_{jk} distribution of the second cluster (squares) of the Monte Carlo double-shower event determined from the time-versus-angle distribution of figure F.15 after the spurious points are removed. Note the mean x value shifts from 6.63 ± 0.28 of Figure F.17 to 5.67 ± 0.31, 2.5σ away.

Table F.1: These are the $|X|$ values obtained for the Monte Carlo event that is distinctive in the event display but similar in time-versus-angle distributions of figure F.2. Note that the means of the second cluster are different by 2.5σ depending upon which shower-detector plane is used.

Cluster	SDP	$\overline{r}$	$\overline{\theta}$
1	Separate	6.63 ± 0.28	146.1 ± 5.2
2	Separate	6.63 ± 0.28	142.3 ± 6.3
1	Same	6.63 ± 0.28	146.1 ± 5.2
2	Same	5.67 ± 0.31	145.3 ± 6.8

$$\sigma_{\theta_{mn}} = \sqrt{\sigma_{\theta_m}^2 + \sigma_{\theta_n}^2} \tag{F.12}$$

as the uncertainty in the respective r and θ axes for the different clusters, m and n. Three comparisons were made in order to do this: 1) calculating the difference of the separate clusters using the separate SDPs; 2) calculating the difference of the separate clusters using the same SDP; and 3) calculating the difference of the second cluster using separate SDPs compared to the same SDP.

A direct comparison was made between double-shower Monte Carlo and the single-shower Monte Carlo. Figure F.21 shows the difference between cluster 1 and cluster 2 using the individual, separate SDPs. Figure F.22 shows the same comparisons between cluster means, but using the same SDP for both clusters. Neither of these plots shows a significant difference between the two distributions and cannot be used for discriminating between double and single showers. In contrast, Figure F.23 shows two very different distributions to the mean deviation for cluster 2 if cross-SDP values are compared. Those events with a $|X| < 2.00$ were considered to be too close to distinguish a shift and were removed.

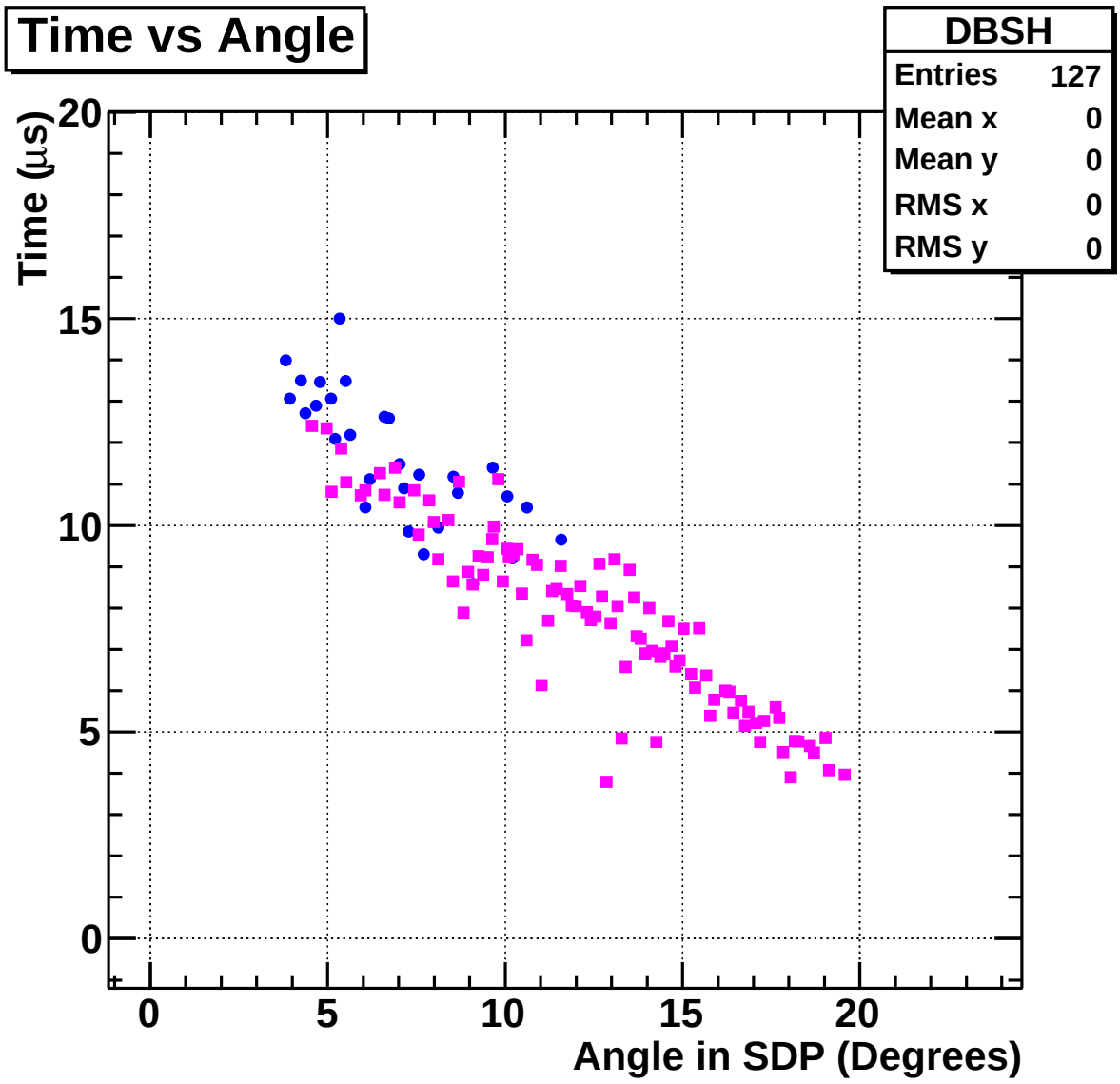

Figure F.18: The time-versus-angle distribution of the Monte Carlo double-shower event with overlapping time-trajectories from Figure F.3 using individual shower-detector planes.

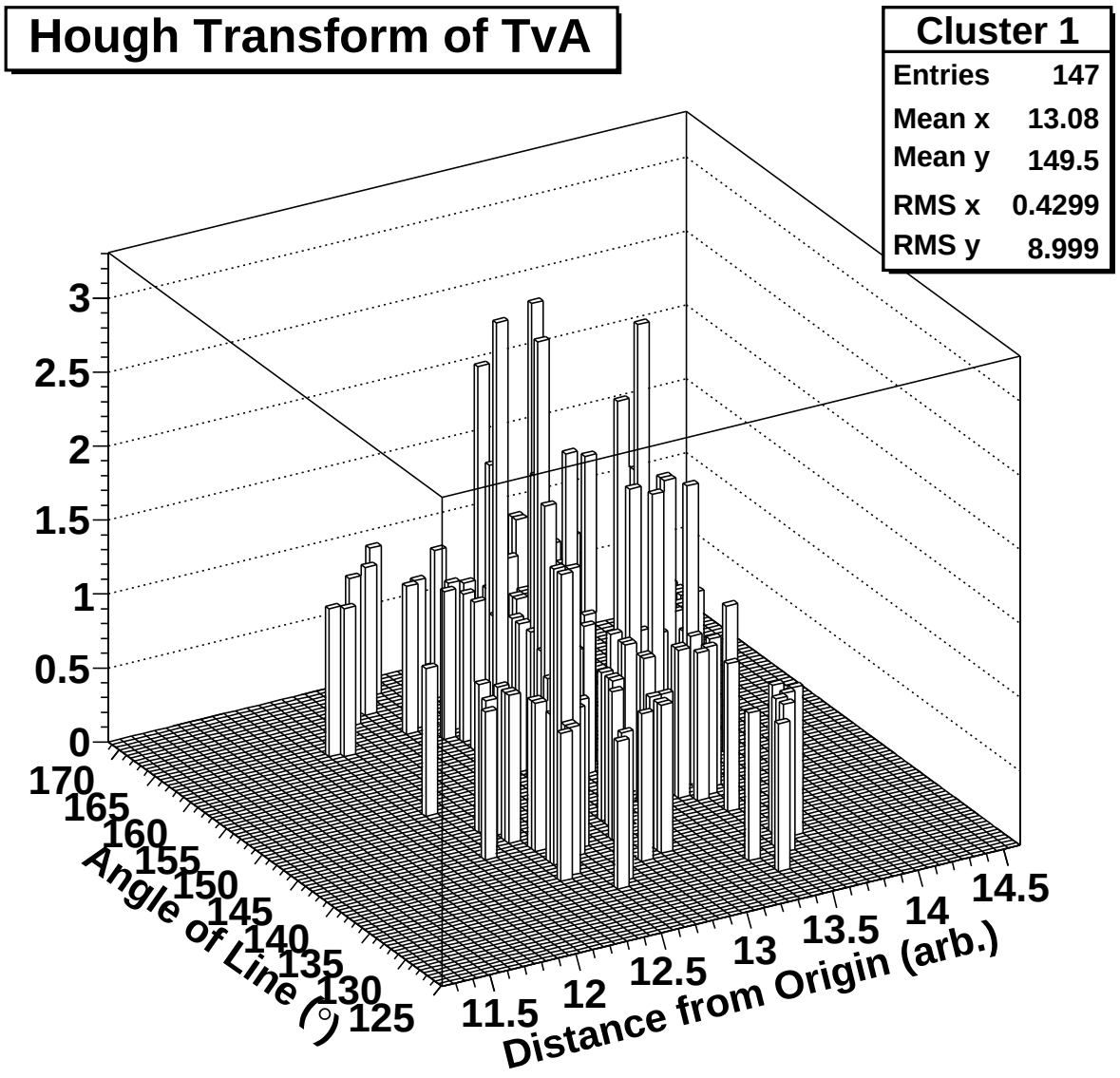

Figure F.19: The d_{jk} and θ_{jk} distribution of the first cluster (circles) of the Monte Carlo double-shower event determined from the time-versus-angle distribution of Figure F.18 after the spurious points are removed.

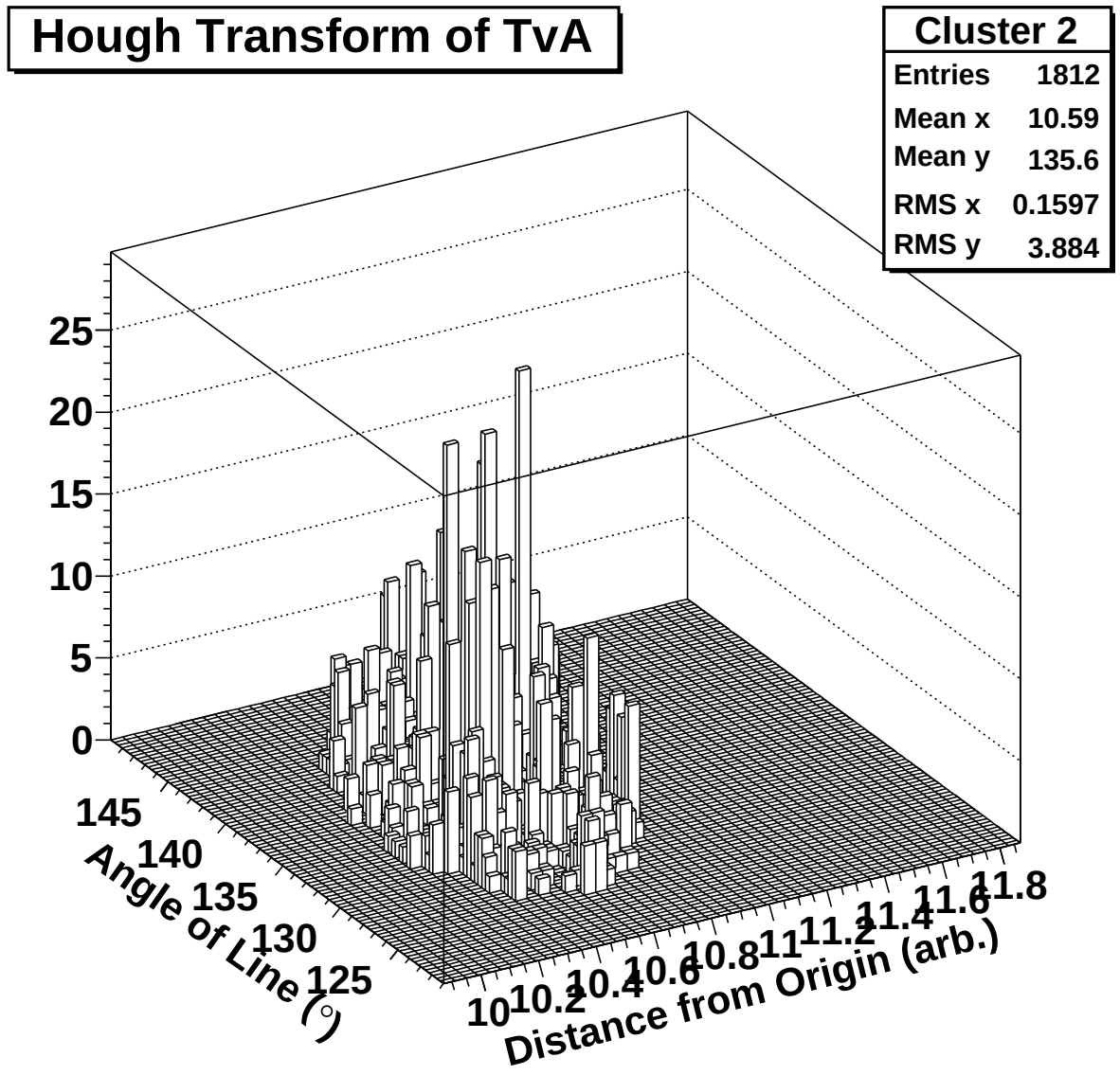

Figure F.20: The d_{jk} and θ_{jk} distribution of the second cluster (squares) of the Monte Carlo double-shower event determined from the time-versus-angle distribution of Figure F.18 after the spurious points are removed.

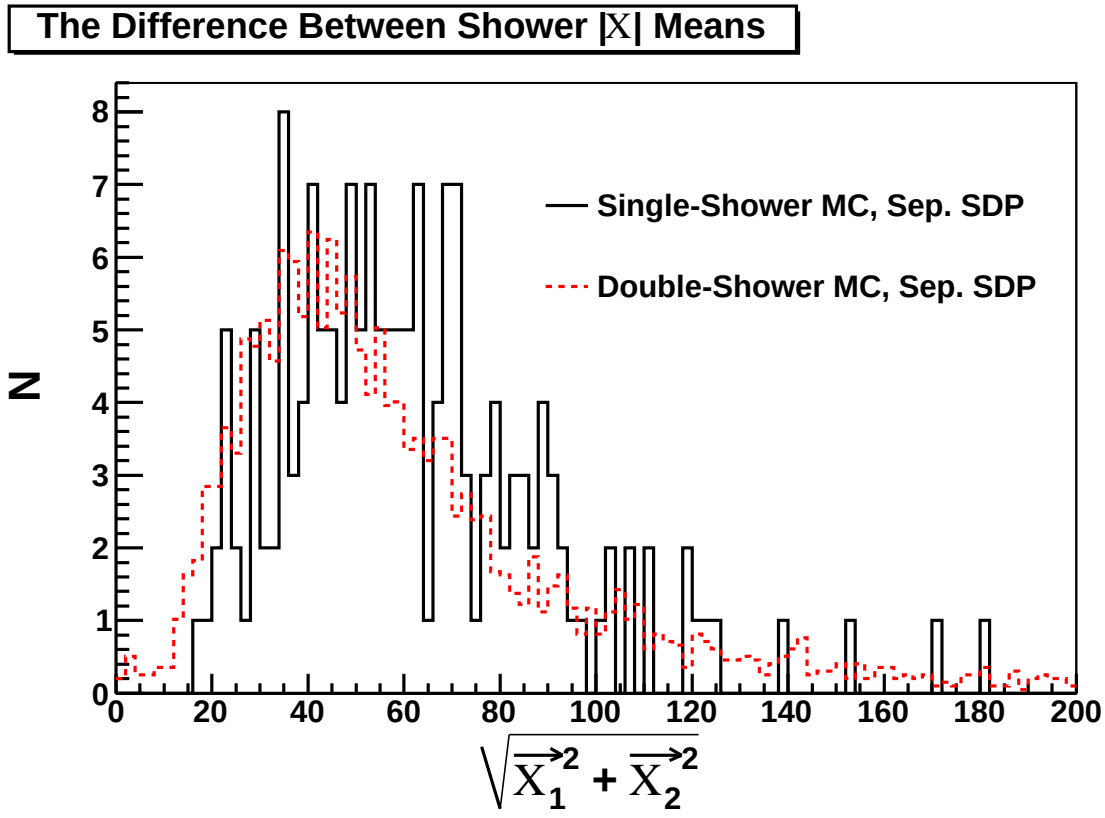

Figure F.21: The distribution of $|\vec{X}|$ for the difference between the means of cluster-1 and cluster-2 using individual, separate SDPs for double-shower Monte Carlo and single-shower Monte Carlo.

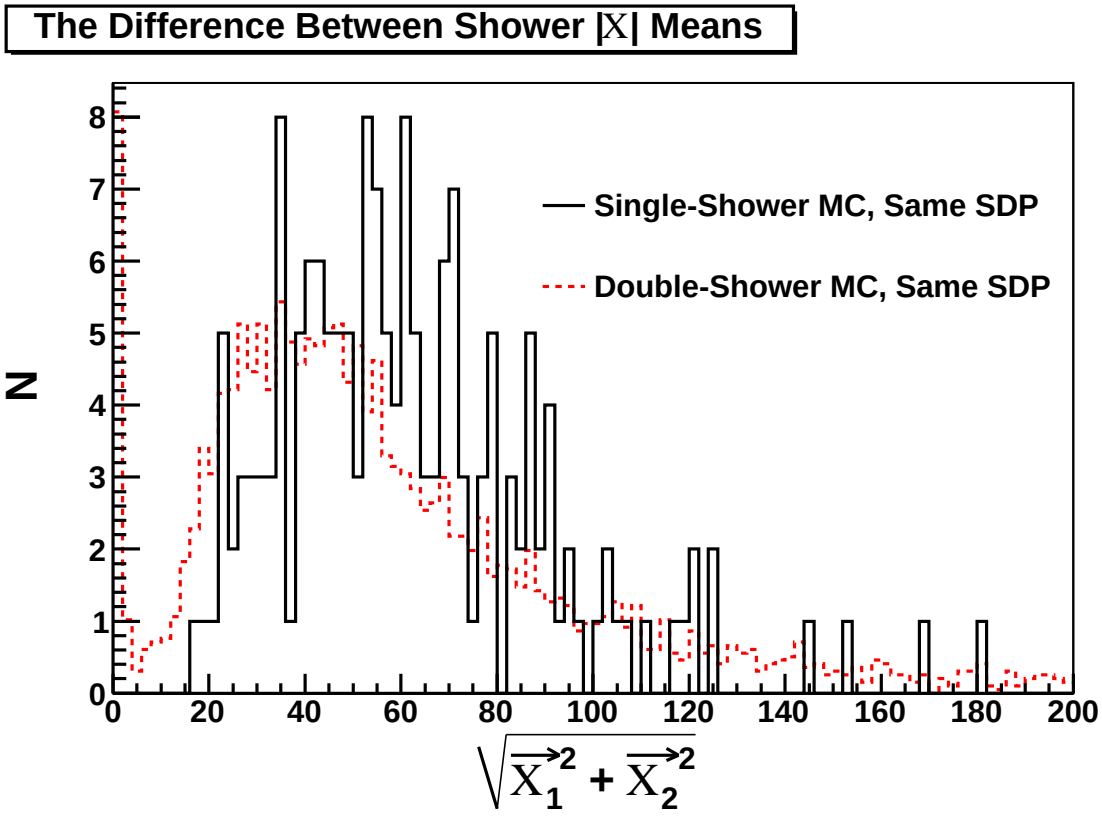

Figure F.22: The distribution of $|\vec{X}|$ for the difference between the means of cluster-1 and cluster-2 using the same SDP of cluster 1 for double-shower Monte Carlo and single-shower Monte Carlo.

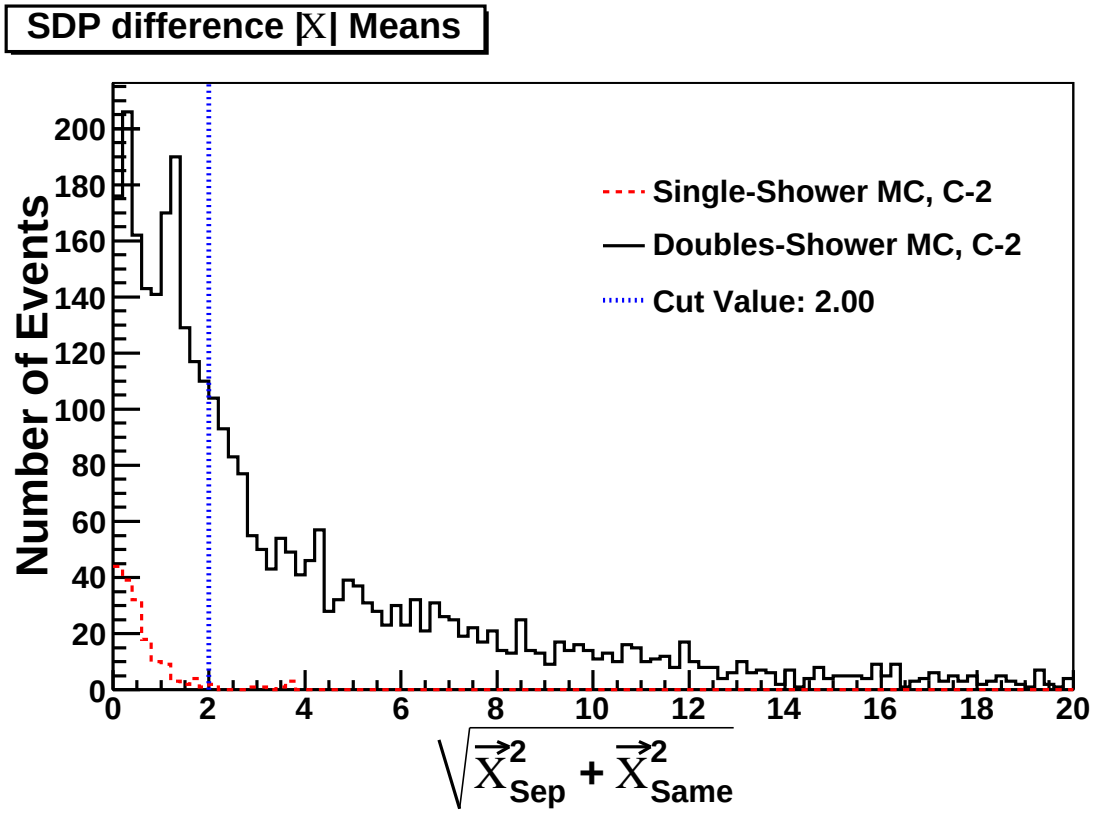

Figure F.23: The distribution of $|\vec{X}|$ for the difference between the means of cluster-2 using individual, separate SDPs and cluster-2 using the same SDP of cluster 1 for double-shower Monte Carlo and single-shower Monte Carlo.

REFERENCES

[1] R. U. Abbasi. *Alternative Methods to Finding Patterns in HiRes Stereo Data*. PhD diss., University of Utah, 2007.

[2] R. Abbasi et al. The FLASH thick-target experiment. *Nuclear Instruments and Methods in Physics Research A*, 597:37–40, Nov. 2008.

[3] R. U. Abbasi et al. First observation of the Greisen-Zatsepin-Kuzmin suppression. *Physical Review Letters*, 100, 2008.

[4] R. U. Abbasi et al. Search for Correlations between HiRes Stereo Events and Active Galactic Nuclei. *Astroparticle Physics*, 2009.

[5] J. Abraham et al. Correlation of the highest-energy cosmic rays with the positions of nearby active galactic nuclei. *Astropart. Phys.*, 29:188–204, Apr 2008.

[6] T. Z. Abu-Zayyad. *The energy spectrum of ultra high energy cosmic rays*. PhD diss., University of Utah, 2000.

[7] T. Abu-Zayyad et al. Atmospheric Monitoring at the High Resolution Fly's Eye: Data from the HiRes2 Flasher Array. In *International Cosmic Ray Conference*, volume 5 of *International Cosmic Ray Conference*, pages 361–+, 1997.

[8] T. Abu-Zayyad et al. Atmospheric Monitoring at the High Resolution Fly's Eye: Monitoring Data via the HiRes Laser/Lidar System. In *International Cosmic Ray Conference*, volume 5 of *International Cosmic Ray Conference*, pages 365–+, 1997.

[9] T. Abu-Zayyad et al. Radio Controlled Light Sources for Atmospheric Monitoring at HiRes. In *International Cosmic Ray Conference*, volume 5 of *International Cosmic Ray Conference*, pages 357–+, 1997.

[10] T. Abu-Zayyad et al. The HiRes Detector: Absolute Calibration and Alignment. In *International Cosmic Ray Conference*, volume 5 of *International Cosmic Ray Conference*, pages 333–+, 1997.

[11] T. Abu-Zayyad et al. Evidence for Changing of Cosmic Ray Composition between 10^{17} and 10^{18} eV from Multicomponent Measurements. *Phys. Rev. Lett.*, 84(19):4276–4279, May 2000.

[12] AGASA: Akeno Giant Air Shower Array. http://www-akeno.icrr.u-tokyo.ac.jp/AGASA. Accessed Mar. 4, 2011.

[13] Pierre Auger et al. Extensive cosmic-ray showers. *Rev. Mod. Phys.*, 11(3-4):288–291, Jul 1939.

[14] M. Ave. Energy Dependance of Air fluorescence Yield measured by AIRFLY. *ArXiv e-prints*, Nov 2007.

[15] R. M. Baltrusaitis et al. The Utah Fly's Eye Detector. *Nuclear Instruments and Methods in Physics Research A*, 240:410 – 428, 1985.

[16] K. Belov et al. Proton-air Inelastic Cross-Section Measurement at Ultra-High Energies by HiRes. In *International Cosmic Ray Conference*, volume 4 of *International Cosmic Ray Conference*, pages 687–690, 2008.

[17] J. W. Belz et al. Measurement of pressure dependant fluorescence yield of air: Calibration factor for UHECR detectors. *Astroparticle Physics*, 25:129–139, Mar 2006.

[18] D. R. Bergman et al. Can Experiments Studying Ultrahigh Energy Cosmic Rays Measure the Evolution of the Sources. http://arxiv.org/abs/astro-ph/0603797v1, 2006.

[19] D. Bird et al. The calibration of photomultiplier tubes in the hires experiment. In *In Proceedings of the Tokyo Workshop on Techniques for the study of Extremely High Energy Cosmic Rays*, pages 269–+, 1993.

[20] D. J. Bird et al. Coincident Observation of Air Showers by the HiRes Prototype and CASA/MIA Experiments. In *International Cosmic Ray Conference*, volume 4 of *International Cosmic Ray Conference*, pages 283–+, 1993.

[21] D. J. Bird et al. Evidence for correlated changes in the spectrum and composition of cosmic rays at extremely high energies. *Phys. Rev. Lett.*, 71(21):3401–3404, Nov 1993.

[22] D. J. Bird et al. The cosmic-ray energy spectrum observed by the Fly's Eye. *The Astrophysical Journal*, 424:491–502, Mar 1994.

[23] D. J. Bird et al. Study of broad-scale anisotropy of cosmic-ray arrival directions from to 10^{20} electron volts from fly's eye data. *The Astrophysical Journal*, 511(2):739–749, 1999.

[24] S. A. Blake. *A Search for Exotic Particles in the HiRes Data Set*. PhD diss., University of Utah, 2009.

[25] M. M. Block. Ultra-high Energy Predictions of proton-air Cross Sections from Accelerator Data. *Phys. Rev.*, D76:111503, 2007.

[26] K. Boothby et al. A New Measurement of Cosmic-Ray Composition at the Knee. *ApJL*, 491:L35+, Dec 1997.

[27] Alan Newton Bunner. *Cosmic Ray Detection by Atmospheric Fluorescence*. PhD diss., Cornell University, 1967.

[28] M. Bzowski et al. Density of neutral interstellar hydrogen at the termination shock from Ulysses pickup ion observations. *Astronomy and Astrophysics*, 491:7–19, Nov 2008.

[29] M. Cassidy et al. Casa-Blanca: A Large non-imaging Cerenkov Detector at Casa-Mia. In *International Cosmic Ray Conference*, volume 5 of *International Cosmic Ray Conference*, pages 189–+, 1997.

[30] R. W. Clay et al. Cloud Detection at the High Resolution Fly's Eye. In *International Cosmic Ray Conference*, volume 2 of *International Cosmic Ray Conference*, pages 649–+, 2001.

[31] Peter S. Cooper. Searching for modifications to the exponential radioactive decay law with the Cassini spacecraft. *Astroparticle Physics*, 31(4):267 – 269, 2009.

[32] Richard O. Duda and Peter E. Hart. Use of the Hough Transform to detect lines and curves in pictures. *Comm. ACM*, 15:11–15, 1972.

[33] S. Eidelman et al. Review of Particle Physics. *Physics Letters B*, 592:1+, 2004.

[34] J. W. Elbert. The HiRes filter and its effect on the aperture. In *In Proceedings of the Tokyo Workshop on Techniques for the study of Extremely High Energy Cosmic Rays*, pages 232–+, 1993.

[35] Thomas Erber. High-Energy Electromagnetic Conversion Processes in Intense Magnetic Fields. *Rev. Mod. Phys.*, 38(4):626–659, Oct 1966.

[36] T. K. Gaisser and A. M. Hillas. Reliability of the method of constant intensity cuts for reconstructing the average development of vertical showers. In *International Cosmic Ray Conference*, volume 8 of *International Cosmic Ray Confernece*, pages 353–357, 1978.

[37] Thomas K. Gaisser. *Cosmic Rays and Particle Physics*. Cambridge University Press, 1990.

[38] R. Glauber. High-energy scattering of protons by nuclei. *Nuclear Physics B*, 21, Jan 1970.

[39] K. Greisen. End to the cosmic-ray spectrum? *Phys. Rev. Lett.*, 16(17):748–750, Apr 1966.

[40] W. Hanlon. *The Energy Spectrum of Ultra High Energy Cosmic Rays Measured by the High Resolution Flys Eye Observatory in Stereoscopic Mode*. PhD diss., University of Utah, 2008.

[41] Andreas Haungs et al. Energy spectrum and mass composition of high-energy cosmic rays. *Rep. Prog. Phys.*, 66:1145–1206, 2003.

[42] D. Heck and T. Pierog. Extensive Air Shower Simulation with CORSIKA: A User's Guide.

[43] D. Heck and T. Pierog. Extensive Air Shower Simulation with CORSIKA: A User's Guide.

[44] D. Heck et al. CORSIKA: A Monte Carlo Code to Simulate Extensive Air Showers, 1998.

[45] Walter Heitler. *The Quantum Theory of Radiation*. Clarendon Press, 1936.

[46] C. T. Hill and D. N. Schramm. Ultrahigh-energy cosmic-ray spectrum. *Phys. Rev. D*, 31:564, 1984.

[47] G. Hughes. *First Observation of the Greisen-Zatsepin-Kuzmin Cutoff.* PhD diss., Rutgers University, 2009.

[48] Information Technology. Physics Analysis Workstation User's Guide, 1986.

[49] Vlad Izmodenov, Brian E. Wood, and Rosine Lallement. Hydrogen wall and heliosheath Ly α absorption toward nearby stars: Possible constraints on the heliospheric interface plasma flow. *J. Geophys. Res.*, 107(A10), 2002.

[50] Jere H. Jenkins et al. Evidence of correlations between nuclear decay rates and earth-sun distance. *Astroparticle Physics*, 32(1):42 – 46, 2009.

[51] J. R. Jokipii and J. Giacalone. Radial Streaming Anisotropies of Charged Particles Accelerated at the Solar Wind Termination Shock. *The Astrophysical Journal Letters*, 605(2):L145, 2004.

[52] Adolph S. Jursa and Air Force Geophysics lab Hanscom AFB MA. Handbook of Geophysics and the Space Environment, 1985.

[53] F. Kakimoto et al. A measurement of the air fluorescence yield. *Nuclear Instruments and Methods in Physics Research Section A: Accelerators, Spectrometers, Detectors and Associated Equipment*, 372(3):527 – 533, 1996.

[54] A. Karle et al. Design and performance of the angle integrating Cerenkov array AIROBICC. *Astroparticle Physics*, 3(4):321 – 347, 1995.

[55] K. Kasahara. Cosmos Monte Carlo simulation program, 1999.

[56] M. J. Kidd. *Properties of Extensive Air Showers Around* 10^{17} *eV.* PhD diss., University of Illinois at Urbana-Champaign, 1997.

[57] K. Kim, C. Song, and P. Sokolsky. Signatures of UHE Gamma Ray Flux for Fluorescence Detectors. In *International Cosmic Ray Conference*, volume 5 of *International Cosmic Ray Conference*, 1999.

[58] L. Landau and I. Pomeranchuk. Limits of applicability of the theory of bremsstrahlung electrons and pair production for high energies. *Doklady Akad. Nauk S.S.S.R.*, 92(4):735, 1953.

[59] J. Linsley. Structure of Large Air Shower at Depth 834 G cm^{-2} Applications. In *International Cosmic Ray Conference*, volume 12 of *International Cosmic Ray Conference*, pages 89–+, 1977.

[60] K. Lodders. Solar system abundances and condensation temperatures of the elements. *Astrophysical Journal*, 591:1220 – 1247, 2003.

[61] M. S. Longair. *High Energy Astrophysics*, volume 2. Cambridge University Press, 1992. Chapter 21.

[62] RealVNC Ltd. VNC: Virtual Network Computing.

[63] Mengzhi Luo. *Tropospheric Aerosol Study by Fly's Eye and Lidar Technique*. PhD diss., University of Utah, 1991.

[64] J. N. Matthews et al. The absolute calibration of HiRes-I, 1997.

[65] B. McBreen and C. J. Lambert. Interactions of high-energy ($E > 5 \times 10^{19}$ eV) photons in the Earth's magnetic field. *Phys. Rev. D*, 24(9):2536–2538, Nov 1981.

[66] A. B. Migdal. Bremsstrahlung and Pair Production in Condensed Media at High Energies. *Phys. Rev.*, 103(6):1811–1820, Sep 1956.

[67] C. Wright Mills. *The Promise*. Oxford University Press, 1959.

[68] H. R. Müller, G. Zank, and A. Lipatov. Selfconsistent hybrid simulations of the interaction of the heliosphere with the local interstellar medium. *J. Geophys. Res.*, 105(A12):27419–27438, 2000.

[69] J. R. Mumford et al. for the High Resolution Fly's Eye Collaboration. A Steerable Laser System for Atmospheric Monitoring at the High Resolution Fly's Eye. In *International Cosmic Ray Conference*, volume 5 of *International Cosmic Ray Conference*, pages 377–+, 1999.

[70] Nichia Corporation. Specifications for Nichia UV LED Model: NSHU590A.

[71] HAWC: High Altitude Water Cerenkov observatory. http://hawc.umd.edu. Accessed Mar. 4, 2011.

[72] Pierre Auger Observatory. http://www.auger.org. Accessed Mar. 4, 2011.

[73] The Milagro Gamma-Ray Observatory. http://www.lanl.gov/milagro/index.shtml. Accessed Mar. 4, 2011.

[74] A. R. Ong et al. Preliminary Results from the Chicago Air Shower Array. In *International Cosmic Ray Conference*, volume 2 of *International Cosmic Ray Conference*, pages 357–+, 1990.

[75] M. Opher, E. C. Stone, and T. I. Gombosi. The Orientation of the Local Interstellar Magnetic Field. *Science*, 316(5826):875–878, 2007.

[76] Merav Opher, Edward C. Stone, and Paulett C. Liewer. The Effects of a Local Interstellar Magnetic Field on Voyager 1 and 2 Observations. *The Astrophysical Journal Letters*, 640(1):L71, 2006.

[77] KEK High Energy Accelerator Research Organization. http://www.kek.jp/intra-e/index.html. Accessed Mar. 4, 2011.

[78] E. N. Parker. The Dynamical State of the Interstellar Gas and Field. *The Astrophysical Journal*, 145:811–+, September 1966.

[79] A. A. Penzias and R. W. Wilson. A Measurement of Excess Antenna Temperature at 4080 Mc/s. *Astrophysics Journal*, 142:419–421, Jul 1965.

[80] Philips Photonics. XP3062 Photomultiplier Tubes, 1994.

[81] R. E. Smith. ESPSX3 Ethernet Serial Port Server X 3.

[82] K. Rayleigh. On the problem of the random walk. *Nature*, 72, 1905.

[83] R. A. Riehle et al. Portable, Single-mirror, Air Fluorescence Detector. In *International Cosmic Ray Conference*, volume 2 of *International Cosmic Ray Conference*, pages 907–+, Jul 2003.

[84] B. Rossi. *High-Energy Particles*. Prentice-Hall, Inc., 1952.

[85] K. Scherer and H. J. Fahr. Breathing of heliospheric structures triggered by the solar-cycle activity. *Annales Geophysicae*, 21(6):1303–1313, 2003.

[86] S. J. Sciutto. Air Shower Simulations with the AIRES System, 1999.

[87] L. M. Scott et al. Test of the Telescope Array Low-energy Extension Tower Prototype. In *International Cosmic Ray Conference*, International Cosmic Ray Conference, 2009.

[88] J. A. Simpson. Elemental and isotopic composition of the galactic cosmic rays. *Ann. Rev. Nucl. Part. Sci.*, 33:323 – 381, 1983.

[89] Jeremy Smith. Personal communication.

[90] Jeremy Smith. Personal communication.

[91] Jeremy Smith. Personal communication.

[92] P. Sokolsky, John Belz, and the HiRes Collaboration. Composition of UHE Composition Measurements by Fly's Eye, HiRes-prototype/MIA and Stereo HiRes Experiments. In *International Cosmic Ray Conference*, volume 0 of *International Cosmic Ray Conference*, pages 101–104, 2005.

[93] Pierre Sokolsky. *Introduction to ultrahigh energy cosmic ray physics*. Addison-Wesley Publishing Company, Inc., 1989. 5:1.

[94] Pierre Sokolsky. *Introduction to ultrahigh energy cosmic ray physics*. Addison-Wesley Publishing Company, Inc., 1989. 3:4.

[95] Pierre Sokolsky. *Introduction to ultrahigh energy cosmic ray physics*. Addison-Wesley Publishing Company, Inc., 1989. 15:2.

[96] P. Sokolsky et al. Proposal for the U.S. Part of the Telescope Array (TA) Experiment, Including the TA Low Energy Extension (TALE), 2006.

[97] VERITAS: Very Energetic Radiation Imaging Telescope Array System. http://veritas.sao.arizona.edu/. Accessed Mar. 4, 2011.

[98] The HiRes Collaboration. Measurement of the cosmic ray energy spectrum and composition from 10^{17} to 10^{19} ev using hires prototype detector. In *International Cosmic Ray Conference*, volume 1 of *International Cosmic Ray Conference*, pages 358–+, 2001.

[99] The ROOT Team. ROOT: An Object-Oriented Data Analysis Framework, 2009.

[100] G. Thomson. The "test beam" of high-energy events, 2007.

[101] Gordon Thomson. Personal communications.

[102] T. Ueta et al. Detection of a Far-Infrared Bow Shock Nebula around R Hya: The First MIRIAD Results. *The Astrophysical Journal Letters*, 648(1):L39, 2006.

[103] L. Wiencke. Stereo Measurements of Cosmic Ray Events at the High Resolution Fly's Eye Prototype. In *International Cosmic Ray Conference*, volume 5 of *International Cosmic Ray Conference*, pages 381–+, 1999.

[104] L. R. Wiencke et al. Radio-controlled xenon flashers for atmospheric monitoring at the HiRes cosmic ray observatory. *Nuclear Instruments and Methods in Physics Research A*, 428:593–607, June 1999.

[105] G. T. Zatsepin and V. A. Kuz'min. Upper limit of the cosmic-ray spectrum. *Sov. Phys. JETP Lett.*, 4:78, 1966.